# Understanding past abrupt climatic change through the reduction of chronological uncertainty

Rebecca Kearney
St. Anne's College, University of Oxford

Thesis submitted for DPhil in Environmental Research (NERC DTP) – Archaeological Science

Michaelmas Term 2020

# Abstract

Across Europe, palaeoclimatic records dated to the Last Glacial-Interglacial Transition (LGIT; 16-8 cal. ka BP) provide evidence for several abrupt climatic oscillations on millennial and centennial-timescales. Understanding the spatial and temporal environmental response to these climatic events on a continental scale is important for providing insight into future climate scenarios. This relies on providing precise chronologies for palaeoenvironmental records, but issues with large dating uncertainties, and the practice of tuning/wiggle-matching different records together, has limited our ability to test for (a)synchroneity for abrupt climate transitions.

In this study, the temporal and spatial complexity of LGIT climatic events, specifically, the Younger Dryas (YD) and earliest Holocene (EH) were investigated. Several of the most precisely dated pollen records were selected, spanning from northern to southern Europe. These sites were chosen using selection criteria that required independent chronologies based on radiocarbon dating and tephrochronology. To broaden the geographic range, a cryptotephra investigation was also undertaken on two palaeoenvironmental records from Romania (Lake Lia and Lake Brazi).

Using Bayesian chronological modelling, each site's ages and the widespread tephra layers were remodelled. Pollen records were also re-investigated using the statistical methods of Principal Curve analysis to assist in identifying abrupt climatic transitions. The INTIMATE Integration tool was utilised to enable quantified comparisons between these terrestrial sites and the high-resolution Greenland ice core records.

The results from the Romanian cryptotephra investigation highlight the importance of this region to expand tephrostratigraphic frameworks across Europe, the Mediterranean and Anatolia. The identification of ultra-distal tephra layers allowed for a broader investigation into the timing of LGIT events.

This study showed that even with the most precisely dated sites and, despite the methodological approaches employed here, identifying a clear time-transgression for the YD and centennial-scale events within the EH remains difficult due to chronological uncertainties. Issues with proxy and dating resolutions currently limit the chronological approach undertaken. Nonetheless, using widespread tephra layers and statistical methods on proxy records can help to evaluate the potential asynchrony of abrupt climate transitions and the possible climatic drivers.

Overall, this study highlights the need to provide robust chronologies by undertaking high-resolution radiocarbon dating and proxy reconstruction, supplemented by tephrochronology. By employing these approaches with Bayesian age modelling, the temporal and spatial response to abrupt climatic shifts can be further explored.

# Acknowledgements

There are many people who have helped me throughout my DPhil journey over the past four years. I would especially like to thank Prof Christopher Bronk Ramsey, Dr Richard Staff and Dr Paul Albert for being fantastic supervisors. Your help, guidance and support throughout this part of my research career has been instrumental in allowing me to submit this research.

I would also like to thank Dr Eniko Magyari, Dr Daniel Veres and Dr Ilona Pál for allowing me to work on providing a cryptotephra record for the Romanian sites of Lake Lia and Lake Brazi. I never would of dreamed of the exciting cryptotephra results that came from those sites! I feel privileged to highlight the importance of the region for future cryptotephra studies. I especially thank Eniko and Ilona for teaching me statistical analysis to further understand pollen records.

My thanks to Dr Ian Matthews and Dr Ashley Abrook for teaching me the ways of Principal Curve analysis. This technique was highly useful for my thesis, so thank you for giving me the time and energy in answering my many questions about it. For those who have helped me in other ways throughout my thesis, I would like to thank Prof Christine Lane (Ioannina tephra samples), Dr Victoria Smith (EPMA analysis), Dr Victoria Cullen (teaching tephra lab techniques).

In particular, I would like to thank the following people who shared with me their published and unpublished data used throughout this thesis. Prof John Birks and Prof Hilary Birks (Kråkenes), Prof Kevin Edwards and Prof Graeme Whittington (Crudale Meadow), Prof Svante Björck (Lake Madtjärn), Prof Barbara Wohlfarth (Hässeldala port), Dr Pim de Klerk (Endinger Bruch), Dr Florin Ott and Dr Michał Słowiński (Lake Czechowskie), Dr Dorota Nalepka and Dr Rupert Housley (Węgliny), Prof Christine Lane and Dr Stefan Engels (Lake Hämelsee), Prof Andrew Lotter (Rotsee and Soppensee), Dr Walter Finsinger (Lago di Piccolo Avigliana), Dr Maja Andrič (Bled), Dr Eniko Magyari and Dr Ilona Pál (Lake Lia and Brazi).

There are many I would like to thank who kept me sane throughout these past four years. Thank you to Dr Rebecca Smith and Dr Danielle McLean who are the best tephra lab buddies a DPhil student could ask for. Thank you to Dr Cyndi Goh (and Oscar the dog) and Dr Mimi Harrison for accompany on many, many bike cake rides. And to many, many others.

I would like to thank my family for their unwavering support and love throughout this research. To my Dad who has supported me throughout the last ten years of my university life, I could not of done this without you. You should receive an honourable degree in Quaternary Science. To my brothers, Nick and Phil, thank you so much for your support. I hope this ‘door stopper’ shows you I do more things than just look at “mud”.

And finally, to my Mum, who saw me begin my DPhil but never saw me finish. Thank you for giving me the tenacity to finish this. Without the things you taught me and the love you showed, this research would never have existed. I hope I did you proud.

*This thesis is dedicated to my Mum,*
Yvonne Kearney

# Table of Contents


**Abstract** i

**Acknowledgements** ii

**Table of contents** iv

**Lift of Figures** xii

**List of Tables** xvi

**List of Equations** xix

**Chapter 1. Introduction** 1

1.1 Research rationale 5

1.2 Project outline and hypothesis' 8

1.3 Aims and objectives 9

1.4 Conventions adopted 10

1.5 Thesis structure 11

**Chapter 2. Millennial and centennial-scale abrupt climatic events of the Last Glacial-Interglacial transition** 12

2.1 Terminology and the INTIMATE approach – events stratigraphy and protocols 12

2.2 Climatic and environmental response to millennial and centennial scale abrupt climatic events 17

2.2.1 The Younger Dryas 19

2.2.2 Centennial oscillation in the earliest Holocene 23

2.3 Mechanisms of abrupt climate for the Younger Dryas and Early Holocene oscillations 24

2.3.1 Oceanic circulation 25

2.3.2 Solar forcing 27

2.4 The timing of abrupt climatic transitions across Europe 29

2.4.1 Providing chronologies - Radiocarbon dating 29

2.4.1.1 Calibration of radiocarbon ages 30

2.4.1.2 Bayesian age modelling 30

2.4.1.3 Limitations of radiocarbon dating 32

2.4.2 The Younger Dryas onset and termination across Europe 33

2.4.3 The timing and characteristics of Early Holocene oscillations across Europe 36
2.5 Integrating records 40
2.5.1 Tephrochronology 40
2.5.1.1 Limitations of tephrochronology 44
2.5.1.2 Tephra in lacustrine sediments 46
2.5.1.3 An ideal tephra layers for correlating sedimentary archives 47
2.5.1.4 Tephrochronology in the LGIT 48
2.5.1.5 Potential for tephrostratigraphy in Romania 55
2.5.2 The INTIMATE database – Integration tool 58
2.6 Chapter summary 58

**Chapter 3. Methodology 59**
3.1 Site selection criteria 59
3.1.1 Tephrochronology of Romania 59
3.1.2 Terrestrial records 60
3.2 Palaeoenvironmental methods – pollen analysis 61
3.2.1 Data collection and presentation 62
3.2.2 Pollen diagram zonation 64
3.2.3 Statistical analysis 65
3.2.4 Abrupt event definition and identification in the pollen record 71
3.3 Tephrochronology 74
3.3.2 Sediment sampling 74
3.3.3 Cryptotephra sample preparation 75
3.3.4 Geochemical analysis 79
3.3.4.1 Sample preparation 79
3.3.4.2 Major and minor element composition analysis 80
3.3.4.3 Trace element composition analysis 81
3.4 Age-depth modelling 82
3.5 INTIMATE database – the Integration tool 86

**Chapter 4. Study sites** **88**
4.1 Sites selected for tephrochronology for Romania 88
4.1.1 Lake Brazi 89
4.1.2 Lake Lia 90
4.2 Terrestrial sites selected 90
4.2.1 Kråkenes, Norway (KRA) 91
4.2.2 Crudal Meadow, Scotland (CRU) 91
4.2.3 Lake Madtjärn, Sweden (MAD) 96
4.2.4 Hässeldala port, Sweden (HAS) 97
4.2.5 Endinger Bruch, Germany (HBG) 97
4.2.6 Lake Czechowskie, Poland (JC) 98
4.2.7 Lake Hämelsee, Germany (HAM) 99
4.2.8 Węgliny, Poland (WE) 100
4.2.9 Soppensee, Switzerland (SOP) 100
4.2.10 Rotsee, Switzerland (RO) 101
4.2.11 Lago Piccolo di Avigliana, Italy (LPA) 102
4.2.12 Lake Bled, Slovenia (BLE) 102
4.2.13 Lake Brazi, Romania (TDB) 103
4.2.14 Lake Lia, Romania (LIA) 103

**Chapter 5. The results of tephrostratigraphy investigations of the Sediments of Lake Lia and Lake Brazi (Romania)** **105**
5.1 Tephrostratigraphy and glass geochemistry of Lake Lia 106
5.2 Tephrostratigraphy and glass geochemistry of Lake Brazi 126

**Chapter 6. Discussion of the tephrostratigraphy and tephrochronology of Lake Lia and Lake Brazi** **140**
6.1 Anatolian province – unknown eruption 140
6.2 Central Mediterranean derived cryptotephra 146
6.2.1 LIA_796/ Campi Flegrei caldera (Neapolitan Yellow Tuff) 147
6.2.2 LAD_612-613/Ischia (unknown eruption) 152
6.2.3 LIA_613/Pantelleria (unknown eruption) 153
6.2.4 TDB_564/Lipari (Aeolian Islands) 155
6.3 Icelandic tephra deposits 160

6.3.1 LIA_603/TDB_540-541/ Askja-S tephra 160
6.3.2 Katla-type tephra 163
6.3.3 Icelandic unknowns 168
6.4 Uncorrelated tephras 170
6.5 Identifying primary and secondary cryptotephra deposits 172
6.6 Chronological modelling 174
6.7 Expansion of the tephrostratigraphic framework 176
6.8 Synchronising palaeoenvironmental records 179

**Chapter 7. Chronological and palynological statistical analysis results from across Europe 181**
7.1 Results of refined chronological modelling 181
7.1.1 New tephra age estimates 182
7.1.1.1 Neapolitan Yellow Tuff (NYT) 183
7.1.1.2 The Borrobol and Pennifiler tephras 184
7.1.1.3 Laacher See Tephra (LST) 184
7.1.1.4 Late Glacial Lipari tephra (LG Lipari) 185
7.1.1.5 Vedde Asha (VA) 185
7.1.1.6 Pomici Principali tephra (PP) 186
7.1.1.7 Hässeldalen tephra 186
7.1.1.8 Ulmener Maar tephra (UMT) 186
7.1.1.9 Askja-S tephra 187
7.1.10 Saksunvartn Ash (Saks.) 188
7.1.2 Age-modelling results for sites 189
7.1.2.1 Kråkenes, Norway 189
7.1.2.2 Crudale Meadow, Scotland 188
7.1.2.3 Lake Madtjärn, Sweden 193
7.1.2.4 Hässeldala port, Sweden 194
7.1.2.5 Endinger Bruch, Germany 194
7.1.2.6 Lake Czechowskie, Poland 194
7.1.2.7 Lake Hämelsee, Germany 195
7.1.2.8 Węgliny, Poland 195
7.1.2.9 Soppensee, Switzerland 196
7.1.2.10 Rotsee, Switzerland 196

7.1.2.11 Lago Piccolo di Avigliana, Italy 196
7.1.2.12 Lake Bled, Slovenia 197
7.1.2.13 Lake Brazi, Romania 197
7.2 Palynological results 198
7.2.1 Kråkenes, Norway 199
7.2.1.1 Statistical analysis 200
7.2.1.2 Palaeoclimatic and palaeoenvironmental Interpretation 206
7.2.2 Crudale Meadow, Scotland 208
7.2.2.1 Statistical analysis 209
7.2.2.2 Palaeoclimatic and palaeoenvironmental Interpretation 214
7.2.3 Lake Madtjärn, Sweden 216
7.2.3.1 Statistical analysis 217
7.2.3.2 Palaeoclimatic and palaeoenvironmental Interpretation 219
7.2.4 Hässeldala port, Sweden 223
7.2.4.1 Statistical analysis 224
7.2.4.2 Palaeoclimatic and palaeoenvironmental Interpretation 227
7.2.5 Endinger Bruch, Germany 231
7.2.5.1 Statistical analysis 233
7.2.5.2 Palaeoclimatic and palaeoenvironmental Interpretation 236
7.2.6 Lake Czechowskie, Poland 238
7.2.6.1 Statistical analysis 241
7.2.6.2 Palaeoclimatic and palaeoenvironmental Interpretation 243
7.2.7 Lake Hämelsee, Germany 246
7.2.7.1 Statistical analysis 247
7.2.7.2 Palaeoclimatic and palaeoenvironmental Interpretation 252
7.2.8 Węgliny, Poland 255
7.2.8.1 Statistical analysis 257

7.2.8.2 Palaeoclimatic and palaeoenvironmental Interpretation 260
7.2.9 Soppensee, Switzerland 262
7.2.9.1 Statistical analysis 264
7.2.10 Rotsee, Switzerland 267
7.2.10.1 Statistical analysis 270
7.2.10.2 Palaeoclimatic and palaeoenvironmental Interpretation of Soppensee and Rotsee 272
7.2.11 Lago Piccolo di Avigliana, Italy 276
7.2.11.1 Statistical analysis 278
7.2.11.2 Palaeoclimatic and palaeoenvironmental Interpretation 281
7.2.12 Lake Bled, Slovenia 283
7.2.12.1 Statistical analysis 285
7.2.12.2 Palaeoclimatic and palaeoenvironmental Interpretation 287
7.2.13 Lake Brazi, Romania 290
7.2.13.1 Statistical analysis 293
7.2.13.2 Palaeoclimatic and palaeoenvironmental Interpretation 296
7.3 Chapter summary 298

**Chapter 8. The timing of millennial-scale vegetation response: the onset and termination of the Younger Dryas 300**
8.1 Identification of the Younger Dryas across Europe 301
8.1.1 Kråkenes, Norway 301
8.1.2 Crudale Meadow 306
8.1.3 Lake Madtjärn, Sweden 308
8.1.4 Hässeldala port, Sweden 309
8.1.5 Endinger Bruch, Germany 310
8.1.6 Lake Czechowskie, Poland 311
8.1.7 Lake Hämelsee, Germany 312
8.1.8 Węgliny, Poland 313
8.1.9 Soppensee and Rotsee, Switzerland 314

8.1.10 Lago Piccolo di Avigliana, Italy 315
8.1.11 Lake Bled, Slovenia 316
8.1.12 Lake Brazi, Romania 317
8.2 The magnitude of Younger Dryas vegetation response
Across Europe 318
8.2.1 The Younger Dryas onset 318
8.2.2 The Younger Dryas termination 322
8.3 Timing of the Younger Dryas vegetation response 324
8.3.1 Younger Dryas onset 324
8.3.2 Younger Dryas termination 332
8.4 Correlation to the Greenland Ice Cores 338
8.5 Proposed climatic driver 340
8.6 Evaluating climatic synchronicity across Europe 344
8.7 Chapter summary 345

**Chapter 9 – The timing of centennial-scale vegetation response(s) in the earliest Holocene 347**
9.4 Identification of vegetation revertences across Europe 348
9.4.1 Kråkenes, Norway 353
9.4.2 Crudale Meadow, Scotland 356
9.4.3 Lake Madtjärn, Sweden 357
9.4.4 Hässeldala port, Sweden 358
9.4.5 Endinger Bruch, Germany 360
9.4.6 Lake Czechowskie, Poland 362
9.4.7 Lake Hämelsee, Germany 363
9.4.8 Węgliny, Poland 364
9.4.9 Soppensee, Switzerland 365
9.1.10 Rotsee, Switzerland 366
9.1.11Lago Piccolo di Avigliana, Italy 368
9.1.12 Lake Bled, Slovenia 369
9.1.13 Lake Brazi, Romania 370
9.5 The magnitude of EH vegetation response across Europe 371
9.6 Timing of proposed vegetation revertences 375
9.6.1 The onset of Early Holocene cooling events 379

9.6.2 Termination of Early Holocene cooling events 381
9.6.3 Additional younger Early Holocene cooling events 382
9.7 Correlation to the Greenland ice-core record 384
9.8 Proposed climatic drivers 388
9.9 Evaluating climatic synchronicity across Europe 391
9.9.1 Identifying the classical PBO of Björck et al. (1996, 1997) 394
9.10 Chapter summary 395

**Chapter 10. Synthesis and conclusions 397**
10.1 Cryptotephra investigations in Romania – summary of findings 397
10.2 The (a)synchronicity of millennial and centennial-scale climatic oscillations across Europe 398
10.2.1 The Younger Dryas 399
10.2.2 The earliest Holocene oscillations 400
10.3 Synthesis and future research 401

**References 405**

**Appendix 1 – List of abbreviations 452**
**Appendix 2 – Tephra geochemistry data 453**
**Appendix 3 – Chronological problems of Lake Lia 492**
**Appendix 4 – Radiocarbon dates for all sites 493**
**Appendix 5 – OxCal coding for age models 511**
**Appendix 6 – This study's publication on the Askja-S tephra 532**

**Figures**

**Chapter 1 - Introduction**

Figure 1.1 The NGRIP oxygen stable isotope and event stratigraphy record of the LGIT 2

**Chapter 2 - Millennial and centennial-scale abrupt events of the Last Glacial-Interglacial transition**

Figure 2.1 The different Greenland ice-core records and their climatic reconstruction of the LGIT 14
Figure 2.2 The LGIT vegetation and climate changes across the different regions in Europe 22
Figure 2.3 Schematic of the Atlantic Meridional Overturning circulation and North Atlantic Deep Water 26
Figure 2.4 The different modes of the North Atlantic Oscillation 28
Figure 2.5 LGIT calibration curve and precision and accuracy in dating 31
Figure 2.6 Timings of Early Holocene cooling events identified at sites across Europe 38
Figure 2.7 Schematic of tephra deposition 41
Figure 2.8 The possible different tephra shard concentration profiles in lacustrine sediment archive 47
Figure 2.9 Map of volcanic centres active during the Late Glacial and Early Holocene period 56
Figure 2.10 Schematic of how different palaeoclimatic records can be successfully integrated together 58

**Chapter 3 - Methodology**

Figure 3.1 Diagram of the taphonomic process that need to be considered when undertaking pollen analysis 62
Figure 3.2 Schematic to interpreting PCA bi-plots 68
Figure 3.3 Diagram of Principal Component Analysis and Principal Curve 69
Figure 3.4 Flow chart for abrupt event identification 73
Figure 3.5 Illustration of the cryptotephra sampling process 76
Figure 3.6 Diagram of the cryptotephra laboratory methods 78
Figure 3.7 Schematic of glass shard morphologies 79

Figure 3.8 Images of the equipment used for picking individual tephra shards 81
Figure 3.9 The OxCal output for the Hässeldalen and Askja-S tephras 84
Figure 3.10 Schematic of the Bayesian age model run for refining tephra ages 85
Figure 3.11 INTIMATE integration tool interface 87

**Chapter 4 - Selected study sites information**

Figure 4.1 Maps showing the location of Lake Brazi and Lake Lia 89
Figure 4.2 Map showing selected sites with their relevant tephra layers 96

**Chapter 5 - The results of tephrostratigraphy investigations of the Sediments of Lake Lia and Lake Brazi (Romania)**

Figure 5.1 Glass shard concentration profile for Lake Lia 110
Figure 5.2 TAS plot for glass composition in Lake Lia 111
Figure 5.3 Harker diagram of major element glass geochemistry for Lake Lia 112
Figure 5.4 Trace element profile for Lake Lia normalised to primitive mantle 114
Figure 5.5 Trace element bi-plots of glasses for Lake Lia and Lake Brazi 115
Figure 5.6 Glass shard concentration profile for Lake Brazi 126
Figure 5.7 TAS plot for glass composition in Lake Brazi 130
Figure 5.8 Harker diagram of major element glass geochemistry for Lake Brazi 131
Figure 5.9 Trace element profile for Lake Brazi normalised to primitive mantle 133

**Chapter 6 – Discussion of the tephrostratigraphy and tephrochronology of Lake Lia and Lake Brazi**

Figure 6.1 Major element bi-plots of high silica glasses from Lake Lia and Brazi 141
Figure 6.2 Trace element bi-plots for Lake Lia and Lake Brazi 144
Figure 6.3 Major element bi-plots of glass shard from Lake Lia with comparison to the Neapolitan Yellow Tuff, Ischia and Pantelleria 148
Figure 6.4 Trace element bi-plots of LIA_796 to the Neapolitan Yellow Tuff 149
Figure 6.5 Dispersal maps of tephra from the Mediterranean region 151
Figure 6.6 Peralkaline classification for LIA_613 154
Figure 6.7 Major and trace element bi-plots of proximal and distal comparisons of Lake Lia and Brazi to eruptions from Lipari 156
Figure 6.8 Major element bi-plots of Lia and Brazi to Icelandic volcanic eruptions 161
Figure 6.9 Dispersal maps of Icelandic tephras 163

Figure 6.10 Trace element comparison to LIA_631 and TDB_556 to Icelandic tephras 164
Figure 6.11 Major element bi-plots to uncorrelated tephra of TDB_541 and LIA_633 171
Figure 6.11 Age-depth model for Lake Lia 175

**Chapter 7 - Chronological and palynological statistical analysis results from across Europe**

Figure 7.1 Schematic of the tephra layer age estimates from this study 183
Figure 7.2 Presentation of age estimates for Hässeldalen and Askja-S tephra 187
Figure 7.3 Age model results for each site involved in the large age model 190
Figure 7.4 Pollen percentage record of key taxa from Kråkenes 201
Figure 7.5 Pollen accumulation rate record of key taxa from Kråkenes 202
Figure 7.6 Ordination diagram of the PCA results from Kråkenes during the LGIT 204
Figure 7.7 The statistical results for the pollen percentage data from Kråkenes 205
Figure 7.8 Pollen percentage record of key taxa from Crudale Meadow 210
Figure 7.9 Pollen accumulation rate record of key taxa from Crudale Meadow 211
Figure 7.10 Ordination diagram of the PCA results from Crudale Meadow 212
Figure 7.11 The statistical results for the pollen percentage data from Crudale 213
Figure 7.12 Pollen percentage record of key taxa from Lake Madtjärn 217
Figure 7.13 Ordination diagram of the PCA results from Lake Madtjärn 218
Figure 7.14 The statistical results for the pollen percentage data from Lake Madtjärn 220
Figure 7.15 Pollen percentage record of key taxa from Hässeldala port 225
Figure 7.16 Pollen accumulation rate record of key taxa from Hässeldala 226
Figure 7.17 Ordination diagram of the PCA results from Hässeldala port 227
Figure 7.18 The statistical results for the pollen percentage data from Hässeldala 228
Figure 7.19 Pollen percentage record of key taxa from Endinger Bruch 232
Figure 7.20 Ordination diagram of the PCA results from Endinger Bruch 234
Figure 7.21 The statistical results for the pollen percentage data from Endinger 235
Figure 7.22 Pollen percentage record of key taxa from Lake Czechowskie 239
Figure 7.23 Pollen accumulation rate record of key taxa from Lake Czechowskie 240
Figure 7.24 Ordination diagram of the PCA results from Lake Czechowskie 242
Figure 7.25 The statistical results for the pollen percentage data from Czechowskie 243
Figure 7.26 Pollen percentage record of key taxa from Lake Hämelsee 248
Figure 7.27 Pollen accumulation rate record of key taxa from Lake Hämelsee 249
Figure 7.28 Ordination diagram of the PCA results from Lake Hämelsee 250

Figure 7.29 The statistical results for the pollen percentage data from Hämelsee 251
Figure 7.30 Pollen percentage record of key taxa from Węgliny 256
Figure 7.31 Ordination diagram of the PCA results from Węgliny 258
Figure 7.32 The statistical results for the pollen percentage data from Węgliny 259
Figure 7.33 Pollen percentage record of key taxa from Soppensee 263
Figure 7.34 Pollen accumulation rate record of key taxa from Soppensee 264
Figure 7.35 Ordination diagram of the PCA results from Soppensee 266
Figure 7.36 The statistical results for the pollen percentage data from Soppensee 267
Figure 7.37 Pollen percentage record of key taxa from Rotsee 269
Figure 7.38 Pollen accumulation rate record of key taxa from Rotsee 270
Figure 7.39 Ordination diagram of the PCA results from Rotsee 271
Figure 7.40 The statistical results for the pollen percentage data from Rotsee 273
Figure 7.41 Pollen percentage record of key taxa from Lago Piccolo di Avigliana 277
Figure 7.42 Ordination diagram of the PCA results from Lago Piccolo di Avigliana 279
Figure 7.43 The statistical results for the pollen percentage data from LPA 280
Figure 7.44 Pollen percentage record of key taxa from Lake Bled 284
Figure 7.45 Pollen accumulation rate record of key taxa from Lake Bled 285
Figure 7.46 Ordination diagram of the PCA results from Lake Bled 286
Figure 7.47 The statistical results for the pollen percentage data from Lake Bled 288
Figure 7.48 Pollen percentage record of key taxa from Lake Brazi 291
Figure 7.49 Pollen accumulation rate record of key taxa from Lake Brazi 292
Figure 7.50 Ordination diagram of the PCA results from Lake Brazi 294
Figure 7.51 The statistical results for the pollen percentage data from Lake Brazi 295

**Chapter 8 - The timing of millennial-scale vegetation response: the onset and termination of the Younger Dryas**

Figure 8.1 Comparisons of Principal Curve from sites across Europe 303
Figure 8.2 Map of percentage change for the onset of the Younger Dryas 319
Figure 8.3 Map of percentage change for the termination of the Younger Dryas 322
Figure 8.4 Schematic of the ages for the onset and termination of the Younger Dryas across Europe 325
Figure 8.5 Individual age model results for each site for the Younger Dryas 329
Figure 8.6 Map of the climatic drivers for the Younger Dryas 342

**Chapter 9 – The timing of centennial-scale vegetation response(s) in the earliest Holocene**

Figure 9.1 Comparisons of Principal Curve from sites across Europe 350

Figure 9.2 Map of percentage change for the vegetation events during the earliest Holocene 372

Figure 9.3 The timings of vegetation revertences in the earliest Holocene across Europe 377

**Appendix 3. Chronological problems of Lake Lia**

Figure A3.1 Pollen record for Lia highlighting the chronological problems 492

**Tables**

**Chapter 2 - Millennial and centennial-scale abrupt events of the Last Glacial-Interglacial transition**

Table 2.1 Further information on proxies discussed in this thesis 20

Table 2.2 The limitations of radiocarbon dating in lacustrine archives 32

Table 2.3 Laboratory protocols for radiocarbon dating 33

Table 2.4 List of tephras and volcanic eruptions during LGIT 51

**Chapter 3 - Methodology**

Table 3.1 Criteria for defining vegetation revertences in pollen records 74

**Chapter 4 - Selected study sites information**

Table 4.1 List of selected sites and their relevant background information 93

Table 4.2 Information on the sites and their relevant cores used in the thesis 95

**Chapter 5 - The results of tephrostratigraphy investigations of the Sediments of Lake Lia and Lake Brazi (Romania)**

Table 5.1 Representative grain specific major element data for Lake Lia 107

Table 5.2 Representative grain specific trace element data for Lake Lia 109

Table 5.3 Representative grain specific major element data for Lake Brazi 127

Table 5.4 Representative grain specific trace element data for Lake Brazi 128

**Chapter 6 - Discussion of the tephrostratigraphy and tephrochronology of Lake Lia and Lake Brazi**

Table 6.1 List of eruptions from Lipari 157
Table 6.2 Table of the depths, ages and tephra layers identified in Lake Lia and Brazi 166

**Chapter 7 - Chronological and palynological statistical analysis results from across Europe**

Table 7.1 The best age estimates for selected tephra layers 182
Table 7.2 The local pollen assemblage zones for Kråkenes 199
Table 7.3 Detrended correspondence analysis results for Kråkenes 200
Table 7.4 Vegtation oscillations identified in the PrC for Kråkenes 204
Table 7.5 The local pollen assemblage zones for Crudale Meadow 208
Table 7.6 Detrended correspondence analysis results for Crudale Meadow 209
Table 7.7 Vegtation oscillations identified in the PrC for Crudale Meadow 212
Table 7.8 The local pollen assemblage zones for Lake Madtjärn 216
Table 7.9 Detrended correspondence analysis results of Lake Madtjärn 218
Table 7.10 Vegtation oscillations identified in the PrC for Lake Madtjärn 219
Table 7.11 The local pollen assemblage zones for Hässeldala port 223
Table 7.12 Detrended correspondence analysis results for Hässeldala port 224
Table 7.13 Vegtation oscillations identified in the PrC for Hässeldala port 227
Table 7.14 The local pollen assemblage zones for Endinger Bruch 231
Table 7.15 Detrended correspondence analysis results for Endinger Bruch 233
Table 7.16 Vegtation oscillations identified in the PrC for Endinger Bruch 234
Table 7.17 The local pollen assemblage zones for Lake Czechowskie 238
Table 7.18 Detrended correspondence analysis results for Lake Czechowskie 241
Table 7.19 Vegtation oscillations identified in the PrC for Lake Czechowskie 242
Table 7.20 The local pollen assemblage zones for Lake Hämelsee 246
Table 7.21 Detrended correspondence analysis results for Lake Hämelsee 247
Table 7.22 Vegtation oscillations identified in the PrC for Lake Hämelsee 252
Table 7.23 The local pollen assemblage zones for Węgliny 255
Table 7.24 Detrended correspondence analysis results for Węgliny 257
Table 7.25 Vegtation oscillations identified in the PrC for Węgliny 258
Table 7.26 The local pollen assemblage zones for Soppensee 262

Table 7.27 Detrended correspondence analysis results for Soppensee 265
Table 7.28 Vegtation oscillations identified in the PrC for Soppensee 266
Table 7.29 The local pollen assemblage zones for Rotsee 268
Table 7.30 Detrended correspondence analysis results for Rotsee 271
Table 7.31 Vegtation oscillations identified in the PrC for Rotsee 272
Table 7.32 The local pollen assemblage zones for Lago Piccolo di Avigliana 276
Table 7.33 Detrended correspondence analysis results for LPA 278
Table 7.34 Vegtation oscillations identified in PrC for LPA 279
Table 7.35 The local pollen assemblage zones for Lake Bled 283
Table 7.36 Detrended correspondence analysis results for Lake Bled 286
Table 7.37 Vegtation oscillations identified in the PrC for Lake Bled 287
Table 7.38 The local pollen assemblage zones for Lake Brazi 290
Table 7.39 Detrended correspondence analysis results for Lake Brazi 293
Table 7.40 Vegtation oscillations identified in the PrC for Lake Brazi 294

**Chapter 8 - The timing of millennial-scale vegetation response: the onset and termination of the Younger Dryas**

Table 8.1 Summary of modelled ages for the onset of the Younger Dryas 324
Table 8.2 Summary of modelled ages for the termination of the Younger Dryas 333

**Chapter 9 - The timing of centennial-scale vegetation response(s) in the earliest Holocene**

Table 9.1 The criteria for establishing a vegetation revertence at sites across Europe 349
Table 9.2 Modelled ages for the onset and termination of vegetation revertences 376

**Appendix 2 – Tephra geochemistry data**

Table A2.1 Lake Lia tephra major geochemistry non-normalised 453
Table A2.2 Lake Brazi tephra major geochemistry non-normalised 462
Table A2.3 Secondary standard of StHS6/80-G 469
Table A2.4 Secondary standard of ATHOG 474
Table A2.5 Secondary standard of GOR132 478
Table A2.6 Lake Lia trace geochemistry 483
Table A2.7 Lake Brazi trace geochemistry 487
Table A2.8 Secondary standards for trace elements geochemistry StHS6/80-G 490

**Appendix 4 – Radiocarbon dates for all sites**

Table A4.1 AMS $^{14}$C dates for Kråkenes used in the large age model 493
Table A4.2 AMS $^{14}$C dates for Lake Madtjärn used in the large age model 496
Table A4.3 AMS $^{14}$C dates for Hässeldala port used in the large age model 497
Table A4.4 AMS $^{14}$C dates for Endinger Bruch used in the large age model 499
Table A4.5 AMS $^{14}$C dates for Lake Czechowskie used in the large age model 500
Table A4.6 AMS $^{14}$C dates for Lake Hämelsee used in the large age model 500
Table A4.7 AMS $^{14}$C dates for Węgliny used in the large age model 501
Table A4.8 AMS $^{14}$C dates for Soppensee used in the large age model 501
Table A4.9 AMS $^{14}$C dates for Rotsee used in the large age model 503
Table A4.10 AMS $^{14}$C dates for LPA used in the large age model 508
Table A4.11 AMS $^{14}$C dates for Lake Bled used in the large age model 509
Table A4.12 AMS $^{14}$C dates for Lake Brazi used in the large age model 509
Table A4.13 AMS $^{14}$C dates for Lake Lia used in the large age model 510

**Equations**

**Chapter 3 - Methodology**

Equation 3.1 Calculation for pollen concentration 64
Equation 3.2 Calculation for PAR 64

# Chapter 1
# Introduction

The climate of the Last Glacial-Interglacial transition (LGIT, ~16-8 calibrated (cal.) ka BP) has been widely studied in Europe, with a plethora of highly detailed and dated palaeoenvironmental reconstructions. The high-resolution Greenland ice core records (GIC) provide detailed evidence for climatic variability (Figure 1.1). Variations in oxygen stable isotope ratios ($\delta^{18}O$) show clearly defined millennial-scale climatic fluctuations between stadials (cold conditions) and interstadials (warm conditions) with abrupt and short-lived (centennial to decadal-scale) oscillations superimposed upon these fluctuations (Dansgaard et al., 1993; Rasmussen et al., 2006, 2014; Lowe et al., 2008). The timing, duration, and magnitude of this climatic variability are recognised at local and regional scales in European terrestrial proxy records (e.g. Lotter et al., 1992a; Brauer et al., 2008; Moreno et al., 2014). The term 'proxy' is defined as the line of evidence used to provide information on past climates or environments (Lowe and Walker, 2013). Terrestrial proxies include pollen, chironomids (non-biting midges) and stable isotopes. Comparing the temporal and spatial variability of environmental responses using proxies gives insight into past abrupt climatic shifts can reveal the complex interplay between the ocean, atmosphere and cryosphere and the overall climatic driving mechanisms.

The LGIT has been sub-divided into climatically delineated events with terms derived from biostratigraphic classifications from Northern Europe (Figure 1.1; Andersson, 1896; Mangerud et al. 1974; Björck et al., 1998). This includes the warm Bølling-Allerød interstadial with superimposed centennial to decadal scale cooling events (e.g. Gerzensee Oscillation (Eicher, 1980; Lotter et al., 1992)), before the return of the near glacial conditions of the Younger Dryas stadial (YD). The warmer Holocene

interstadial followed, with abrupt short-lived interruptions of cooler conditions (e.g. Preboreal Oscillation, Björck et al., 1997).

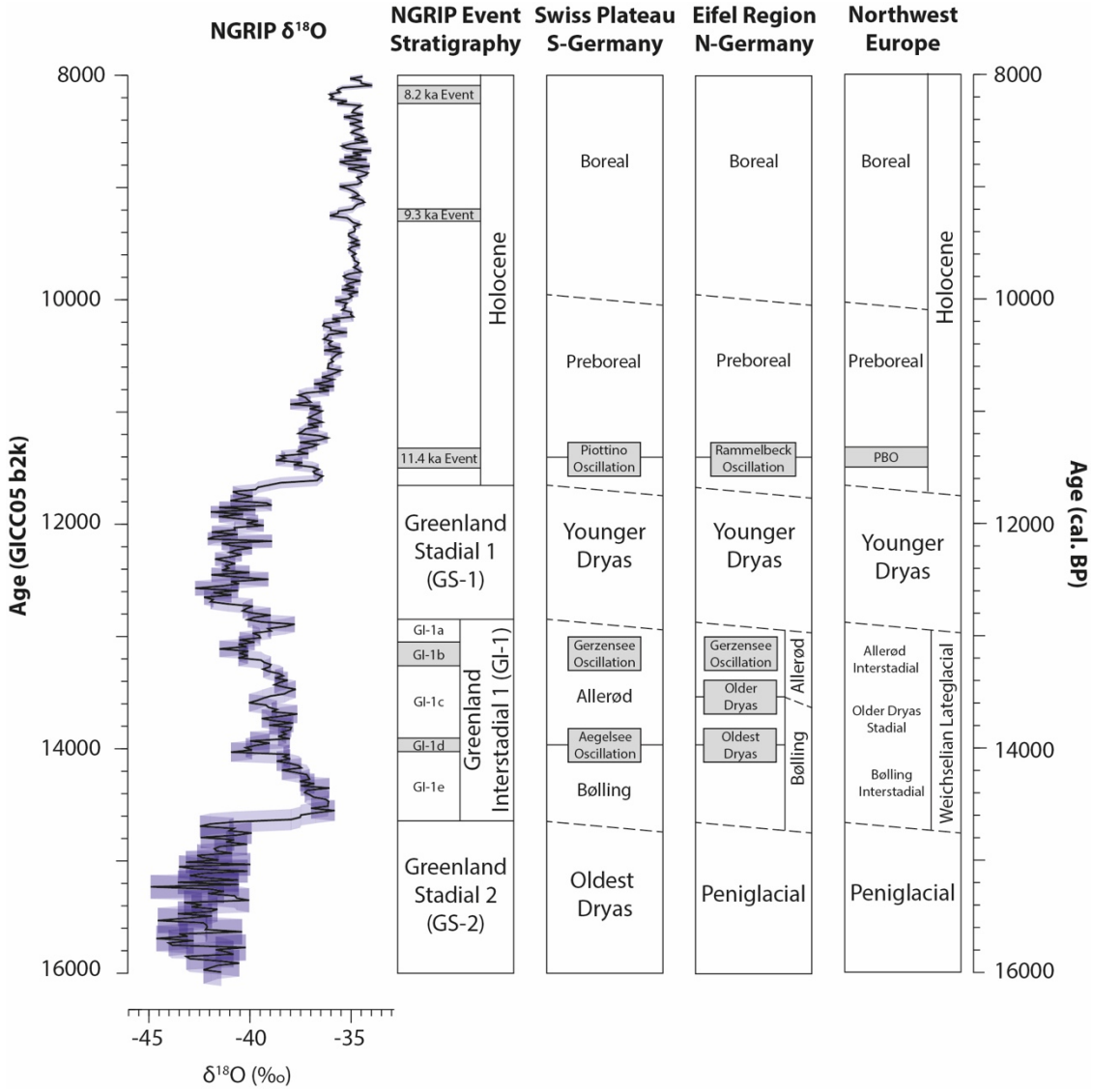


**Figure 1.1** The NGRIP oxygen stable isotope and event stratigraphy record of the Last Glacial-Interglacial transition. Note the timescale is on GICC05 (left, Rasmussen et al., 2006, 2014) and timescale is on Age cal. BP (right, IntCal13). On NGRIP, the colour shade presented is the age uncertainty at 1 sigma, in the Greenland ice-core records this is half of the maximum counting errors (MCE). LGIT NGRIP event stratigraphy with the millennial-scale events are Greenland stadial 2 (GS-2), Greenland Interstadial 1 (GI-1), GS-1 into the Holocene period. Centennial-scale events are superimposed upon these timescales seen in GI-1 and throughout the Holocene. The bio- and climatostratigraphy of LGIT events for the different regions in Europe are also presented. The different names for its climatostratigraphic equivalent in the NGRIP highlights the confusion around understanding the timing of climatic oscillations across Europe. The dashed lines represent rough calibrated ages compared to the GICC05 timescale. Adapted from van Raden et al. (2013) and Lowe and Walker (2014).

The millennial-scale climatic oscillation of the Younger Dryas (YD) stadial is a highly studied period of the LGIT, recognised and radiocarbon dated across Europe around ~12.9-11.5 ka cal. BP (Walker et al., 2009). The term 'Younger Dryas' is derived from the presence of the indicator vegetation species of *Dryas octopetala* ('Dryas'), an alpine-tundra taxa in Scandinavia (Figure 1.1, Andersson, 1896). The 'Younger' relates to the youngest of two 'Dryas' stadials (Andersson, 1896). The abrupt nature of the onset and termination of this event is a paradigm for investigating future climate change (Broecker et al., 2010). Many past studies have assumed temporal and spatial synchronicity in the onset and termination of the YD (e.g. Schwander et al., 2000; Lane et al., 2011). This implies a common climatic forcing mechanism based on poorly temporally constrained data. However, the study of high-resolution palaeoenvironmental records that are chronologically constrained show that climatic transitions can be time-transgressive (Brauer et al., 2008; Bakke et al., 2009; Lane et al., 2013; Rache et al., 2014; Muschitiello and Wohlfarth, 2015; Bartolomé et al., 2015; Baldini et al., 2015).

The Holocene period, defined through the term 'holocènes' meaning 'entirely recent' (Gervais, 1867-69, pg.32), witnessed several centennial-scale climatic oscillations. The earliest Holocene (EH), defined in this thesis as between ~11.5-10.5 ka cal. BP, saw one such climatic event the Preboreal Oscillation (PBO). This event is dated to 11,300-11,150 cal. BP by Björck et al. (1997). The term 'Preboreal' is in reference to the expansion of pine and birch tree taxa within northern European pollen records (Mangerud et al., 1974). The PBO saw a decline in the pine-birch woodland while herbaceous taxa expanded (Björck et al. 1997). This cooling event has been widely recognised and dated across Europe in several palaeoenvironmental records (e.g. Rasmussen et al., 2007, Wohlfarth et al., 2006; Lotter al., 1992; Pál et al., 2018). However, issues remain in precisely dating this event with evidence for additional climatic cooling oscillations

recorded during the EH (e.g. Bochnek and Hoek, 2007; Fiłoc et al., 2018; Blockley et al., 2018).

As demonstrated, the understanding of the environmental responses to these particular abrupt climatic oscillations of the LGIT are still spatially and temporally complex. Challenges remain in providing precise chronologies for palaeoenvironmental records. Chronological problems with large dating uncertainties and tuning/wiggle-matching different records together limit the ability to test the (a)synchroneity of climate between the widely used NGRIP stratotype (Lowe et al., 2008; Rasmussen et al., 2014) and European palaeoenvironmental records (Brauer et al., 2014). Recent studies have highlighted the need to test the assumptions of climatic synchroneity and the inherent time-transgressive nature of abrupt climatic transitions, with questions over the climatic regime, forcing factors and environmental responses to these climatic oscillations during this period (e.g. Lane et al., 2013; Muschitiello and Wohlfarth, 2015).

As a result, there is a need to generate proxy data on properly quantified chronologies for individual palaeoenvironmental records to investigate the climactic sequence of different LGIT millennial and centennial-scaled climatic events. This protocol, as proposed by the INTIMATE group (INTegration of Ice, MArine and TErresterial records), allows for the interpretation, integration and correlation of records during the LGIT (Björck et al., 1998; Lowe et al., 2008). The use of tephra layers (volcanic ash) preserved in sedimentary records provides an ideal method to tie together independent site chronologies. These instantaneous deposits can be geochemically identified and correlated to dated volcanic eruptions providing precise age-markers or isochrons (Davies et al., 2012). The innovative use of cryptotephra layers (volcanic ash invisible to the naked eye) has allowed a broader application on continental to hemispheric scales (e.g. McLean et al., 2016; Haflidason et al., 2019). Identifying known tephra layers

allows sites to be independently correlated and investigation into the environmental response to LGIT climatic oscillations. Also, the application of Bayesian statistical modelling has improved the calibration of radiocarbon dates and generated optimised age models for palaeoenvironmental records (Blaauw et al., 2018). Combining these chronological methods, presenting age uncertainty and conforming to the INTIMATE protocol, allows investigation into the assumption of climatic synchronicity.

## 1.1 Research Rationale

Across Europe, there is a vast number of dated terrestrial palaeoenvironmental records available covering the LGIT (e.g. Lotter et al., 1992a; Birk et al., 2000; Wohlfarth et al., 2006). A transect of sites across Europe is ideal for investigating the spatial and temporal differences of environmental response to the abrupt climatic oscillations of the YD and EH. The North Atlantic ocean is seen as the main driver for many climatic oscillations during the LGIT (e.g. Clark et al., 2001; Björck et al., 1997; Lane et al., 2013; Muschitiello and Wohlfarth, 2015).

Many studies have shown the importance of changes in oceanic circulation, mainly the Atlantic Meridional Overturning Circulation (AMOC), that transports latent heat from the tropics to the northern latitudes (see section 2.3; Clark et al., 2002; Broecker et al., 2006). Disruption to this circulation through the input of freshwater from terrestrial sources (i.e. ice sheets), has been linked to climatic cooling events witnessed in European palaeoenvironmental records (e.g. Björck et al., 1997; Broecker et al., 2006). The timing and amplitude of the corresponding terrestrial site response can depend on the latitude and longitude within Europe (e.g. Magyari et al., 2012; Heiri et al., 2014; Moreno et al., 2014; Muschitiello and Wohlfarth, 2015; Candy et al., 2016; Pál et al., 2018). Sites situated closer to the North Atlantic have a stronger environmental response compared to records

further east, showing the propagation of climatic effect across a continent through changes in atmospheric circulation (Lane et al., 2011a; Heiri et al., 2014; Candy et al., 2016; Pál et al., 2018). Other studies have gone on to demonstrate that the shifts in atmospheric circulation, namely the polar front, is also a crucial climatic mechanism that is linked to changes in the North Atlantic ocean circulation (e.g. Bakke et al., 2009; Lane et al., 2013). The use of tephra layers and Bayesian statistical modelling to reduce chronological uncertainties has been key to understanding these climatic mechanisms and the time-transgressive patterns of climatic response (Lane et al., 2013; Muschitiello and Wohlfarth, 2015; Wohlfarth et al., 2018). However, in those studies, only sites in northern Europe were investigated.

The type of proxy archive for palaeoenvironmental reconstructions that is most widely available on large spatial scales are pollen records, mainly terrestrial pollen from lake sediments. The method of pollen analysis is a technique has been widely adopted to reconstruct past climatic changes for nearly a century (von Post, 1946). It can be applied to a wide variety of sedimentary archives with a plethora of pollen records covering the LGIT. Compared to other proxies that can need specific environmental and sedimentary conditions to form (i.e. sedimentary stable isotopes; Leng and Marshall, 2004), pollen records are widely available across Europe. Where other biological proxies need a large amount of sediment to reconstruct past climate (e.g. plant macrofossils, Coleoptera), the temporal resolution from pollen sequences allows past vegetation to be linked to millennial and centennial-scale climatic events identified in Greenland ice-cores (Bennett and Willis, 2001).

Despite the numerous dated high-resolution palaeoenvironmental records available across northern, western and central Europe, the regions of central-eastern Europe lack the same intense, well-dated climatic reconstructions (Feurdean et al., 2014; Mindrescu and

Veres, 2016; Pál et al., 2018). The incomplete understanding of the impact and mechanisms of climate change on a continental scale can be addressed by the inclusion of records from central-eastern Europe, for example, Romania. This region is particularly sensitive to climatic variation due to being at the confluence of several climatic systems (Magyari et al., 2012; Pál et al., 2018).

In the last two decades, Romania has seen a steady rise in the publication of dated, high-resolution proxy studies of past climate and environmental conditions. This offers the potential to investigate short term climatic transitions (e.g. Wohlfarth et al., 2001; Magyari et al., 2012; Pál et al., 2018). However, dating problems characterised by poor dating resolution (Farcas et al., 1999; Feurdean et al., 2007), large dating errors (Wohlfarth et al., 2001; Björkman et al., 2002) and sample contamination (Magyari et al., 2009) have resulted in chronological uncertainty, limiting our ability to fully understand the critical questions of rapid climatic transitions across Europe (Brauer et al., 2014; Bronk Ramsey et al., 2014; Mindrescu and Veres, 2016). The application of tephra marker-layers to palaeoenvironmental records can allow regions such as Romania, to be linked to other European sites, enabling investigation of the broader spatial and temporal migration of abrupt, short-lived climate events during the LGIT period.

Overall, there is a need for investigating the possibility of time-transgression for abrupt climatic shifts during the LGIT over a larger spatial scale. The utilisation of widespread tephra marker layers and Bayesian age modelling can improve chronological uncertainty surrounding abrupt climatic changes (Lowe et al., 2008; Blaauw et al., 2018). By extending the transect to a continental scale, further insight into the behaviour of the climate system can be investigated. It is essential to provide insight for climatic modellers in producing realistic computer simulations for future climate scenarios, potentially allowing us to mitigate impacts on future societies (Broecker et al., 2010).

## 1.2 Project outline and hypothesises

This DPhil research seeks to investigate and assess the synchroneity or asynchrony of the millennial and centennial-scale abrupt climatic shifts during the LGIT period across Europe. There are two parts to this research. Firstly, a cryptotephra investigation will be applied to palaeoenvironmental records from Romania to identify widespread tephra marker layers. This improves chronological uncertainty for the records as well as providing a direct tephra linkage to other palaeoenvironmental archives in Europe. Romania was chosen to provide a broader continent-scale investigation into climatic patterns.

The second part involves investigating the central hypothesis of whether there are regional spatial and temporal differences in the palaeoenvironmental responses to abrupt climatic events recorded across Europe for specific times of the LGIT period. Specifically, it is hypothesised that the Greenland ice-cores and northern European localities experience the onset of these oscillations earlier than those sites in central and southern Europe (Lane et al., 2013; Mustichiello and Wohlfarth, 2015). The terminations of these climatic events would be later at northern localities. This can be linked to changes in the North Atlantic Ocean circulation (Ibid). If this hypothesis is correct, there should be a time-transgressive pattern of the environmental response to these different temporal climatic events recorded along the northwest to southeast transect of the European region.

The LGIT provides the potential to test the (a)synchronicity of different temporal scale climatic oscillations with the millennial-scale climatic cooling of the Younger Dryas (Section 2.2.1) and the shorter centennial-scale cooling during the earliest part of EH period, i.e. the Preboreal Oscillation (~11.5 to 10.5 ka cal. BP, Section 2.2.2). Both of these climatic oscillations have been identified across Europe with the reconstruction of local and regional environmental response (e.g. Lane et al., 2011a; Fiłoc et al., 2018). This

is based on mainly terrestrial pollen records from lake archives (e.g. Lotter et al., 1992a; Björck et al., 1997; Wohlfarth et al., 2006, 2017; Magyari et al., 2012).

## 1.3 Aims and objectives

The main aim of this thesis is to investigate the temporal and spatial (a)synchroneity of abrupt climatic events during the LGIT across Europe, specifically the YD and EH oscillations. To achieve this aim, the following objectives were set:

1. To provide a complete high-resolution LGIT cryptotephra record for two palaeoenvironmental sites in Romania. Only two sites were chosen due to time constraints.
2. To collect dated pollen records across Europe that conform to a strict site selection criteria and that include key tephra isochrones for the YD and/or EH.
3. To perform high precision Bayesian age modelling to produce precise and accurate age models for the selected sites and ages for widespread tephra layers.
4. To undertake a re-examination of palynological data through statistical analysis from the chosen sites to clearly identify the onset and terminations of climatic events and the magnitude of these environmental shifts.
5. To integrate these selected sites on their properly quantified timescales using an integration tool to allow comparisons in timings of climatic onsets and terminations across a continental scale transect and with the Greenland ice-core records.
6. To visually and quantitively present chronological uncertainties associated with the timings of climatic onset and terminations from each record.

## 1.4 Conventions adopted

As this study refers to timescales throughout, and to ensure consistency with the timescale chosen, certain conventions are adopted. Firstly, 'cal. BP' refers to calibrated radiocarbon ages, as used by the radiocarbon community. 'BP' refers to 'before present' which is 'before AD 1950'. The 'cal. BP' is applied as an 'absolute age' timescale (i.e. real timescale) in this study, which is in principle equivalent to the calibrate radiocarbon ages. For uncalibrated radiocarbon ages, the notion of '$^{14}$C BP' is used and is based upon the radiocarbon half-life of 5,568 years, as adopted by the radiocarbon dating community (Mook, 1986).

Another timescale used in this study is the GICC05 (Greenland Ice-Core Chronology 2005) 'b2k' (before AD 2000) from the Greenland ice-cores (Rasmussen et al., 2006, 2014). As ice-cores are annually counted, an age uncertainty is calculated termed maximum counting errors (MCE) in years. Previously, when studies compared terrestrial records on 'cal. BP' timescales to Greenland ice-cores on 'b2k' timescales, they were assumed to be equivalent in 'absolute age' with a difference of 50 years due to the 'before AD 1950' and 'before AD 2000'. However, work by Muscheler et al. (2014) and Adolphi and Muscheler (2016) have provided a time-transfer function to synchronise these two different timescales while also providing quantified uncertainty estimates. As a result, this study will use this time-transfer function when comparing 'cal. BP' and 'b2k' timescales.

For ages presented in the text, figure and graphs of this study, the mean and one sigma ($\mu \pm 1\sigma$ (68.2%)) are used unless otherwise stated. The timescale used in all figures is the calibrated IntCal13 timescale as 'age cal. BP', unless otherwise stated. Abbreviations used in this study are written out in full on their first depiction in text with a full list in Appendix 1.

## 1.5 Thesis structure

This thesis is divided into ten chapters. Chapter 2 will provide an overview of the LGIT climatic structure with particular focus on the Younger Dryas and earliest Holocene oscillations (i.e. the Preboreal Oscillation), the climatic and environmental responses within the vegetation record in these periods and the proposed driving mechanism behind these changes. Issues regarding the accuracy and precision of dating these transitions will be addressed, with a review of the methods that can be employed to resolve these problems. Chapter 3 introduces the methods that will be used throughout this thesis. Chapter 4 will present the sites selected for both the tephrochronological investigation in Romania as well as the sites chosen for palaeoclimatic and environmental analysis. Chapter 5 gives the results of the cryptotephra investigation with Chapter 6 presenting the discussion and identification of tephra layers from Romania. Chapter 7 shows the results of the large age model with new tephra ages and age models for individual sites. The pollen records from sites across Europe are re-interpreted using the newly derived chronology. Chapter 8 synthesises the climatic and environmental data to look into the timing of the Younger Dryas across Europe providing insight into the timing, duration and magnitude allowing insights into the climatic driver(s) behind this millennial-scale climatic oscillation. Chapter 9 follows the same approach focusing on the earliest Holocene climatic event(s). Chapter 10 summarises the significant findings in this project and further areas for study.

# Chapter 2

# Millennial and centennial-scale abrupt climatic events of the Last Glacial-Interglacial transition

This chapter provides a literature review of the climatic and environmental response to two different temporal scale abrupt climatic cooling oscillations: the millennial-scale Younger Dryas (YD) stadial and a centennial-scale earliest Holocene (EH) events (i.e. the Preboreal Oscillation (PBO)). These are the climatic oscillations that are the focus of this thesis. The timing of these events across Europe are based on radiocarbon dating, which will also be presented, with current chronological issues surrounding our understanding into the complex interplay between ocean, atmosphere and terrestrial elements. Finally, an introduction into tephrochronology and the INTIMATE database integration tool which will provide further insight into the temporal and spatial characteristics for these different oscillations.

## 2.1 Terminology and the INTIMATE approach - event stratigraphy and protocols

The terminology of the Last Glacial-Interglacial Transition (LGIT) derives from palynological studies in Northern Europe (Mangerud et al., 1974). The YD and PBO derive their terminology from these Northern European pollen records (see Chapter 1). There has been a transference of this terminology across different European localities and other proxy records. Where different proxies have shown similar timing and environmental response to climatic oscillations during the LGIT, authors have replaced regional terminology to these terms (Figure 1.1). The term YD is commonly applied to records outside Scandinavia and also to different proxy records other than pollen. This can result in assumed identical temporal and spatial response, especially when chronologies

associated with this event are commonly transferred across. Regional diachrony may exist (Björck et al., 1998; Walker et al., 2001; Lowe, 2001; Lowe et al., 2019).

There are similar problems in using the term PBO. The term was first devised by Lotter et al. (1992a) using pollen in lacustrine records from the Swiss Plateau. Björck et al. (1997) went on to identify the PBO in northern European pollen records. However, since then, there has been the universal application of the term to EH climatic oscillations across Europe (e.g. Tóth et al., 2012; Fiłoc et al., 2018). There are also regional names for this EH oscillation of the 'Youngest Dryas' (Behre, 1978), the 'Piottino Oscillation' in Switzerland (Zoller 1960) or the 'Rammelbeek Phase' in NW Europe (e.g. Bos et al., 2005; Theuerkauf et al., 2014). Without a formally resolved unit and with an increasing number of high-resolution records highlighting the climatic complexity of the EH, using the term PBO can confuse and be inappropriately applied.

The INTIMATE group (INTegration of Ice, MArine and TErresterial records) have suggested an application of a new event stratigraphy. The Greenland ice core record of NGRIP (North GReenland Ice core Project) is a high-resolution isotopic record on an annually resolved timescale called the Greenland Ice-Core Chronology 2005 (GICC05) (Rasmussen et al., 2006, 2014). Across the LGIT period, the record has the smallest age uncertainty with a maximum counting error (MCE) of 186-68 years (Rasmussen et al., 2006; 2014; Blockley et al., 2012). The isotopic records are also highly sensitive to climatic change and show the abrupt nature of the climatic variability (Steffensen et al., 2008; Rasmussen et al., 2006, 2014). There are two isotopic records used in the event stratigraphy. Firstly, the variations in oxygen stable isotope ($\delta^{18}O$) values that reflect air temperature (Dansgaard et al., 1984; Masson-Delmotte et al., 2005). Secondly, the changes in deuterium excess ($d = \delta D - 8\delta^{18}O$) show alterations in temperature and moisture sources (Masson-Delmotte et al., 2005; Steffensen et al., 2008). Changes in these proxies reflect

the climatic variability seen in other European records on a highly precise chronological template (Lowe et al., 2008, 2019). Overall, Greenland ice cores are the best resolved and dated archive, providing an ideal regional stratigraphic standard for LGIT climatic change (Lowe et al., 2008; Figure 2.1).

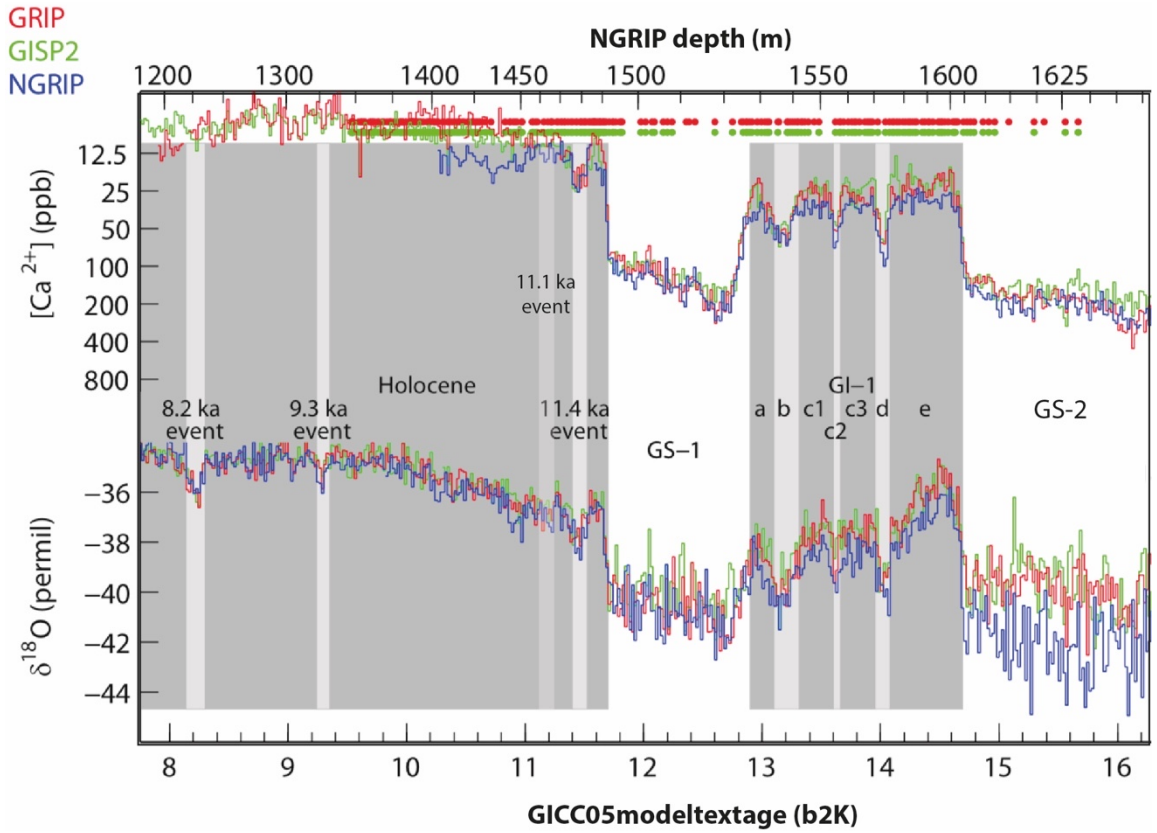


**Figure 2.1** The different Greenland ice-cores and their climatic reconstruction of the LGIT; GRIP (red), GISP2 (green) and NGRIP (blue) 20-year average stable isotope record ($\delta^{18}O$) and Calcium ($Ca^{2+}$) plotted on the GICC05 timescale (b2k) with millennial- and centennial-scale climatic events during the LGIT period. The 11.1ka event in NGRIP has also been highlighted from Rasmussen et al. (2007). Source: Rasmussen et al. (2014).

The scheme provides a chronostratigraphic definition for climatic events identified in NGRIP. The stadials (cold), termed Greenland stadials (GS), and interstadials (warm), Greenland interstadials (GI) with individual events numbered successively. These events were defined using multiple proxy indicators with clear lower and upper climatic boundaries dated by the GICC05 chronology using b2k (see section 1.4; Rasmussen et al., 2014). The cooling event associated with the YD is termed GS-1 (12.9-11.7 ka b2k ± 138

and 99 MCE) with changes in deuterium excess defining the onset and termination of the event (Rasmussen et al., 2006, 2014).

The Early Holocene in INTIMATE stratigraphy (11.7-8 ka b2k ± 99 MCE) is not sub-divided. This is the period covers the earliest Holocene (EH) defined in this thesis. However, centennial- and decadal-scale oscillations are identified within the EH in the ice cores. An event was identified through large scale changes in accumulation rate (10-15%) and $\delta^{18}O$ values at 11,585-11,255 b2k (± 97-86 MCE) by Rasmussen et al. (2007), termed the 11.4ka event. The PBO is tentatively associated with this Greenland ice-cores (GIC) event (Rasmussen et al., 2016). Another event, the 11.1ka event, has only been identified in NGRIP only with smaller changes in $\delta^{18}O$ and no significant accumulation rate (Rasmussen et al., 2007, 2016).

The INTIMATE group stressed that the terminology and dates presented in this event stratigraphy were to be used as a format to compare the timing and response between climatic oscillations identified in European records and NGRIP. Protocols published by INTIMATE stipulated that records should have their independent proxy data upon their own independently generated chronologies (Björck et al., 1998; Lowe et al., 2008). Once completed, then comparisons between regional stratotypes can be undertaken with dating uncertainties also taken into consideration (Ibid). This allows testing of climatic mechanisms driving abrupt climatic change (Lowe et al., 2008). However, there are continuing problems with studies interchanging between the YD and GS-1 terminology. Also, the chronostratigraphy of GS-1 is used to tune terrestrial records (e.g. Heiri et al., 2005; Magny et al., 2007). This results in a loss of information for understanding the propagation of abrupt climatic events across different spatial scales.

With the main aim of this project being to investigate the timing of abrupt climatic events across Europe, the protocol established by INTIMATE will be used (Lowe et al.,

2008). The terminology used throughout this thesis for the climatic oscillations to be studied will be as follows:

- The Younger Dryas will be used in reference to European terrestrial records. The central proxy used to investigate former climatic oscillations will be pollen (see section 2.2). As the YD was defined using pollen records, be it from northern Europe, the term can be justifiable to use here. The use of YD with other proxies (e.g. chironomids, stable isotopes in lacustrine sediments) will be considered when the concerning depths are primarily identified through the pollen record.
- GS-1 will be used in reference to the Greenland ice-cores record only.
- The term Preboreal Oscillation will not be used in reference to EH climatic and environmental oscillations within the terrestrial record. This is due to the unresolved geological/temporal unit definition of this oscillation. Instead, identified EH climatic oscillations around the time of the proposed PBO (~11.5 to 10.5 ka cal. BP) within pollen records will be referred to as a number (site_E*n*) to allow an unbiased investigation.
- 11.4ka and 11.1ka events will only be used in reference to the Greenland ice-core records.
- Timings of these climatic oscillations will be generated using the site records' chronology.

## 2.2 Climatic and environmental response to millennial- and centennial-scale abrupt climatic events

The following section will discuss the climatic and environmental structure for the millennial-scale YD and centennial-scale EH oscillations within European records.

The reconstruction of past climates and environments use various proxies (e.g. chironomids, stable isotopes) from sedimentary archives. Pollen analysis was chosen as the main proxy for this thesis due to: 1) the high-resolution potential of pollen analysis (Bennett and Willis, 2001); 2) vegetation response are considered sensitive to changing climatic conditions as demonstrated throughout the LGIT (Merkt and Müller, 1999; Lotter et al., 2012; Theuerkauf et al., 2014); 3) the YD and PBO were initially defined in pollen records (e.g. Björck et al., 1997); and 4) the near-ubiquitous application of pollen analysis as a primary palaeoenvironmental reconstruction across the whole of Europe. As a result, the climatic and environmental reconstruction will focus on vegetation changes.

The shifts in vegetation have been proposed as responding to changes in climatic conditions, mainly temperature and precipitation (Davis and Shaw, 2001; Williams et al., 2011). As a result, vegetation changes presented by pollen can be seen as responding to climatic oscillations during the LGIT (Seppä and Bennett, 2003; Davis and Shaw, 2001). This is due to individual taxon shift their distribution range rather than their climatic tolerance (Seppä and Bennett, 2003; Davis and Shaw, 2001). This is the dynamic equilibrium hypothesis (Prentice et al., 1991).

Another hypothesis is that of disequilibrium (Huntley, 1991; Prentice et al., 1991). Other factors can also affect vegetation assemblages and individual taxa distributions. Site factors such as soil type, nutrient availability, soil drainage are known to affect vegetation (e.g. Prentice et al., 1991; Thereukauf et al., 2014). Also, dispersal factors can also affect the migration of certain taxa to a region (e.g. Bunting, 1996), resulting in a lag between

climate change and vegetation response (Prentice et al., 1991; Clark et al., 1998). As a result, vegetation response can be complex and driven by numerous factors (Williams et al., 2011). However, the view taken in past pollen investigations (e.g. Birks and Ammann, 2000) and shown in computer simulations (e.g. Davis and Shaw, 2001), vegetation shifts can be linked to overall changes in climatic conditions and can respond rapidly (within decades; e.g. Ammann et al., 2001; Engels et al., 2016)

Under changing conditions, i.e. climate, vegetation assemblages can be resilient to this external forcing factor. However, a threshold can be reached that may 'tip' the vegetation into a new state (Scheffer and Carpenter, 2003; Williams et al., 2011; Reyer et al., 2015). This would result in a new vegetative regime that is in equilibrium with the new climatic state (Reyer et al., 2015).

When using pollen analysis to reconstruct past vegetation change, and thus past climatic oscillations, caveats also need to be taken into consideration. Firstly, certain taxa within a pollen record can be under/over-represented (e.g. *Pinus* and *Quercus*; Odgaard, 1995; Whitmore et al., 2005). Secondly, far-travelled pollen grains (~100km) can obscure representation of local species (Odgaard, 1995; Farcas and Benneike, 2004). Thirdly, identification of species to a low taxonomic level is difficult due to pollen grain preservation and similar grain morphologies (Birks and Birks, 2000). This is especially important when different taxa identified to species (i.e. *Betula* vs *Betula nana*) can have different environmental tolerances (warm vs cold; Birks and Birks, 2000). Lastly, there is a known lag (within decades) in vegetation response to abrupt climatic change (Hoek, 2001; Birks and Birks, 2008). However, these problems are known in numerous pollen records and can be disentangled by using other proxy evidence to provide insight into the environmental and climatic conditions during the LGIT.

### 2.2.1 The Younger Dryas

The warm interstadial of the Allerød was interrupted by the climatic downturn of the YD stadial. The abrupt decrease in temperatures resulted in a dramatic environmental response that is recorded in sequences across Europe.

The equivalent to the YD is the GS-1 in the GICs due to tehir broadly chronological correspondence. These records highlighted the abrupt nature of this shift with enrichment in deuterium excess of ~2-3‰ occurring within 1-3 years (Steffensen et al., 2008). In comparison, changes in the depletion in $\delta^{18}O$ values were more gradual, happening over 200 years (Rasmussen et al., 2014). Steffensen et al. (2008) highlighted that these changes were due to the rapid reorganisation of the Northern Hemispheric atmospheric circulation associated with changing sea surface temperatures linked to sea-ice extent.

Within the terrestrial record across Europe, there were clear indications of environmental responses to this climatic deterioration. The Scandinavian Ice Sheet (SIS) front re-advanced after a major retreat during the Bølling-Allerød (Mangerud et al., 2013) with local glacier re-advanced in mountainous regions, evident from moraine features across Europe (e.g. Ballantyne, 2010; Ivy-Ochs et al., 2008).

Quantitative palaeotemperature reconstructions from chironomid-inferred summer temperature (C-IT) and coleopteran mutual climatic ranges (MCR) show a marked decline in temperatures. Additional information on these proxies and their caveats are given in Table 2.1. There is a demonstrated decline in summer and winter temperatures presented by C-IT and MCR. Northern latitudes experienced the greatest declines in temperature at the onset of the YD with an ~5-6$^{o}$C drop (e.g. Coope et al., 1998; Brooks and Birks, 2001; Brooks et al., 2012). Central and southern Europe experienced smaller temperature decreases of ~1-2$^{o}$C (e.g. van Asch et al., 2012; Heiri et al., 2005; Larocque and Finsinger,

2008). Eastern Europe recorded a <1°C decline (e.g. Tóth et al., 2012). Computer modelling studies of past temperature also show similar results, with declines in summer temperatures as a driver for vegetation change (Renssen and Isarin, 1997, 2001). Recent modelling studies using indicator species (e.g. birch, deciduous tree taxa) from plant macrofossils (e.g. leaved, seeds) show that short warm summers and harsh winters typical of continental conditions influenced environmental change (Schenk et al., 2018).

**Table 2.1** Further information on additional proxies and their limitations discussed in this thesis

| Proxy | Reconstruction | Limitations |
|---|---|---|
| **Chironomids** (non-biting midges) | **Quantitative inferred summer temperatures** – using training sets based on modern day species enviro. Tolerances (e.g. temperature, lake trophic level). | Other environmental factors (e.g. lake depth, trophic levels) may affect chironomid assemblages (Brooks and Birks, 2000; Lang et al., 2010), preservation of head capsules not ideal especially during YD (Heiri et al., 2005), training sets based on Alps and Scandinavian assemblages and may not be appropriate to reconstruct temperatures outside these regions (Heiri et al., 2005; Larocque and Finsinger, 2008; Tóth et al., 2012). |
| **Coleopteran** (beetles) | **Quantitative Temperature reconstruction** – summer and winter | Coarse resolution sampling, large range of temperatures (Coope and Lemdahl, 1995), preservation of organic remains, habitat preference of certain species may have changed over time so cannot use completely to reconstruct past vegetation and temperature (Ribera and Vogler, 2004) |
| **Oxygen stable isotopes** in carbonate within lacustrine sediments ($\delta^{18}O$) | **Temperature and/or precipitation source** – controlled by isotopic fractionation which is temperature at vapour condensation (Dansgaard, 1964; Leng and Marshall, 2004) | Only mean annual temperature, changes in moisture sources affects isotopic composition (Marshall et al., 2002), need to understand past lake system (open or closed, Talbot, 1990), detrital carbonate can influence isotopic values (Leng and Marshall, 2004) |
| **Hydrogen isotope** from lipid biomarkers ($\Delta\delta D_{terr-aq}$) | **Paleohydrological changes** - δD of precipitation from rainfall or lake signal from terrestrial or aquatic plant *n*-alkanes (Sachse et al., 2012) | δD from terrestrial plants can be affected by evaporation (Kahmen et al., 2013). Also changes in moisture sources, differences in terrestrial and aquatic lipid biomarkers, variation in δD fraction between different plant species and life stages (Sachse et al., 2012). |

Stable isotopes measurements from sediment archives (carbonate precipitation in lakes) also reveal a clear climatic signal. There is a consensus that variations in $\delta^{18}O_{bulk}$ values from authigenic sediments are related to temperature and/or precipitation changes (see Table 2.1; Dansgaard et al., 1993; Leng and Marshall, 2004). Absolute temperature cannot be accurately calculated, yet relative temperature changes can be inferred (Leng and Marshall, 2004; Candy et al., 2016). Nonetheless, $\delta^{18}O_{bulk}$ records show a climatic downturn with a decline in temperatures (e.g. Lotter et al., 1992a; Schwander et al., 2000). Some records show a hiatus in $\delta^{18}O_{bulk}$ recorded during the YD, indicative of low temperatures (e.g. Lotter et al., 1992a; Whittington et al., 2015).

There was a pronounced vegetation response to this climatic deterioration (Figure 2.2). Northern and north-western Europe experienced a marked decline in woody taxa of *Betula* and *Pinus* with an increase in herbaceous taxa of Arctic heathland (e.g. *Artemisia, Rumex*, Poaceae). Landscapes became open and largely treeless (e.g. Walker et al., 2003; Birks et al., 2012). There were some occurrences of *Betula* and especially *Pinus* in local records at these latitudes during the YD. However, this can be related to: 1) either the localised presence of these taxa; 2) the presence of the dwarf shrub *Betula nana,* due to the similar morphology between this taxon and *Betula* trees (mainly *Betula pubescens*; Birks, 1968); 3) reworking from older sediments (Mortensen et al., 2011) or wind-blown from other regions such as central Europe (Birks et al., 2000; Mortensen et al., 2014). The presence of macrofossils for these taxa can help to confirm their local occurrence (Birks and Birks, 2000). In central and western Europe, the woodland declined with a general increase in herbaceous and shrub taxa of *Juniperus*. There were some stands of tree *Betula* and *Pinus* remaining in many locations (e.g. Mortensen et al., 2014; Lotter et al., 1992a; Theurukauf et al., 2014). In mountainous areas, the altitude of treelines descended (e.g. Lotter et al., 1992a,b). In southern and eastern Europe there was a decline in *Pinus* and

deciduous tree taxa (e.g. *Quercus*-type, *Picea*) with an increase in cold herbaceous steppe taxa of *Artemisia* and Chenopodiaceae (e.g. Guiter et al., 2005; Tanţău et al., 2003; Magyari et al., 2013). Deciduous trees retreated to refugial sites located in northern Romania (e.g. Feurdean and Bennike, 2004, Feurdean et al., 2007). However, some sites show no vegetation response to the YD (e.g. Farcas et al., 1999). This can be related to either hiatus within the record or problems associated with low-resolution sampling undertaken in studies, rather than an authentic lack of response (e.g. Reille and Lowe, 1991).

Changes in the temperature and precipitation regime resulted in large scale environmental responses. There are further climatic and environmental variations during the YD stadial (e.g. Lane et al., 2013), but this is beyond the scope of this investigation.

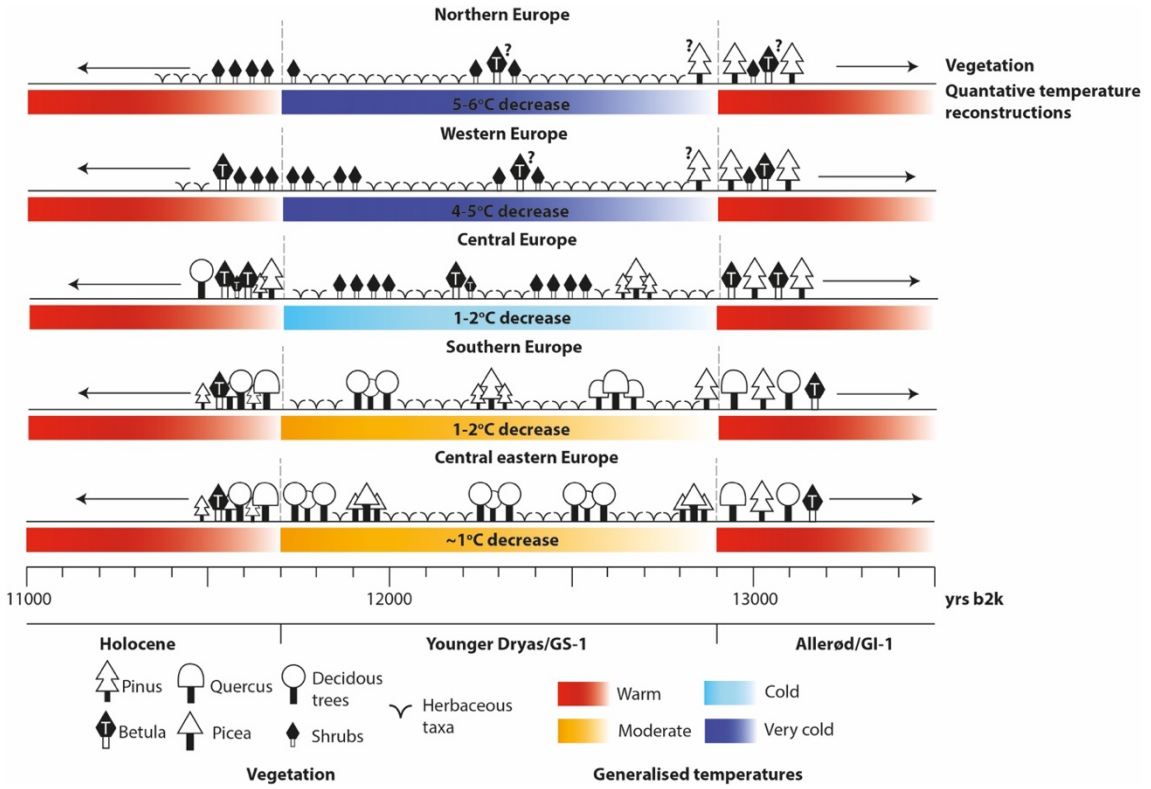


**Figure 2.2** The LGIT vegetation and climatic changes across the different regions in Europe. Local variations to the generalised view of vegetation change can be present and is due to additional factors such as soil, evaporation, growing season length, etc. For references, see text.

### 2.2.2 Centennial-oscillations in the earliest Holocene

After the cold YD period, a transition to warmer and drier conditions was recorded around 11.7ka b2k in the GIC, the Holocene onset (Blockley et al., 2012). The termination of the YD period is as abrupt as the onset with depletion in deuterium excess within three years and enrichment of $\delta^{18}O$ within 60 years (Steffensen et al., 2008).

There was a clear climatic response to amelioration with an increase in summer temperatures, indicated by C-IT (e.g. Brooks et al., 2012; Heiri et al., 2005) and a rise in relative mean annual temperatures from $\delta^{18}O$ records (e.g. Starkel, 1991; Lotter et al., 1992a). This resulted in ice retreat (e.g. Mangerud et al., 2013) and expansion of pioneer vegetation (*Pinus*, *Betula*) across the region (Figure 2.2, e.g. Ammann et al., 2000; Theuerkauf et al., 2014). With the expansion of tree taxa, herbaceous pollen species became a minor vegetation component due to competition and vegetation succession.

Within the GIC records, several rapid cooling events have been identified by Rasmussen et al. (2007, 2014) during the earliest part of the EH. The 11.4ka event, recorded in the decline of $\delta^{18}O$ values of NGRIP, GRIP and GISP archives and tentatively correlated to the classic PBO of Björck et al. (1997) (Rasmussen et al., 2014). Kobashi et al. (2008) showed a gradual decline in temperatures over 100-150 years. There are additional decreases in GIC $\delta^{18}O$ values following the 11.4ka event. This includes the identification of the 11.1ka event seen in the NGRIP record only (Rasmussen et al., 2007, 2014; Blockley et al., 2018).

Within European environmental records, the initial amelioration was interrupted by a cold event around 11,300 cal. years BP (Björck et al., 1997). Climatic proxy records reveal a deterioration in summer temperatures of ~0.5-1°C by C-IT (e.g. Brooks and Birks, 2001; Tóth et al., 2015) and either a change in temperatures and/or precipitation source from $\delta^{18}O_{bulk}$ (e.g. Lotter et al., 1992a; Whittington et al., 2015). Several climatic records

see an additional proxy response to subsequent EH climatic changes (e.g. Whittington et al., 2015; Blockley et al., 2018)

Within the vegetation record, an early cooling oscillation, defined termed by Björck et al. (1997) as the PBO, was predominantly recognised within pollen records within northern and western European records (e.g. Björck and Wastegård, 1999; Bos et al., 2007; Vorren et al., 2009) with further identification of this event in central-eastern Europe (e.g. Usinger, 2004; Magyari et al., 2012; Pál et al., 2018; Ott et al., 2016). This event was characterised by a general decline in arboreal pollen, mainly *Pinus* and thermophilous (warm-loving) species, with an expansion of birch forests, light-demanding shrubs and open grassland species across northern Europe (e.g. Björck et al., 1997; Björck and Wastegård, 1999; Vorren et al., 2009; Paus et al., 2015), western Europe (e.g. Lotter et al., 1992a; Bos et al., 2005, 2007; Finsinger and Tinner, 2006), central Europe (e.g. Goslar et al., 1995; Ralska-Jasiewiczowa et al., 2003; Bos and Urz, 2003; Bos et al., 2008; Boettger et al., 2009; Wacnik, 2009; Lauterbach et al., 2011; Stančikaitė et al., 2009, 2017) and southern Europe (e.g. Magyari et al., 2012, Pál et al., 2018, Drescher- Schneider et al., 2007). However, there have also been additional cooling events recorded in pollen records across Europe within the EH period (e.g. Bochnek and Hoek, 2007; Fiłoc et al., 2018; Blockley et al., 2018). This indicates a complicated climatic time.

## 2.3 Mechanisms of abrupt climate change for the Younger Dryas and earliest Holocene oscillations

There have been several possible causes proposed for these abrupt cooling events during the LGIT. There is wide acceptance for the onset of the YD to be related to the mass release of glacial freshwater into the North Atlantic changing ocean circulation (McManus et al., 2004; Praetorius et al., 2008). The source of this input has been disputed

between Lake Agassiz in North America (Broecker et al., 1985), Laurentide Ice sheet (Broecker et al., 1989) and the SIS (Muschitiello et al., 2015). Climatic modelling simulations and comparisons to proxy data have suggested that a combination of oceanic, solar and atmospheric changes resulted in the trigger for the onset of the YD (Renssen et al., 2015). The use of proxy data in these computer models highlights the need to provide robust chronologies for records to allow a better understanding of these drivers.

A similar scenario involving the North Atlantic has been suggested for the EH oscillations (specifically the PBO) with freshwater inputs from Lake Agassiz (Fisher al., 2002; Teller et al., 2002; Aharon, 2003; Nesje et al., 2004) and/or the Baltic ice lake via the Nordic Seas (Björck et al., 1996, 1997; Hald and Hagen, 1998; Husum and Hald, 2002). A decrease in solar activity may also be connected to these cooling events. Van der Pilcht et al. (2004) presented an increase in cosmogenic nuclides ($^{14}C$ and $^{10}Be$) that has been dated to or around the same time as the cooling event, indicating a solar minimum event (Teller et al., 2000; Björck et al., 2001; Magny, 2007; Wanner et al., 2011). These several possible mechanisms for the EH cooling event(s) show the complexity of the Earth's climatic system and subsequent environmental response (Björck and Wastegård, 1999; van der Pilcht et al., 2004; Bos et al., 2007, 2008). The following section provides a review on the climatic forcing of these hypotheses.

### 2.3.1 Oceanic circulation

Ocean circulation is the main mechanism behind heat transport between the Tropics and northern latitudes (Figure 2.3). Differences in salinity and water temperature drive the thermohaline conveyor of the Atlantic Meridional Overturning Circulation (AMOC; Clark et al., 2002). The warm, salty water of the Gulf Stream is driven by prevailing winds to the northern latitudes, transferring heat to Europe. As it cools, density

increases resulting in sinking and formation of the North Atlantic Deep Water (NADW) current. This then flows southwards, returning to the tropics (Figure 2.3). Freshwater input into the North Atlantic changes oceanic density, disrupting NADW formation, causing a weakening or termination of AMOC (Rahmstorf, 2002; Clark et al., 2002, Figure 2.3).

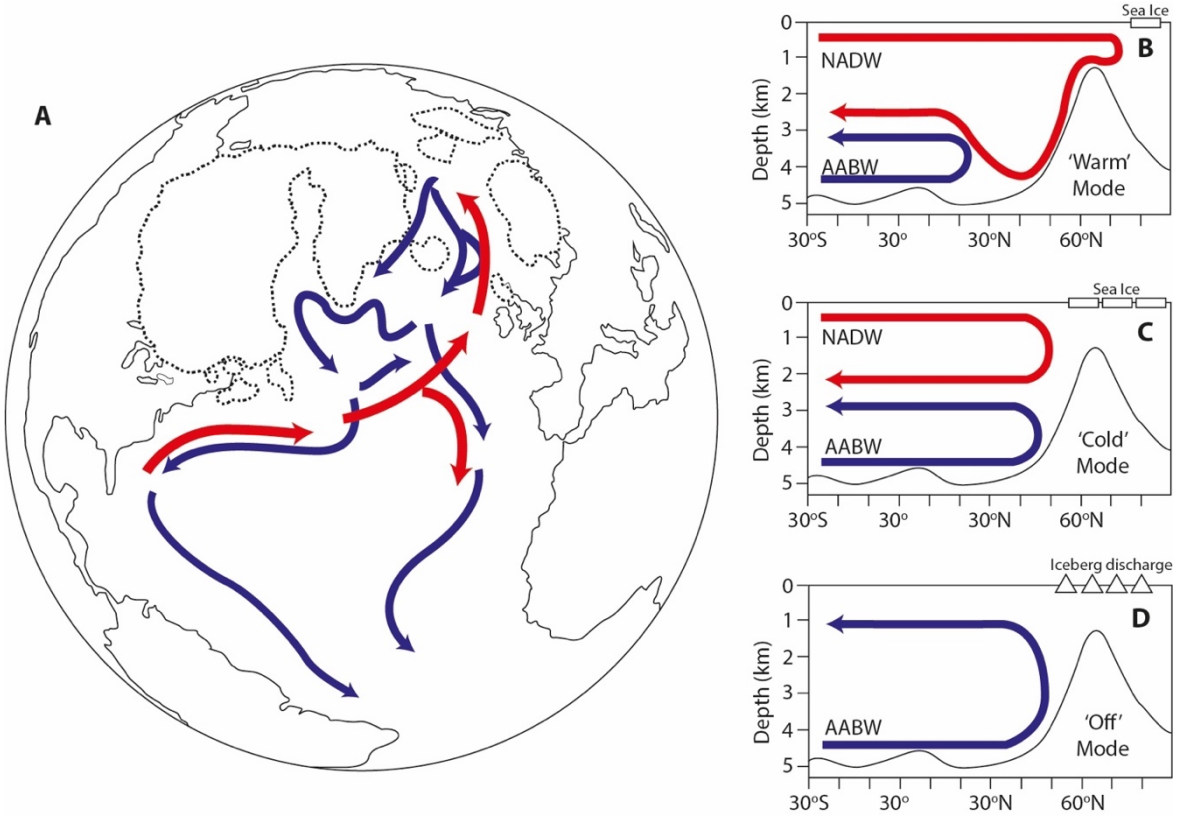


**Figure 2.3** Schematic of ocean circulations A) Adapted map of Atlantic Meridional Overturning Circulation from Muschitiello et al. (2019) with red arrows showing the direction of warm Atlantic flow to the Nordic Seas and the blue arrows of the returning colder bottom waters. B-C additional schematic on the three different modes of the North Atlantic circulation. B) Is the 'warm' mode experienced in interglacials such as the Holocene with North Atlantic Deep Water (NADW) being active with deep water circulation; C) 'cold' mode or glacial as NADW has a shallower circulation with an increase in sea-ice expanse; D) 'off' mode results from pulses of meltwater into the North Atlantic resulting in the collapse of the NADW and governance of the Antarctic Bottom Water (AABW) with ice berg discharge related to Heinrich events. The YD has been associated with Heinrich event 0 (Andrews et al., 1995). Adapted image from Böhm et al. (2015).

The latent heat transfer is affected, resulting in cooler oceanic temperatures allowing the sea-ice limit to extend further south into the Nordic Seas (Isarin et al., 1998;

Broecker et al., 2006). This produces thermal gradients between the colder north and warmer southern latitudes (Ruddiman and McIntyre, 1981). Changes in sea-ice coverage and placement have been demonstrated to displace the polar front to the south with westerly winds bringing colder climatic conditions to Europe (Broecker et al., 2006; Bakke et al., 2009). This interplay between ocean and atmospheric circulations has been primarily regarded as the scenario for the YD (e.g. Ruddiman and McIntyre, 1981; Isarin and Renssen, 1999; Brauer et al., 2008). Similar changes in the AMOC have also been proposed as a driver for colder oscillations during the EH (Björck et al., 1996, 1997; Nesje et al., 2004).

### 2.3.2 Solar forcing

Variations in the Sun's magnetic activity, recorded as total solar irradiance (TSI), are superimposed on more extended timescale changes of orbital forcing of the Milankovitch cycles (e.g. Martinson et al. 1987). TSI shifts, recorded by fluctuations in cosmogenic nuclides of Beryllium-10 ($^{10}$Be) and carbon ($^{14}$C) (Steinhilber et al., 2009; Reimer et al., 2013), have been shown to affect past climate on various time scales (e.g. 11-year Schwabe cycle; Engels and van Geel, 2012). In the upper atmosphere, $^{10}$Be reacts with aerosols and is recorded in sediments and ice-cores, while $^{14}$C enters the global carbon cycle (van Geel et al., 1999; Adolphi et al., 2018). When solar activity is low, cosmogenic nuclide production increases as more cosmic rays penetrate Earth's atmosphere (van Geel et al., 1999; Steinhilber et al., 2009).

Changes in TSI results in feedback mechanisms. The 'bottom-up' mechanism involves solar radiation being absorbed by the oceans, affecting evaporation and moisture, which leads to changes in precipitation patterns and trade wind locations (Meehl et al., 2003). The 'top-down' mechanism involves solar heating of the stratosphere and effects on

ozone feedback; this then impacts on the tropospheric circulations, such as the North Atlantic Oscillation (NAO; Haigh, 1996). During a solar minimum, there were reduced pressure gradients with a negative NAO over Europe. North Atlantic storm tracks are shifted south with northern Europe being cold and dry, with moist air to central and southern Europe (Figure 2.4; Martin-Puertas et al., 2012). It is proposed that both these mechanisms work together, amplifying the effect of solar minima (Gray et al., 2010).

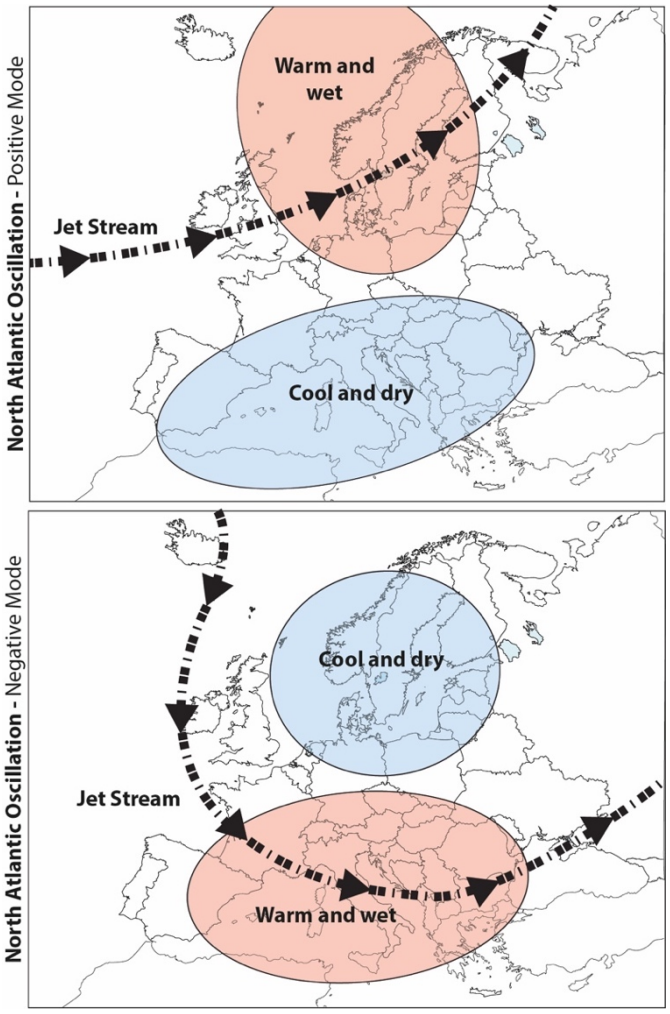


**Figure 2.4** The different modes of the North Atlantic Oscillation (NAO). During the positive mode, northern Europe experiences warm and wet winters while central and southern Europe are cooler and dry. During a negative mode, northern Europe becomes cold with central and southern Europe are warm and wet (adapted from text in Magyari et al., 2013). Changes in the strength and mode of the NAO is understood to have changed throughout the Last Glacial-Interglacial period.

The effects of TSI variability on climatic conditions in Europe are well known during the EH (e.g. van Geel et al., 1999; Martin-Puertas et al., 2012). During the LGIT,

studies have suggested the influence of TSI on climatic variability (e.g. Magny et al., 2006; Aldophi et al., 2014). Many studies have proposed that the ocean can be amplifying low TSI (e.g. van Geel et al., 1999; Bos et al., 2007).

## 2.4 The timing of abrupt climatic transitions across Europe

To resolve the timing of transitions for abrupt climatic oscillations during the LGIT, and thus provide insight into the climatic and environmental drivers, a robust chronology must be derived for the records. The most widely applied dating technique during this period is radiocarbon dating, providing a chronostratigraphic framework for the LGIT oscillations in many European records. This section will focus on providing an introduction into the technique, it's caveats and application to dating the YD and EH oscillations.

### 2.4.1 Providing chronologies - Radiocarbon dating

Radiocarbon dating is based on the radioactive decay of the naturally occurring radioisotope carbon-14 ($^{14}C$). This cosmogenic isotope is oxidised to $^{14}CO_2$ with atoms of $^{14}C$ incorporated into carbon-bearing material, e.g. wood, seeds, bulk sediment (Libby et al., 1949). The half-life of $^{14}C$ is 5,730 ± 40 years allowing apparent radiocarbon ages to be calculated from organic materials (Godwin, 1962). This involves the measurement of $^{14}C$ relative to the stable carbon isotopes of $^{13}C$ and $^{12}C$ using Accelerator Mass Spectrometry (AMS). However, radiocarbon can only provide accurate ages to ~50,000 years ago as a result of its half-life.

#### 2.4.1.1 Calibration of radiocarbon ages

To provide a 'true' calendar age for samples after dating, the reported radiocarbon dates ($^{14}$C yrs BP, see section 1.4) have to be calibrated. This is due to underestimating of the $^{14}$C half-life (e.g. Chiu et al., 2007) and the natural variability of the production and uptake of $^{14}$C between the atmosphere (e.g. solar minima (Steinhilber et al., 2009) and oceans (e.g. changes in THC (Broecker et al., 1989)). Using independently dated archives of annually dated tree-rings (dendrochronology) and plant macrofossils in varved sediments with independently dated corals and speleothems using U-series dating (to reduce the problems of the reservoir effect), changes in atmospheric $^{14}$C can be measured and presented as a 'best-estimate' curve with uncertainty, termed IntCal(International Calibration). With time, IntCal has undergone many advances with the recent curve of IntCal13 producing a tree-ring $^{14}$C data up to 13,900 cal. BP (Reimer et al., 2013). Using the IntCal13 curve allows for more accurate and precise ages than previous calibration curves, which is key for understanding climatic (a)synchronicity (Figure 2.5).

#### 2.4.1.2 Bayesian age modelling

To provide further accuracy and precision in calibrating radiocarbon dates, Bayesian statistics can be used (Blaauw et al., 2018). The Bayesian approach allows prior information and assumptions about the data to be incorporated into the process of calibrating ages. The 'prior model' is information on the sedimentary sequence (e.g. linear deposition, stratigraphic position of dates) together with the 'likelihood' of the radiocarbon dates themselves ($^{14}$C yrs BP ± uncertainty). This produces an updated 'posterior' probability density of the calibrated age which includes statistical uncertainties, the key to understanding the timing of climatic transitions (Bronk Ramsey, 2008). Several computer

packages allow for radiocarbon calibration using Bayesian statistics. OxCal was used in this project (Bronk Ramsey, 1994, 1995).

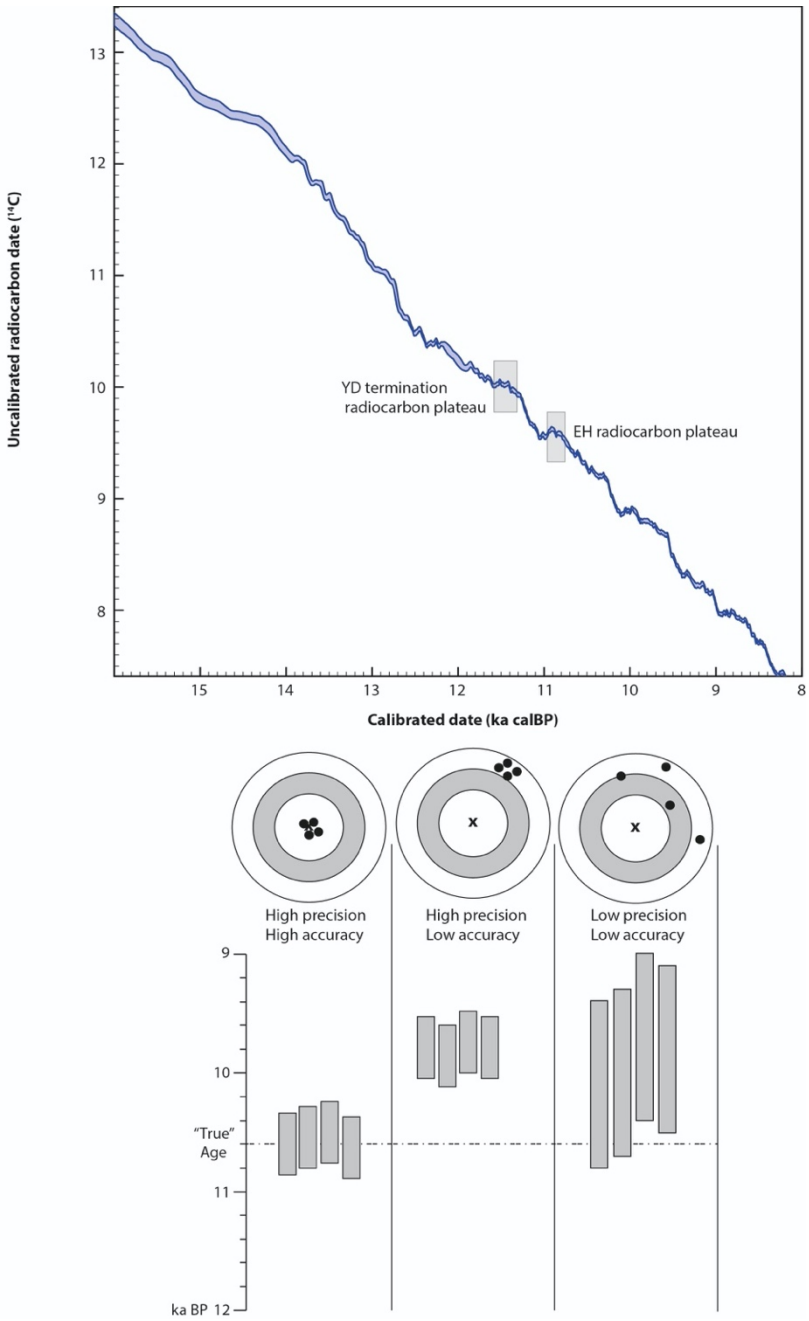


**Figure 2.5** The IntCal13 calibration curve for the LGIT is presented in the top panel (Reimer et al., 2013; Bronk Ramsey, 2019). Highlighted are radiocarbon plateaus at the termination of the YD and earliest Holocene (EH) that produces errors when calibrating radiocarbon ages around these terminations. The lower panel presents the difference between precision and accuracy in dating. Precision refers to the uncertainty associated with a date while accuracy is how well the dates corresponds to the "true" age. To regard a date as reliable or uncertain, precision and accuracy need to be taken into account as well as additional information associated with the record (i.e. taphonomy). Adapted from Schoene et al. (2013).

### 2.4.1.3 Limitations of radiocarbon dating

As with every dating technique, there are caveats with using radiocarbon dating (Table 2.2). When using published radiocarbon dates produced for a site by different researchers, how the $^{14}C$ measurement was obtained also needs to be taken into account. This includes the material that has been dated (i.e. terrestrial plant macrofossils, bulk sediment, shells), the site setting (terrestrial or marine), the laboratory methods undertaken for sample preparation and the instrument precision (Table 2.2, Lowe and Walker, 2000).

The following sections present the issues associated with radiocarbon dating when investigating the timing of the YD and the earliest EH oscillations. INTIMATE produced several quality assurance protocols associated with obtaining and reporting precise ages from LGIT samples (Björck et al., 1998; Lowe and Walker, 2000; Lowe et al., 2008). This is outlined in Table 2.3.

**Table 2.2** Table presenting the limitations of radiocarbon dating lacustrine archives. Protocols can be applied to records to ensure these limitations are kept to a minimum (Lowe and Walker, 2000; Walker et al., 2001; Lowe et al., 2008).

| Limitations | References/ examples |
|---|---|
| Contamination from older or younger carbon from inwash (inorganic), root penetration, etc. | Walker et al., 2001 |
| Hard water error – dating aquatic macrofossils that have a diluted uptake of $^{14}C$ in carbonate rich waters. | Cwynar and Watts, 1989 |
| Reservoir effect dating lake sediments (bulk) – the slow mixing of lake waters with the atmosphere results in a lower exchange of $^{14}C/^{12}C$ ratio with consequences of variations in ages of up to 1,000 years. | Geyh et al. (1998) |
| Dating shells can have problems with older or younger carbon. | Lawson et al., (2004) |
| Dating bulk organic samples – used at sites that lack organic macrofossils for dating (e.g. Hubay et al., 2018). Bulk ages can be different to plant macrofossils from the same depth. | Walker et al., 2001 |
| If the age produced from dated material are a true representation of the material from a particular horizon. | Lowe et al., 2007 |
| Carbon plateaus during the LGIT (Figure 2.5) - A radiocarbon plateau is when the atmospheric radiocarbon ration $^{14}C/^{12}C$ became equal to the radiocarbon decay (Guilderson et al., 2005). This can result in large age uncertainties from dates obtained around these plateaus. | Björck et al., 1997 |
| Limitation of current calibration models to convert $^{14}C$ dates to calibrated ages. The IntCal13 currently has problems surrounding the end of the YD-EH transition | Reimer et al., 2013 |

**Table 2.2** cont.

| Limitations | References/ examples |
|---|---|
| Larger age uncertainties with older material – limit of radiocarbon ~50 kya | Brauer et al., 2014 |
| Low carbon in dating samples can affect precision resulting in larger age errors | Preece and Bridgland, 1999 |
| Instrument precision – AMS machines vary standard errors produced. Typically errors range from <100-30 $^{14}$C years. | Olsson, 2009 |

**Table 2.3** The laboratory protocols and reporting outlines for radiocarbon dating (adapted from Lowe and Walker, 2000).

| | |
|---|---|
| **Sample integrity** | • Laboratory number for sample<br>• Stratigraphic information from where sample was obtained (depth, sample resolution)<br>• Material type dated (terrestrial plant macrofossils, shells)<br>• Organic carbon content and carbonate content<br>• Wet weight of sample submitted to laboratory<br>• Total organic dry weight of carbon used in radiocarbon measurement<br>• Tests for radiocarbon activity on bulk material (humic vs humin, other fractions tested) |
| **Laboratory handling** | • Date of sample collection<br>• Date of submission to laboratory for dating<br>• Storage conditions of sample and treatment<br>• Nature of solvents, dispersants used<br>• Conditions samples where extracted and packaged to laboratory |
| **Radiocarbon laboratory procedures** | • Dates samples received and counted<br>• Storage conditions<br>• Pre-treatment procedures<br>• Laboratory sample number<br>• Count statistics<br>• Corrections applied – fractionation, reservoir effect<br>• Comments on unusual chemical effects during pre-treatment |
| **Calibration procedures applied** | • Calibration data-set employed – IntCal13<br>• Specify any smoothing or rounding procedures applied<br>• Single calibration or series of calibrations |

### 2.4.2 The Younger Dryas onset and termination across Europe

The abrupt onset and termination of the YD stadial have been widely presented as synchronous on regional, hemispheric and global spatial scales (e.g. Goslar et al., 1995). However, there is now growing evidence for time-transgression of abrupt climatic changes

across different spatial scales (e.g. Pedro et al., 2011; Lane et al., 2013; Buizert et al., 2015; Muschitiello and Wohlfarth, 2015). The INTIMATE protocol calling for records to be independently dated and proxies examined upon their timescale has allowed for an investigation into the spatially synchronous nature of the YD to be called into question (Björck et al., 1998; Lowe et al., 2008). However, chronological problems remain when investigating the spatial and temporal expression of this stadial.

Dating terrestrial palaeoenvironmental records has been extensive since the introduction of radiocarbon dating (e.g. Willkomm and Erlenkeuser, 1973). The chronostratigraphic framework for the YD of Mangerud et al. (1974) has led to the transference of this terminology to different archives, records, proxies and regions with many studies using the dates for this chronozone for their record. Despite the introduction of the INTIMATE event stratigraphy and adoption of GS-1 for this period in the ice cores (only), there is continued misuse of this term in a chronostratigraphic sense (Lowe et al., 2019). Many studies use the ages of the YD or GS-1 to "date" their record (e.g. Marshall et al., 2002; Brooks et al., 2012). Using the terminology in this manner has limited the discussion and understanding of the propagation of abrupt climatic change and how it impacted on different environments (Lane et al., in preparation).

The resolution of radiocarbon dates applied to terrestrial archives varies significantly between individual sites. Many records have dates at a low resolution, with poor distribution of dates across the LGIT (Blaauw et al., 2018). Around the YD, low organic production has resulted in limited dating material which makes obtaining dates particularly difficult (e.g. Hubay et al., 2018). Precision and accuracy of chronologies is key to answering many palaeoenvironmental questions (Blaauw et al., 2018). At many sites across Europe, the low chronological resolution can have a detrimental effect on assessing (a)synchronicity due to the large age uncertainties produced. In addition, low

proxy resolution can also have a negative effect when identifying climatic transitions in the pollen record (Wohlfarth et al., 2006; Engels et al., 2016; Abrook et al., 2019).

To address difficulties in direct dating, many studies use dates of regional biostratigraphic changes to adjust a record's chronology (e.g. Reille and Lowe, 1993; Farcas et al., 1999; Heiri et al., 2007). This limits the understanding of past climate and environmental synchronicity due to: 1) the known slower response of vegetation development to climatic change; and 2) regional and local vegetational differences. Many other studies tune their records to the well-resolved archive of the GICs. This is to either: 1) attempt to improve the existing age model (e.g. Hoek and Bohncke, 2001; Heiri et al., 2005, 2007); or 2) provide an age model for a record that lacks dating (e.g. Marshall et al., 2002; van Asch et al., 2012). Tuning involves pattern matching in proxy signals through either statistical or visual analysis. Differences in the magnitude of proxy response can be undertaken, yet no independent chronology can be created (Lane et al., in preparation). This results in assumptions that climatic change is synchronous. However, the local or regional climatic response may exist and be time-transgressional (Lane et al., 2013; Brauer et al., 2014).

The problem of radiocarbon calibration plateaus over the YD transition can result in dates obtained from this period having large age uncertainties (Figure 2.5, Table 2.2; e.g. Reille and Lowe, 1993; Birks et al., 2012; Brooks et al., 2012; Lascu et al., 2015). This produces issues when investigating the timing of environmental and climatic response across Europe as age uncertainties may obscure centennial or decadal-scale time-transgression.

Several studies have recently shown the asynchronous nature of the YD climatic transition, highlighting the need to test assumptions of climatic synchronicity. Muschitiello and Wohlfarth (2015) undertook Bayesian age modelling on dated palynological records

within northern Europe. Results showed a time-transgression in vegetation response to the onset of the YD. It was postulated that freshwater input from the SIS resulted in sites situated at 56-54°N responding before sites at 60-58°N. This difference was linked to the resilience of vegetation in the furthest northern sites of Kråkenes, Norway and Lake Madtjärn, Sweden (Muschitiello and Wohlfarth, 2015). An additional site, Hässeldala port, Sweden investigated by Wohlfarth et al. (2016), provided further pollen evidence for a time-transgression response to the onset of the YD. However, additional proxies, other than pollen, were used to define the YD boundary at some sites. Rach et al. (2014) identified a 170 year lag between hydrological changes in a terrestrial varved record and GS-1 in GIC. Variations in hydrogen isotopes in lipid biomarkers (δD, see Table 2.1) were related to the displacement of the Westerly storm track. These studies are confined to the northern latitudes. However, there several dated palaeoenvironmental records currently available from across Europe investigate the synchronicity of the YD onset and termination further.

### 2.4.3 The timing and characteristics of earliest Holocene oscillations throughout Europe

Since Björck et al. (1997) dated the Preboreal Oscillation (referred to hereafter as the 'classic PBO') from northern European pollen records, numerous other investigations over the EH period have identified multiple "PBOs" within their proxy records (e.g. Whittington et al., 1996; Theuerkauf et al., 2014). The timing of PBOs vary from terrestrial records across Europe (Figure 2.6), e.g. the Netherlands (11,430-11,350 cal. BP - Bos et al., 2007; 11,400-11,300 cal. BP – Bohncke and Hoek, 2007), Lithuania (11,200 to 11,100 cal. BP – Stančikaitė et al., 2017), Poland (11,300 to 10,800 cal. BP – Wacnik, 2009), Switzerland (11,450-11,350 cal. BP – Ilyashuk et al., 2009) and Romania (11,480-

11,390 cal. BP – Tóth et al., 2012). Other sites have recorded several cooling events in the EH, with studies correlating these environmental responses to the classic PBO event despite apparent differences in their timing (e.g. Whittington et al., 1996; Björck and Wastegård 1999; Ralska-Jasiewiczowa et al., 2003; van der Pilcht et al., 2004; Andresen et al., 2007; Bos et al., 2008; Magny et al., 2012; Fiłoc et al., 2018; Figure 2.6).

Additional confusion around the climatic characteristics of the PBO has led to difficulty in identifying the proposed climatic event. The Rammelbeck Phase is palynologically defined by Bohncke and Hoek (2007) as a drier period and is seen as a different climatic event to the PBO. However, the climatic conditions for both events are debatable. It seems to be dependent on the latitudinal and longitudinal position of sites and their chronological controls (e.g. Magny et al., 2007). Diachrony may exist. Discrepancies in the age of the cooling event labelled as the 'PBO' across Europe, coupled with evidence for multiple early-Holocene cooling events in high-resolution archives (i.e. GIC) means that it can be hypothesised that not all reported "PBOs" relate to the same overall climatic cooling.

In contrast, many dated palynological records have highlighted an absence or lack of clear environmental response to this cooling event(s) (e.g. Jahns, 2000; Hoek and Bohncke, 2001; Bos et al., 2007). Problems with proxy resolution and response may have resulted in the short, abrupt climatic EH oscillations not being recorded at some sites (Lotter, 1999; Hoek, 2001; Birks and Birks, 2008; Theurkauf et al., 2014; Fiłoc et al., 2018). The events identified within different site records correlated to the classic PBO have shown that the duration of the abrupt event is short, varying from ~50-400 years (e.g. Amman et al., 2000; Ott et al., 2016; Fiłoc et al., 2018; Martin-Pilertas et al., 2017). As a result, many sedimentary records do not have the temporal resolution to resolve this event.

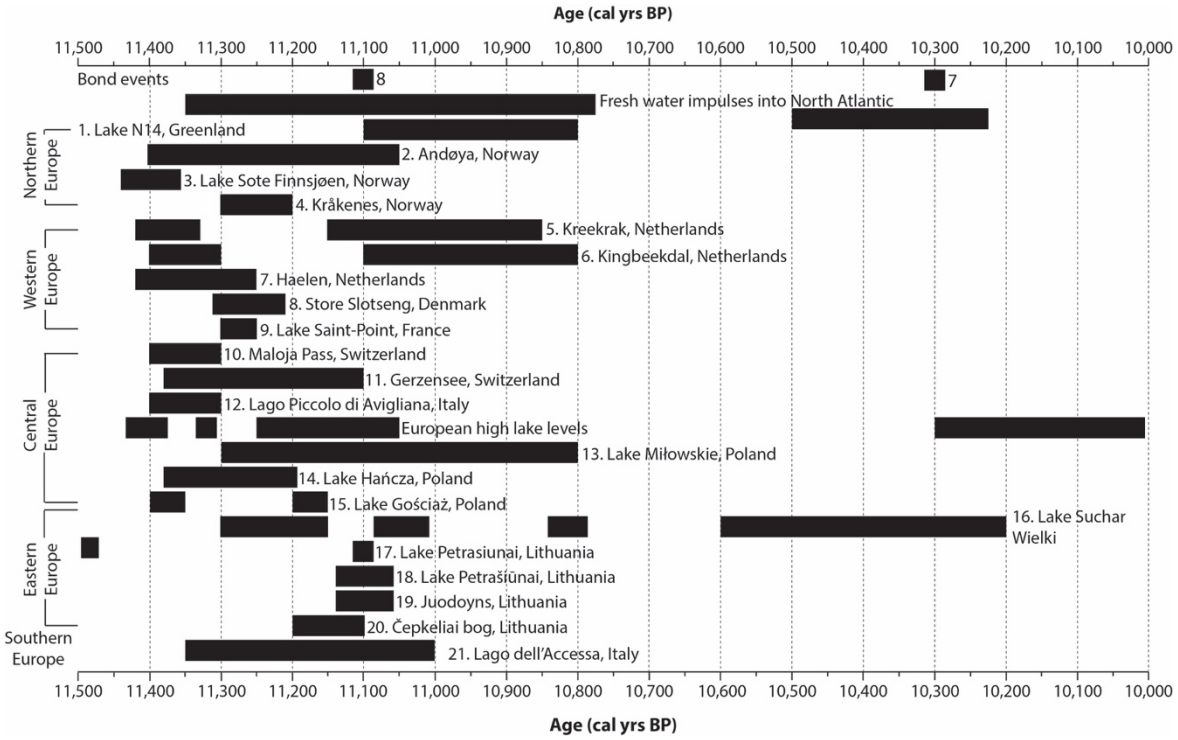


**Figure 2.6** Timings of earliest Holocene cooling events identified at sites across Europe in different proxies (adapted from Fiłoc et al., 2018). The solid black lines show the timing of these cooling events. There is a cluster of events around 11.3kya across Europe that may suggest a continental scale environmental response to a climatic cooling, indicative of the classic PBO. However, there is evidence of environmental feedbacks to other cooling climatic events during the earliest Holocene which could be due to chronological problems associated with the record .The sources for these timing are; Bond cold events (Bond et al., 1997, 2001); Fresh water impulses into the North Atlantic (Nesje et al., 2004); 1) Lake N14, Greenland (Andresen et al., 2007); 2) Andøy, Norway (Vorren et al., 2009); 3) Lake Sote Finnsjøen, Norway (Paus et al., 2015); 4) Kråkenes, Norway (Birks and Birks, 2008); 5) Kreekrak, Norway (Bos et al., 2005, 2007); 6) Kingbeekdal, Netherlands (Bohncke and Hoek, 2007); 7)Haeleen, Netherlands (Bos and van Geel, 2017); 8) Store Slotseng, Denmark (Larsen and Noe-Nygaard, 2014); 9) Lake Saint-Point, France (Magny et al., 2013); 10) Maloja Riegel, Switzerland (Ilyashuk et al., 2009); 11) Gerzensee, Switzerland (Lotter et al., 1992a, b, 1999; Brooks et al., 2013); 12) Lago Piccolo di Avigliana, Italy (Finsinger and Tinner, 2006; Larocque and Finsinger, 2008); and periods of higher lake levels in mid-European lakes (Magny et al., 2007); 13) Lake Miłowskie, Poland (Wacnik, 2009); 14) Lake Hańcza, Poland (Lauterbach et al., 2011); 15) Lake Gościaz, Poland (Pazdur et al., 1995; Ralska-Jasiewiczowa et al., 2003); 16) Lake Suchar Wielki, Poland (Fiłoc et al., 2018); 17) Lake Petrasiunai, Lithuania (Stančikaitė et al., 2009); 18) Lake Petrašiūnai, Lithuania (Stančikaitė et al., 2009); 19) Juuodonys, Lithuania (Stančikaitė et al., 2009); 20) Čepkeliai bog, Lithuania (Stančikaitė et al., 2017); 21) Lago dell'Accesa, Italy (Drescher-Scheider et al., 2007).

Problems such as low sedimentation rates that decrease temporal resolution, bioturbation and poor proxy preservation can also affect the sampling and temporal resolution for many

records. The lack of response to these cooling event(s) within lacustrine records has been recognised in some studies (Björck et al., 1997; Ott et al., 2016).

Thoroughly investigating the timing of the EH oscillations within disparate European terrestrial records is restricted by dating limitations. There is a radiocarbon plateau present from 10,000-9,900 and 9,600-9,500 uncalibrated $^{14}$C yrs, coinciding with the timing of the proposed PBO (Figure 2.5; Björck et al., 1996; van der Pilcht et al., 2004; Bos et al., 2007). This results in large calibrated age uncertainties that can be larger than the short duration of the EH events themselves. The lack of or limited dating applied at some sites has resulted in chronological uncertainty around the timing of the EH period (e.g. Anderson et al., 2004; Bos et al., 2007; Stanačikaitė et al., 2009).

Also, the use of wiggle-matching of records using similar palaeoenvironmental responses results in the assumption that climatic change is synchronous across a region where there may be local variances (e.g. Lotter et al., 1999; Pál et al., 2018). These chronological uncertainties result in limiting our ability to fully understand the possible timing and characteristics of abrupt cooling events during the earliest Holocene across Europe.

Investigations into the time-transgressive nature of EH oscillations have not previously been undertaken using proxy records (Wiersma et al., 2011). This is possible due to the issues previously stated. However, spatial and temporal expression of centennial-scale oscillations throughout the Holocene period has been examined. Wiersma et al. (2011) used climatic model simulations to investigate the potential of the abrupt climatic event of the 8.2ka. Computer simulations on decadal scales presented changing temperature patterns across the globe. A lag in the order of several decades showed that the cooling was not synchronous. A delayed response of ~30 years was recorded over Greenland after the initial freshwater impulse (the proposed driver for the 8.2ka climatic

event) into the North Atlantic Ocean. In addition, simulations highlighted response to this cooling event diminished the further from the North Atlantic Ocean a site was located (Wiersma et al., 2011).

However, there are limited investigations into centennial-scale abrupt events within the proxy record. Lane et al. (2013) demonstrated that using varve records in northern Europe, coupled with a tephra layer, can provide insight into centennial-scale drivers. The climatic change is demonstrated to be asynchronous, and the migration of the polar front is hypothesised as the causative mechanism. This was with the mid-YD climatic shift which may have been a larger amplitude climatic forcing in comparison to EH oscillations. Similar climatic mechanisms are believe to drive centennial-scale climatic oscillations that could be identified as time-transgressive in palaeoenvironmental records.

## 2.5 Integrating records

To investigate the temporal and spatial characteristics of millennial- and centennial-scale abrupt climatic oscillations, different proxy records from different sites must be compared on their own timelines. Additional techniques can improve the accuracy and precision of age modelling, helping to test the synchronicity of individual archives. The following section provides insight into two of these techniques: 1) tephrochronology; and 2) the INTIMATE database integration tool.

### 2.5.1 Tephrochronology

Tephra is a product of an explosive volcanic eruption, comprised of unconsolidated pyroclastic materials ranging in particle size (e.g. bombs, pumice fragments and volcanic ash). The fine ash product of these eruptions can travel far from the volcanic source (Figure 2.7). Individual ash/tephra layers can be geochemically identified through their

glass shard chemical properties (Westgate and Gorton, 1981). This allows linkages to be made between sites and several different sedimentary records (e.g. marine, terrestrial, archaeological sites) in both proximal and distal settings (tephrostratigraphy). The dispersal and deposition of tephra in these sedimentary archives are believed to be virtually instantaneous (e.g. few days to months after the initial eruption), producing isochronous layers in sedimentary archives (Thórarinsson, 1944). In principle, this allows tephra to improve the dating of other archives through the transfer of ages from a relative or absolute dating site (tephrochronology).

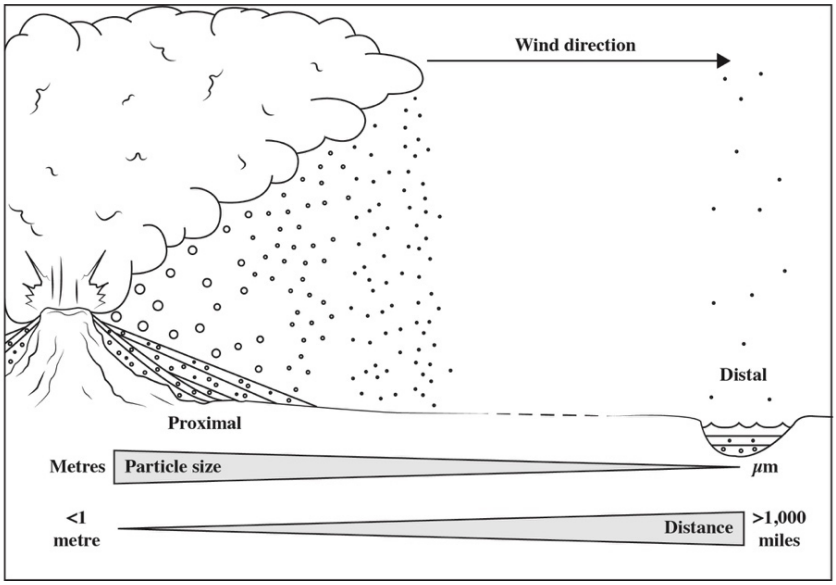


**Figure 2.7** Schematic of tephra deposition. Thick and coarse deposits are found closest to the volcanic source. The smallest shard sizes are transported the furthest and deposited into distal records in the dominant wind direction at the time of plume formation.

The study of visible tephra layers and their chronostratigraphic linkages has been extended across the world (e.g. Davies et al., 2012; Moriwaki et al., 2016). Within the last few decades, microtephra or cryptotephra, non-visible volcanic ash, investigations have greatly extended the application of tephrochronology (Lowe et al., 2015; Lane et al., 2017). The development of the density separation method (Turney, 1998; Blockley et al., 2005) has been vital in extracting these fine-grained glass shards (<125μm) from

sedimentary archives. The smallest glass shards are carried long distances with the volcanic ash found to be dispersed across continental distances (Figure 2.7; e.g. Jensen et al., 2014; van der Bilt et al., 2017). A European example is that of the wide dispersal of the Vedde Ash. This tephra erupted from Katla volcano, Iceland during the middle of GS-1 and formed a visible layer seen in many records from the Greenland ice cores, across the North Atlantic region (Waelbroeck et al., 2001; Lowe et al., 2008). The cryptotephra horizons identified and associated with this ash dispersal extends further across Europe, from Scotland (Lowe and Turney, 1997; Matthews et al., 2011) to Russia (Wastegård et al., 2000a; Haflidason et al., 2019) and as far south as Slovenia (Lane et al., 2011a).

In many cases, the geochemical composition of tephra is unique to a volcanic source and/or eruption as this is controlled by crustal material, crystal fractionation and other processes (Hall, 1996). These geochemical compositions of the glass shards are important in distal cryptotephra investigations when other diagnostic elements, such as mineralogy and lithology found in proximal settings, are lacking (Shane, 2000; Lowe, 2011).

The geochemical composition of tephra is typically determined using an Electron Probe Micro-analyser (EPMA) with wavelength dispersive spectrometry, measuring the major and minor element composition of individual glass shards and presenting them as percentage weight ($SiO_2$, $Al_2O_3$, FeO, $TiO_2$, MnO, MgO, CaO, $Na_2O$, $K_2O$, $P_2O_5$; Lowe, 2011). The results are then normalized (to remove water content from the glass) and can then be compared to other compositional data of known volcanic sources and/or geochemically characterised eruptions. Database tools such as that of the RESET project (RESponse of humans to abrupt Environmental Transitions, Bronk Ramsey et al., 2015) and Tephrabase (www.tephrabase.org) can be used to compare individual tephra geochemical datasets to help identify tephra. Additionally, trace element analysis by laser

ablation inductively coupled plasma-mass spectrometry (LA-ICP-MS) can be used as an additional discrimination tool to avoid miscorrelation of tephra (Lowe, 2011; Pearce et al., 2011; Lind et al., 2016). Due to the size constraints of cryptotephra, the beam size must be reduced resulting in less accurate results and robust tephra correlations (Tomlinson et al., 2012).

Tephra units can also be dated. At proximal sites, radiocarbon dating can provide relative ages from organic material found close to the tephra deposit (e.g. Lowe et al., 2007). Absolute dating by $^{40}$Argon/$^{39}$Argon through single-crystal laser fusion can be undertaken directly on tephra deposits (material containing, e.g. sanidine, anorthoclase, e.g. Smith et al., 2011). If the same geochemical tephra is found at other sites, especially distal locations, the given tephra age can be transferred to that record and used in subsequent age models (e.g. Lane et al., 2011a, Timms et al., 2017). Also, distal tephra can be dated through relative dating methods of radiocarbon age-depth models (e.g. Wohlfarth et al., 2006), varves (e.g. Brauer et al., 1999) and annual chronologies (ice cores, varve counting, e.g. Rasmussen et al., 2014; Ott et al., 2016). A tephra age can also be refined through a tephra framework or lattice. A tephra lattice is the linkage of chemically distinct tephra horizons in several well-dated sedimentary records (Lowe et al., 2015). For example, the RESET tephra lattice by Bronk Ramsey et al. (2015) has resulted in new, highly constrained ages for numerous widespread tephras identified across Europe, allowing these dates to be used to improve age models in which the tephra are found.

Tephrochronology and tephrostratigraphy are powerful tools that can be useful in providing insights into the timing and understanding of synchronisation of past climatic changes over large distances. Tephras that are well characterised and clearly identified to a dated eruption allow records to be more precise and reliable.

#### 2.5.1.1 Limitations of tephrochronology

As with every correlative tool, there are limitations associated with the successful application of tephrochronology/tephrostratigraphy. The activity and frequency of eruption of a volcanic centre can influence the occurrence of tephra within a record. The magnitude of the event, direction and strength of the prevailing wind has a considerable influence on the occurrence and horizon thickness of the tephra layer within the sedimentary archive. Sites situated near the volcano and under the path of prevailing wind directions have a higher chance of tephra deposition than those sites located further away and upwind.

Precise geochemical characterization of individual tephra shards is key to tephrochronology. Robustly correlating tephra layers to known volcanic sources and eruptions can be problematic, especially at distal sites. Having proximal deposits that can be fully geochemically analysed is useful to match distal occurrences of tephra to volcanic sources. However, older deposits can be removed by subsequent eruptions. This can limit the number of direct correlations made to tephra horizons in proximal archives.

Tephras of similar geochemical composition is particularly problematic for Icelandic derived cryptotephra layers deposited in European sedimentary records during the Late Glacial period (Davies et al., 2012). The temporally and stratigraphic similar Borrobol and Penifiler tephra layers that erupted during GI-1 are geochemically indistinguishable at a major and minor element level resulting in uncertainties in synchronizing archives using these tephra layers (Davies et al., 2012; Lind et al., 2016). Attempts were made to distinguish these two tephra layers through LA-ICP-MS of trace elements by Lind et al. (2016), but this was unsuccessful. Further investigation is needed, as the volcanic source on Iceland of these two tephra layers remains unresolved (Davies, 2015; Lind et al., 2016; Macleod and Davies, 2016).

Consideration of other factors, such as local geology, can also impact robust tephra geochemical correlations. This is seen at Sluggan Bog, Ireland, where previous investigations have highlighted particular tephra layers that remained uncorrelated to volcanic sources (Lowe et al., 2004). MacLeod and Davies (2016) recently equated these layers to the erosion of the local obsidian, close to the site. This is even though these shards looked morphologically 'fresh' (Macleod and Davies, 2016). Such effects must be taken into consideration when tephra correlation is undertaken.

The relative dating of tephra layers is limited by the dating method employed, mainly due to the absolute dates used. Radiocarbon dating is widely used during the LGIT period and up to its temporal limit of ~50 kya. There are uncertainties associated with each date, which, through age-depth modelling, are transferred to the tephra age. These uncertainties are usually larger than the related depth uncertainty within the specific records (potentially identifiable to the year). By combining several well-dated records that have tephra with the same geochemistry, these uncertainties can be substantially reduced.

Cryptotephras are extracted from sediments through continuous sampling within the laboratory. Shard concentration profiles are created across the sedimentary record (Davies et al., 2012; Lane et al., 2014). Low-resolution sampling (incorporating 5-10cm of sediment) and high-resolution (1-0.05cm of sediment) which are then processed by similar laboratory techniques outlined by Blockley et al. (2005). Individual tephra shards are counted under a high- powered microscope. This is the most effective and reliable practice for cryptotephra studies extensively employed in several investigations (e.g. Lane et al., 2011b; Timms et al., 2017).

#### 2.5.1.2 Tephra in lacustrine sediments

For cryptotephra research, understanding the depositional processes of the glass shards is essential in the identification of primary tephra deposition so that an isochron can be recognised. For this thesis, taphonomic processes affecting lacustrine records will be discussed.

Lacustrine archives are ideal for cryptotephra studies due to the rapid accumulation of sediments, preserving the tephra layers and producing higher chronological precision (Lowe, 2011; Davies, 2015). There have been extensive studies from such archives in Europe (e.g. Lane et al., 2011a, 2012a).

The peak in glass shard concentration within a record is seen to be associated with the timing of the volcanic eruption, the primary fallout or isochron. However, taphonomic processes can result in secondary deposition of shards, resulting in dispersion of shards up/down the profile (Figure 2.8). These taphonomic processes include;

- Bioturbation, where organisms living in the sediment of the lake activities can affect the sediment and tephra deposition by burrowing and feeding (Ruddiman and Glover, 1972).
- Underwater currents are disturbing the primary sediment deposition.
- Secondary mobilisation of shards due to entrapment by snow cover and subsequent melting (Davies et al., 2007) or erosion of the local landscape due to low vegetation into the lake (Pyne-O'Donnell et al., 2008).
- Physical features such as inlets and catchment size can influence tephra shard distribution and preservation across a lake (Pyne-O'Donnell, 2011).
- Low sedimentation rates can decrease chronological precision and no clear cryptotephra tephra horizons.

There are problems when there is no distinct peak in glass shard concentrations, with more than one seen (e.g. Davies et al., 2007; Pyne-O'Donnell et al., 2008). Undertaking high-resolution shard concentration investigations can provide insight into these taphonomic processes (Davies et al., 2012; Davies, 2015; Timms et al., 2017).

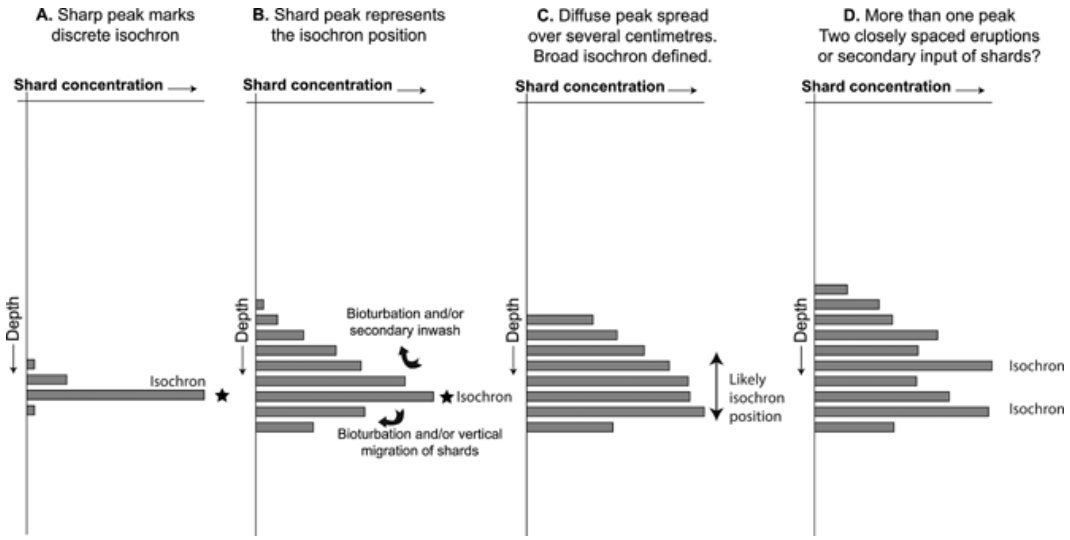


**Figure 2.8** Diagram showing the possible different shard concentration profiles that can occur in lacustrine sedimentary environments. The depth with the highest shard concentration is defined as the isochron (A). Sediment and catchment processes can result in an unclear isochron (B and C). Two isochrones in stratigraphically found close together, can indicate two different eruptions or secondary shard input (D). Image after Davies et al. (2012, 2015).

#### 2.5.1.3 An ideal tephra layer for correlating sedimentary archives

For a tephra layer to be useful within palaeoclimatic studies, it ideally needs to be (Lowe, 2011):

1. Geographically widespread and found in multiple and diverse sedimentary records across a region.
2. Geographically distinguishable from other tephra deposits erupted from the same source volcano and other volcanoes in the same volcanic field.
3. Stratigraphically well constrained.
4. In association with an important climatic oscillation.

5. Robustly dated at volcanic source or in multiple distal sedimentary archives (e.g. $^{40}Ar/^{39}Ar$, $^{14}C$, or annual layer counting).

#### 2.5.1.4 Tephrochronology in the LGIT

The use and identification of tephra layers within palaeoenvironmental records can provide a way to reduce this chronological uncertainty in records for investigations into YD and EH oscillations in Europe. The application of tephrochronology to records allows the successful integration of local and regional palaeo-records (Lowe, 2011; Davies, 2015). Previous investigations have shown the usefulness of tephra in providing insight into past regional abrupt climatic change (e.g. Lane et al., 2013; Ott et al., 2016). Numerous tephra layers and their associated eruptions have been dated and identified across Europe during the LGIT (Table 2.4). With questions focusing on the timing and identification of abrupt climatic oscillations, the application of tephrochronology to records across Europe will provide insight into the spatial and temporal occurrence of these abrupt, short-lived climatic events during the LGIT.

Two important tephra layers have been widely documented which date to around the YD. The Laacher See Tephra (LST) has been securely dated to the Allerød period in the varved record of Meerfelder Maar (MFM) to 12,880 ± 40 varve years (Brauer et al., 1999) or 12,937 ± 23 cal. BP in radiocarbon records (Bronk Ramsey et al. 2015). This tephra's distinct geochemistry has resulted in identification in numerous central European records (e.g. Housley et al., 2013; Lane et al., 2015; Jones et al., 2018; Kletetschka et al., 2019). The LST provides a time marker for the late Allerød with ~200 varve years before the YD onset (Lane et al., 2015). The second tephra, the Vedde Ash (VA), is one of the most widely documented tephras with identifications in the GIC (Rasmussen et al., 2013) and across Europe (e.g. Lane et al., 2011a, 2013; Timms et al., 2018; Haflidason et al.,

2019). The date for this eruption from Katla has been constrained to 12,023 ± 43 cal. BP, mid-YD and produces a clear isochron at many sites (Table 2.4; Bronk Ramsey et al., 2015). Additional eruptions from Katla have produced tephra layers of near identical major, minor and trace geochemistry (i.e. Abernethy Tephra; Lane et al., 2012b). However, having robust chronological and stratigraphic controls is need to identifying the VA at sites during the YD, confidently (Lane et al., 2012b). Both LST and VA tephras can be used together to constrain the timing of the YD demonstrated in several studies (e.g. Lane et al., 2011b; Wulf et al., 2016a).

During the EH period, the Askja-S tephra has been documented at several sites across Europe (e.g. Wohlfarth et al., 2006, 2017; Lane et al., 2011b; Timms et al., 2017, 2018). Wohlfarth et al. (2006) noted that this tephra layer is stratigraphically close to the observed PBO climatic oscillation of Björck et al. (1997). Other authors have also suggested the usefulness of this tephra within north-west European records in investigating the possible climate time-transgression and identification of cooling oscillations associated with the classic PBO within proxy records (e.g. Kelly et al., 2017; Timms et al., 2017). This tephra dispersion over Europe provides a continental scale time-parallel marker which can be used to examine the timing of EH oscillations across the continent. With the addition of the refined age of this eruption to 10,830 ± 57 cal BP (68.4% confidence; Bronk Ramsey et al., 2015), the Askja-S can be used to: 1) provide a chronological tie point across Europe; and 2) improve site chronologies that have recorded this tephra to provide understanding into the timing of EH oscillations.

The Hässeldalen tephra has been suggested as a useful isochron which coincides with the beginning of the climatic shift of the classic PBO (Davies et al., 2003; Wohlfarth et al., 2006). However, only northern European sites have recorded this tephra, limiting the additional information for the timing of cooling events in the EH across the region (e.g.

Davies et al., 2003; Housley et al., 2013; Ott et al., 2016). The identification of both the Hässeldalen and Askja-S tephras within the independently annually dated, floating varved record of Lake Czechowskie, Poland, provides an opportunity to refine the age of both tephras (Ott et al., 2016). Both can be used as a marker layer for the proposed EH cooling events in palaeoenvironmental records.

**Table 2.4** Summarised information for the main volcanic eruptions that occurred before and during the LGIT from volcanic centres situated close to Europe and Romania. The dispersal of these tephras from these eruptions may have the potential to be identified within palaeoenvironmental records in Romania. Information on the tectonic setting can help to identify particular volcanic sources using trace elements (Tomlinson et al., 2015). UM = Upper member; LM = Lower member. Geochemical composition relates to Silica ($SiO_2$) vs Potassium ($K_2O$) content (Peccerillo and Taylor, 1976).THO = Tholeiitic ; CA = Calc-alkaline; HKCA = High potassium calc-alkaline, SHO = Shoshonitic.

| | Eruption/tephra name | Volcano | Tectonic setting | Age | Magnitude (VEI) | Known dispersal | Geochemical composition | Reference |
|---|---|---|---|---|---|---|---|---|
| North Atlantic | Saksunarvartn Ash | Grímsvötn, Iceland | Anorogenic | 10,176 ± 49 cal BP ($^{14}$C, Bronk Ramsey et al., 2015) | VEI 5, Ultra-Plinian | SE Northern Europe only | Basaltic, THO | Dugmore et al., 1997; Lind and Wastegård, 2011 |
| | Askja-S | Askja, Iceland | Anorogenic | 10,842 ± 97 cal BP ($^{14}$C , Kearney et al., 2018) | VEI 5, Ultra-Plinian | NNE and NE over continental Europe | Rhyolitic, CA | Davies et al., 2003; Wohlfarth et al., 2006 |
| | Hässeldalen | Unknown (Thórðarhyrna ?) Iceland | Anorogenic (?) | 11,316 ± 124 cal BP ($^{14}$C, Wastegård et al., 2018) | ? | SE Northern Europe only | Rhyolitic, HKCA | Wohlfarth et al., 2006; Wastegård et al., 2018 |
| | Abernethy Tephra | Katla, Iceland | Anorogenic | 11,462 ± 122 cal BP ($^{14}$C, Bronk Ramsey et al., 2015) | VEI 4, Plinian | SE Confined to Scotland and Sweden | Rhyolitic, HKCA | Matthews et al., 2011; Timms et al., 2018; |
| | Vedde Ash | Katla, Iceland | Anorogenic | 12,023 ± 43 cal BP ($^{14}$C, Bronk Ramsey et al., 2015) | VEI 6, Ultra-Plinian | SE over continental Europe towards Russia | Rhyolitic, HKCA | Davies et al., 2001; Blockley et al., 2007; |
| | Penifiler | Unknown, Iceland | Anorogenic (?) | 13, 939 ± 66 cal BP ($^{14}$C, Bronk Ramsey et al., 2015) | VEI 5, Plinian | SE Northern Europe only | Rhyolitic, HKCA | Turney et al., 2001; Pyne-O'Donnell et al., 2007 |
| | Borrobol | Unknown, Iceland | Anorogenic (?) | 14,098 ± 47 cal BP ($^{14}$C, Bronk Ramsey et al., 2015) | VEI 5, Plinian | SE Northern Britain only | Rhyolitic, HKCA | Turney et al., 2001; Cook et al., 2018 |

**Table 2.4** Cont.

| | Eruption/tephra name | Volcano | Tectonic setting | Age | Magnitude (VEI) | Known dispersal | Geochemical composition | Reference |
|---|---|---|---|---|---|---|---|---|
| **Central Europe** | Ulmener Maar | Ulmener, Eifel Complex, Germany | Intra plate volcanism | 11,096 ± 117 cal BP ($^{14}$C, Bronk Ramsey et al., 2015) | Maar | Central Europe, Germany only | Phonolithic, SHO | Zolitschka et al., 1995; Brauer et al., 1999 |
| | Laacher See Tephra | Eifel Complex, Germany | Intra plate volcanism | 12,937 ± 23 cal BP ($^{14}$C, Bronk Ramsey et al., 2015) | VEI 5, Phreato-Plinian (Textor et al., 2003 | NE to SW, Central Europe only | Phonolithic, SHO | Finsinger et al., 2008; Housley et al., 2013 |
| | Roxolany Tephra, Younger Turia, Bixad | Ciomadul, Romania | Post subduction | 29,600 ± 620 cal BP ($^{14}$C, Wulf et al., 2016) | VEI | E towards the Black Sea | Rhyolite, CA | Wulf et al., 2016; Cullen et al., 2014 |
| **Central Mediterranean** | Vallone del Gabellotto | Lipari, Aeolian Islands, Italy | Subduction | 8,430-8,730 cal BP ($^{14}$C, Albert et al., 2017) | VEI 3-4, sub-Plinian | N and E as far as Greece | Rhyolite, HKCA | Albert et al., 2012, 2017 |
| | Pomici Principali Tephra | Campi Flegrei, Neapolitan Volcanic area, Italy | Post subduction | 11,999 ± 52 cal BP ($^{14}$C, Bronk Ramsey et al., 2015) | VEI 4, Plinian | E into Adriatic Sea | Phonolite, SHO | Mastrolorenzo et al., 2008; Tomlinson et al., 2012 |
| | Neapolitan Yellow Tuff | Campi Flegrei, Neapolitan Volcanic area, Italy | Post subduction | 14,194 ± 172 cal BP ($^{14}$C, Bronk Ramsey et al., 2015) | VEI 5, Ultra-Plinian | Mainly to the E with plumes to the N as far as Germany | NYT UM Phonolite-trachyte, NYT LM bimodal Phonolite-tracyte, SHO | Mastrolorenzo et al., 2008; Tomlinson et al., 2015, 2012 |

**Table 2.4** cont.

| | Eruption/tephra name | Volcano | Tectonic setting | Age | Magnitude (VEI) | Known dispersal | Geochemical composition | Reference |
|---|---|---|---|---|---|---|---|---|
| **Central Mediterranean** | Casa Lentia | Vulcano, Aeolian Islands | Subduction | 13,000 ± 300 cal BP | VEI 3-4, sub-Plinian | Local to Aeolian Islands, E into Tyrrhenian Sea | Basaltic, Trachyte-rhyolite, SHO | Albert et al., 2017 |
| | Upper Vancori | Stomboli, Aeolian Islands | Subduction | 13,000 cal BP | VEI 3-4, sub-Plinian | Local to Aeolian Islands, E into Tyrrhenian Sea | Trachyte, SHO | Albert et al., 2017 |
| | Upper Pollara | Salina, Aeolian Islands | Subduction | 15,200 ± 800 cal BP | VEI 3-4, sub-Plinian | Local to Aeolian Islands, E into Adriatic Sea | Dacite-rhyolite, CA | Albert et al., 2017 |
| | Biancavilla Ignibrite (Y1) | Etna, Sicily, Italy | Anorogenic | 17,335 ± 278 cal BP ($^{14}$C, Bronk Ramsey et al., 2015) | VEI 4, Plinian | E and S to Red Sea | Trachyte, HKCA | Albert et al., 2013 |
| | Monte Gaurdia | Lipari, Aeolian Islands, Italy | Subduction | 24,650 – 17,100 cal BP (Albert et al., 2017) | VEI 3-4, sub-Plinian | E as far as Greece | Rhyolite, HKCA | Albert et al., 2012, 2017 |
| **Eastern Mediterranean** | Upper Pumice | Nisyros, Aegean Arc | Subduction | ~47,700 cal BP | VEI 3-4, sub-Plinian | N and S | Rhyolite, HKCA | Tomlinson et al., 2012 |
| | Cape Riva (Y2) | Santorini, Aegean Arc | Subduction | 22,024 ± 321 cal BP ($^{14}$C, Bronk Ramsey et al., 2015) | VEI 5, Plinian | E and S to Red Sea | Dacite-Rhyolite, CA-HKCA | Wulf et al., 2002; Lee et al., 2013 |
| | Dikkartin (S1) | Ericyles Dagi, Central Anatolia, Turkey | Subduction | 8,939 ± 83 cal BP ($^{14}$C, Neugebauer et al., 2017) | VEI 4-5?, Plinian | S towards Saudi Arabia, Dead Sea | Rhyolite, CA | Hamann et al., 2010; Neugebauer et al., 2017 |
| | Perikartini | Ericyles Dagi, Central Anatolia, Turkey | Subduction | 10,200-7,900 cal BP ($^{36}$Cl cosmogenic, Sarikaya et al., 2006) | VEI 4-5?, Plinian? | Localised to central Turkey | Rhyolite, CA | Hamann et al., 2010; Cullen et al., 2014 |

**Table 2.4** Cont.

| | Eruption/tephra name | Volcano | Tectonic setting | Age | Magnitude (VEI) | Known dispersal | Geochemical composition | Reference |
|---|---|---|---|---|---|---|---|---|
| **Eastern Mediterranean** | Karagüllü | Ericyles Dagi, Central Anatolia, Turkey | Subduction | 10,200-7,900 cal BP ($^{36}$Cl cosmogenic, Sarikaya et al., 2006) | VEI 4-5?, Plinian? | Localised to central Turkey | Rhyolite, CA | Hamann et al., 2010; Cullen et al., 2014 |
| | Güneydag | Acigöl, Central Anatolia, Turkey | Subduction | 23,800 ± 2,100 cal BP (U-Th/He, Schmitt et al., 2011) | VEI 4-5?, Plinian? | Localised to central Turkey | Rhyolite, CA | Cullen et al., 2014; Tomlinson et al., 2015 |
| | Korudag | Acigöl, Central Anatolia, Turkey | Subduction | 24,900 ± 2,100 cal BP (U-Th/He, Schmitt et al., 2011) | VEI 4-5?, Plinian? | Localised to central Turkey | Rhyolite, CA | Cullen et al., 2014; Tomlinson et al., 2015 |

#### 2.5.1.5 Potential for tephrostratigraphy in Romania

As described, cryptotephra horizons are a powerful tool to integrate geographically disparate records to understand the dynamics of abrupt climatic change. Numerous European records have been subjected to detailed cryptotephra investigations, especially in northern and western Europe (e.g. MacLeod et al., 2015; Lowe et al., 2015). However, regions such as Central Eastern Europe, especially Romania, have been largely overlooked for cryptotephra application.

Identification and investigation of visible volcanic ash layers in sedimentary archives across Romania have been studied for some time. The location of Romania is close to several volcanic centres during the Late Quaternary (Figure 2.9; Table 2.4). This includes the more distal volcanic centres of the central and eastern Mediterranean (Wulf et al., 2004; Sulpizio et al., 2010; Smith et al., 2011) and central Anatolia, Turkey (Tryon et al., 2009; Cullen et al., 2014), which have the potential to disperse volcanic ash to Romania.

Many past researchers have focused on studying the past eruptive activity of the Ciomadul volcano, located in the eastern Carpathians. Proximal volcanic ash deposits close to the volcano have been described since the 1700s with additional dating in the recent decade (e.g. von Fichtel, 1780; Bányai, 1964; Harangi et al., 2010; Wulf et al., 2016b; Karáston et al., 2017), with present research providing an age of ~29,600 cal yrs BP for the last eruption at Ciomadul (Wulf et al., 2016b). Other studies have looked at the potential of volcanic ash in sedimentary deposits such as loess, to provide tephrostratigraphic correlation to other regional archives (e.g. Ghena 1967; Mârza, 1991; Veres et al., 2013; Obreht et al., 2017). This is seen with the Campanian Ignimbrite/Y5 tephra, which has been extensively described across the Lower Danube region in Romania (Horvath et al., 2001; Veres and Mîndrescu, 2013; Obreht et al., 2017).

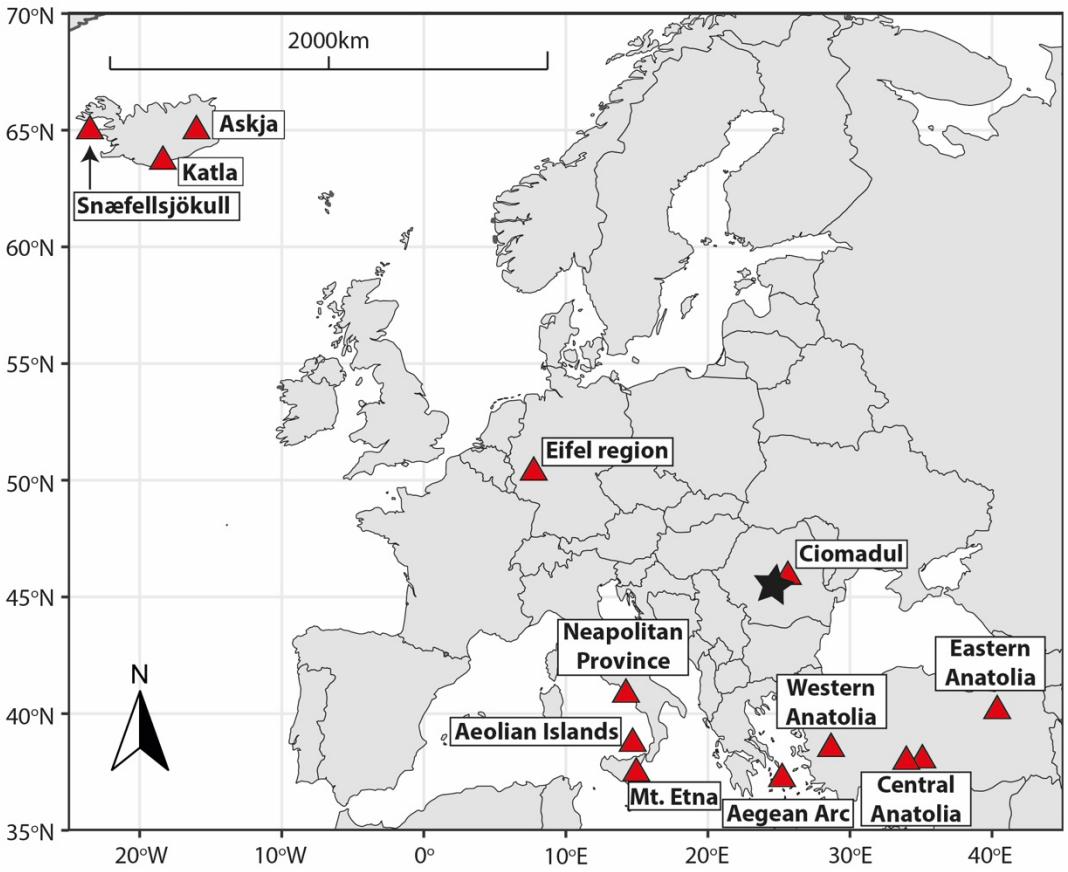


**Figure 2.9** Map of Europe showing the proximity of known active volcanic centres during the LGIT period. The star indicate the location of the sites in Romania that are investigated in this study.

These past studies have concentrated on visible volcanic layers. To date, no research has pursued the study of distal cryptotephra within the palaeoenvironmental records of the Romanian region. This may be due to the emphasis placed on radiocarbon dating and the perceived little chance of finding key tephra marker horizons that allow correlations to other important climatic records, especially in north-west Europe. However, the potential to find distal tephra is high with recent cryptotephra studies showing that fine volcanic ash can travel >1,000km across the world (e.g. Jensen et al., 2014, van der Bilt et al., 2017). Completing detailed cryptotephra investigations in Romanian sedimentary archives has the potential to facilitate the synchronisation of these records with those from across Europe. This would enable the assessment of the spatial and temporal variation of

climatic change over a wider geographical distance providing insight into the mechanisms and drivers of climatic change during the LGIT period.

### 2.5.2 INTIMATE database – Integration tool

Using tephra marker layers as event-stratigraphy allows researchers to compare the timing of climatic oscillations in different records. However, this is only over short periods where the tephra layer is present. Individual records also have their associated uncertainty with their chronology (i.e. age uncertainty, different timescales (IntCal13 vs GICC05)) and proxy (proxy error, depth error) in addition to the additional uncertainty of comparing records on different timescales. As a result, there is a need to calculate, quantify and visualise the uncertainties when correlating to different records to provide insight and understanding into the temporal and spatial expression of abrupt climatic transitions. The development of the INTIMATE database Integration tool (Bronk Ramsey et al., 2014, 2019) allows these issues to be addressed.

This tool uses a time-transfer function based on the identification of common events between different records and the known chronological relationships between different archives (Figure 2.10; Bronk Ramsey et al., 2014). The identification of tephra layers to a well-known, and widely recognised volcanic event allows many records to be integrated. To allow comparisons between the terrestrial records that are within the IntCal13 timescale and the GICC05 timescale, the tool utilises the variations between the cosmogenic nuclides of $^{14}C$ and $^{10}Be$ (Bronk Ramsey et al., 2014). As these isotopes co-vary and are dependent on solar intensity, it allows these two different timescales to be synchronised. Muscheler et al. (2014) and Adolphi and Muscheler (2016) have developed and quantified the uncertainty associated with correlating these two records. Exploiting these relationships allows different timescales to be integrated and their uncertainty

derived. As a result, this Integration tool will be key to understanding the synchronicity of terrestrial records and their comparisons to the GICs for the YD and EH transition.

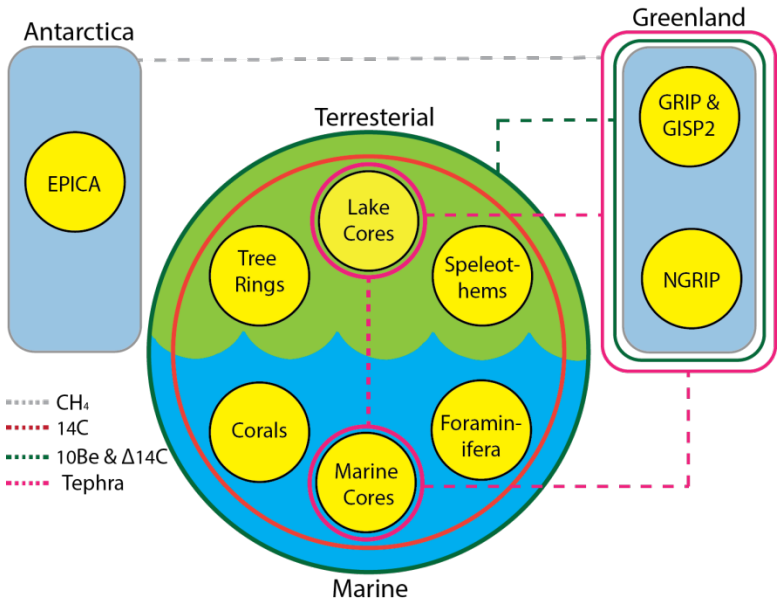


**Figure 2.10** Schematic showing how different palaeoclimatic records can be successfully integrated through the Integration tool of the INTIMATE database (adapted from (Bronk Ramsey et al., 2014). Light blue = ice cores, blue = marine, green = terrestrial.

## 2.6 Chapter summary

This chapter has presented an overview of the climatic and environmental conditions for the LGIT with specific reference to the millennial-scale climatic oscillation of the Younger Dryas and centennial-scale earliest Holocene events of the Preboreal Oscillation. In addition, the vegetation response to these abrupt climatic transitions. The current challenges of: 1) the confused usage of the terms YD and PBO; 2) chronological problems with tuning/wiggle matching records; 3) large age uncertainties; and 4) lack of focus on eastern Europe, i.e. Romania, has limited our understanding into the temporal and spatial characteristics of these different scale oscillations across Europe. As a result, the this thesis will focus on improving chronological uncertainty around these events using tephra layers, Bayesian age-modelling and the INTIMATE Integration tool to address these limitations. This will improve the understanding of the climatic drivers and propagation of these abrupt events across Europe.

# Chapter 3

# Methodology

This chapter provides details on the methodological procedures that were used in this thesis. Firstly, Section 3.1 outlines the rationale for selecting appropriate sites to provide insight into the timing of the terrestrial environmental response to climatic fluctuations during the LGIT. As there are two parts to this thesis, the site selection rationale is separated into: 1) site selection for tephrochronological investigations with a focus on Romania and 2) the site selection for the integration of terrestrial records across Europe. Section 3.2 focuses on pollen analysis with a general outline on the method and its caveats. This is followed by how the pollen data was obtained and processed from the selected site records. Information is given on the statistical analysis applied to these datasets. Section 3.3 presents the laboratory procedures undertaken for collecting, processing, identifying and characterising tephra samples from the Romanian sites. Section 3.4 outlines the age-depth model approaches for the overarching large age model encompassing all chosen terrestrial sites. Finally, section 3.5 provides insight into how records were added to the INTIMATE database and the use of the integration tool.

## 3.1 Site selection criteria

### 3.1.1 Tephrochronology of Romania

There were three criteria for sites selected to provide a tephrochronology for Romania. These were that they should:

1. Be a lacustrine record with rapid sediment accumulation that can provide the highest potential for preserving tephra layers (e.g. Lane et al., 2014; Davies, 2015).

2. Already have been subjected to extensive high-resolution palaeoclimatic and palaeoenvironmental investigations, in line with the main research rationale of this thesis.
3. Have no known hiatus(es) within the periods of interest.

### 3.1.2 Terrestrial records

To compile the most appropriate terrestrial palaeoenvironmental records from across Europe, as outlined in Chapters 1 and 2, the selection criteria were for sediments that:

1. Span the majority of the LGIT period that includes the Younger Dryas and earliest Holocene (~13,500 to ~10,500 cal yrs BP).
2. Have been subject to detailed palynological investigations over the relevant time interval of at least one sample per ~50-100 years to accurately capture potential vegetation change associated with abrupt climatic oscillations. To ensure a suitable transect across Europe from north to south, certain sites, with lower resolution samples, were chosen as long as they fulfilled other site selection criteria. Although not ideal, these sites were chosen to fulfil the main aim of this project on a continental scale.
3. Have been subject to independent dating over the time interval (radiocarbon dating or well-known tephra layers).
4. Contain the key tephrostratigraphic markers of the Vedde Ash or Laacher See Tephra for investigating the YD and/or the Hässeldalen and Askja-S tephras for investigating the earliest Holocene period. These tephra layers are crucial in reducing chronological uncertainty around the transitions of interest, as outlined in section 2.5.1.4.

## 3.2 Palaeoenvironmental methods – pollen analysis

Pollen analysis is a powerful technique for the reconstruction of vegetational responses to past climatic changes, and thus was the principal method used in this thesis. Pollen grains are used for reproductive purposes to carry the male gamete from the anther to the stigma in female plants (Moore et al., 1991). The dispersal of pollen is either by wind, water, insects, birds and animals. Some species produce large quantities of pollen with grain sizes ranging from 10-100μm in diameter to ensure successful pollination (Odgaard, 1999; Bennett and Willis, 2001). Many of these liberated pollen grains can become incorporated into sediment archives and preserved in anaerobic environments such as the lake archives studied here (Moore et al., 1991). The preservation of unique morphological features of individual pollen grains can allow identification of different plant taxa and inferences of vegetation patterns around a site (Birks, 1968; Moore et al., 1991). These different pollen grains can then be counted and a past vegetation pattern inferred.

Interpreting the pollen data relies on modern observations and studies of current plant communities and their interactions under different climatic and environmental conditions (Seppä, 2007). Changes in the pollen grain assemblage are inferred to be variations in past vegetation patterns. It is assumed that these changes reflect different climatic and environmental conditions with understanding of how the pollen arrives at the site (Moore et al., 1991; Figure 3.1). In addition, transport and taphonomic processes also need to be considered before interpreting pollen data in terms of past vegetation composition (Prentice, 1988; Sugita 1994). Ideally, the proportion of pollen taxa identified from the sediment has an exact relationship to the proportion of vegetation composition on the landscape, but this is rarely the case. Figure 3.1 highlights the main issues published in the literature. As a result, these processes have to be kept in mind when making assumptions

about past vegetation changes. These taphonomic processes can be identified and disentangled using dating and multi-proxy investigations (Birks and Birks, 2010).

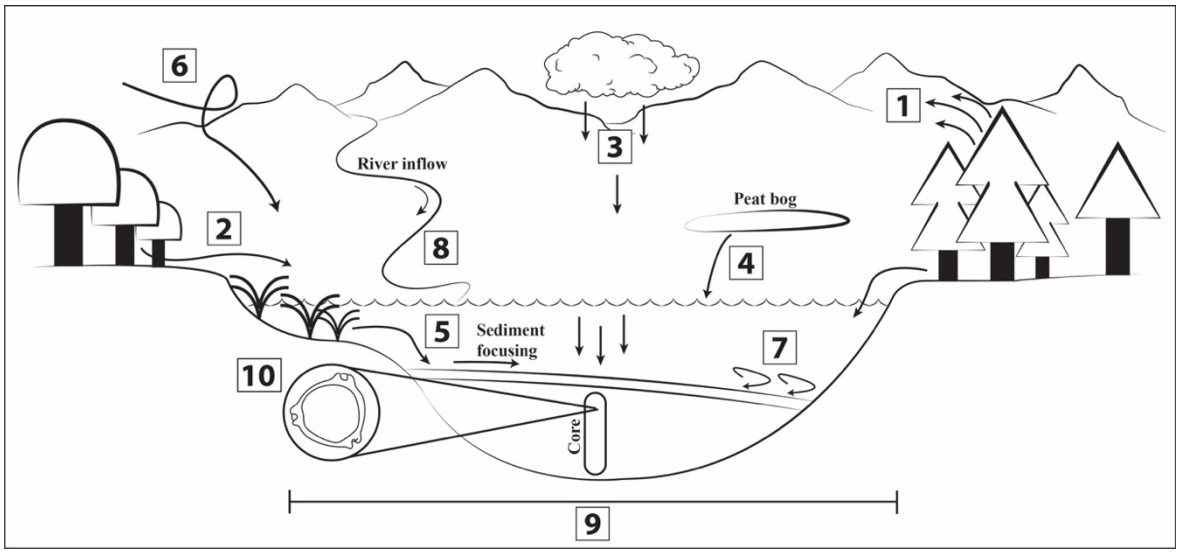


**Figure 3.1** Diagram showing the taphonomic processes that need to be considered when undertaking pollen analysis. This is especially for inferring past vegetation composition (adapted from Moore et al., 1991). These include; 1) Over representation of some pollen producers (local and distal component; Björkman et al., 2002); 2) Pollen transported at low wind speeds along the area directly below the canopy in the trunk space between the trees (local component; Tauber, 1965; Moore et al., 1991); 3) Rain component as pollen fallout (local and distal component; Tauber, 1965; Moore et al., 1991); 4) Secondary remobilisation through erosion (secondary component); 5) local aquatic input can lead to over representation within the pollen record (local component); 6) secondary sources from outside catchment (distal component); 7) bioturbation and resuspension of sediment (secondary component); 8) distal component from river inflow (local and distal component); 9) size of lake and catchment with smaller lakes having a local vegetation component vs larger lakes and a regional component (Giescke and Fontana, 2008); 10) preservation of pollen grain after deposition with some grain types being more susceptible to corrosion than others equalling an under representation in the pollen record for some taxa (Moore et al., 1991).

### 3.2.1 Data collection and presentation

For the terrestrial sites that met the selection criteria for this investigation, the relevant site authors were contacted to ask for the original raw pollen counts for the depths that covered the LGIT. By receiving and working on raw pollen counts, the same techniques of presenting and analysing the data can be applied to all sites. There are numerous different ways that pollen data can be handled and presented, which varies between authors (Bennett

and Willis, 2001). These differences include: the various pollen taxa that can be included/excluded in the total pollen counts (e.g. aquatics or spore-producing taxa), the pollen taxa that are included/excluded in terrestrial land pollen sum (TLP) (e.g. Cyperaceae, Ericales), as well as the numerous different numerical techniques in presenting the data (e.g. as percentage, concentration).

For this study, the TLP included tree, shrubs and herbaceous species and were counted as the pollen sum. Cyperaceae is included in the TLP due to some of the sedges being terrestrial plants (Bennett and Willis, 2001). Aquatic species (e.g. *Potamogeten*) and spores (e.g. *Sphagnum*) were excluded and not used. This is due to the problem of over-representation of these taxa within the pollen assemblage (Moore et al., 1991). The majority of the sites selected are lake sediments with aquatic plants growing in or at the site margins resulting in inundation of these pollen types into the record. This is similar to fern spores, which are produced differently and have a different biological function to pollen (Bennett and Willis, 2001).

The resulting pollen assemblages were then plotted as pollen percentage diagrams, calculated using the TLP. This type of diagram is prevalent in palynological investigations. However, problems with statistical interdependence can affect the representation of pollen taxa within the assemblage. A rise in one pollen taxon can result in a decline in other taxon (Davis and Deevey, 1964). Different plant taxa produce varying amounts of pollen such as *Pinus*, which is dispersed by the wind and so produces a large amount of pollen that can be over-represented within the record (Moore et al., 1991).

As a result, pollen accumulation rate (PAR) was also calculated where possible. This allowed for absolute changes in concentration per unit measure of time (Davis and Deevey, 1964; Thompson, 1980). This involved using exotic marker pollen counts to calculate pollen

concentration (Equation 3.1.1). As all sites will have an age model allowing sediment accumulation rate was obtained and PAR calculated using Equation 3.2.

**Equation 3.1** Calculation for pollen concentration (Bennett and Willis, 2001)

$$\text{Fossil pollen concentration} = \frac{\text{exotic pollen added x fossil pollen counted}}{\text{exotic pollen counted}}$$

**Equation 3.2** Calculation for PAR (Bennett and Willis, 2001)

$$\frac{\text{pollen concentration } (\text{cm}^3)}{\text{sediment accumulation rate } (\text{cm yr}^{-1})}$$

By using PAR, the problem of interdependence from percentage diagrams is reduced (Leunda et al., 2017; Seppä and Hicks, 2006). However, due to the interpolation of radiocarbon dates, sedimentation rate is locally assumed to be constant were, in reality, this may not be the case (Davis and Deevy, 1964; Colinvaux, 1978; Telford et al., 2004). There are also errors associated with radiocarbon calibration (Colinvaux, 1978; Telford et al., 2004). Also, a high number of radiocarbon dates are needed to make an accurate sediment accumulation model (Seppä and Hicks, 2006). These problems will be taken into consideration when interpreting PAR results.

Several pollen data programmes are available to run and create pollen diagrams. This study used *psimpoll* due to the various plotting options available (Bennett, 2000).

### 3.2.2 Pollen diagram zonation

Each pollen diagram was divided into Local Pollen Assemblage Zones (LPAZ) to aid in the description, interpretation and correlation of the pollen records (Gordon and Birks,

1972; Grimm, 1987; Moore et al., 1991). These biostratigraphic zones contain pollen assemblages of a broadly similar character which may be associated with a strong environmental response to an overarching control (e.g. climate change) (Gordon and Birks, 1972; Bennett, 1996; Birks, 2012). Zonation of pollen diagrams can be undertaken using objective numerical techniques to allow repeatable and unbiased results in contrast to zonation's undertaken purely by 'eye' (Bennett, 1996).

In this investigation, diagram zonation was undertaken using the numerical method of Constrained Incremental Sum of Squares Cluster Analysis (CONISS) developed by Grimm (1987) on untransformed pollen data. The 'sum-of-squares' refers to the dispersion or variance (mean dispersion) within a suggested zone of two stratigraphically adjacent clusters. This binary approach splits the data set into zones where a minimal dispersion (sum-of-squares) is found. A hierarchy or splitting of zones can be formed as smaller and smaller zones can be calculated. The zone boundaries were placed between two adjacent stratigraphic samples determined by the site's own pollen resolution undertaken by the primary investigator.

The number of zones were statistically determined through the Broken-stick model (Mac-Arthur, 1957; Bennett, 1996). This method calculates the total variance related to the allocation of samples into zones (Bennett, 1996). The results produce the number of zones that is appropriate in capturing the variance within the dataset. (Bennett, 1996; Birks, 2012).

### 3.2.3 Statistical analysis

To provide additional evidence, and not to reinforce the need to fit data-sets to a preferred hypothesis (Ammann et al., 2000), numerical analysis of the pollen data was undertaken. This type of approach would allow variability in the data to be captured and

scrutinised for the presence of 'events' in the EH which may not be captured by CONISS alone (Ammann et al., 2000; Abrook et al., 2019).

As a result of the pollen data being multivariate, with counts for species and depth, several indirect ordination statistical techniques can be employed to display and explore the relationships between the data. This is usually displayed in a graph with a few dimensions that examine all variables within the dataset at once (ter Braak and Prentice, 1988; Legendre and Birks, 2012). The dimensions (or axes) are considered as hypothetical environmental variables that are constructed from the best fit of the species data (ter Braak and Prentice, 1988). These variables can then be inferred from the composition of the species and their position along the gradient (ter Braak and Prentice, 1988). The ordination techniques chosen in this investigation include: Detrended Correspondence Analysis (DCA); Principal Component Analysis (PCA); Correspondence Analysis (CoA); Principal Curve Analysis (PrC) and Rate of Change Analysis (RoC).

Within this investigation, DCA was used as a preliminary process to assist in PrC modelling (see below). DCA detrends and non-linearly rescales the assemblage data set to produce an estimate of the gradient length or axis length (Hill and Gauch, 1980; ter Braak and Prentice, 1988).This is given in the units of standard deviation (SD) related to composition turnover (Hill and Gauch, 1980). The first axis length is seen as the most important for choosing the most appropriate ordination method as it incorporates the majority of the data (Legendre and Birks, 2012). The variance around these axes is explained by eigenvalues (Legendre and Birks, 2012). The higher the eigenvalue, the more significant that axis is. As a result, where the first axis is <1.5 SD, the variation of the assemblage is low, implying that linear approaches, such as PCA, is appropriate to further investigating the dataset (ter Braak and Prentice, 1988; Simpson and Birks, 2012). If the axis length is

1.5-3SD, the assemblage variation is larger over a wider range and so a unimodal-based approach, such as CoA, should also be considered (Ibid).

Using PCA allows large datasets to be refined to orthogonal linear axes of variation. The first few principal components (or axes) encompasses the most data variation and are used to indicate the known response variables (Figure 3.2; Birks, 1974). The principal components are naturally linear (Figure 3.3). The key taxa that are important along the first two axes are usually displayed in ordination plots. The particular taxa and their position along these axes can provide insight into the governing variables upon a data set. These variables can include climate (e.g. temperature, precipitation, evapotranspiration), environmental (e.g. soil, shading) and biology (e.g. species competition). This is where knowledge of a taxon's or group of taxa's environmental preferences and stratigraphic changes can provide insight into the overarching control on the assemblage (e.g. climate change).

When interpreting results, PCA can be subjected to the 'horseshoe' effect, an artefact of the data (Gauch et al., 1977). This is when the first two axes are not independent of each other resulting in the second axis curving relative to the first. This is caused by a unimodal distribution (ter Braak and Prentice, 1988). As a result, CoA may be more appropriate to explore the relationships in the dataset. CoA was applied as a secondary analysis tool to compare to PCA in relation to creating a PrC (see below). It is similar to PCA (producing variables (axis)) to access the data variation but CoA assumes a Gaussian response compared to PCA, removing the 'horseshoe' effect (Gauch et al., 1977; Hill and Gauch, 1980).

In PCA, the first axis is deemed as the most crucial axis with the total amount of data variation captured by this axis usually equating to <40%. The complexity of the pollen data may not be completely captured by one dimension alone. As a result, PrC was used to capture more variance within the pollen record and identify minor changes associated with

possible climatic events (Hastie and Stuetzle, 1989; De'ath, 1999; Simpson and Birks, 2012; Abrook et al., 2019).

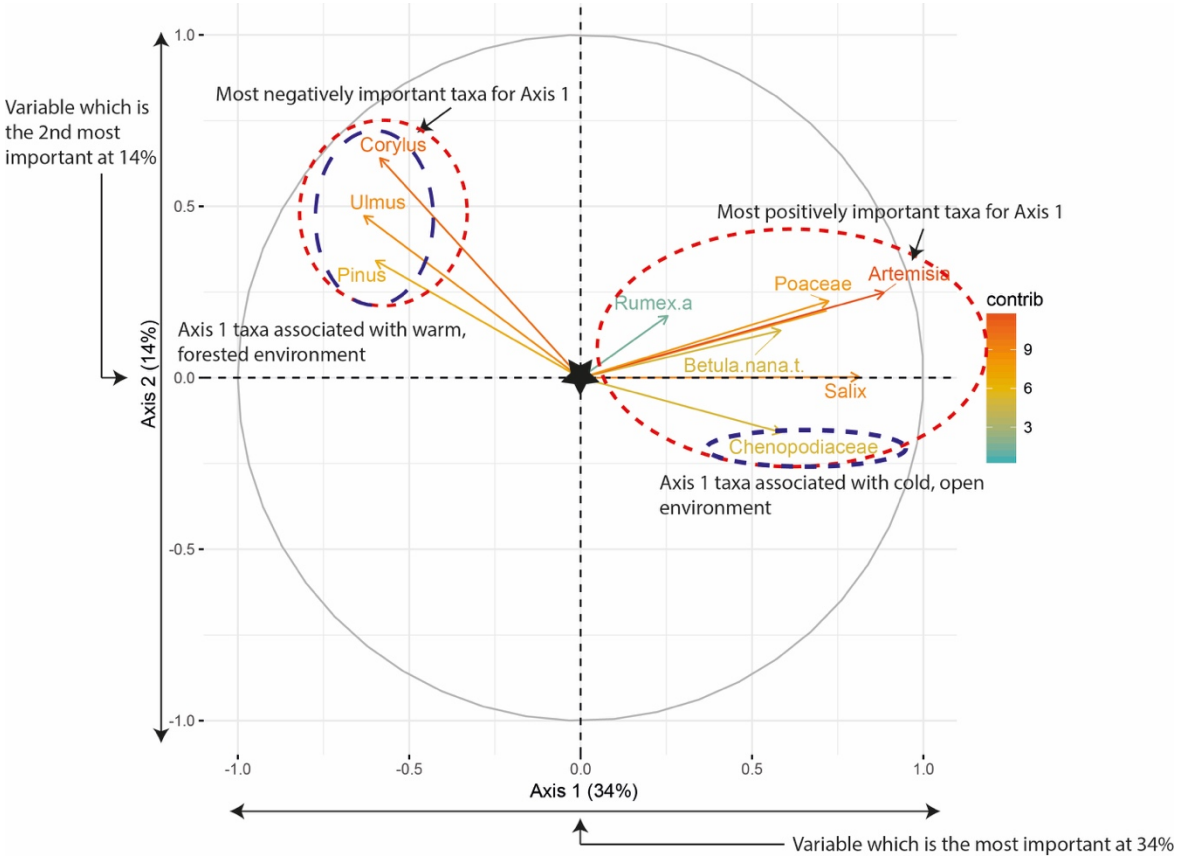


**Figure 3.2.** Schematic of how to interpret PCA biplots in this thesis using example data. The data is plotted using the two most important variables which encompass the most data variance (Axis 1 and Axis 2). The pollen taxa is placed along the axis with the length and colour of the arrow indicating the dominance of that taxa along Axis 1 and Axis 2. The further the taxa is away from the origin (the star), the more that taxa is important for either Axis 1 or Axis 2. This example data shows positively and negatively correlated taxa are grouped together on the opposite side on Axis 1 (circled red). It is important to know the climatic and environmental conditions for each taxa to correctly interpret possibly variables. The most important variable of Axis 1 can be interpreted as climate, mainly temperature due to the opposing positions (positive vs negative) of taxa along this axis. For the second most important variable of Axis 2 (circled blue), it can be assumed to be associated with another variable of potentially moisture availability due to the taxa involved: trees (positive = drier environments) versus Chenopodiaceae (negative = wetter environments). Axis 1 is deemed as the most important encompassing 34% of the data variability and is associated with climate.

The PrC method captures data variation by using a smooth one-dimensional curve that is fitted through the data (Simpson and Birks, 2012). This curve minimises the distance between the observations, the sum of squares distance (Figure 3.3; Simpson and Birks, 2012;

Abrook et al., 2019). It has been shown to capture more data variation (>70%) than the other ordination techniques, allowing identification of changes in pollen records (Simpson and Birks, 2012; Bennion et al., 2015; Shumilovskikh et al., 2017; Abrook, 2019; Abrook et al., 2019).

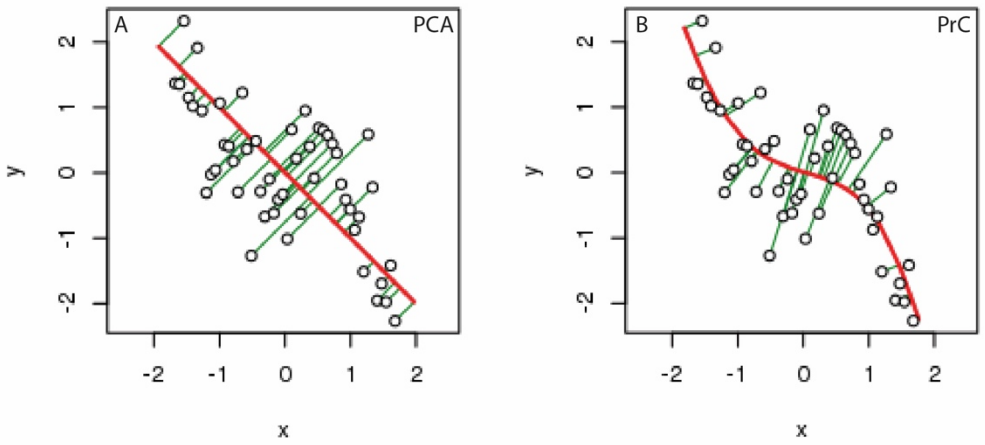


**Figure 3.3** Diagram from Simpson and Birks (2012) showing the differences between A) Principal Component Analysis (PCA) and B) Principal Curve (PrC). The fitted relationship is shown with the solid red line and errors are shown by the green lines. The sum of squared errors in minimised by reducing the distance from a point to the location of principal component to the line as orthogonal creating a straight line in PCA. Combining PCA and splines the PrC produces a smooth curve that reduces these errors, allowing more variation in the data to be captured on the first axis compared to PCA.

PrC's are generated through stages. Firstly, a smooth curve is generated through the data using either a PCA or CoA axis as a starting curve. The length of primary axis determines the application of an appropriate starting point from DCA results.

Where the axis is 1.5-3SD both PCA and CoA are effective, while <1.5 SD PCA was chosen (ter Braak and Prentice, 1988; Simpson and Birks, 2012). Then the curve is smoothed to "best fit" the data using a degree of smoothness through a penalty value. The appropriate "best fit" is determined by: 1) the number of iterations it takes for the model to converge (becoming stable, ideally <10 iterations); 2) the degrees of freedom calculated and 3) monitoring the algorithm to ensure no over-fitting (Simpson and Birks, 2012).

To further identify abrupt changes within vegetation records from sites across Europe during the LGIT period, the method of Rate of Change (RoC) was used. Developed by Jacobson and Grimm (1986) and Grimm and Jacobson (1992) to investigate the synchronicity of vegetation change across North America, this method quantifies the amount of palynological change per unit of time between adjoining pollen samples (Lotter et al., 1992a). In this study, intervals of 50 years were deemed appropriate due to the detail provided at this resolution. This in comparison to more intervals of 100 years, where detail linked to abrupt centennial-scale climatic events is lost (i.e. PBO). In contrast, shorter interval of ~1 year can result in "noise" obscuring an accurate environmental "signal" (Bennett and Humphry, 1995). In this thesis, the same interpolation interval is applied to all sites to provide appropriate comparisons (Bennett and Humphry, 1995). Interpolating to the same interval for each site reduces the problems of artefact features being produced, due to the variation in the number and resolution of radiocarbon dates and pollen samples (Bennett and Humphry, 1995).

All statistical analysis was performed on percentage of pollen data. This approach has been consistently applied in other studies (e.g. Simpson and Birks, 2012). Care needs to be taken as the taxa may not be independent from each other with possible problems of reworked pollen affecting the results (Pollard et al., 2006; Abrook et al., 2019). However, these effects can easily be disentangled from the data when reviewing the statistical results (Abrook et al., 2019).

The method of Simpson and Birks (2012) was followed to perform the statistical analysis on the pollen data. For each site, an appropriate down-weighting of rare taxa was undertaken between 2-5% abundance. The specific value used was dependent on the number of taxa left to provide reliable trends within the pollen data. By down-weighting, the effects of data skew by taxa less than 2-5% abundance would be removed. Statistical analysis of

PCA, DCA, CoA and PrC was performed using the 'R' computer program software using the statistical packages of 'Rioja', 'Vegan' and 'Analogue' (Juggins, 2017; Oksanen, 2018). The R-script was created by B. Simpson and further developed by A. Abrook and I. Matthews. For the calculation of RoC, *psimpoll* v4.26 computational programme (Bennett, 2000) was used. An appropriate dissimilarity coefficient of Hellinger distance was used to provide chord distance values as this was proven to be statistically appropriate for species abundance data (Prentice 1980; Bennett et al., 1992; Lotter et al., 1992; Bennett, 2000; Legendre and Gallagher, 2001; Legendre and Birks, 2012). RoC values were displayed as exaggerated chord-distance per half a century.

The results were displayed as 1) DCA table; 2) PCA ordination biplots with axis one and two scores; 3) chronostratigraphic plot for axis one sample scores from PCA or CoA modelled outputs and the PrC with RoC analysis; 4) individual species response curves.

### 3.2.4 Abrupt event definition and identification in the pollen record

Many palaeoclimatological and palaeoenvironmental investigations refer to and describe an event within their records. The definition of an event, in terms of how it can be characterised and identified, has never been securely defined, with variations in definition dependent upon a climatic or environmental perspective (Watts, 1970; Tipping, 1991; Edwards and Whittington, 2010; Rasmussen et al., 2014). Within ice-core research, Rasmussen et al. (2014) identified event onsets as crucial characteristics in defining the event stratigraphy from the NGRIP record. Recently, Botta et al. (2019) have provided a coherent definition for the term 'abrupt' as 'when a climatic system crosses a tipping point and switches to a new state' (pg. R1047). However, defining suitable and coherent criterion for identifying these abrupt climatic events across the many disciplines of palaeoclimatology is lacking.

For this investigation, methods of statistical analysis were used to 'define' and identify abrupt events during the LGIT in pollen records across Europe (Figure 3.4). In identifying the YD, CONISS was the main method used due to this method's wide application to identifying and describing local and regional pollen assemblage changes across the palynological field (Gordon and Birks, 1974; Grimm 1986). In this way, similar pollen zones from different sites can then be discussed and compared, with investigation into the potential overarching driver(s), i.e. climatic downturn associated with the YD (Gordon and Birks, 1974; Grimm, 1986). The YD is seen as a large scale and large magnitude climatic event (section 2.2.1). Other statistical methods, such as PrC, were also calculated. PrC did mirror CONISS in determining the timing of the onset and termination of the YD at the majority of selected sites. However, PrC was deemed not to be confidently reliable at some sites due to issues raised in Chapter 8. With this and CONISS zonation being widely applied and accepted by the palynological community as broadly identifying a common driver to environmental changes across a wide spatial scale, CONISS was the primary method used for the YD.

For identifying the EH oscillations, CONISS alone cannot clearly identify short, abrupt pollen events. PrC can capture more variance within a dataset (Birks and Simpson, 2012). To identify and then ensure an 'event' seen at a site is related to EH climatic event(s), other criteria were used, as demonstrated in Figure 3.3. This included Watts (1970) established criteria in which to identify a climatic fluctuation within the pollen record through vegetation response termed 'vegetation revertence' (Table 3.1). The term is defined as 'clear evidence for climatic reversion. Revertence is what distinguished an oscillation from a long slowly developing plant succession' (Watts, 1970 pg.144). This criterion provided a distinction from natural succession as the vegetation assemblage reached a tipping point and then crossed into a new state to become in equilibrium with the new climate

and environment (Tipping, 1991). This criterion provides a greater degree of evidence for inferring vegetation change related to possible climatic events (Abrook, 2019). The same criteria can then be applied to multiple records to ensure reproducibility in distinguishing vegetation revertences and avoid biases in trying to find a 'signal' in the complex data (Ammann et al., 2000).

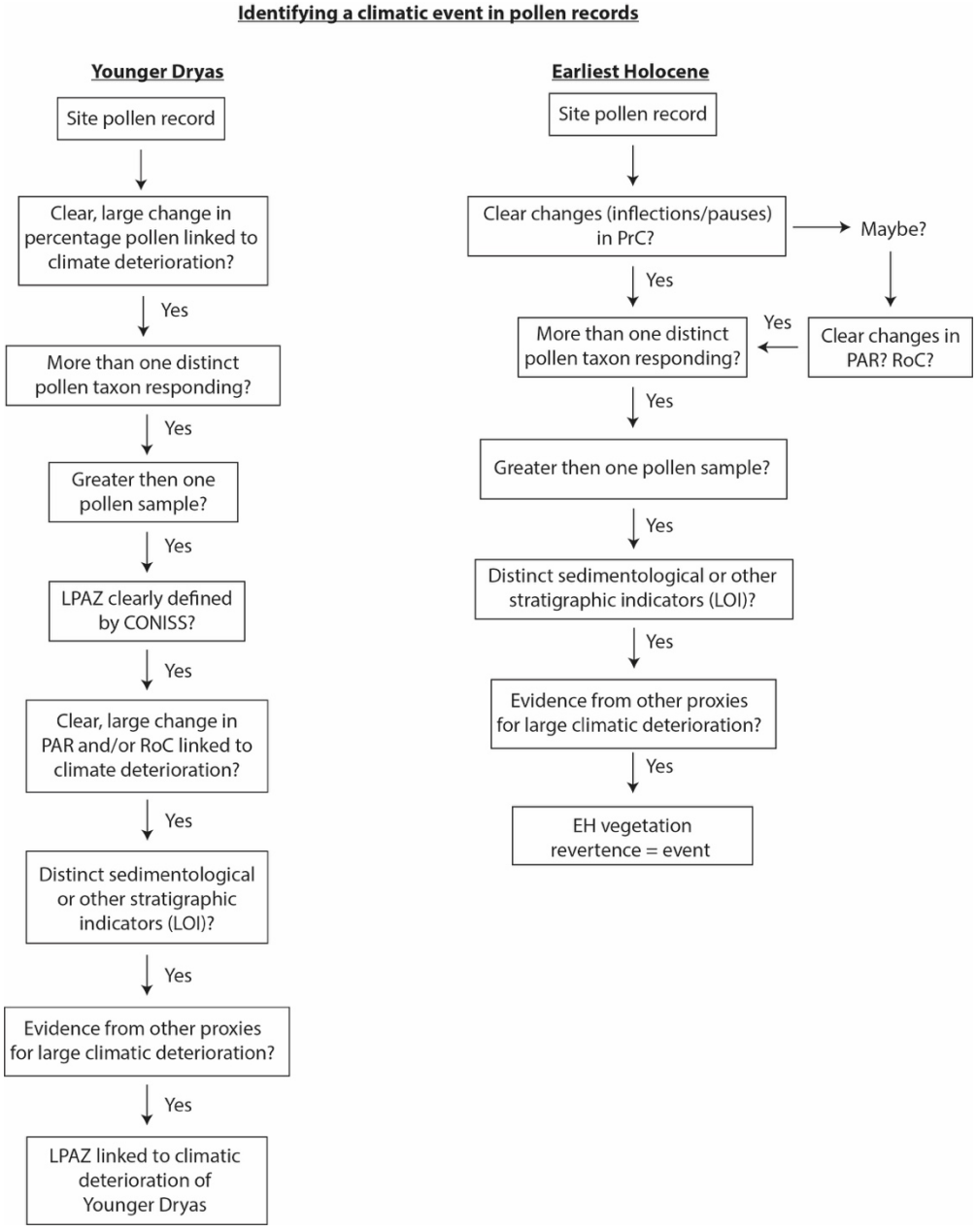


**Figure 3.4** Flow chart explaining the use of different statistical methods for identifying the large magnitude climatic event of the Younger Dryas and the smaller, abrupt event(s) of the earliest Holocene. If one step could not be completed (following 'Yes') then no event could be identified. PAR = Pollen accumulation rate; RoC = Rate of change.

Additional criteria outlined by Abrook (2019) can be added to those of Watts (1970) to provide further confirmation for a climate forced vegetation response (Figure 3.3). These include: 1) that the changes in the pollen record are seen over more than one sample, separating it from a potential statistical anomaly; 2) using a multi-proxy approach with changes in both pollen and other climatic proxies (e.g. stable isotopes, chironomids), then climate is driving this change. The addition of modelling vegetation response through PrC subjects the data to unbiased statistical analysis. If all or the majority of criteria are met, then a vegetation revertence in response to a climatic event can be inferred.

**Table 3.1** Adapted criteria for defining vegetation revertence in pollen records and thus climatic events. Main criteria is from Watts (1970) (Tipping, 1991; Edwards and Whittington, 2010) with additional criteria from Abrook (2019).

| Criteria | Refence |
|---|---|
| 1. Pollen flora identified to a good modern standard with high pollen counts, sampling and level of taxonomic<br>2. Clear evidence of climatic reversion in pollen<br>3. More than one distinct pollen taxon responding<br>4. Distinctive sedimentological or other stratigraphic indicators (LOI) | Watts (1970) |
| 5. Greater than one pollen sample so not to be an anomaly<br>6. Evidence for climatic deterioration in other proxies – if other proxies available at the site | Additional criteria from Abrook (2019) |

## 3.3 Tephrochronology

The following section outlines the laboratory procedures for collecting, processing, identifying and characterising tephra samples from selected Romanian sites. The sites selected are outlined in Chapter 4 and are Lake Brazi (TDB) and Lake Lia (LIA).

### 3.3.1 Sediment sampling

Sediment from both cores, TDB-1 and LIA-1, were collected by Dr Eniko Magyari, Dr Ilona Pál and Dr Daniel Veres and stored at 2ºC in the MTA-MTM-ELTE Research Group for the Palaeontology Laboratory, Eötvös Lóránd University, Budapest, Hungary. These cores were then cleaned prior to sampling with the outer ~1cm sediment around the whole core removed to ensure no contamination from the coring method, i.e. smearing (Figure 3.5). The remaining sediment was then cut every 1cm in-depth and stored in individually numbered sample bags (Figure 3.5).

### 3.3.2 Cryptotephra sample preparation

The sampling process for cryptotephra investigation at Lake Brazi and Lake Lia followed a modified version of the non-destructive, density separation technique outlined by Turney (1998) and Blockley et al. (2005).

Sediment from both lake sites was subsampled at low resolution. This involved the amalgamation of sediment from each contiguous 1cm sample bag across a depth of 5cm into a single ~0.5 gram sample (Figure 3.5, Figure 3.6). This low-resolution process was carried out to check for the presence or absence of tephra within the sediment record. These samples were dried overnight at 70ºC in an oven and were then individually weighed and recorded. This allowed the calculations of the number of glass shards per dry weight.

Samples that were deemed to contain high amounts of organic matter (peaty) were then ashed. The weighed individual samples were put into a furnace at 550ºC for two hours to remove organic material. Carbonates were removed by adding 10% of Hydrochloric acid (HCl) to each sample.

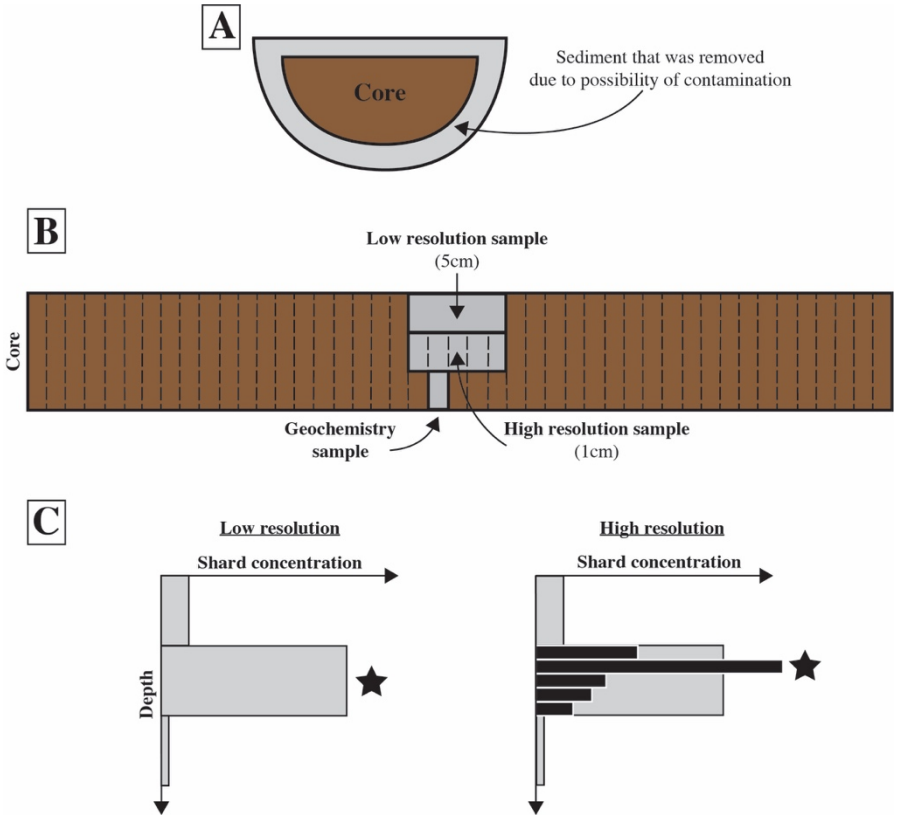


**Figure 3.5** Illustration of (A) the removal of possibly contaminated sediment from the core edge in the laboratory (B) Low-resolution sampling involved the amalgamation of ~0.5g sediment from 5cm depth while high-resolution sampling involved ~0.5g of sediment: (C) Shard concentration profile (shards/gram), grey bars show low-resolution sample results. The highest low-resolution shard concentration is identified (star) and high-resolution sampling is applied to those depths (black bars). The isochron position is identified and geochemical analysis is conducted on shards at this depth (star).

Samples were then sieved at 80µm and 15µm (modified from the of 80µm and 25µm of Blockley et al., 2005). The decrease in size fraction to 15µm allows smaller cryptotephra shards to be retained that may have travelled further from the source volcano. Samples were first sieved through an 80µm sized mesh to remove >80µm fraction. A plastic spatula, tap water and a mild detergent were used to break up the sediment sample. After the samples were sieved, the >80µm fraction was kept and transferred to a separate labelled conical test tube. The <80µm fraction was suspended in water and subsequently passed through a 15µm sized mesh using the same disaggregation technique. The remaining >15µm sized sediment fraction was retained in a test tube. In between each sieving operation, all the equipment was cleaned and surfaces wiped down. Sieve meshes were disposed of after each sample to

reduce the risk of contamination between samples. Following the same procedure, every tenth sample, a 'blank' was used to monitor for contamination.

After sieving, the retained samples were put through a density separation process, used to isolate cryptotephra shards from other materials (e.g. organics, quartz) at a density between 1.95 and 2.55g/cm$^3$ (Blockley et al., 2005). Sodium Polytungstate (SPT) was used to separate these fractions. Four millimetres of 1.95g/cm$^3$ SPT is added to each sample and is centrifuged for 15 minutes at 2500 rpm (no brake) was used to remove any remaining organic material from the sample (termed the cleaning float). The SPT and >1.95g/cm$^3$ floating material were carefully siphoned off and the 1.95g/cm$^3$ SPT added again to repeat the procedure. The remaining sample had four millilitres of 2.55g/cm$^3$ SPT was added and was centrifuged for 15 minutes at 2500 rpm (no brake) to isolate cryptotephra shards. The SPT and 1.95-2.55g/cm$^3$ floating material were carefully siphoned off to a separate labelled test tube. This was repeated again. After the density separation, all samples were thoroughly cleansed with deionised water. The 1.95-2.55g/cm$^3$ sample was then mounted onto an optical slide with Canada balsam.

The volcanic glass was identified and counted under a high-powered, polarizing optical microscope. The tephra shards were identified based on their morphology. Shard morphologies (e.g. blocky, platy, cuspate, fluted; Mclean et al., 2018; Figure 3.7) and sizes (measured on the longest axis) were recorded. The number of shards per gram of dry weight sediment were calculated. Once all the 'low resolution' samples were counted, higher resolution sampling at 1cm resolution were carried out on the peaks. These depths were prepared and counted, as outlined above.

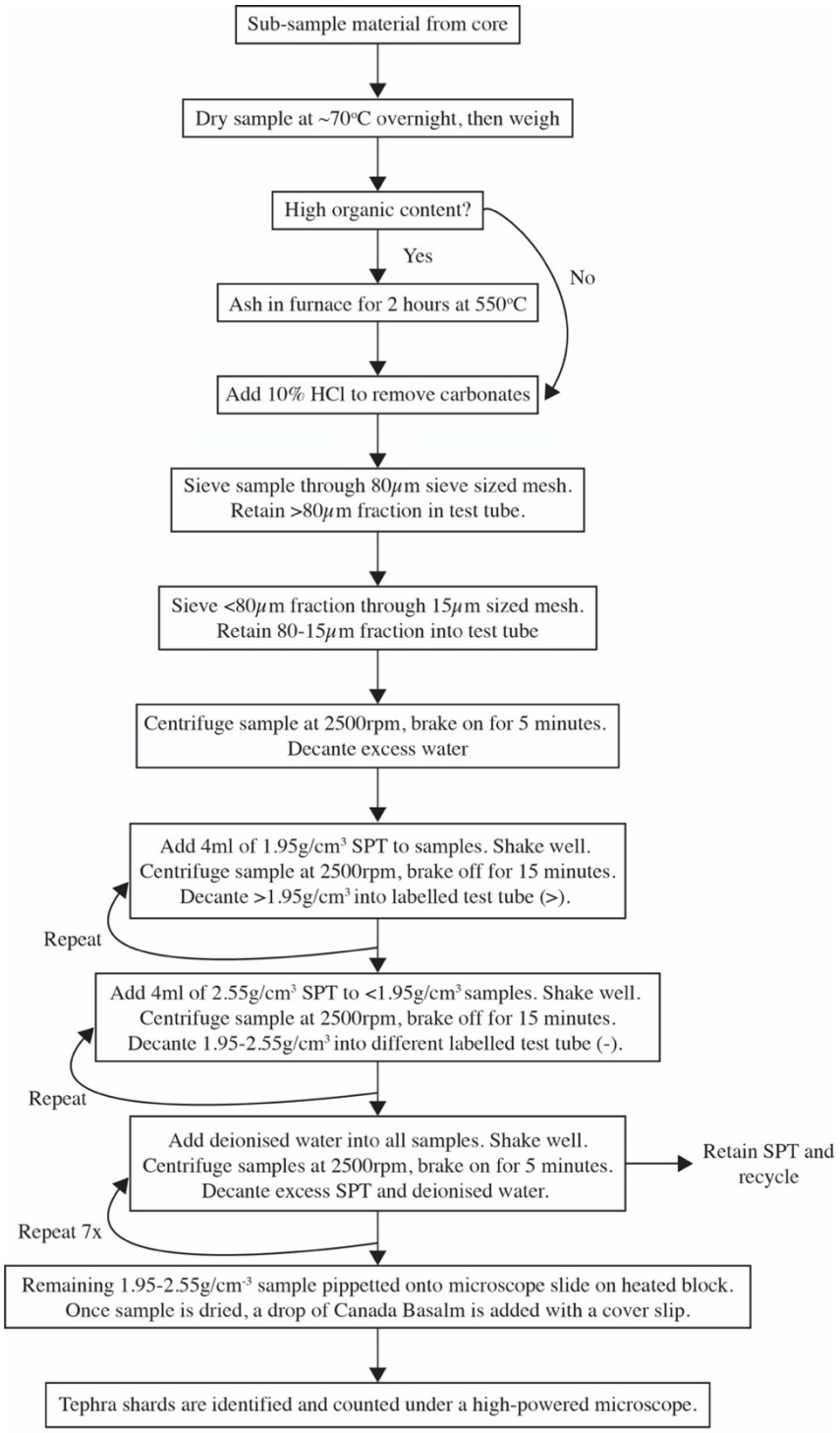


**Figure 3.6** Diagram of the cryptotephra laboratory methods modified from Blockley et al. (2005) and Turney (1998).

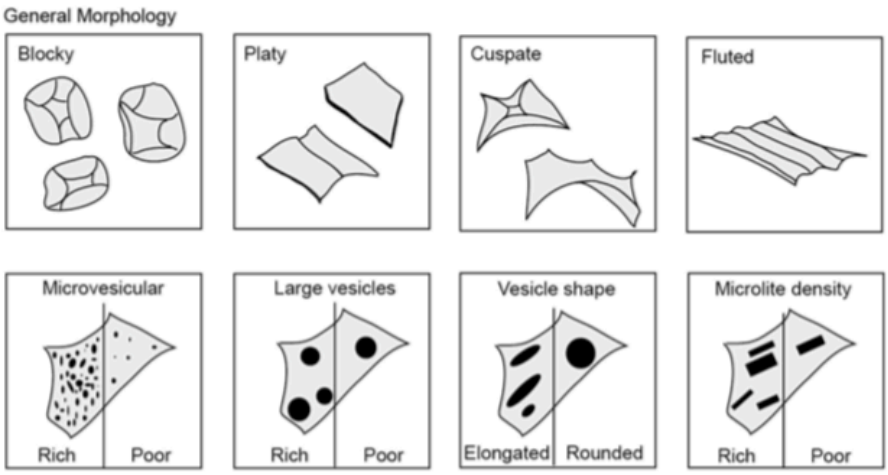


**Figure 3.7** Schematic from Mclean et al. (2018) used to describe the glass shard morphologies in this thesis.

### 3.3.3 Geochemical analysis

#### 3.3.3.1 Sample preparation

After identifying the depths at which peaks in shard concentrations occurred, samples were prepared for geochemical analysis. The samples were prepared as described above. However, the ashing of samples in a furnace was avoided due to the possibility of the high temperatures altering the geochemical composition of the glass shards (Blockley et al., 2005) and were not mounted. Instead, the samples were suspended in water.

The sample were then pipetted onto a welled slide under a high-powered microscope. Individual glass shards were identified and extracted using a gas chromatography syringe attached to a micromanipulator (Figure 3.8, Lane et al., 2014). These shards were then placed on an epoxy resin stub. Once the shards had been removed, the samples were left to dry and then sealed with additional epoxy resin and cured in an oven >40$^{o}$C for 3.5 hours.

The stubs were ground by hand to expose the individual shards using silicon carbide paper. The stubs where then polished, using a 3-micrometre diamond paste using an automatic polisher at 150 rpm for ~30 minutes. This was followed by a 1-micrometre diamond polish for ~5 minutes at 150 rpm on the same sample.

Due to the small number of shards 'picked' from some samples, only a few shards in each stub were exposed at a time and so stubs were re-ground after geochemical analysis to expose additional shards. This allowed additional geochemical analyses to be obtained on a single peak.

#### 3.3.3.2 Major and minor element composition analysis

Major and minor element compositions of individual glass shards were measured using a JEOL-8600 wavelength-dispersive electron microprobe (WDS-EPMA) at the Research Laboratory for Archaeology and History of Art (RLAHA), University of Oxford. WDS-EPMA, allows high precision on grain-specific analysis (Lowe, 2011). All analyses used an accelerating voltage of 15 kV, beam current of 6 nA and 10 and 5 μm-diameter beam. Peak counting time was 30 seconds for all elements apart from Na (12s), M (40s), Cl (50s) and P (60s). The electron microprobe was calibrated using a suite of mineral standards, and the PAP absorption correction method was used for quantification.

The accuracy and precision of the analyses were assessed using analyses of the MPI-DING reference glasses of ATHO-G, GOR132 and St/Hs6/80-g secondary glass standards (Jochum et al., 2006), which were run alongside the unknown tephra samples. All major element glass data determined on the Lake Lia and Brazi cryptotephra deposits, including the associated reference standard glass analyses, can be found in Appendix 2. All data was filtered to remove accidental analyses of minerals and biogenic silica. Volcanic glass with analytical totals <92% were also removed (See Chapter 5 for criteria).

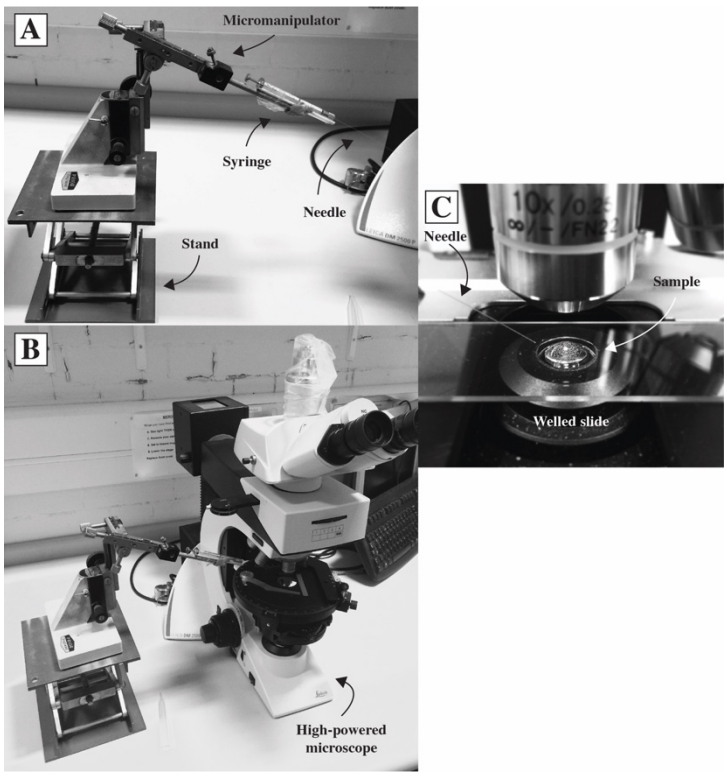


**Figure 3.8** Images of the equipment used for picking individual tephra shards for geochemical analysis.

### 3.3.3.3 Trace element composition analysis

Trace element analysis of volcanic glass shards were performed using an Agilent 8900 triple quadrupole ICP-MS (ICP-QQQ) coupled to a Resonetics 193nm ArF excimer laser-ablation system housed in the Department of Earth Sciences, Royal Holloway, University of London. Full analytical methods for analysis of volcanic glass are reported in Tomlinson et al. (2010). Owing to the small shards analysed a 20 μm ablation crater was used. The repetition rate was 5 Hz, with a count time of 40 s on the sample, and 40 s on the gas blank to allow the subtraction of the background signal. Analytical runs comprised of blocks of unknown glass shards and a MPI-DING reference glass bracketed by the NIST612 glass calibration standard (GeoREM 11/2006). The internal standard applied was $^{29}Si$ (determined by the EPMA analysis). Analyses of the MPI-DING reference glasses were used to monitor analytical accuracy (Jochum et al., 2006). LA-ICP-MS data reduction was

performed in Microsoft Excel using the approaches outlined in Tomlinson et al. (2010). Accuracies of LA-ICP-MS analyses of ATHO-G and StHs6/80-G MPI-DING glass were typically ≤ 5%. The full trace element geochemical dataset can be found in Appendix 2, including the analyses of the reference glasses. Each unknown glass analysis can be linked to a reference standard analysis using their common analysis date and analytical run number.

### 3.4 Age-depth modelling

Using the published radiocarbon datasets from the selected terrestrial sites (see Chapter 4 for these sites), a large age model was constructed using OxCal version 4.3 (Bronk Ramsey, 2017) and applying the IntCal13 calibration curve (Reimer et al., 2013).

The '*P_Sequence*' deposition procedure were applied to all sites (Bronk Ramsey, 2008). This 'Poisson process sequence' involves defining a *k* value parameter that governs the rigidity of the sedimentary process (Bronk Ramsey, 2008). By applying this type of model, the complexity (randomness) of a depositional process can provide a more realistic representation of sedimentation rate within a record. The Poisson distribution describes the random variation of individual particle sizes that contribute to a sedimentary record. Using the *k* value, the 'number of accumulation events per unit depth' can be dictated, resulting in rigidity of the depositional model through the depositional rate (Bronk Ramsey, 2008). All sequences were given a variable *k* value with 1.0 $cm^{-1}$ being the centre value with two orders of magnitude each site. This allowed flexibility with a variable sedimentary rate within the models. Markov Chain Monte Carlo (MCMC) was then used by OxCal to generate an age-depth model (Bronk Ramsey, 1994, 2008; Bronk Ramsey and Lee, 2013).

Outlier analysis was included in the model for each sites. The radiocarbon dates that were outliers (either due to wrong radiocarbon dates for the particular depth or the individual

site model refusing to run) were removed from the overall age model (Bronk Ramsey, 2009a). Additional *Outlier_Model* analysis was performed on the remaining radiocarbon dates with a prior probability of 5% applied to each sample/radiocarbon date (Bronk Ramsey, 2009a). This type of approach was chosen rather than manually excluding dates that exceed a particular probability threshold. Instead, dates are down-weighted within the model with the prior probability as the user cannot determine if the particular date is truly an outlier (Bronk Ramsey, 2009a). These type of outliers were defined as *General* in the coding for individual radiocarbon dates. The outlier analysis of *SSimple* were used for combined radiocarbon dates from a single depth (Bronk Ramsey, 2009a).

With the identification of tephras throughout all sites and the assumption that tephra layers are laid down synchronous within depositional records, linking the same tephra through cross-referencing can be applied through the '=' character (Bronk Ramsey 2009b). Due to the extensive use of cross-referenced tephras within the age model, the MCMC analysis is negatively affected, resulting in low convergence or false representative solutions of the model runs (Bronk Ramsey, 2009b). To ensure no circular argument is imposed on the overall age model, broad prior age distributions for each tephra layer were created. Age distributions were defined in OxCal using the *Top_Hat* or *U* function for uniform probability distributions (Bronk Ramsey, 2008). The *Top_Hat* function allows for a date to lie around a certain deviation from the average (e.g. *Top_Hat*(200,20)) while the *U* function allows for a date to be between two ages (e.g. *U*(180,220)). The tephra were also incorporated into a *Sequence* at the beginning of the age-model. The *Sequence* provided the prior information on the stratigraphic order of tephra deposits. The relative order could not be made if the tephras were not found in a single site. This would not biases the prior information on the tephras.

Tephras that have been dated and modelled precisely at multiple sites, such as the Vedde Ash and Laacher See tephras, prior age distributions were given with smaller distributions, yet are still broad enough to allow no bias towards a certain date. A preliminary age model was run using a *Top_Hat* function for all tephras. This resulted in a double peak in the probability density ranges for the ages for the Askja-S and Hässeldalen tephras (Figure 3.9). The convergence for these tephras is also low (3-5%), which is not ideal to use in the larger age model. The double peak can be linked to the radiocarbon plateau during this time in the earliest Holocene (Björck et al., 1996).

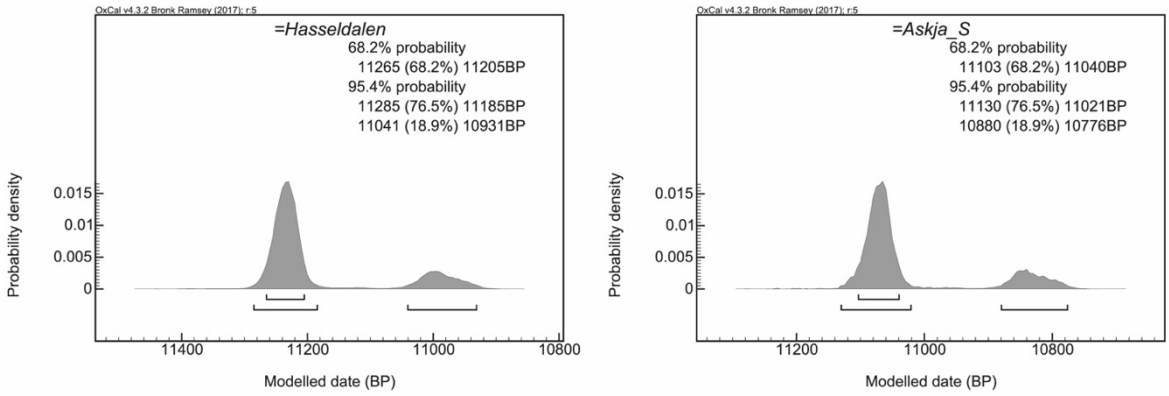


**Figure 3.9** OxCal output of Hässeldalen and Askja-S tephras when using broad ages with Top_Hat function. The bimodal peak is due to the carbon plateau experienced at this time on the IntCal13 curve. The peak with the higher probability density for both tephras is the age give from the model in Figure 3.8

In the case of providing an appropriate prior age for the Hässeldalen and Askja-S tephras that would allow the model to run correctly, a separate age model was created that involved radiocarbon dates associated with these tephras (Figure 3.10). A *Sequence* deposition model comprising of *Phases* and a sub-*Sequence* was created (Bronk Ramsey, 2008). Prior information in the order of events was used from depth information associated with the dates from the sites of Soppensee and Hässeldala port. *Phase* models were created that contained dates from before the Hässeldalen tephra and after the Askja-S deposition. A sub-*Sequence* model was used to provide age information in between the Askja-S and

Hässeldalen tephra. This was obtained from Hässeldala port, the only site that contained dating information between these two tephras. A *Tau-Boundary* was applied to the top and bottom of the overall *Sequence* model allowing flexibility in the dates with possible depositions just before/after the eruptions, yet also have the probability being deposited substantially before the eruption (Bronk Ramsey, 2009b).

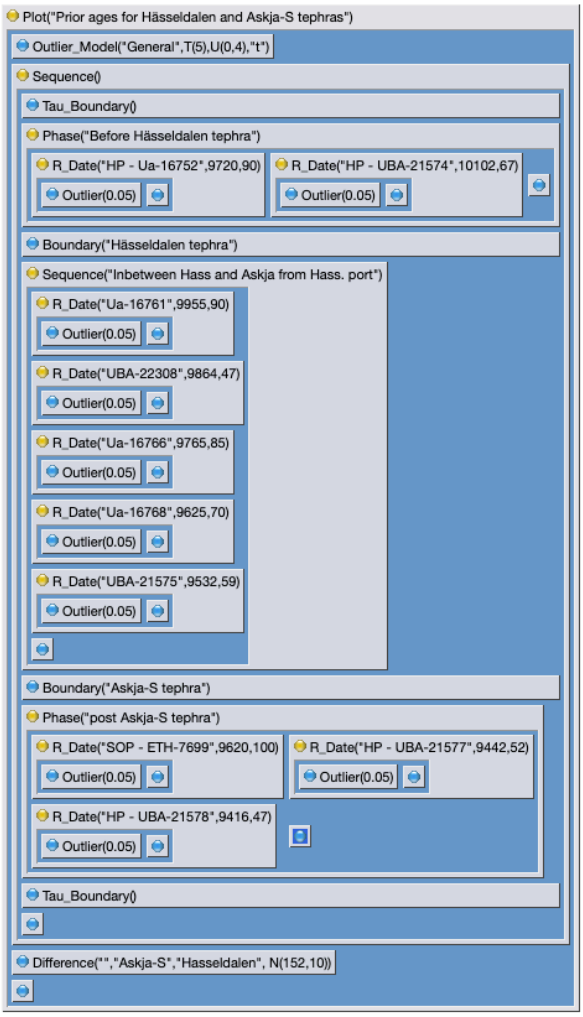


**Figure 3.10** Schematic representation of the Bayesian model run for providing a refined prior age for the Hässeldalen and Askja-S tephras to be used in the larger age-model. The model is constructed from a Sequence with nested sub-phases and sub-sequences. HP = Hässeldala port dates (Wohlfarth et al., 2006) and SOP = Soppensee date (Lotter et al., 1999). Hässeldala port is the only site with radiocarbon dates between the two tephras (Wohlfarth et al., 2006). The Difference is the counted varve years between the two tephras at Lake Czechowskie (Ott et al., 2016).

Once the appropriate prior age for both the Askja-S and Hässeldalen tephras were calculated using this separate age model run, these ages were inserted as *U* functions with

an additional larger age to ensure as a little circular argument as possible, yet with enough restriction to allow the large model to run correctly with better convergence. As a result, convergence of the model was improved to >75%. An additional four model runs were made using the same model code to test the similarities in ages. There was a good agreement between all model age outputs. A full list of the radiocarbon dates for each site that were used in the large age model, can be found in Appendix 4.

### 3.5 INTIMATE database – the Integration tool

The INTIMATE database Integration tool has been discussed in detail in section 2.5.2. The use of this novel tool in this project provides insight into the timing of climatic events across Europe as well as the associated chronological uncertainties. For each site in this project, a *Record* was produced that contain several *Series* for age models, tephra and individual proxy records for that site (Figure 3.11). The ages (on the IntCal13 timeline) for these sites were taken from the large OxCal age model output with their relevant depth. To allow integration of the records with the Greenland ice core record of NGRIP, a series relationship between IntCal13 and GICC05 using the time-transfer function calculated by Adolphi and Muscheler (2016) were used. This allowed the NGRIP record to be presented on the IntCal13 timescale with associated uncertainties with the time-transfer.

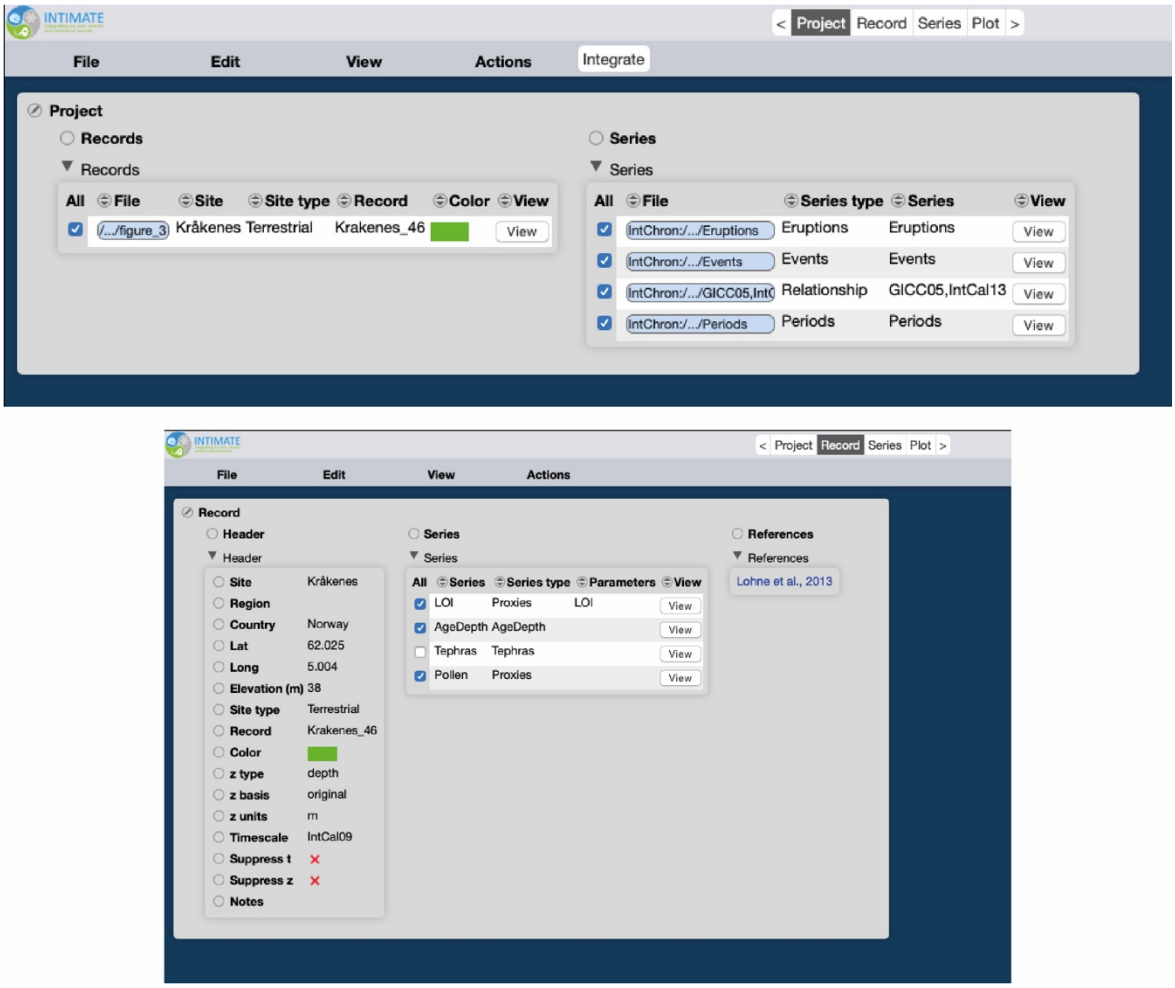


**Figure 3.11** Example of the INTIMATE Integration tool. The top image shows the *Project* interface set up. The *Record* is Kråkenes, as an example. The *Series* shows the *Eruptions* (tephras with ages), *Events* (abrupt climatic events i.e. GI-1e), *Relationship* (the time transfer-function between GICC05 and IntCal13), *Periods* (climatic periods i.e. GI-1). The bottom image shows the *Record* of Kråkenese with associated site information. The different *Series* of Proxies (LOI, Pollen), AgeDepth (depth and ages for the record), Tephras (from the site, in this example Vedde Ash).

# Chapter 4
# Study sites

This chapter introduces the sites that fulfilled the site selection criteria outlined in section 3.1. An introduction to each site's setting and past research is specified. As this thesis is composed of two parts, the sites selected are separated. Section 4.1 provides information for the chosen sites for tephrochronological investigations in Romania. Section 4.2 introduces the terrestrial records selected from across Europe. This section provides background information on the temporal and spatial response to the Younger Dryas (YD) and the centennial-scale climatic oscillations during the earliest Holocene (EH).

## 4.1. Sites selected for tephrochronology for Romania

The Retezat Mountains, located in southern Romania, form the western massif of the Southern Carpathian Mountains (Figure 4.1). During the Last Glacial Maximum (LGM), the area underwent extensive glaciation (Urdea, 2004; Reuther et al., 2007; Ruszkiczay-Rüdiger et al., 2016).

The present-day climate of the Retezat Mountains is influenced by precipitation regimes from the Mediterranean region and the Atlantic region (Magyari et al., 2013). It is one of the wettest massifs in the Carpathians receiving precipitation of ~1400mm/year. The coldest temperatures are experienced during January (-11-+5$^{o}$C) while the warmest temperatures are during July (6-16$^{o}$C) below 1,800m a.s.l. At the highest peaks (2,500m a.s.l.), summer and winter temperatures are -2$^{o}$C and -10$^{o}$C, respectively. Snow can persist in areas during summer, with snowpacks remaining for ~100 days a year at low altitudes and ~170 days at 2,000m a.s.l.

The retreat of glacial ice during the Last Glacial period resulted in 58 permanent glacial lakes (Jancsik, 2001). In the Galeşul valley, the two glacial lakes that were available

for cryptotephra research and met the criteria outlined in section 3.1.1 were chosen for tephrochronological investigations. These are Lake Brazi and Lake Lia.

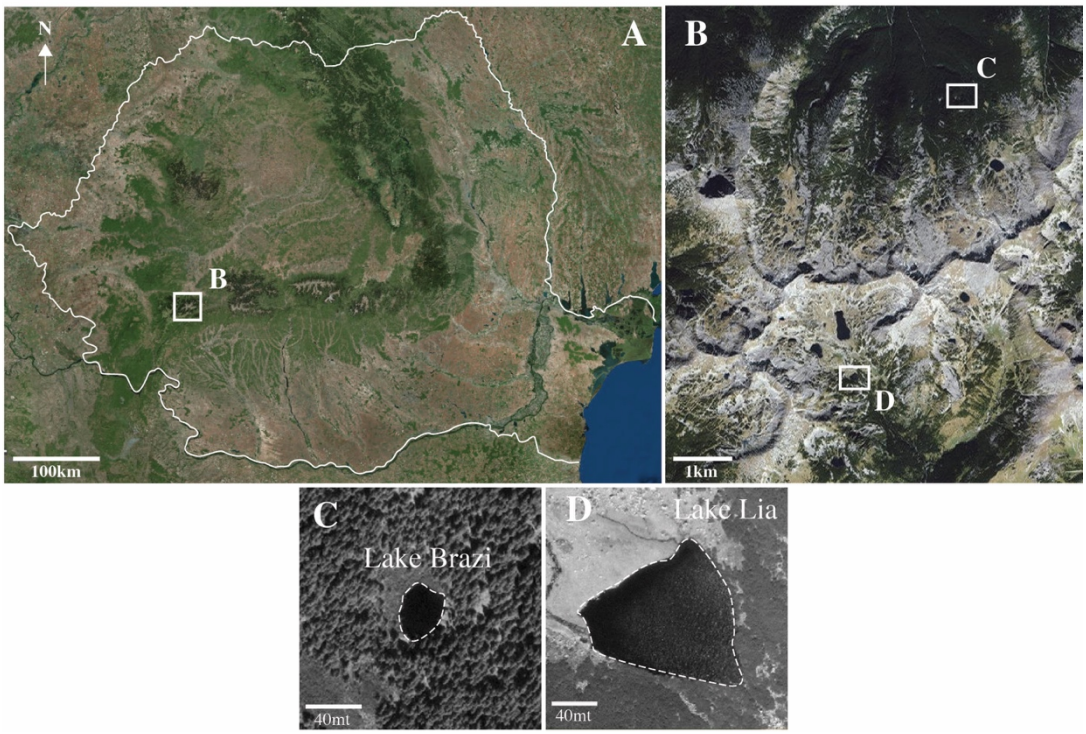


**Figure 4.1** Landsat image (EU-DEM, 2016) of Romania (A), the Retezat Mountains (B) with Lake Brazi (C) and Lake Lia (D).

### 4.1.1 Lake Brazi

Lake Brazi (Figure 4.1C) is located in the west of the Galeşul valley, on the northern flank of the mountains. It is a kettle hole formation with a shallow depth (1.1m max depth) and a small surface area (0.5ha; Magyari et al., 2009; Hubay et al., 2018). The lake receives seasonal underground inflow along its northern edge in addition to water from slope inwash and rainfall. It has a single outflow located on the southern shore.

A sedimentary core was taken from the central part of Lake Brazi during August 2007 with a modified Livingstone piston corer (Magyari et al., 2009) as part of the PROLONG project (Providing long environmental records of Late Quaternary climatic

oscillations in the Retezat Mountains). The core, TDB-1, is 490cm in length and has been used in numerous palaeoenvironmental studies (see Table 4.1). A chronology is provided from twenty-one radiocarbon dates (Table 4.1; Hubay et al., 2018).

### 4.1.2 Lake Lia

Lake Lia (Figure 4.1D) is located on the southern side of the mountain range. This is a small (1.26ha), shallow glacial lake (0.8m max depth). The lake receives inflow from Lake Bucura and several other smaller lakes through two inflow streams and has one outflow.

This lake is also part of the PROLONG project. An 880cm long sediment core (LIA-1) was taken close to the western shore of Lake Lia in July 2008 by a modified Livingstone corer. Currently, multiple palaeoenvironmental studies are underway at the site with chronology provided by seventeen radiocarbon dates (Table 4.1; Hubay et al., 2018).

## 4.2 Terrestrial sites selected

A total of thirteen sites met the criteria set out in section 3.1.2. Investigating the timing of abrupt climatic oscillations at millennial- and centennial-scale relied on the results of the tephrochronology. All these sites were included in the large age model. As a result, all sites were part of the investigation into the timing of the YD and EH oscillations. However, depending on the tephra identified in each record, and their association to the climatic oscillation under investigation, they were identified as either primary (have the appropriate tephra for the climatic period being investigated i.e. the VA with the YD or Hässeldalen tephra with the EH) or secondary sites (have tephra and dating but not the tephra for investigating the climatic period e.g. VA with the YD) (see Table 4.2).

### 4.2.1 Kråkenes, Norway (KRA)

Kråkenes lake is situated on the west coast of Norway (Figure 4.2). Sediment accumulation began around the Allerød period. A cirque glacier close to the lake developed during the YD and subsequently retreated in the EH (Birks et al., 2000). The meltwater from the glacier drained into the lake. Detailed multi-proxy investigations from the lake sediments have shown that this glacier did not considerably influence environmental changes at the site (see Table 4.1). A total of 118 radiocarbon dates from terrestrial macrofossils and bulk sediment samples were produced for the record. Seventy of which are in the LGIT section of the core. In addition, the identification of the Vedde Ash (VA) and Saksunarvatn Ash has resulted in additional chronological tie-points to improve the chronology at the site (Birks et al., 1996; Lohne et al., 2013).

The sediments at Kråkenes show distinct lithostratigraphic change with the transition to the YD period (Birks and Wright, 2000; Birks et al., 2000). Within the pollen record, this period showed an increase in *Salix* and a general opening of the vegetation with a rise in herbaceous pollen (Birks et al., 2000). To identify the pollen transition to the YD, Birks et al. (2000) used the statistical tool of rate-of-change analysis. During the EH, Birks et al. (2000) did not identify any distinct vegetation changes associated with centennial-scale cooling events. However, chironomid-inferred temperatures by Brooks and Birks (2001) show a response to these events during this time.

### 4.2.2 Crudale Meadow, Scotland (CRU)

Crudale Meadow is located on the Orkney Mainland, northern Scotland (Figure 4.2). This infilled lake formed after the retreat of the LGM ice sheet (Whittington et al., 2015). Whittington et al. (2015) conducted high-resolution multi-proxy investigations at the site, identifying numerous climatic oscillations typical of the LGIT period (Table 4.1). There are

radiocarbon dates available from this site by Whittington et al. (2015); however, problems with hard water effects from calcareous sediments resulted in older ages, and so these dates were rejected by those authors. Timms et al. (2018) subsequently identified several well-dated ash layers at the site, providing a basic chronology on a different sediment core (Table 4.2). Based on lithostratigraphy and Loss-On-Ignition (LOI), core alignment between Whittington et al. (2015) and Timms et al. (2018) was performed. The master depth scale is from Whittington et al. (2015; Table 4.2).

The YD at the site is identified in the pollen record: Poaceae dominates and *Salix* and *Artemisia* expand, to the detriment of tree species such as *Betula* and *Pinus*. There is no bulk sediment stable isotope record ($\delta^{18}O$) for this period (Whittington et al., 2015). After the EH warming, there was a rise in thermophilous woodland vegetation. An apparent expansion of *Empetrum nigrum* with a fall in *Pinus sylvestris, Salix* and Poaceae is attributed to the cooling event of the Preboreal Oscillation (PBO) by Björck et al. (1997). Depletion of $\delta^{18}O$, was observed at this time. There is a second isotopic event soon afterwards, with no accompanying vegetation response visible (Whittington et al., 2015).

**Table 4.1** List of the compiled sites selected from across Europe that meet the site selection criteria for both tephrochronology and integration part of this thesis. Information depicts the location of the site, the type of archive, the dating methods available, the tephras identified at each site and the types of proxies available at each site. Definition of codes for the proxies are as follows: P = pollen, B$\delta^{18}$O = bulk oxygen isotopes, B$\delta^{13}$C = bulk carbon isotopes, Ch = chironomids, Di = diatoms, PMF = plant macrofossils, LiBi = Lipid Biomarkers, Ost = Ostracods, Cl = Cladocera, MiCh = micro charcoal, Geoch = geochemistry, BGeoch = bulk geochemistry. Definition of tephras as follows: LST = Laacher See Tephra, VA = Vedde Ash, Häss. = Hässeldalen tephra.

| Site | Country | Archive | Altitude (m a.s.l.) | Type of dating | Tephras available | | | | | Proxies | References |
|---|---|---|---|---|---|---|---|---|---|---|---|
| | | | | | *LST* | *VA* | *Häss.* | *Askja-S* | *Other* | | |
| Kråkenes | Norway | Lake sediments | 38 | $^{14}$C (118 dates, ~66 LGIT dates) | | ✓ | | | ✓ | P, Ch, Di, PMF, GeoCh | Birks et al. (2000); Birks and Wright (2000); Lohne et al. (2013); Brooks and Birks (2000); Bakke et al. (2009) |
| Crudale Meadow | Scotland | Lake sediments | 9 | $^{14}$C (problems) | | ✓ | ✓ | ✓ | ✓ | P, B$\delta^{18}$O, B$\delta^{13}$C | Whittington et al. (2015); Timms et al. (2018) |
| Lake Madtjärn | Sweden | Lake sediments | 135 | $^{14}$C (28 dates LGIT) | | ✓ | | | | P | Björck et al. (1996, 1998); Wastegård et al. (1998) |
| Hässeldala port | Sweden | Palaeolake | 9.25 | $^{14}$C (~40 LGIT dates) | | | ✓ | ✓ | | P, LiBi | Davies et al. (2003); Wohlfarth et al. (2006, 2017); Muschitiello and Wohlfarth (2015) |
| Endinger Bruch | Germany | Palaeolake | 65 | $^{14}$C (1 date LGIT) | | ✓ | ✓ | ✓ | | P | de Klerk (2002); Lane et al. (2012a) |
| Lake Czechowskie | Poland | Lake sediments | 108 | $^{14}$C (4 dates) | | | ✓ | ✓ | | P, BGeoch | Ott et al. (2016); communication with Florian Ott |
| Lake Hämelsee | Germany | Lake sediments | 19.5 | $^{14}$C (5 LGIT dates) | ✓ | ✓ | | ✓ | | P, Ch, LiBi | Previously Merkt and Müller (1999), communication with Stefan Engels and Christine Lane |

| Site | Country | Archive | Altitude (m a.s.l.) | Type of dating | Tephras available | | | | | Proxies | References |
|---|---|---|---|---|---|---|---|---|---|---|---|
| | | | | | *LST* | *VA* | *Häss.* | *Askja-S* | *Other* | | |
| Węgliny | Poland | Palaeolake | 8 | $^{14}$C (9 dates, problems) | ✓ | | ✓ | | | P | Jurochnik and Nalepka, (2013); Housley et al. (2013) |
| Soppensee | Switzerland | Lake sediments | 595 | $^{14}$C (89 dates) | ✓ | ✓ | | ✓ | | P, B$\delta^{18}$O, B$\delta^{13}$C | Hajdas et al. (1993); Lotter et al. (1999); Blockley et al. (2008); Lane et al. (2011a, 2012c) |
| Rotsee | Switzerland | Lake sediments | 420 | $^{14}$C (85 dates) | ✓ | ✓ | | | | P, B$\delta^{18}$O, B$\delta^{13}$C | Zbinden et al. (1989); Ammann and Lotter (1989); Lotter et al. (1989); Lotter et al. (1992a,b); Lane et al. (2012c) |
| Piccolo di Avigliana | Italy | Lake sediments | 365 | $^{14}$C (13 dates) | ✓ | ✓ | | | | P, B$\delta^{18}$O, Ch, Ost, MiCh, PMF | Finsinger et al. (2006, 2008); Finsinger and Tinner (2006); Belis et al. (2008); Larocque and Finsinger (2008); Lane et al. (2012c) |
| Lake Bled | Slovenia | Lake sediments | 475 | $^{14}$C (2 dates) | | ✓ | | | ✓ | P, B$\delta^{18}$O, Ch, Cl, PMF | Andrič et al. (2009); Lane et al. (2011b) |
| Lake Brazi | Romania | Lake sediments | 1740 | $^{14}$C (21 dates, 6 LGIT dates) | | | | ✓ | ✓ | Di$\delta^{18}$O, Ch, Di, PMF, Cl, BGeoCh | Buczkó et al. (2009; 2013; 2018); Korponai et al. (2011); Magyari et al. (2012); Tóth et al. (2012, 2015); Braun et al. (2013); Pál et al (2018); Hubay et al. (2018); Kearney et al. (2018) |
| *Lake Lia* | Romania | Lake sediments | 1910 | $^{14}$C (17 dates, 7 LGIT dates) | | | | ✓ | ✓ | P, PMF, MiCh, Di, BGeoCh | Hubay et al. (2014); Vincze et al. (2017); Orbán et al. (2017); Buczkó et al. (2017); Finsinger et al. (2018); Hubay et al. (2018) |

**Table 4.2** Information on the different cores from each site with the overall master depth and code that will be used for these selected sites throughout the thesis. ✓ indicates site was used, x indicates site was not used in specific chapter as primary site while * indicates used as secondary site due to no specific tephra identified at the site for that climatic period i.e. VA with the YD.

| Site | Pollen core | Chronology core | Core depth used | Site used in | | Site code |
|---|---|---|---|---|---|---|
| | | | | *YD chapter* | *PBO chapter* | |
| Crudale Meadow | CRU (Whittington et al., 2015) | CRUM (Timms et al., 2018) | CRU | ✓ | ✓ | CRU |
| Kråkenes | Core 46 (Birks et al. 2000) | Core 46 (Lohne et al., 2013, 2014) | Core 46 | ✓ | * | KRA |
| Lake Madtjärn | MA (Björck et al., 1996) | MA (Björck et al., 1996) | MA | ✓ | * | MAD |
| Hässeldala port | Core 3 (Wohlfarth et al. 2006; 2018) | Core 2 and Core 5 (Davies et al., 2003; Wohlfarth et al. 2006; 2018) | Core 5 | * | ✓ | HAS |
| Endinger Bruch | HBG (de Klerk et al., 2002 | HBG (Lane et al., 2012a) | HBG | ✓ | ✓ | HBG |
| Lake Czechowskie | JC (Florian Ott, personal communication) | JC (Ott et al., 2016; Florian Ott, personal communication) | JC | * | ✓ | JC |
| Lake Hämelsee | HAM (Stefan Engels, personal communication) | HAM (Jones et al., 2018; Stefan Engels, personal communication) | HAM | ✓ | ✓ | HAM |
| Węgliny | WE'10/2 (Jurochnik and Nalepka, 2013) | WE'10/2 (Housley et al., 2013) | WE'10/2 | ✓ | ✓ | WE |
| Soppensee | SO89-23 (Lotter et al. 1999) | SO89-17 (Hajdas et al., 1993; Lane et al., 2011a, 2012c) | SO89-17 | ✓ | ✓ | SOP |
| Rotsee | RL205 (Lotter et al., 1992a, b) | RL05 (Lane et al. 2012c, Christine Lane, personal communication) | RL05 | ✓ | * | RO |
| Piccolo di Avigliana | AVP1 (Finsinger et al., 2006) | AVP1 (Finsinger et al., 2006; Lane et al. 2012c) | AVP1 | ✓ | * | LPA |
| Lake Bled | Bled C (Andrič et al., 2009) | Bled C (Lane et al., 2011) | Bled C | ✓ | x | BLE |
| Lake Brazi | TDB (Magyari et al., 2012, Pál et al., 2018) | TDB (Hubay et al., 2018, Kearney et al., 2018) | TDB | ✓ | ✓ | TDB |
| Lake Lia | LIA (Eniko Magyari and Ilona Pál personal communication) | LIA (Hubay et al., 2018, Kearney et al., 2018) | LIA | x | x | LIA |

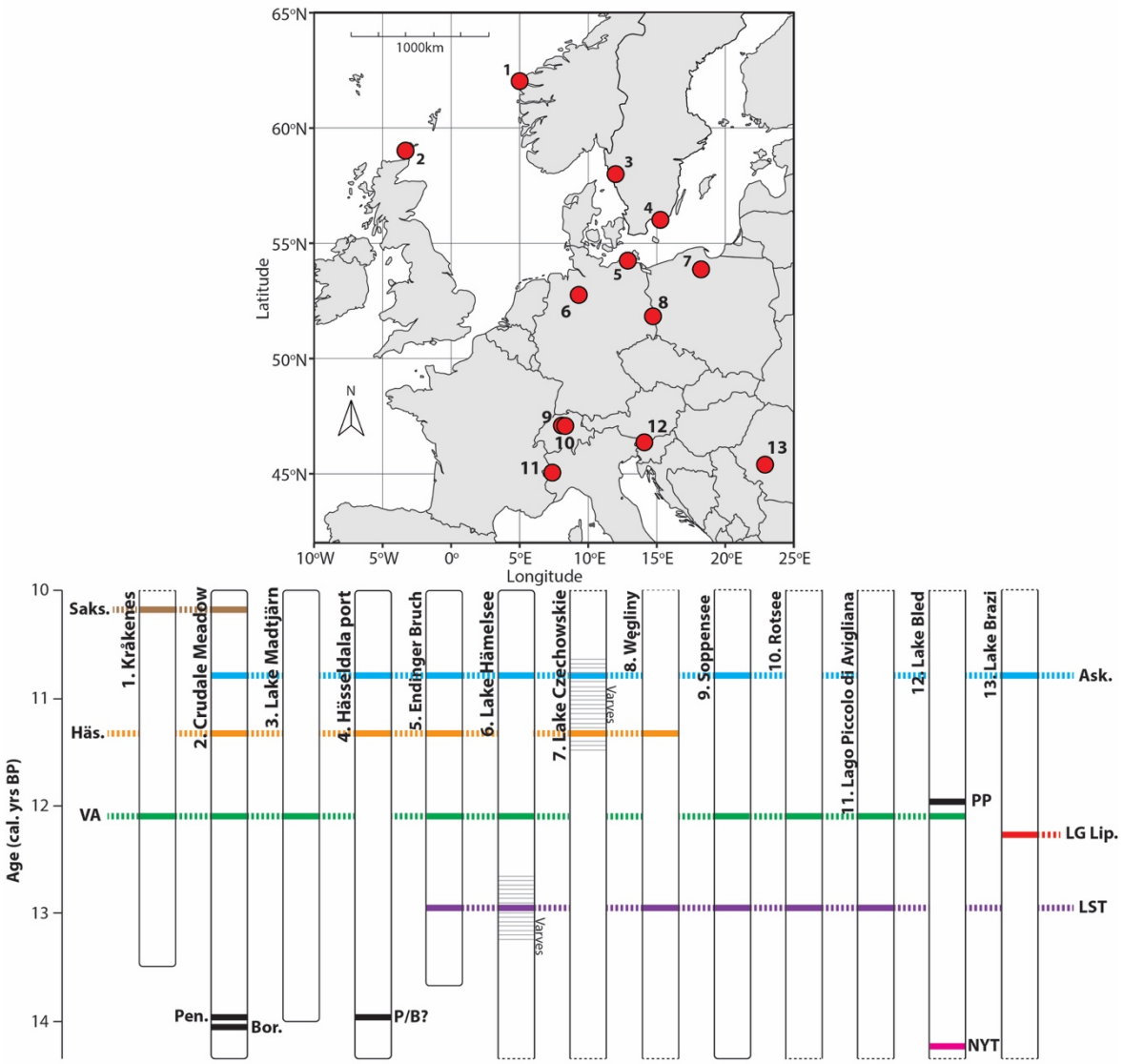


**Figure 4.2** Map of the selected sites with a schematic of the published tephra layers found at each site. The solid coloured lines depict in which sites a certain tephra has been identified. Ages of these tephras are based on Bronk Ramey et al. (2015). Bor. = Borrobol tephra, Pen. = Pennifiler, P/B? = uncertain Borrobol or Pennifiler (Davies et al., 2012; Lind et al., 2016), NYT = Neapolitan Yellow Tuff, LST = Laacher See Tephra, LG Lip. = Late Glacial Lipari tephra (see Chapter 6 and 7), VA = Vedde Ash, PP = Pomici Principali tephra, Häs = Hässeldalen, Ask. = Askja-S, Saks. = Saksunarvatn.

### 4.2.3 Lake Madtjärn, Sweden (MAD)

Lake Madtjärn is located in southwestern Sweden (Figure 4.2). During the Allerød, this lake was located close to the southern margin of the remaining Scandinavian Ice Sheet. The site was isolated on an island during the early Allerød and surrounded by a separate body of water from the sea (Björck et al., 1996). The pollen record spans from the late

Allerød to EH (Björck et al., 1998). A total of twenty-eight radiocarbon dates were obtained from the site, in addition to the VA (Björck et al., 1996, 1998; Wastegård et al., 1998). The YD period has been identified within the pollen record by Björck et al. (1996) with a decline in *Betula alba* and *Pinus* species and a rise in *Artemisia*. Björck et al. (1997) used Lake Madtjärn, with other northern European pollen records, to identifying and date the timing of the PBO. The pollen record shows a decrease in *Betula alba* and *Pinus* with a rising peak in *Empetrum* and *Betula nana* (Björck et al. 1997).

### 4.2.4 Hässeldala port*, Sweden (HAS)

Hässeldala port is situated on the south coast of Sweden (Figure 4.2) This palaeolake record was studied extensively using several proxies from different cores (see Table 4.1). A total of forty-nine radiocarbon dates are available for the site, providing a high-resolution chronology. These radiocarbon dates are from Core 2 and Core 5. Muschitiello et al. (2015) provided core correlations to the master depth of Core 5. The pollen record is from Core 3, correlated across to Core 5 (Table 4.2). Within the pollen record of Core 3, the YD sees a rise in *Betula* and herbaceous taxa of Poaceae and *Artemisia*. In the EH, a cooling event linked to the PBO of Björck et al. (1997) was identified (Wohlfarth et al., 2006). A *Pinus* decline and a peak in *Betula* along with a rise in the shrub *Salix*, accompanied by a decline in LOI, shows this cooling event. Wohlfarth et al. (2006) have identified the Askja-S and Hässeldalen tephra either side of this cooling event in Core 3. Additional tephra of Borrobol-type geochemistry was identified at the site.

### 4.2.5 Endinger Bruch, Germany (HBG)

Endinger Bruch is in north-eastern Germany (Figure 4.2). The Hoher Birkengraben (HBG) core is from an infilled lake within a kettle hole feature from the LGIT. A high-

resolution pollen record was produced by de Klerk (2002). An age-depth model was created by Lane et al. (2012a) through the identification of the LST, VA, Hässeldalen and Askja-S tephras. A single radiocarbon date for the site was also used (Lane et al., 2012a, Pim de Klerk, personal communication).

In the pollen record, the YD is apparent with an opening of the local vegetation, with a rise in NAP, *Betula nana* and *Juniperus* and a constant increase in *Pinus* and *Betula* (de Klerk, 2002). During the EH, vegetation responses to cooling events were not identified at the site (de Klerk, 2002). With the identification of the Hässeldalen and Askja-S tephras, Lane et al. (2012a) highlighted a stepwise increase in *Betula* and decrease of *Pinus* between these tephras which may, or may not, be indicative of the proposed PBO.

### 4.2.6 Lake Czechowskie, Poland (JC)

Lake Czechowskie is in central-northern Poland (Figure 4.2). This lake formed in a subglacial channel since the retreat of the LGM ice sheet (Ott et al., 2016; Wulf et al., 2016a). The sediment record revealed a largely annually laminated record with the lower depths with homogenous sediments (Ott et al., 2016; Wulf et al., 2016a). A systematic cryptotephra investigation revealed two tephra layers during the LGIT: the Askja-S and Hässeldalen tephras. The identified tephras are in a floating varved section with counted layers of 152 +11/-8 varve years between them. Three radiocarbon dates are from the LGIT section of the core.

No current pollen record is published for Lake Czechowskie with data in this thesis supplied by Dr Florian Ott. The YD in the region is identified in the pollen record with a rise in *Juniperus* and herbaceous taxa of *Artemisia* and Poaceae (e.g. Słowiński et al., 2017). The identification of the Askja-S and Hässeldalen tephras in the Lake Czechowskie record allowed Ott et al. (2016) to identify changes in geochemical composition of the varve layers.

A decrease in titanium and a rise in calcium indicated a drying between the positions of the two tephras (Ott et al. 2016). However, there was no change in varve thickness or composition at this time. The high-resolution pollen record during the earliest Holocene is complicated with oscillations in *Betula* and *Pinus,* which makes identifying a clear vegetation response to EH events difficult (Florian Ott, personal communication).

### 4.2.7 Lake Hämelsee, Germany (HAM)

Lake Hämelsee is in northern Germany (Figure 4.2). This shallow lake's sedimentation began before the Late Glacial period and continued throughout the Holocene (Merkt and Müller, 1999). There are partially varved sediments within the LG period. The new core of HÄM13 has recently undergone numerous multi-proxy studies (Christine Lane personal communication). Radiocarbon dates, varves and five tephra layers provide the chronology for the site. (Jones et al., 2018). The floating varve chronology contains the LST, with the counted layers providing additional chronological controls (Jones et al., 2018; Christine Lane and Stefan Engels, personal communication).

Within the HÄM13 pollen record, the transition to the YD is progressive with a slow decline in *Betula* and rise in *Poaceae* (Stefan Engels, personal communication). The YD is overall characterised by higher herbaceous pollen with a rise in *Artemisia* and *Cyperaceae*. During the EH, previous investigations by Merkt and Müller (1999) at the site showed a decline in *Betula* pollen and a rise in NAP. This change was termed the Rammelbeck oscillation, similar to the PBO. Little change in the lithology was noted at this time. In the new core of HÄM13, investigations have not focused upon identifying similar vegetation response (Stefan Engels, personal communication).

### 4.2.8 Węgliny, Poland (WE)

This palaeolake site is in south-western Poland on the Lubsza Plain (Figure 4.2). Situated north of the maximum extent of the LGM ice-sheet, this low-lying feature is hypothesised to have formed from dead-ice structures. The ice then melted and become open water during the Bølling. This was replaced by peat during the Holocene (Jurochnik and Nalepka, 2013; Housley et al., 2013). The master core of WE'10/2 has undergone palynological and tephrochronological investigations (Jurochnik and Nalepka, 2013; Housley et al., 2013). Nine radiocarbon dates provide a chronology for the whole record (Housley et al., 2013). However, with a lack of plant macrofossils and high carbonate levels, problems with hard water affected the older parts of the sequence (Ibid). Identification of the key LST and Hässeldalen tephra layers provides additional chronological tie points for the site (Table 4.1).

Within the pollen record the YD stadial is defined by Jurochnik and Nalepka (2013) with an increase in herbaceous taxa, with a rise in *Hippophaë rhamnoides*, Poaceae, *Artemisia* and *Rumex acetosella*. However, during the EH, there was no vegetation response to EH cooling oscillations identified by Jurochnik and Nalepka (2013).

### 4.2.9 Soppensee, Switzerland (SOP)

Soppensee is a lacustrine record in the Swiss Alps (Figure 4.2). Sedimentation started at the site after the last glaciation (Lotter, 1989). The site has undergone several environmental proxy investigations (e.g. Lotter et al., 1999; Lotter et al., 2001; Tinner et al., 2005). It has a high-resolution chronology from the master core SO89-17 core with tephra layers (see Table 4.1). The pollen record is from the core SO89-23 by Lotter et al. (1999), with correlations made to SO89-17 using event layers (Lotter et al., 1997).

The YD saw a decline in *Betula* and increase in NAP such as *Juniperus*, *Artemisia* and Gramineae (Poaceae) (Lotter et al., 1999). There is a significant shift in bulk sediment stable isotopes ($\delta^{18}O$) at this time (Lotter et al., 1999). The identification of the proposed EH oscillation, the PBO, in the pollen record was questioned due to lack of clear vegetation response (Lotter et al., 1992a). However, a decline in LOI and decrease in *Betula* may show a vegetation response to this cooling event (Lotter et al., 1999).

### 4.2.10 Rotsee, Switzerland (RO)

Rotsee is a lacustrine record ~20 km away from neighbouring Soppensee in the Swiss Alps, with sedimentation dating back to the last glaciation (Figure 4.2; Lotter, 1989; Lotter et al., 1992a). There have been detailed palaeoenvironmental studies conducted on several cores from this site, with the identification of two key tephra layers (see Table 4.1). The cores of RL-300 and RL-305 have provided a chronology for the site using radiocarbon dates and tephra (Table 4.1). Lane et al. (in preparation) correlated these to depths in a new core, RL05 (Verbruggen et al., 2010) using event layers. Additional, repeated radiocarbon dates at certain depths were also carried out by Dr Richard Staff from RL05 (Appendix 4). Another core, RL250, has had extensive pollen investigations and, as a result, was correlated to RL05 depths based upon event layers (Table 4.2; Lotter et al., 1997).

In RL250's pollen record, the decline in *Pinus*, a rise in *Juniperus,* and an increase in NAP such as Poaceae and *Artemisia,* indicate the YD stadial (Lotter et al.,1992a). Within the $\delta^{18}O$ from bulk sediment record, there is an apparent depletion of values indicating a climatic cooling (Lotter et al., 1992a). For the EH period, as with Soppensee, there is difficulty in identifying EH oscillations within the vegetation record (Lotter et al., 1992a).

### 4.2.11 Lago Piccolo di Avigliana, Italy (LPA)

The Lago Piccolo di Avigliana is situated in north-western Italy, Southern Alps (Figure 4.2). The lake was formed by damming of a moraine system originating after the LGM (Finsinger et al. 2008; Lane et al., 2012c). Sediment accumulation continues into the Holocene (Finsinger et al., 2006; 2008). The record has undergone extensive high-resolution, multi-proxy investigations with chronology provided by radiocarbon dates and the identification of key tephra layers (see Table 4.1).

The YD has been identified within the pollen record with a decline in *Quercus* and a rise in *Betula* and *Artemisia*, indicating an opening of the woodland established in the Allerød period (Finsinger et al., 2008). An apparent lowering of bulk sediment $\delta^{18}O$ and chironomids also show an evident cooling at this time (Finsinger et al., 2008; Larocque and Finsinger, 2008). EH oscillations have also been identified in the vegetation and chironomid records (Finsinger and Tinner, 2006).

### 4.2.12 Lake Bled, Slovenia (BLE)

Lake Bled is in north-western Slovenia (Figure 4.2). Formed in a depression left by a glacier from the LGM, sediment accumulation began before 16kya and continued to the mid-Holocene (Andrič et al., 2009). The location of the lake results in influences by the North Atlantic and Mediterranean climatic zones (Andrič et al., 2009; Lane et al., 2011b). The site has undergone multi-proxy palaeoenvironmental. The chronology is provided by radiocarbon dating and the identification of several key tephra layers (see Table 4.1). The YD has been seen in the pollen record with an increase in *Artemisia* and Chenopodiaceae taxa (Andrič et al., 2009). The tree species *Larix* became more abundant, indicating cooler and drier climatic conditions (Andrič et al., 2009). Limited investigations into the EH period have been undertaken by Andrič et al. (2009) due to their project aims.

### 4.2.13 Lake Brazi, Romania (TDB)

Lake Brazi is the southernmost site included in this investigation, located in the Southern Carpathian Mountains, Romania (Fig. 2.1). The palaeoenvironmental information is described in section 4.2.1.1 and Table 4.1. Additional tephrochronological information and results are given in Chapters 6 and 7. The identification of the Askja-S tephra (Kearney et al. 2018) and the Late Glacial Lipari tephra allows Brazi to meet the site selection criteria of section 3.1.2.

The YD is identified at Brazi with an increase in NAP, with *Artemisia* and Chenopodiaceae with a decline in *Pinus* subspecies Diploxylon and thermophilous species such as *Ulmus* and *Quercus* (Magyari et al., 2012). The proposed PBO is identified clearly with a decline in *Pinus mugo* and decrease in *Ulmus* and *Fraxinus excelsior*-type pollen and an overall increase in NAP (Pál et al., 2018).

### 4.2.14 Lake Lia, Romania (LIA)

Lake Lia was not selected as part of the overall investigation into the temporal and spatial response to millennial and centennial-scale climatic oscillations across Europe during the LGIT. The tephrochronological results presented in Chapters 6 and 7, with the independent age control of radiocarbon dating, fulfilled the majority of the site selection criteria for this part of the project. However, issues remain when providing an age model for the pollen record in this thesis. There are discrepancies in the timing of key climatic transitions (i.e. the termination of the YD, see Appendix 3). Compared to the previous age model by Hubay et al. (2018), the YD transition is ~400 years to young in comparison to the Lia age model in this project. Inherited problems may be present with the use of the corrected depths due to a known discrepancy with the core occurred during the coring process. This is in contrast with neighbouring Brazi and the previous age-models for Lia by Dr Eniko

Magyari and Dr Ilona Pál (personal communication). Potential problems exist with the identification of an isochron for many tephras layers due to the influence of the ice melts from the local glacier. This has resulted in re-working of older tephras into the record. As a result, Lia was not chosen. However, Brazi is not affected in the same way as Lia, providing a key site from the central-eastern European region.

# Chapter 5

## The results of tephrostratigraphy investigations of the sediments of Lake Lia and Lake Brazi (Romania)

The following chapter presents the results of the detailed cryptotephra investigation undertaken on sediment cores retrieved from the two Romania lakes, Lia and Brazi.

Following cryptotephra investigations, volcanic glass shard concentrations shown are expressed as shards per gram (shards/g) of dry sediment. Neither cores contained visible tephra layers. The individual tephra layers are named according to the site/core name and their respective depth (e.g. LIA_cm, TDB_cm).

Many of the analysed shards from both sites had consistently low analytical totals of > 92 wt.%. These low totals may be due to the challenges of analysing such small shards, with a small beam spot size (10μm) and/or due to high water content within the tephra shard itself (Hunt and Hill, 1993; Pollard et al., 2006). Whilst it is preferred that geochemical data with analytical totals below 95% are discarded (Hunt and Hill, 1993; Pollard et al., 2006), it is widely recognised that evolved magmas (rhyolites and trachytes) contain high water content and result in total lower than > 95% (e.g. Lowe et al., 2017; Albert et al., 2019). A lower analytical total cut-off of 92% was selected due to the number of glass shards that yielded consistently low totals between 92-95 wt.%, across different analytical runs. The major element and trace element compositions are presented in Tables (Tables 5.1-5.4), data described in text represent averages of the glass shard populations and ± two standard deviations, unless otherwise stated. The error ranges reported in the chemical bi-plots show 2σ standard deviations on replicated analysis of MPI-DING StHs6/80-G glass standard.

## 5.1 Tephrostratigraphy and Glass Geochemistry of Lake Lia

A total of eighteen cryptotephra peaks were identified and geochemically investigated within this sequence (Figure 5.1). The low-resolution shard counts reveal low shard concentrations, with certain intervals being completely sterile of glass shards. Identified peaks in shard concentrations ranged from 38 shards/g (LIA_713) to 908 shards/g (LIA_603). Low shard concentrations are generally observed in the lower portion of the core, with higher concentrations observed towards the top of the core (Figure 5.1). Each cryptotephra layer is describe below, including glass shard concentrations, morphologies, size (long-axis) and chemical composition. Representative analyses of glass shards population for each depth are shown in Table 5.1. Major element geochemical glass data for Lake Lia are shown in Figure 5.2 and Figure 5.2, with the trace element data presented in Figure 5.4 and Figure 5.5. For comparative purposes all data described throughout the text, and presented in the figures and Tables has been normalised to 100 wt.%.

**Table 5.1** Representative grain specific major (WDS-EPMA) element data for Lake Lia. CA= Calc-alkaline; HKCA=High potassium calc-alkaline; SHO = Shoshonitic; $FeO_t$ = all Fe as FeO.

| Depth | LIA_829 | | LIA_815 | | LIA_805 | | LIA_796 | | | | LIA_769 | | LIA_713 | LIA_686 |
|---|---|---|---|---|---|---|---|---|---|---|---|---|---|---|
| Shards | n = 4 | | n = 9 | | n = 12 | | n =29 | | | | n = 4 | | | n = 12 |
| Population | Pop. 1 | | Pop. 1 | | Pop. 1 | | Pop. 1 | | Pop. 1 | Single | Pop. 1 | | Single | Pop.1 |
| Major | | | | | | | | | | | | | | |
| $SiO_2$ | 78.42 | 78.09 | 78.50 | 77.74 | 78.05 | 78.17 | 78.29 | 78.10 | 77.86 | 61.69 | 78.27 | 77.43 | 78.54 | 78.66 |
| $TiO_2$ | 0.01 | 0.12 | 0.07 | 0.09 | 0.11 | 0.00 | 0.15 | 0.09 | 0.02 | 0.46 | 0.04 | 0.07 | 0.05 | 0.11 |
| $Al_2O_3$ | 12.83 | 12.08 | 12.44 | 12.58 | 12.35 | 12.31 | 12.52 | 12.45 | 12.40 | 18.54 | 12.42 | 12.45 | 12.46 | 12.66 |
| $FeO_t$ | 0.57 | 1.04 | 1.06 | 1.03 | 1.15 | 1.05 | 1.09 | 0.47 | 0.95 | 2.91 | 1.12 | 0.95 | 0.86 | 0.92 |
| MnO | 0.00 | 0.00 | 0.03 | 0.00 | 0.04 | 0.00 | 0.01 | 0.00 | 0.00 | 0.01 | 0.01 | 0.13 | 0.00 | 0.00 |
| MgO | 0.01 | 0.01 | 0.07 | 0.02 | 0.06 | 0.05 | 0.06 | 0.05 | 0.05 | 0.46 | 0.12 | 0.02 | 0.07 | 0.12 |
| CaO | 0.54 | 0.64 | 0.78 | 0.56 | 0.81 | 0.62 | 1.02 | 0.87 | 0.77 | 2.16 | 1.02 | 0.69 | 0.60 | 0.94 |
| $Na_2O$ | 4.52 | 4.52 | 3.61 | 3.43 | 4.29 | 3.23 | 3.93 | 3.71 | 2.61 | 4.53 | 3.68 | 3.60 | 3.63 | 3.99 |
| $K_2O$ | 2.95 | 4.33 | 2.91 | 4.37 | 2.96 | 4.41 | 2.78 | 4.14 | 5.20 | 8.50 | 3.13 | 4.53 | 3.63 | 2.45 |
| Total | 93.16 | 93.77 | 93.55 | 93.15 | 94.19 | 92.11 | 93.48 | 94.25 | 95.84 | 97.76 | 92.65 | 95.32 | 93.20 | 93.24 |
| CA/HKCA | CA | HKCA | CA | HKCA | CA | HKCA | CA | HKCA | HKCA | HKCA | CA | HKCA | CA/HKCA | CA |

| Depth | LIA_686 | | LIA_637 | | | LIA_633 | | | | LIA_631 | | | | LIA_613 |
|---|---|---|---|---|---|---|---|---|---|---|---|---|---|---|
| Shards | n = 12 | | n = 9 | | | n = 18 | | | | n =16 | | | | |
| Population | Pop. 1 | Pop. 2 | Pop. 1 | Pop. 2 | | Pop. 1 | Pop. 2 | | Single | Pop. 1 | Pop. 2 | | Single | Pop. 1 |
| Major | | | | | | | | | | | | | | |
| $SiO_2$ | 77.15 | 75.59 | 75.92 | 77.71 | 78.11 | 75.63 | 77.92 | 77.78 | 65.17 | 75.45 | 77.86 | 77.48 | 71.36 | 75.16 |
| $TiO_2$ | 0.09 | 0.11 | 0.06 | 0.10 | 0.04 | 0.10 | 0.01 | 0.01 | 1.01 | 0.04 | 0.11 | 0.12 | 0.17 | 0.08 |
| $Al_2O_3$ | 12.22 | 13.06 | 11.42 | 12.67 | 12.79 | 12.68 | 12.87 | 12.85 | 14.10 | 12.81 | 12.38 | 12.10 | 13.50 | 13.08 |
| $FeO_t$ | 1.08 | 1.35 | 2.46 | 1.03 | 0.82 | 1.23 | 0.94 | 0.83 | 6.48 | 1.49 | 1.19 | 0.93 | 4.04 | 1.39 |
| MnO | 0.00 | 0.00 | 0.13 | 0.00 | 0.00 | 0.26 | 0.05 | 0.02 | 0.29 | 0.06 | 0.11 | 0.02 | 0.28 | 0.05 |
| MgO | 0.01 | 0.04 | 0.00 | 0.07 | 0.05 | 0.00 | 0.02 | 0.00 | 0.95 | 0.04 | 0.03 | 0.08 | 0.23 | 0.01 |
| CaO | 0.43 | 0.66 | 0.15 | 1.04 | 0.71 | 0.57 | 0.58 | 0.57 | 2.96 | 0.72 | 0.85 | 1.18 | 1.43 | 0.80 |
| $Na_2O$ | 3.55 | 4.03 | 4.93 | 4.26 | 3.69 | 3.91 | 4.16 | 4.22 | 5.95 | 4.09 | 4.22 | 3.88 | 5.17 | 3.94 |
| $K_2O$ | 5.12 | 4.79 | 4.54 | 2.97 | 3.60 | 5.22 | 3.32 | 3.62 | 2.64 | 4.88 | 3.09 | 4.06 | 4.04 | 5.08 |
| Total | 97.61 | 95.78 | 96.28 | 93.47 | 92.19 | 94.19 | 95.15 | 93.40 | 94.17 | 95.57 | 93.11 | 92.24 | 98.45 | 93.67 |
| CA/HKCA | HKCA | HKCA | HKCA | CA | HKCA | HKCA | CA | HKCA | HKCA | HKCA | CA | HKCA | CA | HKCA |

**Table 5.1** continued.

| Depth | LIA_613 | | | LIA_612 | | | | LIA_610 | | LIA_607 | | LIA_603 | | LIA_600 | |
|---|---|---|---|---|---|---|---|---|---|---|---|---|---|---|---|
| Shards | n = 9 | | | n = 12 | | | | n = 12 | | n = 8 | | n = 10 | | n = 9 | |
| Population | Pop. 2 | Pop. 3 | Single | Pop. 1 | Pop. 2 | | Pop. 3 | Pop. 1 | Pop. 2 | Pop. 1 | Single | Pop. 1 | Single | Pop. 1 | Single |
| Major | | | | | | | | | | | | | | | |
| $SiO_2$ | 71.31 | 61.96 | 70.87 | 75.23 | 77.38 | 77.89 | 62.93 | 75.30 | 71.22 | 74.89 | 73.05 | 75.32 | 75.51 | 75.80 | 75.03 |
| $TiO_2$ | 0.30 | 0.52 | 0.34 | 0.13 | 0.06 | 0.01 | 0.46 | 0.10 | 0.30 | 0.07 | 0.11 | 0.29 | 0.03 | 0.35 | 0.09 |
| $Al_2O_3$ | 13.55 | 18.67 | 7.58 | 13.04 | 13.98 | 12.64 | 18.21 | 12.72 | 13.44 | 13.16 | 12.82 | 12.42 | 12.93 | 12.34 | 12.71 |
| $FeO_t$ | 3.73 | 2.56 | 8.40 | 1.47 | 0.79 | 0.86 | 2.41 | 1.34 | 3.94 | 1.21 | 3.62 | 2.61 | 1.30 | 2.46 | 1.50 |
| MnO | 0.23 | 0.26 | 0.30 | 0.07 | 0.06 | 0.03 | 0.18 | 0.00 | 0.14 | 0.01 | 0.15 | 0.14 | 0.02 | 0.10 | 0.00 |
| MgO | 0.20 | 0.33 | 0.04 | 0.05 | 0.03 | 0.02 | 0.23 | 0.02 | 0.19 | 0.04 | 0.02 | 0.27 | 0.04 | 0.31 | 0.07 |
| CaO | 1.41 | 1.05 | 0.45 | 0.74 | 0.39 | 0.62 | 1.16 | 0.75 | 1.41 | 0.76 | 0.77 | 1.63 | 0.69 | 1.67 | 0.81 |
| $Na_2O$ | 5.35 | 7.40 | 6.79 | 3.88 | 5.16 | 4.21 | 7.29 | 4.35 | 5.58 | 4.26 | 3.90 | 4.63 | 4.08 | 4.26 | 4.37 |
| $K_2O$ | 3.67 | 6.42 | 4.18 | 4.94 | 2.06 | 3.59 | 6.44 | 5.04 | 3.59 | 5.19 | 5.22 | 2.59 | 5.00 | 2.58 | 5.04 |
| Total | 98.42 | 99.92 | 93.02 | 95.81 | 94.19 | 92.92 | 96.92 | 95.43 | 5.58 | 92.96 | 94.94 | 98.48 | 95.55 | 97.96 | 93.69 |
| CA/HKCA | HKCA | SHO | HKCA | HKCA | CA | HKCA | SHO | HKCA | HKCA | HKCA | HKCA | CA | HKCA | CA | HKCA |

| Depth | LIA_600 | LIA_591 | | LIA_589 | | LIA_576 | | | | |
|---|---|---|---|---|---|---|---|---|---|---|
| Shards | n = 9 | n = 4 | | n = 4 | | n = 11 | | | | |
| Population | Single | Pop. 1 | | Pop. 1 | | Pop. 1 | Pop. 2 | | Pop. 3 | Single |
| Major | | | | | | | | | | |
| $SiO_2$ | 76.33 | 78.50 | 77.60 | 78.00 | 77.56 | 74.70 | 77.23 | 76.75 | 75.79 | 71.52 |
| $TiO_2$ | 0.07 | 0.02 | 0.16 | 0.02 | 0.03 | 0.05 | 0.15 | 0.08 | 0.36 | 0.31 |
| $Al_2O_3$ | 11.25 | 12.69 | 12.64 | 12.89 | 12.69 | 13.10 | 12.68 | 12.57 | 12.38 | 13.41 |
| $FeO_t$ | 2.37 | 0.88 | 0.51 | 0.80 | 0.82 | 1.40 | 1.76 | 1.36 | 2.41 | 3.84 |
| MnO | 0.12 | 0.00 | 0.03 | 0.06 | 0.07 | 0.04 | 0.11 | 0.08 | 0.16 | 0.18 |
| MgO | 0.00 | 0.00 | 0.03 | 0.09 | 0.01 | 0.03 | 0.08 | 0.01 | 0.26 | 0.25 |
| CaO | 0.15 | 0.64 | 0.52 | 0.57 | 0.60 | 0.70 | 1.11 | 0.94 | 1.67 | 1.39 |
| $Na_2O$ | 5.10 | 3.98 | 3.72 | 3.97 | 3.93 | 4.50 | 4.00 | 4.01 | 4.27 | 5.27 |
| $K_2O$ | 4.28 | 3.15 | 4.66 | 3.49 | 4.17 | 5.09 | 2.72 | 4.10 | 2.57 | 3.62 |
| Total | 94.93 | 93.61 | 97.58 | 92.05 | 94.99 | 94.49 | 92.34 | 4.01 | 97.43 | 98.41 |
| CA/HKCA | HKCA | CA | HKCA | CA | HKCA | HKCA | CA | HKCA | CA | HKCA |

**Table 5.2** Representative grain specific trace (LA-ICP-MS) element data for Lake Lia. Shards indicate the number of glass shards analysed for trace elements. Population refers to the major glass populations these shards were analysed from with additional information the average $SiO_2$ and $K_2O$ content representative of the population.

| Depth | LIA_805 | LIA_796 | | | LIA_637 | | LIA_633 | LIA_631 | | |
|---|---|---|---|---|---|---|---|---|---|---|
| **Shards** | n = 1 | n = 5 | | | n = 4 | | n = 7 | n = 4 | | |
| **Population** | Pop. 1 | Pop. 1 | Pop. 2 | Single | Pop.1 | Single | Pop. 1 | Pop.1 | Pop.2 | Single |
| **$SiO_2$ (Av.)** | 78.04 | 77.92 | 77.49 | 61.69 | 75.56 | 77.49 | 75.48 | 75.30 | 77.86 | 71.36 |
| **$K_2O$ (Av.)** | 3.70 | 3.39 | 5.38 | 8.50 | 4.99 | 3.53 | 5.09 | 4.96 | 0.46 | 3.65 |
| **Trace Ppm** | | | | | | | | | | |
| **Rb** | 140.4 | 157.5 | 146.3 | 372.7 | 309.8 | 182.9 | 326.4 | 327.3 | 97.6 | 619.1 |
| **Sr** | 43.9 | 42.9 | 69.1 | 236.8 | 14.4 | 31.9 | 10.6 | 13.8 | 108.0 | 3.9 |
| **Y** | 34.9 | 36.7 | 24.1 | 34.6 | 35.8 | 25.0 | 43.1 | 32.3 | 62.0 | 72.3 |
| **Zr** | 130.6 | 94.1 | 102.8 | 422.9 | 145.8 | 57.5 | 159.0 | 132.2 | 708.2 | 969.2 |
| **Nb** | 16.7 | 16.4 | 11.6 | 65.5 | 34.2 | 11.1 | 36.7 | 35.1 | 131.6 | 156.1 |
| **Ba** | 784.5 | 960.9 | 897.7 | 96.1 | 23.6 | 754.9 | 11.6 | 12.0 | 655.4 | 7.9 |
| **La** | 35.0 | 28.5 | 33.8 | 85.9 | 42.9 | 20.6 | 51.6 | 40.5 | 71.9 | 150.5 |
| **Ce** | 73.3 | 62.6 | 64.5 | 165.7 | 85.7 | 41.2 | 110.0 | 86.6 | 165.1 | 280.6 |
| **Pr** | 8.0 | 6.7 | 6.5 | 15.9 | 9.7 | 4.5 | 12.3 | 8.7 | 18.2 | 27.6 |
| **Nd** | 30.7 | 25.7 | 23.1 | 60.2 | 33.1 | 17.1 | 43.4 | 32.7 | 71.2 | 88.4 |
| **Sm** | 5.6 | 6.6 | 5.5 | 11.7 | 8.0 | 4.1 | 8.5 | 5.6 | 15.3 | 15.4 |
| **Eu** | 0.5 | 0.6 | 0.5 | 2.0 | <LOD | <LOD | 0.2 | 0.2 | 3.5 | 0.9 |
| **Gd** | 6.1 | 5.3 | 3.7 | 7.6 | 6.7 | 3.6 | 7.4 | 5.7 | 13.5 | 11.6 |
| **Dy** | 5.5 | 6.4 | 4.1 | 6.5 | 6.4 | 4.2 | 7.7 | 5.4 | 13.1 | 10.9 |
| **Er** | 4.1 | 3.6 | 2.6 | 3.5 | 3.6 | 2.7 | 4.6 | 3.8 | 6.8 | 7.1 |
| **Yb** | 4.0 | 4.2 | 2.9 | 3.3 | 4.6 | 3.4 | 5.9 | 3.8 | 7.3 | 8.8 |
| **Lu** | 0.5 | 0.6 | 0.4 | 0.5 | <LOD | <LOD | 0.7 | 0.5 | 0.9 | 1.3 |
| **Ta** | 4.5 | 4.3 | 2.9 | 9.1 | 5.3 | 2.9 | 6.1 | 4.7 | 16.0 | 20.1 |
| **Pb** | 1.2 | 1.3 | 1.1 | 3.3 | 2.3 | 1.4 | 2.6 | 2.1 | 5.9 | 6.8 |
| **Th** | 21.0 | 23.3 | 20.3 | 51.0 | 30.1 | 25.3 | 30.1 | 36.7 | 8.3 | 97.2 |
| **U** | 12.9 | 12.9 | 13.6 | 37.7 | 42.2 | 14.2 | 48.0 | 35.8 | 8.2 | 75.4 |

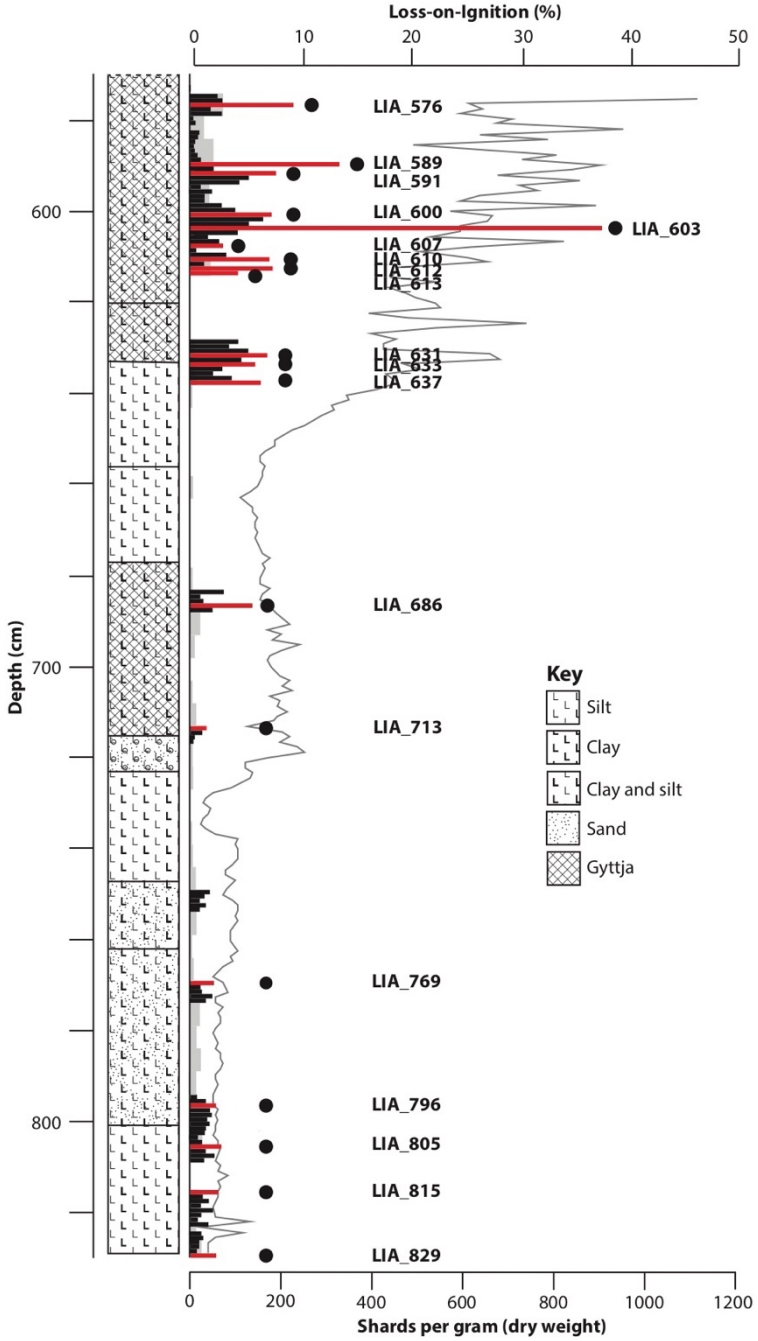


**Figure 5.1** Glass shard concentration profile of Lake Lia, LIA core. Low resolution (5cm) concentrations are indicated by grey boxes. High resolution (1cm) concentrations are shown by black lines with glass shard peak depths that were analysed for glass chemistry highlighted in red and depth marked (e.g. LIA_603). The loss-on-ignition data is plotted with the tephra profile.

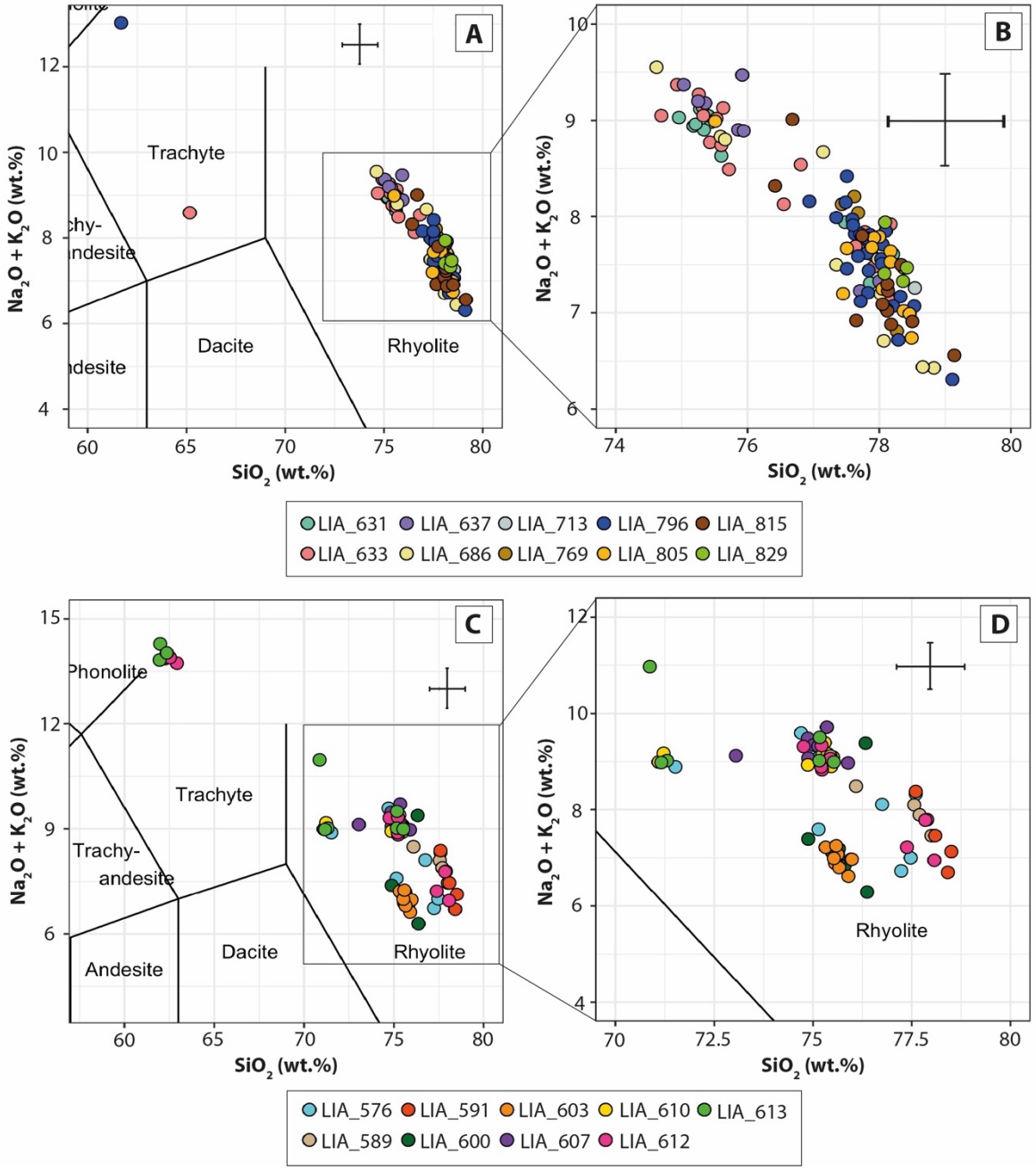


**Figure 5.2** Total Alkali Silica (TAS) plots of glass compositions of cryptotephra layers (e.g. LIA_576) identified in the sediments of Lake Lia (Le Bas et al., 1986). Error bars represent 2 standard deviations of repeat analyses of the MPI-DING StHs6/80-G glass standard.

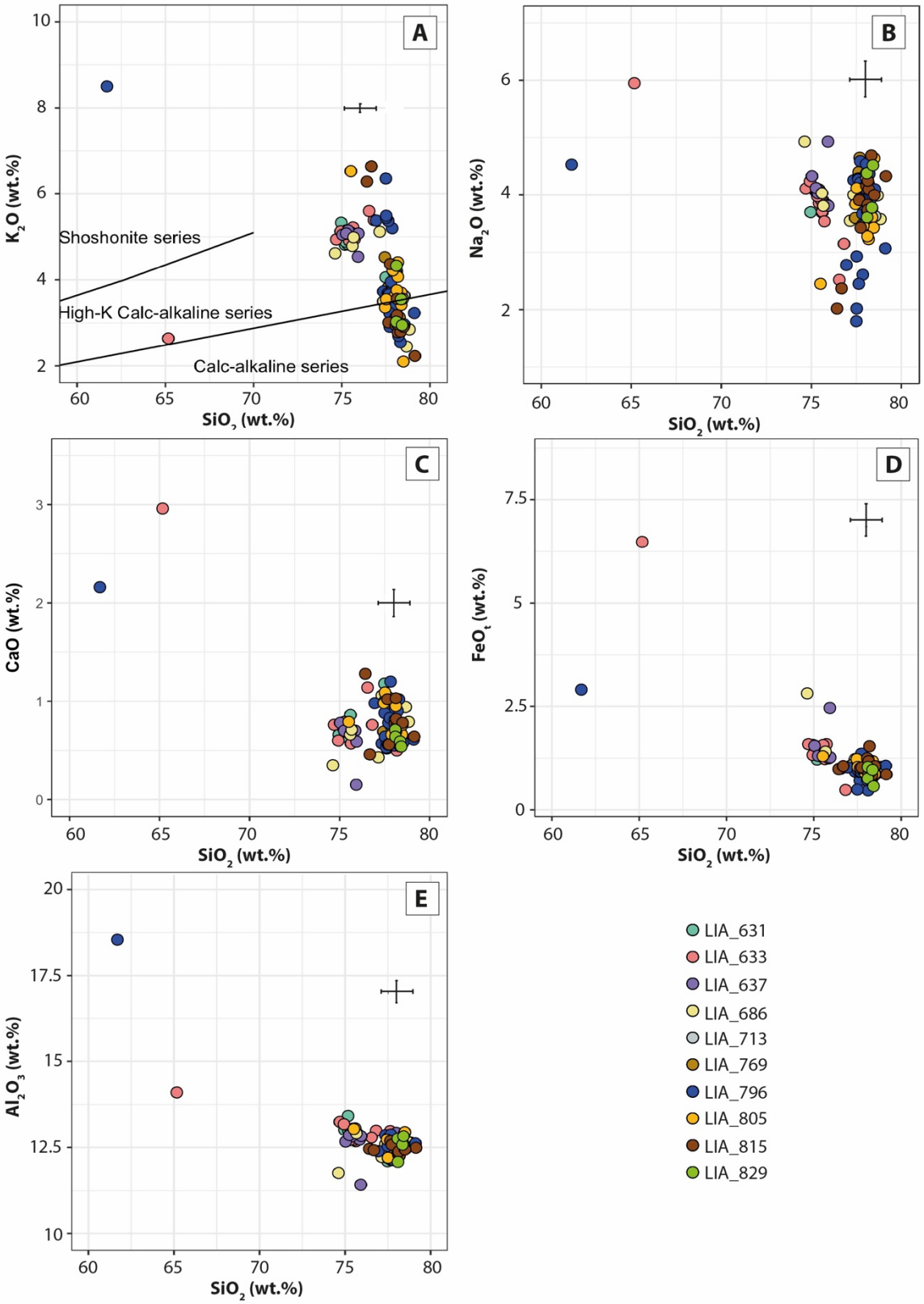


**Figure 5.3** Harker diagram of major element glass geochemical composition for cryptotephra layers identified in the sediments of Lake Lia (A-E). (A) the SiO2 vs. K2O classification diagrams follows Peccerillo and Taylor (1976). Error bars represent 2 standard deviations of repeat analyses of the MPI-DING StHs6/80-G glass standard.

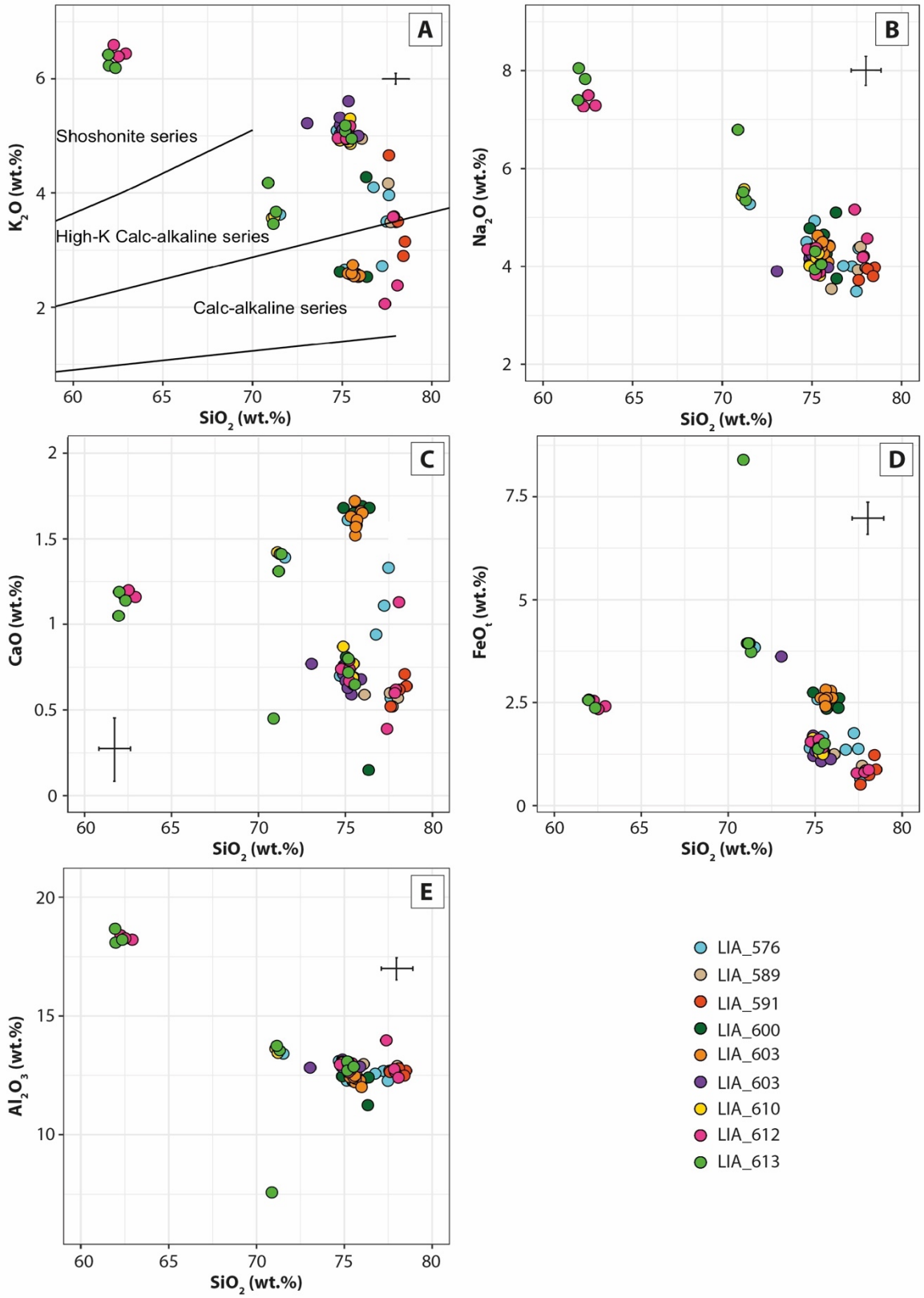


**Figure 5.3 cont.** Harker diagram of major element glass geochemical composition for cryptotephra layers identified in the sediments of Lake Lia (A-E). (A) the SiO2 vs. K2O classification diagrams follows Peccerillo and Taylor (1976). Error bars represent 2 standard deviations of repeat analyses of the MPI-DING StHs6/80-G glass standard

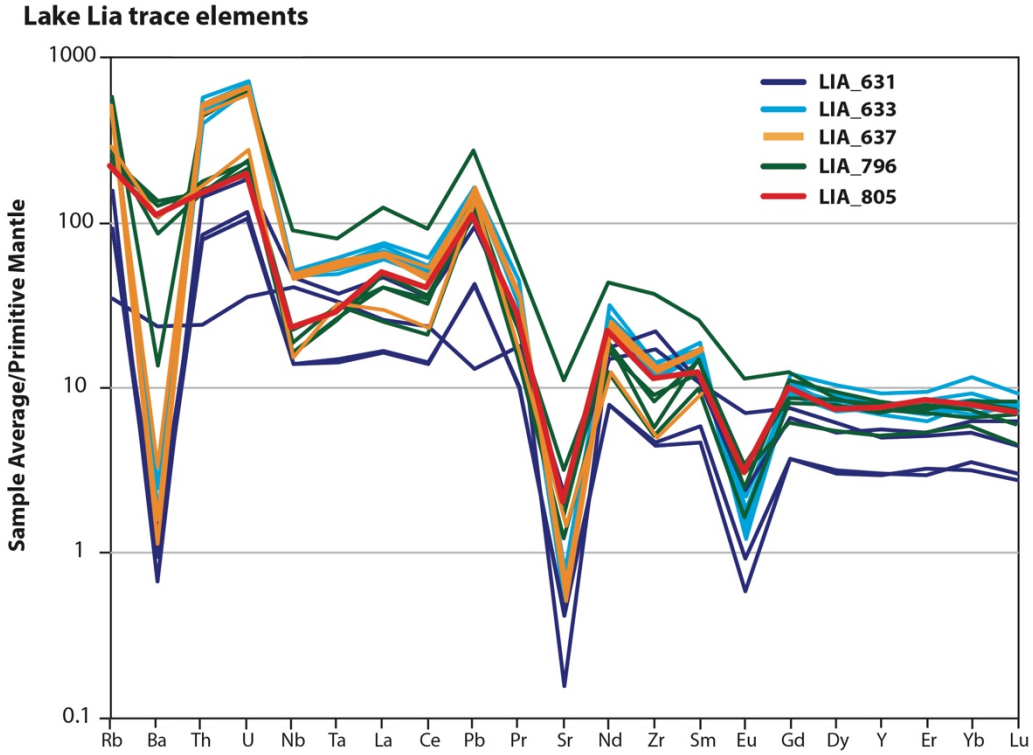


**Figure 5.4** Trace element profiles of Lake Lia glasses normalised to primitive mantle compositions (Sun and McDonough, 1989).

### 5.1.1 LIA_829

This is the oldest cryptotephra horizon with a shard concentration of 59 shards/g. The shards are clear with mixed shard morphologies, dominated by platy (61%) shards, but also comprising cuspate (33%) and fluted glasses (6%). Shard sizes were predominantly 20-50µm (87%), with a few shards larger than 100µm. Geochemical analysis shows LIA_829 to have glass shards ($n$ = 4) that are homogeneous in terms of their high $SiO_2$ (78.24 ± 0.40 wt.%; Figure 5.2) content, whilst in terms of $K_2O$ (3.47 ± 1.27 wt.%) content the glasses are more variable and transition between a CA and HKCA affinity (Figure 5.3).

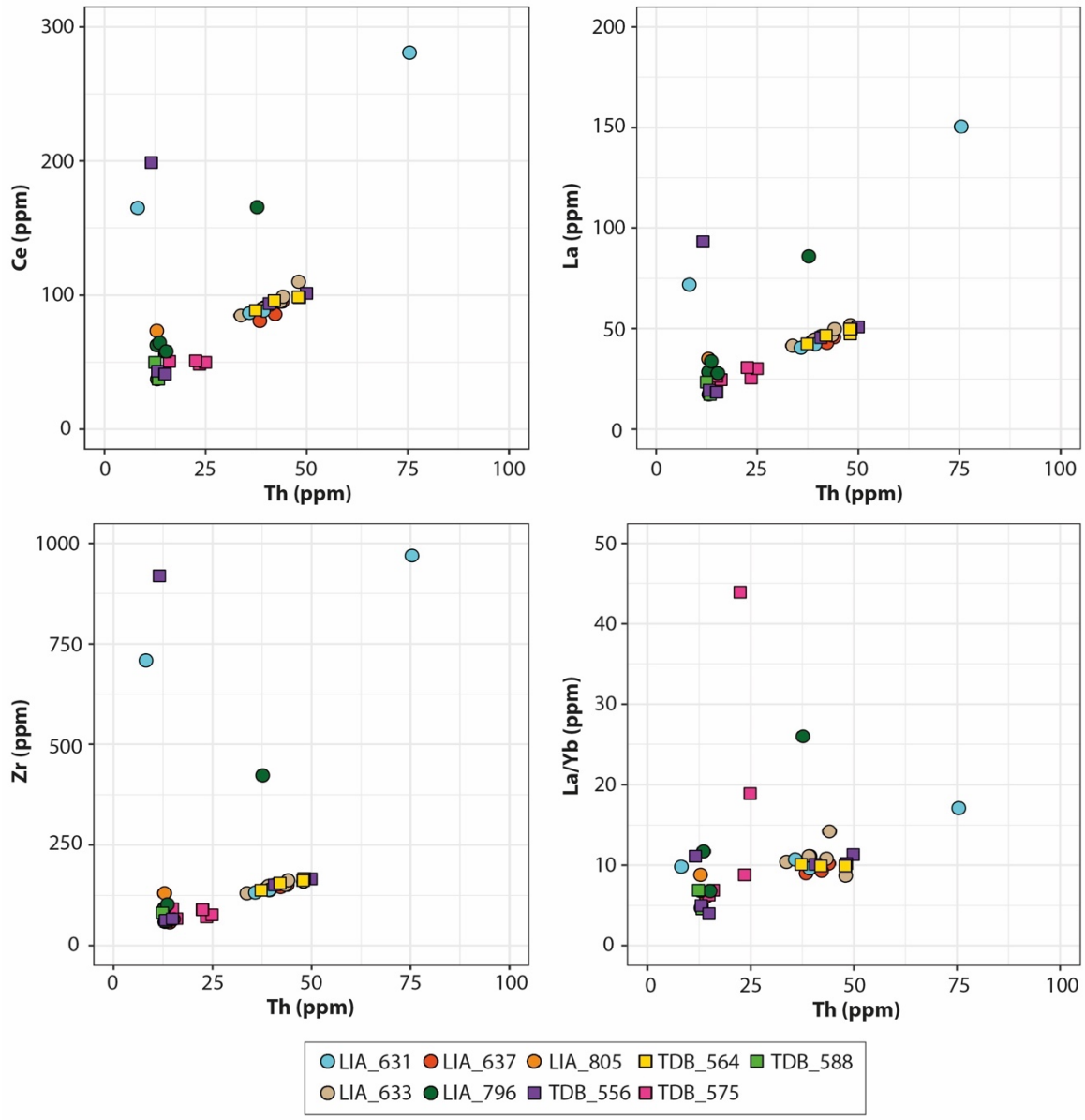


**Figure 5.5** Trace element bi-plots of glasses from certain depths in Lake Lia and Brazi. Error bars of 2 standard deviations of repeat analyses of the MPI-DING StHs6/80-G glass standard were smaller than the points presented in this graph. As a result, they are not displayed.

### 5.1.2 LIA_815

LIA_815 has a shard concentration of 52 shards/g. The cryptotephra morphologies are a mix of platy (50%) and cuspate (50%) shapes with shard size ranging from 20-80µm (89%), with just a few shards larger than 100µm. Geochemical analysis reveals glass

shards ($n$ = 9) that are homogeneous in terms of their high $SiO_2$ (78.09 ± 0.53 wt.%; Figure 5.2) content, whilst in terms of $K_2O$ (3.17 ± 1.02 wt.%) content the glasses are more variable, and transition between a CA and HKCA affinity (Figure 5.3).

### 5.1.3 LIA_805

LIA_805 has a shard concentration of 60 shards/g. The glass shards are clear with mixed morphologies comprising of platy (64%) and cuspate (36%) glasses that range in size between 20-60μm. The geochemical analysis reveals glass shards ($n$ = 12) that are homogeneous in terms of their high $SiO_2$ (78.04 ± 0.63 wt.%; Figure 5.2) content, whilst in terms of $K_2O$ (3.70 ± 0.90 wt.%) content the glasses are variable and transition between a CA and HKCA affinity (Figure 5.3). A single shard was successfully analysed at a trace element level. Normalised to primitive mantle this glass shard shows Light Rare Earth Element (LREE) enrichment relative to the Heavy Rare Earth Elements (HREE) (La/Yb = 8.8), depletions in Nb and Ta typical of an arc signature, and further depletions in Ba, Sr and Eu consistent with feldspar fractionation (Figure 5.4). The glasses contain 21.0 ppm Th, 140.4 ppm Rb, 34.9 ppm Y, 130.6 ppm Zr and 35.0 ppm La (Figure 5.5, Table 5.2).

### 5.1.4 LIA_796

This depth has a shard concentration of 59 shards/g comprising of clear glass shards. Shard morphology is dominantly cuspate (59%) glasses, with a minor platy glass component (32%). These shards range from 20-80μm. There are also larger blocky shards rich in microlites (100μm). Chemical analyses reveals two compositional populations, and a single chemically isolated shard.

Population 1 contains rhyolitic glass shards ($n$ = 20) that are homogeneous in terms of their high $SiO_2$ (77.92 ± 0.57 wt.%) content, whilst in terms of $K_2O$ (3.39 ± 0.90 wt.%)

content these glasses are variable and transition between a CA and HKCA affinity (Figure 5.3). Trace element compositions within these glasses (*n* = 3) normalised to primitive mantle show LREE enrichment relative to the HREE (La/Yb = 4.7-6.9), and depletions at Nb and Ta are consistent with an subduction origin (Figure 5.4).

Glass population 2 (*n* = 5) contains a smaller cluster of homogeneous rhyolitic ($SiO_2$ = 77.49 ± 0.68) glass shards with a HKCA affinity ($K_2O$ = 5.38 ± 0.2). The trace element content of a single glass shard from the HKCA population (2) normalised to primitive mantle reveals LREE enrichment relative to the HREE (La/Yb = 11.6), and depletions in Nb and Ta consistent with an subduction origin (Figure 5.4).

A single glass shard displayed a High-K trachytic affinity ($SiO_2$ = 61.69 wt.%; $K_2O$ = 8.50 wt.%), this K-rich shard also displays high $Al_2O_3$ (18.54 wt.%), FeOt (2.91 wt.%) and CaO (2.16 wt. %) contents with high alkaline ratio ($K_2O/Na_2O$ = 1.88 wt.%). Trace element analysis of this shard reveals high levels of incompatible trace element enrichment (e.g., Rb = 372.65 ppm; Th = 37.69 ppm; Zr = 422.86 ppm). Trace element content normalised to primitive mantle reveals LREE enrichment relative to the HREE (La/Yb = 26.1), depletions in Nb and Ta are consistent with an arc origin, and strong negative anomalies in Ba, Sr and Eu typical of K-feldspar fractionation (Figure 5.4, 5.5).

### 5.1.5 LIA_769

LIA_769 has a shard concentration of 54 shards/g. Shard morphologies are dominated by cuspate (82%) glasses, but also comprise fluted shards (18%). The geochemical analysis reveals glass shards (*n* = 4) that are relatively homogeneous in terms of their high $SiO_2$ (77.75 ± 0.73 wt.%; Figure 5.2) content, whilst in terms of $K_2O$ (3.72 ±

1.22 wt.%) content the glasses are highly variable and transition between CA and HKCA affinities (Figure 5.3).

### 5.1.6 LIA_713

LIA_713 has a shard concentration of 38 shards/g. These colourless shards have variable morphologies; platy (56%), cuspate (32%) and fluted (12%) with a shard size typically 20-80μm insert. A single chemical analysis of this cryptotephra reveals a high-$SiO_2$ (78.54 wt.%) rhyolitic composition which straddles the CA/HKCA boundary ($K_2O$ = 3.63 wt.%; Figures 5.2, 5.3).

### 5.1.7 LIA_686

This cryptotephra peak yielded a shard concentration of 136 shards/g. Shards exhibited mixed morphology with dominance of cuspate (73%) along with blocky, platy and fluted shards with sizes ranging 25-80μm. Twelve analyses reveal overall a heterogeneous rhyolitic compositions (Figure 5.2), a dominant population can be distinguished, with a second smaller population and a single outlier. The dominant glass population 1 ($n$ = 9) are homogenous in terms of their high $SiO_2$ (77.75 ± 0.73 wt.%) content, whist more variable in terms of their $K_2O$ (3.72 ± 1.22 wt.%) content and transition between a CA and HKCA affinity (Figure 5.3). Glass population 2 ($n$ = 2) are homogenous with lower $SiO_2$ (75.62 ± 0.1 wt.%) with similar CaO (0.68 ± 0.07 wt.%) content compared to population 1 (Table 5.1). A single analysis has lower $SiO_2$ (74.62 wt.%) compared to population 1, with high $K_2O$ (4.62 wt.%) content displaying a HKCA affinity (Table 5.1, Figure 5.3).

### 5.1.8 LIA_637

LIA_637 has a peak of 156 shards/g with mixed morphologies, dominated by platy shards (56%), but also containing cuspate (32%) and fluted (12%) shards, and shard sizes ranging 20-60 μm. Nine analyses yielded two heterogeneous rhyolitic composition groups (Figure 5.2). Glass population 1 ($n$ = 6) has high $SiO_2$ (75.56 ± 0.79 wt.%) content with high $K_2O$ (4.99 ± 0.45 wt.%) and high $FeO_t$ (1.52 ± 0.95 wt.%; Figure 5.3). Trace element concentrations ($n$ = 4) from this population show enrichment in LREE relative to the HREE (La/Yb = 9.5 ± 1.1). Normalised to primitive mantle, the glasses reveal depletions in Ba, Sr and Eu, consistent with K-feldspar fractionation (Figure 5.4).

Glass population 2 ($n$ = 3) are homogenous in terms of their high $SiO_2$ (77.94 ± 0.41 wt.%) content, which is distinctly higher than population 1. While in terms of $K_2O$ (3.53 ± 1.64 wt.%) content have shards that transition between a CA and HKCA affinity (Table 5.1, Figure 5.3). A single shard from this population underwent trace element analysis. Normalised to primitive mantle it shows LREE enrichment to the HREE (La/Yb = 6.0; Table 5.2, Figure 5.5) and depletions in Nb and Ta, with enrichment in Rb and Th, indicative of an arc origin (Figure 5.4).

### 5.1.9 LIA_633

This depth has a shard concentration of 155 shards/g. Glass shards are clear with mixed morphologies comprising of cuspate (57%), platy (21%) and fluted (21%) glasses. Shard size ranges 20-80μm. Geochemical analysis reveals glass shards ($n$ = 18) have heterogenous chemical compositions (Figure 5.2). Glass population 1 ($n$ = 11) has high $SiO_2$ (75.48 ± 1.08 wt.%) and high $FeO_t$ (1.35 ±0.63 wt.%) with HKCA affinity ($K_2O$ = 5.09 ± 0.27 wt.%). Trace element analysis of shards from this population ($n$ = 7) are

depleted in Ba, Sr and Eu when normalised to primitive mantle. Glasses show LREE enrichment relative to HREE (10.9 ± 3.41; Figure 5.4).

Glass population 2 (*n* = 5) is homogenous in higher $SiO_2$ (77.93 ± 0.46 wt.%) and with variable higher $K_2O$ (3.50 ± 0.33 wt.%) of CA and HKCA affinities in comparison to population 1 (Table 5.1).

A single shard displays a trachytic composition with lower $SiO_2$ (65.17 wt.%), lower $K_2O$ (2.64 wt.%) and higher $Al_2O_3$ (14.10 wt.%) in relation to population 1. Another outlier analysis displays a rhyolitic composition with high $SiO_2$ (76.55 wt.%) and HKCA affinity ($K_2O$ = 5.60 wt.%; Figure 5.3).

### 5.1.10 LIA_631

LIA_631 has a shard concentration of 171 shards/g. Glass shards are clear with mixed morphologies of cuspate (54%), fluted (38%) and platy (8%). Shard size ranges 20-80μm. The geochemical analysis reveals glass shards (*n* = 16) are rhyolitic, with two glass populations, and a single outlier (Figure 5.2). Glass population 1 (*n* = 8) is homogenous with high $SiO_2$ (75.30 ± 0.39 wt.%) content with high $FeO_t$ (1.46 ± 0.24 wt.%) and a HKCA affinity ($K_2O$ = 4.96 ± 0.33 wt.%; Figure 5.3). Trace element concentrations (*n* = 2) are enriched in LREE relative to HREE (La/Yb = 9.6-10.6). Normalised to primitive mantle reveals, depletions at Nb and Ta consistent with a subduction source, and pronounced depletions in Ba, Sr and Eu, consistent with K-feldspar fractionation (Figure 5.4).

Population 2 glass shards (n = *6*) are homogenous in terms of high $SiO_2$ (77.86 ± 0.46 wt.%) content, whilst more variable in terms of their $K_2O$ (4.96 ± 0.33 wt.%) content in comparison to population 1, with transitions between a CA and HKCA affinity (Figure

5.3). Trace element content from a single shard normalised to primitive mantle show LREE enrichment to HREE (La/Yb = 9.9) and depletions in Nb and Ta (Figure 5.4).

A single shard displayed with lower $SiO_2$ (71.36 wt.%) content with a composition of high $FeO_t$ (4.04 wt.%) compared to population 1 (Figure 5.2, 5.3). The shard has a CA affinity ($K_2O$ = 3.65 wt.%). Trace element analysis normalised to primitive mantle shows enrichment of Rb, Th, Nb and Ta, inconsistent with the dominant glasses of this layer, and indicative of anorogenic volcanic settings (Figure 5.4, Table 5.2).

### 5.1.11 LIA_613

This depth yielded a shard concentration of 108 shards/g. Glass shards are clear with mixed cuspate (62%), fluted (33%) and platy (5%) morphologies with shard size ranging 25-80μm. Chemical analyse reveals shards of three compositional populations, and a single chemically isolated glass composition. Population 1 contains rhyolitic glass shards ($n$ = 3; Figure 5.2) high in $SiO_2$ (75.29 ± 0.43 wt.%) content and low $FeO_t$ (1.43 ± 0.14 wt.%). Glass population 2 has rhyolitic shards ($n$ = 2) with lower $SiO_2$ (71.24 ± 0.21 wt.%) content than population 1, and higher $FeO_t$ (3.83 ± 0.28 wt.%) content. Glass population 3 ($n$ = 3) are High-K trachytic glasses ($SiO_2$ = 62.10 ± 0.44 wt.%; $K_2O$ 6.28 ± 0.25 wt.%, Figure 5.2), also containing high-Na (7.76 ± 0.66) than $K_2O$ content, manifested in a low alkali ratio ($K_2O/Na_2O$ = 0.81 ± 0.10 wt. %).

A single rhyolitic glass shard exhibits lower $SiO_2$ (70.87 wt.%) content than the other rhyolitic glasses in this layer, whilst also showing higher $FeO_t$ (8.40 wt.%) and lower $Al_2O_3$ (7.58 wt.%) content with high $K_2O$ (4.18 wt.%) content, classified as having a HKCA affinity (Figure 5.3).

### 5.1.12 LIA_612

LIA_612 has a shard concentration of 184 shards/g. Shard morphologies are clear with mixed morphologies of cuspate (77%), platy (33%), fluted (8%) and blocky (4%) with shard sizes ranging 20-80µm. The geochemical analysis reveals three compositional populations. Population 1 contains rhyolitic glass shards (*n* = 5*;* $SiO_2$ 75.17 ± 0.50 wt.%; Figure 5.2) with $K_2O$ that can be classified as HKCA (5.02 ± 0.20 wt.%; Figure 5.3). Glass population 2 reveals rhyolitic shards (*n* = 4) of homogenous composition in terms of their high $SiO_2$ (77.80 ± 0.59 wt.%) content, but are lower in their overall $K_2O$ content relative to population 1 glasses, and are also more variable $K_2O$ (2.90 ± 1.90 wt.%) where they transition between a CA and HKCA affinities (Figure 5.3). Population 3 displays glass shards of High-K trachytic composition ($SiO_2$ = 62.57 ± 0.68 wt.%; $K_2O$ = 6.47 ± 0.21 wt.%, Figure 5.2), these glasses also show high-Na content, where $Na_2O$ (7.35 ± 0.26) is > $K_2O$ reflected in a low alkali ratio ($K_2O/Na_2O$ = 0.88).

### 5.1.13 LIA_610

This depth has a shard concentration of 175 shards/g. The glass shard show mixed morphologies with cuspate (54%), fluted (38%) and platy (8%) with shard sizes ranging from 25-70µm. Geochemical analysis yielded two distinct but homogenous rhyolitic populations (Figure 5.2). Glass population 1 (*n* = 6) rhyolites are high in $SiO_2$ (75.28 ± 0.44 wt.%) and display a HKCA affinity ($K_2O$ = 4.99 ± 0.33 wt.%). Glass population 2 (*n = 2*) are again HKCA rhyolites ($K_2O$ = 3.57 ± 0.05 wt.%; Figure 5.3), but are lower in their $SiO_2$ (71.15 ± 0.20 wt.%) content, and consequently higher in CaO (1.41 ± 0.01 wt.%) and $FeO_t$ (3.94 ± 0.01 wt.%) than the population 1 glasses (Figure 5.3).

### 5.1.14 LIA_607

This depth has a shard concentration of 75 shards/g. The glass shards are clear with mixed morphologies of cuspate (67%), platy (17%) and fluted (8%), with shard sizes ranging 20-80µm. Geochemical analysis reveals a dominant rhyolitic glass shard population, with a chemically distinct rhyolitic outlier (Figure 5.2). The dominant rhyolitic glass population ($n$ = 7) has $SiO_2$ content of 75.15 ± 0.74 wt.% and displays a HKCA affinity ($K_2O$ = 5.17 ± 0.46 wt.%). Whilst the single outlying HKCA ($K_2O$ = 5.22 wt.%; Figure 5.3) rhyolitic glass shard shows a lower $SiO_2$ (73.05 wt.%) content, and coupled with a higher $FeO_t$ (3.62 wt.%) content relative to the dominant glass population 1 (Table 5.1).

### 5.1.15 LIA_603

LIA_603 has a high shard concentration of 908 shards/g with clear glass. Shard morphology comprises of cuspate (55%), fluted (34%) and platy (11%) glasses. Glass shard sizes range from between 20-50µm. Geochemical analysis reveals one dominant rhyolitic glass population with a single outlier rhyolitic analysis (Figure 5.2). The dominant rhyolitic glass population 1 ($n$ = 9) is characterised by glass shards with a $SiO_2$ content of 75.64 ± 0.39 wt.% and they are classified as having a CA ($K_2O$ = 2.60 ± 0.13 wt.%) affinity, with a CaO (1.61 ± 0.12 wt.%) content that is relatively high given their $SiO_2$ content. A single rhyolitic glass shard displays similar $SiO_2$ content (75.51 wt.%) and a HKCA affinity ($K_2O$ = 5.00 wt.%; Figure 5.3A), this outlying glass analysis also shows significantly lower CaO (0.69 wt.%) content relative to the dominant glass population (1).

### 5.1.16 LIA_600

This depth contains a shard concentration of 183 shards/g. Shard morphologies comprised of clear platy glasses (50%) with fluted (23%) and cuspate (27%) components. Shard sizes ranged between 20-80μm. Geochemical analysis shows a dominant rhyolitic glass population and two outlier rhyolitic analyses. Rhyolitic glass population 1 shards (*n* = 7) have $SiO_2$ content of 75.67 ± 0.92 wt.% and are show a CA affinity ($K_2O$ =2.56 ± 0.06 wt.%), with CaO (1.67 ± 0.04 wt.%) content that is relatively high at their given $SiO_2$ content (Figure 5.2). A single rhyolitic shard ($SiO_2$ = 75.03 wt.%) displays a HKCA affinity ($K_2O$ = 5.04 wt.%; Figure 5.3A), which also displays lower CaO (0.81 wt.%) and $FeO_t$ (1.50 wt.%) content than the dominant population (Table 5.1). Another shard is higher in $SiO_2$ content (76.33 wt.%) than the other rhyolitic glasses characterised and show a HKCA affinity ($K_2O$ = 4.28 wt.%; Figure 5.3). .

### 5.1.17 LIA_591

This depth has a shard concentration of 190 shards/g. Shard morphology is largely dominated by clear platy glasses (75%), but also contains fluted (17%) and cuspate (8%) glass shards. Shard size ranges from between 25-90μm. The glass shards analysed shows a homogenous rhyolitic population in terms of their very high $SiO_2$ (78.15 ± 0.81 wt.%) content, whilst in terms of $K_2O$ (3.55 ± 1.55 wt.%) content these glasses display more variability and transition between a CA and HKCA affinity (Figure 5.3, Table 5.1).

### 5.1.18 LIA_589

LIA_589 has a shard concentration of 333 shards/g. Shard morphology is predominated by clear platy glasses (65%) with fluted (25%) and cuspate (10%). Shard

size ranges 25-80µm. The geochemistry analysis shows rhyolitic glass shards ($n$ = 4) that are homogenous in terms of their high $SiO_2$ (77.34 ± 1.71 wt.%) content, but are more variable with respect to their $K_2O$ content (4.02 ± 1.39 wt.%), where they transition between a CA and HKCA affinity (Figure 5.3; Table 5.1).

### 5.1.19 LIA_ 576

This depth has a shard concentration of 228 shards/g. The glass shards are colourless with fluted (55%), cuspate (42%) and platy (3%) morphologies with shard sizes ranging 20-70µm. Chemical analyses reveal that this depth comprises of distinct rhyolitic glass components. The most dominant population (1) observed comprises shards ($n$ = 4) that have a rhyolitic ($SiO_2$ = 75.07 ± 0.61 wt.%; Figure 5.2) HKCA affinity ($K_2O$ = 5.09 ± 0.12 wt.%), with 1.51 ± 0.25 wt.% and 0.71 ± 0.06 wt.% of FeOt and CaO, respectively. Glass population 2 shards ($n$ = 4) are homogenous in terms of their high $SiO_2$ (77.26 ± 0.75 wt.%) content, whilst more variable with respect to their $K_2O$ (3.57 ± 1.24 wt.%) content that transitions between a CA and HKCA affinities. Glass population 3 rhyolitic shards ($n$ = 2) have a CA affinity ($K_2O$ = 2.62 ± 0.14), and are higher in $FeO_t$ (2.50 ± 0.25 wt.%) and CaO (1.64 ± 0.09 wt.%) content than population 1. A single outlying rhyolitic shard consists of lower $SiO_2$ (71.52 wt.%; Figure 5.2) content than the other observed components, whilst displaying a clear HKCA affinity ($K_2O$ = 3.62 wt.%). Consistent with it lower $SiO_2$ content this rhyolitic glass displays higher CaO and FeOt content than the other rhyolitic glasses observed at this depth (Table 5.1).

## 5.2 Tephrostratigraphy and geochemistry of Lake Brazi

A total of twelve cryptotephra horizons were identified within a constant background of shard throughout the record (Figure 5.6). There is a distinct peak at TDB_564 (1,135 shards/g). Other peaks are not clearly defined within the record (e.g. TDB_540 and TDB_541). Represented examples of glass shards population for each depth are shown in Table 5.3 and Table 5.4. All major geochemical results for Lake Brazi are displayed in Figure 5.7 and Figure 5.8 with trace element results displayed in Figure 5.5 and Figure 5.9.

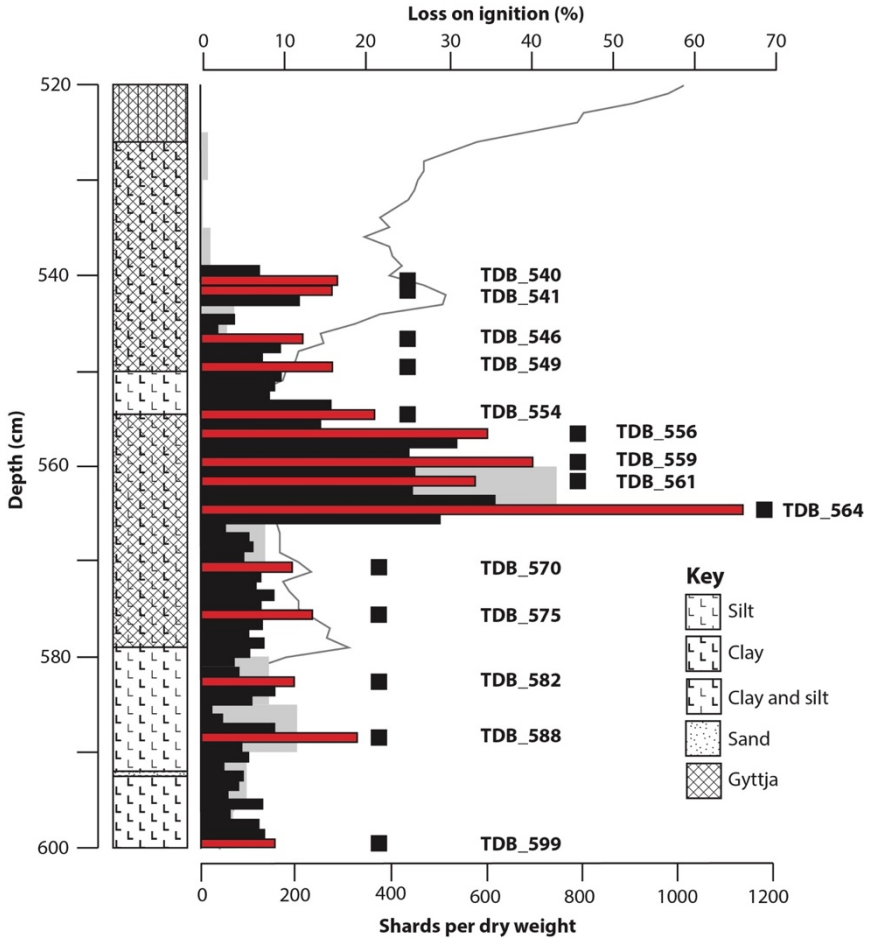


**Figure 5.6** Glass shard concentration profile of Lake Brazi, TDB core. Low resolution (5cm) concentrations are indicated by grey boxes. High resolution (1cm) concentrations are shown by black lines with depths that were analysed for glass chemistry are highlighted in red. The loss-on-ignition data is plotted with the tephra profile.

**Table 5.3** Representative grain specific major (WDS-EPMA) element data for Lake Brazi. CA= Calc-alkaline; HKCA=High potassium calc-alkaline; SHO = Shoshonitic; $FeO_t$ = all Fe as FeO.

| Depth | TDB_599 | | TDB_588 | | | TDB_575 | TDB_570 | | TDB_564 | | TDB_561 | | TDB_559 | |
|---|---|---|---|---|---|---|---|---|---|---|---|---|---|---|
| Shards | n = 14 | | n = 15 | | | n =13 | n = 5 | | n = 21 | | n = 2 | | n = 8 | |
| Population | Pop. 1 | | Pop. 1 | | Single | Pop.1 | Pop. 1 | Single | Pop. 1 | Pop. 2 | Single | Single | Pop. 1 | Pop. 2 |
| Major | | | | | | | | | | | | | | |
| $SiO_2$ | 77.61 | 78.56 | 77.43 | 78.29 | 75.59 | 77.45 | 77.92 | 74.20 | 75.45 | 77.80 | 75.36 | 71.67 | 77.86 | 75.20 |
| $TiO_2$ | 0.05 | 0.12 | 0.14 | 0.09 | 0.09 | 0.01 | 0.08 | 0.20 | 0.00 | 0.09 | 0.06 | 0.25 | 0.04 | 0.05 |
| $Al_2O_3$ | 12.53 | 12.42 | 12.47 | 12.40 | 12.66 | 12.74 | 12.53 | 12.56 | 12.94 | 12.47 | 12.96 | 13.33 | 12.70 | 13.01 |
| $FeO_t$ | 0.79 | 1.00 | 1.21 | 1.22 | 1.54 | 0.88 | 1.05 | 2.15 | 1.41 | 1.12 | 1.44 | 3.78 | 0.84 | 1.35 |
| MnO | 0.02 | 0.05 | 0.09 | 0.05 | 0.14 | 0.00 | 0.00 | 0.11 | 0.06 | 0.11 | 0.05 | 0.15 | 0.03 | 0.11 |
| MgO | 0.07 | 0.12 | 0.10 | 0.03 | 0.02 | 0.00 | 0.01 | 0.19 | 0.01 | 0.04 | 0.00 | 0.21 | 0.02 | 0.03 |
| CaO | 0.65 | 1.02 | 1.01 | 0.82 | 0.79 | 0.61 | 0.65 | 0.52 | 0.70 | 0.65 | 0.75 | 1.42 | 0.59 | 0.71 |
| $Na_2O$ | 4.22 | 3.48 | 3.82 | 4.24 | 3.83 | 4.30 | 4.12 | 3.69 | 3.88 | 3.31 | 3.74 | 5.39 | 3.96 | 3.97 |
| $K_2O$ | 3.94 | 3.10 | 3.61 | 2.72 | 5.05 | 3.89 | 3.47 | 6.00 | 5.07 | 4.27 | 5.20 | 3.56 | 3.80 | 5.15 |
| Total | 94.04 | 92.55 | 93.38 | 94.12 | 96.17 | 92.47 | 92.05 | 94.90 | 93.27 | 94.00 | 95.18 | 95.74 | 94.49 | 96.66 |
| CA/HKCA | HKCA | CA | CA | HKCA | HKCA | HKCA | HKCA | HKCA/sh. | HKCA | HKCA | HKCA | HKCA | HKCA | HKCA |

| Depth | TDB_556 | | | | TDB_554 | TDB_549 | TDB_546 | | | TDB_541 | | | |
|---|---|---|---|---|---|---|---|---|---|---|---|---|---|
| Shards | n = 38 | | | | n = 3 | n = 1 | n = 6 | | | n = 7 | | | |
| Population | Pop. 1 | | Pop. 2 | Single | Pop. 1 | Single | Pop. 1 | | Single | Pop. 1 | Pop. 2 | Single | Single |
| Major | | | | | | | | | | | | | |
| $SiO_2$ | 78.53 | 77.90 | 75.38 | 76.69 | 77.67 | 75.47 | 77.87 | 78.05 | 71.75 | 75.89 | 75.89 | 75.74 | 77.44 |
| $TiO_2$ | 0.02 | 0.03 | 0.07 | 0.04 | 0.02 | 0.09 | 0.04 | 0.01 | 0.23 | 0.33 | 0.10 | 0.05 | 0.07 |
| $Al_2O_3$ | 12.87 | 12.82 | 12.91 | 12.97 | 12.58 | 13.06 | 12.64 | 12.77 | 13.56 | 12.42 | 13.21 | 11.89 | 12.47 |
| $FeO_t$ | 0.82 | 0.96 | 1.46 | 1.29 | 0.80 | 1.43 | 1.01 | 0.76 | 3.85 | 2.42 | 1.13 | 2.33 | 1.02 |
| MnO | 0.00 | 0.07 | 0.04 | 0.11 | 0.07 | 0.10 | 0.00 | 0.04 | 0.15 | 0.22 | 0.00 | 0.07 | 0.03 |
| MgO | 0.04 | 0.05 | 0.02 | 0.02 | 0.00 | 0.04 | 0.06 | 0.00 | 0.21 | 0.17 | 0.09 | 0.00 | 0.01 |
| CaO | 0.57 | 0.79 | 0.61 | 0.93 | 0.61 | 0.66 | 0.84 | 0.60 | 1.35 | 1.51 | 0.78 | 0.23 | 0.70 |
| $Na_2O$ | 4.21 | 3.28 | 3.83 | 4.30 | 4.17 | 3.74 | 4.22 | 3.86 | 5.19 | 4.33 | 3.60 | 5.40 | 3.46 |
| $K_2O$ | 2.82 | 3.93 | 5.28 | 3.54 | 3.94 | 5.05 | 3.22 | 3.84 | 3.47 | 2.63 | 5.00 | 3.85 | 4.66 |
| Total | 92.74 | 92.81 | 95.31 | 93.31 | 93.46 | 96.25 | 95.85 | 94.84 | 96.20 | 99.69 | 95.53 | 96.43 | 93.92 |
| CA/HKCA | CA | HKCA | HKCA | HKCA | HKCA | HKCA | CA | HKCA | HKCA | CA | HKCA | HKCA | HKCA |

**Table 5.3** continued.

| **Depth** | **TDB_540** | | | |
|---|---|---|---|---|
| **Shards** | n = 7 | | | |
| **Population** | Pop. 1 | | Pop. 2 | Single |
| **Major** | | | | |
| **$SiO_2$** | 77.27 | 78.58 | 75.35 | 74.98 |
| **$TiO_2$** | 0.10 | 0.01 | 0.34 | 0.06 |
| **$Al_2O_3$** | 13.05 | 12.47 | 12.37 | 13.26 |
| **$FeO_t$** | 0.92 | 0.76 | 2.63 | 1.35 |
| **MnO** | 0.00 | 0.00 | 0.16 | 0.10 |
| **MgO** | 0.04 | 0.05 | 0.26 | 0.05 |
| **CaO** | 0.83 | 0.58 | 1.73 | 0.74 |
| **$Na_2O$** | 4.38 | 3.69 | 4.42 | 4.09 |
| **$K_2O$** | 3.31 | 3.73 | 2.61 | 4.93 |
| **Total** | 96.02 | 96.25 | 95.89 | 97.30 |
| **CA/HKCA** | CA | HKCA | CA | HKCA |

**Table 5.4** Representative grain specific trace (LA-ICP-MS) element data for Lake Brazi. Shards indicate the number of glass shards analysed for trace elements. Population refers to the major glass populations these shards were analysed from with additional information the average $SiO_2$ and $K_2O$ content representative of the population

| **Depth** | **TDB_588** | **TDB_575** | **TDB_564** | **TDB_556** | | |
|---|---|---|---|---|---|---|
| **Shards** | n = 2 | n = 5 | n = 4 | n = 6 | | |
| **Population** | Pop. 1 | Pop. 1 | Pop. 1 | Pop. 1 | Pop. 2 | Single |
| **$SiO_2$ (Av.)** | 77.60 | 77.16 | 75.29 | 77.79 | 75.23 | 76.69 |
| **$K_2O$ (Av.)** | 4.12 | 5.38 | 5.04 | 3.59 | 5.05 | 3.54 |
| **Trace Ppm** | | | | | | |
| **Rb** | 4849.0 | 4427.1 | 5879.1 | 171.0 | 325.6 | 92.6 |
| **Sr** | NA | NA | NA | 27.2 | 13.9 | 130.3 |
| **Y** | NA | NA | NA | 35.9 | 41.6 | 85.4 |
| **Zr** | 163.1 | 170.3 | 338.1 | 66.9 | 166.0 | 918.5 |
| **Nb** | 28.3 | 25.6 | 13.9 | 13.6 | 36.7 | 136.8 |
| **Ba** | 36.8 | 30.5 | 38.8 | 657.4 | 12.5 | 742.0 |
| **La** | 81.6 | 67.3 | 155.5 | 18.5 | 50.8 | 93.1 |
| **Ce** | 15.5 | 25.1 | 35.5 | 41.2 | 101.4 | 198.8 |
| **Pr** | 885.4 | 691.9 | 16.3 | 5.0 | 10.8 | 23.1 |
| **Nd** | 23.5 | 24.7 | 46.6 | 18.5 | 38.9 | 94.4 |
| **Sm** | 49.9 | 50.6 | 96.0 | 5.0 | 8.1 | 18.4 |
| **Eu** | 5.8 | 5.4 | 9.8 | 0.3 | 0.2 | 3.8 |
| **Gd** | 24.3 | 19.4 | 36.7 | 4.3 | 7.4 | 15.5 |
| **Dy** | 5.9 | 4.3 | 7.5 | 6.4 | 6.4 | 17.6 |
| **Er** | 0.4 | 0.3 | 0.3 | 3.5 | 4.5 | 8.9 |
| **Yb** | 5.2 | 4.6 | 5.7 | 4.6 | 4.5 | 8.4 |
| **Lu** | 6.5 | 4.9 | 5.7 | 0.6 | 0.7 | 1.2 |
| **Ta** | 3.8 | 3.3 | 3.8 | 3.0 | 5.7 | 21.5 |
| **Pb** | 3.4 | 3.6 | 4.7 | 1.4 | 2.6 | 7.5 |
| **Th** | 0.6 | 0.5 | 0.6 | 49.5 | 31.1 | 8.3 |
| **U** | 3.0 | 3.1 | 5.5 | 14.9 | 49.9 | 11.6 |

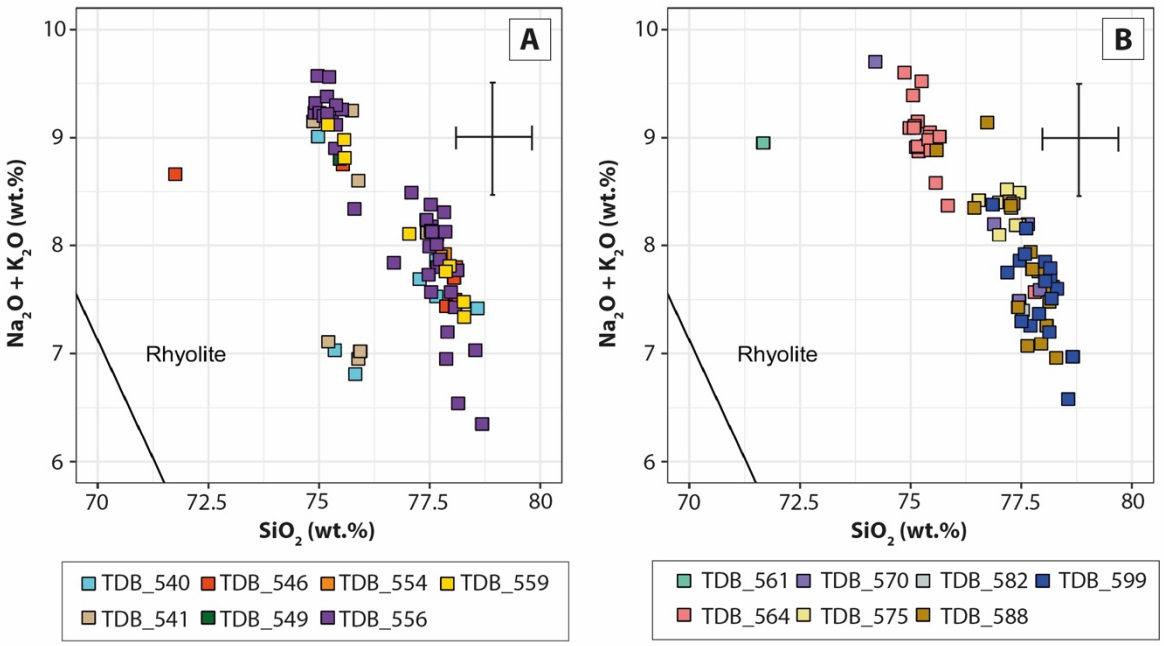


**Figure 5.7** Total Alkali Silica (TAS) plots of glass compositions of cryptotephra layers (e.g. TDB_541) identified in the sediments of Lake Brazi (Le Bas et al., 1986). Error bars represent 2 standard deviations of repeat analyses of the MPI-DING StHs6/80-G glass standard.

### 5.2.1 TDB_599

This is the oldest tephra peak with a shard concentration of 163 shards/g. The shards are clear with mixed morphologies cuspate (89%) and platy (11%) components. Shard sizes (long-axis) were pre-dominantly 20-50µm, with a few shards larger than 100µm. Geochemical analysis shows the rhyolitic glass shards ($n$ = 14) are homogenous in terms of their high $SiO_2$ (77.88 ± 0.96 wt.%; Figure 5.7) content, whilst these glasses display more variability in their $K_2O$ (4.10 ± 1.43 wt.%) content, spanning between a CA and HKCA affinity (Figure 5.8).

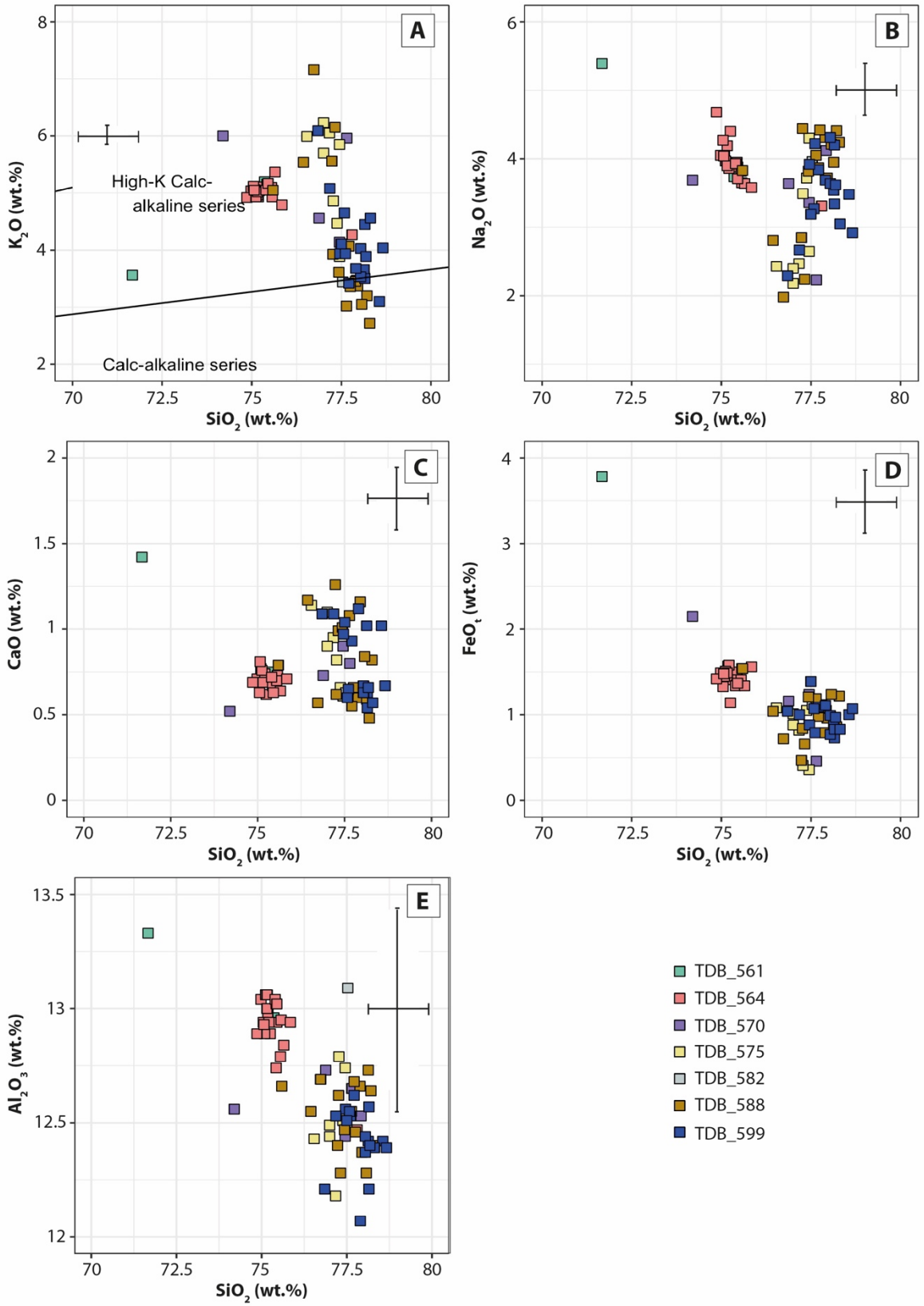


**Figure 5.8** Harker diagram of major element glass geochemical composition for cryptotephra layers identified in the sediments of Lake Brazi (A-E). (A) the SiO2 vs. K2O classification diagrams follows Peccerillo and Taylor (1976). Error bars represent 2 standard deviations of repeat analyses of the MPI-DING StHs6/80-G glass standard.

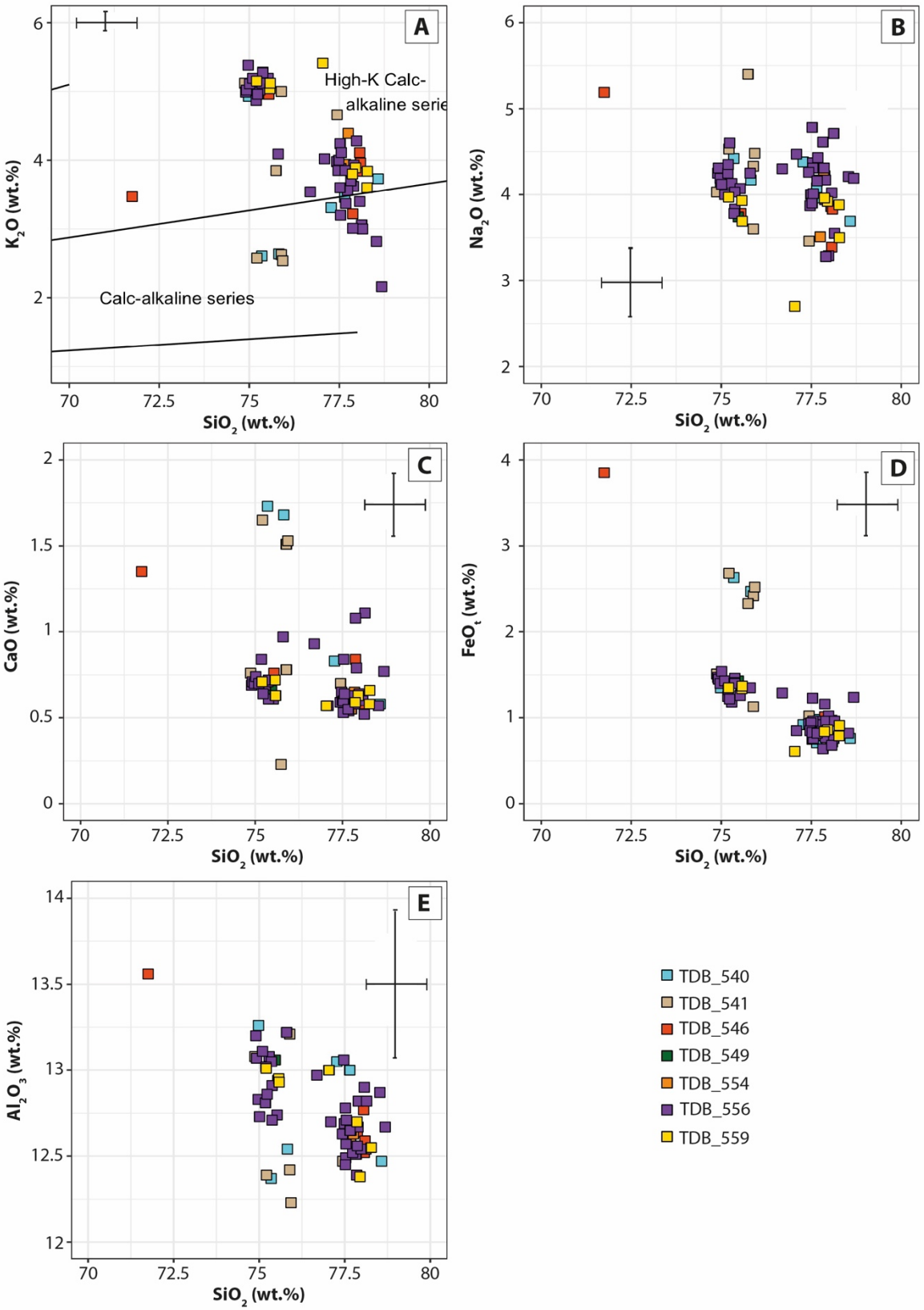


**Table 5.8 cont.** Harker diagram of major element glass geochemical composition for cryptotephra layers identified in the sediments of Lake Brazi (A-E). (A) the SiO2 vs. K2O classification diagrams follows Peccerillo and Taylor (1976). Error bars represent 2 standard deviations of repeat analyses of the MPI-DING StHs6/80-G glass standard.

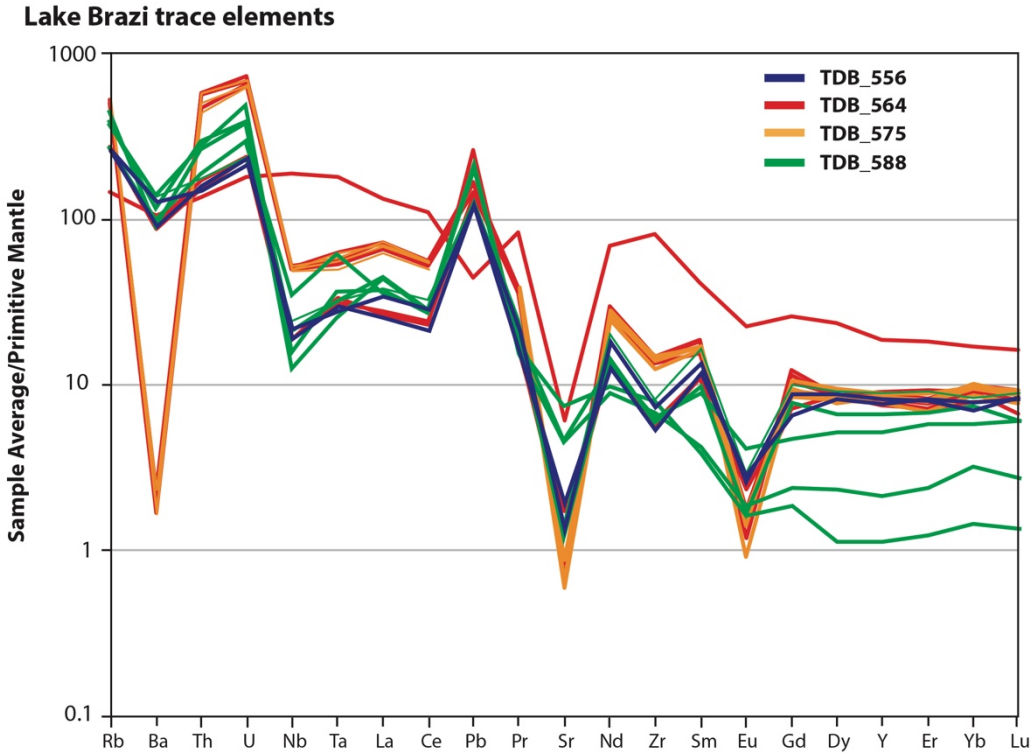


**Figure 5.9** Trace element profiles of Lake Brazi glasses normalised to primitive mantle compositions (Sun and McDonough, 1989).

### 5.2.2 TDB_588

TDB_588 has a shard concentration of 279 shards/g. The cryptotephra morphologies are a mix of cuspate (65%), platy (25%) and fluted (10%) with shard size ranging from 25-100µm. Chemical analyses reveals rhyolitic glass shards of two compositional populations (Figure 5.7). Glass population 1 shards ($n$ = 15) are relatively homogenous in $SiO_2$ (77.60 ± 1.08 wt.%) content, yet in terms of their $K_2O$ (4.12 ± 2.66 wt.%) content these glasses are more variable and spanning between CA and HKCA affinity (Figure 5.8). Trace element compositions within these glasses ($n$ = 2) normalised to primitive mantle show LREE enrichment to the HREE (La/Yb = 4.5 – 6.8), with depletions in Nb and Ta consistent with a subduction related origin (Figure 5.9). A single glass shard displayed lower $SiO_2$ (75.58 wt.%) rhyolitic composition with a HKCA affinity

($K_2O$ = 5.05), whilst this outlier displayed higher FeOt content than the dominant glass population (Table 5.3).

### 5.2.3 TDB_582

This depth has a shard concentration of 197 shards/g. The shards are clear with a mix platy (63%) and cuspate (37%) shard morphologies. Shard size ranges 25-100µm. A single chemical analysis of the cryptotephra reveals a high-$SiO_2$ (77.53 wt.%) rhyolitic composition which straddles the CA/HKCA transition ($K_2O$ 3.44 wt.%) (Figure 5.7, 5.8).

### 5.2.4 TDB_575

TDB_575 has a shard concentration of 234 shards/g. Shard morphologies are mixed with cuspate (48%), platy (48%) and fluted (4%). Shard size ranges 20-80µm. Geochemical analysis reveals these rhyolitic glass shards ($n$ = 8) are homogenous in terms of their $SiO_2$ (77.16 ± 0.62 wt.%; Figure 5.7) content, but more variable in terms of their $K_2O$ (5.38 ± 1.72 wt.%) content showing affinities that span between CA and HKCA affinities (Figure 5.8). Trace element content of these glass shards ($n$ = 5) normalised to primitive mantle reveals LREE enrichment relative to HREE (La/Yb = 6.4 – 43.1), with depletions at Nb and Ta consistent with an arc origin, whilst those at Ba, Sr and Eu are consistent with K-feldspar fractionation (Figure 5.5, 5.9).

### 5.2.5 TDB_570

This depth has a shard concentration of 196 shards/g. The shards are clear with mixed morphologies of platy (46%) and cuspate (49%). Shard sizes range 20-70µm. Geochemical analysis reveals a dominant rhyolitic population with high $SiO_2$ (77.47 ± 0.88

wt.%; Figure 5.7) that display a variable $K_2O$ contents (4.53 ± 2.10 wt.%) that can be classified as HKCA (Figure 5.8). A single glass shard displayed lower $SiO_2$ (74.20 wt.%) rhyolitic composition with a higher $K_2O$ (6.00 wt.%) $FeO_t$ (2.15 wt.%) content which resides on the HKCA/Shoshonitic boundary (Figure 5.8).

### 5.2.6 TDB_564

This cryptotephra has the highest shard concentration within the Lake Brazi succession with 1,135 shards/g. Shard morphology is largely composed of cuspate glasses (78%), and a smaller sub-population of platy glass shards (19%). Shard sizes range from 20µm to over a 100µm. The glass shards analysed ($n$ = 20) show a very homogeneous rhyolitic ($SiO_2$ = 75.29 ± 0.50 wt.%) glass population HKCA affinity ($K_2O$ = 5.04 ± 0.24 wt.%) (Figure 5.7, 5.8). These rhyolitic glasses contain 1.43 ± 0.21 wt.% FeOt and 0.70 ± 0.10 wt.% CaO. Trace element composition within these glasses ($n$ = 4) normalised to primitive mantle show LREE enrichment relative to the HREE (La/Yb = 9.9 ± 0.2). The glasses show a depletion in Nb and Ta relative to U and Th, indicative of an arc origin, whilst pronounced depletions in Ba, Sr and Eu are consistent with K-feldspar fractionation (Figure 5.9).

### 5.2.7 TDB_561

This depth has a shard concentration of 550 shards/g. Shard morphology is mixed with cuspate (65%) and platy (35%) components. Shard size ranges 20-80µm. Chemical analysis reveals two distinct rhyolitic glass compositions. A single rhyolitic shard ($SiO_2$ = 75.36 wt.%; Figure 5.7) displays a HKCA affinity ($K_2O$ = 5.20). The second lower $SiO_2$ (71.67 wt.%) rhyolitic shard also shows a HKCA affinity (Figure 5.8), but contains higher

CaO and FeOt content relative to the other glasses analysed in this layer (Table 5.3; Figure 5.8).

### 5.2.8 TDB_559

TDB_599 has a shard concentration of 697 shards/g. Shard morphology is dominantly cuspate (69%) and with a minor platy component (31%). Shard sizes range 20-80µm. The geochemical analysis reveals rhyolitic glass shards forming two populations (Figure 5.7). Population 1 glass shards ($n$ = 5) have a high $SiO_2$ (77.88 ± 1.01 wt.%) with high yet variable $K_2O$ (4.11 ± 1.47 wt.%) content and a HKCA affinity (Figure 5.8). Glass population 2 ($n$ = 3) are more homogeneous in terms of bother their lower $SiO_2$ (75.45 ± 0.43 wt.%) and higher $K_2O$ (5.10 ± 0.11 wt.%) content compared to population 1(Table 5.3; Figure 5.8).

### 5.2.9 TDB_556

This depth has a shard concentration of 600 shards/g with shard morphologies have a cuspate (65%), platy (25%) and fluted component (10%). Shard size range 25-100µm. Geochemical analysis reveals two dominant rhyolitic glass populations, and a single chemically isolated shard. Population 1 reveals glass shards ($n$ = 23) are homogenous in terms of their high $SiO_2$ (77.79 ± 0.72 wt.%; Figure 5.7) content, yet display great variability in terms of their $K_2O$ (3.59 ± 1.04 wt.%) content which extend between CA and HKCA affinities (Figure 5.8). Trace element concentrations of these glass shards ($n$ = 2) show enrichment of LREE to HREE (La/Yb = 4-5) when normalised to primitive mantle along with depletions in Nb and Ta consistent with an arc origin (Figure 5.5, 5.9).

Population 2 ($n$ = 14) are homogenous rhyolitic ($SiO_2$ = 75.23 ± 0.50 wt.%) glasses with a HKCA affinity ($K_2O$ = 5.05 ± 0.62 wt.%). They also comprise of homogenous 1.37

± 0.21 wt.% FeOt, and 0.72 ± 0.18 wt.% CaO contents (Figure 5.8). Trace element concentrations ($n$ = 3) are enriched in LREE relative to HREE (La/Yb = 10.5 ± 1.3), normalised to primitive mantle, whilst pronounced depletions in Ba, Sr and Eu, consistent with K-feldspar fractionation (Figure 5.9).

A single rhyolitic shard displays higher $SiO_2$ (76.69 wt.%) with similar $FeO_t$ (1.29 wt.%) and higher CaO (0.93 wt.%) compared to population 1 (Figures 5.7, 5.8). Trace element analysis normalised to primitive mantle shows enrichment of Rb, Th, Nb and Ta, indicative of anorogenic volcanic settings (Figure 5.9).

### 5.2.10 TDB_554

This depth contained a shard concentration of 363 shards/g with mixed shard morphologies of platy (55%), cuspate (35%) and fluted (10%). Shard sizes range 20-80µm. Geochemical analysis reveals homogenous rhyolitic glass shards ($n$ = 3; $SiO_2$ = 77.75 ± 0.18 wt.%) with a HKCA affinity (3.99 ± 0.76 wt.%) and low CaO (0.60 ± 10 wt.%) and $FeO_t$ (0.81 ± 0.04 wt.%) content (Figure 5.8).

### 5.2.11 TDB_549

TDB_549 has a shard concentration of 275 shards/g with a mixture of platy (44%), cuspate (28%), blocky (16%) and fluted (13%) shard morphologies. Sizes range 20-60µm. A single glass shard displayed high $SiO_2$ (75.47 wt.%), with HKCA affinity ($K_2O$ = 5.05 wt.%) and low FeOt (1.43 wt.%) content (Figure 5.8).

### 5.2.12 TDB_546

This depth has a shard concentration of 213 shards/g with clear glass shards. Shards are clear with mixed morphology of cuspate (60%), platy (30%) and fluted (10%) components with sizes of 20-80µm. Geochemical analysis revealed a homogenous rhyolitic glass shard population, and two geochemically distinct shards (Figure 5.7). The dominant population 1 contains rhyolitic shards ($n$ = 4) that are homogenous in terms of their high $SiO_2$ (78.02 ± 0.20 wt.%) content, but show more variability in their $K_2O$ (3.78 ± 0.79 wt.%) content which transitions between CA and HKCA affinity (Figure 5.8). One single rhyolitic glass shard has high $SiO_2$ (75.54 wt.%) with a HKCA affinity ($K_2O$ = 4.96 wt.%) and low in $FeO_t$ (1.35 wt.%) and CaO (0.76 wt.%) content. Another single rhyolitic shard is lower in $SiO_2$ (71.75 wt.%) with a HKCA affinity with higher $FeO_t$ (3.85 wt.%) and CaO (1.35 wt.%) compared to population 1 (Figure 5.7, 5.8).

### 5.2.13 TDB_541

This depth has a shard concentration of 275 shards/g with clear glass shards of mixed morphology with cuspate (59%) and platy (49%) components. Shard size range 20-70µm. Geochemical analysis shows distinct rhyolitic glass shard populations, none of which are clearly dominant (Figure 5.7). Population 1 glass shards ($n$ = 3) is high in $SiO_2$ (75.68 ± 0.81 wt.%) with a CA affinity ($K_2O$ = 2.58 ± 0.81 wt.%). Glass population 2 shards ($n$ = 2) are similar in $SiO_2$ (75.38 ± 1.44 wt.%) with HKCA affinity ($K_2O$ = 5.06 ± 0.18 wt.%) and lower $FeO_t$ (1.32 ± 0.54 wt.%) content (Figure 5.8). A single shard displays a lower $SiO_2$ (75.54 wt.%) with a HKCA affinity ($K_2O$ = 3.85 wt.%) and higher $FeO_t$ (2.33 wt.%) content. A second single glass shard is higher in $SiO_2$ (77.44 wt.%) with a HKCA affinity ($K_2O$ = 4.66 wt.%) and low $FeO_t$ (1.02 wt.%) and CaO (0.70 wt.%) content compared to population 1 (Figure 5.8).

### 5.2.14 TDB_540

This depth has a shard concentration of 288 shards/g. The clear glass shards have a mixed morphology of platy (44%), cuspate (44%) and fluted (11%) component. Shards size range <20µm-60µm. Geochemical analysis revealed rhyolitic glass shards of heterogenous composition with three different populations (Figure 5.7). Population 1 shards ($n$ = 4) is homogenous in high $SiO_2$ (77.78 ± 1.11 wt.%) content, whilst in terms of $K_2O$ (3.60 ± 0.53 wt.%) content these glasses are variable and transition between a CA and HKCA affinity (Figure 5.8). Population 2 shards ($n$ = 2) have lower $SiO_2$ (75.58 ± 0.66 wt.%) with CA affinity ($K_2O$ = 2.62 ± 0.03 wt.%). A single glass shard displays similar $SiO_2$ (74.98 wt.%) content with a HKCA affinity ($K_2O$ = 4.93 wt.%; Table 5.3; Figure 5.8).

# Chapter 6

# Discussion of the tephrostratigraphy and tephrochronology of Lake Lia and Lake Brazi

Detailed tephrostratigraphical investigations of the sediments of Lake Lia and Lake Brazi revealed thirty cryptotephra peaks, eighteen were resolved in Lake Lia and twelve in Lake Brazi (Chapter 5). The following chapter will discuss the geochemical correlations of these tephra layers to volcanic sources and where possible known volcanic eruptions using their major, minor and trace element signatures. Section 6.1 to 6.4 focuses on provenancing the cryptotephra to known volcanic sources (Anatolian, Mediterranean and Icelandic) and where possible specific eruptions. Section 6.5 discusses issues surrounding deciphering primary vs reworked cryptotephra. Section 6.6 provides an age-depth model for Lake Lia incorporating the identified cryptotephra layers. Section 6.7 discusses the potential of the Carpathian region to expand and integrate the tephrostratigraphic frameworks of north-west Europe and the Mediterranean region. Section 6.8 brings together the importance of the tephra layers identified in both lakes and how these results allow Lake Brazi to be used in the following chapters.

## 6.1 Anatolian province – unknown eruption(s)

The majority of cryptotephra horizons in Lake Lia and Lake Brazi are rhyolitic volcanic glasses that are very evolved, with high $SiO_2$ content (> 76 wt.%) and with low CaO (<1.2 wt.%) and $FeO_t$ (<1.5 wt.%). Within these glass populations, there is often considerable variation in $K_2O$, resulting in a transition across the calc-alkaline (CA) and high-K calc-

alkaline (HKCA) boundary (Figure 6.1). It is unclear if late-stage fractionation (e.g., K-feldspar) drives this $K_2O$ variation, or whether it reflects distinct magmas and consequently

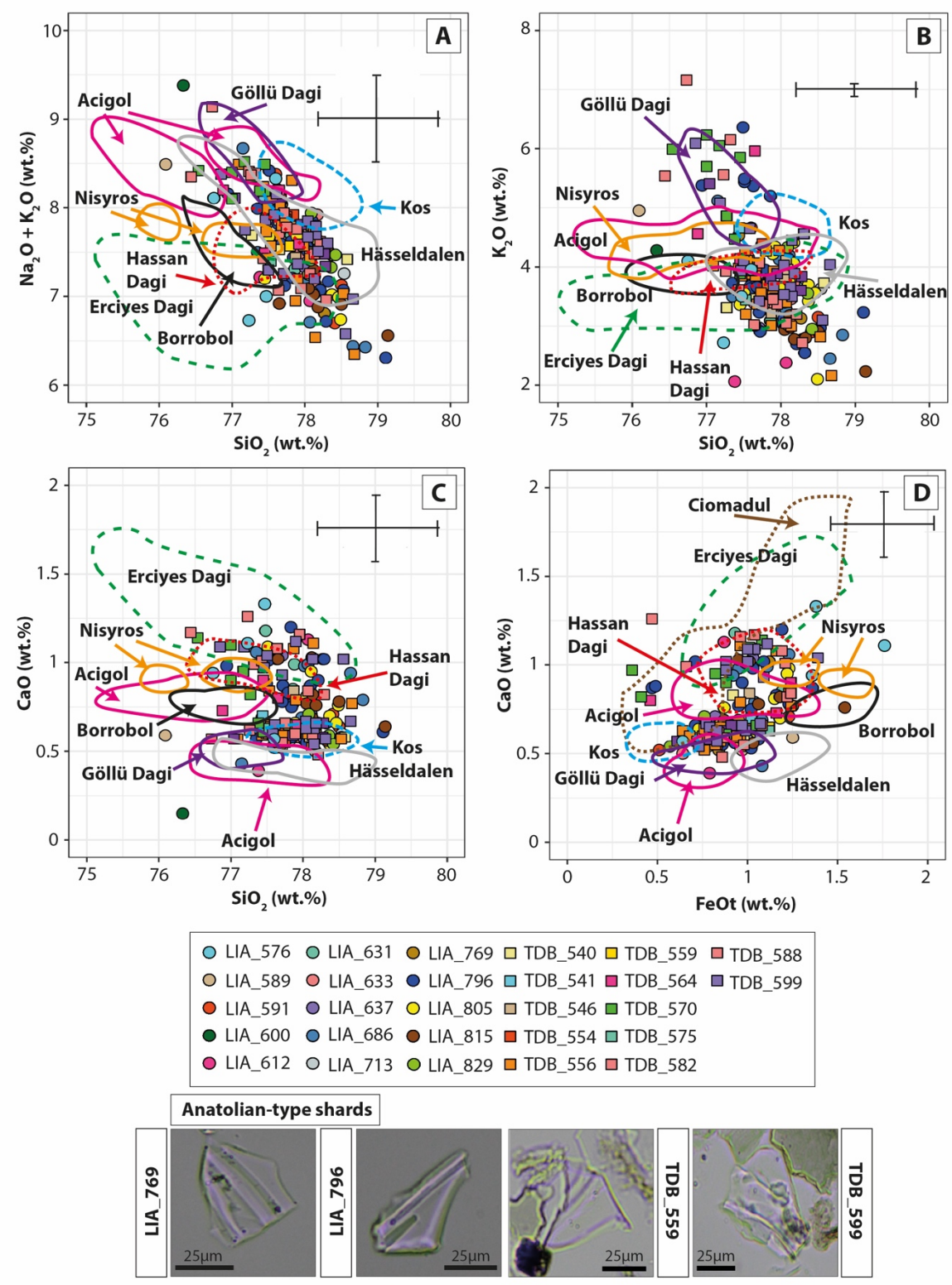

**Figure 6.1** (Previous page) Major element bi-plots of high silica glass shards from Lake Lia and Brazi compared to similar high silica glass shards of: Ciomadul, Romania (Harangi et al., 2020); Anatolian tephras from Acigöl, Ericyles Dagi, Hassan Dagi and Göllu Dagi (Tryon et al., 2009; Hamann et al., 2010; Cullen et al., 2014; Tomlinson et al., 2015; Barton et al., 2015; Neugebauer et al., 2017); Icelandic tephra units of Hässeldalen and Borrobol (no exact Icelandic volcanic source; Turney et al., 1997; Pyne-O'Donnell, 2007; Davies et al., 2003; Matthews et al., 2011; Lane et al., 2012a; Lilja et al., 2013; Lind and Wastegård, 2013; Housley et al., 2013; Lind et al., 2016; Wulf et al., 2016a; Cook et al., 2018); Aegean Arc tephras from Nisyros and Kos (Eastwood et al., 1999; Kwiecien et al., 2008; Tomlinson et al., 2012a; Karkanas et al., 2015; Satow et al., 2015). Photos of these glass shards from certain depths in Lia and Brazi. Error bars represent 2 standard deviations of repeat analyses of the MPI-DING StHs6/80-G glass standard.

different but chemically similar volcanic sources. Cryptotephra layer containing these glasses include high-$SiO_2$ rhyolitic glasses in Lia are: LIA_829, LIA_815, LIA_805, LIA_796 (pop.1 and pop.2), LIA_769, LIA_686 (pop.1), LIA_637 (pop.2), LIA_633 (pop.2), LIA_631 (pop.2), LIA_612 (pop.2), LIA_591, LIA_589, LIA_576 (pop.2); and in Brazi they are: TDB_599, TDB_588 (pop.1), TDB_575, TDB_570 (pop.1), TDB_559 (pop.1), TDB_556 (pop.1), TDB_554, TDB_546 (pop.1), TDB_540 (pop.1).

The chemical composition of these glass shards are similar but inconsistent with known eruptions from the local volcano of Ciomadul, Romania. In Figure 6.1D, there is a subtle offset between Ciomadul tephra geochemistry (Harangi et al., 2020) and cryptotephra peaks analysed in lakes Lia and Brazi. The timing of volcanism at Ciomadul also precludes a correlation, with the most recent explosive eruptions in the region is dated at 33-24 kya (Harangi et al., 2010, 2020; Wulf et al., 2016b), significantly older than interval of sedimentation investigated here in Lakes Lia and Brazi. Furthermore, the reworking of these older deposits is limited and localised around the volcano (Daniel Veres, personal communication).

Italian volcanic sources are known to erupt evolved rhyolitic magmas in the relevant timeframe are restricted to the Aeolian Islands (Southern Tyrrhenian Sea; Albert et al., 2012, 2017). Lipari, Vulcano and Salina islands have all erupted rhyolites in the last 15 ka. Those produced by Lipari (and Vulcano) typically have lower $SiO_2$ (75-76 wt.%) and higher $FeO_t$ >1.5 wt.% (Albert et al., 2012, 2017) than the glasses described here (Figure 6.1). Salina eruptions can also produce variable high $SiO_2$ (70-77 wt.%) with higher CaO (~1-3 wt.%) than Brazi and Lia glasses described (Albert et al., 2017). Tephra from the Aegean Arc volcanoes including Nisyros and Kos that have similar $SiO_2$ content, yet can be excluded due to having higher CaO (>1.1 wt.%) and lower $FeO_t$ (<0.75 wt.%) (Tomlinson et al., 2012a; Karkanas et al., 2015; Satow et al., 2015) (Figure 6.1).

It is plausible that far travelled ash from Icelandic volcanic eruptions during the LGIT could be deposited in the Carpathian mountain lakes. Particularly tephras, such as the Vedde Ash, derived from Katla volcano has been recognised in lacustrine sequences from central-southern Europe, including those south of the Alps (e.g. Lane et al., 2012b, c). Numerous eruptions have been recorded at sites across Europe with similar geochemistry to these Icelandic tephras throughout the LGIT period (e.g. Cook et al., 2018; Timms et al., 2018). The Icelandic Borrobol and Hässeldalen cryptotephra deposits are derived from an unknown volcanic source (Lind et al., 2016; Cook et al., 2018; Wåstegard et al., 2018). While these tephras have high-$SiO_2$ characteristics (>76 wt.%), they can be discriminated easily from the glasses described here by comparing $FeO_t$ and CaO content (Figure 6.1D). Thus major element data reviewed here indicates that Icelandic volcanoes are not the source of these high-$SiO_2$ cryptotephra deposits. Trace element analyses of volcanic glasses associated with these high-$SiO_2$ rhyolitic shards were observed at multiple depths in both lakes. Their glasses show

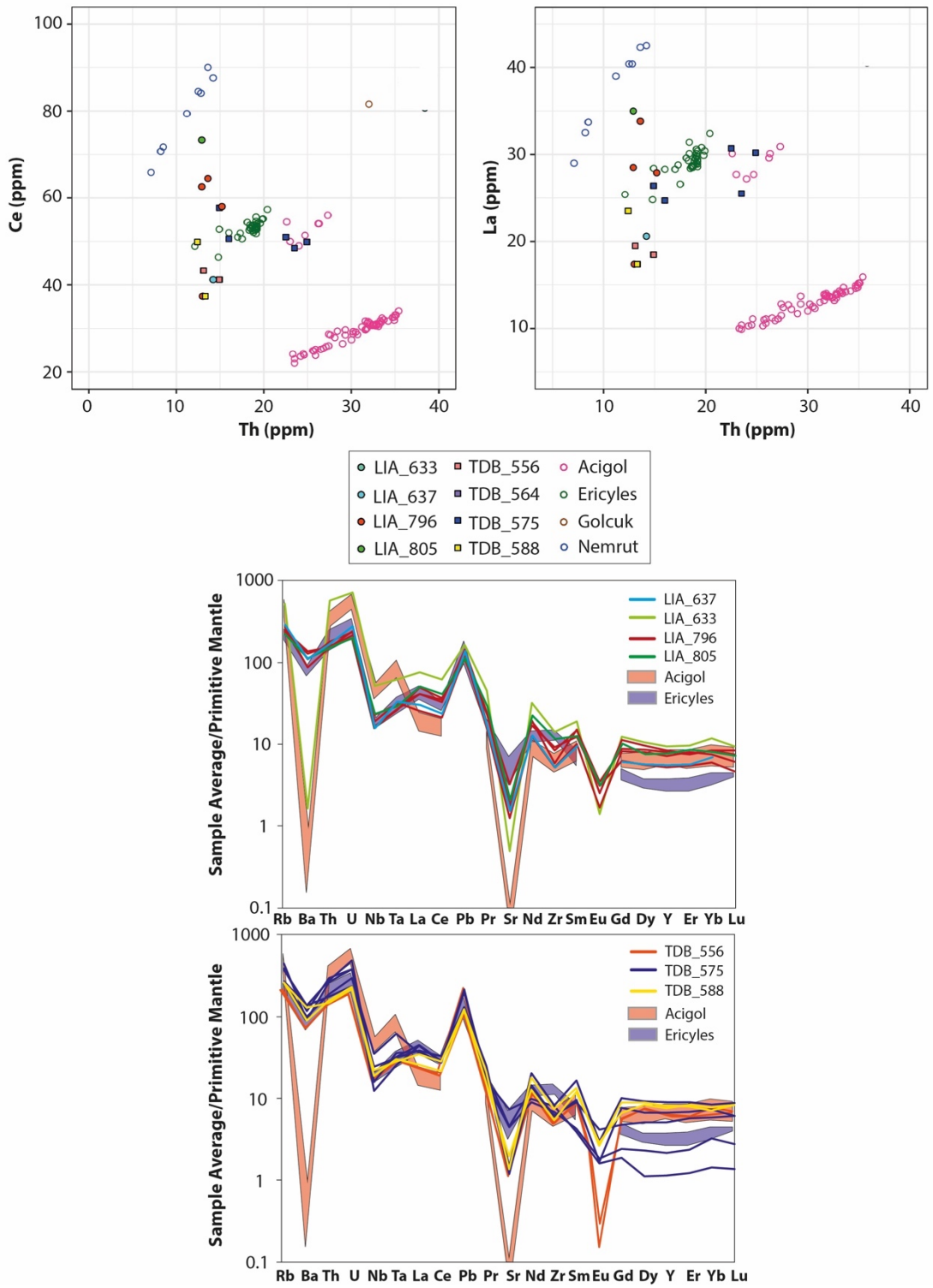


**Figure 6.2** Trace element bi-plots and diagrams of mantled normalised (Sun and McDonough, 1989) of glasses from Lia and Brazi in comparison to glass shards from known Anatolian eruptions (Tomlinson et al., 2015; RESET database, 2019). Error bars were smaller than the symbols and are not presented.

evident depletion in Nb and Ta with an enrichment of Th, indicating a continental subduction setting, and thus confirming that an Icelandic volcanic origin is impossible (Figure 6.2; Tomlinson et al., 2015).

With local subduction-related rhyolites, and those of Italian and Aegean arc settings excluded, the most plausible source region are the subduction related volcanoes of Anatolia, where high-$SiO_2$ rhyolites and frequently erupted (Figure 6.1; Tyron et al., 2009; Sumita and Schminck, 2013; Neugebauer et al., 2017). Glass shards with HKCA affinity are similar in composition to known deposits originating from Central Anatolian Volcanic Provenance such as Acigöl, Ericyles Dagi and Göllü Dagi (Tryon et al., 2009; Hamann et al., 2010; Zanchetta et al., 2011; Tomlinson et al 2014). Nemrut located in Eastern Anatolian Volcanic Provence (EAVP) has less evolved compositions (<76 wt.% $SiO_2$) compared to the glass shards found in Lia and Brazi (Sumita and Schminck, 2013; Cullen et al., 2014). Other volcanoes located in the EAVP, such as Süphan, lack sufficient glass chemistry to make a comparison (Pearce et al., 1990; Yilmaz et al., 1998; Sumita and Schminck, 2013; Cullen, 2015). With the glass shards with CA affinity, there is a lack of a known volcanic sources with this chemical composition in the region, especially to Western Anatolian Volcanic Provenance (Tomlinson et al., 2015).

Comparisons to sparse trace element data from Central Anatolia shows broadly similar mantle-normalised profile to those observed in Lake Lia and Brazi (Figure 6.2). However, a precise source attribution remains extremely tentative. Due to the major lack of volcanic glass geochemistry at volcanoes across the Anatolian region, coupled with limited stratigraphic and geochronological constraints on the volcanic activity, establishing precise tephra correlations is a major challenge that, for the moment, cannot be overcome (Cullen et al., 2014). However,

through the geochemical evidence presented for these Lake Lia and Brazi cryptotephra deposits, with a process of source elimination (Italian, Icelandic and Aegean), it seems that high-$SiO_2$ rhyolites might derive from the east and the volcanoes of Central Anatolia ~1,000km away, despite the prevailing westerlies.

## 6.2 Central Mediterranean derived cryptotephra

Throughout Lia and Brazi, several LGIT cryptotephra horizons contain sub-populations or outlying glass shards that can be attributed to explosive activity at Mediterranean volcanoes. In Lake Lia, there are K-rich trachytes identified and can be linked to explosive volcanism of the Campanian Volcanic Zone, southern Italy (Figure 6.3; Smith et al., 2011; Tomlinson et al., 2012b, 2015). Specifically, Campi Flegrei and Ischia are the dominant sources of K-rich trachytic tephra (Wulf et al., 2008; Tomlinson et al., 2014, 2015). The glasses of Ischia typically contain higher $Na_2O$ content than those of Campi Flegrei (Figure 6.3). Consequently, the alkaline ratio ($K_2O/Na_2O$) of the volcanic glass provides a useful discriminator when assigning source (Tomlinson et al., 2014, 2015). Campi Flegrei trachytic glasses typically display higher alkaline ratios ($K_2O/Na_2O$ >1.5-3) than those erupted from the neighbouring island of Ischia located to the west in the bay of Naples ($K_2O/Na_2O$ <1) (Tomlinson et al., 2015; Albert et al., 2015; Donato et al., 2016; Giaccio et al., 2017). Trachytic tephra deposits erupted from Ischia also usually contain lower CaO and MgO content than those produced by Campi Flegrei (Tomlinson et al., 2014, 2015).

Other LGIT cryptotephra layers identified in both lake sequences can be attributed to explosive activity in the Aeolian Islands. Here, deciphering source is primarily achieved through the island differences in $SiO_2$ and $K_2O$ content (Albert et al., 2017). The volcano of

Lipari produces rhyolitic tephra deposits with glass compositions that show an apparent HKCA affinity, Vulcano ranges from basaltic-andesite through to rhyolite, with Shoshonitic (SHO) to K-series affinities. Vulcano rhyolites do not extend to the same degree of evolution as those of Lipari (Albert et al., 2017). The rhyolites produced by Salina Island display glass compositions that straddle the boundary between a CA/HKCA affinities (Albert et al., 2017).

Distinctive volcanic glass chemistries are recognised in the eruption deposits of Mediterranean intra-plate volcanoes, Pantelleria Island (Sicily Channel) and Mount Etna (Sicily). Pantelleria has erupted distinctive trachy-rhyolites that are peralkaline in nature ($Na_2O + K_2O > Al_2O_3$) (MacDonald, 1974; Civetta, 1988; Tomlinson et al., 2015). The rhyolitic tephra deposits (ca. 70 wt.%) erupted on Pantelleria display distinctively high $FeO_t$ content ( ca. 8 wt.%) . In contrast, Mount Etna, Italy produces benmoreites, with a Na-alkaline affinity with trachy-andesite to trachyte glass shards, where $Na_2O$ content is greater than $K_2O$ (Albert et al., 2013; Tomlinson et al., 2015).

### 6.2.1 LIA_796/ Campi Flegrei caldera (Neapolitan Yellow Tuff)

The chemistry of the single glass shard from LIA_796 has a trachytic glass composition characterised by a high alkali ratio (1.88 wt.%) consistent with the eruptive products of Campi Flegrei caldera, Naples (Figure 6.3). The largest known eruption at Campi Flegrei during this time-interval of this investigation is the last caldera-forming eruption of the volcano, the Neapolitan Yellow Tuff (NYT) (Figure 6.3; Figure 6.4). The best age estimates for this eruption are 14,433-13,795 cal. BP (95.4%, Bronk Ramsey et al., 2015, see section 7.1). The ash from this caldera-forming eruption is widely distributed to the north and east of

the Campanian Volcanic Zone (e.g. Wulf et al., 2004; Siani et al., 2004), currently the most distal occurrence reported at 1200 km north (Lane et al., 2015) (Figure 6.5).

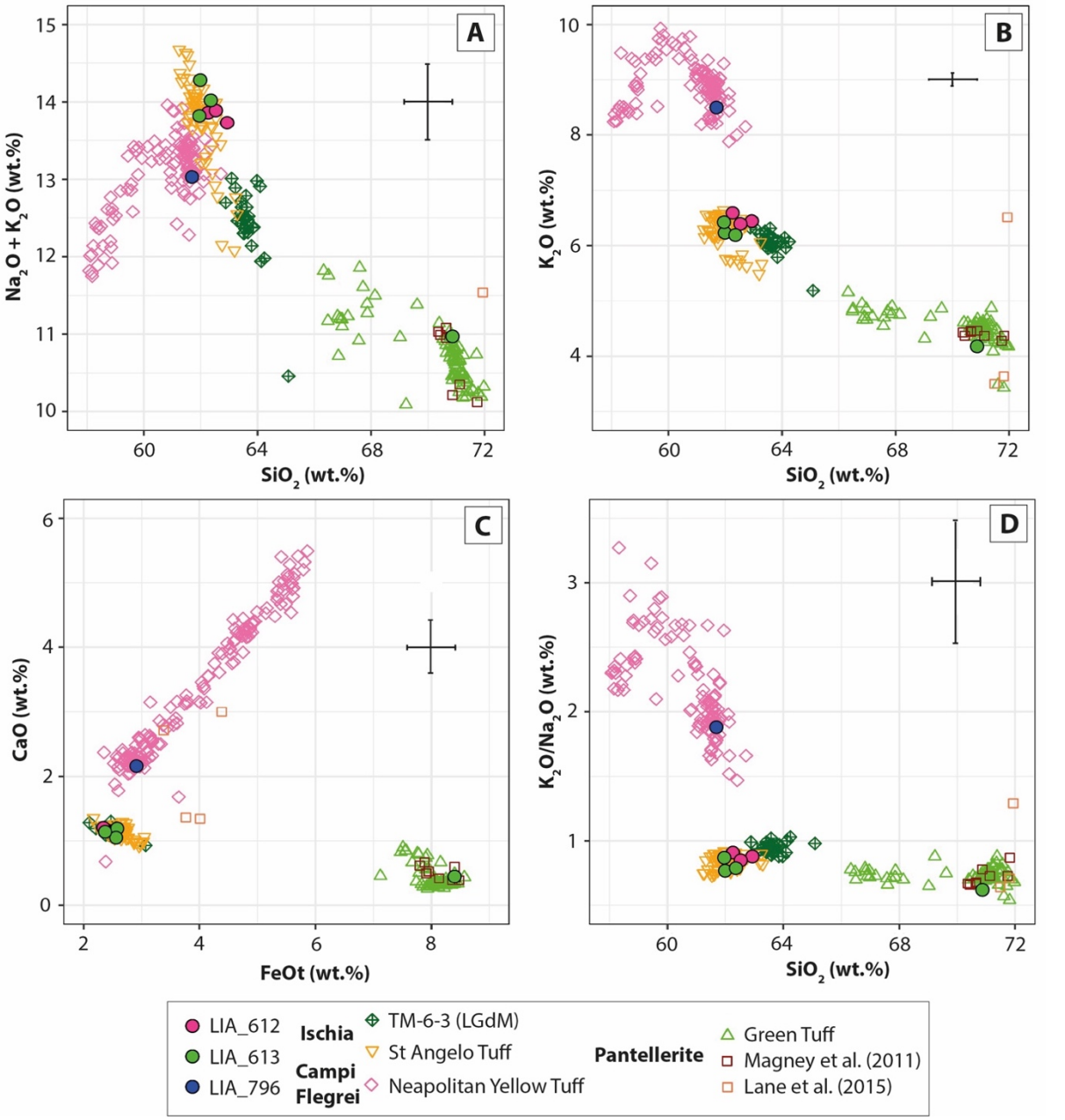


**Figure 6.3** Major trace element of glass shards from Lia with comparisons to the Neapolitan Yellow Tuff from Campi Flegrei (Wulf et al., 2004, 2007; Magny et al., 2006; Bourne et al., 2010; Lane et al., 2011a; Tomlinson et al., 2012a), known eruptions for Ischia (Wulf et al., 2008 (TM-6-3 (LGdM Lago Grande di Monticchio)); Tomlinson et al., 2015) and eruptions from Pantelleria (Wulf et al., 2004, 2007; Margari et al., 2007; Vogel et al., 2009; Magney et al., 2011; Tamburrino et al., 2012; Lane et al., 2015). Error bars represent 2 standard deviations of repeat analyses of the MPI-DING StHs6/80-G glass standard.

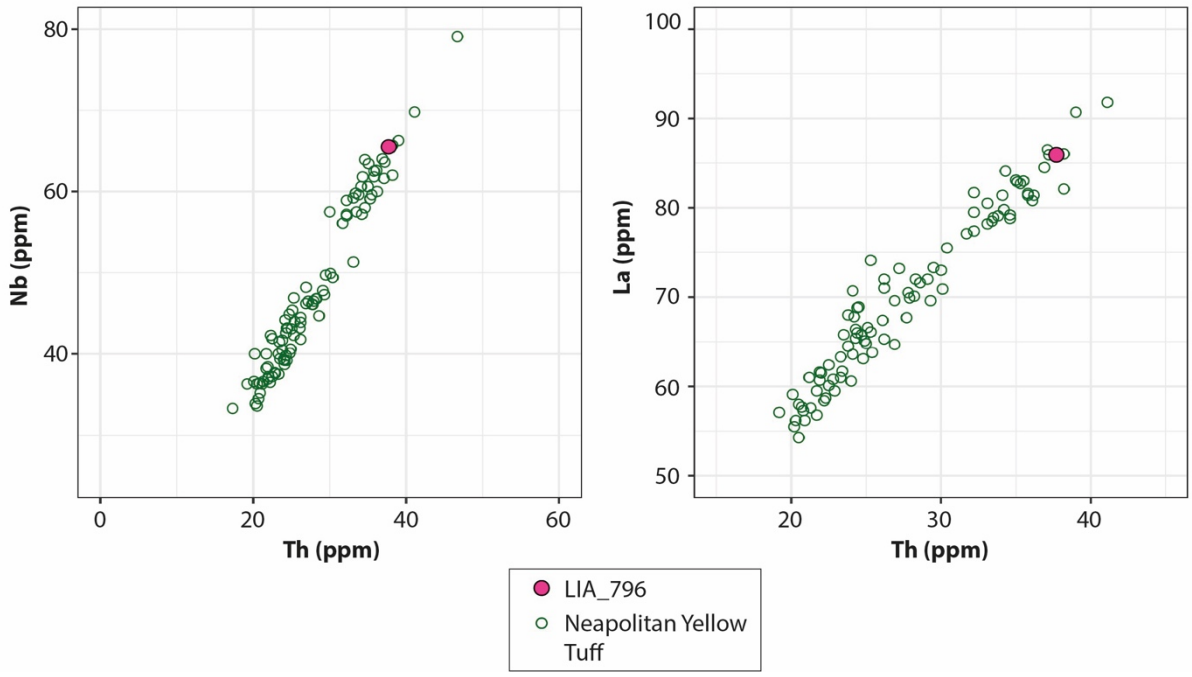


**Figure 6.4** Trace element plots comparing LIA_796 to the Neapolitan Yellow Tuff (Tomlinson et al., 2012a; Wulf et al., 2004). Error bars were smaller than the symbols and are not presented.

The single analysis of LIA_796 is consistent with the evolved lower-member NYT glasses (Figure 6.3; Figure 6.4; Tomlinson et al., 2012a,b, 2015). A diagnostic characteristic of the NYT is it's heterogeneous chemical signature. The eruptive products straddle the phono-trachytic boundary (Tomlinson et al., 2012a). The Lower Member is bi-modal with a trachytic component (>61 wt.% $SiO_2$) and a phono-trachytic component (<59 wt.% $SiO_2$). The Upper Member of the NYT spans the entire continuum between the two end-members of the Lower Member, and also shows marginally less evolved compositions (Tomlinson et al., 2012a). Unfortunately, with just a single chemical analysis corresponding to the NYT it is not possible to unequivocally attribute this to the NYT Lower Member. This evolved end-member of the NYT is a commonly erupted composition from the volcano that is the most widespread

eruption deposit originating from the volcano in this time interval, indicating that it is the most likely candidate (Schmidt et al., 2002; Lane et al., 2012b, 2015; Tomlinson et al., 2012a,b).

The potential discovery of NYT ash 870 km from Campi Flegrei in the sediments of Lake Lia would greatly expand the north-eastern distribution of tephra from this eruption (e.g. Lane et al., 2012b; Bronk Ramsey et al., 2015; Figure 6.5). However, without the identification of more glass shards with the NYT chemical signature at this depth, it is unclear if it represents a primary fall deposit or if it is perhaps reworked. Regardless, such a discovery of ash from this eruption provides enormous incentive to examine other archives closer to the source along a similar dispersal axis. The results from the age-depth model for Lake Lia show large age uncertainties at this depth interval which encompasses the age estimates of NYT supporting this potential correlation (see section 6.6). Without more evidence to verify this as a primary NYT cryptotephra deposit, it cannot be used as an isochronous marker in the Lake Lia sequence.

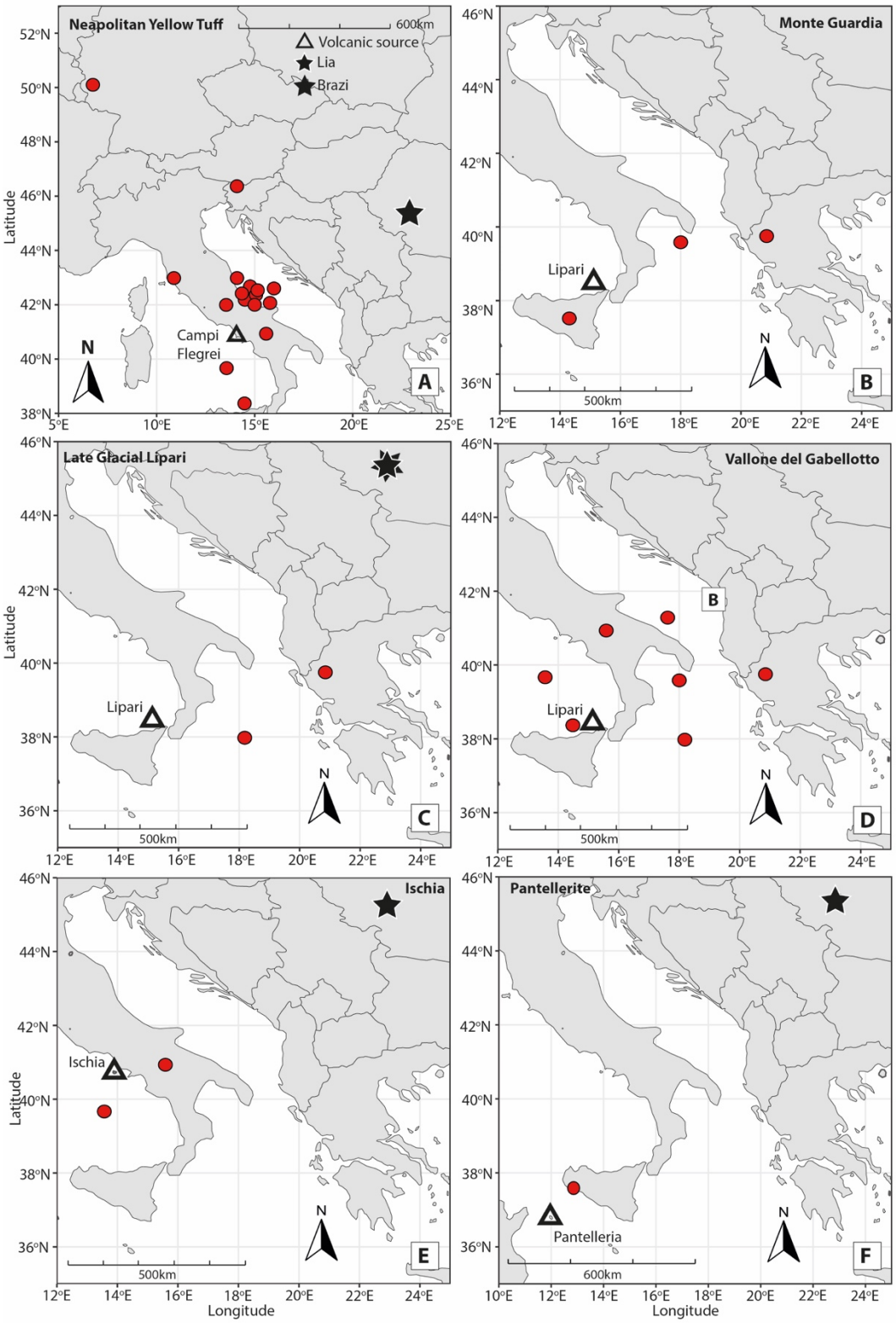


**Figure 6.5** Dispersal maps of tephras from the Mediterranean region identified in Lake Lia and Brazi. Black circles represent single site occurrences of tephra layers. Maps E and F show sites with similar geochemical tephras to those found in Lia with difference in ages.

### 6.2.2 LIA_612-613/ Ischia (unknown eruption)

K-rich trachytic glass shards identified in LIA_612 and LIA_613 also display high-Na content and consequently a low-alkali ratio (0.85 ±0.10 wt.% [2 s.d]), distinguishable from Campi Flegrei and instead consistent with the eruptive products of Ischia island (Figure 6.3; Paterne et al., 1988; Civetta et al., 1991; Wulf et al., 2008; Tomlinson et al., 2015). The largest known eruption from this volcano is the Mount Epomeo Green Tuff (MEGT), dated at ~56 ka yrs BP (Watts et al., 1996). This eruption was responsible for enormous ash dispersal traced throughout the Tyrrhenian, Ionian and the Adriatic Sea and is known as the Mediterranean Y-7 tephra marker (Tomlinson et al., 2014). Ischia has also been active throughout the Holocene (10 ka yrs BP- 1302 AD; Civetta et al., 1991; de Vita et al., 2006). The most recent period of activity represents the thirds post-MEGT eruptive cycle of the volcano, where the most intense activity concentrated around 5.5kya (Civetta et al., 1991; de Vita et al., 2006; Wulf et al., 2008).

Due to the similar shard count and identification of Ischia geochemical shards across both depths, the position of the peak or isochron is taken at the mid-point of these depths (612.5cm). The age for LIA_612.5 is 11,216 - 10,952 cal yrs BP (95.4%). A distal occurrence of an unknown Ischia eruption recorded at the site of Lago Grande di Monticchio (LGdM), TM-6-3, is dated to 12,100 – 10,950 varve cal yrs BP (Wulf et al., 2008; 95.4%), overlapping in age with LIA_612.5. TM-6-3 is characterised by three chemically indistinguishable sub-layers at LGdM, resulting in a large age error compared to the cryptotephra at Lake Lia (Wulf et al., 2008). Geochemical comparisons between LIA_612.5 and TM-6-3 are made through CaO vs $FeO_t$ correlations (Figure 6.3C). This is due to the TM-6-3 analyses used very different analytical conditions which manifested in $Na_2O$ loss, and consequently inflated $SiO_2$

content. An Ischia eruption deposit is also found in the Late Glacial sediments of the KET8004 Tyrrhenian Sea marine core (Paterne et al., 1988). Thus LIA_612.5 provides further evidence for a major widespread ash dispersal originating from Ischia during the Late Glacial period, and clearly captures the onset of the most recent eruptive cycle at the volcano (Figure 6.5).

### 6.2.3 LIA_613/Pantelleria (unknown eruption)

A single shard from LIA_613 can be geochemically identified as a pantellerite, a Fe-rich peralkaline rhyolite (Figure 6.3, 6.6; MacDonald, 1974; Civetta et al., 1988; Tomlinson et al., 2015). This shard can be seen as originating from Pantelleria Island, located in the Sicily Channel (Figure 6.5; Civetta et al., 1988). This volcanic island has been active throughout the Late Quaternary, with the largest known eruption the caldera-forming Green Tuff dated to 45,700 ± 500 yrs BP by $^{40}Ar/^{39}Ar$ technique (Scaillet et al., 2013) and has been identified in records throughout the region (e.g. Wulf et al., 2004; Margari et al., 2007; Paterne et al., 1988; 2008; Vogel et al., 2009; Tamburrino et al., 2012; Kakanas et al., 2015; Ntinou and Kyparissi-Apostolika, 2016). Volcanic activity following this large eruption has been recorded on the island (Civetta et al., 1988; Genova et al., 2013). Localised pyroclastic and lava flows with lava dome formations recorded during the Late Glacial and Early Holocene period (Mahood and Hildreth 1986; Civetta et al., 1988; Speranza et al., 2010).

Previously, only one occurrence of distal ash from Pantelleria erupted during the Late Glacial and Holocene has been reported. Magny et al. (2011) identified several rhyolitic pantellerites shards in Lago Preola, southern Sicily, Italy, during the Holocene at 7,444 – 7,136 cal yrs BP (95.4%) related to the VI cycle of volcanic activity of Pantelleria (Civetta et

al., 1988). The single pantellerite rhyolitic shard found in Lake Lia (LIA_613) is significantly older at 11,220 - 10,948 cal yrs BP (95.4%), chrono-stratigraphically this coincides with volcanic cycle V of Pantelleria (Civetta et al., 1988). However, no prominent explosive eruption deposits have been identified on the island making a correlation for now challenging.

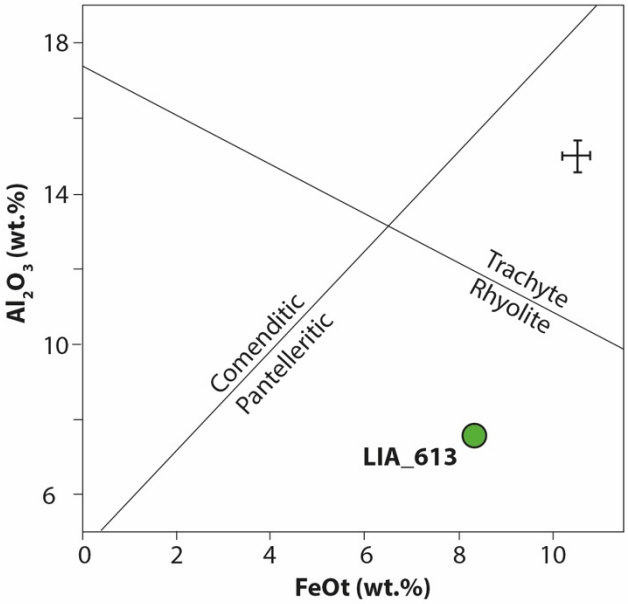


**Figure 6.6** A single glass shard from Lake Lia cryptotephra peak LIA_613 plotted on the Peralkaline classification diagram following MacDonald, 1974. Error bars represent 2 standard deviations of repeat analyses of the MPI-DING StHs6/80-G glass standard.

### 6.2.4 TDB_564/ Lipari (Aeolian Islands)

A high number of glass shard populations identified in cryptotephra deposits across several depths in the Late Glacial (LG) sediments of Lake Lia and Brazi display a chemical signature characteristic of volcanism on Lipari Island (Aeolian Islands; Figure 6.7; Albert et al., 2012, 2017). A high concentration peak in HKCA Lipari rhyolites are found at TDB_564 in Lake Brazi. For Brazi, these shard concentrations far exceed other occurrences of peaks displaying similar compositions, and this peak is extremely homogeneous (Figure 5.6) as such it is considered the primary depth of deposition. In Lia, there is also a potential deposition of primary Lipari rhyolitic layer at LIA_637. However, there are shards with similar Lipari HKCA type geochemistries and shard concentrations extending across a wider interval above this initial depth (LIA_637), including LIA_633 and LIA_631. As a result, no clear primary isochron in Lia can be stratigraphically resolved consistent with the layer in Lake Brazi (see section 6.5).

Throughout the past 50 ka years BP, Lipari volcano has erupted HKCA trachytes, but predominantly rhyolitic tephra units (Forni et al., 2013; Albert et al., 2017). There are several known eruptions dated before and during, and after the LGIT period (Table 6.1). Distal occurrences of these tephras are limited and are mainly confined to marine records in the Tyrrhenian, Adriatic and Ionian Seas (e.g. Paterne et al., 1988; Siani et al., 2004; Caron et al., 2012; Albert et al., 2017) with limited distal terrestrial records (e.g. Narcisi, 2002; Di Roberto et al., 2018; Figure 6.5).

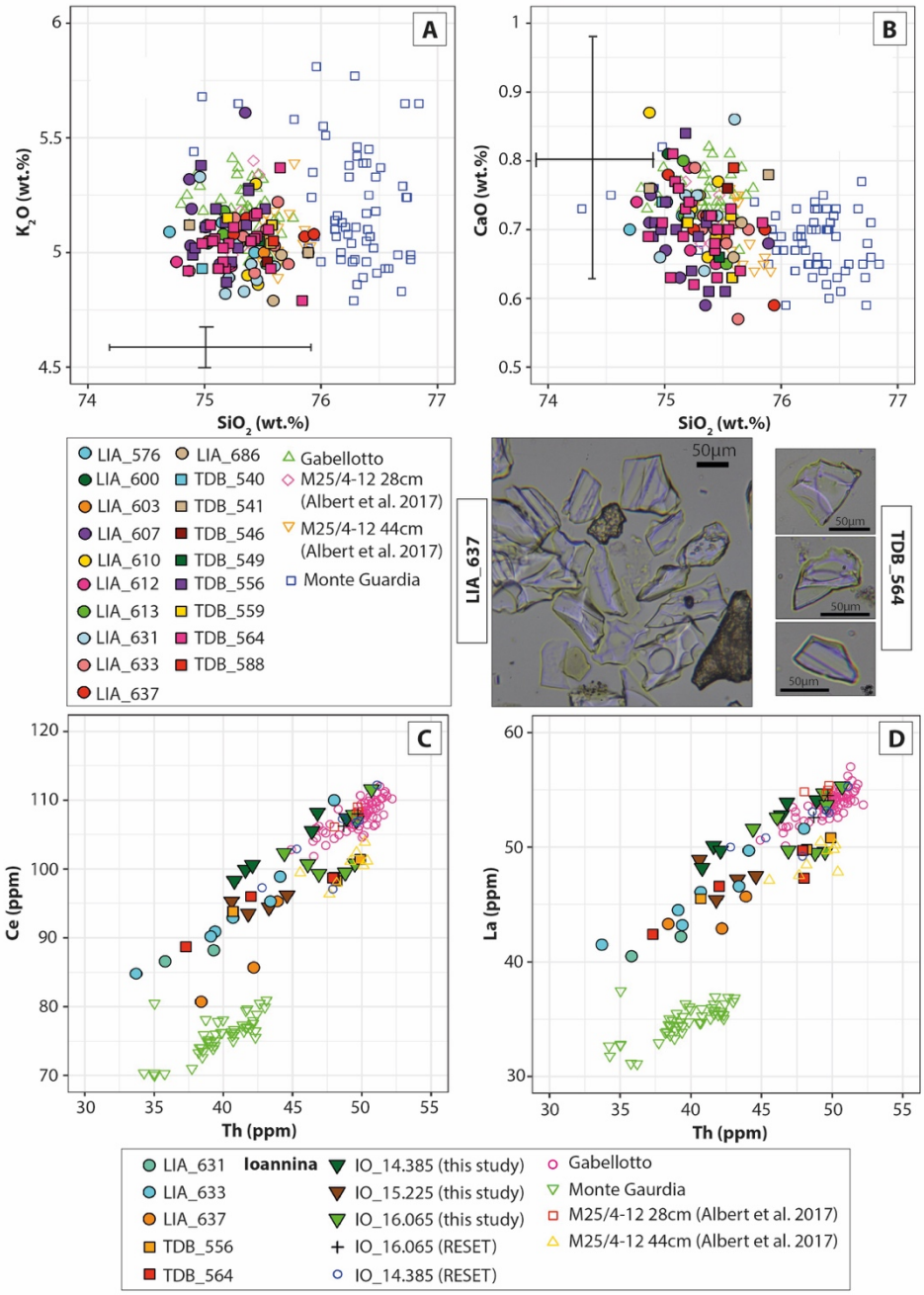


**Figure 6.7** Major element biplots of proximal and distal comparisons of Lia and Brazi to known eruptions from Lipari for the last 30 kya of Monte Guardia, Vallone del Gabellotto (VdG) and newly identified Late-glacial Lipari eruption from Ionian Sea marine core M25/4-12 (Albert et al., 2012, 2017; A-B). Trace element correlations to these eruptions with additional evidence for a LG Lipari eruption from Ioannina, previously geochemically analysed as part of the RESET project with trace element analysis carried out on these shards in this project (Albert et al., 2012, 2017; C-D). Photos of the Lipari glass shards are also presented from both cores. Error bars represent 2 standard deviations of repeat analyses of the MPI-DING StHs6/80-G glass standard on the major element graphs. Error bars on the trace element graphs were smaller than the symbols and are not presented.

**Table 6.1** List of eruptions from Lipari during the last ~30 kya. Ages presented are 95.4% probability range.

| Tephra | Age | Proximal deposits | Distal deposits | References |
|---|---|---|---|---|
| Monte Guardia | 24,650-27,100 cal. BP (Albert et al., 2017) | ✓ | ✓ | Crisci et al., 1981; Colella and Hiscott, 1997; Narcisi, 2002; Lucchi et al., 2008, 2013; Albert et al., 2012, 2017; Caron et al., 2012; Forni et al., 2013; De Rita et al., 2007; Caron et al., 2008 |
| Late Glacial Lipari | 12,847 – 11,430 cal BP (This study) | x | ✓ | Albert et al., 2017; Christine Lane, personal communication |
| Vallone del Gabellotto (VdG) | 8,430 – 8,730 cal BP (Albert et al., 2017) | ✓ | ✓ | Cortese et al., 1986; Siani et al., 2004; Albert et al., 2012, 2017; Caron et al., 2012; Lucchi et al., 2013; Forni et al., 2013; Marchini et al., 2014 |

The Vallone del Gabellotto (VdG) tephra is recorded in the Early Holocene period (8,430 – 8,730 cal yrs BP; Albert et al., 2017) is the most widely trace tephra deposits from the volcano, with distal occurrences residing in Sapropel 1 marine sediments of the central Mediterranean (Paterne et al., 1988; Siani et al., 2004; Caron et al., 2012; Albert et al., 2017; Figure 6.7). The glass shards identified in Lake Lia and Brazi display similar major and minor element compositions to those of the VdG tephra. However, these glass shards identified in both Lake Lia and Brazi sediments are chronological older dated at 12,139-11,881 cal yrs BP (this study, see Chapter 7) than the well constrained age of the VdG precluding a correlation (Table 6.1, Table 6.2). Trace element analysis undertaken from TDB_564 and LIA_637-631 highlight subtle differences in LREE concentrations relative to the younger VdG tephra, specifically their La and Ce contents being lower (Figure 6.7).

Interestingly, Albert et al. (2017) also identified a LG period Lipari cryptotephra stratigraphically below the VdG within the sediments of a Ionian Sea marine core M25/4-12 (44 cm), its chrono-stratigraphic position being constrained by the cores oxygen isotope stratigraphy (Negri et al., 1999). Albert et al. (2017) recognised that this tephra could be distinguished from the VdG by subtly lower LREE concentrations, as is illustrated by the Lake Lia and Brazi Lipari deposits (Figure 6.7). Further evidence for a Late Glacial Lipari (LG Lipari) eruption and a widespread ash dispersal is also derived from Lake Ioannina in Greece. New chemical analysis of a Lipari cryptotephra deposits from this site also reveal a LG Lipari eruption deposit which is distinguishable from the overlying VdG tephra at the site using trace element signatures (Figure 6.7). This now widely traced LG distal Lipari eruption deposit highlights a significant issue with completeness of the proximal eruption stratigraphy preserved on the island, with no prominent or widely trace eruption unit identified in the correct chrono-stratigraphic position between the Monte Guardia (ca. 27ka yrs BP) and the VdG. The incompleteness of volcanic stratigraphies is not uncommon, particularly at volcanic islands, where owing to limited on-land exposure and much of the erupted material enters the sea (Albert et al., 2012; Cassidy et al., 2014), these discoveries away from volcanic source merely reinforce the importance of ash fall preserved in distal sedimentary records for understanding eruptive history of volcanic centres. The rhyolitic HKCA Lipari derived TDB_564 cryptotephra clearly presents a useful tephrochronological marker for the Mediterranean region capable of synchronising sedimentary archives in the LG period.

Additional HKCA rhyolitic glass shards derived from Lipari that are chrono-stratigraphically older than this LG cryptotephra, and are identified in Lia at LIA_686 and Brazi TDB_588 (Figure 6.7. Only one shard is found in LIA_686 while two are resolved in

TDB_588. This may indicate a yet another older, unknown eruption from Lipari. In Lia, there is sterile glass free sediments between the LG Lipari isochron of LIA_637 and LIA_686 suggesting a different eruption. The age for these stratigraphically older glass shards from both sites overlap, be it at the larger statistical confidence (13,633-13,092 cal. BP LIA_686; 14,225-13289 cal. BP; 95.4%). Interestingly, a third Lipari layer has been identified in Ioannina sequence, during the Glacial period, (ca. 18 ka; Lawson et al., 2004; Christine Lane, personal communication; RESET database) but the poorly constrained age of this deposit mean it is unlikely to relate to the deposits identified in this study.

Another explanation for Lipari type glass chemistries occurring beneath the high-concentration LG Lipari cryptotephra at Lake Brazi is that whilst extracting the core some minor stratigraphic contamination was noted. Specifically, Magyari et al. (2009) described that a pine cone seed was dragged from 545cm to a depth of 591 cm during the core extraction. To minimise contamination during core sampling the outer core edge was avoided, but it might be possible that this issue was responsible for the down core movement of HKCA rhyolitic glass shards associated with the high-concentration LG Lipari cryptotephra layer (TDB_564).

Due to problems of; 1) dating distal material and hard water affect at Ioannina (Lawson et al., 2014); 2) the demonstrated difficulty in distinguishing different Lipari eruptions based on major geochemistry alone; 3) the lack of trace element data from these shards in this study and; 4) the possibility of sediment contamination from the coring processes, assigning these stratigraphically older Lipari shards earlier activities on Lipari would be for the moment be highly speculative, and requires further investigation.

## 6.3 Icelandic tephra deposits

### 6.3.1 LIA_603 / TDB_540-541 /Askja-S tephra

The depths of LIA_603 and at Brazi over 2cm at TDB_540 and TDB_541 are rhyolitic glass shards that are geochemically similar to the Askja-S tephra from Askja volcano eruption in Iceland (Figure 6.8). This Plinian eruption, coinciding with Icelandic glacial retreat after YD/GS-1, formed the Askja caldera at the Dyngjuföll volcanic centre (Sigvaldason, 2002). The estimated volume of this rhyolitic eruption is 1.5 ± 0.5 $km^3$ dense-rock equivalent (DRE), relative to a Volcanic Explosive Index (VEI) of 5 (Newhall and Self, 1982; Sigvaldason, 2002). Proximal Askja-S Plinian fall deposits are distributed along the north-eastern coast of Iceland (Figure 6.9; Sæmundsson, 1991; Norðdahl and Hjort, 1993; Sigvaldason, 2002; Gudmundsdóttir et al., 2011), confirming a dominant NNE plume dispersal off Iceland.

Combining the distinctive glass geochemistry, the fluted appearance of the colourless shards (Figure 6.8) and chronostratigraphic position of these layers within the locally described pollen zones associated with the transition from the YD to EH (Magyari et al., 2009, 2012; Vincze et al., 2017) there is confirmation that these depths can be correlated to the Askja-S tephra. The first reported distal occurrence of the Askja-S was by Davies et al. (2003) as a cryptotephra horizon in a sediment core from Hässeldala Port, Sweden. Since them, the Askja-S has been observed in as far north as Borge, Norway (Pilcher et al., 2003) as far east as Lake Czechowskie, Poland (Wulf et al., 2016a) and as far south as Soppensee, Switzerland (Lane et al., 2011b) with a recent discovery in Pant-y-Llyn, South Wales (Jones et al., 2018). This ultra-distal discovery of the Askja-S, over 3,000 km away from volcanic source in the Southern Carpathian Mountains dramatically extends the known dispersal of the fine ash

(typically <25µm in size; Figure 6.9). Further identification of Askja-S type shards are seen in younger depth of LIA_600 and LIA_576, but do not represent primary cryptotephra deposits.

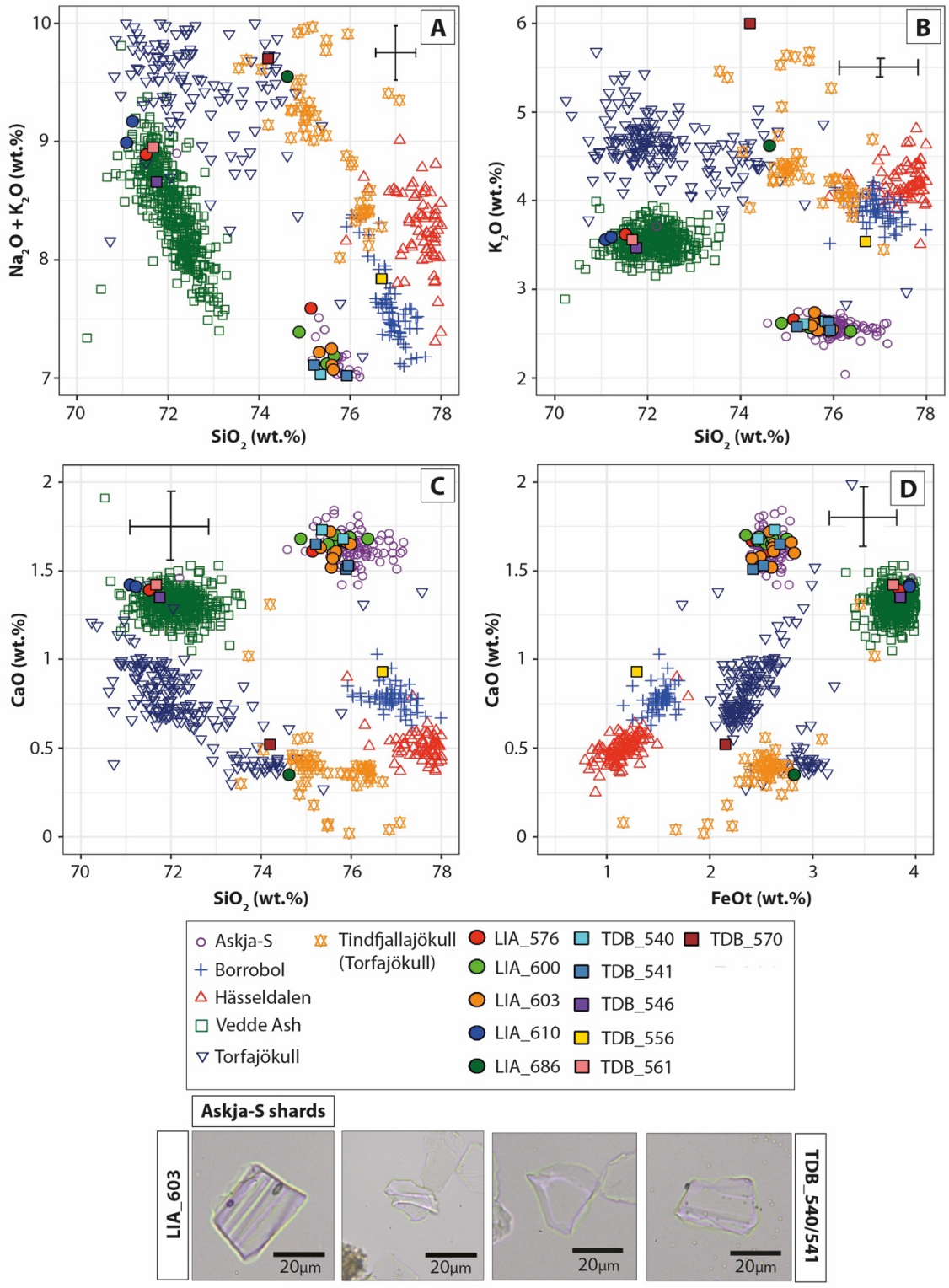

**Figure 6.8** (previous page) Geochemical bi-plots of the major elemental data from Lake Brazi and Lake Lia with known rhyolitic eruptions during the Late Glacial to Early Holocene from Icelandic volcanic sources. Borrobol (Turney et al., 1997; Davies et al., 2003; Pyne-O'Donnell, 2007; Matthews et al., 2011; Lind et al., 2016); Vedde Ash (Birks et al., 1996; Wastegård et al., 1998, 2000; Turney et al., 1997, 2006; Raner et al., 2005; Pilcher et al., 2005; Davies et al., 2005; Blockley et al., 2007; Lane et al., 2011b, c, 2012a, b); Torfajökull/Tindfjallajökull (Ram et al., 1996; Sigurdsson et al., 1998; Thordason et al., 2007; Moles et al., 2019); Hässeldalen (Davies et al., 2003;Lane et al., 2012b; Housley et al., 2013; Lind and Wastegård, 2011; Lilja et al., 2013; Larsen and Noe-Nygaard., 2014; Wulf et al., 2016) Askja-S (Sigvaldason, 2002; Davies et al., 2003; Turney et al., 2006; Lane et al., 2011b; Lind and Wastegård, 2011; Wulf et al., 2016; Kelly et al., 2016; Jones et al., 2017b; Lowe et al., 2017). Error bars represent 2 standard deviations of repeat analyses of the MPI-DING StHs6/80-G glass standard on the major element graphs.

Whilst other, younger tephra deposits from Askja volcano have been reported (e.g. the Askja-L and Askja-H; Jóhannsdottir, 2007; Striberger et al., 2012; Gudmundsdóttir et al., 2016), there is no evidence to date of these tephra deposits having been identified beyond Iceland indicating that these shards are possibly reworked from the Askja-S.

Dating of this tephra has been refined within the larger chronological model of this project to 11,120-11,040 cal. BP (95.4%). Please see Chapter 7 for the chronological discussion and newly modelled age of this tephra.

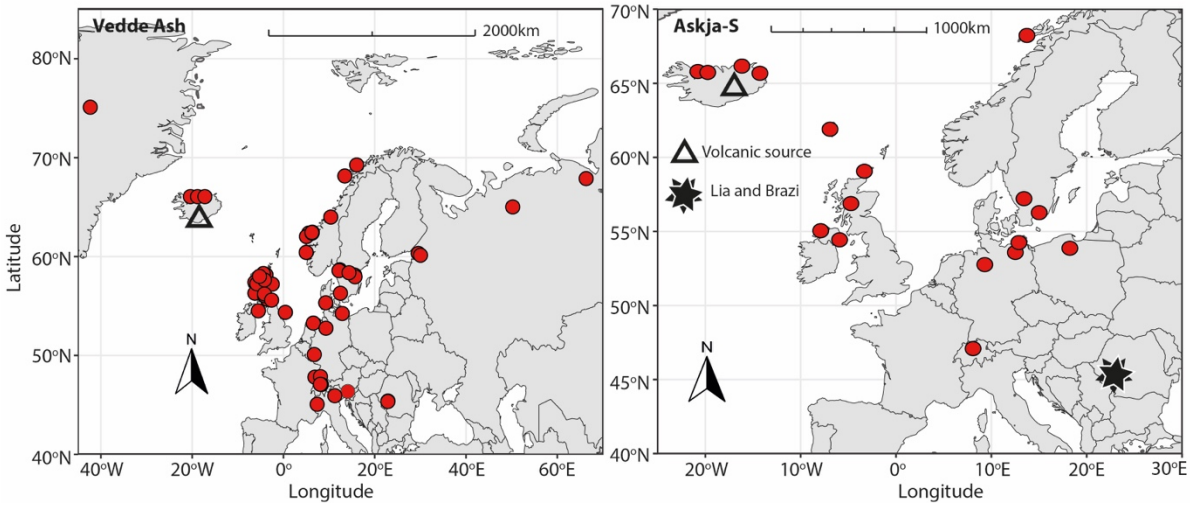


**Figure 6.9** Dispersal maps of Icelandic tephras identified in Lake Lia and Brazi. Black circles represent single site occurrences of tephra layers.

### 6.3.2 Katla-type tephra

Isolated glass shard within cryptotephra deposits LIA_631, LIA_610, LIA_576, TDB_561 and TDB_546 all exhibit glass chemistries similar to the rhyolitic products of Katla volcano (e.g., Vedde Ash), Iceland (Figure 6.8). Further evidence for the major element similarities between these glass shards and those erupted by Katla is illustrated by the trace element signature of the Katla-type shard in LIA_631 (Figure 6.10). During the LGIT period, multiple tephra units are produced by Katla volcano, these eruption deposits display similar rhyolitic chemical compositions and have been recorded at sites across Europe (e.g. Bond et al., 2001; Pilcher et al., 2005; Koren et al., 2008; Thornalley et al., 2011; Matthews et al., 2011; MacLeod et al., 2015).

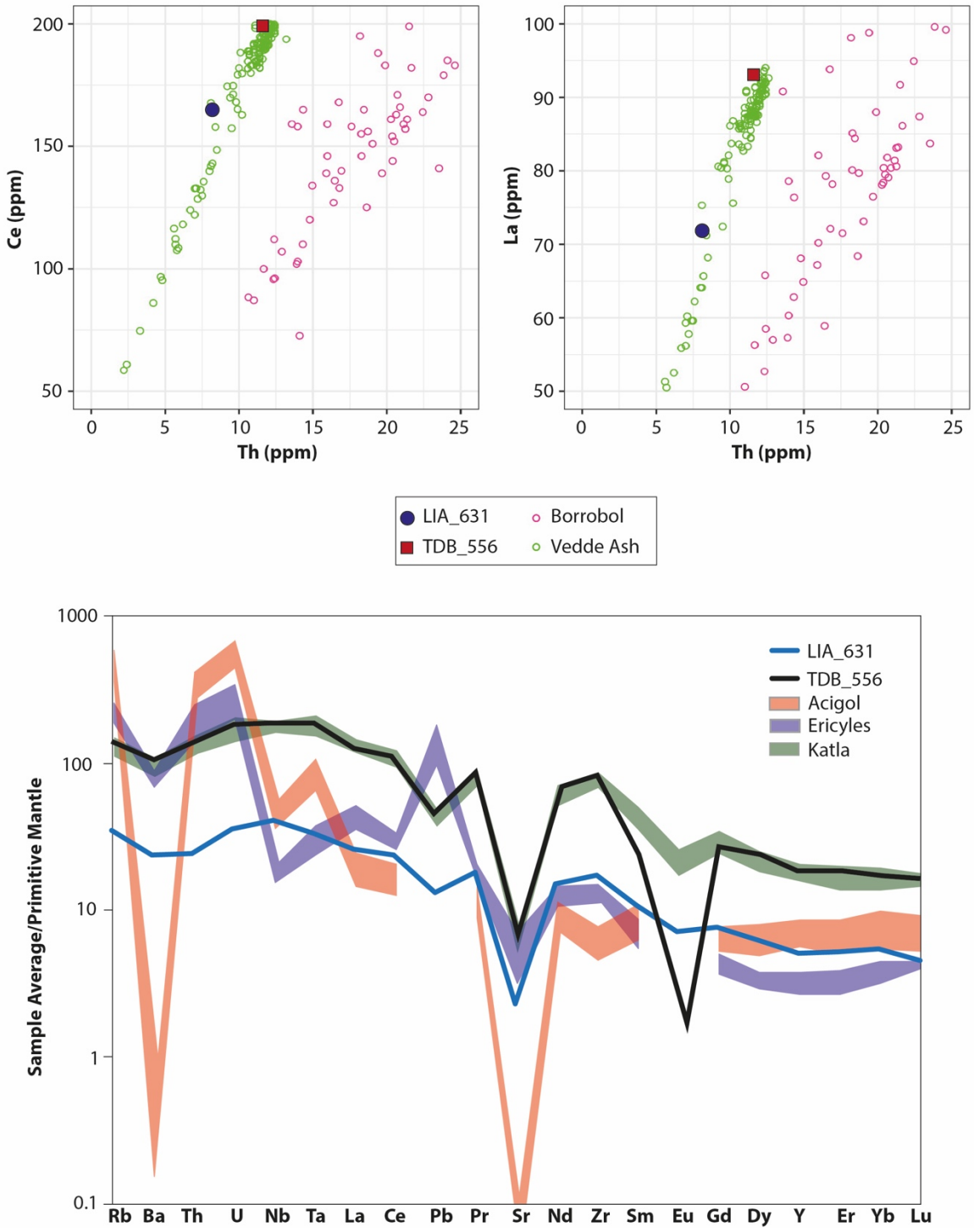


**Figure 6.10** Trace element comparison of LIA-631 and TDB_556 to Icelandic tephra deposits the distally characterised Borrobol tephra (Lind et al., 2016; Cook et al., 2018) and Vedde Ash (Lane et al., 2012b) bi-plots and normalised to primitive mantle (Sun and McDonough, 1989). Error bars were smaller than the symbols and are not presented.

The chrono-stratigraphic position of these glass shards in Lia and Brazi suggest a GS-1 to Early Holocene transition deposition (see section 6.6; Table 6.2). The widespread Vedde Ash is traced across much of Europe including northern (e.g. Timms et al., 2018; Birks et al., 1996), central (e.g. Lane et al., 2013; Blockley et al., 2007) and southern regions (e.g. Lane et al., 2012b, c) with extension into Russia (e.g. Wastegård et al., 2000; Haflidason et al., 2019). This tephra layer has been dated to 12,101-11,914 cal yrs BP with radiocarbon dating (95.4%, Bronk Ramsey et al., 2015) and to 12,171 ± 114 b2k (GICC05; Rasmussen et al., 2006). The age estimates of LIA_613, LIA_610, LIA_631, LIA_576, TDB_561 and TDB_546 produced in the age-models of this work (Table 6.2) suggest that these cryptotephra deposits are too young to represent primary deposition from the widespread Vedde Ash. Another Katla-type tephra, the Abernethy Tephra, has been identified and dated to 11,584-11,340 cal yrs BP (95.4%, Bronk Ramsey et al., 2015) at the GS-1 and Early Holocene boundary (Matthews et al., 2011; MacLeod et al., 2015). This could be considered a potential correlative of TDB_561 owing to their overlapping age. However, this Abernethy tephra is significantly more restricted in terms of distribution, particularly relative to the Vedde Ash, with occurrences limited to lacustrine records in Scotland (Matthews et al., 2011; MacLeod et al., 2015; Timms et al., 2017, 2018), thus making a link to the deposits found in Lake Brazi unlikely.

The yet younger LIA_631, LIA_613, LIA_610 and LIA_576 are not chronologically consistent with known eruptions of Katla (c. 11,700 to 10,800 cal yrs BP). Several authors have identified single Katla-type shards within European records at this time (e.g. Timms et al., 2017, 2018; Jones et al., 2018), however re-working of material from the underlying Vedde Ash layers have been suggested as responsible.

**Table 6.2** Table presenting the depths, ages and type of tephra layer in Lake Lia and Brazi. Those marked in bold are recognised here as robust chrono-stratigraphic markers with Lake Lia record

| Site | Depth code | Mean age (cal. BP) | ± 1 sigma | Tephra correlations | Layer type |
|---|---|---|---|---|---|
| **Lia** | LIA_576 | 10,796 | 138 | Anat. Unknown, LG Lipari, Askja-S, Katla-type | Mixed |
| | LIA_589 | 10,941 | 120 | Anat. Unknown | Mixed |
| | LIA_591 | 10,961 | 113 | Anat. Unknown | Mixed |
| | LIA_600 | 11,038 | 62 | Anat. Unknown, Askja-S, LG Lipari | Mixed |
| | **LIA_603** | **11,065** | **17** | **Askja-S, Anat. Unknown,** | **Askja-S Isochron** |
| | LIA_607 | 11,073 | 40 | LG Lipari, Unknown | Mixed |
| | LIA_610 | 11,079 | 55 | LG Lipari, Katla-type | Mixed |
| | LIA_612 | 11,083 | 64 | Anat. Unknown, Ischia, LG Lipari | Mixed |
| | **LIA_612.5** | **11,084** | **66** | **Ischia** | **Ischia Isochron** |
| | LIA_613 | 11,085 | 68 | Anat. Unknown, Ischia, LG Lipari, Unknown Pantellerite | Mixed |
| | LIA_631 | 11,595 | 457 | Anat. Unknown, LG Lipari, Katla-type | Mixed |
| | LIA_633 | 11,733 | 462 | Anat. Unknown, LG Lipari | Mixed |
| | LIA_637 | 12,011 | 413 | LG Lipari Anat. Unknown, | LG Lipari ? |
| | LIA_686 | 13,292 | 184 | Anat. Unknown, Lipari unknown(?), Ice. Unknown | Mixed |
| | LIA_713 | 13,866 | 649 | Anat. Unknown | Mixed |
| | LIA_769 | 15,051 | 1141 | Anat. Unknown | Mixed |
| | LIA_796 | 15,622 | 1332 | Anat. Unknown, NYT | Mixed |
| | LIA_805 | 15,814 | 1391 | Anat. Unknown | Mixed |
| | LIA_815 | 16,027 | 1456 | Anat. Unknown | Mixed |
| | LIA_829 | 16,322 | 1546 | Anat. Unknown | Mixed |

**Table 6.2** (cont.) Table presenting the depths, ages and type of tephra layer in Lake Lia and Brazi. Those marked in bold are recognised here as robust chrono-stratigraphic markers with the Lake Brazi record.

| Site | Depth code | Mean age (cal. BP) | ± 1 sigma | Tephra correlations | Layer type |
|---|---|---|---|---|---|
| Brazi | TDB_540 | 11,057 | 63 | Anat. Unknown, Askja-S, LG Lipari | Mixed |
| | **TDB_540.5** | **11,076** | **19** | **Askja-S** | **Askja-S Isochron** |
| | TDB_541 | 11,079 | 22 | Anat. Unknown, Askja-S, LG Lipari, Unknown | Mixed |
| | TDB_546 | 11,142 | 92 | Anat. Unknown, LG Lipari, Katla-type | Mixed |
| | TDB_549 | 11,251 | 161 | LG Lipari | Mixed |
| | TDB_554 | 11,431 | 199 | Anat. Unknown | Mixed |
| | TDB_556 | 11,503 | 198 | Anat. Unknown, LG Lipari, Ice. Unknown, | Mixed |
| | TDB_559 | 11,746 | 343 | LG Lipari | Mixed |
| | TDB_561 | 11,950 | 407 | Katla-type, LG Lipari | Mixed |
| | **TDB_564** | **12,156** | **421** | **LG Lipari** | **LG Lipari Isochron** |
| | TDB_570 | 12,840 | 153 | Anat. Unknown, Ice. Unknown (?) | Mixed |
| | TDB_575 | 13,181 | 221 | Anat. Unknown | Mixed |
| | TDB_582 | 13,529 | 265 | Anat. Unknown | Mixed |
| | TDB_588 | 13,744 | 410 | Anat. Unknown, Lipari unknown | Mixed |
| | TDB_599 | 14,140 | 608 | Anat. Unknown, Unknown | Mixed |

Re-working of Vedde Ash material from within the lake catchments is the most plausible explanation for successive identifications of Katla-type glass chemistries through the Lake sequences. Factors that support this interpretation are; (1) very low concentrations of Katla-type glass chemistries (1-2 shards) at the different core depths in the two lakes; (2) only the Vedde Ash has been traced into central-southern Europe (Blockley et al., 2007; Lane et al., 2012b, c); and (3) the inclusion of other mixed glass chemistries within the cryptotephra layers examined. (Table 6.2).

The Vedde Ash particles found in the sediments of Lake Lia and Brazi are mostly likely the result of secondary deposition, probably following the melting of ice and/or snow beds in the region. Nonetheless, their discovery here indicates that ash fall from this enormous Katla eruption did reached the Carpathian Mountains (Figure 6.9). This expands the distribution of ash fall from the Vedde Ash which is already extensive across Europe (e.g. Wastegård et al., 2000; Blockley et al., 2007; Lind et al., 2013; Lane et al., 2011b, 2012b). Modern day tephra dispersal from Iceland is known to have reached south eastern Europe (Gudmundsson et al., 2012).

### 6.3.3 Icelandic unknowns

There are several glass shards at TDB_570, TDB_556 and LIA_686 possess chemical compositions of Icelandic origin (Figure 6.8). However, correlating them to a known volcanic source and/or eruption is difficult. Yet, with the ultra-distal occurrence of the Askja-S and Vedde Ash in both records, additional Icelandic eruptions may also be recorded at Lia and Brazi

Tentative correlations of single glass shards from TDB_570 and LIA_686 can be made to the contentious Torfajökull volcano as a source for these shards (Figure 6.8). The data for these correlations comes from the recently re-examined a volcanic source for the Thórsmörk Ignimbrite eruption by Moles et al. (2019) to Torfajökull rather than previously Tindfjallajökull volcano. Similar correlations were made to Torfajökull with rhyolitic shards of the Crudale Tephra from the British Isles by Timms et al. (2019). Both TDB_570 and LIA_686 plot within this volcanoes chemical envelopes (Figure 6.8). However, the age for both these tephras is older than the proposed Crudale Tephra age that is placed between

12,111-11,174 cal. BP (Table 6.2; Timms et al., 2019). The Lia and Brazi tephras may present evidence for additional eruptions from Torfajökull during the LGIT. However, only single shards are present at different ages in both sites. In addition, further geochemical and chronological examination of the Crudale Tephra and Torfajökull proximal outcrops need to be undertaken before direct correlations to this volcano/eruption cam be securely made.

The single glass shard from TDB_556 can be described as a "Borrobol-type" due to correlating within the broad geochemical envelope of this tephra with low FeOt and CaO (Figure 6.8). Trace element data has been obtained from this shard further corroborates an Icelandic origin (Figure 6.10). Comparisons to Cook et al. (2018) Borrobol-type trace element data sees no overlap in key elements suggesting a different volcanic source (Figure 6.10). The volcanic source on Iceland of the distally traced Borrobol-type tephra deposits across NW Europe remains contentious and unresolved (e.g. Pyne-O'Donnell, 2007; Lind et al., 2016; Cook et al., 2018; Plunkett and Pilcher, 2018). In addition, the date for this Lake Brazi tephra is placed within the EH period, significantly younger than the age of the Borrobol which is dated within the LG (Bronk Ramsey et al., 2015). As a result, the volcanic source and eruption for this shard remains largely unknown.

Overall, even with the vast number of Icelandic tephra layers geochemically analysed and identified in distal records, there are still knowledge gaps associated with the volcanism of Iceland during the LGIT elucidated by several distal records (e.g. Lane et al., 2015; Timms et al., 2019).

## 6.4 Uncorrelated tephras

A single glass shard found at TDB_541 is rhyolitic geochemistry and has no correlation to a known volcanic source or eruption can be made. This population can be provisionally identified as Icelandic from an unknown volcano (Figure 6.11). The high $FeO_t$ and low $SiO_2$ cannot be correlated to any known Anatolian volcanoes or previous unknown Anatolian tephras from both records. The geochemistry is similar to the Askja-S, yet the CaO content is too low to make assumptions of reworked Askja-S shards. As a result, further investigation is need.

Another single glass shard of distinct trachytic composition from LIA_633 currently cannot be correlated to any known volcanic sources from the Anatolian, Mediterranean, or Icelandic (Figure 6.11). As a result, this tephra remains uncorrelated.

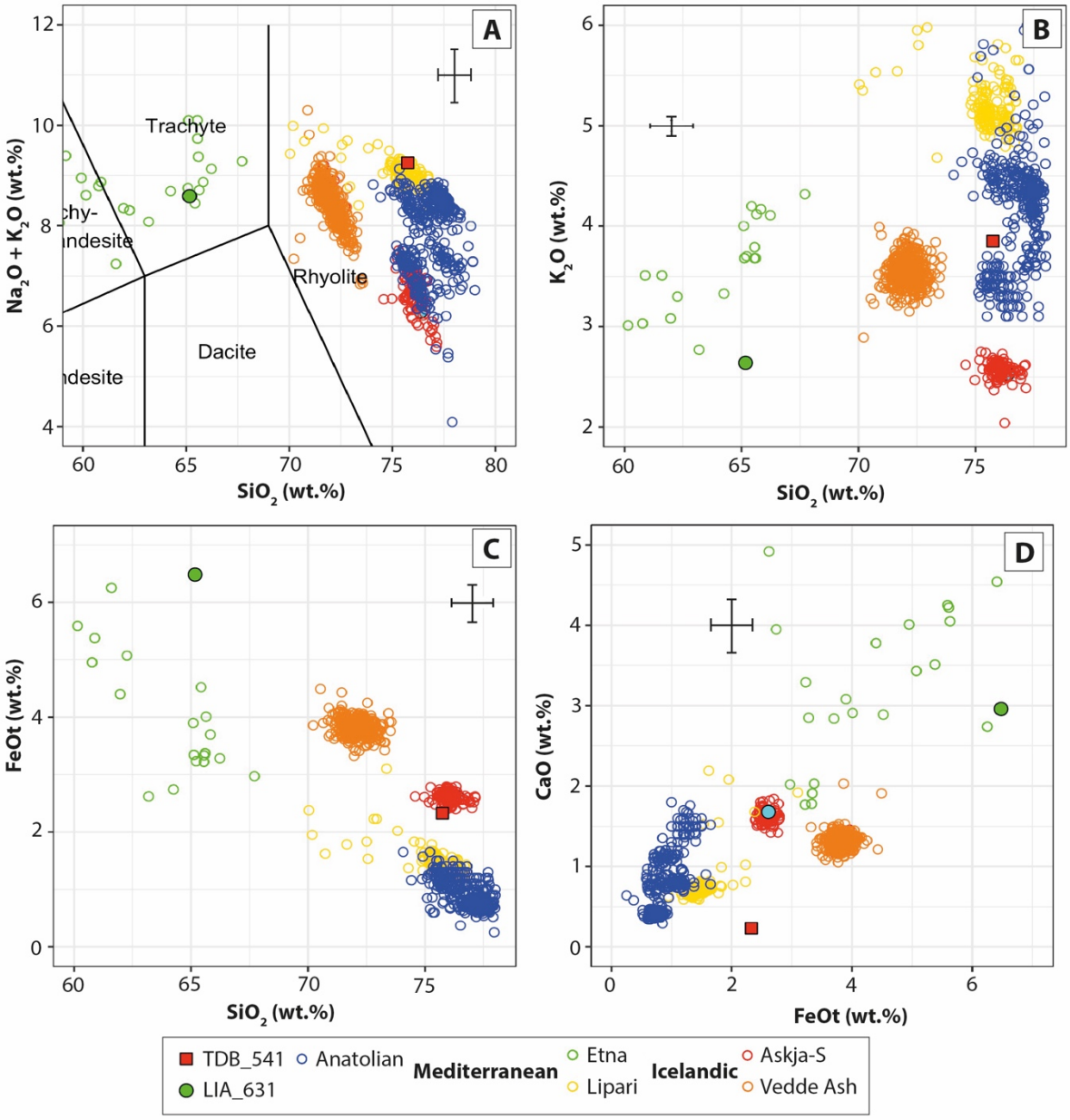


**Figure 6.11** Major element geochemistry of uncorrelated tephras of TDB_541 and LIA_633. LIA_633 single shard is similar to Etna glass shards from Wulf et al. (2003) yet vary on many elements resulting in no current correlation to a volcanic source or eruption.

## 6.5 Identifying primary and secondary cryptotephra deposits

Within cryptotephra concentration profiles, the largest shard peak is described as an isochron, representing the specific timing of the volcanic eruption and thus primary deposition (Lowe et al., 2011; Davies et al., 2012). Within lake records, low levels of shard concentrations located above this peak can be associated with secondary mobilisation of shards from the local catchment from melting of snow-beds (Hunt 1994; Bergman et al., 2004; Davies et al., 2007) and/or lake ice cover melting (Harning et al., 2018). Bioturbation and currents can also be linked to shard remobilisation within a profile (Davies et al., 2012; Pyne-O'Donnell, 2008).

The clear peak of TDB_564 and LIA_603 with homogenous geochemistry and shard morphologies can be both interpreted as robust isochrons (Table 6.2). Lower concentrations peak situated in sterile sediment (above and below) can be considered primary isochrons (e.g., LIA_637). Due to the near identical shard concentrations of TDB_541 and TDB_540, the position of the isochron can be taken at the mid-point of these depths (TDB_540.5). This is also appropriate in the case of LIA_613 and LIA_612 (LIA_612.5) due to the sterile nature of the shard profile before these depth.

Defining the stratigraphic position for the LG Lipari eruption in Lia is more challenging due to processes related to inwashing of shards from the surrounding catchment. The primary deposit of LG Lipari in Lia can be identified as LIA_637 due to the first occurrence of these shards after a sterile period of the core. Further deposition of Lipari thereafter in LIA_633, 631 and beyond can be due to the prolonged input of shards from perennial snow-beds within the catchment. In Brazi, the clear isochron of Lipari at TDB_564 and successive shards of Lipari chemistry thereafter can also be linked to existence of snow-

beds at the site. Davies et al. (2007) has highlighted that the presence of snow-beds can become 'tephra traps', and with subsequent melting, release this tephra into the catchment and lake over an extended period of time. Multi-proxy evidence from both Lia and Brazi have indicated the presence of prolonged snow-beds during the early part of GS-1 with a subsequent increasing in melting around the time of the Lipari eruption (Buczko et al., 2009, 2017; Magyari et al., 2009, 2012; Finsinger et al., 2018). In addition, Lia also had a rock glacier located on the western side of the lake at this time (Urdea, 2004). A glacier is also located near Lake Bucura that would have influenced inflow to Lia (Urdea, 2004). This type of ice can also be interpreted as 'traps' for tephra shards, which are then released into the catchment system with melting and subsequently deposited into the record (Davies et al., 2007). The continuous lower shard concentrations with heterogeneous glass chemistry within both lake profiles as indicated in Table 6.2 may also be due to melting of snow and ice tephra traps after an eruptions primary deposition at the sites. This has resulted in identifying additional clear isochrons difficult. Additional occurrences of tephras in younger depths after a clearly identified isochrone (Table 6.2) can also be due to re-working and inwash from snow traps in the catchment.

The identification of the Vedde Ash within the records of Lia and Brazi at a younger chronostratigraphic age indicates inwashing of these older shards from the surrounding landscape. Evidence for a younger Katla-type eruption this far south-east from Iceland is limited (see section 6.3.2; Timms et. Al., 2018, 2019) It can be hypothesised that the Vedde Ash did make it to the Southern Carpathians at the time of Katla's eruption. However, with the eruption from Lipari and subsequent near constant inwash of Lipari shards from the surrounding landscape, identifying the Vedde Ash isochron is difficult due to the high number

of background shards especially presented in Brazi. A more continuous high-resolution sampling (at 0.5cm) throughout the profile may have allowed the Vedde Ash isochron to be identified (Timms et al., 2017). However, the high amount of shard concentration witnessed would have made this difficult.

Within the lower depths of Lake Brazi and Lia, multiple peaks of mixed >76 wt.% $SiO_2$ chemistry which have identical major element composition correlated here to unknown volcanic eruptions at sources in Anatolia (Table 6.2). Repeat major and minor element glass chemistries produced over prolonged timescales is commonly recognised at many volcanic systems (e.g. Smith et al., 2011; Lane et al., 2012b; Cook et al., 2018). While trace element analysis can sometimes help distinguish between eruptions (Tomlinson et al., 2012a; Albert et al., 2015), certain volcanoes can also produce identical trace element compositions with each eruption (e.g. Lane et al., 2012b; Cook et al., 2018) resulting in unclear correlations to a particular eruption. Not all cryptotephra peaks from Lia and Brazi have undergone trace element analysis due to the shards being too small. Yet, where trace geochemistry data was obtained, there is little geochemical information from volcanic regions such as Anatolia to make a clear comparison. As a result, it is uncertain if these shards are from separate, closely spaced eruptions or reworking of older tephra deposited in the surrounding catchment and periodically released.

## 6.6 Chronological modelling

Both Lia and Brazi records have radiocarbon dates across their sequences. Due to the overarching aim of this project focusing on the refining the timing of abrupt climatic

oscillations during the LGIT, Brazi was selected as a site to be involved in the larger age model. This was due to identification of the Askja-S and a new tephra in the YD, the LG Lipari, in combination with other selection criteria outlined in section 3.1.2. However, there are issues when producing an age model for Lia and it's pollen record (see Appendix 3 and explained in 4.2.14). As a result, Lia was not involved in the subsequent large age model of Chapter 7.

However, the new ages for the Askja-S and LG Lipari that have been produced from this larger age model (see section 7.1) can subsequently be used to improve the age-model for Lia. Figure 6.12 presents the age model for Lia with focus on the Last Glacial Interstadial transition.

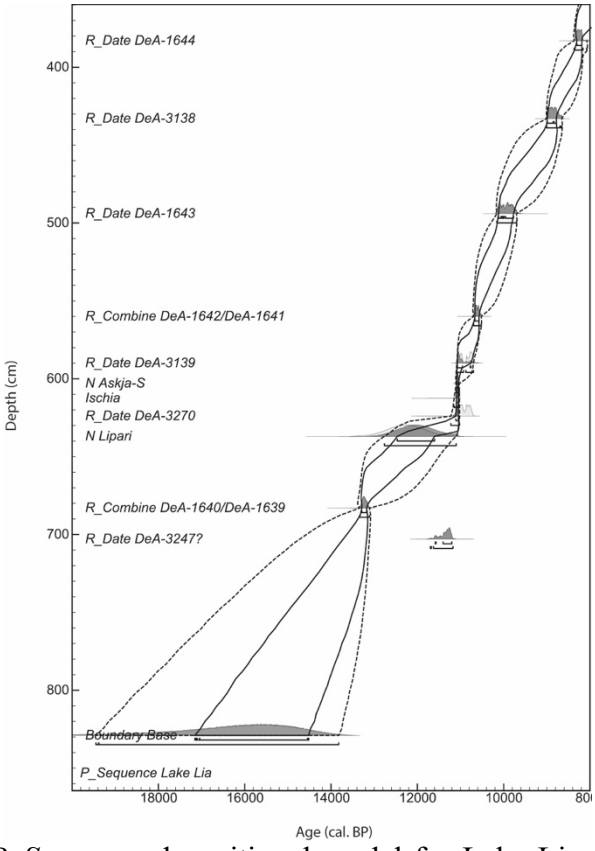


**Figure 6.12** Bayesian *P_Sequence* depositional model for Lake Lia using radiocarbon dates (Hubay et al., 2018) and tephra ages from Chapter 7 for Askja-S and LG Lipari.

## 6.7 Expansion of the tephrostratigraphic framework

Both the records of Lake Brazi and Lia provides the first detailed LGIT tephrostratigraphy for Romania. Three different cryptotephra horizons successfully identified and can be utilised as isochrons, importantly these derive from different source regions: Iceland, Askja (TDB_540.5 and LIA_603); the Aeolian Islands (Italy), Lipari (TDB_564 and LIA_637(?)); and the Campanian Volcanic Zone (Southern Italy), Ischia (LIA_612.5). The chronology of both sites allows these eruptions to be precisely dated and their eruption ages improved upon. These findings extend the European and Mediterranean tephrochronological framework eastward. As a result, these Romania cryptotephra records provide a pivotal link between a large number of palaeoenvironmental archives throughout the North Atlantic region, Europe and the Mediterranean during the LGIT time period.

The discovery of Anatolian geochemical compositions within the records highlights the potential of new regional tephra markers. However, with the lack of glass geochemistry (major, minor and trace elements) currently available from this region, coupled with a poor chronology of past eruptions from these volcanic sources, the usefulness for these tephras to be regional markers will be a future endeavour. Once established, further correlations can be made between palaeoenvironmental archives between Europe and beyond into the Middle East and the Caucuses, allowing future understanding of climate time-transgression from the North Atlantic region.

The identification of the Askja-S tephra within these ultra-distal records highlights the possibility of finding further Icelandic tephras in the far corners of Europe. The presence of Vedde-like shards, yet with no clear isochron, demonstrates the possibility of identifying this important horizon within this region's palaeoenvironmental records. The depositional

processes at Lakes Lia and Brazi have hindered the possible identification of this important, European wide tephra horizon. Nonetheless, there is potential to identifying important Icelandic tephra horizons in south-eastern Europe.

The confirmation and dating of a LG Lipari eruption highlights the importance of distal records in constructing accurate volcanic eruption histories were no proximal deposit has yet been recognised (Albert et al., 2012). By examining this tephra for major, minor and trace element composition, this approach allowed for this particular tephra to be distinguished from younger/older eruptions from the same volcano and be successfully correlated to other sedimentary records. This highlights trace elements analysis as an important tool in making correct correlations than just solely based upon major and minor elements. There is potential for further discovery of the LG Lipari in records along, and possibly beyond, the trajectory of the ash dispersal with refinement of the age for this tephra (Figure 6.5). This also true with the validation of a LGIT Ischia tephra and the furthest north-eastern dispersal of the NYT.

A number of factors could be responsible for the distal occurrences of the widespread ash from Iceland, the Mediterranean and Anatolia. The region of the Southern Carpathians is governed by three air circulations; the Atlantic, the Mediterranean and the Siberian High resulting in ash fall from the three different volcanic sources to be deposited at the sites (Obreht et al., 2016; Longman et al., 2017a,b). Variable and evolving concomitant weather patterns may have led to varying directions of ash plume dispersals from the volcanic sources, resulting in patchy distribution of tephra identifications at sites across Europe (Jones et al., 2018). In addition, different atmospheric circulations at varying elevation of the ash plumes height may have resulted in divergent directions against prevailing wind directions (Fisher, 1964). This is especially seen in the case of Anatolian tephra distribution.

The resulting complex atmospheric circulations over Lake Brazi and Lia have governed the distribution of ash fall from the these volcanic sources. It could be suggested that the dominance of tephra from a volcanic source could indicate the dominance of prevailing palaeo wind directions, i.e. the presence of Mediterranean tephra shows the influence of Mediterranean sources (Bogaard and Schmincke, 1985). Shard geochemistry from Lake Lia shows a higher occurrence of Mediterranean derived glass shards from different eruptions compared to Lake Brazi (Table 6.2). This may be due to the location of Lia on the southern side of the Carpathian Mountains, mainly influenced by the Mediterranean atmospheric circulation.

The use of a 15μm sieve mesh size is believed to have been crucial in retaining and the identification of the finest grain ash particles produced during some eruptions (<25μm). Typically in cryptotephra studies, an approach of using 25μm mesh is undertaken which may have resulted in fine-grain material not being recovered by the cryptotephra procedures. This adaptation has allowed the identification of the furthest south-eastern deposits for the Askja-S horizon and Vedde-like shards as well as geochemical characterisation of a number of previously unknown eruptions from Anatolia. Therefore, these findings provide encouragement in implementing a smaller sieve mesh size in providing a highly detailed cryptotephra investigation.

A speculative factor for the identification of cryptotephra in Lake Brazi and Lia records may have been influenced by orography of the Carpathian mountain range. The Carpathians raises up out of the low topography of central Europe forming a large barrier to atmospheric circulations. Turbulence caused by these mountains can influence the localised deposition of tephra transported within atmospheric circulation (Watt et al., 2015). In addition,

orographic precipitation can enhance tephra deposition (Stevenson et al., 2013; Watt et al., 2015). The Retezat Mountains, where Lake Lia and Brazi are located, is one of the wettest alpine regions in the Carpathian Mountains, influenced by three difference climatic systems (Atlantic, Mediterranean and Siberian High) (Magyari et al., 2012; Obreht et al., 2016; Longman et al., 2017b). Additional factors such as regional bias of cryptotephra investigations especially in south-eastern Europe (Watson et al., 2017), site-specific sedimentary taphonomic processes (Pyne-O'Donnell, 2011) and lack of continuous high-resolution cryptotephra searches (Timms et al., 2016) may have all influenced the currently limited known spatial distribution of these tephrostratigraphic markers in other European records.

## 6.8 Synchronising palaeoenvironmental records

For tephra layers to be useful in providing insight into past climatic events, an identified tephra horizon must be: 1) geographically widespread and found in multiple palaeoenvironmental records; 2) geochemically disguisable from other tephra layers; 3) robustly dated and 4) be associated with a climatic oscillation. The discovery of a number of tephra layers in two palaeoenvironmental records from the Southern Carpathians can provide key tephrostratigraphic linkages between western and northern Europe, the Mediterranean and into the Middle East with south-eastern Europe.

The identification of the Askja-S in both Lia and Brazi is chrono-stratigraphically important due to the eruptions position close to an abrupt climatic transition within the Early Holocene, namely the Preboreal Oscillation (PBO; see section 2.5.1.4) which has been identified in numerous European palaeoclimate records (Björck et al., 1997; Wohlfarth et al.,

2006; Lowe et al., 2015; Ott et al., 2016). However, these events remain poorly understood in terms of environmental impacts and geographical expression (e.g. Björck et al., 1996, 1997; Wohlfarth et al., 2006; section 2.4.3). Both Lake Brazi and Lia have undergone high-resolution, multi- proxy palaeoenvironmental investigations across this time period (e.g. Magyari et al., 2012; Buczkó et a., 2013; Tóth et al., 2015, 2018; Pál et al., 2016; 2018; Finsinger et al., 2014; 2016; Vincze et al., 2017). With the identification of the Askja-S within both records, this presents an ideal opportunity to investigate comparative environmental dynamics of Early Holocene oscillations through improving chronological modelling from north-western Europe to the Southern Carpathians. The identification of LG Lipari tephra within both Lake Brazi and Lia and subsequent refined age for this eruption of 12,139-11,881 cal yrs BP provides an additional opportunity to investigate the timing of the onset and termination of GS-1 (Younger Dryas) across Europe.

With the discovery of the Askja-S and LG Lipari tephra as clear isochrones in Brazi, only Brazi will be used in the following chapters. This is due to the highlighted problems of the reworking of LG Lipari in Lia. In addition, problems associated with the new age-model developed in this project with the Askja-S and LG Lipari, and comparisons to the currently unpublished pollen record of Lia has resulted in large disparities in ages for known vegetation changes (see Appendix 3). Further investigation is need to resolve these discrepancies. Nonetheless, the high-resolution dated pollen record from Brazi alone, now with the supplementary of the Askja-S and LG Lipari tephras, provides an ideal palaeoenvironmental record to investigate the timing of abrupt climatic oscillations during the LGIT.

# Chapter 7

# Chronological and palynological statistical analysis results from across Europe

The following chapter presents the results for both the age modelling and the palynological reinvestigation of this study's selected sites. Section 7.1 focuses on the chronological results from the large age model described in Chapter 3. Included are the new tephra age estimates obtained from this model with the age-depth results for each site. Section 7.2 follows on with the palynological results for the LGIT period. Each sites pollen record was reinvestigation using statistical analysis (as outlined in Chapter 3). The pollen records are on age, using the new chronology devised from this thesis's large age model.

## 7.1 Results of refined chronological modelling

Within the large age model, there are thirteen sites with eleven different tephra layers cross-referenced (outlined in Chapter 3). The age model code was run three times to test the similarity of ages for each tephra and radiocarbon date. These ages differed by <10 years each time. The run with the best convergence (>75%) obtained for each tephra and radiocarbon age is the most robust. This model produced the ages that are in the remainder of this thesis. The ages are presented as calibrated radiocarbon ages (cal. BP) unless otherwise stated as uncalibrated radiocarbon ages ($^{14}$C yrs BP). The ages are presented as the mean ± one sigma ($\mu \pm 1\sigma$) in figures and graphs unless otherwise stated. The timescale presented in the figure is on the IntCal13 cal. BP.

The previous most robust age estimates for these tephras originate from Bronk Ramsey et al. (2015). A similar methodology was employed using Bayesian chronological depositional modelling and links between similar tephra layers. However, compared to this

investigation, different sites were used by Bronk Ramsey et al. (2015) due to the specific aim of the present investigation being on the YD and EH. As a result many tephras have similar ages to those previously published, with several older tephras (i.e. NYT, Borrobol) having larger uncertainties because of this aim.

### 7.1.1 New tephra age estimates

Table 7.1 summaries the previous best age estimates and this thesis age estimates for the tephra layers. Many of these tephras were only identified at one site, which resulted in a greater age uncertainty (Figure 7.1). Several of the older tephras were used within the age model to increase chronological constraints for sites that have a lower density of radiocarbon dates (i.e. Crudale and Bled).

**Table 7.1** The best age estimates for selected tephra layers. Ages included are from previous investigations involving radiocarbon modelling along with new ages that are produced in this study. Bold indicates the best age estimate for the selected tephra.

| Tephra name | Volcanic source | Modelled age (μ ± 1σ cal. BP) | | References |
|---|---|---|---|---|
| | | Prev. estimates | This study | |
| **Neapolitan Yellow Tuff (NYT)** | Campanian Volcanic Field, Italy | **14,194 ± 172** | 14,408 ± 245 | Bronk Ramsey et al. (2015) |
| **Borrobol** | Unknown, Icelandic | **14,098 ± 47** | 12,945 ± 791 | Bronk Ramsey et al. (2015) |
| **Pennifiler** | Unknown, Icelandic | **13,939 ± 66** | 12,813 ± 710 | Bronk Ramsey et al. (2015) |
| **Laacher See Tephra (LST)** | Laacher See, Germany | **12,937 ± 23** | 12,910 ± 31 | Bronk Ramsey et al. (2015) |
| **Late Glacial Lipari** | Lipari, Aeolian Islands, Italy | NA | **12,258 ± 421** | This study |
| **Vedde Ash (VA)** | Katla, Iceland | 12,023 ± 43 | **12,068 ± 31** | Bronk Ramsey et al. (2015) |
| **Pomici Principali (PP)** | Campanian Volcanic Field, Italy | **11,999 ± 52** | 12,019 ± 76 | Bronk Ramsey et al. (2015) |
| **Hässeldalen** | Unknown, Iceland | 11,316±124 | **11,239 ± 18** | Wastegård et al. (2018) |
| **Ulmener Maar** | Ulmener, Germany | 11,096 ± 117 | **11,141 ± 52** | Bronk Ramsey et al. (2015) |
| **Askja-S** | Askja, Iceland | 10,824 ± 48 | **11,076 ± 19** | Kearney et al. (2018) |
| **Saksunarvartn Ash** | Grimsvotn, Iceland | **10,176 ± 49** | 10,317 ± 91 | Bronk Ramsey et al. (2015) |

#### 7.1.1.1 The Neapolitan Yellow Tuff (NYT)

The NYT is from an ultra-Plinian eruption from Campi Flegrei, Italy (see section 6.3.1 for further information; Tomlinson et al., 2012). The Lower Member is found across the Mediterranean and as far north as Germany (e.g. Wulf et al., 2004; Lane et al., 2015). Radiocarbon dates from a marine core gave an age estimate of 14,870-13,510 cal. BP (95.4%; IntCal04, Siani et al., 2004). The Bayesian age modelling of Bronk Ramsey et al. (2015) produced a refined age of 14,433-13,795 cal. BP (95.6%, IntCal13). This study generated an age of 14,965-13,941 cal. BP which is in good agreement, albeit with a wider age range.

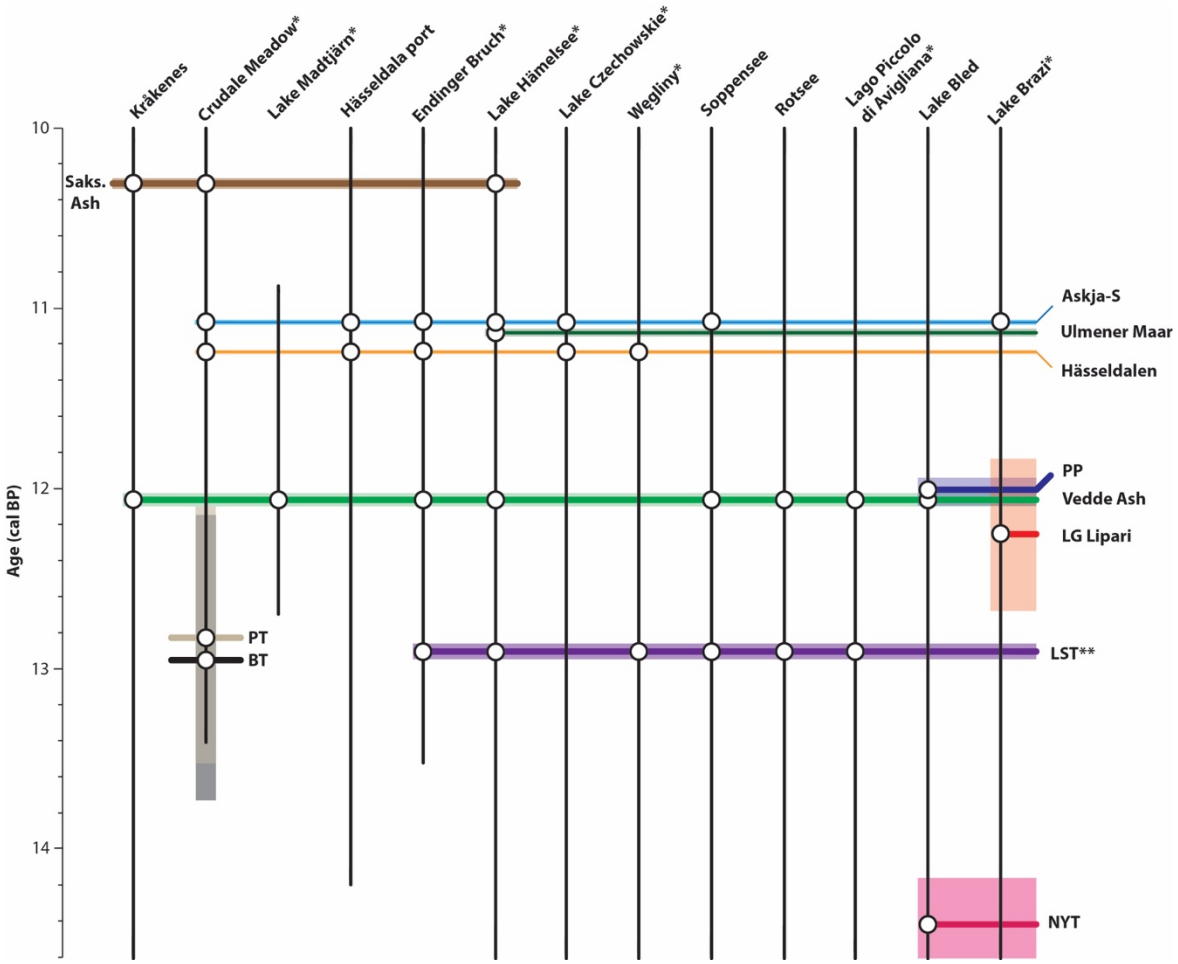


**Figure 7.1** Schematic of the tephra layer age estimates from this study. The vertical lines represent the records, horizontal lines link together tephra layers and are presented at mean ± 1σ deviation in lighter colour). The circles show which tephra layer is deposited within

each record. * = sites not included in Bronk Ramsey et al. (2015). ** = tephra with additional age constraints from proximal eruption deposits used in age model.

#### 7.1.1.2 The Borrobol and Pennifiler tephras

The Pennifiler and Borrobol tephras are in the large age model from the site of Crudale (Timms et al., 2018). However, there are no radiocarbon dates associated with these layers. As a result, the age estimates were large for both Borrobol at 14,276-12,066 cal. BP (95.4%) and the Pennifiler 14,039-12,039 cal. BP (95.4%) compared to the age estimates produced by Bronk Ramsey et al. (2015) (Borrobol:14,190-14,003; Pennifiler: 14,063-13,808 cal. BP. However, due to the problems of geochemically distinguishing between these tephras and the close sedimentary deposition in between, it is hard to identify which tephra is which formally (Davies et al., 2012; Lind et al., 2016). Also, within the Greenland ice-core records, numerous other closely timed Borrobol-like tephras are identified (Cook et al., 2018). The Borrobol is identified within Core 3 at Hässeldala port (Wohlfarth et al., 2006). However, with the ambiguity behind the identification, this was not included in the age modelling. Due to the large age ranges for tephras, they do not help in refining age in this age model.

#### 7.1.1.3 Laacher See tephra (LST)

The LST is in numerous archives across northern and central Europe (e.g. Lane et al., 2012a, c; Housley et al., 2013). The eruption has been dated to the late Allerød by varve counting and radiocarbon dating. The varve age for the LST from Meerfelder Maar, Germany is 12,880±120 varve years BP (Brauer et al., 1999) with radiocarbon dating from counted tree rings of 13,010-13,200 cal. yrs BP (IntCal98; Friedrich et al., 1999). Bronk Ramsey et al. (2015) produced a refined age of 12,979-12,889 cal. BP (95.4%, IntCal13). This study has produced a similar age estimate of 12,967-12,846 cal. BP with also including Friedrich et al. (1999) tree ring data (Figure 7.1).

#### 7.1.1.4 Late Glacial Lipari tephra (LG Lipari)

This new tephra identified in this study from both Lake Lia and Lake Brazi (Chapter 6). Due to possible taphonomic problems at Lake Lia in the deposition of this tephra (section 6.6), as well as problems in chronology with Lia (Appendix 3), Lake Lia was not included within the large age model. This thesis produced an age estimate for the LG Lipari of 12,847-11,430 cal. BP (95.4%) which is based solely on its position in the Brazi sequence. The low precision in this age estimate is due to only being identified at Brazi in this age model. Also, there are no radiocarbon dates close to this tephra's deposition. Other records that contain the geochemically identified LG Lipari, are not dated (Albert et al., 2017) or have chronological problems (e.g. Lia see Chapter 6; Lawson et al., 2004). Albert et al. (2017) assigned the LG Lipari to the LG period due to the interpretation from the marine isotopic record. The involvement of the other cross-referenced tephra at Brazi, the Askja-S, to other multiple dated sites would have also influenced the LG Lipari age. Further identification of this tephra from well-dated records in the future will refine the age of this eruption.

#### 7.1.1.5 Vedde Ash (VA)

The VA is one of the most widely identified tephras across the majority of Europe (e.g. Wastegård et al., 2000; Blockley et al., 2007; Lane et al., 2011a, b, 2012a, c). It has been key tephra dated to mid-way through the Younger Dryas (YD), at a time of abrupt climatic change (Lane et al., 2013). Within the Greenland ice cores, a date of 12,171 ± 114 b2k (GICC05; Rasmussen et al., 2006) is from counted annual layers. Bayesian modelling by Bronk Ramsey et al. (2015) provided an age of 12,101-11,914 cal. BP (95.4%, IntCal13). An age of 12,134-11,996 cal. BP from this study is within agreement with these age estimates. This age is slightly older than that produced by Bronk Ramsey et al. (2015), yet

can be explained by the use of different sites and tephras involved in the modelling (Figure 7.1).

#### 7.1.1.6 Pomici Principali tephra (PP)

This tephra is from the Campanian volcanic field, Italy and is largely confined to the Mediterranean region (e.g. Magny et al., 2006; Lane et al., 2011b). An age estimate of 12,158-11,915 cal. BP (95.4%, IntCal09) used an age model combining radiocarbon dates from different sites (Di Vito et al., 2008; Smith et al., 2011). A refined Bayesian modelled age of 12,091-11,850 cal. BP (95.4%, IntCal13) is from Bronk Ramsey et al. (2015). This thesis produced an age of 12,139-11,881 cal. BP (95.4%) using only the site of Bled.

#### 7.1.1.7 Hässeldalen tephra

The Hässeldalen tephra is important in dating abrupt climate change during the earliest Holocene (EH), namely the classic PBO (Wohlfarth et al., 2006; 2017). There have been limited age estimates for this tephra. Re-modelled radiocarbon ages from Hässeldala port have generated ages of 11,117-11,657 cal. yrs BP (95.4%, IntCal13, Ott et al., 2016) with remodelled ages from Høvdarhagi bog, the Faroe Islands providing an estimate of and 11,192-11,440 cal. BP (95.4%, IntCal13, Wastegård et al., 2018). Within this study, the inclusion of the tephra within the floating varve chronology of Czechowskie has produced a refined modelled age estimate of 11,204-11,277 cal. BP (95.4%) (Figure 7.2).

#### 7.1.1.8. Ulmener Maar tephra (UMT)

This tephra identification has been limited to a few sites in central Europe (e.g. Hajdas et al., 1995; Jones et al., 2017) and dated to the EH. Varve counting from Holzmaar provides a date of 11,000 varve years BP (Zolitschka et al., 1995) with a good agreement

with radiocarbon dating from the same site and MFM of 11,215-10,586 and 11,161-10,775 cal. BP (95.4%, IntCal13 recalibrated here; Hajdas et al., 1995; Endres, 1997). Previous Bayesian modelling provided a range of 11,400-10,907 cal. BP (IntCal13; Bronk Ramsey et al., 2015). The Hämelsee sequence provides a new age range of 11,242-11,055 cal. BP. The age refinement of tephras either side of the UMT (i.e. Hässeldalen and Askja-S (see below) has constrained the timing of this eruption.

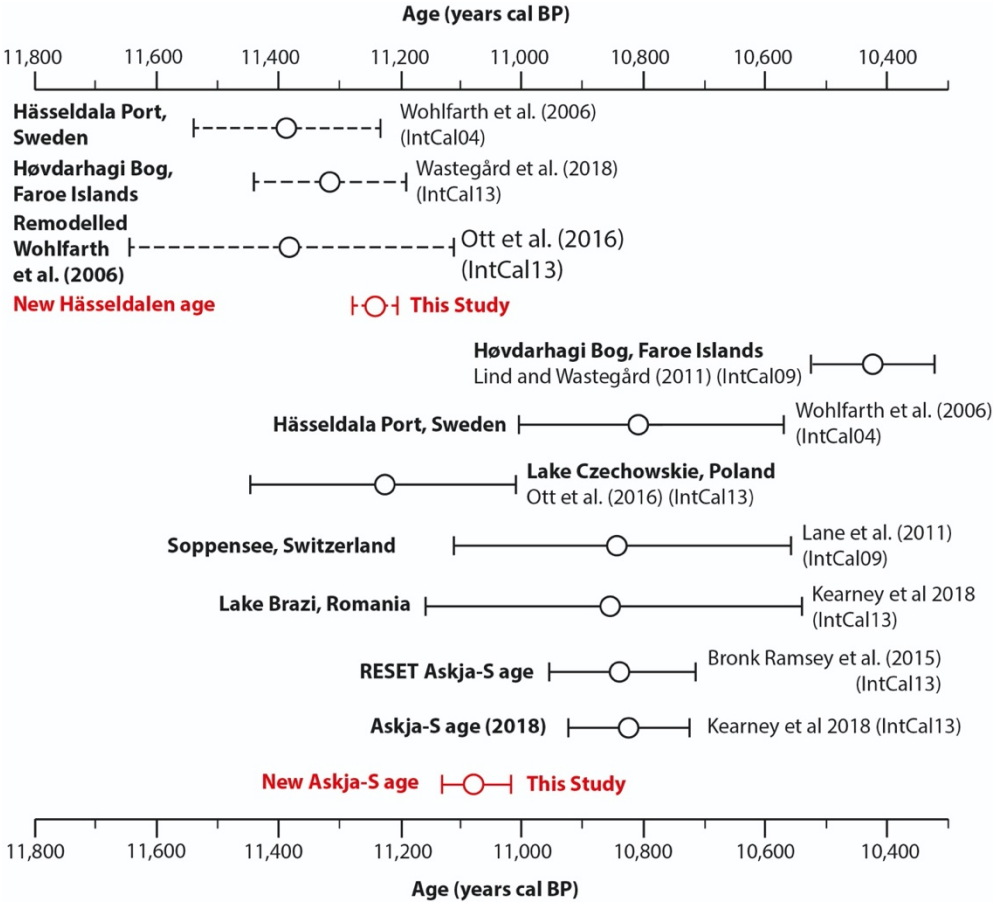


**Figure 7.2** Schematic representation of age estimates (μ ± 1σ) for Hässeldalen and Askja-S tephra. Ages are from published records and the newly remodelled data from this study. Different radiocarbon calibration curves were used by the authors, depending on the IntCal curve available at the time of quoted publications. The difference between these different calibrations (IntCal13, IntCal09, IntCal04) for the earliest Holocene is very similar (possible minor <~25 years). The curves use the same tree-ring data for IntCal04 to IntCal09 with additional data points added for this time period for IntCal13 (Reimer et al., 2009; 2013).

### 7.1.1.9 Askja-S tephra

The Askja-S tephra is also important in the EH (section 2.5.14). Dating of the eruption from the volcanic source provides a broad estimate of c.10,000 $^{14}$C years due to the

radiocarbon plateau at this time (Sigvaldason, 2002). Radiocarbon dating of sediments from Hässeldala port provided a more precise age of 11,050-10,570 cal. BP (95.4%, IntCal04; Wohlfarth et al., 2006). Ott et al. (2016) remodelled Wohlfarth et al. (2006) age for the Hässeldalen tephra and using the varve counts between the two tephras in Lake Czechowskie, produced an older age estimate of the Askja-S tephra of 11,454-11,002 cal. BP (95.4% IntCal13; Ott et al., 2016). However, there are younger age estimates for the Askja-S tephra by Bronk Ramsey et al. (2015) with 10,956-10,716 cal. BP (95.4%, IntCal13), Kearney et al. (2018) with 10,921-10,727 cal. BP (95.4%, IntCal13) and by Wastegård et al. (2018) with 10,526-10,322 cal. BP (95.4%, IntCal13). The results from this thesis that included several sites and the varve counted layers of Czechowskie, provided an older age of 11,120-11,040 cal. BP (Figure 7.1; Figure 7.2), within good agreement with age estimates for the Askja-S tephra from Wohlfarth et al. (2006).

Issues exist trying to date the Askja-S when using radiocarbon dating. During the EH, around the proposed time of the Askja-S eruption, there is a radiocarbon plateau, resulting in the vast difference in calibrated ages (Björck et al., 1996; van der Pilcht et al., 2004; Bos et al., 2007). The use of the Czechowskie varve chronology between the Hässeldalen and Askja-S tephras has reduced this problem, resulting in the older age estimate presented here. The only other site with radiocarbon dates between the Hässeldalen and Askja-S tephras is Hässeldala port, of which the broad age estimates agree with this new modelled age (Wohlfarth et al. 2006). However, there may be taphonomic problems at Czechowskie such as missing varves, which are currently unknown. Additional dated sites with both the Hässeldalen and Askja-S tephras would provide insight into the timing of both eruptions.

#### 7.1.1.10 Saksunvartn Ash (Saks.)

The Saksunvartn Ash has been found across Northern Europe (e.g. Dugmore and Newton, 1997; Lind and Wastegård, 2011). Age estimates for this eruption include 10,347±89 b2k from the Greenland ice cores (GICC05; Rasmussen et al., 2006) and a radiocarbon age estimates of 10,245-10,185 cal. BP (95.4%, IntCal09; Lohne et al., 2013). Bayesian age modelling by Bronk Ramsey et al. (2015) provides a refined age estimate of 10,257-10,056 cal. BP (95.4%, IntCal13). In this study, the age estimate for the Saksunvartn has larger uncertainty, with an age of 10,485-10,176 cal. BP (95.4%). Both Kråkenes and Crudale have Saksunvartn identified in their record. However, only Kråkenes is independently dated, resulting in larger are uncertainties. However, there are questions with the correlation of Saksunvartn Ash to a single eruption. There are multiple Saksunvartn-type tephras identified in Europe around this time (Davies et al., 2012).

### 7.1.2 Age-modelling results for sites

#### 7.1.2.1 Kråkenes, Norway

There are sixty-seven radiocarbon dates from Core 46 in the large age model (Lohne et al., 2013; Figure 7.3A) The dating material included terrestrial macrofossils with bulk samples of gyttja (Appendix 4). The VA and Saksunarvatn ash were incorporated and cross-referenced to these tephras in other sites within the model. Three of the dates had a >50% probability of being an outlier with three dates were rejected by the model using the outlier analysis. The resulting age-model is precise, with age errors of <90 years (1$\sigma$).

#### 7.1.2.2 Crudale Meadow, Scotland

Due to hard water affecting the radiocarbon dates from Crudale (Whittington et al., 2015), well-known tephra layers identified by Timms et al. (2018) and correlated to

Whittington et al. (2015) core depths, constructed the age model (see section 4.2.2 for details). The age-model produced age errors (1σ) of ~800-700 years for the lower part of the core due to the poorly constrained Borrobol and Pennifiler tephras (Figure 7.3B). Age precision increased to <20-300 around the well-dated tephras of VA, Hässeldalen and Askja-S tephras.

#### 7.1.2.3 Lake Madtjärn, Sweden

There were twenty-eight radiocarbon dates used in the age model for the LGIT period. The outlier analysis gave a posterior outlier probability of >5% for five of these dates. The age model is precise, with age errors ranging from ~250-35 years (1σ). The depths with a higher number of radiocarbon dates and the VA have higher precision (Figure 7.3C).

#### 7.1.2.4 Hässeldala port, Sweden

There were forty-eight radiocarbon dates from Core 5 used to produce the age-depth model for Hässeldala, of which the majority of the dates cover the LGIT period (Figure 7.3D). Muschitiello and Wohlfarth (2015) made core correlations to the pollen Core 3. Eleven ages had a posterior outlier probability of >5%, one of which is >50% and one resulted in being rejected by the outlier analysis. The age errors produced (1σ) range from ~18-200 years with higher precision and accuracy around the depths of the Hässeldalen and Askja-S tephras.

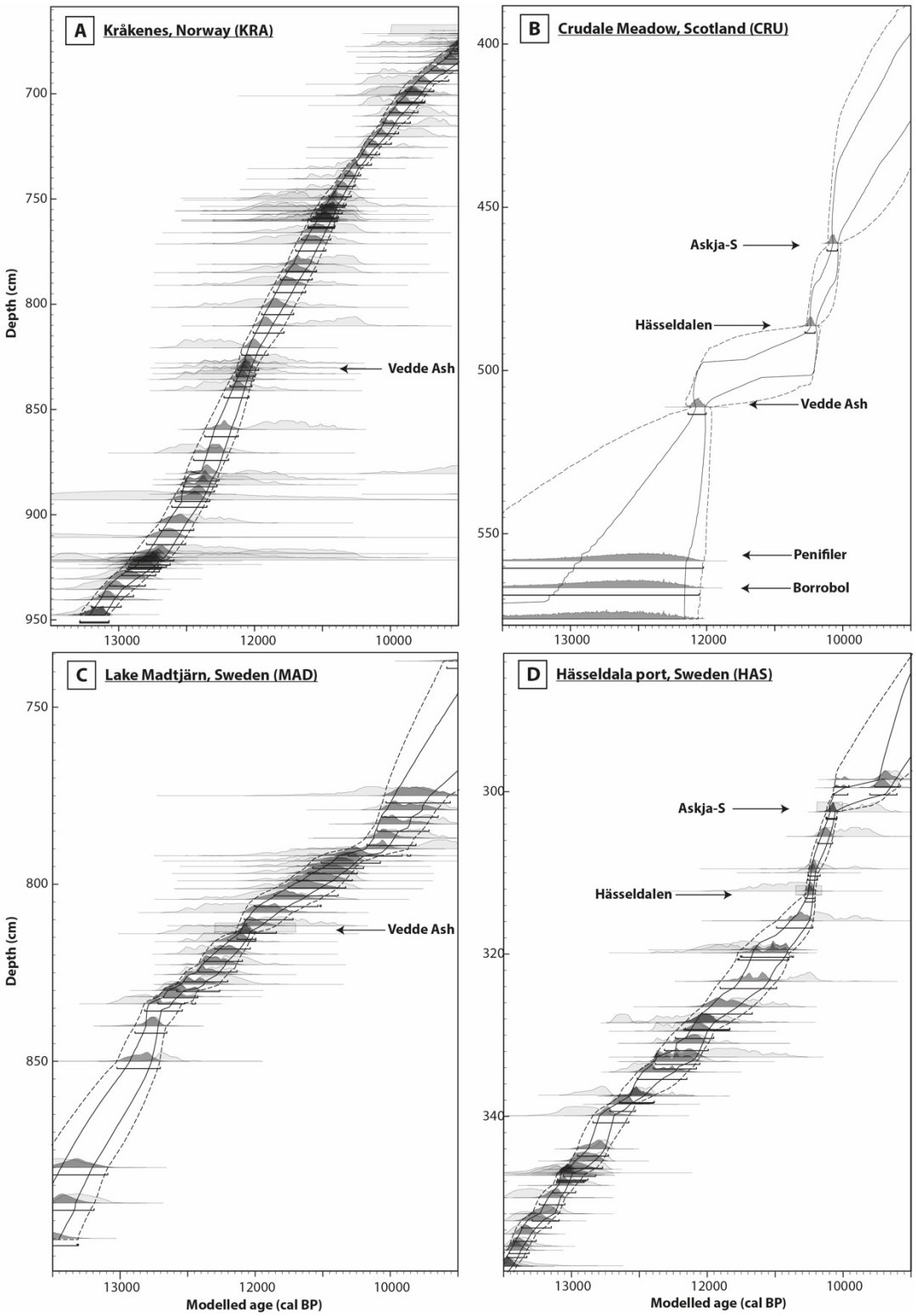


**Figure 7.3** Age model results for each site involved in the large age model. Y-axis shows depth with the position of the individual tephras identified at each site. X-axis plots modelled at 1σ (68.2%, solid line) and 2σ (95.4%, dashed line) age ranges for each calibrated radiocarbon date. With outlier analysis applied to the age model, outliers detected were down-weighted and are shown in lighter grey colour. The models were generated in OxCal. version 4.3.2 (Bronk Ramsey et al. 2015) using the IntCal13 atmospheric calibration curve (Reimer et al., 2013).

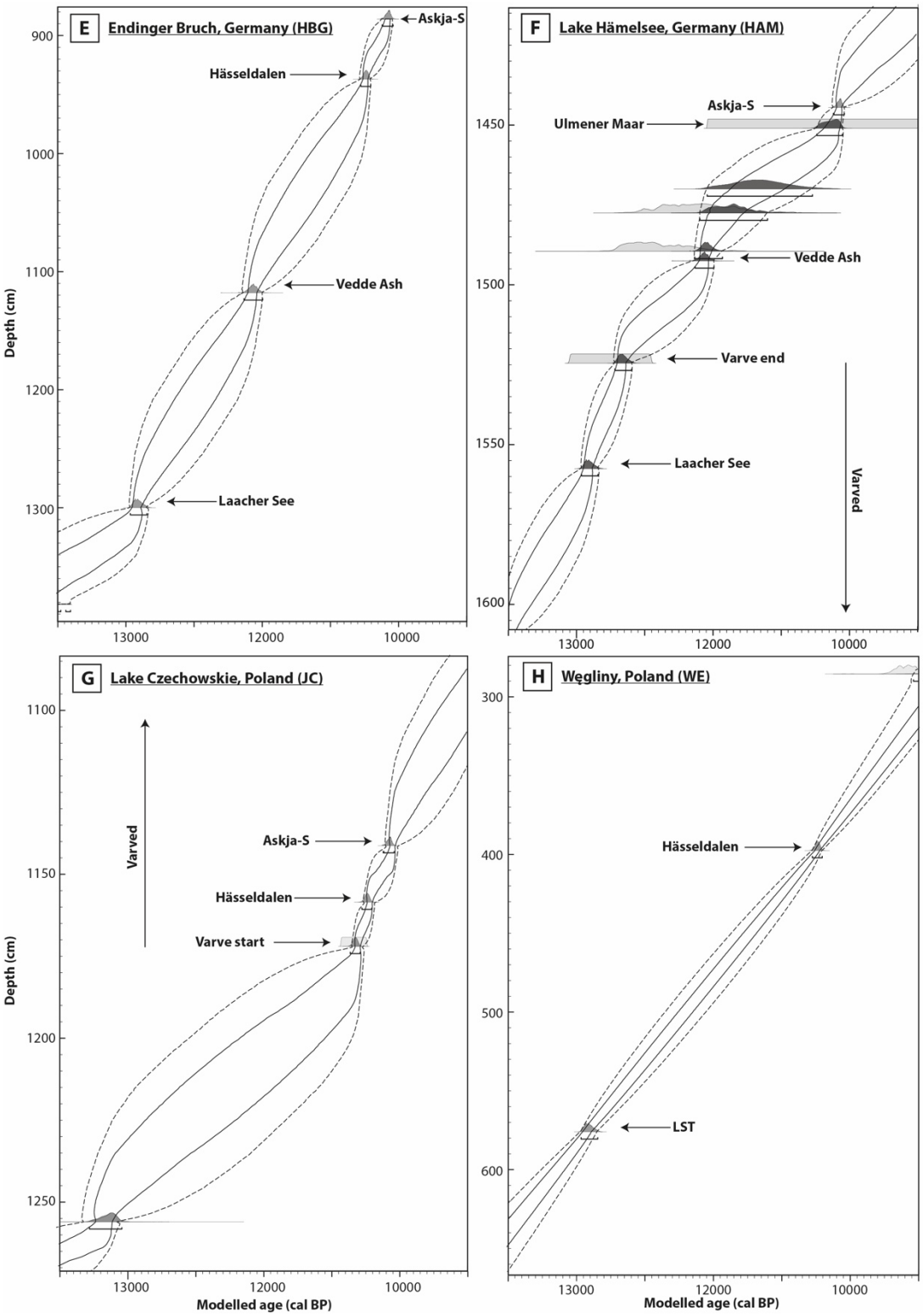


**Figure 7.3 cont.** Age model results for each site involved in the large age model. Y-axis shows depth with the position of the individual tephras identified at each site. X-axis plots modelled at 1σ (68.2%, solid line) and 2σ (95.4%, dashed line) age ranges for each calibrated radiocarbon date. With outlier analysis applied to the age model, outliers detected were down-weighted and are shown in lighter grey colour. The models were generated in OxCal. version 4.3.2 (Bronk Ramsey et al. 2015) using the IntCal13 atmospheric calibration curve (Reimer et al., 2013).

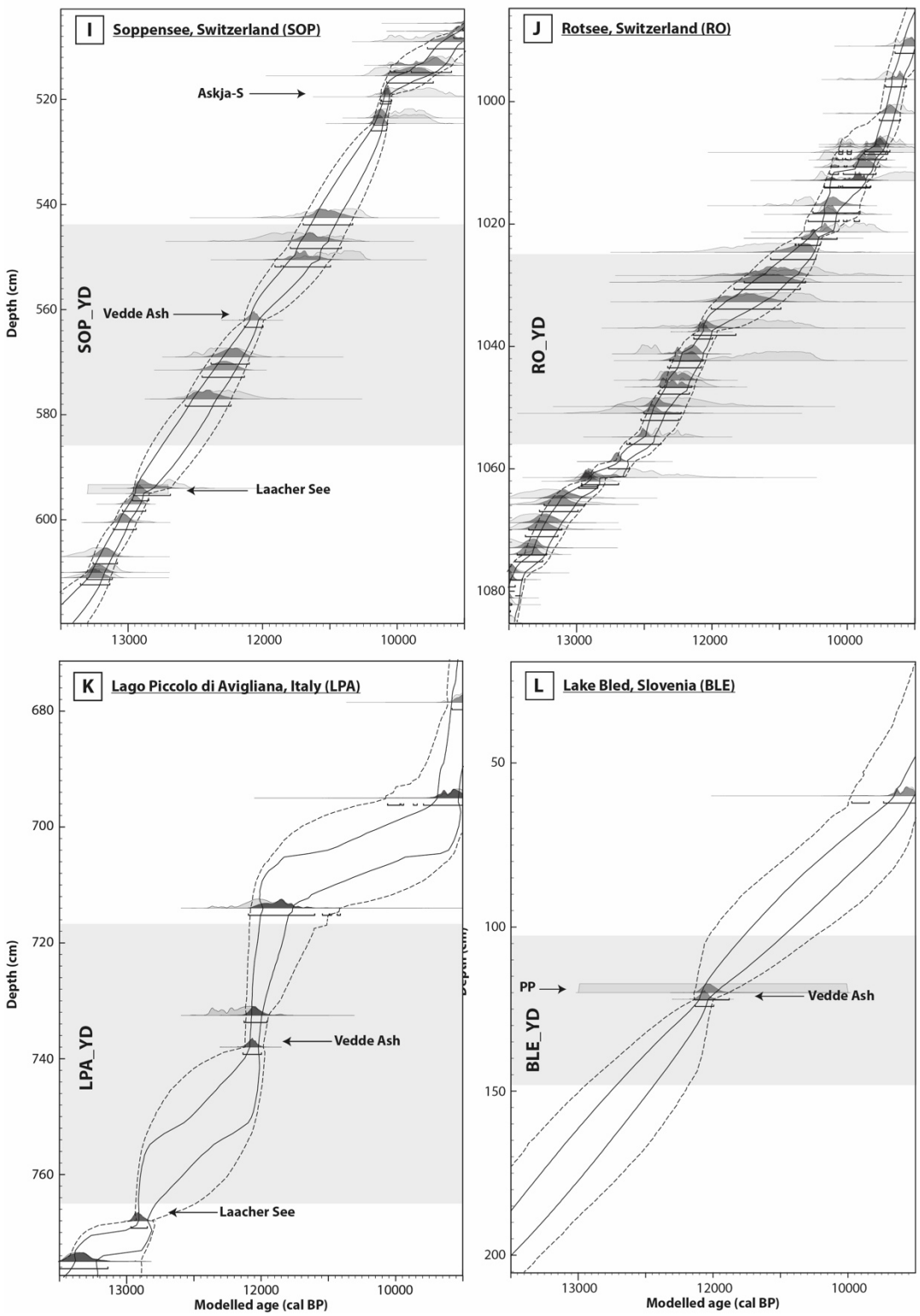


**Figure 7.3 cont.** Age model results for each site involved in the large age model. Y-axis shows depth with the position of the individual tephras identified at each site. X-axis plots modelled at 1σ (68.2%, solid line) and 2σ (95.4%, dashed line) age ranges for each calibrated radiocarbon date. With outlier analysis applied to the age model, outliers detected were down-weighted and are shown in lighter grey colour. The models were generated in OxCal. version 4.3.2 (Bronk Ramsey et al. 2015) using the IntCal13 atmospheric calibration curve (Reimer et al., 2013).

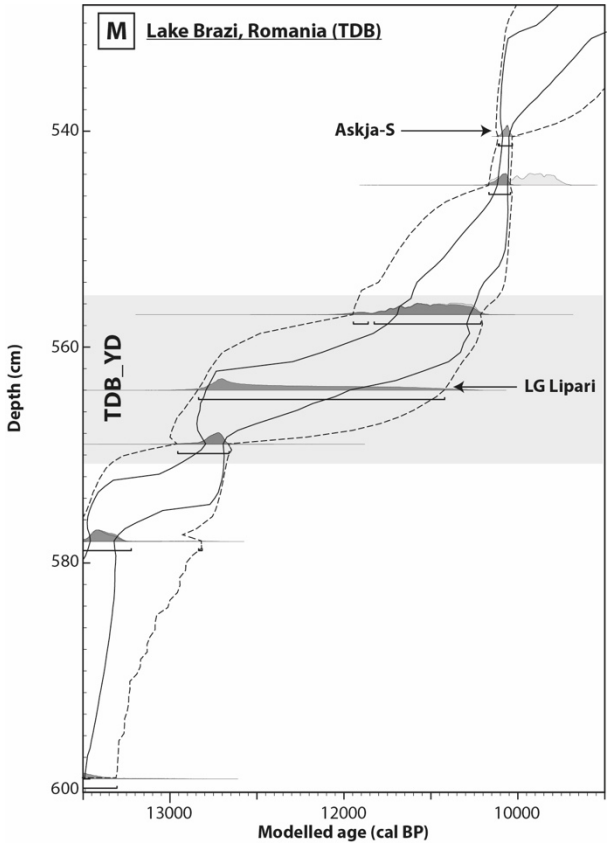


**Figure 7.3 cont.** Age model results for each site involved in the large age model. Y-axis shows depth with the position of the individual tephras identified at each site. X-axis plots modelled at 1σ (68.2%, solid line) and 2σ (95.4%, dashed line) age ranges for each calibrated radiocarbon date. With outlier analysis applied to the age model, outliers detected were down-weighted and are shown in lighter grey colour. The models were generated in OxCal. version 4.3.2 (Bronk Ramsey et al. 2015) using the IntCal13 atmospheric calibration curve (Reimer et al., 2013).

### 7.1.2.5 Endinger Bruch, Germany

Only one radiocarbon date near the base of the record was in the age-depth model, with four well known and widely identified tephra layers of the LST, VA, Hässeldalen and the Askja-S (Lane et al., 2012a). No boundaries related to pollen stratigraphy were applied, allowing the model to be flexible. Figure 7.3E shows the uncertainty between the multiple tephra layers, providing an age model with high precision.

#### 7.1.2.6 Lake Czechowskie, Poland

Four radiocarbon dates were used in the age model, with one dating to the LGIT period. The record also includes a floating varve chronology during the EH period with both the Hässeldalen and Askja-S tephras within (Figure 7.3G). A total count of 967 ± 14 varve years is in the entire varve interval with 152 +11/-8 varve years counted between these tephras (Ott et al., 2016). The varve interval entered as 152±10 varve years in the age model to cover this error as it was not possible to use the age error stated by Ott et al. (2016) in the OxCal coding. The incorporation of these varve counts between Hässeldalen and Askja-S tephras greatly influenced the age estimates for these tephras and subsequent age-depth models for other sites including these tephras. As a result of applying the "Interval" function in OxCal between these two tephras, the model was rigid, providing high precision and accurate ages.

#### 7.1.2.7 Lake Hämelsee, Germany

There are five radiocarbon dates available for the whole Hämelsee core (HÄM13; Jones et al., 2018; Stefan Engels and Christine Lane, personal communication), with three covering the LGIT period. Four well-known tephra layers were identified by Jones et al. (2018), providing additional chronological markers (Figure 7.3F). Hämelsee also has a floating varve chronology between the depths of 1610-1524.5cm which incorporated the LST at 1557.5cm. Counted annual layers between these depths provide a precise age where there are no radiocarbon dates. The VA and the newly constrained age estimate for the Askja-S tephra provide age errors (1σ) of ~50-200 years for dates between these layers.

#### 7.1.2.8 Węgliny, Poland

There are a total of nine radiocarbon dates produced for the whole sequence by Housley et al. (2013). There were problems with the majority of bulk gyttja samples. Housley et al. (2013) rejected these bulk gyttja samples due to hard water affects. However, with the cross-correlation of the LST and Hässeldalen tephra within this model, only three of these dates were manually rejected to allow the large age model to run (Appendix 4). The age estimates for the tephras of LST and Hässeldalen resulted in a uniform sedimentation rate between these layers with very precise age errors (1σ) of ~30-18 years (Figure 7.3H).

#### 7.1.2.9 Soppensee, Switzerland

There were twenty-four radiocarbon dates used in the age-model, the majority within the LGIT period (Figure 7.3I, Hajdas et al., 1993). The outlier analysis provided a posterior outlier probability of >5% for two of these ages. The tephras of the LST, VA and Askja-S provided addition chronological markers to constrain the age precision of the model. Age errors (1σ) ranged ~19-100 years, providing a rigorous age-depth model for the site.

#### 7.1.2.10 Rotsee, Switzerland

There were eighty-seven radiocarbon dates used in this age-model from cores RL305 and RL300 with correlations to the master core of RL05 (see section 4.2.10). The 'R_combine' function was used on duplicates at the same depth to produce one age. The majority of these dates cover the LGIT period (Figure 7.3J). The LST and VA tephras provided additional chronological constraints. The outlier analysis gave a posterior of five dates that had >50% probability of being an outlier. The age errors (1σ) ranged ~50-200 years showing a precise age model. However, the accuracy of these ages declines after the VA, yet still have high precision.

#### 7.1.2.11 Lago Piccolo di Avigliana, Italy

Thirteen radiocarbon dates from terrestrial plant material were obtained from the whole core by Finsinger et al. (2006). Five of these dates are within the LGIT period (Figure 7.3K). With the incorporation of the LST and VA (Lane et al., 2012c), the age-depth model is precise between these cross-correlated tephras (~30-40 years, 1σ). Age ranges for the individual radiocarbon dates range from ~150-80 years (1σ).

#### 7.1.2.12 Lake Bled, Slovenia

Two radiocarbon dates were available for the whole record at Bled, with one within the LGIT period (Andrič et al., 2009; Figure 7.3L). Three cryptotephra layers of NYT, VA and PP provide additional chronological markers (Lane et al., 2011b). The age uncertainties are large, ~100 years.

#### 7.1.2.13 Lake Brazi, Romania

There were eight radiocarbon dates from Brazi used in this age model, of which five were within the LGIT period (Figure 7.3M, Hubay et al., 2018). However, one radiocarbon date, Poz-26113, was manually removed from the age model due to being inconsistent with the majority of the radiocarbon dates at these depths (Hubay et al., 2018). All remaining dates had posterior outlier probabilities of <5%. The identification of the Askja-S tephra improved the precision and accuracy of the ages (Kearney et al., 2018). Brazi is the only site with the LG Lipari tephra. The large age-error for LG Lipari is due to the widely spaced radiocarbon dates.

## 7.2. Palynological results

The following section focuses on the palynological results from each site selected from the criteria outlined in Chapter 3. Authors of original investigations supplied raw pollen data. Each site has percentage pollen, and pollen accumulation rate (PAR, where available) displayed with divisions of each pollen diagram into Local Pollen Assemblage Zones (LPAZ) through the method outlined in Chapter 3. Statistical analysis of Principal Component Analysis (PCA); Correspondence Analysis (CoA); Detrended Correspondence Analysis (DCA); Principal Curve Analysis (PrC) and Rate of Change Analysis (RoC), outlined in Chapter 3, was also undertaken for each site. The presented data is on calibrated radiocarbon ages (IntCal13) with ages devised for each site from the large-age model undertaken in this thesis.

This study focuses upon abrupt climatic oscillations of the YD and EH during the LGIT. Identifying the YD and EH in the pollen records used different approaches (see section 3.2.4, Figure 3.4). For the YD, CONISS (LPAZ) was deemed appropriate to use in establishing the YD transitions. This is due to being associated with a clear, large vegetation shift which is reliably picked out by CONISS. For EH oscillations, PrC was the main tool in identifying vegetation shifts due capturing more variance than CONISS and other ordination statistics (Simpson and Birks, 2012, Abrook et al., 2019). Other additional information from RoC, PAR and other proxies were also used to describe vegetation revertences associated with these climatic events (section 3.2.4).

This section focuses on simple vegetation discussions in terms of identifying the YD transitions and EH events using these two different methods for the chosen sites pollen record. Further extensive discussion on the climatic and environmental interpretations from these pollen records are in Chapter 8 for the YD and Chapter 9 for EH oscillations.

### 7.2.1 Kråkenes, Norway

Kråkenes Core 46 was sampled with the pollen identified and counted by Birks et al. (2000). Sixty pollen samples have been dated in this project to the LGIT with a resolution of 4-2cm. These samples' terrestrial land pollen (TLP) counts range from 420-220 with the highest count during the EH. Six LPAZ (KRA_*n*) were identified and described in Table 7.2 and shown in Figure 7.4. PAR was also calculated (Figure 7.5)

**Table 7.2** The local pollen assemblage zones for Kråkenes. Included are the name of zones, depth, ages for the beginning and end of the zones (μ±1σ) with key taxa observations and changes within each zone. Symbols depict:↑ increases and ↓ decreases in taxa percentage; ↕ oscillating or ↔ stability of values for particular taxa; ▲ taxa peak; ● taxa present at <5%; ⨯ taxa disappears in that zone.

| Zone | Depth (cm) | Age (μ±1σ, cal. BP) | Taxa changes through zone | Key taxa | LOI | Lithology |
|---|---|---|---|---|---|---|
| **KRA_1** | 962-948 | 13,321±60 to 13,177±59 | ▲ *Rumex;* ↑ *Salix* undiff., *Salix herbaceae, Betula, Juniperus;* ↓ Poaceae; ● *Capsella*-type, Carex-type, Cyperaceae | *Rumex,* Poaceae | ↕ | Gyttja with coarse organic detritus |
| **KRA_2** | 948-925.375 | 13,177±59 to 12,842±68 | ↑ *Betula, Salix* undiff., *Carex*-type; ▲↓ *S. herb.;* ↓ *Rumex*; ↔ Poaceae | *Betula*, *Salix undiff*., *Salix herbaeae, Gramineae* | General ↑ | Gyttja with coarse organic detritus |
| **KRA_3a** | 925.375-852.5 | 12,842±68 to 12,195±56 | ▲↑ *Salix* undiff. before gradual ↓; Gradual ↑ Capsella-type; ↓ *Betula, Salix herb., Carex*-type *Rumex,* Poaceae; ● Campanula | *Salix undiff., Gramineae* | Sharp ↓ | Sharp transition to silt then laminated silt and sand |
| **Zone** | **Depth (cm)** | **Age (μ±1σ, cal. BP)** | **Taxa changes through zone** | **Key taxa** | **LOI** | **Lithology** |
| **KRA_3b** | 852.5-752.5 | 12,195±56 to 11,437±46 | Gradual ↑ to ▲ Capsella-type; ↓ *Salix* undiff.; ↕ *Betula, Salix herb., Rumex,* Poaceae; ● Carex-type | *Salix undiff*., Capsella-type | ● | Laminated silt and sand into gyttja |
| **KRA_4** | 752.5-732.5 | 11,437±46 to 11,228±32 | ▲*Carex*-type, *Filipendula*; ↑ *Betula,* Cyperaceae; ↓ *Salix* | *Betula,* Carex-type, *Gramineae* | Sharp ↑ | Gyttja |

| | | | | | | |
|---|---|---|---|---|---|---|
| | | | undiff., *S. herb.;* ↕ Poaceae; ● *Rumex*, Capsella-type, Cyperaceae, *J. comm., E. nigrum, Sedum* | | | |
| **KRA_5** | 732.5-700.5 | 11,228±32 to 10,842±52 | ▲ *E. nigum;* ↑ *Betula, J.comm.;* ↕ Gramineae; ↔ *Salix* undiff., Carex-type; ● *Filipendula,* Cyperaceae, *Rumex* | *Betula, Empetrum nigrum* | ↑ | Gyttja |
| **KRA_6** | 700.5-682 | 10,842±52 to 10,508±68 | ↓ *E. nigrum*; ↑ *Betula, J. comm.,* Gramineae; ↔ *Salix* undiff.; ● Cyperaceae *Filipendula, Rumex* | *Betula, Juniperus communis* | ↑ | Gyttja |

#### 7.2.1.1 Statistical analysis

An abundance of <5% was performed on the terrestrial taxa of Kråkenes. DCA results in Table 7.3 show a short axis length indicating both PCA and CoA starting curves for PrC are suitable to explore Kråkenes pollen data (1.5-3SD).

**Table 7.3** Detrended correspondence analysis results for Kråkenes. The dataset shows short axis lengths and that axis 1 explains the most variation compared to the other axis.

| | **DCA1** | **DCA2** | **DCA3** | **DCA4** |
|---|---|---|---|---|
| **Eigenvalue** | 0.3965 | 0.09590 | 0.08667 | 0.08665 |
| **Axis length** | 2.2202 | 1.21720 | 1.50851 | 1.17223 |

PCA results are shown in Figure 7.6 with the first axis in ordination space representing 34.0% of data variation, while axis two represents 10.9% of the variation. Taxa plotting negatively along axis one include: *Betula, Empetrum nigrum, Pinus slyvestris, Juniperus communis.* Taxa that plots positively include: *Capsella* type (most significant contributor), *Artemisia, Rumex acetosella*, *Salix herbaceae*-type, *Salix undiff*. Intermediate taxa, plots roughly equal to axis 1 and 2, includes: *Filipendula*, Cyperaceae, Poaceae.

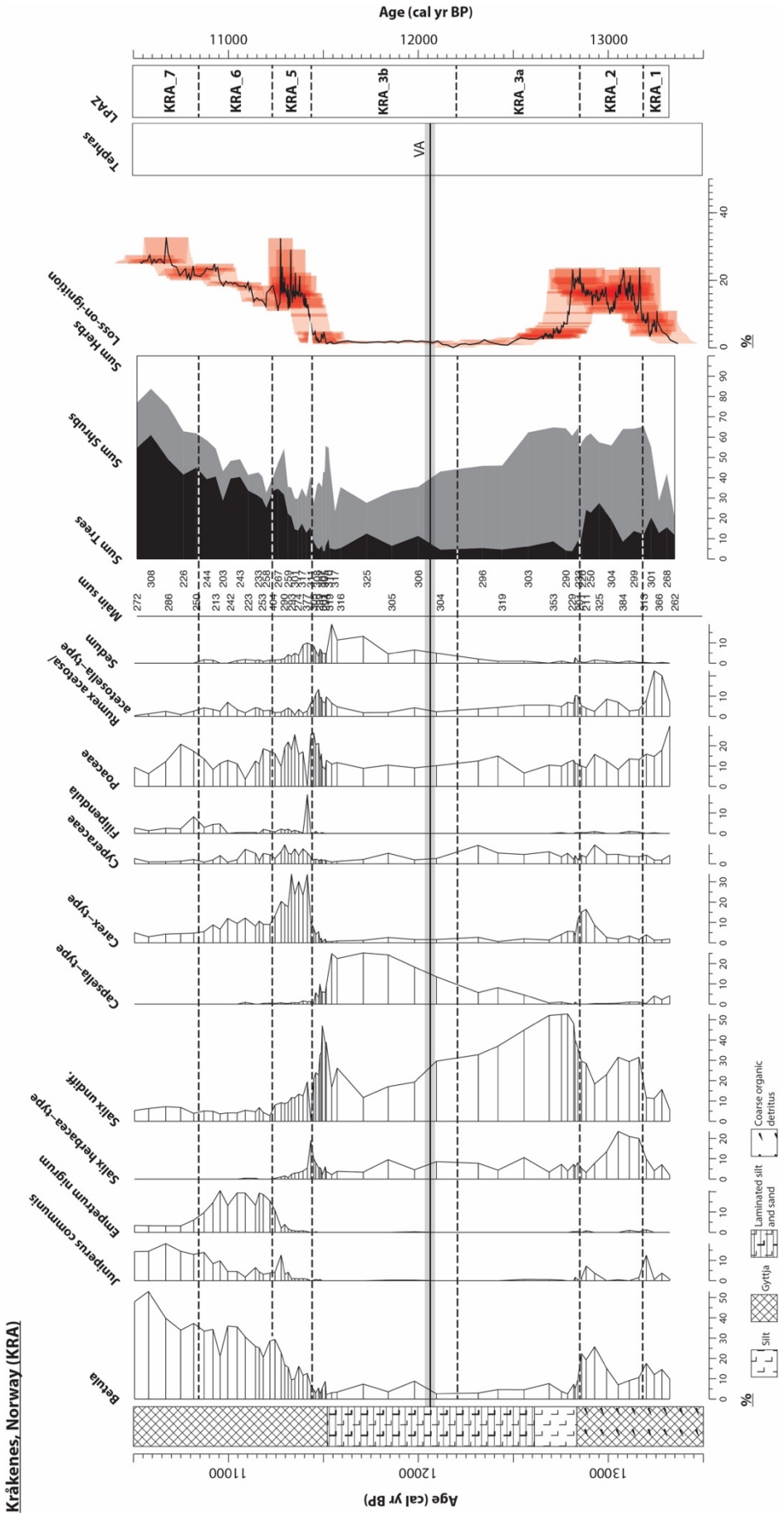


**Figure 7.4** Pollen percentage record of key taxa from Kråkenes. The record is plotted against calibrated age (μ ±1σ ). All values are presented against TLP. Lithology presented as described by Birks et al. (2000) and Lohne et al. (2013). Percentage loss-on-ignition (LOI) is plotted. LPAZ are divided based upon changes in major taxa and CONISS. The Vedde Ash (VA) is identified in Kråkenes and is plotted with this studys new age estimate at μ ±1σ . Light shading shows 1σ age error.

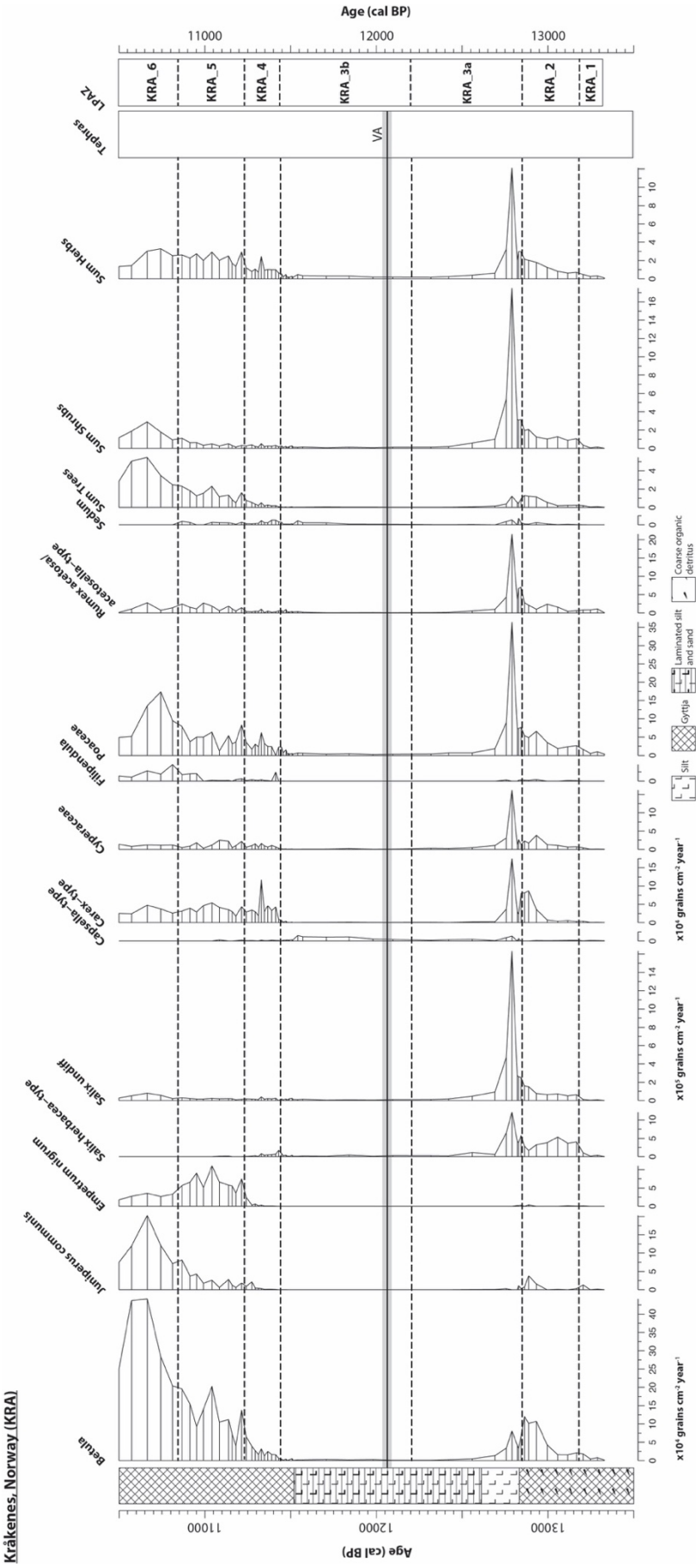


**Figure 7.5** Pollen accumulation rate (PAR) record of key taxa from Kråkenes. The record is plotted against calibrated age ($\mu \pm 1\sigma$ ). Note the difference in x-axis scales used in the diagram. Lithology presented as described by Birks et al. (2000) and Lohne et al. (2013). LPAZ are divided based upon changes in major taxa and CONISS in percentage diagram. The Vedde Ash (VA) is identified in Kråkenes and is plotted with this studys new age estimate at $\mu \pm 1\sigma$ .

PrC was calculated using a PCA-based output rather than a CoA-based approach. This was due to PCA-based output underwent fewer iterations before convergence with less degrees of freedom when similar penalty values were applied. Similar data variation is captured by PCA (74.2%) and CoA (75.1%) yet due to more iterations and greater degrees of freedom for CoA, PCA-based output was deemed more accurate for the model.

PrC results show during the LGIT a single major oscillation (MO) with three additional oscillations (Figure 7.7). These oscillations are identified by 1) a pause in the general shift of values and; 2) an increase variance in the distance along the gradient (Abrook, 2019). The oscillations for the focus of this thesis are after the MO (Table 7.4). Single data points indicate variation from the trend, yet being a single data point, their significance can be questioned and will be kept in mind when inferring vegetation revertences linked to climatic oscillations. Shifts are also seen in RoC (Figure 7.7), indicating palynological changes at the same time.

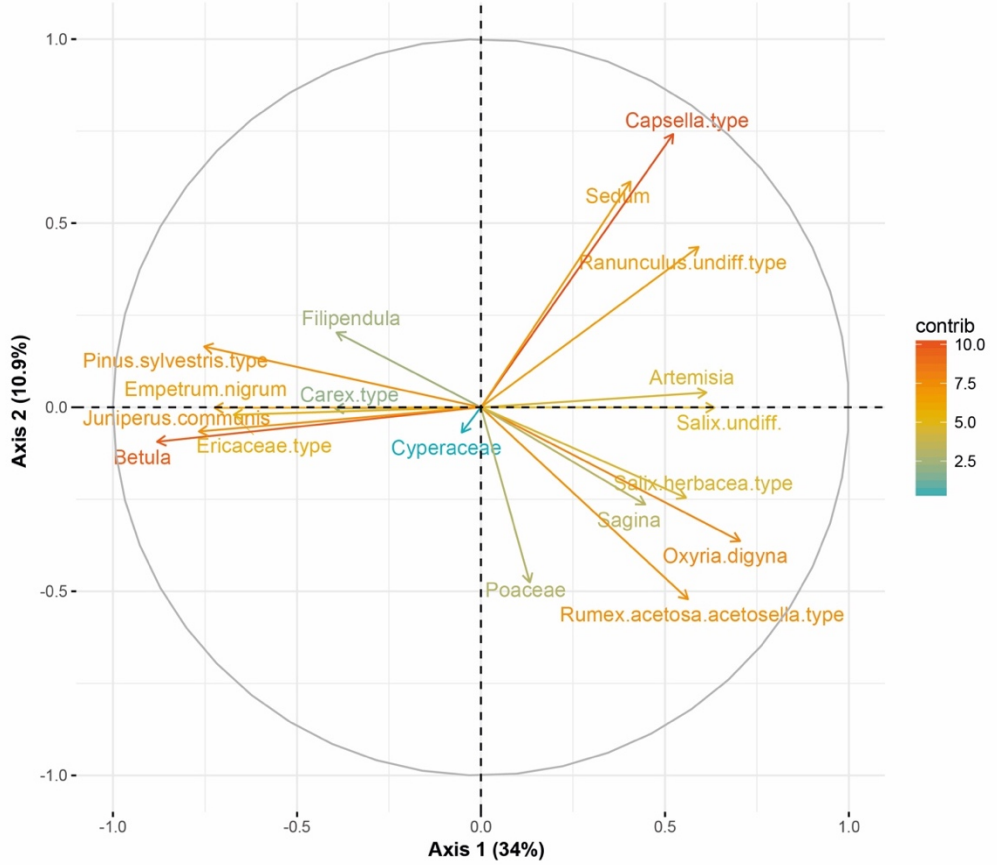


**Figure 7.6** Ordination diagram of the PCA results from Kråkenes. The two axis, axis 1 and 2, present first two principal components. The pollen taxa are placed along the axis with the length and colour of the arrow indicating the taxa dominance along the axis. Along axis 1, woodland taxa plot negatively with taxa associated with wetland while open herbaceous taxa plot positively. Axis 2 has an association with both herbaceous and shrub taxa.

**Table 7.4.** Vegtation oscillations identified in the PrC for Kråkenes. Symbols depict:↑ increases and ↓ decreases in taxa percentage

| Oscillation | Depth (cm) | Age (μ±1σ, cal. BP) | Key taxa influence |
|---|---|---|---|
| KRA_MO | 925.375-752.5 | 12,842±68 to 11,437±46 | ↑↓*Salix* undiff., ↑*Capsella*-type |
| KRA_E1 | 748.5-740.5 | 11,399±43 to 11,321±35 | ↑*Filipendula,* ↑*Carex*-type, ↓*Salix* undiff. |
| KRA_E2 | 728.5-719.75 | 11,177±31 to 11,066±41 | ↓*Carex*-type, ↑*Empetrum nigrum* |
| KRA_E3 | 712.375-708.875 | 10,985±46 to 10,945±51 | ↑*Empetrum nigrum*, ↑*Filipendula* |

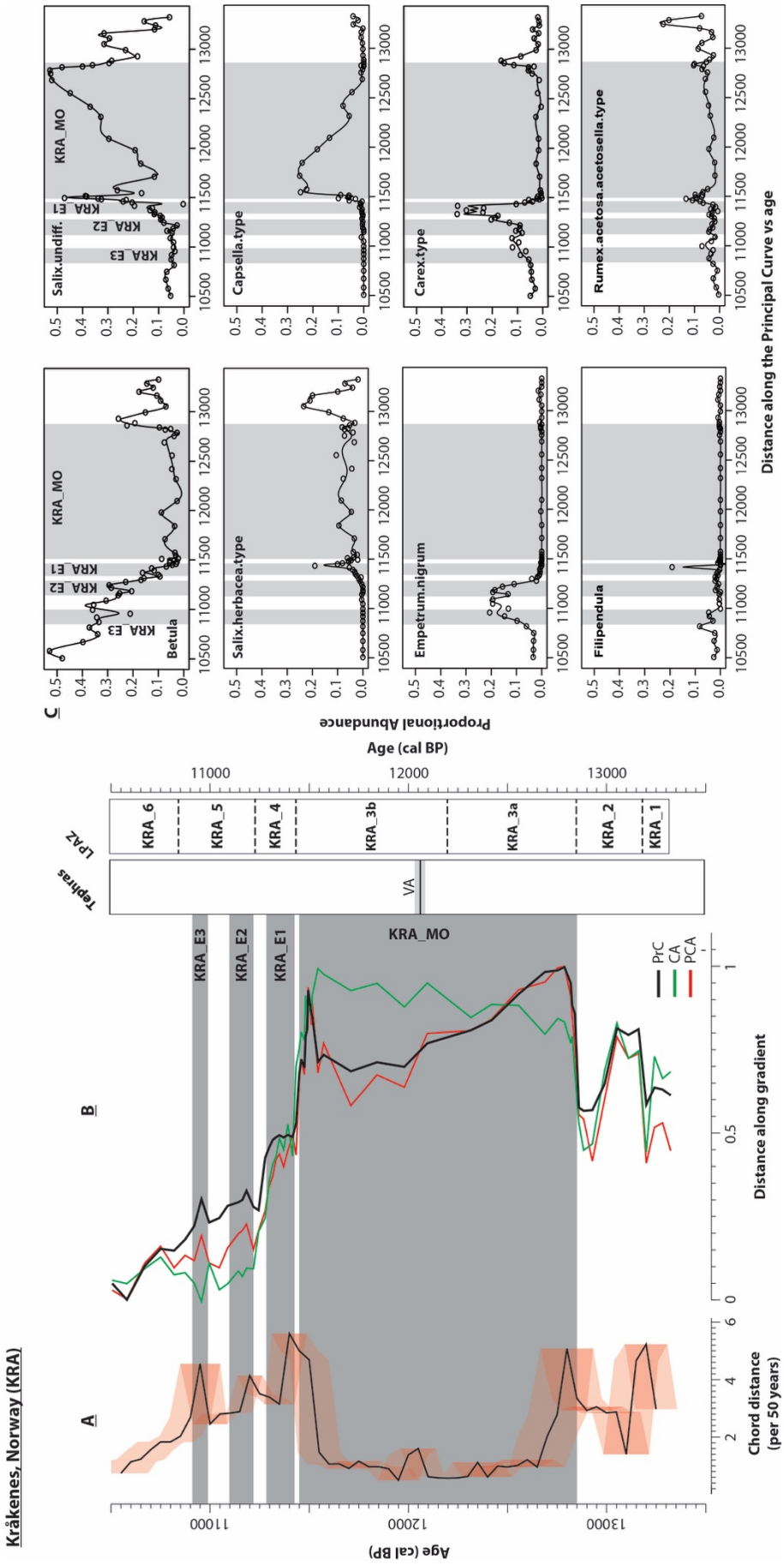


**Figure 7.7** The statistical results for the pollen percentage data from Kråkenes. A) RoC analysis for every 50 years. The values presented are exaggerated to provide clearer results into periods of significant change. The higher the bar, the more significant the composition change was. Light shading shows 1σ age error. B) The results of the different ordination tests (PCA, CoA and PrC). The grey boxes highlight oscillations identified from the PrC curve. C) The key taxa response curves modelled through the PrC. The grey boxes show the timing of the oscillations from the main PrC. Changes in the abundance of individual taxa at certain times provide insight into which taxa are driving the change. The record is plotted against calibrated age (μ ±1σ ) with light shading showing 1σ age error.

#### 7.2.1.2 Palaeoclimatic and palaeoenvironmental interpretation

This section will focus on reconstructing the climate and environmental history of Kråkenes using the pollen data previously presented in this study. Based upon age modelling, identification of the Vedde Ash and evident vegetational changes, LPAZ can be correlated to climatic periods of the Allerød (KRA_1-2), YD (KRA_3) and EH (KRA_4-6).

**Allerød-YD transition (12,842 ± 68 cal. BP)**

At the beginning of this record, open habitat taxa such as *Rumex* and *Artemisia* are present. The dwarf-shrub of *S. herbaceae* with *Salix* undiff. and *Juniperus* gradually replaced this pioneering vegetation as the landscape became more stable. *Betula* was also present, yet macrofossils from the site show that it was the dwarf-shrub of *Betula nana* (van Dinter and Birks, 1996). Low Loss-on-Ignition (LOI) shows little organic matter in the catchment (Figure 7.4; Battarbee et al., 2001). There is the interpretation of an open, treeless environment resembling a mid-alpine zone today (Birks et al. 2000, Birks and Birks, 2013).

At 12,841±126 cal. BP, there is a large overturn in vegetational composition. *Salix* undiff. rises sharply with an expansion of high-alpine or artic taxa of *Rumex, Sedum* and Poaceae (Huntly and Birks, 1983; Birks and Birks, 2013). *S. herbaceae, Saxifraga* presence indicates snow-beds on the landscape (Wijk, 1986). There is an increase in PAR at this time (Figure 7.5). Birks and Birks (2013) highlighted a rise in damaged pollen grains linked to an increase snow-melt inwashing sediment into the lake. LOI values also sharply decreased (~20%) as minerogenic inwash rose. There is a sharp lithological change to glacial silt, linked to the local glacier development (Lohne et al., 2013). The vegetation taxa present are associated with an open, artic-type landscape of the YD period (e.g. Birks et al., 2000; Birks et al., 2014).

**YD-EH transition (11,437±46 cal. BP)**

There is a rapid increase in vegetational turnover with RoC (Figure 7.7). *Betula*, most likely *B. nana* from macrofossils (van Dinter and Birks, 1996), replaced *Salix.* The artic taxa of *Artemisia* and *Rumex* declined along with taxa associated with treeless landscapes (*Capsella*-type). PAR shows an increase in pollen production compared to the YD (Figure 7.5). An increase in wetland taxa such as *Carex*-type, Cyperaceae and *Filipendula* increase as a defining taxa in the onset of the EH with low, mid-alpine grasslands flourishing (Beck et al., 2016; Birks and Birks, 2013). A sharp change from glacial-lacustrine sediments to gyttja is seen as the local glacier retreats (Figure 7.4, Lohne et al., 2013). This is the transition to the EH period with similar vegetation responses seen at other sites (e.g. Birks et al., 2014, Seppä et al., 2002)

**Earliest Holocene oscillations**

There is a continued expansion of *Betula* during the climatic amelioration during the EH. *Juniperus, E. nigrum* and Poaceae also expanded with vegetation succession in Norway with heathland development (e.g. Vorren et al., 2009; Birks et al., 2014). *Betula* and *Juniperus* outcompete *Salix,* becoming a dominant part of the landscape.

From the PrC, three vegetation events are seen along with an increase in RoC vegetation turnover (Figure 7.7). At 11,399 ± 43 cal. BP, a rise in *Filipendula* and *Carex*-type drives the plateau in PrC values. LOI values oscillate. At 11,177 ±3 1 cal. BP, there is a small increase and plateau in PrC values. The curve is possibly identifying increases in *E.nigrum* and *Betula* with decreases in *Carex*-type pollen. At 10,985 ± 46 cal. BP, there is another small increase in PrC, driven by a decline in *Betula* and a rise in *E.nigrum, Filipendula* and *Rumex*, indicating a vegetational disturbance and opening of the landscape. There is also a slight increase in herbaceous taxa at these times (Figure 7.4).

### 7.2.2 Crudale Meadow, Scotland

Crudale Meadow was sampled and counted by Whittington et al. (2015). There are Forty-five pollen samples dated to the LGIT, with a sample resolution of 2-4cm. TLP counts of >100 are from the lower depths due to problems with preservation, with up to 500 counted within the EH section (Whittington et al., 2015). Seven LPAZ (CRU_*n*) have been identified (Table 7.5; Figure 7.8). PAR was also calculated (Figure 7.9).

**Table 7.5** The local pollen assemblage zones for Crudale Meadow. Included are the name of zones, depth, ages for the beginning and end of the zones (μ±1σ) with key taxa observations and changes within each zone. Symbols depict:↑ increases and ↓ decreases in taxa percentage; ↕ oscillating or ↔ stability of values for particular taxa; ▲ taxa peak; ● taxa present at <5%; ✕ taxa disappears in that zone.

| Zone | Composite Depth (cm) | Age (μ±1σ, cal. BP) | Taxa changes through zone | Key taxa | LOI | Lithology |
|---|---|---|---|---|---|---|
| **CRU_1** | 576-556 | 13,095±882 to 12,776±685 | ↑ Poaceae, *Empetrum nigrum*; ↔ *Betula;* ● Salix, *Artemisia*, Aster./Card. | *Betula, Empetrum nigrum,* Poaceae | ↓ | Clay and silt |
| **CRU_2** | 556-540 | 12,776±685 to 12,523±518 | ▲ *E. nigrum*, ↓ *Betula*, Poaceae; ● Salix, *Artemisia*, Aster./Card. | *Empetrum nigrum* | ↑ | Marl |
| **CRU_3** | 540-520 | 12,704±518 to 12,207±262 | ▲ Poaceae; ↓ then ↑ *E. nigrum*; ↔ *Betula*; ● Salix, *Artemisia*, Aster./Card. | Poaceae, *Empetrum* | ↑ | Marl to clay and silt |
| **CRU_4** | 520-496 | 12,207±262 to 11,561±255 | ↑ Salix, *Artemisia*, Aster./Card., Lactuceae; ↓ *E. nigrum,* Poaceae | Poaceae, *Aster./Card. undiff., Artemisia*-type, *Lactuceae* undiff. | Sharp ↓ then ● | Clay and silt |
| **CRU_5a** | 496-484 | 11,561±255 to 11,224±33 | Sharp ↑ Poaceae; ↑ *E. nigrum*, *Betula*; ↓ *Salix*; ● *Artemisia*, Aster./Card, Lactuceae | *Betula,* Poaceae | Sharp ↑ | Clay and silt to marl |

| Zone | Composite Depth (cm) | Age (μ±1σ, cal. BP) | Taxa changes through zone | Key taxa | LOI | Lithology |
|---|---|---|---|---|---|---|
| **CRU_5b** | 484-460 | 11,224±33 to 11,065±41 | ▲ *E. nigrum,* Poaceae; ↕ *Betula, Corylus*; ● Salix, *Artemisia*, Aster./Card. | *Betula,* Poaceae*, Empetrum nigrum* | ↑ | Clay and silt to marl transition to marl |
| **CRU_5c** | 460-428 | 11,065±41 to 10,746±173 | ↑ Poaceae, *Corylus*; ↔ *E. nigrum;* ● Salix; ⨯ *Artemisia*, Aster./Card., Lactuceae | *Betula, Empetrum nigrum.* Poaceae | ▲then ↓ | Marl |
| **CRU_6** | 428-402 | 10,746±173 to 10,487±157 | ↑ *Betula, Corylus;* ↓ *E. nigrum*, Poaceae; ● Salix | *Corylus, Betula Poaceae,* | ↓ | Marl |

### 7.2.2.1 Statistical analysis

There terrestrial taxa with an abundance of >5% underwent statistical analysis. DCA results in Table 7.6 show a short axis length indicating that PCA, CoA and PrC are suitable to explore the data.

**Table 7.6** Detrended correspondence analysis results for Crudale Meadow. The dataset shows the short axis lengths and that axis 1 explains the most variation compared to the other axis.

| | DCA1 | DCA2 | DCA3 | DCA4 |
|---|---|---|---|---|
| **Eigenvalue** | 0.2184 | 0.1244 | 0.06003 | 0.4063 |
| **Axis length** | 1.8317 | 1.5078 | 1.01259 | 0.75811 |

PCA results shown in Figure 7.10 the first two principal components, axis 1 and 2, explain 33.4% and 14.7% of data variation, respectively. The taxa that plot negatively along axis 1 are *Lactuceae* undiff. (most significant contributor), *Artemisia*, Asteroidea*, Caryophyllaceae* undiff. and *Salix*. Taxa that plot positively along axis 1 include *Corylus avellane* type and *Filipendula*. Intermediate taxa with a stronger association with axis 2 are *Empetrum nigrum*, *Poaceae* and *Rumex acetosa.*

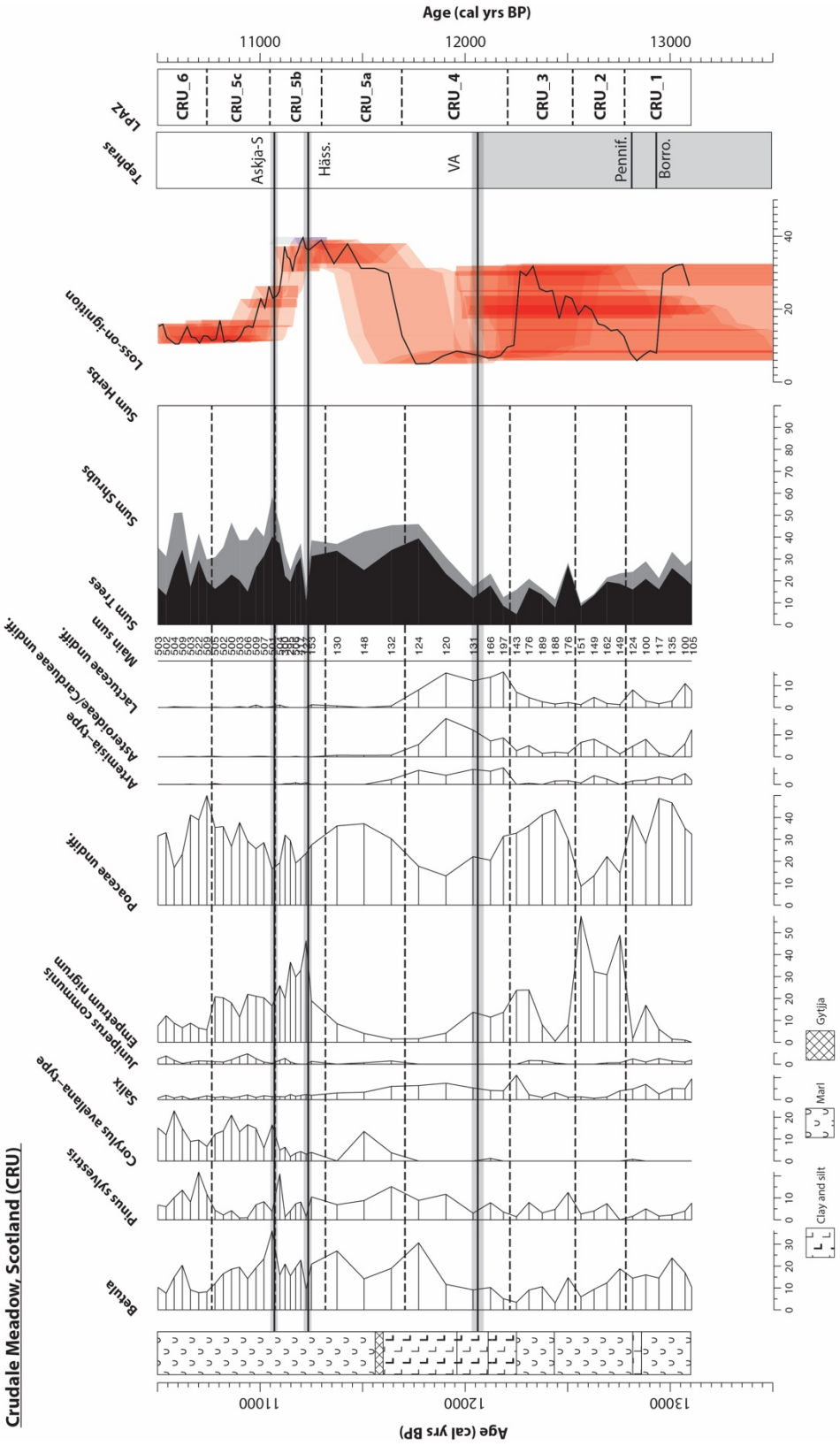


**Figure 7.8** Pollen percentage record of key taxa from Crudale Meadow. The record is plotted against calibrated age (μ ±1σ ). All values are presented against TLP. Lithology presented as described by Whittington et al. (2015). Percentage LOI is plotted. LPAZ are divided based upon changes in major taxa and CONISS. The Vedde Ash (VA), Hässeldalen (Häss.) and Askja-S tephras were identified in Crudale Meadow by Timms et al (2018) and are plotted with this study' s new age estimate at μ ±1σ for each tephra. The Penniflier (Pennif.) and Borrobol (Borro.) tephra ages are also present. But with the continued problems of identifying these tephras (Lind et al., 2016; Cook et al., 2019), they were not involved in creating the age model for Crudale Meadow. Light shading shows 1σ age error.

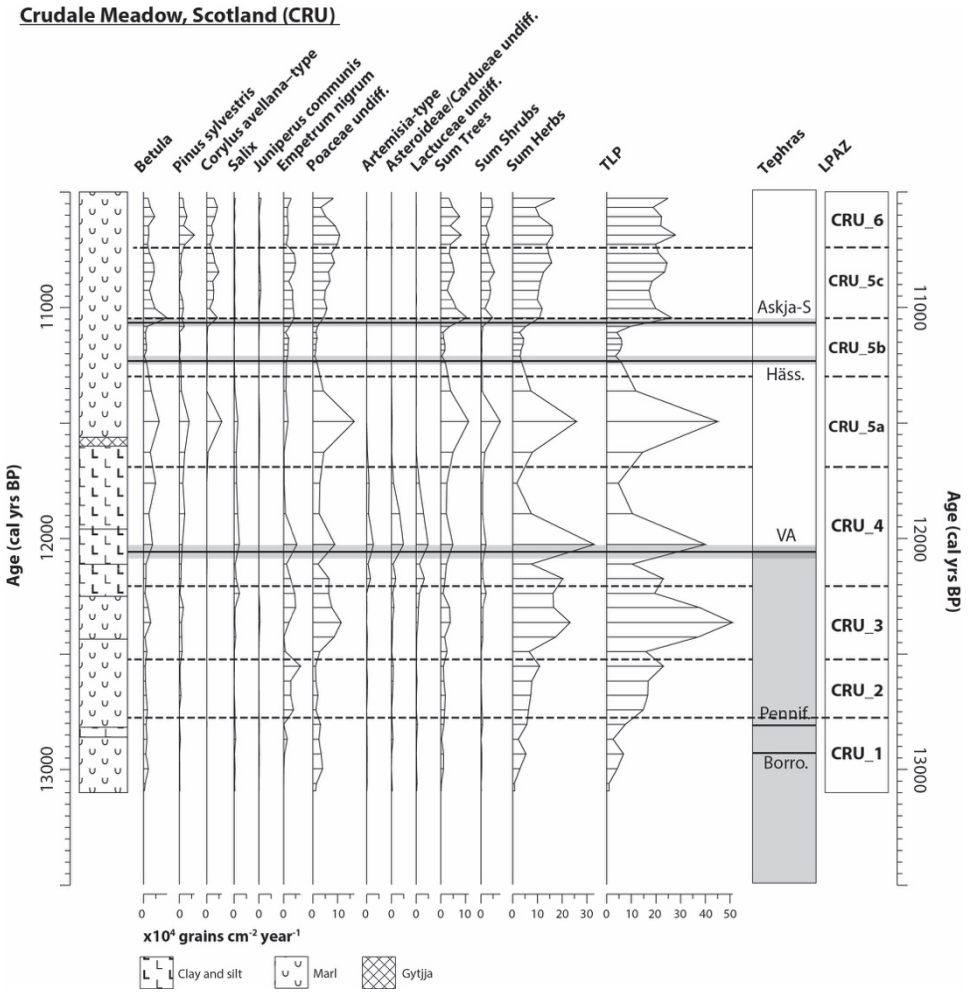


**Figure 7.9** Pollen accumulation rate (PAR) record of key taxa from Crudale Meadow. The record is plotted against calibrated age (μ±1σ). Lithology presented as described by Whittington et al. (2015). LPAZ are divided based upon changes in major taxa and CONISS in the percentage diagram. The Vedde Ash (VA), Hässeldalen (Häss.) and Askja-S tephras were identified in Crudale Meadow by Timms et al (2018) and are plotted with this study's new age estimate at μ±1σ for each tephra. The Pennifiler (Pennif.) and Borrobol (Borro.) tephra ages are also present. But with the continued problems of identifying these tephras (Lind et al., 2016; Cook et al., 2019), they were not involved in creating the age model for Crudale Meadow.

To model PrC a low penalty value of 0.8 was applied to allow both PCA- and CoA-based models to converge. A PCA-based output was chosen as the model captured more data variance than CoA (PCA 57% vs CA 49%). Within the PrC data, one MO and one additional oscillation were identified with an increase in variance (Figure 7.11, Table 7.7).

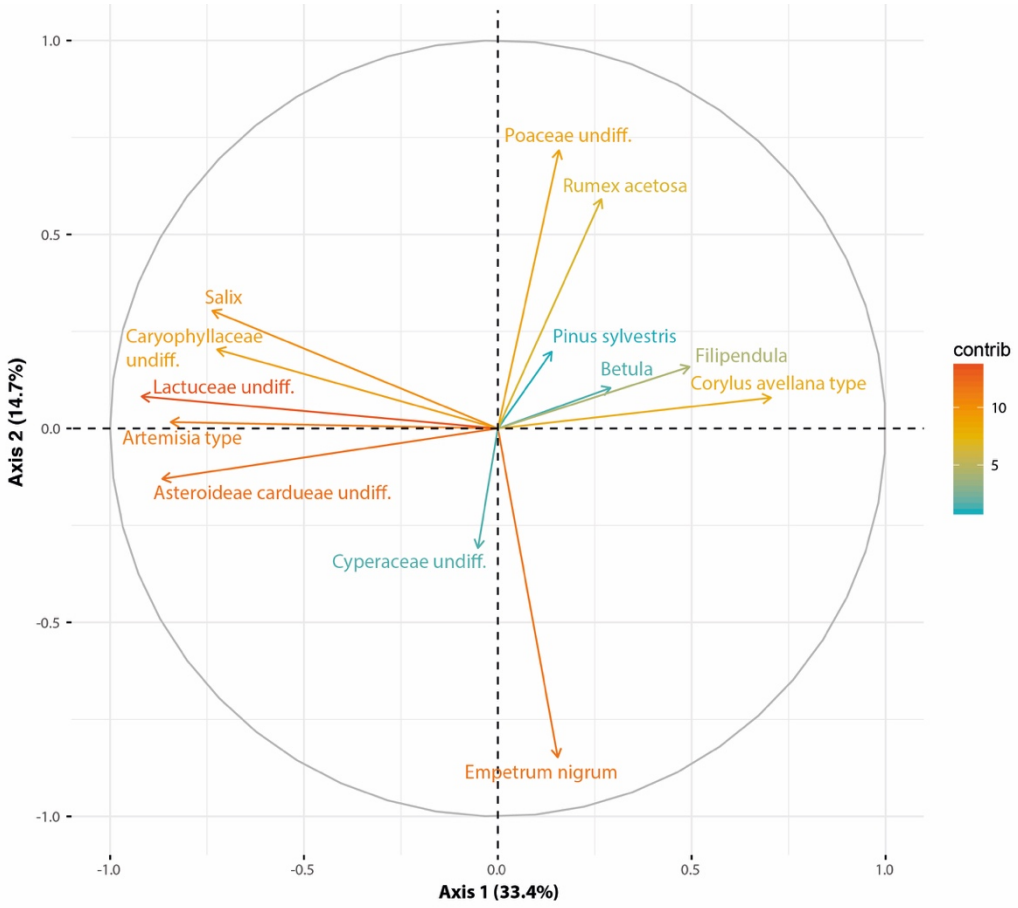


**Figure 7.10** Ordination diagram of the PCA results from Crudale Meadow. The two axis, axis 1 and 2, present first two principal components. The pollen taxa are placed along the axis with the length and colour of the arrow indicating the taxa dominance along the axis. Along Axis 1, taxa of open, colder landscapes plot negatively while mostly tree taxa plot positively. *Empetrum nigrum* is acting independently compared to the other taxa in this assemblage. This could indicate *Empetrum* is responding to a different climatic control. This is unlikely and is related to reworking of this taxa grains at the site (discussed in Chapter 8 and 9).

**Table 7.7** Vegtation oscillations identified in the PrC for Crudale Meadow. Symbols depict:↑ increases and ↓ decreases in taxa percentage.

| Oscillation | Depth (cm) | Age (μ±1σ, cal. BP) | Key taxa influence |
|---|---|---|---|
| CRU_MO | 524-496 | 12,270±322 to 11,561±255 | ↓ *Betula,* ↑*Asteroideae,* ↓Poaceae |
| CRU_E1 | 488-428 | 11,296±127 to 10,746±173 | ↑*Empetrum nigrum,* ↓*Betula,* ↑ Poaceae |

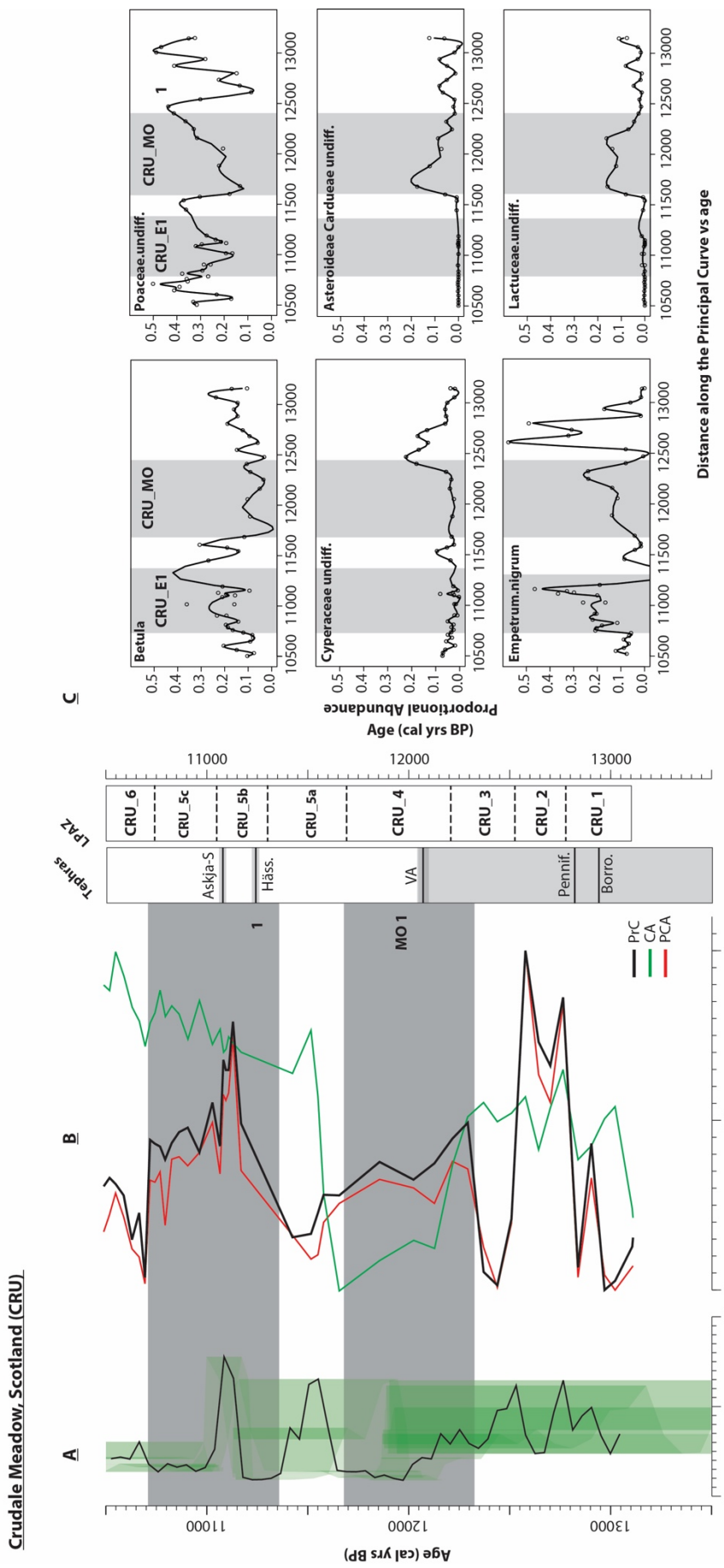


**Figure 7.11** The statistical results for the pollen percentage data from Crudale Meadow. A) RoC analysis for every 50 years. The values presented are exaggerated to provide clearer results into periods of significant change. The higher the bar, the more significant the composition change was. Light shading shows 1σ age error. B) The results of the different ordination tests (PCA, CoA and PrC). The grey boxes highlight oscillations identified from the PrC curve. C) The key taxa response curves modelled through the PrC. The grey boxes show the timing of the oscillations from the main PrC. Changes in the abundance of individual taxa at certain times provide insight into which taxa are driving the change. The record is plotted against calibrated age (μ ±1σ ) with light shading showing 1σ age error.

#### 7.2.2.2 Palaeoclimatic and palaeoenvironmental interpretation

This section will focus on reconstructing the climate and environmental history of Crudale using the pollen data previously presented. Based upon age modelling, identification of the key tephras and evident vegetational changes, LPAZ can be correlated to climatic periods of the Allerød (CRU_1-3), YD (CRU_4) and EH (CRU5-6).

**Allerød-YD transition (12,270±322 cal. BP)**

The landscape was mainly open with herbaceous taxa of *Artemisia,* Asteroideae/Cardueae undiff. and Lactuceae. Poaceae was a dominant part of the vegetation with near 50% while *E nigrum* varied. *Betula* was present yet, this is acknowledged as being *B. nana* (Figure 7.8; Whittington et al., 2015). PAR shows an increase in pollen concentrations as the climate warms and becomes more stable (Figure 7.9). Lithology changes to largely marl, with an increase in LOI values, also indicating climatic warming of the Allerød (Nolan et al., 1999; Figure 7.8).

At 12,270±322 cal. BP there is an increase in open habitat taxa. Poaceae remains a dominant part of the vegetation while increases in taxa the of Lactuceae, *Artemisia* and Asteroideae/Cardueae undiff. indicate an onset of an open, unstable, treeless landscape (Huntley and Birks, 1983). *Betula* is present, with Whittington et al. (2015) making assumptions that it is dwarf-shrub *B.nana*. *Pinus* was also recorded, yet there are no known tree stands present in the UK at this time and is linked to long distant transport from the continent (Birks et al., 2005). A decrease in TLP counts with lower PAR show deterioration in climatic conditions negative effect on the vegetation (Figure 7.9). LOI values decrease (~20%) as minerogenic sediments are in washed with silty deposits (Whittington et al., 2015). These environmental characteristics, with the identification of the VA, indicate the YD stadial.

**YD-EH transition (11,561±255 cal. BP)**

At 11,561±255 cal. BP there is a marked transition from cold, open landscape to heathland. The expansion of *Betula* and *Corylus* are indicative of climate amelioration of the earliest Holocene period (Figure 7.8, Theuerkauf et al., 2012, 2014). Taxa of colder, unstable environments (*Artemisia,* Asteroideae/Cardueae undiff. and Lactuceae) declined and disappeared from the record. Poaceae remained a dominant part of the landscape (Figure 7.8). Vegetation increases as seen in a peak in PAR (Figure 7.9). With the presence of shade-intolerant *E. nigrum*, a heathland developed with a few tree stands of birch (Bell and Tallis, 1973). Marl carbonate began to be redeposited with climatic amelioration (Nolan et al., 1999; Whittington et al., 2015).

**Earliest Holocene oscillations**

Thermophilous taxa (*Betula* and *Corylus avellana*-type) continued to expand (Figure 7.8). Poaceae was still a dominant part of the record with *Salix* and *Juniperus* soon outcompeted with a growing birch-hazel mixed woodland.

At 11,296 ± 127 cal. BP an increase and then a pause in PrC values is seen with a rise in vegetational composition turnover seen in RoC (Figure 7.11). The PrC is identifying an increase in *E. nigrum* with a decline in *Betula*. Cyperaceae also slightly rises with *Corylus* expansion possibly being inhibited. There is a slight increase in taxa of *Artemisia, Rumex* and Lactuceae. PAR shows a decline in pollen production and possibly sedimentation rate (Figure 7.9). An oscillation with a sharp decline in LOI values is also seen.

### 7.2.3 Lake Madtjärn, Sweden

Lake Madtjärn was collected, sampled and counted by Björck et al. (1991, 1996). A total of seventeen samples were processed at varying resolutions of 1-11cm. Based on the chronology, the samples cover the middle part of the LGIT (Allerød, YD and EH). Three LPAZ (MAD_*n*) were identified (Table 7.8; Figure 7.12). No PAR or LOI data is available.

**Table 7.8** The local pollen assemblage zones for Lake Madtjärn. Included are the name of zones, depth, ages for the beginning and end of the zones (μ±1σ) with key taxa observations and changes within each zone. Symbols depict:↑ increases and ↓ decreases in taxa percentage; ↕ oscillating or ↔ stability of values for particular taxa; ▲ taxa peak; ● taxa present at <5%; ✕ taxa disappears in that zone.

| Zone | Depth (cm) | Age (μ±1σ, cal. BP) | Taxa changes through zone | Key taxa | LOI | Lithology |
|---|---|---|---|---|---|---|
| **MAD_1** | 840-832.5 | 12,763±54 to 12,647±68 | ↓ *Pinus;* ↑ *Betula;* ● *Juniperus,* Poaceae, *Artemisia,* Cyperaceae, *Rumex* | *Betula, Pinus* | NA | Silt and clay |
| **MAD_2** | 832.5-800.25 | 12,647±68 to 11,595±117 | ↑ *Artemisia,* Poaceae, Cyperaceae*;* ↓ *Pinus, Betula*; ↕ *Rumex*; ↔ *B. nana;* ● Empetrum, *Filipendula* | *Artemisia,* Poaceae, Cyperacae | NA | Clay gyttja into clay gyttja with moss macrofossils |
| **MAD_3a** | 800.25-798.75 | 11,595±117 to 11,536±112 | ↑ *Pinus, Betula, Empetrum;* ↓ *Salix,* Poaceae, *Artemisia,* Cyperaceae; ● *Rumex, Filipendula* | *Betula, Pinus, Empetrum* | NA | Clay gyttja |
| **MAD_3b** | 798.75-790.5 | 11,536±112 to 11,136±107 | ↑ *Betula, B. nana, Empetrum*, ↓ *Pinus,* Cyperaceae, *Artemisia;* ● *Rumex, Filipendula* | *Betula, Betula nana, Empetrum* | NA | Clay gyttja |
| **MAD_3c** | 790.5-785 | 11,136±107 to 10,977±98 | ↑ *Betula, Pinus, Empetrum*; ↓ Poaceae, *B.nana;* ● *Rumex, Filipendula* | *Betula, Empetrum* | NA | Clay gyttja |

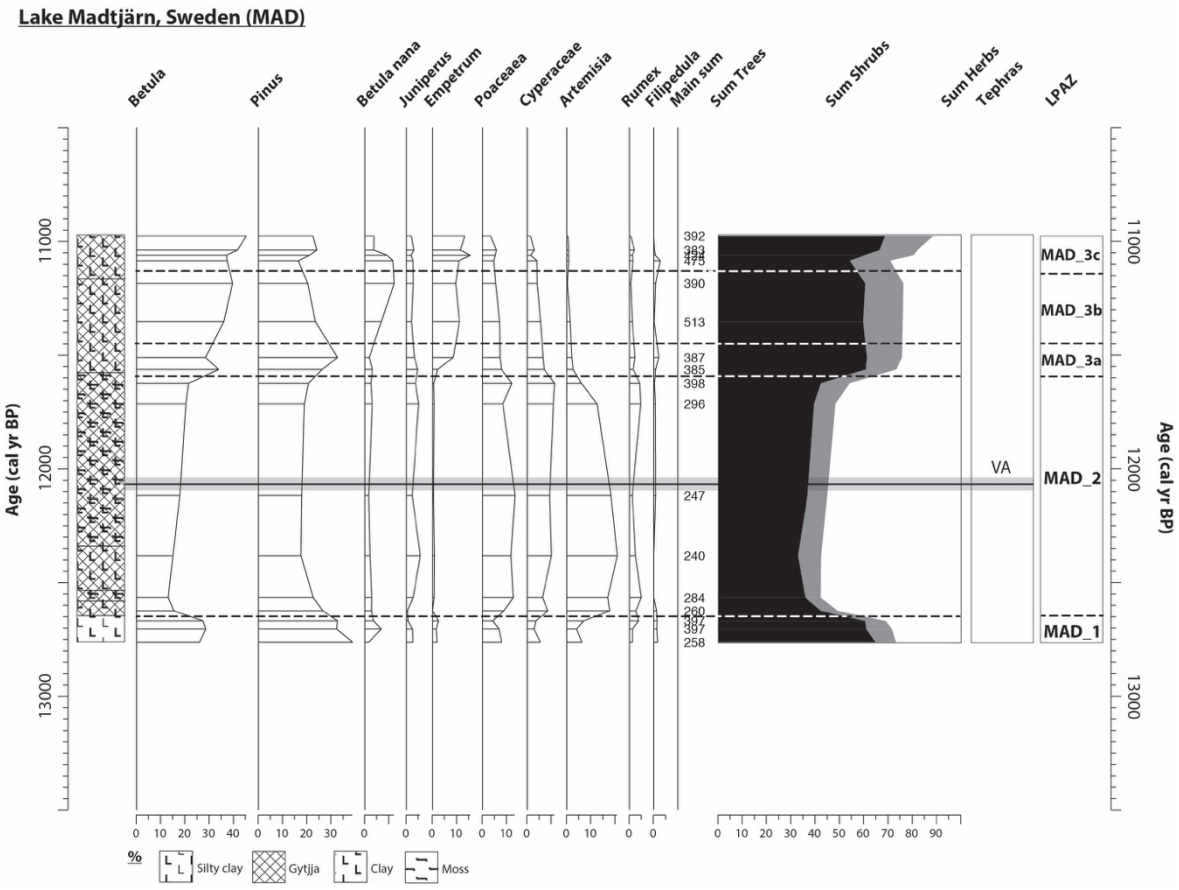


**Figure 7.12** Pollen percentage record of key taxa from Lake Madtjärn. The record is plotted against calibrated age (μ±1σ). All values are presented against TLP. Lithology presented as defined by Björck et al. (1996). No LOI was received for this record LPAZ are divided based upon changes in major taxa and CONISS. The Vedde Ash (VA) is identified in Madtjärn and is plotted with this study's new age estimate at μ±1σ.

### 7.2.3.1 Statistical analysis

A lower limit of taxa with >2% abundance underwent statistical analysis from the Madtjärn percentage pollen dataset. DCA results in Table 7.9 show a short axis length of below >1.5-3 SD. It is appropriate for the dataset to undergo PCA data exploration with this being the approach for modelling PrC.

Figure 7.13 presents the PCA results. Axis 1 accounts for 47% of data variance with axis 2 accounting for 16.9%. Taxa that plots negatively along axis 1 includes: *Empetrum, Betula* (both the largest contributor) and *B. nana*, while taxa that plots positively includes:

*Poaceae*, *Rumex, Artemisia* and Cyperaceae. Taxa that have a greater affinity to axis 2 includes: *Pinus, Salix,* and *Filipendula.*

**Table 7.9** Detrended correspondence analysis results of Lake Madtjärn. The dataset shows short axis lengths and that axis 1 explains the most variation compared to the other axis.

| | DCA1 | DCA2 | DCA3 | DCA4 |
|---|---|---|---|---|
| **Eigenvalue** | 0.1915 | 0.02101 | 0.011361 | 0.014525 |
| **Axis length** | 1.2785 | 0.46176 | 0.364824 | 0.372565 |

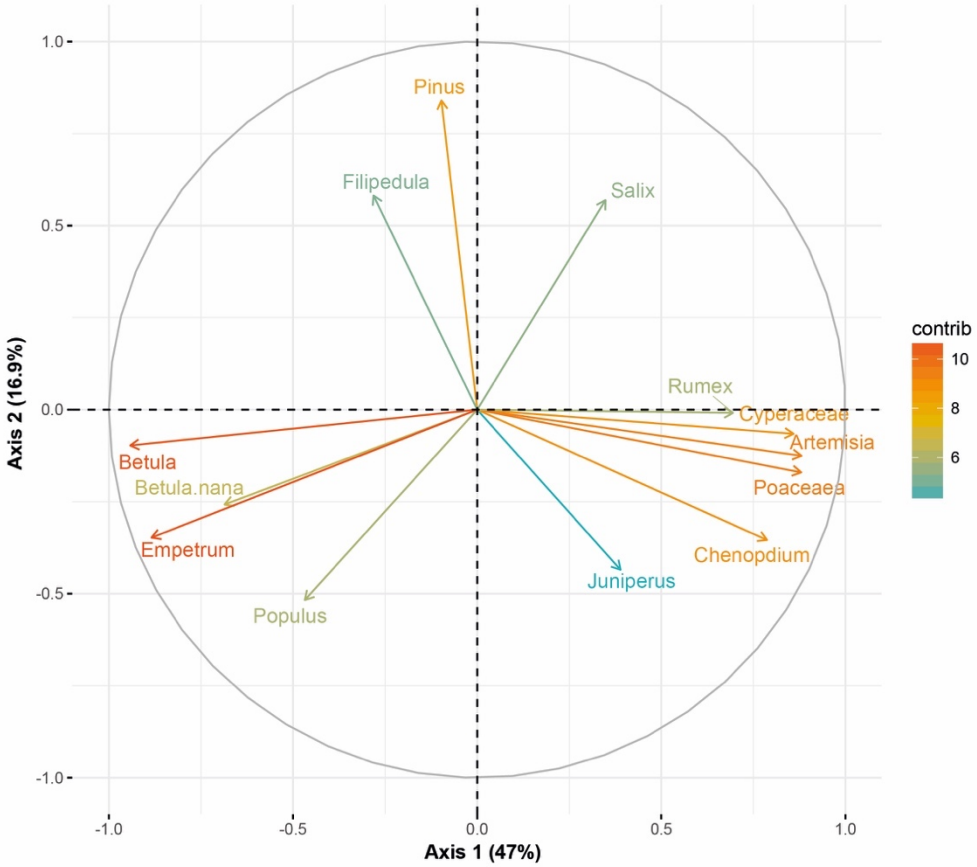


**Figure 7.13** Ordination diagram of the PCA results from Lake Madtjärn. The two axis, axis 1 and 2, present first two principal components. The pollen taxa are placed along the axis with the length and colour of the arrow indicating the taxa dominance along the axis. Along axis 1, taxa associated with stadial conditions plot negatively while taxa associated with interstadial conditions plot positively. Axis 2 has an association with a mix of taxa.

PrC provided further insight into palynological change of the dataset. A PCA-based approach was undertaken due to a short axis length depicted in DCA. This PCA-based output

accounted for 85.8% of data variance within seven iterations. The CoA-based output converged in less but only accounted for 84.5% of data variance.

The PrC output identified one major oscillation and two additional oscillation (Figure 7.14; Table 7.10). These were identified through 1) a pause in a general shift in variance and; 2) a switch to more positive values. Figure 7.14 presents the key taxa driving these PrC changes with RoC.

**Table 7.7 Vegtation oscillations identified in the PrC for Lake Madtjärn.** Symbols depict:↑ increases and ↓ decreases in taxa percentage

| Oscillation | Depth (cm) | Age (μ±1σ, cal. BP) | Key taxa influence |
|---|---|---|---|
| MAD_MO | 831-792.25 | 12,763±54 to 11,595±117 | ↑*Artemisia,* ↓*Pinus,* ↓*Betula* |
| MAD_E1 | 797.25-795.75 | 11,486±108 to 11,435±103 | ↑*Empetrum,* ↑*Pinus,* ↑*Betula* |
| MAD_E2 | 792.25-788.5 | 11,297±103 to 11,051±91 | ↑*Empetrum,* ↓*Pinus,* ↓*Betula* |

### 7.2.3.2 Palaeoclimatic and palaeoenvironmental interpretation

This section will focus on reconstructing the climate and environmental history of Lake Madtjärn using the pollen data previously presented. Based upon age modelling, identification of the VA and evident vegetational changes, LPAZ can be correlated to the LGIT periods of the Allerød (MAD_1), YD (MAD_2) and EH (MAD_3).

**Allerød-YD transition (12,763±54 cal. BP)**

The start of the record shows that *Betula* and *Pinus* are an important part of the vegetation. Pioneering taxa (*Rumex, Artemisia* and Cyperaceae) declined as woody taxa increased (Figure 7.12). *Betula nana* does expand very shortly. The chronology and the increase in woody taxa indicating climatic warming, it is vegetation indictive of the late Allerød period (Björck and Digerfeldt, 1991, Berglund et al., 1994). The sea flooded the site

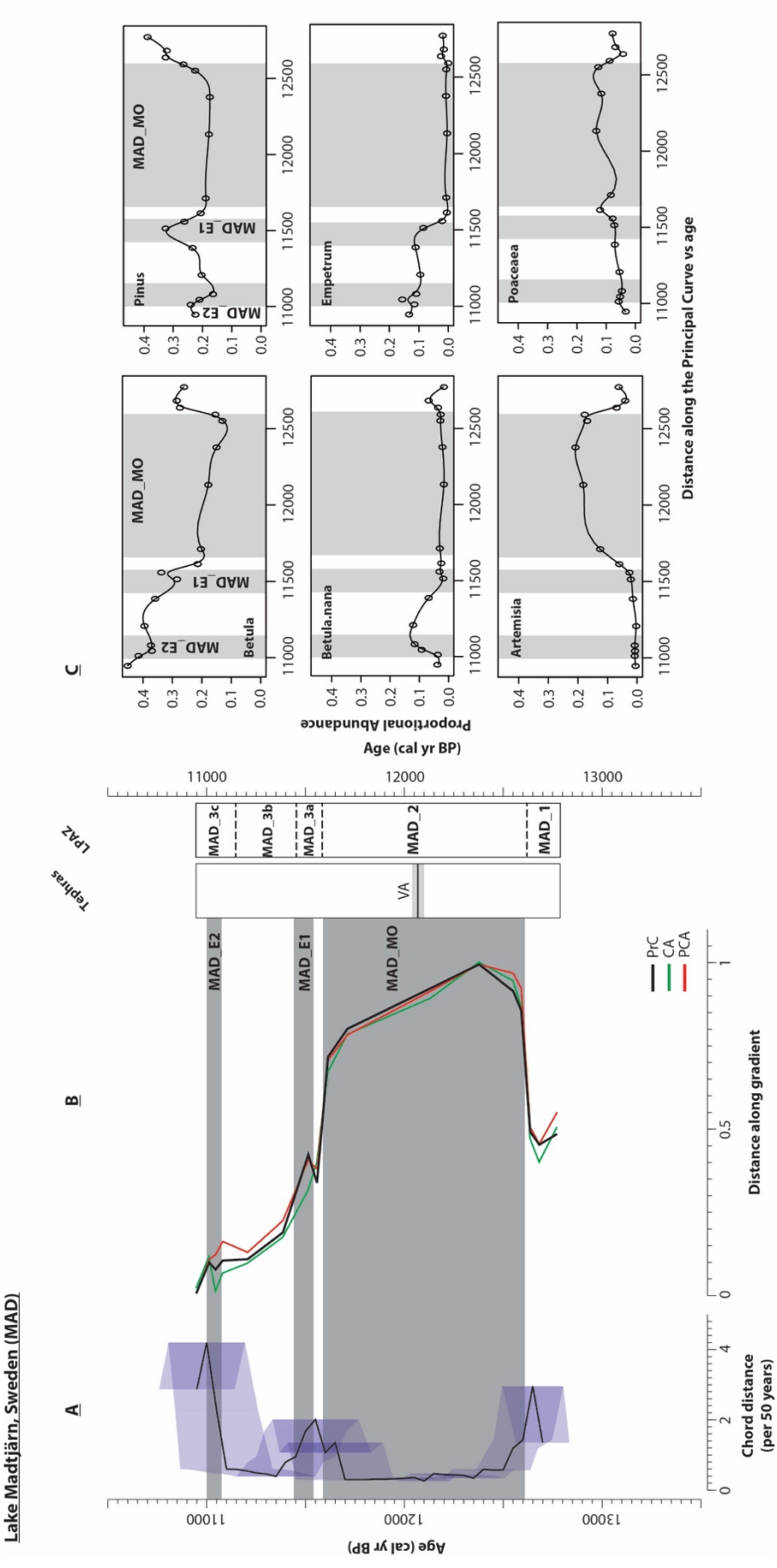


**Figure 7.14** The statistical results for the pollen percentage data from Lake Madtjärn. A) RoC analysis for every 50 years. The values presented are exaggerated to provide clearer results into periods of significant change. The higher the bar, the more significant the composition change was. Light shading shows 1σ age error. B) The results of the different ordination tests (PCA, CoA and PrC). The grey boxes highlight oscillations identified from the PrC curve. C) The key taxa response curves modelled through the PrC. The grey boxes show the timing of the oscillations from the main PrC. Changes in the abundance of individual taxa at certain times provide insight into which taxa are driving the change. The record is plotted against calibrated age (μ ±1σ ) with light shading showing 1σ age error.

until the SIS retreated and isostatic rebound occurred during this period (Björck and Digerfeldt, 1991).

There was a transition to an open, treeless landscape with a sharp decline in *Betula* and *Pinus* and a rise in herbaceous taxa (e.g. *Artemisia*, *Rumex,* Poaceae, Cyperaceae) at 12,763 ± 54 cal. BP. A lithological change to clay gyttja is seen, which is not vastly different from sediments in the Allerød (Figure 7.12). This is due to the continued effect of a cold sea nearby (Björck and Digerfeldt, 1991). The vegetation change indicates a cooling period associated with the YD (e.g. Björck and Möller, 1987; Berglund et al., 1994).

**YD-EH transition (11,595±117 cal. BP)**

Throughout the YD, open tundra taxa of *Artemisia, Rumex* remain dominant in the open landscape with Poaceae and Cyperaceae. The presence of *Juniperus* shrub during MAD_YD indicates that temperatures were cold enough to affect *Betula*, allowing for this light-demanding shrub to expand in the treeless landscape (Thomas et al., 2007). The lithology is clay indicating allochthonous input from this unstable landscape (Björck et al., 1996).

At 11,595 ± 117 cal. BP, woody taxa sharply rose as *Betula* and *Pinus* started to expand in the surrounding area (Figure 7.12). There is a change in lithology to clay gyttja which is brownish, indicating an increase in organic content (Björck et al., 1996). Herbaceous taxa associated with colder environments of YD (e.g. *Artemisia*, Cyperaceae and Poaceae) decline as the landscape becomes more stable and forested. Overall, the climate is warming, indicating the EH transition (Björck and Möller, 1987; Björck et al., 1996).

**Earliest Holocene oscillations**

The record provides a short insight into the EH at Madtjärn. *Betula* continued to gradually increase, becoming a significant part of the habitat. Tree taxa soon outcompeted *Juniperus*, which declined (Huntly and Birks, 1983). *Empetrum* and *Betula nana* are present indicating open heathlands with the dwarf shrub. The climate is warmer and drier.

At 11,486±108 cal. BP, a small increase in the PrC is seen with a rise in vegetational overturn (RoC) (Figure 7.14). The curve is identifying the increase in *Pinus* and *Empetrum* with a decrease in Poaceae (Figure 7.14). Another change in the PrC is at 11,297±216 to 11,051±200 cal. BP with a peak in *Empetrum* and a decline in *Pinus* and *Betula*. There is no change in lithology at these times or LOI available. However, Björck et al. (1997) show a slight oscillation of ~2% in organic content at the site around the depth of the second PrC event.

### 7.2.4 Hässeldala port, Sweden

Hässeldala port pollen record from Core 3 was collected, sampled and counted by Wohlfarth et al. (2006) and correlated to the master core, Core 5. Twenty-one samples were dated to the LGIT with varying resolutions of 1-7 cm. TLP counts ranged from >400-600 with a single sample of <150 due to poor pollen preservation at this point (Wohlfarth et al., 2006). Seven LPAZ (HAS_*n*) were identified (Table 7.11; Figure 7.15). PAR was also calculated (Figure 7.16).

**Table 7.11** The local pollen assemblage zones for Hässeldala port. Included are the name of zones, depth, ages for the beginning and end of the zones (μ±1σ) with key taxa observations and changes within each zone. Symbols depict:↑ increases and ↓ decreases in taxa percentage; ↕ oscillating or ↔ stability of values for particular taxa; ▲ taxa peak; ● taxa present at <5%; ✕ taxa disappears in that zone.

| Zone | Composite Depth (cm) | Age (μ±1σ, cal. BP) | Taxa changes through zone | Key taxa | LOI | Lithology |
|---|---|---|---|---|---|---|
| **HAS_1** | 357-352.425 | 13,419±40 to 13,222±54 | ↑ *Betula, Pinus*; ↓ *Corylus;* ● *Salix, Empetrum, Juniperus communis,* Cyperaceae, *Artemisia, Rumex* | *Betula pubescens, Rumex* | ↑ | Clay gyttja |
| **HAS_2** | 352.425-340.375 | 13,222±54 to 12,733±63 | ↕ *Betula, Pinus;* ↑ *Empetrum, J. comm.,* Cyperaceae; ● *Corylus, Artemisia* | *Betula pubescens, Empetrum* | ↕ then ↑ | Clay gyttja transition to silt and clay gyttja |
| **HAS_3** | 340.375-320.1875 | 12,733±63 to 11,560±103 | ↑ *Betula, Artemisia, Empertrum*; ↓ *Pinus;* ↔ Poaceae, Cyperaceae; ↓ *J. comm., Corylus* | *Betula pubescens, Artemisia,* Juniperus, Cyperaceae | Sharp ↓ | Silt and clay gyttja to clay gyttja |
| **HAS_4** | 320.1875-312.15 | 11,560±103 to 11,236±18 | ▲ *Empetrum;* ↓ *Betula, Artemisia;* ↑ *Pinus, J. comm.,* Poaceae, Cyperaceae | *Empetrum,* Poaceae | Gradual ↑ | Clay gyttja to silt and clay gyttja |

| Zone | Composite Depth (cm) | Age (μ±1σ, cal. BP) | Taxa changes through zone | Key taxa | LOI | Lithology |
|---|---|---|---|---|---|---|
| **HAS_5** | 312.15-300.125 | 11,236±18 to 10,834±126 | ↕▲ *Betula;* ↑ *Salix, J. comm.,* Poaceae; ↕↓ *Pinus;* ● *Corylus, Artemisia* | *Betula pubescens, Salix, Juniperus*, Poaceae | *Sharp* ↓ then ↑ | Gyttja |
| **HAS_6** | 300.125-293.85 | 10,834±126 to 10,577±140 | ↓ *Betula;* ↑ *Pinus, J. comm.,* Poacae; ● *Corylus, Salix, Empetrum, Artemisia* | *Pinus, Juniperus communis* | Gradual ↑ | Gyttja |
| **HAS_7** | 293.85-290.8 | 10,577±140 to 10,478±150 | ↑ *Betula;* ↓ *Pinus, J. comm.,* Poaceae; ● *Corylus, Salix, Empetrum, Artemisia* | *Betula pubescens* | Gradual ↑ | Gyttja |

### 7.2.4.1 Statistical analysis

Statistical analysis was performed on Hässeldala pollen percentage dataset using taxa with abundances >2%. DCA results are shown in Table 7.12 The axis lengths are short, demonstrating the PCA is the most appropriate method to explore the data along with PrC.

**Table 7.8** Detrended correspondence analysis results for Hässeldala port. The dataset shows short axis lengths and that axis 1 explains the most variation compared to the other axis.

| | DCA1 | DCA2 | DCA3 | DCA4 |
|---|---|---|---|---|
| **Eigenvalue** | 0.09312 | 0.07988 | 0.04124 | 0.49854 |
| **Axis length** | 0.98095 | 0.85504 | 0.65476 | 0.700810 |

Figure 7.17 presents the results of PCA. The first axis accounts for 29% of the data variation, while axis two represents 18.7% of data variation. Along axis 1, taxa that plots negatively include *Juniperus communis* (most significant contributor), Cyperaceae, *Corylus* and Poaceae. In contrast, the taxa of *Betula pubescens* plots positively along axis 1. The taxa that plot strongly against axis 2 are *Pinus* and *Betula nana.*

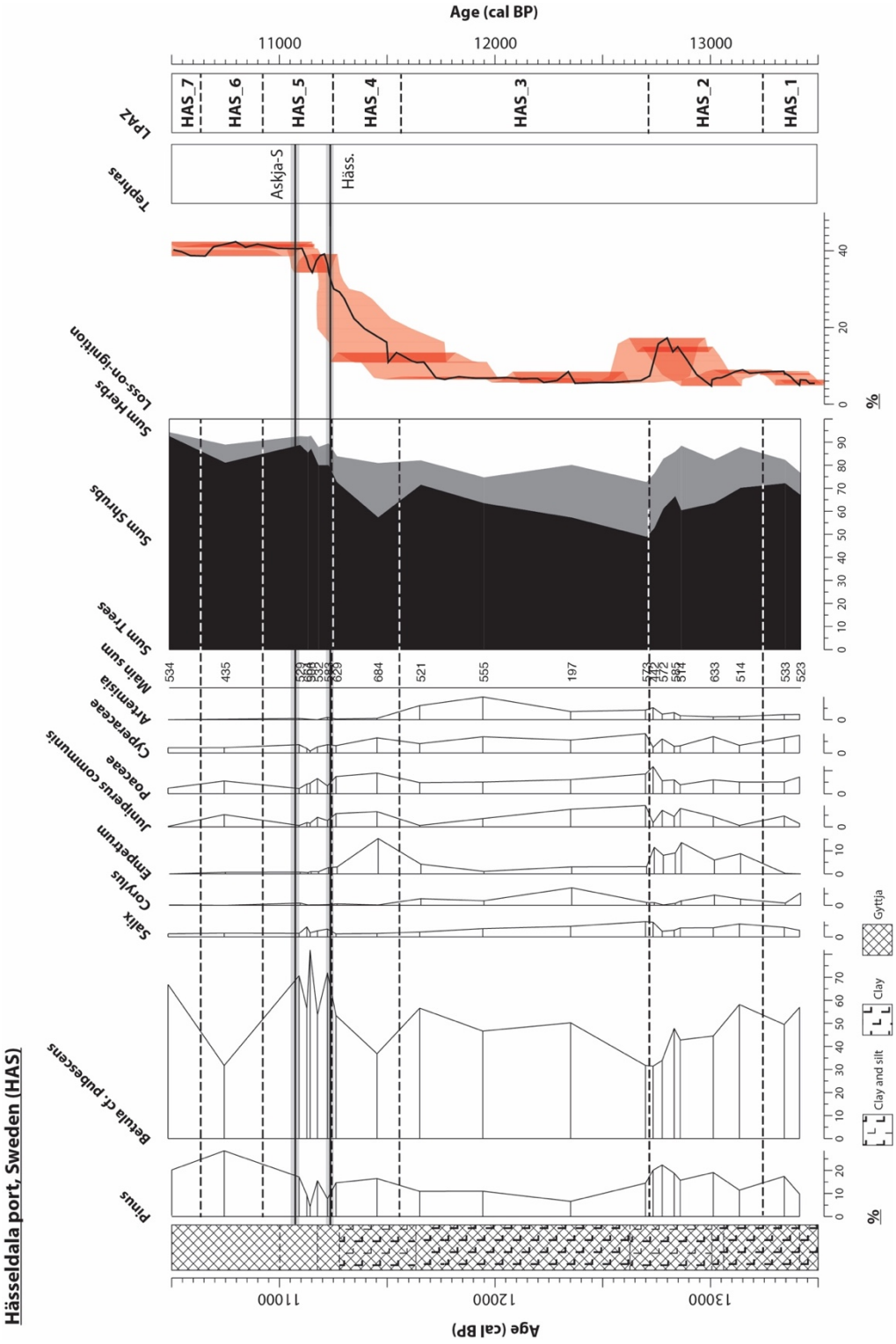


**Figure 7.15** Pollen percentage record of key taxa from Hässeldala port. The record is plotted against calibrated age (μ ±1σ ). All values are presented against TLP. Lithology presented as described by Wohlfarth et al (2006). Percentage LOI is plotted. LPAZ are divided based upon changes in major taxa and CONISS. The Hässeldalen (Häss.) and Askja-S tephra identified by Davies et al. (2003) plotted with this study's new age estimate at μ ±1σ . Light shading shows 1σ age error.

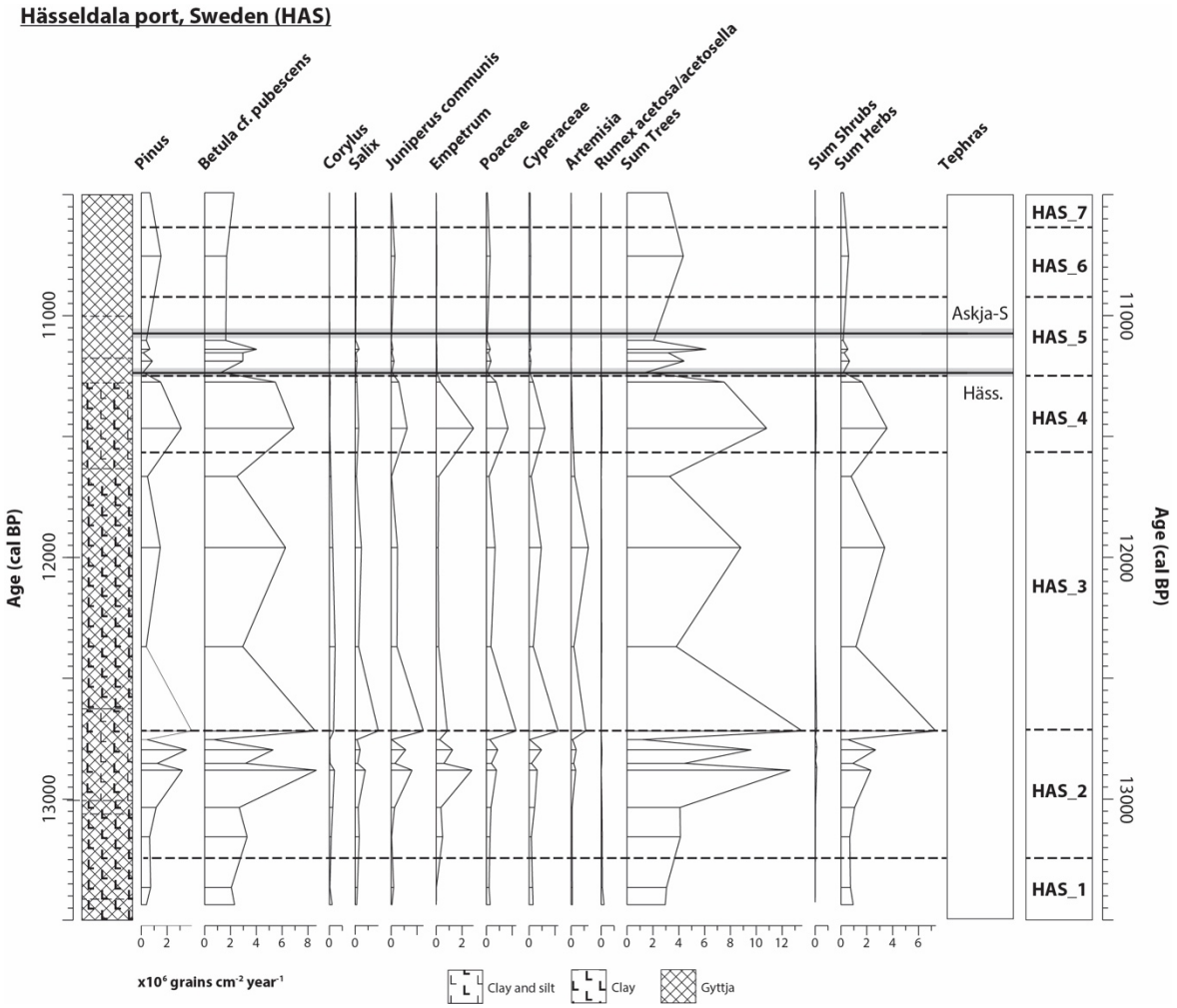


**Figure 7.16** Pollen accumulation rate (PAR) record of key taxa from Hässeldala port. The record is plotted against calibrated age (μ±1σ). Lithology presented as described by Wohlfarth et al (2006). LPAZ are divided based upon changes in major taxa and CONISS in percentage diagram. The Hässeldalen (Häss.) and Askja-S tephra identified by Davies et al. (2003) plotted with this study's new age estimate at μ±1σ.

The PrC allowed further exploration of the pollen dataset. Due to the short axis length from DCA, a PCA-based output for modelling PrC was deemed appropriate, capturing 77.2% of the data variance. Changes within the PrC data show one major oscillation with one additional oscillation indicated by an increase in variance along the gradient (Figure 7.18; Table 7.13). RoC results also show increases in vegetation compositional change at this time (Figure 7.18).

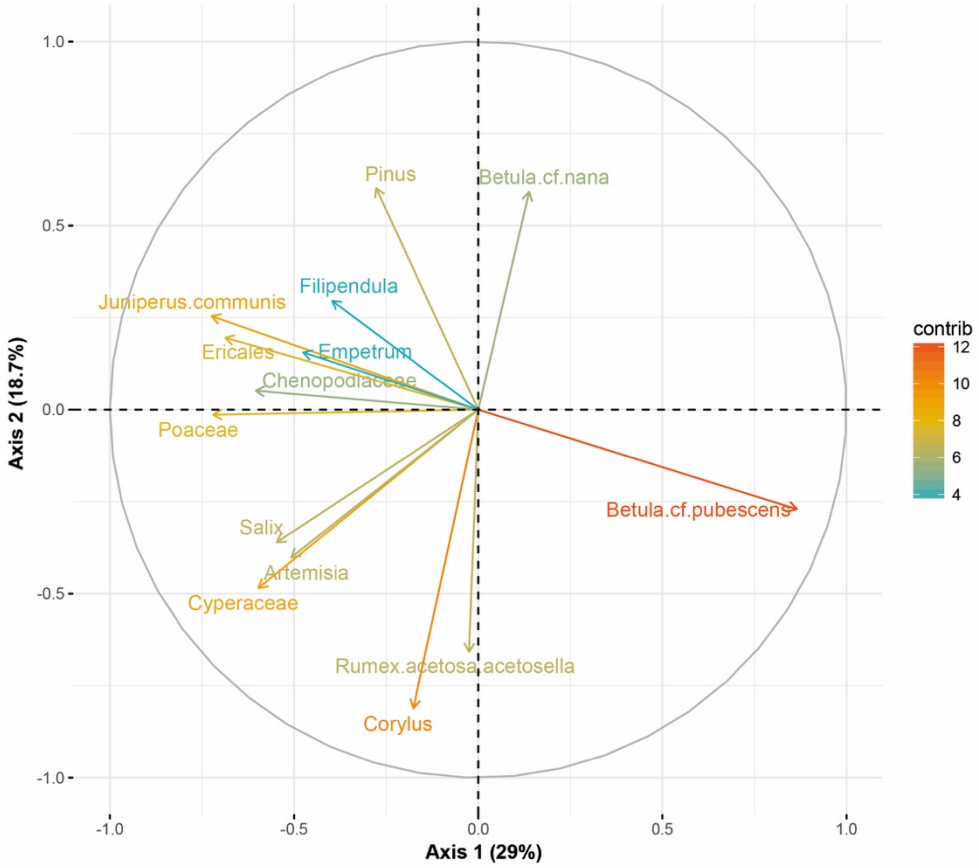


**Figure 7.17** Ordination diagram of the PCA results from Hässeldala port. The two axis, axis 1 and 2, present first two principal components. The pollen taxa are placed along the axis with the length and colour of the arrow indicating the taxa dominance along the axis. It is hard to decipher the principal components for this site. This is due to problems with Corylus being in the record (see Chapter 8 for more details).

**Table 7.13** Vegtation oscillations identified in the PrC for Hässeldala port. Symbols depict:↑ increases and ↓ decreases in taxa percentage

| Oscillation | Depth (cm) | Age (μ±1σ, cal. BP) | Key taxa influence |
|---|---|---|---|
| HAS_MO | 340.375-320.1875 | 12,733±63 to 11,560±103 | ↓*Betula*, ↑*Empetrum*, ↑*Artemisia*, ↑*Juniperus* |
| HAS_E1 | 312.15-304.5 | 11,236±18 to 11,112±27 | ↕*Pinus*, ↕*Betula*, ↕*Salix* |

### 7.2.4.2 Palaeoclimatic and palaeoenvironmental interpretation

This section will focus on reconstructing the climate and environmental history of Hässeldala port using the pollen data previously presented. Based on chronology and the identification of the Hässeldalen and Askja-S tephra, the periods of the Allerød (HAS_1-2), YD (HAS_3) and EH (HAS_4-6) were identified.

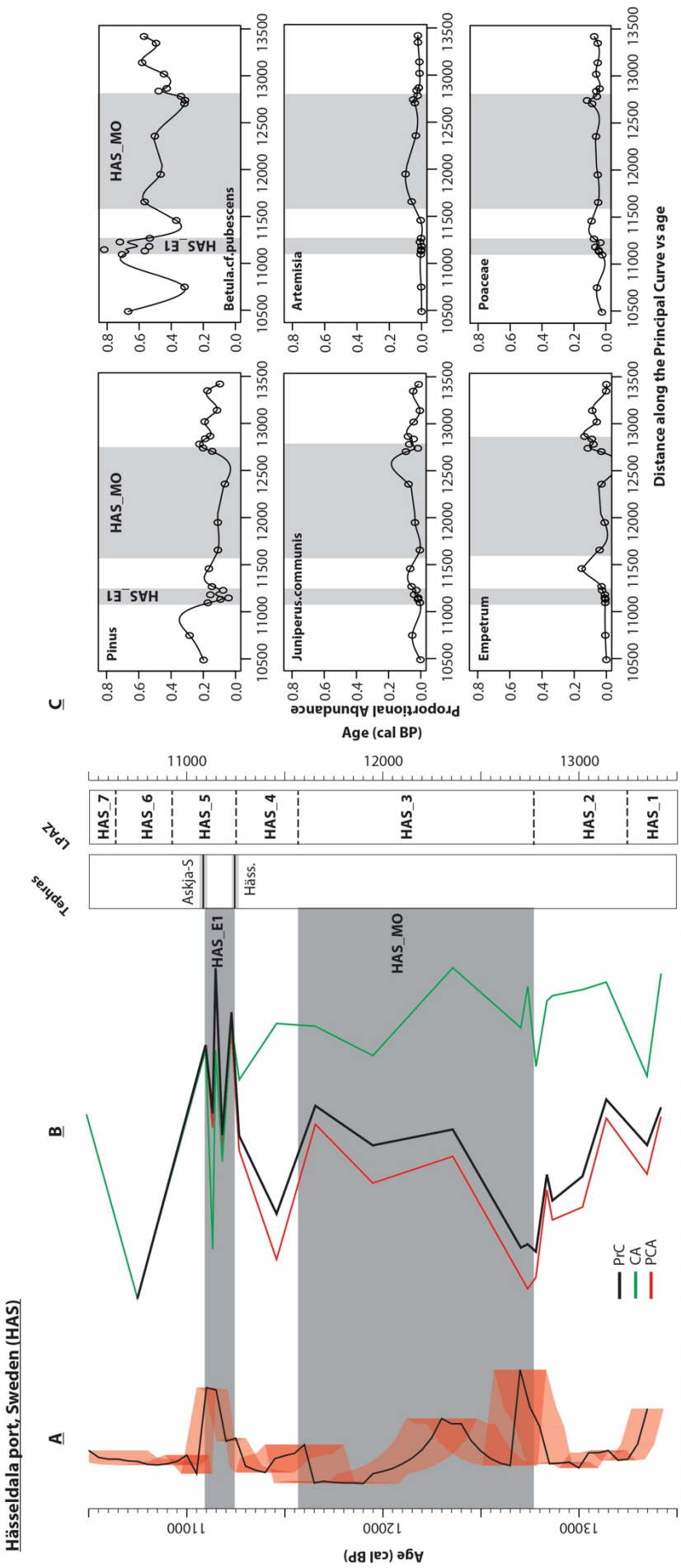


**Figure 7.18** The statistical results for the pollen percentage data from Hässeldala port. A) RoC analysis for every 50 years. The values presented are exaggerated to provide clearer results into periods of significant change. The higher the bar, the more significant the composition change was. Light shading shows 1σ age error. B) The results of the different ordination tests (PCA, CoA and PrC). The grey boxes highlight oscillations identified from the PrC curve. C) The key taxa response curves modelled through the PrC. The grey boxes show the timing of the oscillations from the main PrC. Changes in the abundance of individual taxa at certain times provide insight into which taxa are driving the change. The record is plotted against calibrated age (μ ±1σ ) with light shading showing 1σ age error.

**Allerød-YD transition (12,733±63 cal. BP)**

The record begins with *B. pubescens* being a dominant part of the local vegetation (figure 7.15). *Pinus* may not have present on the local landscape and was far-travelled based on the low percentage values (Huntley and Birks, 1983). *Juniperus* and *Salix* are part of the developing shrub layer. *Empetrum* increased as heathland occupied open areas (Bell and Tallis, 1973). LOI increases towards the end of this period as the climate warms (Figure 7.15). This vegetation succession is associated with the Allerød period (Björck and Möller, 1987; Wohlfarth et al., 2006; 2017).

At 12,733 ± 63 cal. BP, there was a sharp decline in woody taxa (Figure 7.15). There was a sharp decrease in *Empetrum* and increase in herbaceous taxa of *Artemisia*, Cyperaceae and Poaceae as the landscape became mainly open and treeless. PAR indicates a decline in the tree species (Figure 7.16). LOI declines sharply by ~10% as the landscape becomes unstable and lower nutrients are inwashed into the lake (Ampel et al., 2014). This is the YD transition, with other sites in the region showing similar vegetation responses (e.g. Berglund, 1966; Björck and Möller, 1987).

**YD-EH transition (11,560±103 cal. BP)**

At 11,560 ± 103 cal. BP, *Artemisia* declined and subsequent disappeared from the record while *Empetrum* and *Juniperus* rose (Figure 7.15). LOI steadily rises as landscapes become more stable with reforestation of *Betula* woodland. Overall, tree taxa began to rise in both percentage and PAR data, signalling climatic amelioration into the transition into the EH (Berglund, 1966). There is an increase in all taxa concentration in PAR linked to an increase in inwash as local snow-beds melted with rising temperatures (Figure 7.16, Birks et al., 2000).

**Earliest Holocene oscillations**

Tree taxa continued to increase with the presence of *Pinus slyvestris* macrofossils indicating a local occurrence of this taxon (Figure 7.15; Wohlfarth et al., 2006). *Betula* becomes the dominant taxa with possibly mixed birch-pine woodland stands. The shrub layer of *Juniperus* and *Salix* is soon outcompeted within the record.

At 11,236 ± 18 cal. BP, an apparent oscillation in PrC is observed (Figure 7.18). This peak is driven by a rise in *Betula* and decline in *Pinus*. An increase in *Salix* and Poaceae is also seen (Figure 7.15). There is a similar decline witnessed in PAR with a drop of ~5% in LOI values (Figure 7.16). However, there is no change in lithology. This oscillation happens after the Hässeldalen tephra and before the Askja-S.

### 7.2.5 Endinger Bruch, Germany

Endinger Bruch core HBG was collected, sampled and counted by de Klerk (2002). A total of 112 samples were dated to the LGIT in this project at a continuous resolution of 5cm. Five LPAZ (HBG_*n*) were identified (Figure 7.19, Table 7.14). No PAR was calculated due to the lack of exotic pollen data for the majority of samples.

**Table 7.14** The local pollen assemblage zones for Endinger Bruch. Included are the name of zones, depth, ages for the beginning and end of the zones (μ±1σ) with key taxa observations and changes within each zone. Symbols depict:↑ increases and ↓ decreases in taxa percentage; ↕ oscillating or ↔ stability of values for particular taxa; ▲ taxa peak; ● taxa present at <5%; ✕ taxa disappears in that zone.

| Zone | Depth (cm) | Age (μ±1σ, cal. BP) | Taxa changes through zone | Key taxa | LOI | Lithology |
|---|---|---|---|---|---|---|
| **HBG_1** | 1360-1247.5 | 13,503±193 to 12,667±135 | *Betula pubescens* ↑ then ↓; *Pinus* ↓ then ↑; ↕ Wild grasses; ● *Juniperus, Artemisia*, Cyperaceae, | *Betula, Pinus,* Cyperaceae | Gradual ↑ | Silt and sand into detritus gyttja |
| **HBG_2** | 1247.5-997.5 | 12,667±135 to 11,516±137 | ↑ *Betula nana, Picea, Artemisia,* Vaccinium, Cyperaceae; ↓ *B. pub.; ↕ Pinus* | *Picea, Juniperus,* Cyperaceae, *Artemisia,* | Sharp ↓ | Detritus gyttja to silt and sand |
| **HBG_3** | 997.5-937.5 | 11,516±137 to 11,242±22 | ▲ ↑ Wild grasses; ↑ *Filipendula, B. pub.; ↓ B.nana, Artemisia,* Cyperaceae; ✕ *Picea,* Vaccinium | *Wild grasses, Filipendula* | Gradual ↑ | Silt and sand into detritus gyttja |
| **HBG_4** | 937.5-832.5 | 11,242±22 to 10,791±23 | *B. pub.* ↑ then ↓; ↕ *Pinus; ↓* Wild grasses; ● *Artemisia, Salix* | *Betula, Pinus* | Gradual ↑ with peak | Detritus gyttja |
| **HBG_5** | 832.5-780 | 10,791±23 to 10,511±32 | Abrupt ↑ *Corylus; ↓ B. pub. ↕ Pinus,* Wild grasses | *Corylus* | Gradual ↓ | Detritus gyttja |

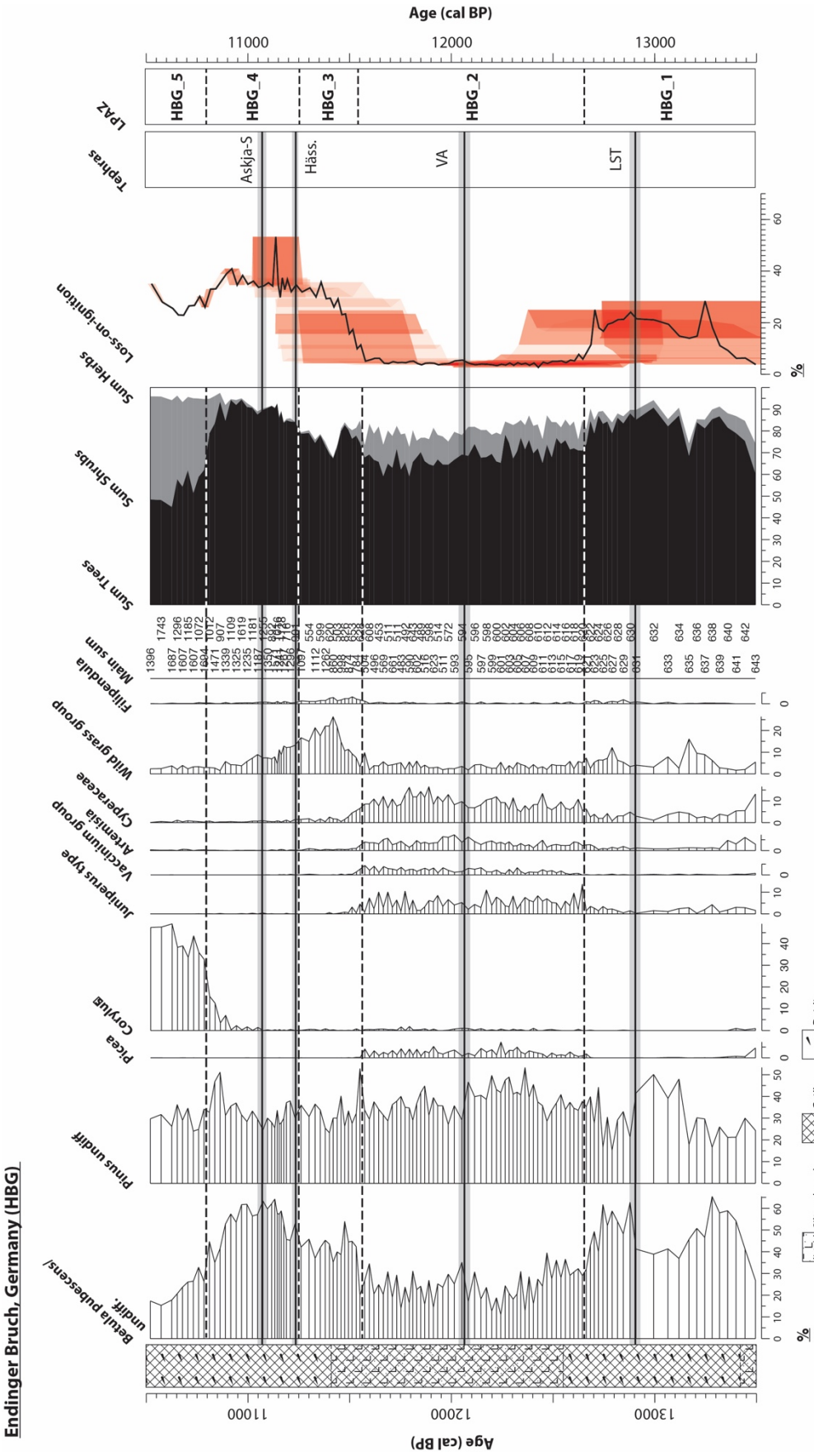


**Figure 7.19** Pollen percentage record of key taxa from Endinger Bruch. The record is plotted against calibrated age (μ ±1σ ). All values are presented against TLP. Lithology presented as described by de Klerk (2002). Percentage LOI is plotted. LPAZ are divided based upon changes in major taxa and CONISS. The Laacher See Tephra (LST), Vedde Ash (VA), Hässeldalen (Häss.) and Askja-S tephra identified by Lane et al. (2012a) is plotted with this study' s new age estimate at μ ±1σ . Light shading shows 1σ age error.

#### 7.2.5.1 Statistical analysis

Statistical analysis was performed on HBG percentage dataset using taxa with abundances >2%. DCA results in Table 7.15 show a short axis length. The lengths (>1.5-3 SD) show PCA, CoA and PrC were appropriate to explore the dataset.

**Table 7.15** Detrended correspondence analysis results for Endinger Bruch. The dataset shows short axis lengths and that axis 1 explains the most variation compared to the other axis

| | DCA1 | DCA2 | DCA3 | DCA4 |
|---|---|---|---|---|
| **Eigenvalue** | 0.1605 | 0.0616 | 0.07287 | 0.03145 |
| **Axis length** | 1.5856 | 0.84848 | 0.92366 | 0.70419 |

Figure 7.20 presents the results of PCA. Axis 1 explains 44.1% of the data variance, while axis 2 explains 16.4% of the dataset. Along axis 1, taxa plotting negative include *B. pubescens*, Wild grasses and *Filipendula* while positive plotting taxa include Cyperaceae (most significant contributor), *Artemisia* and *Picea*. Taxa that are intermediate are *Pinus* and *Salix* with *Corylus* plotting strongly against axis 2.

PrC allowed the dataset to be explored further, with a CoA-based output chosen to produce to the model. The CoA-based output was produced in less iterations needed before convergence (8 versus 10 for PCA). Also, CoA capture more data variation (87% versus 85% for PCA). One major oscillation with two minor oscillations was identified in Figure 7.21 with an increase in the variance from the gradient and a pause in values. Table 7.16 presents the timing of these oscillations, along with the proposed taxa that are driving the change.

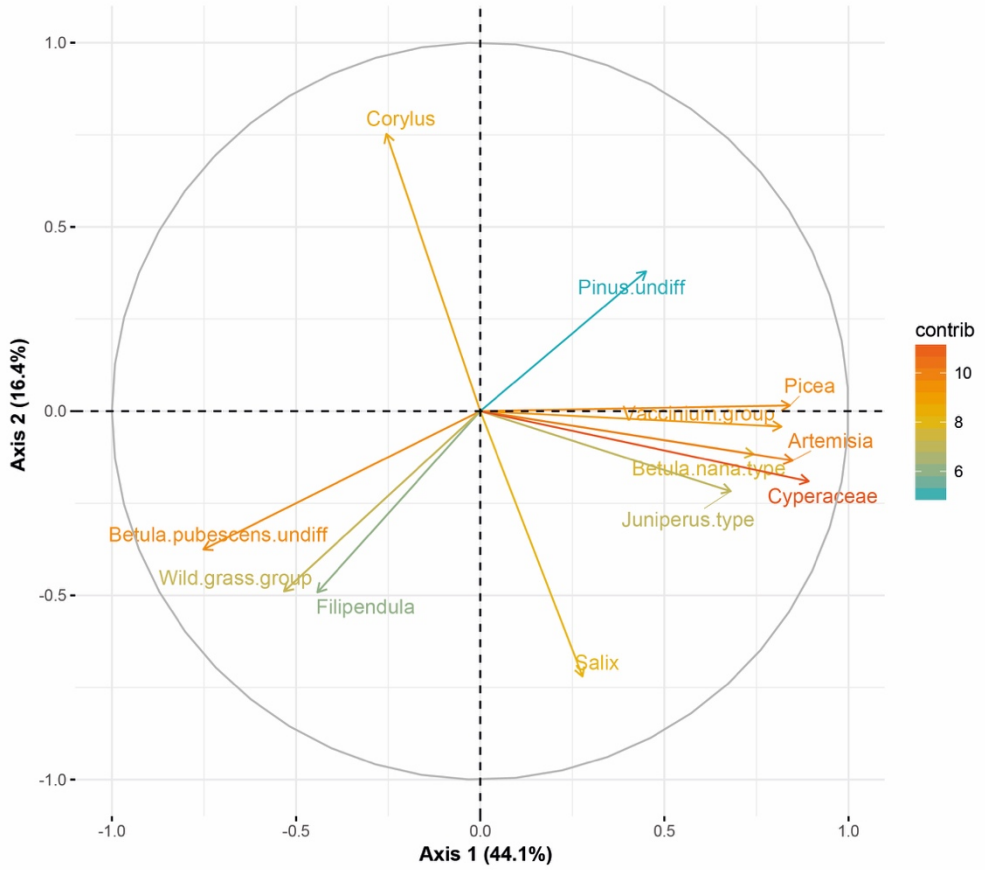


**Figure 7.20** Ordination diagram of the PCA results from Endinger Bruch. The two axis, axis 1 and 2, present first two principal components. The pollen taxa are placed along the axis with the length and colour of the arrow indicating the taxa dominance along the axis. Along axis 1, taxa associated with stadial conditions plot positively while taxa associated with interstadial conditions plot negatively. Axis 2 has an association with Corylus.

**Table 7.16** Vegtation oscillations identified in the PrC for Endinger Bruch. Symbols depict:↑ increases and ↓ decreases in taxa percentage

| Oscillation | Depth (cm) | Age (cal. BP) | Key taxa influence |
|---|---|---|---|
| HBG_MO | 1247.5-997.5 | 12,667±135 to 11,516±137 | ↑*Betula pubescens.*, ↑Cyperaceae |
| HBG_E1 | 982.5-937.5 | 11,447±128 to 11,242±22 | ↑Wild grass group, ↓*Betula pubescens.*, ↓*Pinus* |
| HBG_E2 | 847.5-837.5 | 10,871±21 to 10,818±22 | ↑*Pinus*, ↓*Betula pubescens* |

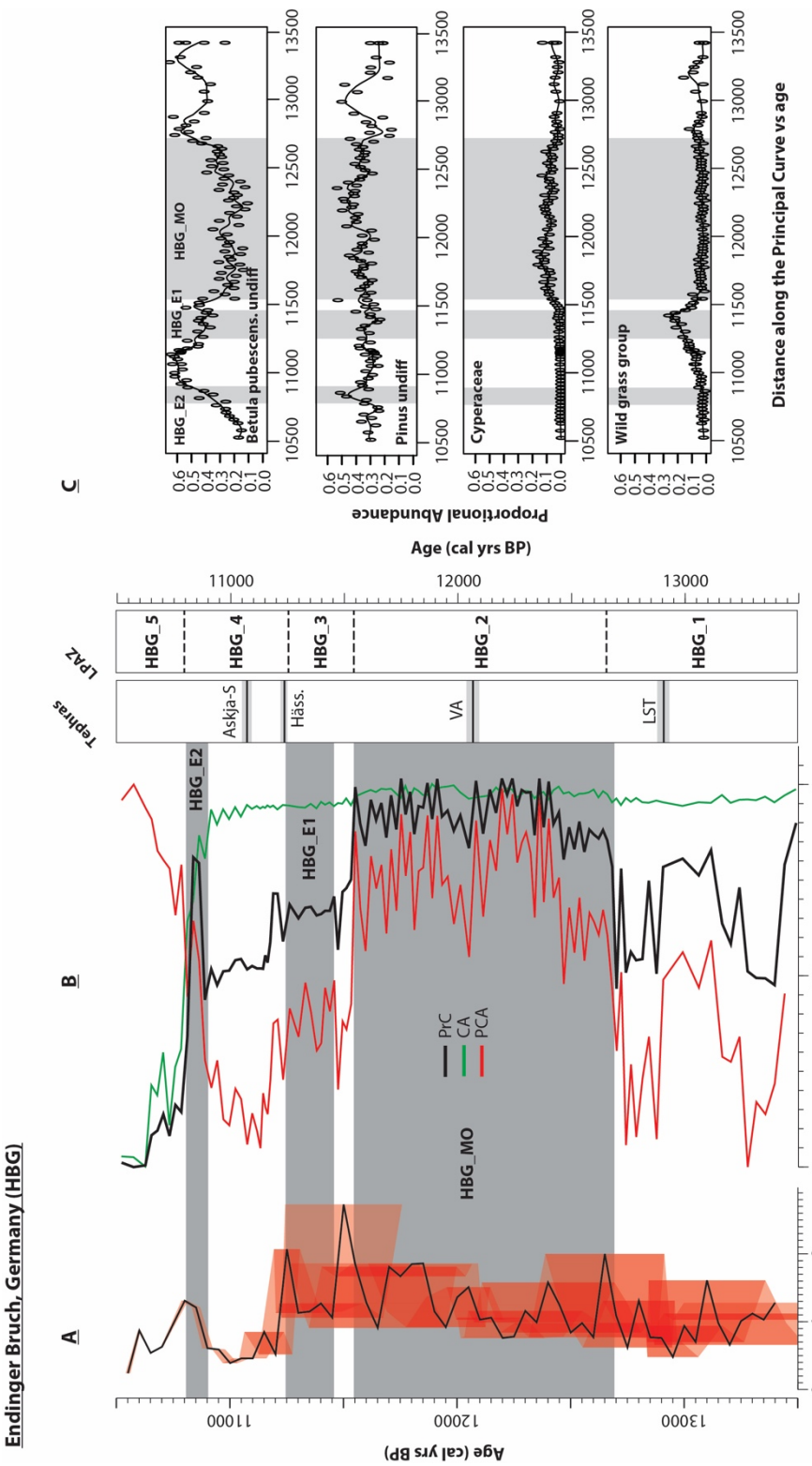


**Figure 7.21** The statistical results for the pollen percentage data from Endinger Bruch. A) RoC analysis for every 50 years. The values presented are exaggerated to provide clearer results into periods of significant change. The higher the bar, the more significant the composition' s change was. Light shading shows 1σ age error. B) The results of the different ordination tests (PCA, CoA and PrC). The grey boxes highlight oscillations identified from the PrC curve. C) The key taxa response curves modelled through the PrC. The grey boxes show the timing of the oscillations from the main PrC. Changes in the abundance of individual taxa at certain times provide insight into which taxa are driving the change. The record is plotted against calibrated age (μ ±1σ ) with light shading showing 1σ age error.

#### 7.2.5.2 Palaeoclimatic and palaeoenvironmental interpretation

This section will focus on reconstructing the climate and environmental history of Endinger Bruch using the pollen data previously presented. Based upon age modelling, identification of the LST, VA, Hässeldalen and Askja-S tephras and evident vegetational changes, LPAZ can be correlated to LGIT periods of the Allerød (HBG_1), YD (HBG_2) and EH (HBG_3-5).

**Allerød-YD transition (12,667±135 cal. BP)**

From the beginning of the record, herbaceous species associated with open grasslands began to decline (e.g. *Artemisia,* Poaceae, Figure 7.19). *Betula* became a dominant part of the local vegetation. *Pinus* soon expanded into the catchment at the expense of *Betula*, resulting in a mixed forest. The high percentage of these taxa indicate local occurrence rather than being far-travelled outside the catchment (Huntley and Birks, 1983; de Klerk, 2002). These forests continued to close resulting in the shrub-layer of *Juniperus* declining. LOI shows a general rise in organic matter with lithology having detritus input (Figure 7.19). This vegetation development indicates a warming climate associated with the Allerød period (e.g. Theuerkauf et al., 2012; van Asch et al., 2012).

After the LST, there is a gradual decline in *Pinus* with a rise in *Betula*. At 12,667 ±135 cal. BP, there is an increase in herbaceous taxa (e.g. *Artemisia*, Cyperaceae) with a rise in *Juniperus* and *Betula nana* shrubs (Figure 7.19). *Betula* declined while *Pinus* remained stable. A sharp decline in LOI with a short delay to silt and sand lithology indicates instability within the local catchment (Figure 7.19; de Klerk, 2002). These lines of evidence indicate the onset of the YD with deterioration in climatic conditions negatively affecting the vegetation assemblage (e.g. Theuerkauf et al., 2012; van Asch et al., 2012).

**YD-EH transition (11,516±137 cal. BP)**

At 11,516 ± 137 cal. BP, herbaceous taxa of *Artemisia,* Cyperaceae and Vaccinium declined (Figure 7.19). The shrub layer of *Juniperus* with *Betula nana* are quickly outcompeted as reforestation of the *Betula/Pinus* woodlands begins. Cyperaceae is still present yet in smaller percentages, indicating wetlands are still around the lake (de Klerk, 2002). LOI gradually rose as the climate continued to warm and the landscape stabilised into the EH (e.g. Theuerkauf et al., 2012; van Asch et al., 2012).

**Earliest Holocene oscillations**

The climate continues to warm with *Betula/Pinus* woodlands being dominant in the landscape (Figure 7.19). *Corylus* migrates into the area as vegetation succession takes overs climatic changes (de Klerk, 2002).

At 11,447 ± 128 cal. BP, a pause is observed in the PrC (Figure 7.21). The plateau in the curve is possibly identifying an increase in Wild grasses with an oscillation in *Betula* and *Pinus*. There is an overall increase in herbaceous taxa at this time (Figure 7.19). However, there is no decline in LOI or changes within lithology. RoC shows a peak at the end of this event (Figure 7.12). At 10,871 ± 21cal. BP, there is sharp increase in PrC with an increase in *Pinus* being the main influencing taxa at this time (Figure 7.21). Overall tree taxa decline. There is a slight decline of ~6% in LOI values yet no lithological change. A peak in vegetational overturn in RoC is seen towards the end of this event.

### 7.2.6 Lake Czechowskie, Poland

The master core, JC-M2015 was collected, sampled and pollen counted and identified by Florian Ott et al. (Ott pers. comms). Hundred and fifty samples were dated to the LGIT in this project with a sample resolution between 1-2cm. These samples TLP counts are >600 grains. Six LPAZ (JC_*n*) were identified (Table 7.17, Figure 7.22). PAR was also calculated (Figure 7.23).

**Table 7.17** The local pollen assemblage zones for Lake Czechowskie. Included are the name of zones, depth, ages for the beginning and end of the zones (μ±1σ) with key taxa observations and changes within each zone. Symbols depict:↑ increases and ↓ decreases in taxa percentage; ↕ oscillating or ↔ stability of values for particular taxa; ▲ taxa peak; ● taxa present at <5%; ✕ taxa disappears in that zone.

| Zone | Depth (cm) | Age (cal. BP) | Taxa changes through zone | Key taxa | LOI | Lithology |
|---|---|---|---|---|---|---|
| **JC_1** | 1270-1248.5 | 13,558±155 to 12,986±193 | ↑ *Pinus*; ↕ *Betula;* ↔ Poaceae; ● *B. nana, Juniperus, Salix, Artemisia* | *Pinus* | NA | Calcite varves into faintly laminated |
| **JC_2** | 1248.5-1176.5 | 12,986±193 to 11,423±143 | ↑ *Betula, Juniperus, Artemisia, Helianthemum,* Poaceae*;* ↓ *Pinus;* ● *B. nana,* Chenopodiaceae | *Betula, Juniperus* | NA | Faintly Laminated |
| **JC_3** | 1176.5-1158.5 | 11,423±143 to 11,239±18 | ↑ *Pinus,* Poaceae; ↓ *Betula;* ● *Juniperus, Salix, Artemisia;* ✕ Chenopodiaceae | *Pinus,* Poaceae | NA | Calcareous diatomaceous varves |
| **JC_4** | 1158.5-1135.5 | 11,239±18 to 11,015±79 | ↑ *Betula;* ↓ *Pinus,* Poaceae; ● *Juniperus, Salix, Artemisia* | *Betula, Pinus* | NA | Calcareous diatomaceous varves |
| **JC_5** | 1135.5-1120.5 | 11,015±79 to 10,854±131 | ↓ Betula; ↑ *Pinus;* ● Poaceae | *Betula, Pinus* | NA | Calcareous diatomaceous varves |
| **JC_6** | 1120.5-1084 | 10,854±131 to 10,464±104 | ↑ *Corylus, Ulmus;* ↔ *Pinus;* ↓ Betula; ● Poaceae | *Corylus, Pinus* | NA | Calcareous diatomaceous varves |

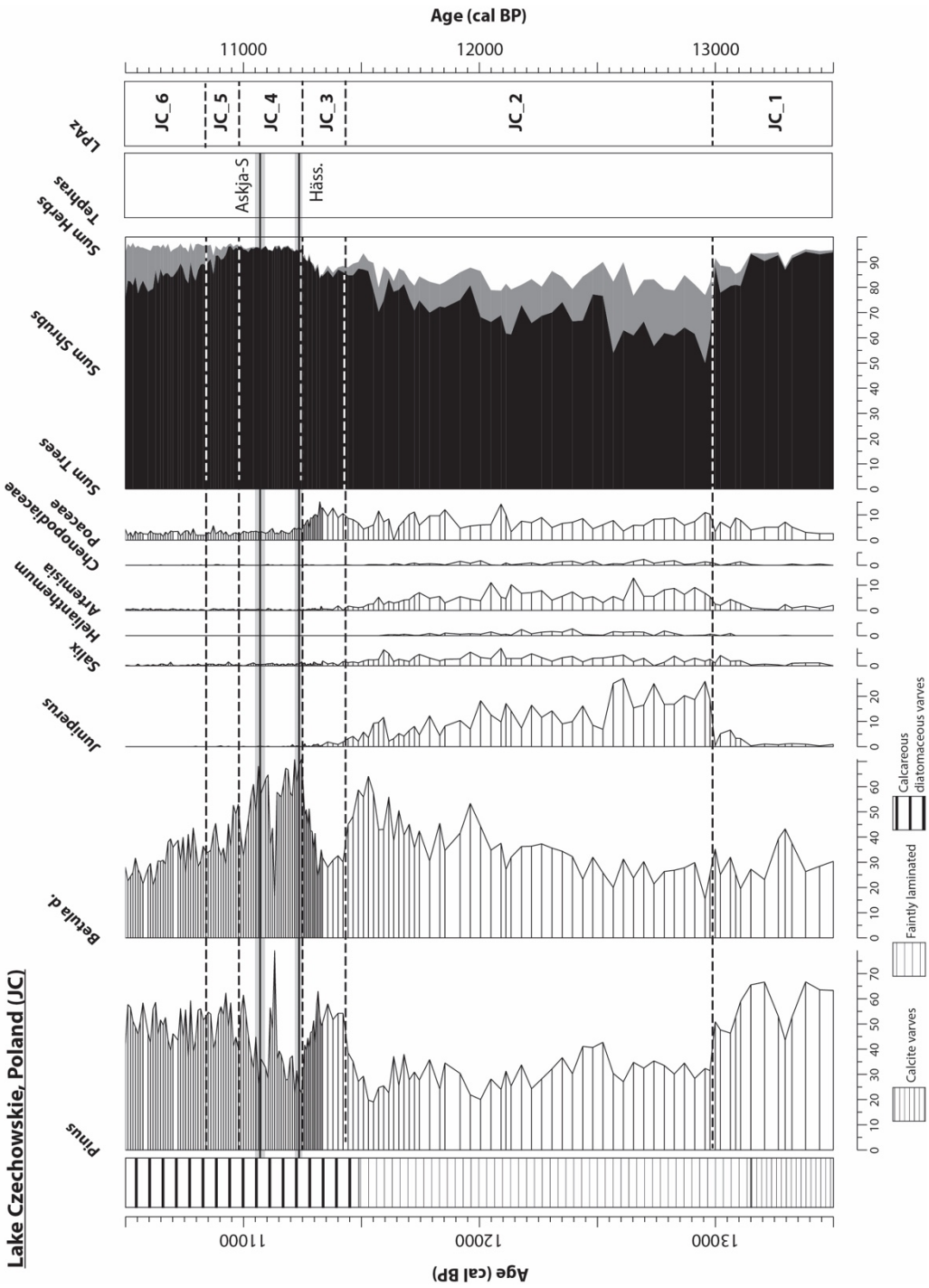


**Figure 7.22** Pollen percentage record of key taxa from Lake Czechowskie. The record is plotted against calibrated age (μ ±1σ ). All values are presented against TLP. Lithology presented as described by Ott et al. (2016). LPAZ are divided based upon changes in major taxa and CONISS. The Hässeldalen (Häss.) and Askja-S tephra were identified by Ott et al. (2016) and are plotted with this study' s new age estimate at μ ±1σ . Light shading shows 1σ age error.

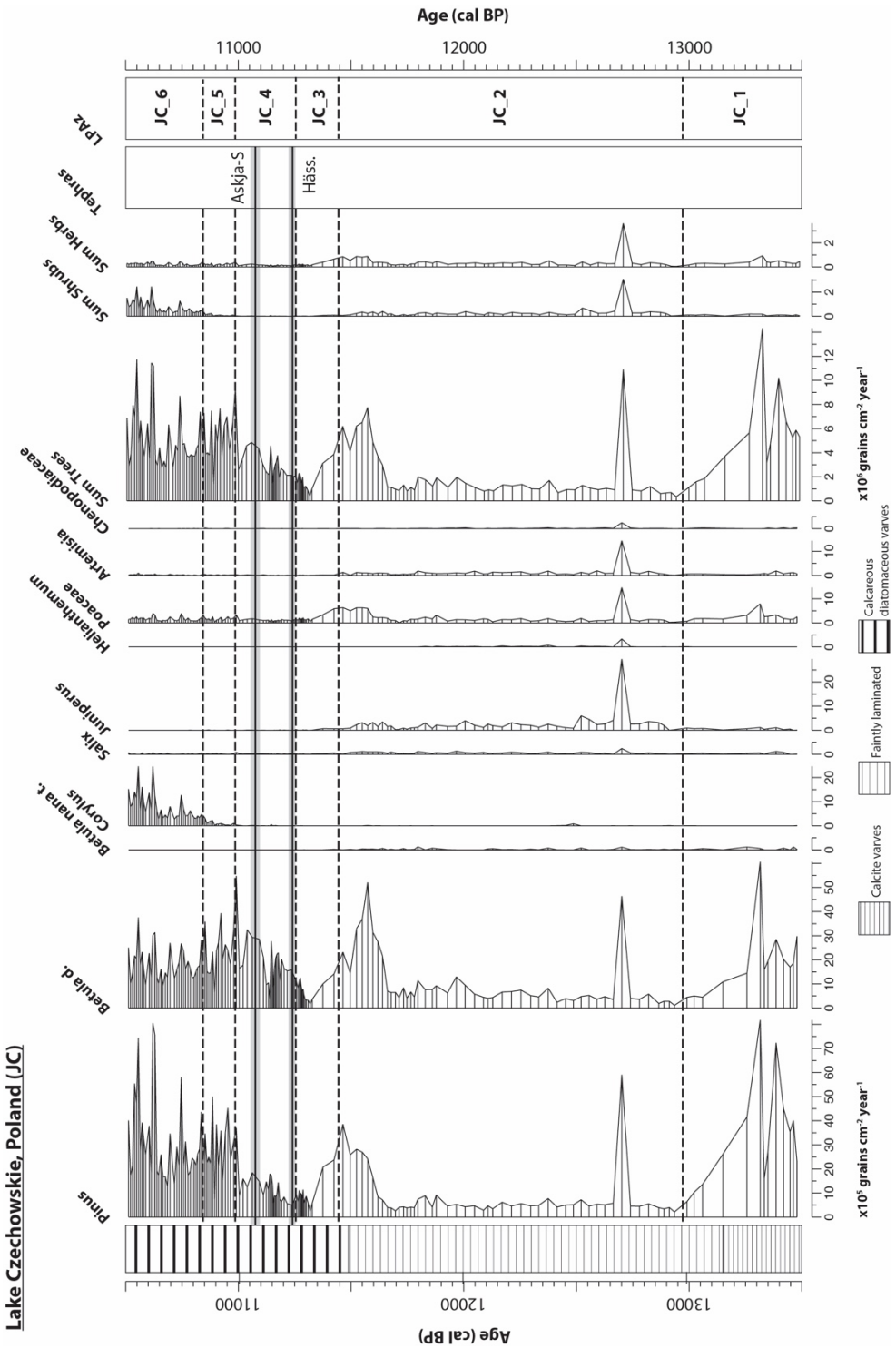


**Figure 7.23** Pollen accumulation rate (PAR) record of key taxa from Lake Czechowskie. The record is plotted against calibrated age (μ ±1σ ). Note the difference in x-axis scales used in the diagram. Lithology presented as described Ott et al. (2016). LPAZ are divided based upon changes in major taxa and CONISS in percentage diagram. The Hässeldalen (Häss.) and Askja-S tephra were identified by Ott et al. (2016) and are plotted with this study' s new age estimate at μ ±1σ . Light shading shows 1σ age error.

### 7.2.6.1 Statistical analysis

Statistical analysis was performed on Czechowskie pollen percentage dataset using taxa with abundances <2%. DCA results in Table 7.18 show a short axis length that is less than <1.5-3 SD, indicating PCA is the most appropriate analyses along with PrC to explore the dataset.

**Table 7.18** Detrended correspondence analysis results for Lake Czechowskie. The dataset shows short axis lengths and that axis 1 explains the most variation compared to the other axis

| | DCA1 | DCA2 | DCA3 | DCA4 |
|---|---|---|---|---|
| **Eigenvalue** | 0.1855 | 0.07513 | 0.04407 | 0.04258 |
| **Axis length** | 1.4243 | 1.07551 | 0.80734 | 0.83401 |

PCA results are shown in Figure 7.24. The first two principal components, axis 1 and 2 explain 34% and 14% of data variation, respectively. Taxa plotting negatively along axis 1 include *Corylus* (largest contributor), *Ulmus* and *Pinus* while taxa plotting positively include *Artemisia, Juniperus, Salix* and Poaceae. Intermediate taxa and those that plot strongly along axis 2 include *Betula*, *Rumex* and *Alnus*.

PrC allowed further exploration of the dataset. DCA results indicate that a PCA-based output is appropriate. However, when testing the PCA- and CoA-based outputs, CoA was deemed more suitable. This was due to converging in fewer iterations when similar penalty values were applied, with less overfitting of the data (PCA 11 versus CoA 7 iterations) as well as more variability captured by CoA (84% versus 75.86% PCA).

The PrC results identified a single MO with two additional oscillations (Table 7.19). These were defined by 1) increase in variance in the distance along the gradient and; 2) a pause in shifts towards lower values. RoC provided additional insight into these oscillations (Figure 7.25).

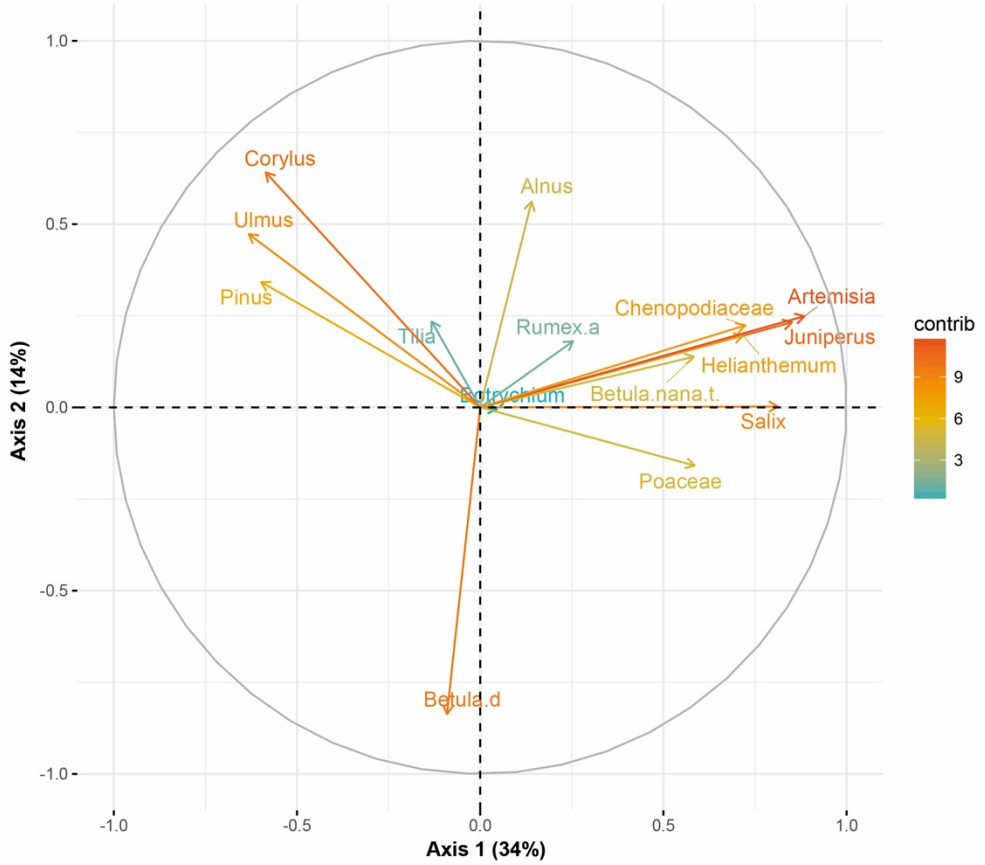


**Figure 7.24** Ordination diagram of the PCA results from Lake Czechowskie. The two axis, axis 1 and 2, present first two principal components. The pollen taxa are placed along the axis with the length and colour of the arrow indicating the taxa dominance along the axis. Along axis 1, woodland taxa plot negatively with taxa associated with cold and open herbaceous taxa plot positively. Axis 2 has an association with tree taxa.

**Table 7.19** Vegtation oscillations identified in the PrC for Lake Czechowskie. Symbols depict:↑ increases and ↓ decreases in taxa percentage

| Oscillation | Depth (cm) | Age (cal. BP) | Key taxa influence |
|---|---|---|---|
| JC_MO | 1248.5-1176.5 | 12,986±193 to 11,423±143 | ↓*Pinus,* ↑*Juniperus,* ↑*Betula* |
| JC_E1 | 1165.5-1146.5 | 11,284±34 to 11,126±49 | ↑*Betula,* ↓*Pinus* |
| JC_E2 | 1143.5-1134.5 | 11,097±38 to 11,004±85 | ↑*Betula,* ↓*Pinus* |

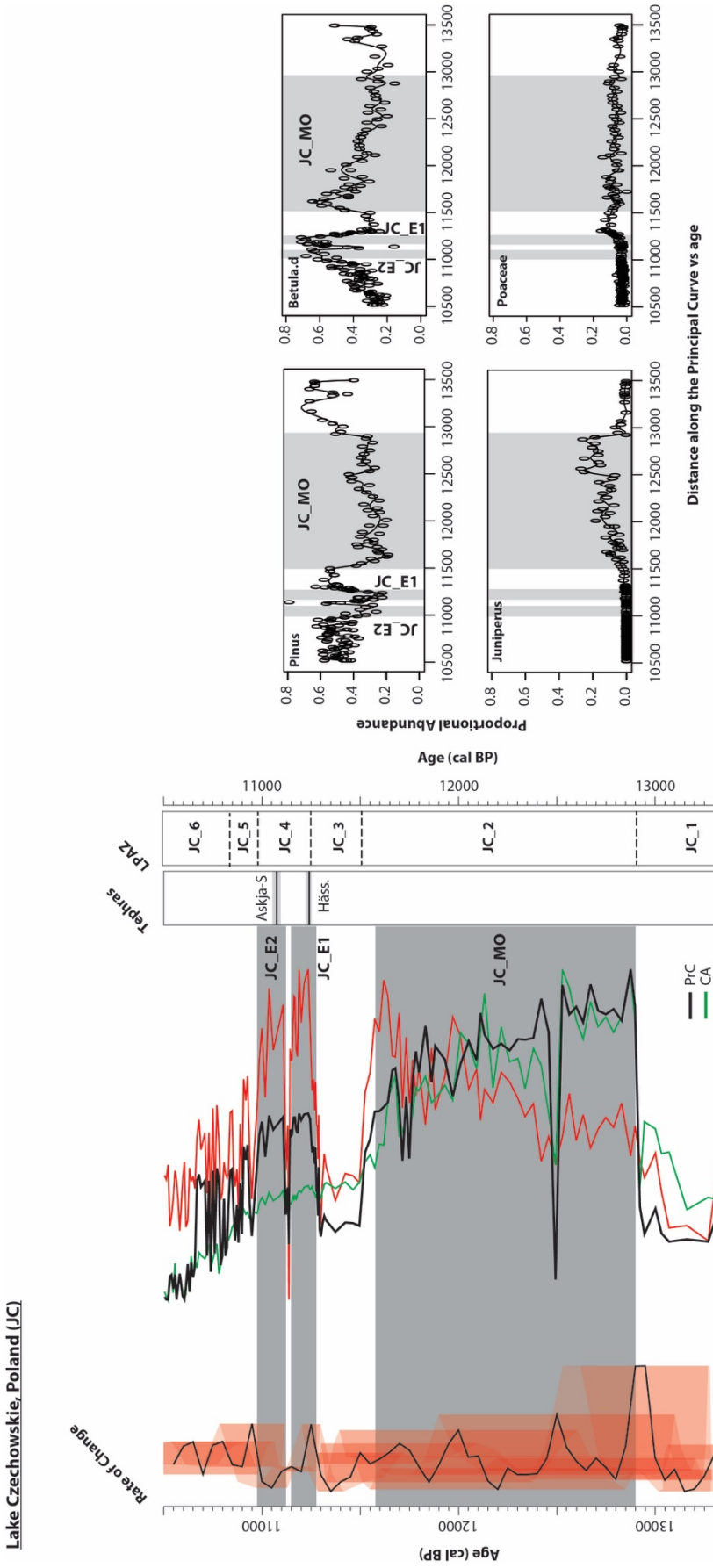


**Figure 7.25** The statistical results for the pollen percentage data from Lake Czechowskie. A) RoC analysis for every 50 years. The values presented are exaggerated to provide clearer results into periods of significant change. The higher the bar, the more significant the composition change was. Light shading shows 1σ age error. B) The results of the different ordination tests (PCA, CoA and PrC). The grey boxes highlight oscillations identified from the PrC curve. C) The key taxa response curves modelled through the PrC. The grey boxes show the timing of the oscillations from the main PrC. Changes in the abundance of individual taxa at certain times provide insight into which taxa are driving the change. The record is plotted against calibrated age (μ ±1σ ) with light shading showing 1σ age error.

### 7.2.6.2 Palaeoclimatic and palaeoenvironmental interpretation

This section will focus on the reconstructing the climate and environmental history using the pollen record previously presented. Based upon age modelling, identification of the Hässeldalen and Askja-S tephras as well as evident vegetational changes, LPAZ can be correlated to LGIT periods of the Allerød (JC_1), YD (JC_2) and EH (JC_3-6).

**Allerød-YD transition (12,986 ± 193 cal. BP)**

The beginning of the record saw a high percentage of tree taxa with *Pinus* being the dominant taxa in the local area (Figure 7.22, Huntley and Birks, 1983). Herbaceous taxa associated with open, tundra habitats (e.g. *Artemisia*, *Helianthemum* and Poaceae) declined as the woodland continued to develop. Pine woodlands were widely seen across NE Poland at this time and can be associated with the Allerød period (e.g. de Klerk, 2007; Kołaczek et al., 2013).

At 12,986 ± 193 cal. BP there was a sharp decline in tree taxa, mainly *Pinus* (Figure 7.22). As this woodland cover decreased, shrubs of *Juniperus* and *Salix* expanded. The steppe tundra taxa of *Artemisia*, Poaceae and Chenopodiaceae began to occupy the open landscape. The faint laminations recorded in the sediment indicate allochthonous material inwashed into the lake (Figure 7.22; Ott et al., 2016). In PAR, there was a decline in all taxa before this transition (Figure 7.23). Changes to a lower sedimentation rate probably affected the record (Engels et al., 2016). The decline in tree and rise in shrubs indicate the colder conditions in the YD stadial in NE Poland (e.g. Lauterbach et al., 2011; Kołaczek et al., 2013).

**YD-EH transition (11,423 ± 143 cal. BP)**

At 11,423 ± 143 cal. BP, *Betula* and *Pinus* increased and became the dominant part of the landscape while *Juniperus* and *Artemisia* declined. The spread of birch signalled the transition to the EH period across the region as temperatures began to warm (e.g. Lauterbach et al., 2011). *Pinus* soon became a dominant part of the landscape again with birch-pine woodlands on the landscape and herbaceous taxa declined (Figure 7.22).

**Earliest Holocene oscillations**

The continued expansion of thermophilous taxa saw the rise of *Corylus* and *Ulmus* within the pollen record as they migrated into the region (e.g. de Klerk, 2007; Kołaczek et al., 2013). At 11,284 ± 34 cal. BP and 11,097 ± 38 cal. BP, there are two positive peaks in the PrC. These events are driven by peaks *Betula* and troughs in *Pinus* (Figure 7.25). This is happens between the Hässeldalen and Askja-S tephras. In Figure 7.25, there is a clear oscillation in *Pinus* and *Betula* percentages. However, there is no clear change in other taxa at this time with no changes recorded in the overall tree or herbaceous taxa. PAR shows similar characteristics with taxa responses indicating that these phenomena are not an artefact expressed by the percentage of pollen data.

### 7.2.7 Lake Hämelsee, Germany

Lake Hämelsee core HÄM13 was collected, sampled and counted as part of Jones et al. (2018) and data supplied by Stefan Engels. Ninety-seven samples are dated to LGIT in this project with a sample resolution ranging from 5-0.5cm. TLP counts ranged from over >500 with a few samples having below 300 due to poor pollen preservation. Seven LPAZ were identified (HAM_*n,* Table 7.20; Figure 7.26) PAR were also calculated (Figure 7.27).

**Table 7.20** The local pollen assemblage zones for Lake Hämelsee. Included are the name of zones, depth, ages for the beginning and end of the zones (μ±1σ) with key taxa observations and changes within each zone. Symbols depict:↑ increases and ↓ decreases in taxa percentage; ↕ oscillating or ↔ stability of values for particular taxa; ▲ taxa peak; ● taxa present at <5%; ✕ taxa disappears in that zone.

| Zone | Depth (cm) | Age (μ±1σ, cal. BP) | Taxa changes through zone | Key taxa | LOI | Lithology |
|---|---|---|---|---|---|---|
| **HAM_1** | 1610.5-1565.5 | 13,495±38 to 12,999±85 | ↑ *Betula;* ↕ *Pinus,* Poaceae*;* ↓ *Salix;* ● *Juniperus, Artemisia, Filipendula* | *Betula* | ↑ | Very faint alternating light/dark layers into fine laminations |
| **HAM_2** | 1565.5-1531.5 | 12,999±85 to 12,716±55 | ↓ *Betula;* ↑ *Pinus;* ↕ *Salix,* Cyperaceae, Poaceae*;* ● *Juniperus, Artemisia, Filipendula* | *Betula, Pinus* | ↓ | Continuous fine laminations |
| **HAM_3** | 1531.5-1515.5 | 12,716±55 to 12,496±126 | ↑ Cyperaceae, Poaceae; ↓ *Betula,* Pinus; ● *Salix, Juniperus, Artemisia, Filipendula* | *Betula,* Cyperaceae | ↓ | Fine laminations into homogenous sediments |
| **HAM_4** | 1515.5-1474 | 12,496±126 to 11,769±171 | ↑ Cyperaceae, *Pinus*, *Salix, Empetrum;* ↓ *Betula;* ● *Juniperus, Artemisia, Filipendula* | Cyperaceae, *Pinus* | ● | Homogenous sediments |
| **HAM_5** | 1474-1454.5 | 11,769±171 to 11,237±133 | ▲ Poaceae; ↑ *Filipendula;* Sharp ↑ then ↓ *Betula;* ↓ *Pinus,* Cyperaceae, *Juniperus, Artemisia;* ✕ *Empetrum* | *Betula, Poaceae* | ↑ with ↓ then ↑ | Homogenous sediments into fine laminations |

| Zone | Depth (cm) | Age (μ±1σ, cal. BP) | Taxa changes through zone | Key taxa | LOI | Lithology |
|---|---|---|---|---|---|---|
| **HAM_6** | 1454.5-1426.5 | 11,237±133 to 10,758±162 | ↑ Betula, Cyperaceae; ↓ Poaceae, *Filipendula*; ↕ *Pinus, Salix;* ● *Juniperus, Artemisia* | *Betula* | ↕ | Concretion into alternating light/dark layers |
| **HAM_7** | 1426.5-1413.5 | 10,758±162 to 10,529±157 | ↑ *Corylus, Pinus;* ↓ *Betula;* ● Cyperaceae, Poaceae | *Corylus* | ↕ | Alternating light/dark layers |

### 7.2.7.1 Statistical analysis

Statistical analysis was conducted on Hämelsee's terrestrial taxa percentage data with taxa of abundances >2%. DCA results in Table 7.21 show the primary axis lengths. Results presented in Table show a short axis length demonstrating that PCA and PrC modelling are appropriate methods to explore the data variation.

**Table 7.21** Detrended correspondence analysis results for Lake Hämelsee. The dataset shows short axis lengths and that axis 1 explains the most variation compared to the other axis.

| | DCA1 | DCA2 | DCA3 | DCA4 |
|---|---|---|---|---|
| **Eigenvalue** | 0.1216 | 0.07611 | 0.02862 | 0.05997 |
| **Axis length** | 1.3446 | 0.97557 | 0.70832 | 0.9007 |

Figure 7.28 presents the PCA results. Axis one explains 27.1% of taxa variability, while axis two explains 18.4%. Along axis 1, taxa observed plotting negatively include Cyperaceae, *Empetrum*, *Artemisia* and *Juniperus*. Taxa that plot positively include *Betula* (most significant contributor) and Brassicaceae. Corylus and *Pinus.* Taxa that are intermediate and those with a stronger affinity with axis 2 include *Pinus*, *Corylus*, and *Filipendula*.

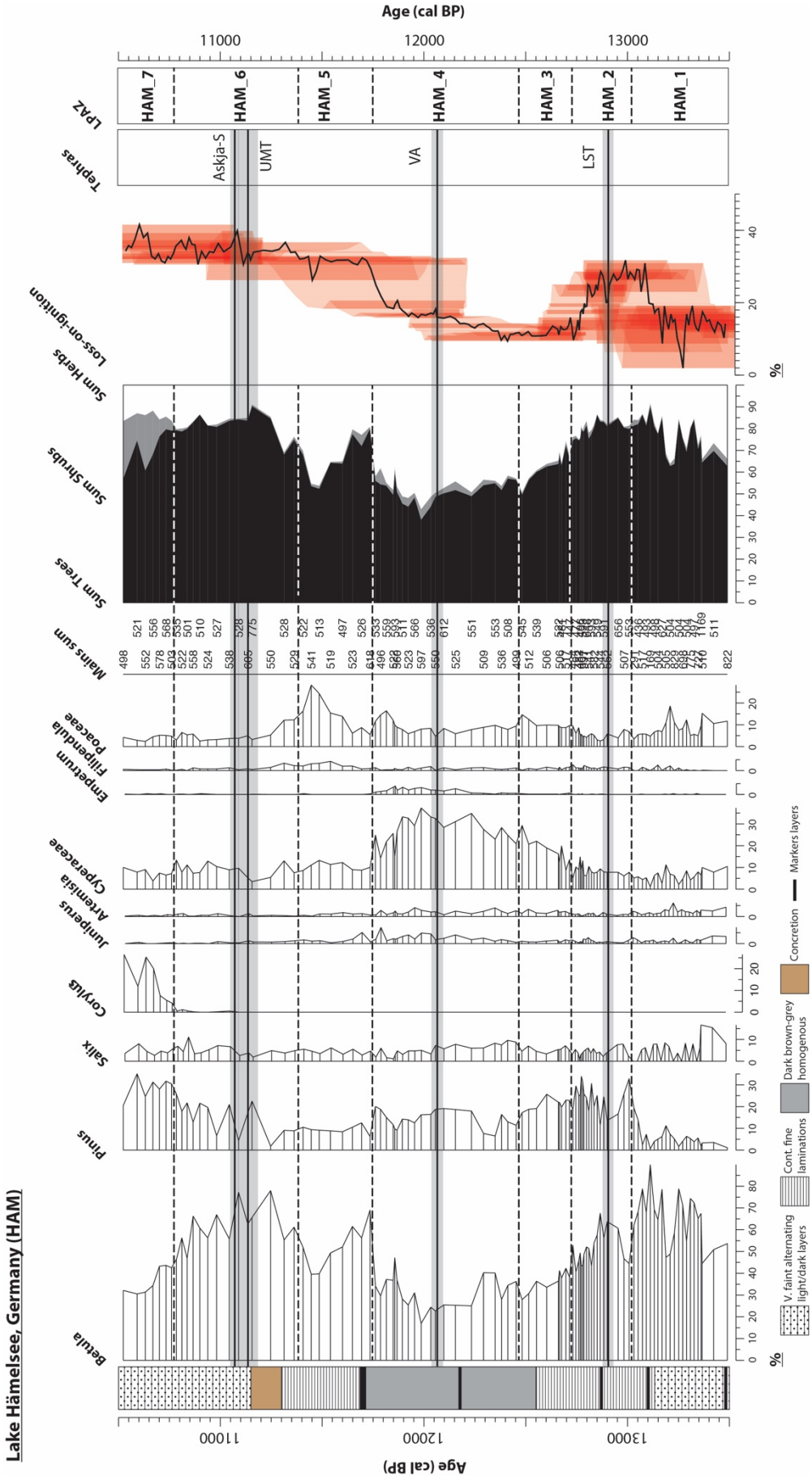


**Figure 7.26** Pollen percentage record of key taxa from Lake Hämelsee. The record is plotted against calibrated age (μ ±1σ ). All values are presented against TLP. Lithology presented as described by Jones et al. (2018). Percentage LOI is plotted. LPAZ are divided based upon changes in major taxa and CONISS. The Laacher See Tephra (LST), Vedde Ash (VA), Hässeldalen (Häss.) and Askja-S tephra was identified by Jones et al. (2018) and is plotted with this study' s new age estimate at μ ±1σ . Light shading shows 1σ age error.

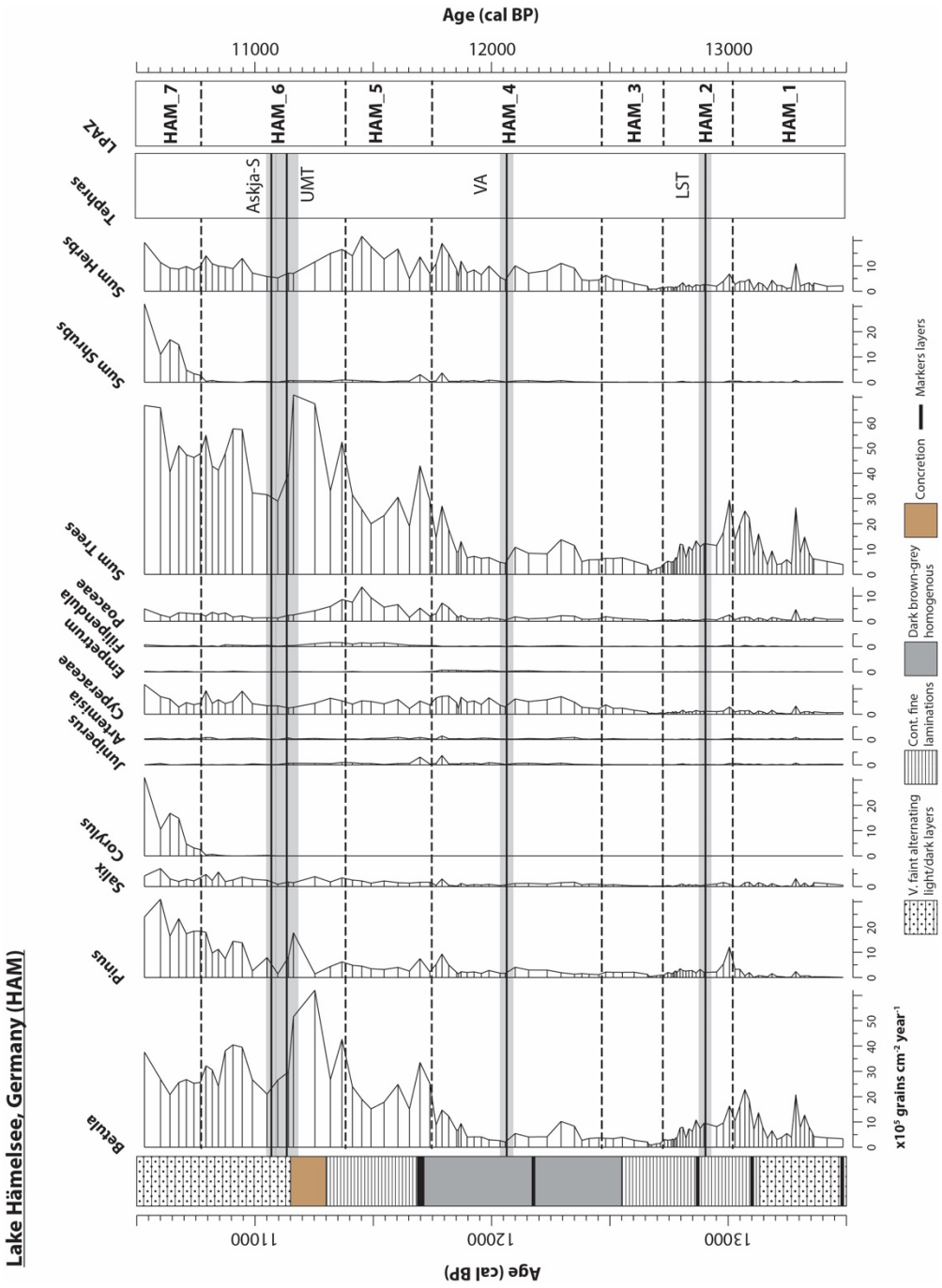


**Figure 7.27** Pollen accumulation rate (PAR) record of key taxa from Lake Hämelsee. The record is plotted against calibrated age ($\mu \pm 1\sigma$ ). Lithology presented as described by Jones et al (2018). LPAZ are divided based upon changes in major taxa and CONISS in percentage diagram. The Laacher See Tephra (LST), Vedde Ash (VA), Hässeldalen (Häss.) and Askja-S tephra was identified by Jones et al. (2018) and is plotted with this study' s new age estimate at $\mu \pm 1\sigma$ . Light shading shows $1\sigma$ age error.

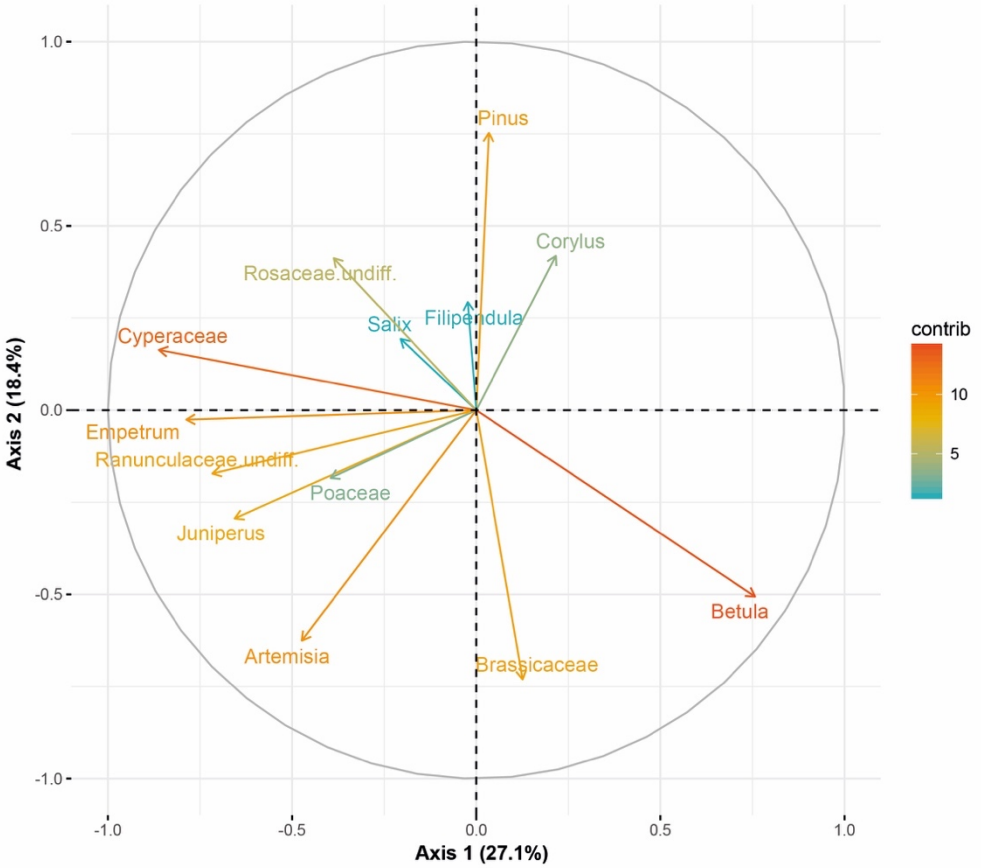


**Figure 7.28** Ordination diagram of the PCA results from Lake Hämelsee. The two axis, axis 1 and 2, present first two principal components. The pollen taxa are placed along the axis with the length and colour of the arrow indicating the taxa dominance along the axis. Along axis 1, taxa associated with stadial conditions plot negatively while taxa associated with interstadial conditions plot positively. Axis 2 has an association with mixed taxa.

To explore the dataset further, PrC was undertaken. The short lengths of the DCA axis length indicate a PCA-based output. The CoA-based approach was also tested to further confirm this approach. Under similar penalty values, PCA-based output explained more data variation (77.2%) than CoA-based output (56.9%) in fewer iterations (4 vs 7 for CoA).

Changes in PrC data show a single MO and two additional oscillations with a decline in PrC values (Figure 7.29). Table 7.22 presents the timing of these oscillations along with the proposed taxa that are driving the change.

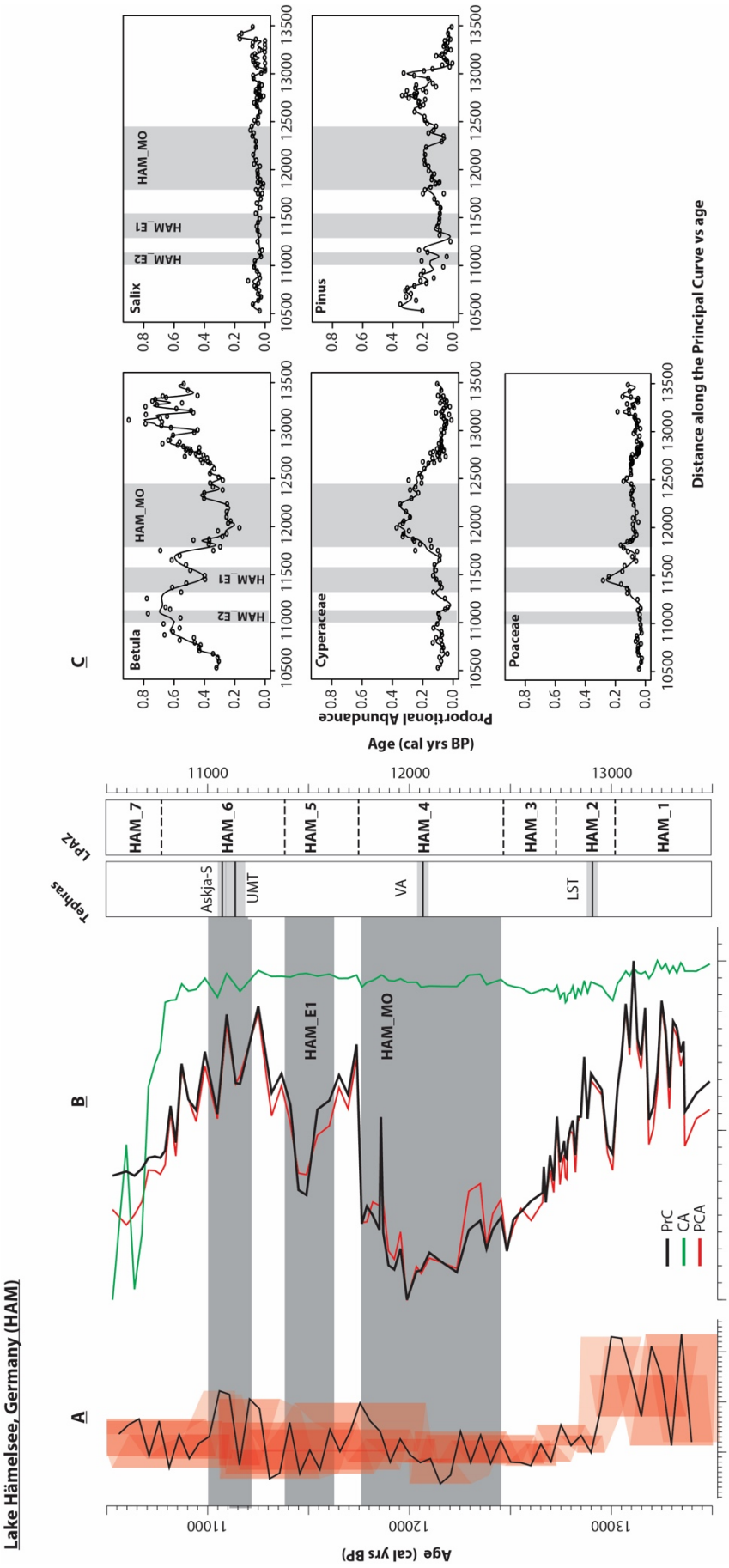


**Figure 7.29** The statistical results for the pollen percentage data from Lake Hämelsee. A) RoC analysis for every 50 years. The values presented are exaggerated to provide clearer results into periods of significant change. The higher the bar, the more significant the composition' s change was. Light shading shows 1σ age error. B) The results of the different ordination tests (PCA, CoA and PrC). The grey boxes highlight oscillations identified from the PrC curve. C) The key taxa response curves modelled through the PrC. The grey boxes show the timing of the oscillations from the main PrC. Changes in the abundance of individual taxa at certain times provide insight into which taxa are driving the change. The record is plotted against calibrated age (μ ±1σ ) with light shading showing 1σ age error.

**Table 7.22** Vegtation oscillations identified in the PrC for Lake Hämelsee. Symbols depict:↑ increases and ↓ decreases in taxa percentage

| Oscillation | Depth (cm) | Age (cal. BP) | Key taxa influence |
|---|---|---|---|
| HAM_MO | 1531.5-1474 | 12,716±55 to 11,769±171 | ↓*Betula,* ↑Cyperaceae, ↕*Pinus* |
| HAM_E1 | 1468.5-1458.5 | 11,619±199 to 11,346±176 | ↑Poaceae, ↓*Betula* |
| HAM_E2 | 1450.5-1440.5 | 11,137±51 to 11,006±93 | ↓ *Betula,* ↕*Pinus* |

### 7.2.7.2 Palaeoclimatic and palaeoenvironmental interpretation

This section will focus on reconstructing the climate and environmental history of Hämelsee using the pollen data previously presented. Based upon age modelling, identification of the LST, VA, UMT and Askja-S tephra with evident vegetational changes, LPAZ can be correlated to LGIT periods of the Allerød (HAM_1-2), YD (HAM_3-4 and EH (HAM_5-7).

**Allerød-YD transition (12,716±55 cal. BP)**

At the beginning of the pollen record, *Betula* increased followed by *Pinus* as the climate continued to warm into the Allerød. Pollen percentages are high for these two species indicating that these were a significant part of the local habitat (Figure 7.26; Huntley and Birks 1983). The herbaceous taxa of *Artemisia*, Cyperaceae declined. The sediment lithology of the core changed to continuous laminations (Figure 7.26). No information was received about these laminations, yet Merkt and Müller (1999) obtained a core from the same site. This older core's laminations contained mineral precipitation with an increased organic matter, linked to a warmer and stable climate (Merkt and Müller, 1999). These results can be assumed to be the same for the new HÄM13 core in this thesis. The LOI shows an increased organic matter as the local catchment became more productive and stable

(Figure 7.26). This is the warm Allerød period (e.g. Brauer et al., 2001; Theuerkauf et al., 2012).

At 12,716 ± 55 cal. BP, there was a gradual decline of *Betula* and *Pinus* and a rise in Cyperaceae, Poaceae and *Artemisia* (Figure 7.26). This opening of the woodland environment is associated with climatic deterioration of the YD stadial (e.g. Litt and Stebich, 1999; Brauer et al., 2001). This progressive vegetation transition is also reflected in PAR (Figure 7.27). LOI values gradually declined after the LST. Lithology changes from laminations to a homogenous layer (probably silty-clay) as the local landscape became more unstable (Merkt and Müller, 1999).

**YD-EH transition (11,769±171 cal. BP)**

At 11,769 ± 171 cal. BP, there was a sharp rise in *Betula* with this taxon becoming dominant in the growing woodland (Figure 7.26, Figure 7.27). There was a decline in herbaceous taxa of *Artemisia* and Cyperaceae occurs as open grasslands receded, indicating climatic amelioration of the EH (Litt and Stebich, 1999; Brauer et al., 2001). The LOI increased as the landscape became more stable and organic matter increased. Lithology shows laminations developed again, possibly with similar sedimentary characteristics to those in the Allerød, indicating warmer climate (Merkt and Müller, 1999).

**Earliest Holocene oscillations**

The EH saw a continued increase in tree taxa, with *Betula* woodlands replaced by Pinus and the thermophilous taxa of *Corylus* and *Ulmus* as the climate continued to warm (Figure 7.26). At 11,619 ± 199 cal. BP there was pronounced decline in the PrC (Figure 7.29). The curve is identifying a decrease in *Betula* with a peak in Poaceae and increases in Cyperaceae and *Filipendula*. There was also a decline of ~6% in LOI values. However, no

considerable change was seen vegetational composition recorded by RoC (Figure 7.29). There is a further decline in the PrC at 11,137±51 cal. BP. The changes in PrC values were driven by a decline in *Betula* and oscillating *Pinus*. This is clearly seen in PAR at this time with peak in RoC too (Figure 7.27). A decline of ~3% was seen in LOI values.

### 7.2.8 Węgliny, Poland

Węgliny WE10/2 core was collected, sampled and counted by Jurochnik and Nalepka (2013). Twenty samples are dated from this project to the LGIT with a varied sample resolution of 10-22cm. TLP counts were above 400 with >1,000 counted in EH samples. Four LPAZ were identified (WE_*n*, Table 7.23, Figure 7.30). No PAR was calculated.

**Table 7.23 The local pollen assemblage zones for Węgliny.** Included are the name of zones, depth, ages for the beginning and end of the zones (μ±1σ) with key taxa observations and changes within each zone. Symbols depict:↑ increases and ↓ decreases in taxa percentage; ↕ oscillating or ↔ stability of values for particular taxa; ▲ taxa peak; ● taxa present at <5%; ✕ taxa disappears in that zone.

| Zone | Composite Depth (cm) | Age (μ±1σ, cal. BP) | Taxa changes through zone | Key taxa | LOI | Lithology |
|---|---|---|---|---|---|---|
| **WE_1** | 645.5-625.25 | 13,552±114 to 13,365±95 | ↓ *Pinus;* ↑ *Betula,* Poaceae; ● *Artemisia* | *Pinus, Betula* | ↑ | Gyttja with organic matter |
| **WE_2** | 625.25-550.5 | 13,365±95 to 12,672±58 | ↑ then ↓ *Pinus;* ↑ *Betula,* ↕ Poaceae; ● *Artemisia* | *Pinus, Betula* | ↑ then ↓ | Gyttja with organic matter |
| **WE_3a** | 550.5-491 | 12,672±58 to 12,115±76 | ↓ *Betula;* ↑ *Pinus, Artemisia;* Poaceae | *Pinus, Betula,* Poaceae | ↕ | Gyttja with organic matter to calcareous gyttja |
| **WE_3b** | 491-430.5 | 12,115±76 to 11,548±59 | ↓ *Pinus;* ↑ *Betula,* Poaceae; ● *Alnus, Artemisia* | *Pinus, Betula,* Poaceae | ↕ | *Gyttja* |
| **WE_4** | 430.5-391 | 11,548±59 to 11,184±28 | ↑ *Betula;* ↓ *Pinus,* Poaceae | *Pinus, Betula* | ↑ | Gyttja to calcareous gyttja |
| **WE_5** | 391-319.5 | 11,184±28 to 10,570±77 | ↕ *Pinus, Betula;* ● *Alnus, Artemisia* | *Pinus, Betula* | ↓ | Calcareous gyttja |

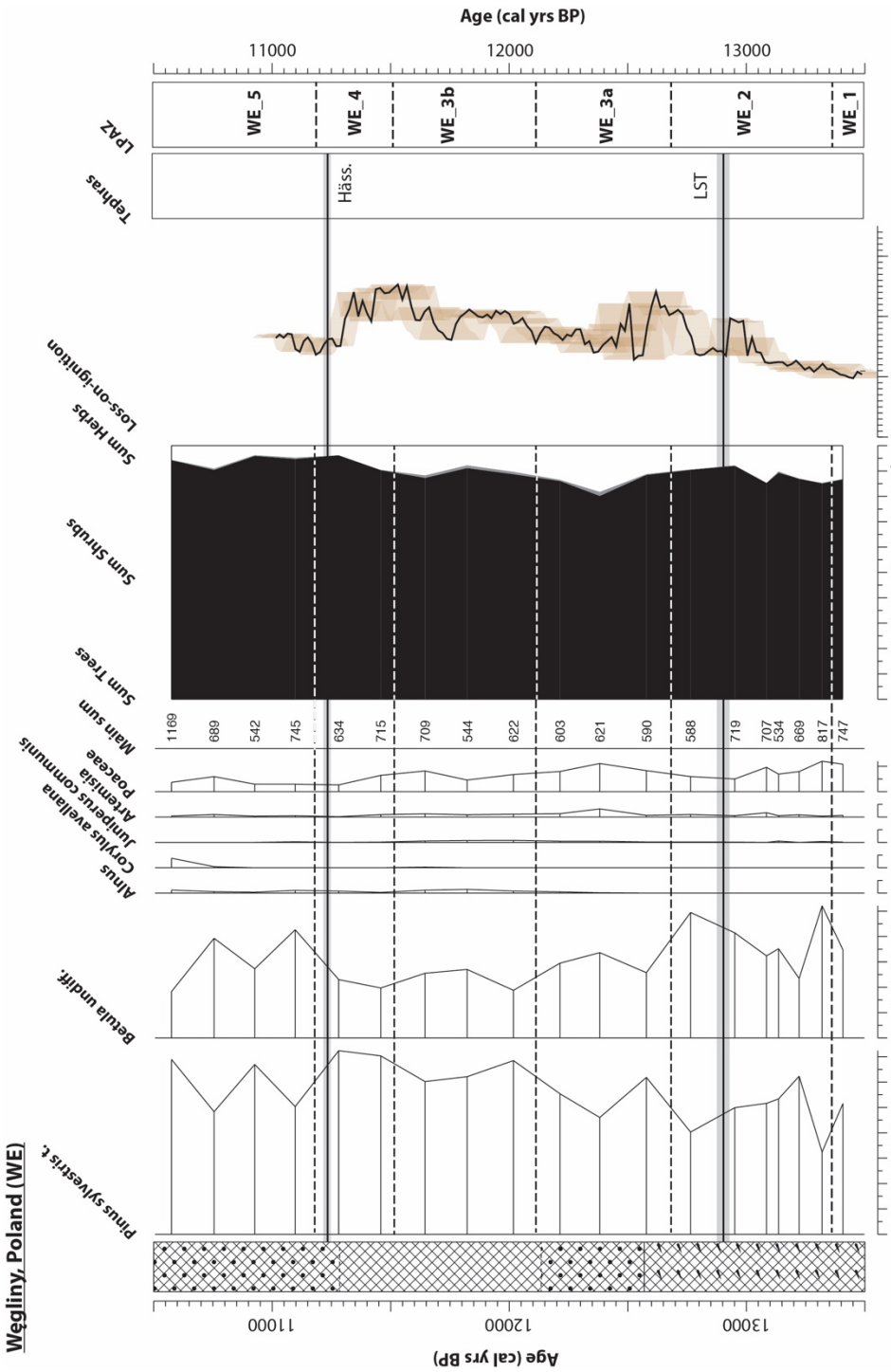


**Figure 7.30** Pollen percentage record of key taxa from Węgliny. The record is plotted against calibrated age (μ ±1σ ). All values are presented against TLP. Lithology presented as described by Jurochnik and Nalepka (2013). Percentage LOI is plotted. LPAZ are divided based upon changes in major taxa and CONISS. The Laacher See (LST) and Hässeldalen (Häss.) tephra identified by Housley et al. (2013) and is plotted with this study' s new age estimate at μ ±1σ . Light shading shows 1σ age error.

#### 7.2.8.1 Statistical analysis

Statistical analysis was performed on taxa with >2% abundances from Węgliny's terrestrial percentage pollen data. DCA results in Table 7.24 show a very short axes lengths, less than 1.5 SD, suggesting PCA is more appropriate method to explore the data, along with PrC modelling.

**Table 7.24** Detrended correspondence analysis results for Węgliny. The dataset shows short axis lengths and that axis 1 explains the most variation compared to the other axis.

| | DCA1 | DCA2 | DCA3 | DCA4 |
|---|---|---|---|---|
| **Eigenvalue** | 0.05138 | 0.01539 | 0.013782 | 0.0139797 |
| **Axis length** | 0.68125 | 0.34217 | 0.337122 | 0.3373543 |

Figure 7.31 shows the results of PCA. Axis 1 shows 43.9% of the data variability, while axis 2 explains 27.3% of the variability. Taxa that plots negatively along axis one are *Pinus* (most significant contributor) and *Corylus* with positive taxa being *Betula,* Poaceae and *Artemisia.* The intermediate taxa is *Betula* undiff.

To explore the data further PrC was undertaken. The DCA results indicated that a PCA-based output would be more appropriate model. Modelling was conducted using both PCA and CoA-based approaches. A CoA-based output was chosen overall due to converging in fewer iterations when the same penalty values was applied (4 versus 6 PCA). When the penalty was set high, PCA produced a straight line through the data resulting in an overfitting and unrealistic results. The PCA-based approach accounted for the high variability of the data 97.1% while CA was 94.4%. However, there were lower degrees of freedom with the CoA-based output.

The PrC results identified one MO and one minor oscillation (Figure 7.32, Table 7.25). The chord distance for RoC show little changes across the whole record (Figure 7.32).

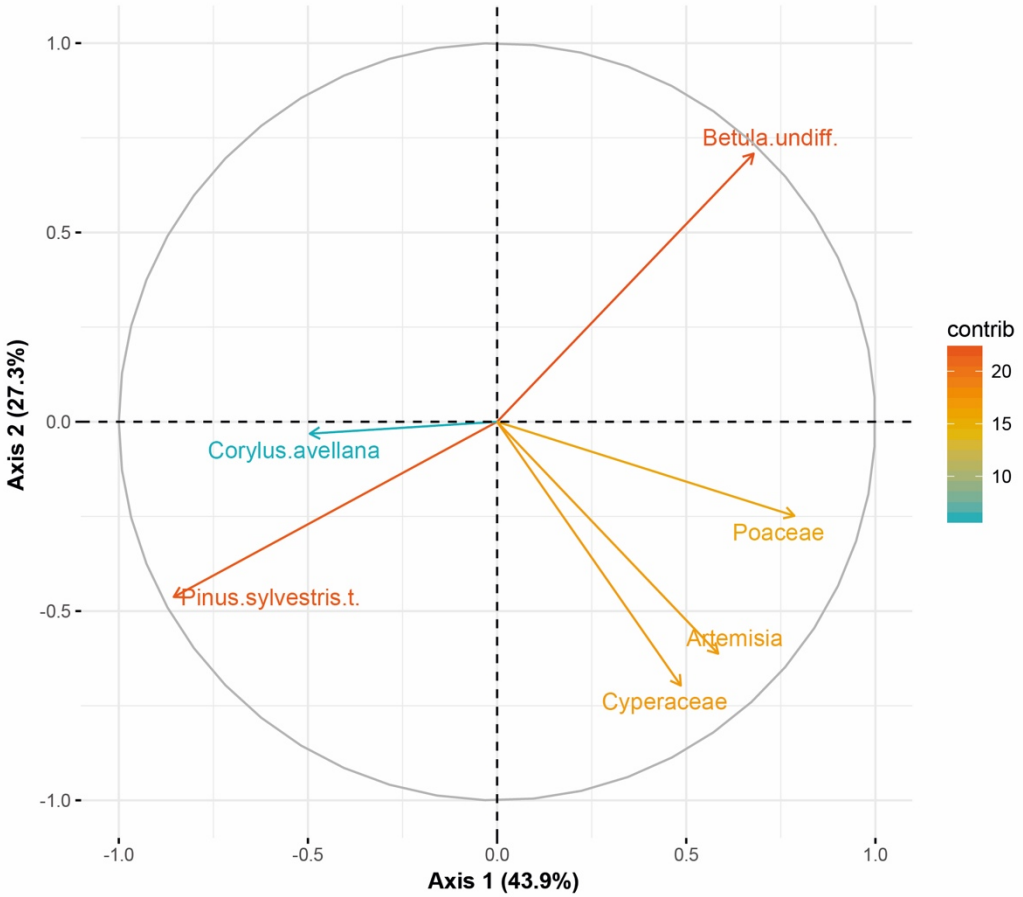


**Figure 7.31** Ordination diagram of the PCA results from Węgliny. The two axis, axis 1 and 2, present first two principal components. The pollen taxa are placed along the axis with the length and colour of the arrow indicating the taxa dominance along the axis. Along axis 1, woodland taxa plot negatively while taxa associated with cold, open herbaceous plot positively.

**Table 7.25** Vegtation oscillations identified in the PrC for Węgliny. Symbols depict:↑ increases and ↓ decreases in taxa percentage.

| Oscillation | Depth (cm) | Age (cal. BP) | Key taxa influence |
|---|---|---|---|
| WE_MO | 550.5-430.5 | 12,672±58 to 11,548±59 | ↓*Betula,* ↑Pinus |
| WE_E1 | 370.5-350.4 | 11,008±48 to 10,836±61 | ↓*Betula,* ↑*Pinus* |

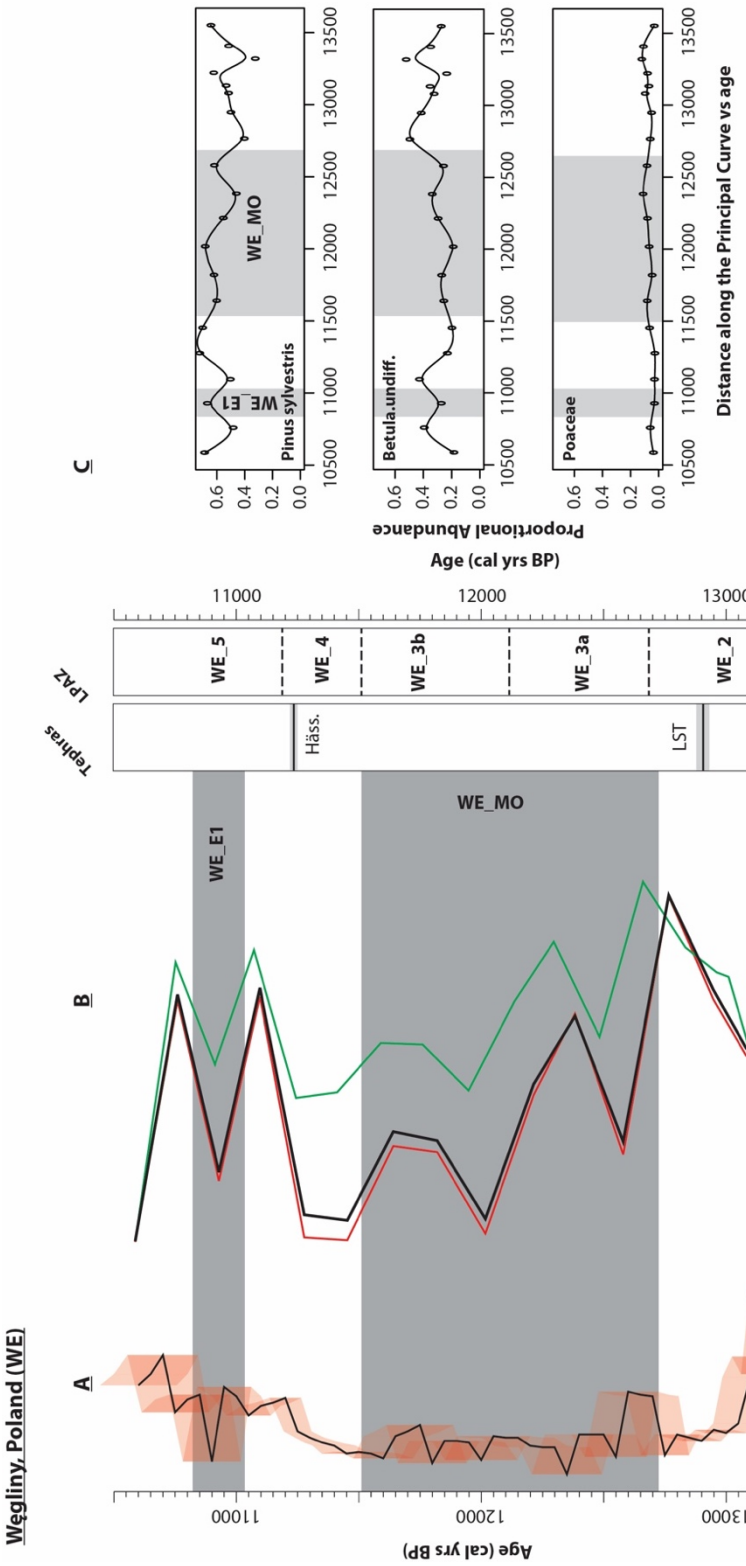


**Figure 7.32** The statistical results for the pollen percentage data from Węgliny. A) RoC analysis for every 50 years. The values presented are exaggerated to provide clearer results into periods of significant change. The higher the bar, the more significant the composition's change was. Light shading shows 1σ age error. B) The results of the different ordination tests (PCA, CoA and PrC). The grey boxes highlight oscillations identified from the PrC curve. C) The key taxa response curves modelled through the PrC. The grey boxes show the timing of the oscillations from the main PrC. Changes in the abundance of individual taxa at certain times provide insight into which taxa are driving the change. The record is plotted against calibrated age (μ ±1σ ) with light shading showing 1σ age error.

#### 7.2.8.2 Palaeoclimatic and palaeoenvironmental interpretation

This section will focus on the reconstructing the climate and environmental history using the pollen record previously presented. Based upon age modelling, identification of the LST, and Hässeldalen tephra with evident vegetational changes, LPAZ is correlated to the LGIT periods of the Allerød (WE_1-2), YD (WE_3) and EH (WE_4-5).

**Allerød-YD transition (12,672±58 cal. BP)**

At the beginning of the record, *Betula* and *Pinus* became a dominant part of the vegetational landscape (Figure 7.30). Woody taxa rose while herbaceous taxa of Poaceae and *Artemisia* declined. *Pinus* was the dominant taxa with local occurrences due to the high percentage (Huntley and Birks, 1983). Organic matter slowly increased as the landscape became more stable with vegetation (Figure 7.30). The presence of *Pinus* and *Betula* indicated warmer temperatures of 12-13$^{o}$C (Theuerkauf et al., 2014). These vegetational assemblages correlate to the regional Allerød period seen in Polish pollen records (e.g. Latałowa and Borówka, 2006; Kulesza et al., 2011).

At 12,672 ± 58 cal. BP, there was a slight decline in *Betula* while *Pinus* increased, continuing its dominance of the landscape (Figure 7.30). The herbaceous taxa of Poaceae increased with the appearance of *Artemisia*. Both taxa indicate an opening of the forest. Overall, the changes in herbaceous pollen help define the transition into the YD (e.g. Gosler et al., 1999; Pawłowski et al., 2016). Also, there was a decline in LOI, linked to increased inorganic matter as fluvial erosion and weathering increased as the climate deteriorated (Brauer et al., 1999).

**YD-EH transition (11,548±59 cal. BP)**

There was limited vegetation change during the YD stadial at Węgliny with *Pinus* remaining the dominant taxon. There were minimal changes in herbaceous taxa of Poaceae and *Artemisia* (Figure 7.30). At 11,548 ± 59 cal. BP, *Corylus* migrated into the record showing a transition to warmer, milder climatic conditions indicative of the EH (Figure 7.30; Theuerkauf et al., 2014). The herbaceous taxa of Poaceae and *Artemisia* declined as *Pinus* reforestation began. Yet, this was a very subtle vegetation transition. LOI showed an increase in organic matter as the landscape became more stable (Figure 7.30).

**Earliest Holocene oscillations**

*Corylus* increased as the climate became warmer. Herbaceous taxa declined as pine-birch forests dominated the landscape. The vegetation remained largely stable with little variation in the percentage data (Figure 7.30). However, at 11,008 ± 48 cal. BP, a decrease in PrC values was observed. The PrC is identifying decreases in *Betula* and increases in *Pinus* (Figure 7.32). There was also a decline in LOI values after the Hässeldalen tephra.

### 7.2.9 Soppensee, Switzerland

Soppensee core of SO89-23 was collected, sampled and, pollen counted by Lotter et al. (1999). These samples were cross-correlated to the master core SO89-17 using event layers (Lotter et al., 1999; Lotter per. comms). Forty-five samples dated to the LGIT in this project with a sample resolution range of ~1-4cm from the transferred resolution onto the master core. TLP is high with ranges from 500 to <1,000 pollen counts. Five LPAZ (SOP_*n*) were identified (Table 7.26, Figure 7.33). PAR was also calculated (Figure 7.34).

**Table 7.26** The local pollen assemblage zones for Soppensee. Included are the name of zones, depth, ages for the beginning and end of the zones (μ±1σ) with key taxa observations and changes within each zone. Symbols depict:↑ increases and ↓ decreases in taxa percentage; ↕ oscillating or ↔ stability of values for particular taxa; ▲ taxa peak; ● taxa present at <5%; ✕ taxa disappears in that zone.

| Zone | Composite Depth (cm) | Age (μ±1σ, cal. BP) | Taxa changes through zone | Key taxa | LOI | Lithology |
|---|---|---|---|---|---|---|
| **SOP_1** | 617.4 - 609.85 | 13,449±103to 13,218±48 | ▲ *Betula;* ↑ *Pinus;* ↔ Poaceae; ● *Juniperus, Artemisia,* Cyperaceae | *Betula* | NA | Homogenous |
| **SOP_2** | 609.85-587.4 | 13,218±48 to 12,680±97 | ↓ *Betula;* ↑ *Pinus;* ↔ Poaceae; ● *Juniperus, Artemisia,* Cyperaceae | *Pinus, Betula* | NA | Laminated fine detritus gyttja |
| **SOP_3** | 587.4-544.95 | 12,680±97 to 11,576±94 | ↕ *Pinus;* ↓ *Betula;* ↑ *Juniperus, Apiaceae, Artemisia,* Cyperaceae, Poaceae | *Pinus,* Poaceae | ↑ | Homogenous layer to Laminated fine detritus gyttja |
| **SOP_4** | 544.95-520.25 | 11,576±94 to 11,089±22 | ↑ *Betula;* ↔ *Pinus;* ↓ *Corylus, Juniperus, Apiaceae, Artemisia,* Cyperaceae, Poaceae | *Pinus, Betula* | ↑ then ↕ | Laminated fine detritus gyttja |
| **SOP_5** | 520.25-506.5 | 11,089±22 to 10,435±72 | ↑ *Corylus, Ulmus;* ↓ *Betula, Pinus;* ● Poaceae, Cyperaceae | *Corylus* | ↓ then ↑ | Laminated fine detritus gyttja |

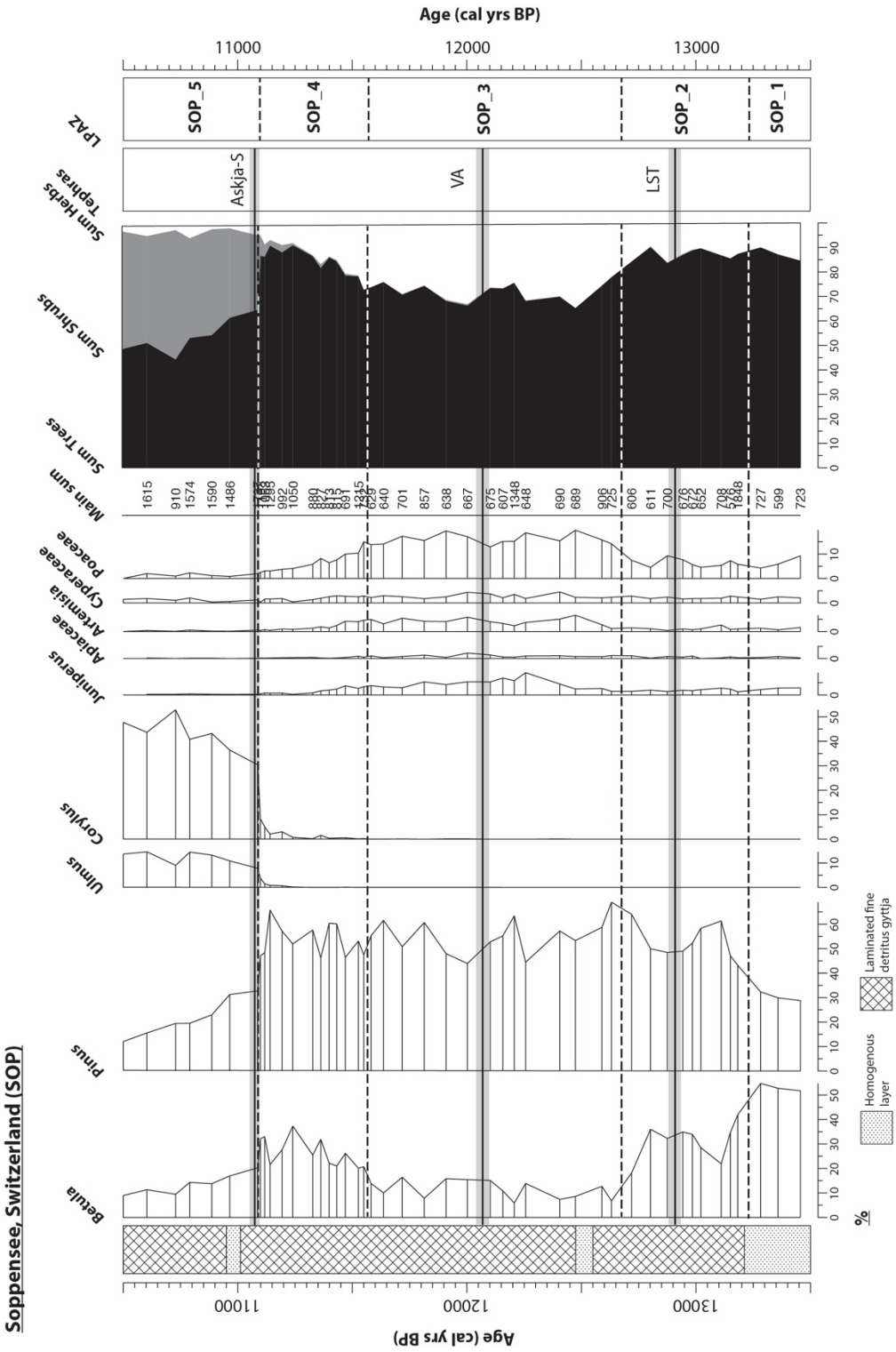


**Figure 7.33** Pollen percentage record of key taxa from Soppensee. The record is plotted against calibrated age (μ ±1σ ). All values are presented against TLP. Lithology presented as described by Lotter et al. (1999). LPAZ are divided based upon changes in major taxa and CONISS. The Laacher See (LST), Vedde Ash (VA) and Askja-S tephra were identified by Lane et al. (2012a) and are plotted with this study' s new age estimate at μ ±1σ . Light shading shows 1σ age error.

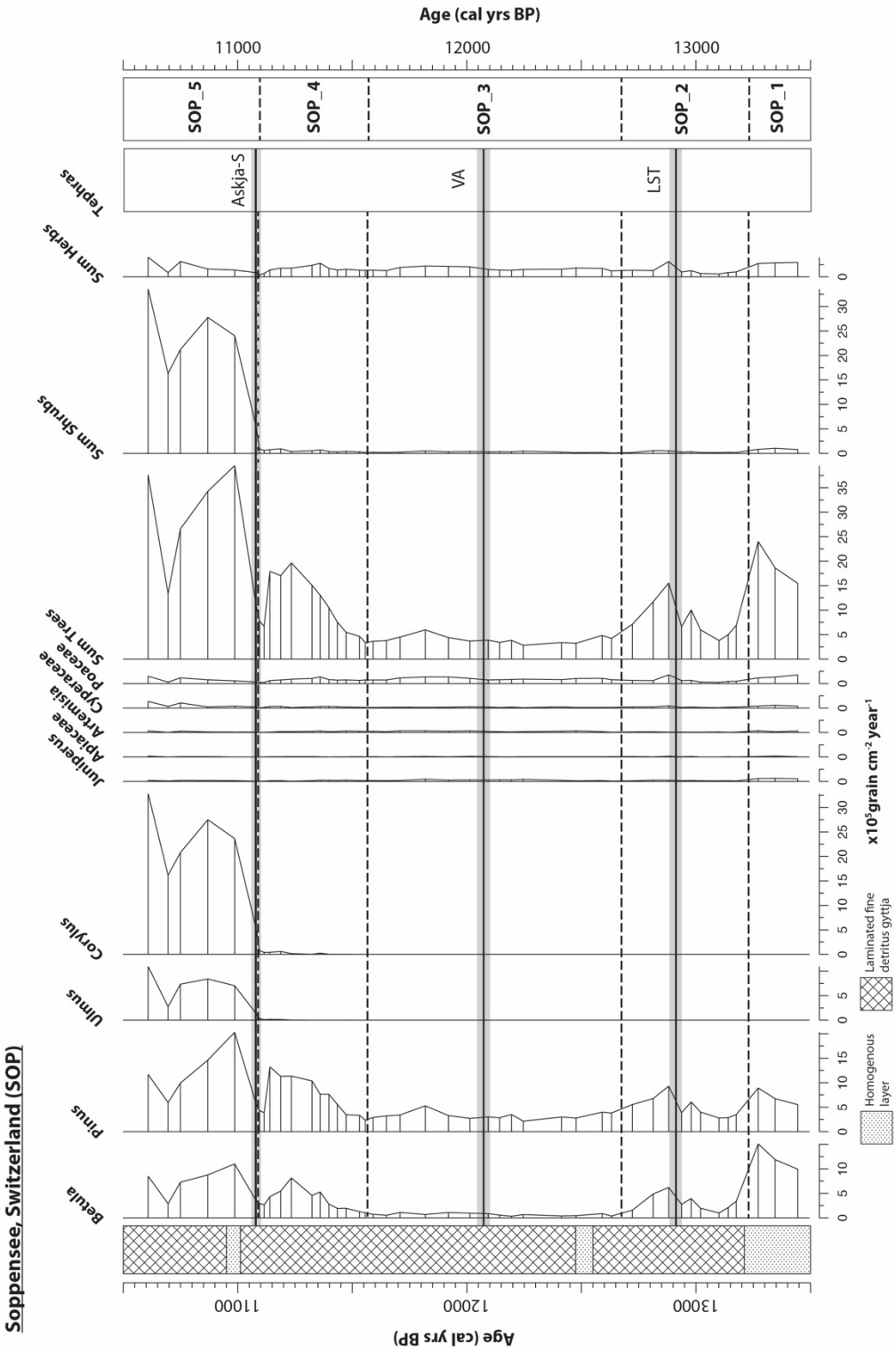


**Figure 7.34** Pollen accumulation rate (PAR) record of key taxa from Soppensee. The record is plotted against calibrated age (μ ±1σ ). Lithology presented as described by Lotter et al. (1999). LPAZ are divided based upon changes in major taxa and CONISS. The Laacher See (LST), Vedde Ash (VA) and Askja-S tephra were identified by Lane et al. (2011a) and are plotted with this study' s new age estimate at μ ±1σ . Light shading shows 1σ age error.

#### 7.2.9.1 Statistical analysis

Statistical analysis was conducted on the terrestrial percentage pollen data of Soppensee with taxa that had abundances of >2%. DCA results in Table 7.27 show short-axis lengths. These lengths demonstrate that PCA, CoA and PrC are appropriate to explore the data (<1.5-3SD).

**Table 7.9** Detrended correspondence analysis results for Soppensee. The dataset shows short axis lengths and that axis 1 explains the most variation compared to the other axis.

| | DCA1 | DCA2 | DCA3 | DCA4 |
|---|---|---|---|---|
| **Eigenvalue** | 0.3636 | 0.04988 | 0.041368 | 0.042340 |
| **Axis length** | 2.0853 | 0.80694 | 0.746149 | 0.751899 |

Figure 7.35 presents the PCA results. Axis 1 explains 56.3% of the data variability, while axis 2 explains 21.4% of the variability. Along axis 1, species that plot negatively includes deciduous tree taxa of *Quercus* (most significant contributor), *Corylus and Ulmus*. Taxa that plot positively along axis 1 include open-habitat taxa of *Artemisia, Juniperus* and Poaceae. Taxa that are intermediate and have a strong affinity to axis 2 include *Betula* and *Pinus*.

PrC allowed further to exploration of changes in vegetation. The DCA results indicated both PCA and CoA-based approaches were appropriate. A PCA-based output was chosen over a CoA output. This was due to a better convergence in fewer iterations (PCA 5 verses CoA 10) when the same penalty conditions were applied, even with CoA capturing higher data variance (PCA 92% versus CoA 96.5%).

PrC results identified one major oscillation with two additional oscillations depicted by 1) a positive increase in the distance along the gradient and; 2) a general pause in the gradient (Figure 7.36, Table 7.28). These were accompanied by oscillations in RoC (Figure 7.36).

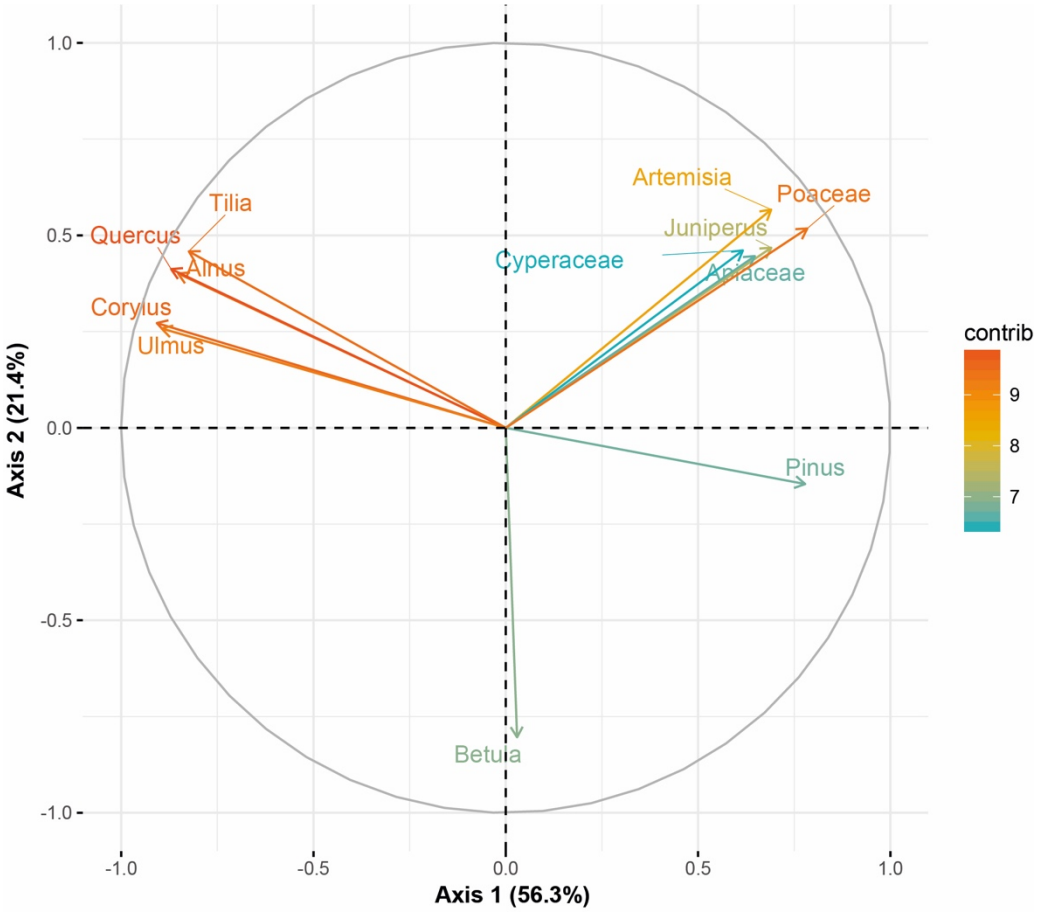


**Figure 7.35** Ordination diagram of the PCA results from Soppensee during the LGIT. The two axis, axis 1 and 2, present first two principal components. The pollen taxa are placed along the axis with the length and colour of the arrow indicating the taxa dominance along the axis. Along axis 1, deciduous tree taxa associated with warmer climates plot negatively while open, colder herbaceous taxa plot positively.

**Table 7.28** Vegtation oscillations identified in the PrC for Soppensee. Symbols depict:↑ increases and ↓ decreases in taxa percentage.

| Oscillation | Depth (cm) | Age (cal. BP) | Key taxa influence |
|---|---|---|---|
| SOP_MO | 587.4-544.95 | 12,680±97 to 11,576±94 | ↑*Pinus*, ↑Poaceae ↓*Betula* |
| SOP_E1 | 541.75-536 | 11,504±92 to 11,381±87 | ↑*Pinus*, ↓*Betula* |
| SOP_E2 | 528.1-520.25 | 11,212±60 to 11,089±22 | ↑*Pinus*, ↓*Betula*, ↔*Corylus* |

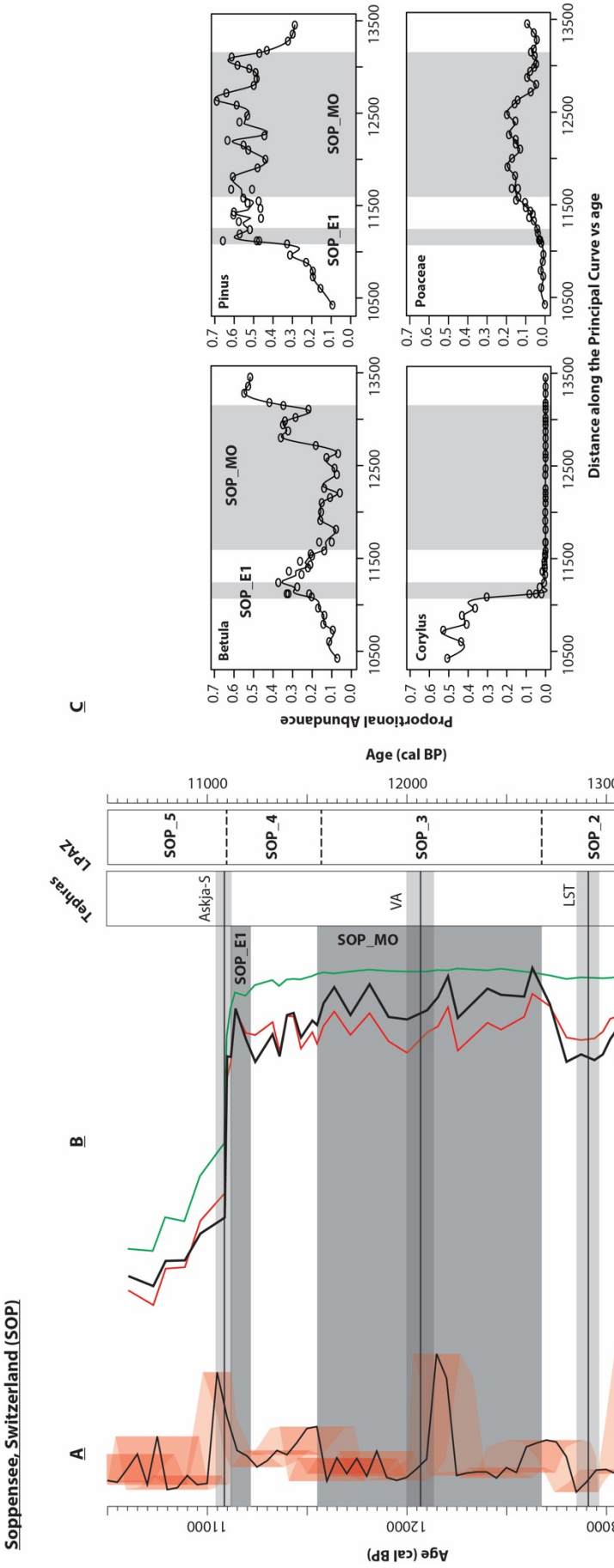


**Figure 7.36** The statistical results for the pollen percentage data from Soppensee. A) RoC analysis for every 50 years. The values presented are exaggerated to provide clearer results into periods of significant change. The higher the bar, the more significant the composition's change was. Light shading shows 1σ age error. B) The results of the different ordination tests (PCA, CoA and PrC). The grey boxes highlight oscillations identified from the PrC curve. C) The key taxa response curves modelled through the PrC. The grey boxes show the timing of the oscillations from the main PrC. Changes in the abundance of individual taxa at certain times provide insight into which taxa are driving the change. The record is plotted against calibrated age (μ ±1σ ) with light shading showing 1σ age error.

### 7.2.10 Rotsee, Switzerland

Rotsee core RL205 was collected, sampled, and the pollen counted by Lotter et al. (1992). These sample depths were cross-correlated to the master core RL05 using event layers and changes in stable isotopes (Verbruggen et al., 2010; Lotter and Lane per. comms). Forty-five were dated to the LGIT in this study project with sample resolution to <1-5cm on RL05. TLP counts are high with 500 to >1,000 individual grains counted. Five LPAZ were identified (RO_*n*, Table 7.29, Figure 7.37). PAR was also calculated (Figure 7.38).

**Table 7.10** The local pollen assemblage zones for Rotsee. Included are the name of zones, depth, ages for the beginning and end of the zones (μ±1σ) with key taxa observations and changes within each zone. Symbols depict:↑ increases and ↓ decreases in taxa percentage; ↕ oscillating or ↔ stability of values for particular taxa; ▲ taxa peak; ● taxa present at <5%; ⨯ taxa disappears in that zone.

| Zone | Composite Depth (cm) | Age (μ±1σ, cal. BP) | Taxa changes through zone | Key taxa | LOI | Lithology |
|---|---|---|---|---|---|---|
| **RO_1** | 1078.89-1058.2 | 13,537±44 to 12,674±49 | ↓ *Betula;* ↑ *Pinus;* ● *Salix, Artemisia,* Cyperaceae, Poaceae | *Betula, Pine* | ↕ | Marl gyttja to Gyttja to Marl gyttja |
| **RO_2** | 1058.2-1024.6 | 12,674±49 to 11,377±92 | ▲ then ↔ *Pinus;* ↓ *Betula;* ↑ *Artemisia,* Cyperaceae, Poaceae | *Betula, Pine,* Poaceae | ● | Marl gyttja transition to silty, marl gyttja |
| **RO_3** | 1024.6-1008.625 | 11,377±92 to 10,847±85 | ↓ *Pinus;* ↑ *Betula;* ↓ Poaceae; ● *Artemisia,* Cyperaceae | *Betula, Pine* | ● | Silty, marl gyttja to marl gyttja |
| **RO_4** | 1008.625-1006.375 | 10,847±85 to 10,774±77 | ▲ *Pinus;* ↓ *Betula;* ● *Corylus, Salix,* Poaceae, Cyperaceae | *Pinus* | Sharp ↑ to ▲ then sharp ↓ | Marl to marl gyttja |
| **RO_5** | 1006.375-991 | 10,774±77 to 10,525±64 | Sharp ↑ *Corylus;* ↑*Alnus, Quercus;* ↓ *Pinus, Betula;* ● Poaceae, Cyperaceae | *Corylus* | Gradual ↑ | marl gyttja |

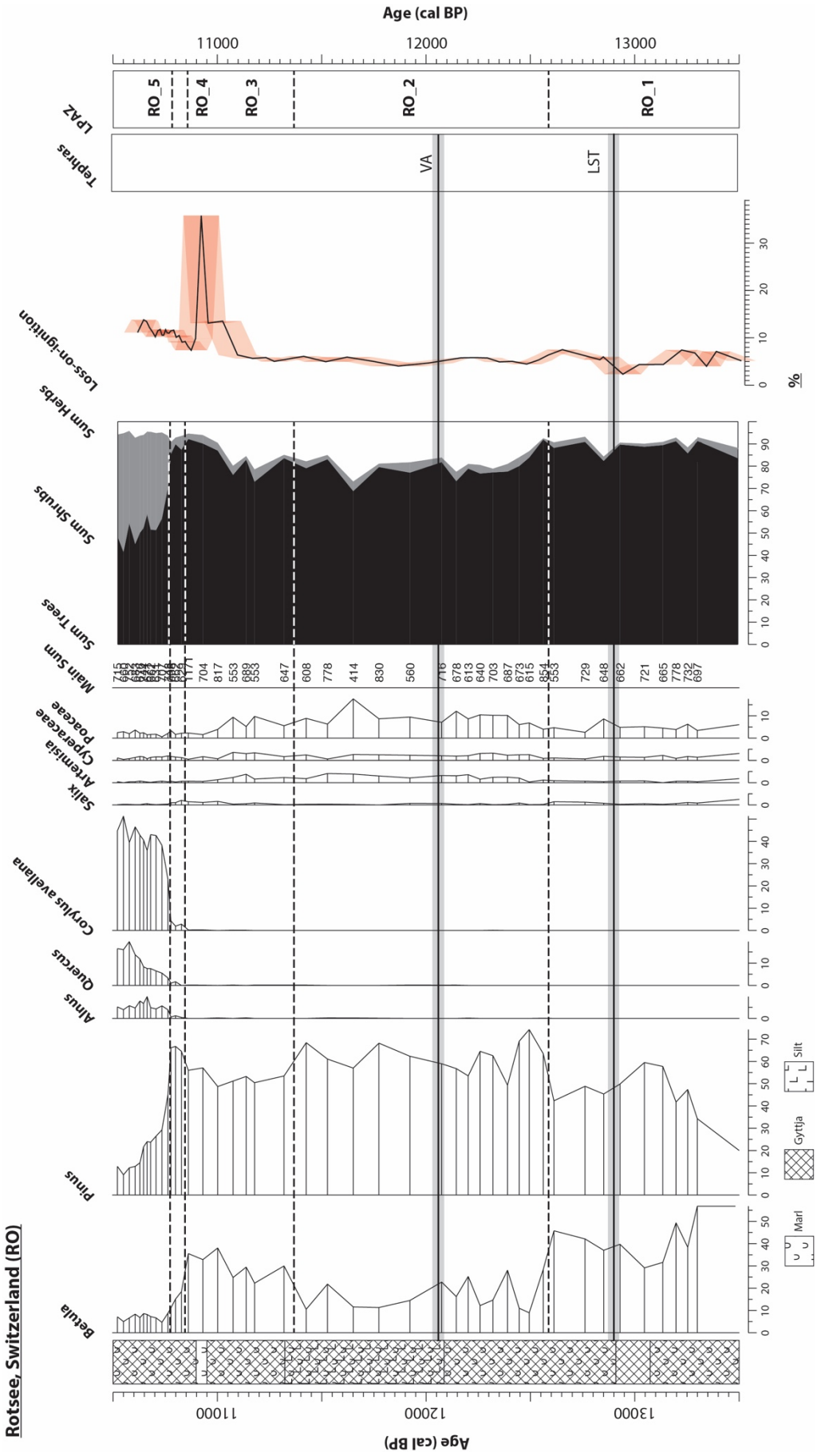


**Figure 7.37** Pollen percentage record of key taxa from Rotsee. The record is plotted against calibrated age (μ ±1σ ). All values are presented against TLP. Lithology presented as described by Lotter et al. (1992). LPAZ are divided based upon changes in major taxa and CONISS. The Laacher See (LST) and Vedde Ash (VA) were identified by Lane et al. (2012c) and are plotted with this study' s new age estimate at μ ±1σ . Light shading shows 1σ age error.

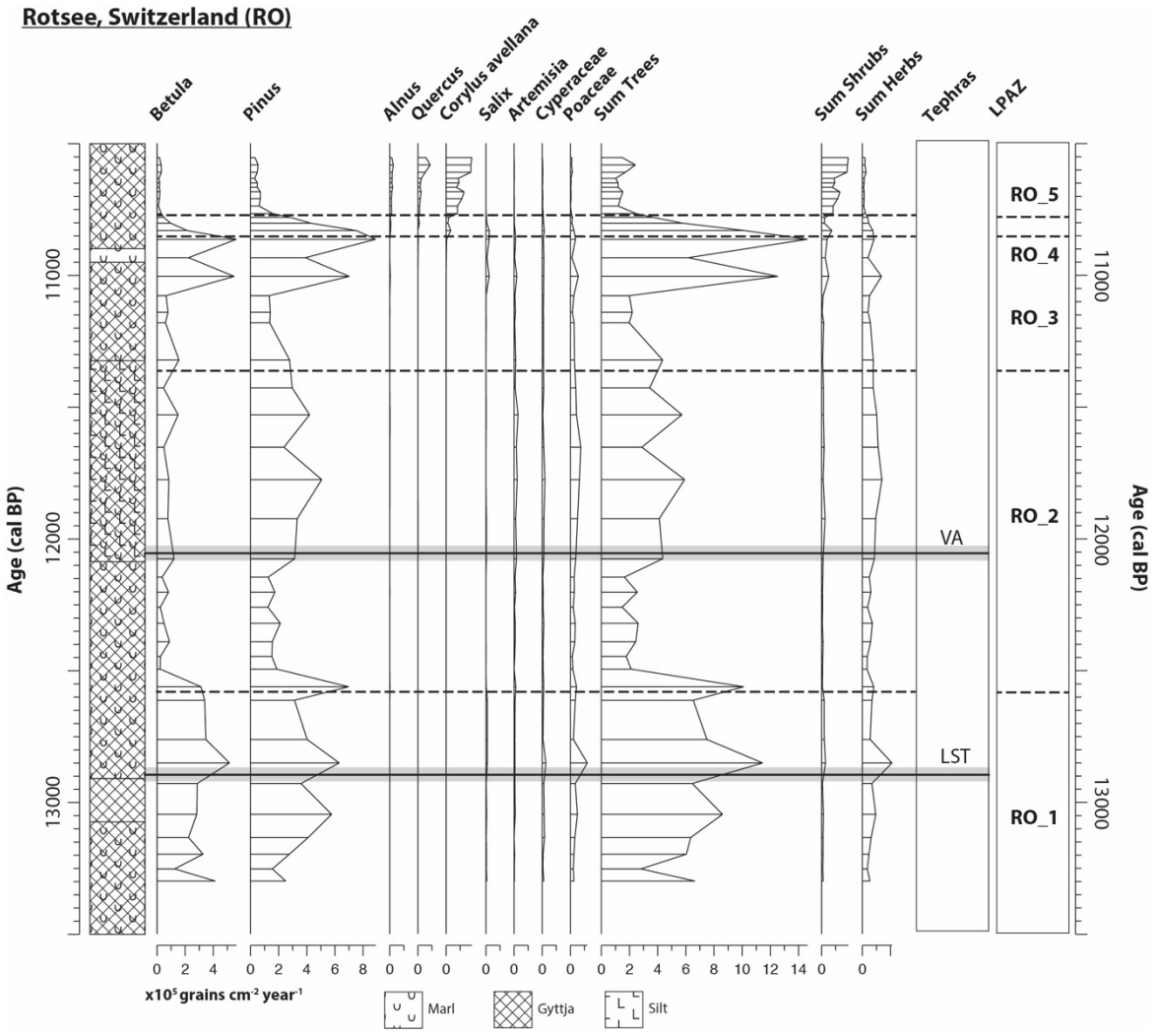


**Figure 7.38** Pollen accumulation rate (PAR) record of key taxa from Rotsee. The record is plotted against calibrated age (μ±1σ). Lithology presented as described by Lotter et al. (1992). LPAZ are divided based upon changes in major taxa and CONISS. The Laacher See (LST) and Vedde Ash (VA) were identified by Lane et al. (2012c) and are plotted with this study's new age estimate at μ±1σ. Light shading shows 1σ age error.

### 7.2.10.1 Statistical analysis

Statistical analysis was conducted on pollen percentage data from Rotsee with taxa that had abundances >2%. DCA results in Table 7.30 show short-axis lengths. These lengths show that PCA, CA and therefore PrC are all appropriate methods in analysing the dataset.

**Table 7.30** Detrended correspondence analysis results for Rotsee. The dataset shows short axis lengths and that axis 1 explains the most variation compared to the other axis.

| | DCA1 | DCA2 | DCA3 | DCA4 |
|---|---|---|---|---|
| **Eigenvalue** | 0.4774 | 0.07793 | 0.029193 | 0.018515 |
| **Axis length** | 2.1005 | 0.97050 | 0.619070 | 0.470084 |

Figure 7.39 presents the PCA results. The first two principal components, axis 1 and 2, explain 53.8% and 18.9% of the data variance. Along axis 1, taxa that plots negatively include deciduous tree species such as *Corylus* (most significant contributor), *Ulmus* and *Quercus*. Taxa that plots positively along axis one includes open habitat species of *Pinus, Artemisia, Juniperus* and Poaceae. Species that plot strongly to axis two include *Betula* and *Salix*.

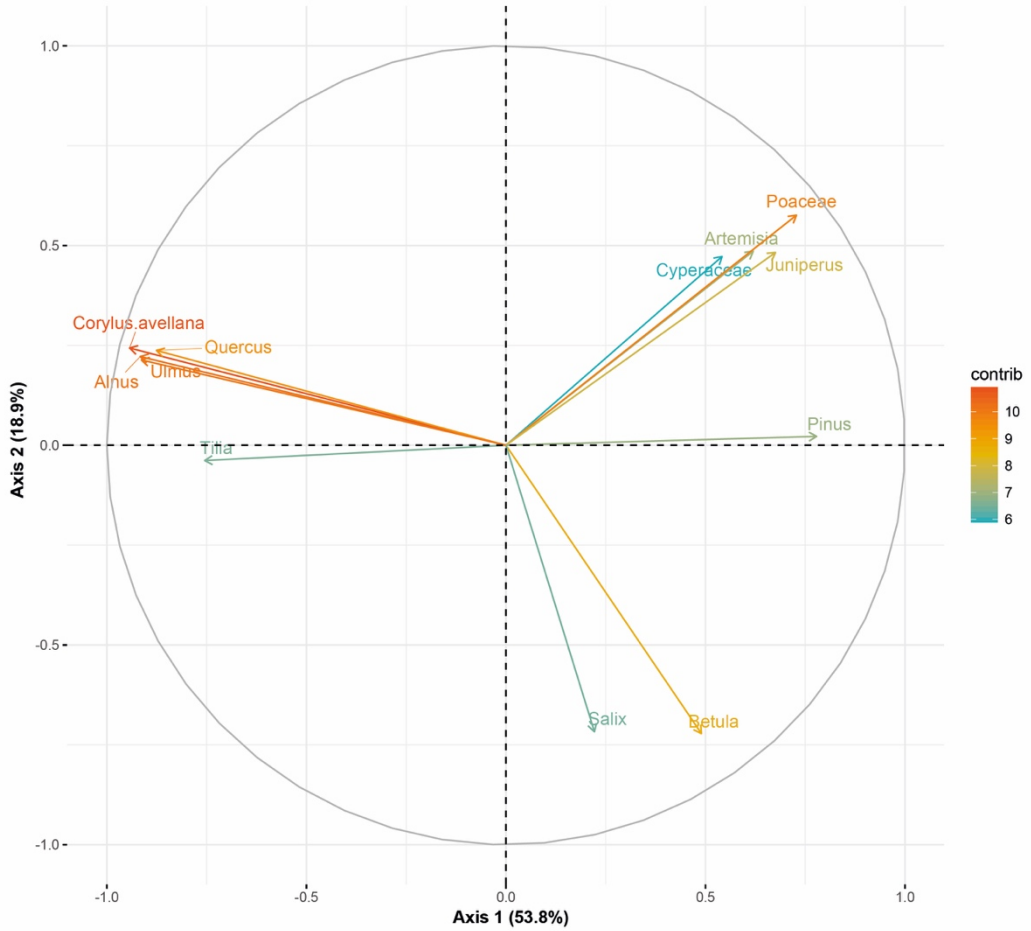


**Figure 7. 39** Ordination diagram of the PCA results from Rotsee. The two axis, axis 1 and 2, present first two principal components. The pollen taxa are placed along the axis with the length and colour of the arrow indicating the taxa dominance along the axis Along axis 1, tree taxa associated with warmer climates plot negatively while open, colder herbaceous taxa plot positively.

The PrC modelling used a PCA-based approach. Compared to CoA, the PCA-based output was produced in fewer iterations with 96% of the variance within the data captured (versus 94% for CoA). The PrC values showed one major oscillation and one additional oscillation with 1) a positive increase in the distance along the gradient and; 2) a general pause in the gradient identified from the curve (Figure 7.40). Table 7.30 describes these oscillations with the driver taxa behind each event. There are also changes in chord distance for RoC (Figure 7.40).

**Table 7.31** Vegtation oscillations identified in the PrC for Rotsee. Symbols depict:↑ increases and ↓ decreases in taxa percentage

| Oscillation | Depth (cm) | Age (μ±1σ, cal. BP) | Key taxa influence |
|---|---|---|---|
| RO_MO | 1058.2-1024.6 | 12,674±49 to 11,377±92 | ↑*Pinus,* ↑*Poaceae,* ↓*Betula* |
| RO_E1 | 1008.625-1006.375 | 10,847±85 to 10,774±77 | ↑*Pinus,* ↓ *Betula,* ↔*Corylus* |

### 7.2.10.2 Palaeoclimatic and palaeoenvironmental interpretation of Soppensee and Rotsee

Due to the proximity and similar vegetation composition of Soppensee and Rotsee on the Swiss plateau, these pollen records will be interpreted together with a simple discussion. Based upon age modelling, identification of the LST, VA and Askja-S tephra with evident vegetational changes, LPAZ can be correlated to the LGIT periods of the Allerød (SOP_1-2; RO_1), YD (SOP_3; RO_2) and EH (SOP_4-5; RO_3-5).

#### Allerød-YD transition (SOP 12,680±97 cal. BP; RO 12,674±49 cal. BP)

The beginning of both records saw an increase in *Pinus* at the expense of *Betula* (Figure 7.33, 7.37). Pine forests developed from an open birch forest (Lotter et al., 1992). The high percentage values of *Pinus* indicated it had a local occurrence (Huntley and Birks, 1983; Lotter

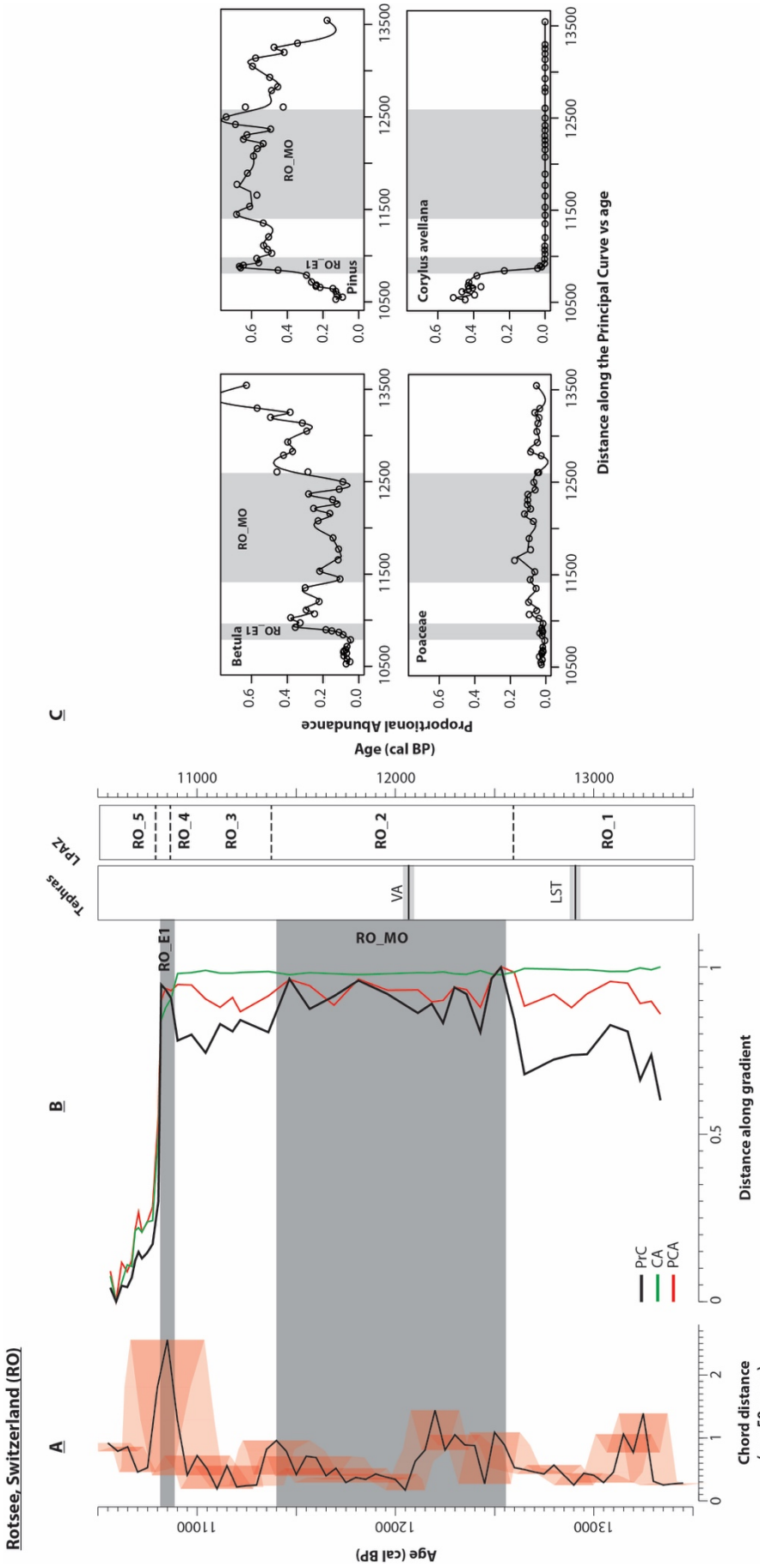


**Figure 7.40** The statistical results for the pollen percentage data from Rotsee. A) RoC analysis for every 50 years. The values presented are exaggerated to provide clearer results into periods of significant change. The higher the bar, the more significant the composition's change was. Light shading shows 1σ age error. B) The results of the different ordination tests (PCA, CoA and PrC). The grey boxes highlight oscillations identified from the PrC curve. C) The key taxa response curves modelled through the PrC. The grey boxes show the timing of the oscillations from the main PrC. Changes in the abundance of individual taxa at certain times provide insight into which taxa are driving the change. The record is plotted against calibrated age (μ ±1σ ) with light shading showing 1σ age error.

et al., 1992). Herbaceous taxa associated with open grasslands decreased (i.e. *Artemisia,* Cyperaceae, Poaceae) as the forest became more enclosed. The *Juniperus* shrub layer decreased as the taxa was affected by increased shading (Huntley and Birks, 1983). LOI at Rotsee showed an oscillation in organic matter (Figure 7.37). Figure 7.34 and 7.38 show an increase in PAR with tree taxa as *Pinus* became a dominant part of the vegetational landscape. The overall climate was warm, and the pollen zones are correlated to the Allerød period (e.g. Lotter et al., 1992; Wick and Tinner, 1997).

At 12,680 ± 97 cal. BP in Soppensee and 12,674 ± 49 cal. BP in Rotsee, *Pinus* reached a peak and remained constant at >50%. There was a notable decline in *Betula* at this time. These characteristics are also represented in PAR (Figure 7.34, 7.38). Overall, tree taxa decreased as herbaceous taxa of *Artemisia* and Poaceae expanded. The shrub taxa of *Juniperus* and *Salix* also increased. It can be interpreted that the pine woodland became open, yet was still very much dominant on the landscape with stands of juniper and birch. These vegetational changes can be related to the YD stadial as climatic conditions became cold (e.g. Lotter et al., 1992, Wick, 2000).

**YD-EH transition (SOP 11,576 ± 94 cal. BP; RO 11,377 ± 92 cal. BP)**

At 11,586 ± 94 cal. BP in Soppensee and 11,377 ± 92 cal. BP in Rotsee, *Betula* started to expand while *Pinus* remained in the high percentage values (Figure 7.33, 7.37). The herbaceous taxa of Poaceae and *Artemisia* declined as the forest began to enclose. *Juniperus* was soon out-competed as tree succession happened. PAR showed an increase in tree taxa at both sites (Figure 7.34, 7.38). It is seen that the climate was warming as the EH period began (e.g. Lotter et al., 1992; Wick, 2000).

**Earliest Holocene oscillations**

Vegetation succession continued throughout the rest of the EH period. The taxon of *Corylus* expanded into both records followed by other thermophilous tree taxa (e.g. *Quercus*, *Ulmus*). Hazel became the dominate part of the woodland and soon outcompeted pine and birch (Figure 7.36, 7.40). At 11,504 ± 92 cal. BP in Soppensee, a peak in PrC values was seen, driven by a peak in *Pinus* and rise in *Betula*. A second peak in PrC is dated to 11,212 ± 60 cal. BP (Figure 7.36). The curve is identifying a peak in *Pinus* and a plateau in *Corylus* while *Betula* declined. There was a decline in tree taxa, seen in Figure 7.33 and 7.37. A clear decline in tree taxa was seen in PAR at both sites (Figure 7.33, 7.37). There was also a peak in RoC vegetation overturning (Figure 7.36, 7.40). At Rotsee, a similar peak in the PrC for the site was seen at 10,847 ± 85 cal. BP with the same taxa response of *Pinus, Corylus* and *Betula* driving the change (Figure 7.40). Rotsee's LOI curve shows a sharp increase, followed by a decline in organic matter (Figure 7.37). This may be linked to an increase in inwash sediments at this time.

### 7.2.11 Lago Piccolo di Avigliana, Italy

Lago Piccolo di Avigliana (LPA) core AVP1 was collected, sampled, and pollen counted by Finsinger et al. (2006). Sixty-six samples dated to the LGIT in this study with variable sample resolution between 7-2cm. TLP counts were >350 pollen grains. Five LPAZ were identified (LPA_*n*, Table 7.32, Figure 7.41). No PAR was calculated due to no exotic pollen counts were obtained from the dataset.

**Table 7.32** The local pollen assemblage zones for Lago Piccolo di Avigliana. Included are the name of zones, depth, ages for the beginning and end of the zones (μ±1σ) with key taxa observations and changes within each zone. Symbols depict:↑ increases and ↓ decreases in taxa percentage; ↕ oscillating or ↔ stability of values for particular taxa; ▲ taxa peak; ● taxa present at <5%; ✕ taxa disappears in that zone.

| Zone | Composite Depth (cm) | Age (μ±1σ, cal. BP) | Taxa changes through zone | Key taxa | LOI | Lithology |
|---|---|---|---|---|---|---|
| **LPA_1** | 779-768.5 | 13,486±225 to 12,941±77 | ↑ *Quercus robur;* ↓ *Betula;* ↔ *Pinus, Artemisia,* Poaceae; ● *Juniperus, Rumex* | *Betula, Pinus* | ↓ | Partly laminated gyttja |
| **LPA_2** | 768.5-764 | 12,941±77 to 12,798±152 | ▲ *Pinus;* ↑ *Q. robur,;* ↓ *Betula, Artemisia;* ↔ Poaceae; ● *Rumex, Juniperus* | *Pinus, Quercus robur* | ↔ | Partly laminated gyttja |
| **LPA_3** | 764-717 | 12,798±152 to 11,877±151 | ↑ *Betula, Alnus, Artemisia,* Poaceae; ↓ *Q. robur;* ● *Rumex, Juniperus* | *Pinus, Artemisia,* Poaceae | ↓ then ↕ | Partly laminated gyttja |
| **LPA_4** | 717-702.5 | 11,877±151 to 11,096±394 | ↑ *Q. robur, Pinus*, Poaceae, *Rumex*; ↓ *Betula;* ▲ *Artemisia;* ● *Juniperus* | *Quercus robur, Pinus* Poaceae | ↕ | Partly laminated gyttja transition to homogenous gyttja |
| **LPA_5** | 702.5-686 | 11,096±394 to 10,522±112 | ↑ *Q. robur;* ↓ *Betula, Pinus;* ↔ Poaceae; ● *Juniperus, Artemisia, Rumex* | *Quercus robur* | ↑ | Homogenous gyttja |

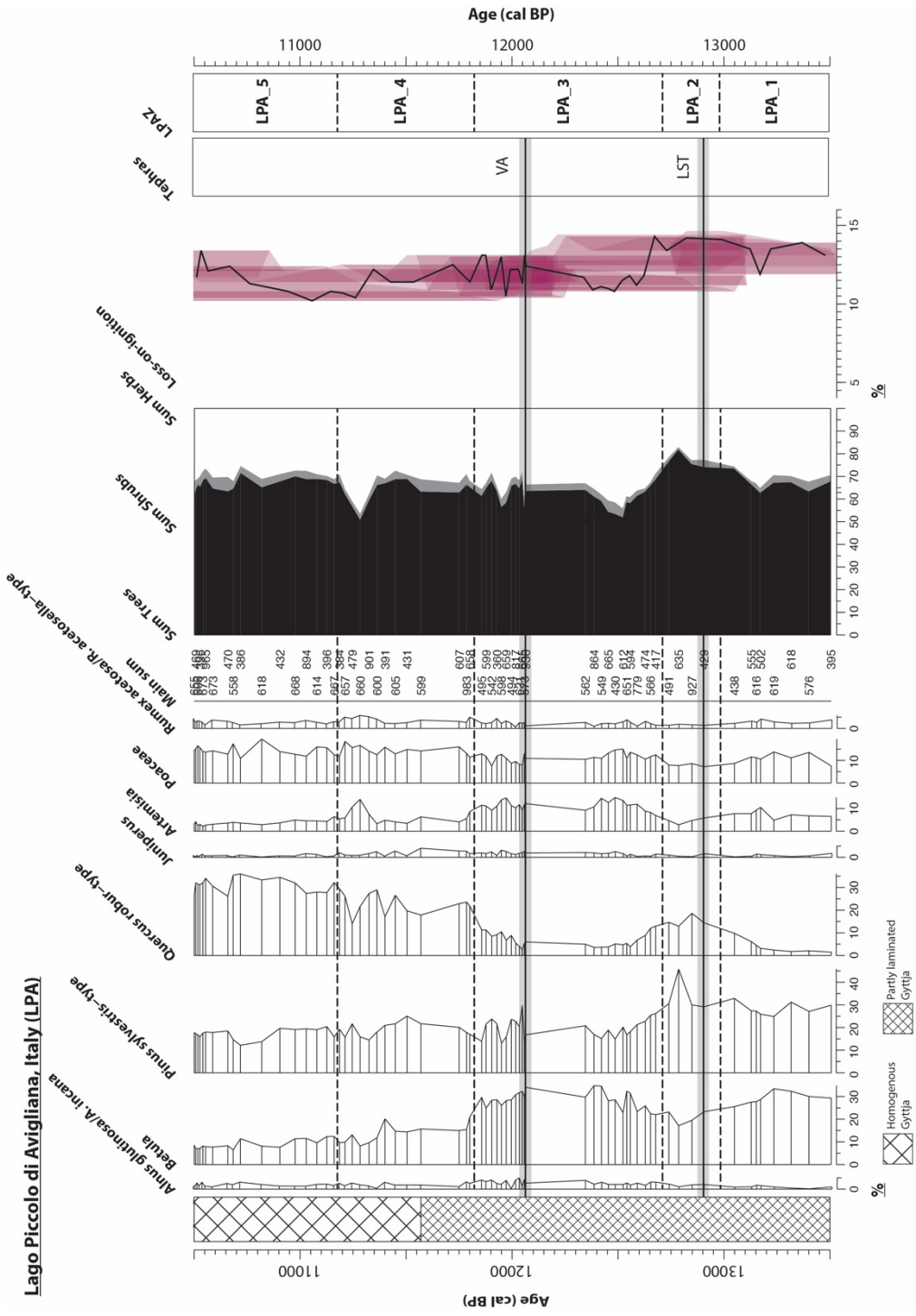


**Figure 7.32** Pollen percentage record of key taxa from Lago Piccolo di Avigliana. The record is plotted against calibrated age ($\mu \pm 1\sigma$ ). All values are presented against TLP. Lithology presented as described by Finsinger et al. (2006, 2008). Local pollen assemblage zones (LPAZ) are divided based upon changes in major taxa and CONISS. The Laacher See (LST) and Vedde Ash (VA) by Lane et al. (2012c) and are presented as the new modelled ages

#### 7.2.11.1 Statistical analysis

Statistical analysis was undertaken on LPA percentage terrestrial taxa dataset with taxa abundances >2%. DCA provided insight into axis lengths. Table 7.33 results show a short axis length demonstrating that PCA and a PCA-based approach to modelling PrC was suitable.

**Table 7.33** Detrended correspondence analysis results for Lago Piccolo di Avigliana. The dataset shows short axis lengths and that axis 1 explains the most variation compared to the other axis.

| | DCA1 | DCA2 | DCA3 | DCA4 |
|---|---|---|---|---|
| **Eigenvalue** | 0.1572 | 0.02471 | 0.009257 | 0.008277 |
| **Axis length** | 1.1452 | 0.65282 | 0.367138 | 0.356051 |

Figure 7.42 presents the PCA results. Axis 1 explains 31.8% of data variability while axis 2 explains 12.5%. The taxa that plot negatively along axis 1 include *Quercus robur* (most significant contributor), *Ulmus* and *Corylus* while *Artemisia, Betula* and *Pinus* plot positively. Taxa that plots strongly to axis 2 include Poaceae, Cyperaceae and *Juniperus*.

PrC provides additional insight into vegetation variance within the record. A PCA-based output model for PrC was suitable due to DCA results. There was further confirmation for a PCA-based output due to converging in fewer iterations (7 versus 15 CoA) under similar penalty values were applied. This approach captured 88.5% of the data variance compared to 87.4% for CoA-based output.

PrC modelling identified one major oscillation and three additional oscillations through 1) a positive increase in the distance along the gradient and; 2) a general pause in the gradient shifts to positive values (Figure 7.43, Table 7.34). These changes occurred alongside peaks in RoC (Figure 7.43).

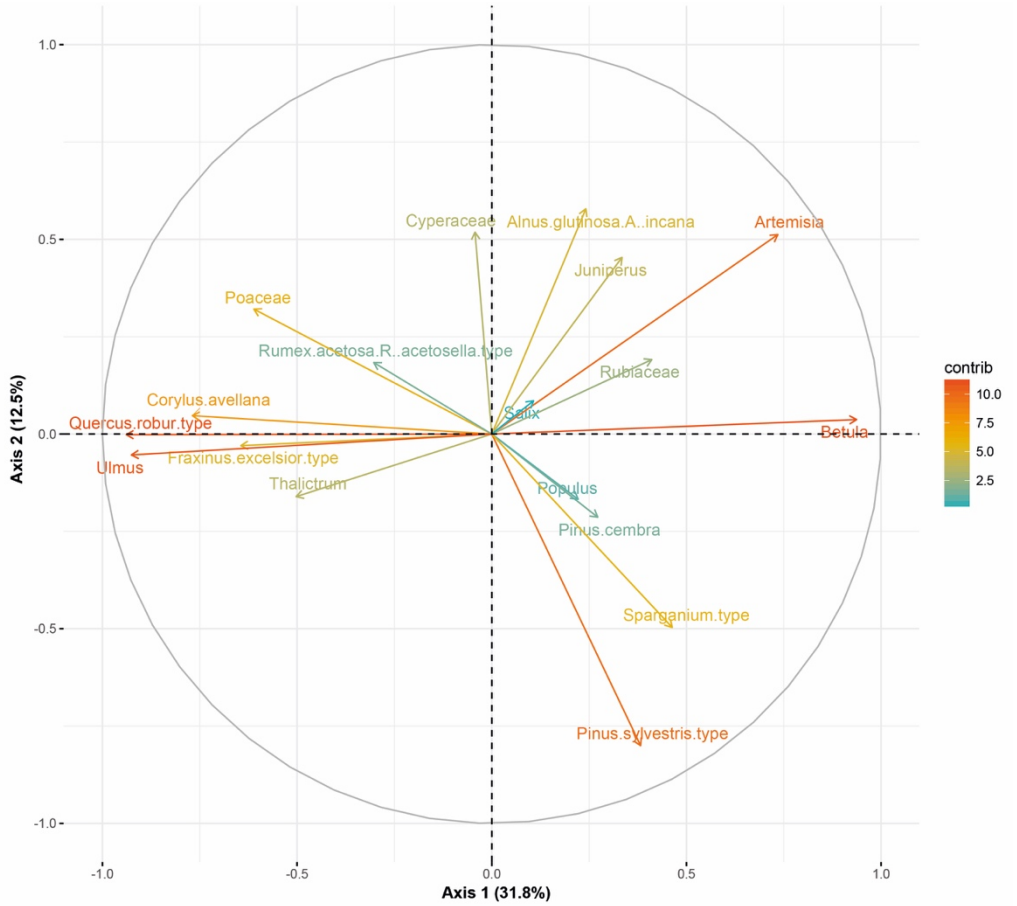


**Figure 7.42** Ordination diagram of the PCA results from Lago Piccolo di Avigliana. The two axis, axis 1 and 2, present first two principal components. The pollen taxa are placed along the axis with the length and colour of the arrow indicating the taxa dominance along the axis. Along axis 1, tree taxa associated with interstadial conditions plot negatively while taxa associated with stadial conditions plot positively.

**Table 7.34** Vegtation oscillations identified in the PrC for Lago Piccolo di Avigliana. Symbols depict:↑ increases and ↓ decreases in taxa percentage

| Oscillation | Depth (cm) | Age (μ±1σ, cal. BP) | Key taxa influence |
|---|---|---|---|
| LPA_MO | 764-717 | 12,798±152 to 11,877±151 | ↑*Betula*, ↓*Quercus robur*, ↓*Pinus*, ↑Poaceae |
| LPA_E1 | 709.5-708.5 | 11,551±353 to 11,487±370 | ↓ *Quercus robur*, ↑*Poaceae* |
| LPA_E2 | 706.5-703.5 | 11,357±395 to 11,160±402 | ↓ *Quercus robur*, ↑*Artemisia*, ↑*Betula* |
| LPA_E3 | 693.5-692.5 | 10,593±144 to 10,584±140 | ↓ *Quercus robur*, ↑*Pinus* |

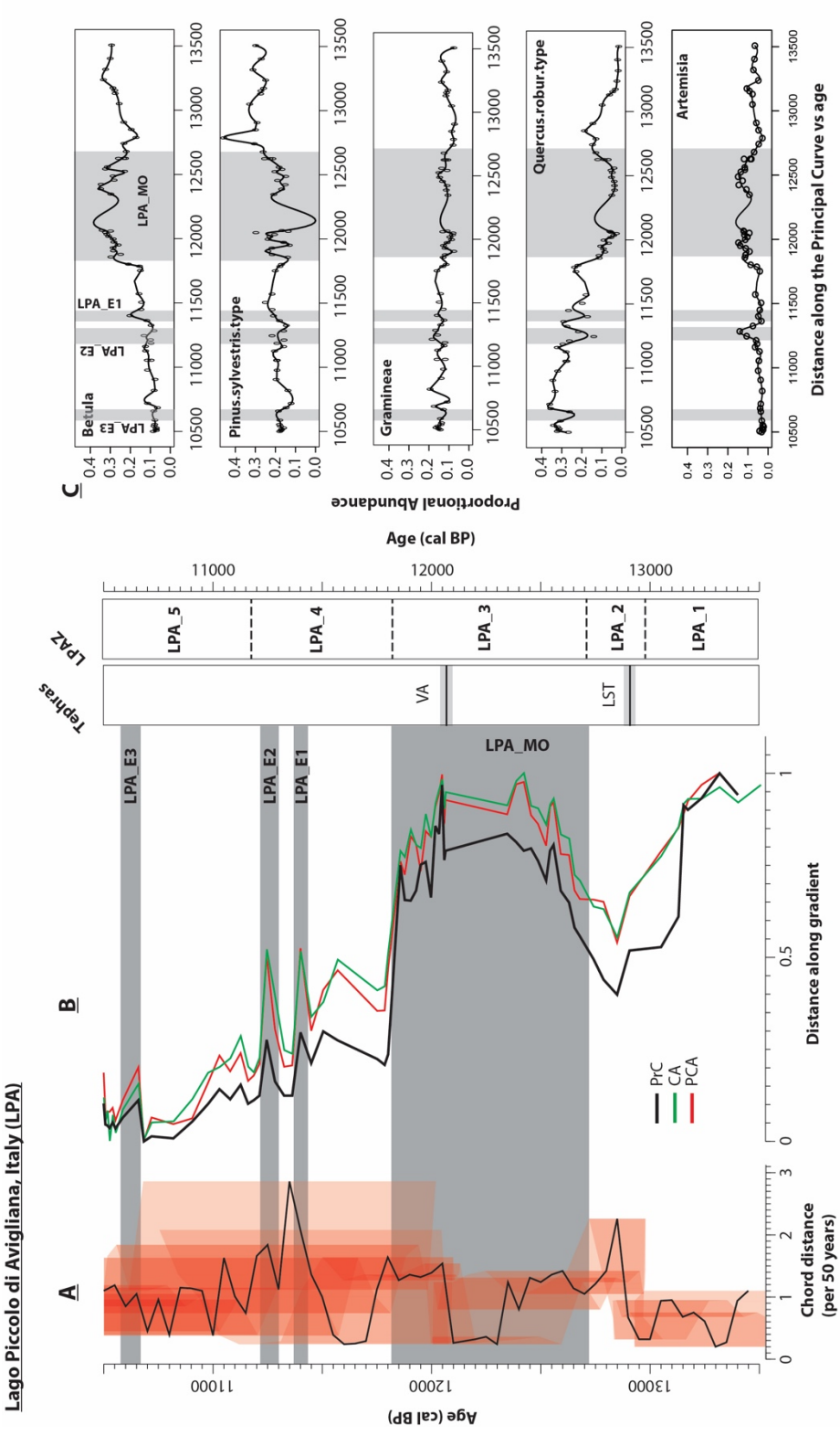


**Figure 7.43** The statistical results for the pollen percentage data from Lago Piccolo di Avigliana. A) RoC analysis for every 50 years. The values presented are exaggerated to provide clearer results into periods of significant change. The higher the bar, the more significant the composition' s change was. Light shading shows 1σ age error. B) The results of the different ordination tests (PCA, CoA and PrC). The grey boxes highlight oscillations identified from the PrC curve. C) The key taxa response curves modelled through the PrC. The grey boxes show the timing of the oscillations from the main PrC. Changes in the abundance of individual taxa at certain times provide insight into which taxa are driving the change. The record is plotted against calibrated age (μ ±1σ ) with light shading showing 1σ age error.

### 7.2.11.2 Palaeoclimatic and palaeoenvironmental interpretation

This section will focus on reconstructing the climate and environmental history of LPA using the pollen data previously presented. Based upon age modelling, identification of the LST and VA, evident vegetational changes, LPAZ are correlated to LGIT periods of the Allerød (LPA-_1-2), YD (LAP_3) and EH (LPA_4-5).

**Allerød-YD transition (12,798±152 cal. BP)**

There was a steady expansion in thermophilous tree taxa such as *Quercus robur* while cold-adapted taxa of *Artemisia* and *Rumex* declined. Percentage pollen shows that *Pinus* was locally significant in the catchment (Figure 7.41; Huntley and Birks, 1983). Mixed deciduous oak forests expanded, closing open habitats indicative of the Allerød period in the southern alps (e.g. Ilyashuk et al., 2009)

At 12,798 ± 152 cal. BP, *Quercus* and *Pinus* declined while herbaceous species of *Artemisia* and Poaceae take advantage of the opening of the woodland (Figure 7.41; Finsinger et al., 2006). A decline in organic matter is also seen (Figure 7.41). This indicated drier and colder climatic conditions of the YD stadial (e.g. Tinner et al., 1999).

**YD-EH transition (11,877±151 cal. BP)**

After the deposition of VA, a gradual rise in *Quercus robur* and *Pinus* was seen indicating climatic amelioration. *Betula*, *Artemisia* and Poaceae declined. There was a sharp rise in *Quercus* while *Artemisia* and *Betula* declined (Figure 7.43). *Juniperus* was a shrub layer in the growing mixed deciduous oak woodland (Finsinger et al., 2006). LOI values oscillated around 12%. This is the transition to the EH, dated to 11,877±151 cal. BP (e.g. Gobet et al., 2000; Vescovi et al., 2007).

**Earliest Holocene oscillations**

EH period saw further expansion of thermophilous taxa (Figure 7.43). *Corylus* expanded into the record as the taxa migrated into the region, indicating a warmer, drier climate (Finsinger et al., 2006). Three short-lived vegetational events were seen during the period. The first at 11,551 ± 353 cal. BP was with a rise in PrC values. This was driven by a decline in *Quercus robur* and a slight rise in Poaceae (Figure 7.43). At 11,357 ± 395 cal. BP, a decline in the PrC curve was observed (Figure 7.43). A high vegetation composition overturn was also witnessed in RoC. There was a slight decline in tree species, mainly *Quercus,* with a rise in NAP, especially *Artemisia* (Figure 7.43). The final event at 10,593 ± 144 cal. BP also saw a decline in *Quercus robur* with a rise in *Pinus* while herbaceous taxa of *Artemisia* and *Rumex* remain stable.

### 7.2.12 Lake Bled, Slovenia

Lake Bled core Bled C was collected, sampled and pollen counted by Andrič et al. (2009). Fourteen samples were dated to the LGIT from this study. The resolution of these samples were undertaken every 8 cm with a large gap of 40cm towards the end of the LGIT. TLP counts ranged from 300 to >500 pollen grains. Five LPAZ (BLE_*n*) were identified (Table 7.35, Figure 7.44). PAR was also calculated (Figure 7.45).

**Table 7.35** The local pollen assemblage zones for Lake Bled. Included are the name of zones, depth, ages for the beginning and end of the zones (μ±1σ) with key taxa observations and changes within each zone. Symbols depict:↑ increases and ↓ decreases in taxa percentage; ↕ oscillating or ↔ stability of values for particular taxa; ▲ taxa peak; ● taxa present at <5%; ✕ taxa disappears in that zone.

| Zone | Composite Depth (cm) | Age (μ±1σ, cal. BP) | Taxa changes through zone | Key taxa | LOI | Lithology |
|---|---|---|---|---|---|---|
| **BLE_1** | 192-188 | 13,435±175 to 13,357±184 | ↑ *Pinus, Picea, Quercus;* ↓ *Betula;* ● *Larix, Artemisia*, Poaceae | *Pinus* | ↑ | Marl |
| **BLE_2** | 188-148 | 13,357±184 to 12,576±174 | ▲ then ↓ *Pinus*; ↕ *Picea, Betula, Quercus*; ● *Larix, Artemisia*, Poaceae | *Pinus, Picea* | ↓ | Marl with moss layers |
| **BLE_3** | 148-108 | 12,576±174 to 11,925±114 | ↔ *Pinus;* ↑ *Piceae;* ↑ *Larix, Artemisia,* Poaceae; ● *Quercus,* Chenopodiaceae | *Pinus, Picea, Artemisia, Larix* | ↕ | Marl with moss layers |
| **BLE_4** | 108-60 | 11,925±114 to 10,600±131 | ↑ *Betula, Quercus, Carpinus,* Poaceae; ↓ *Pinus, Piceae, Artemisia,* Chenopodiaceae | *Betula, Pinus,* Poaceae | ↑ then gradual ↓ | Marl |
| **BLE_5** | 60-56 | 10,600±131 to 10,510±177 | ↑ *Picea, Quercus, Pinus;* ↓ *Betula,* Poaceae | *Picea, Quercus* | ↓ | Marl |

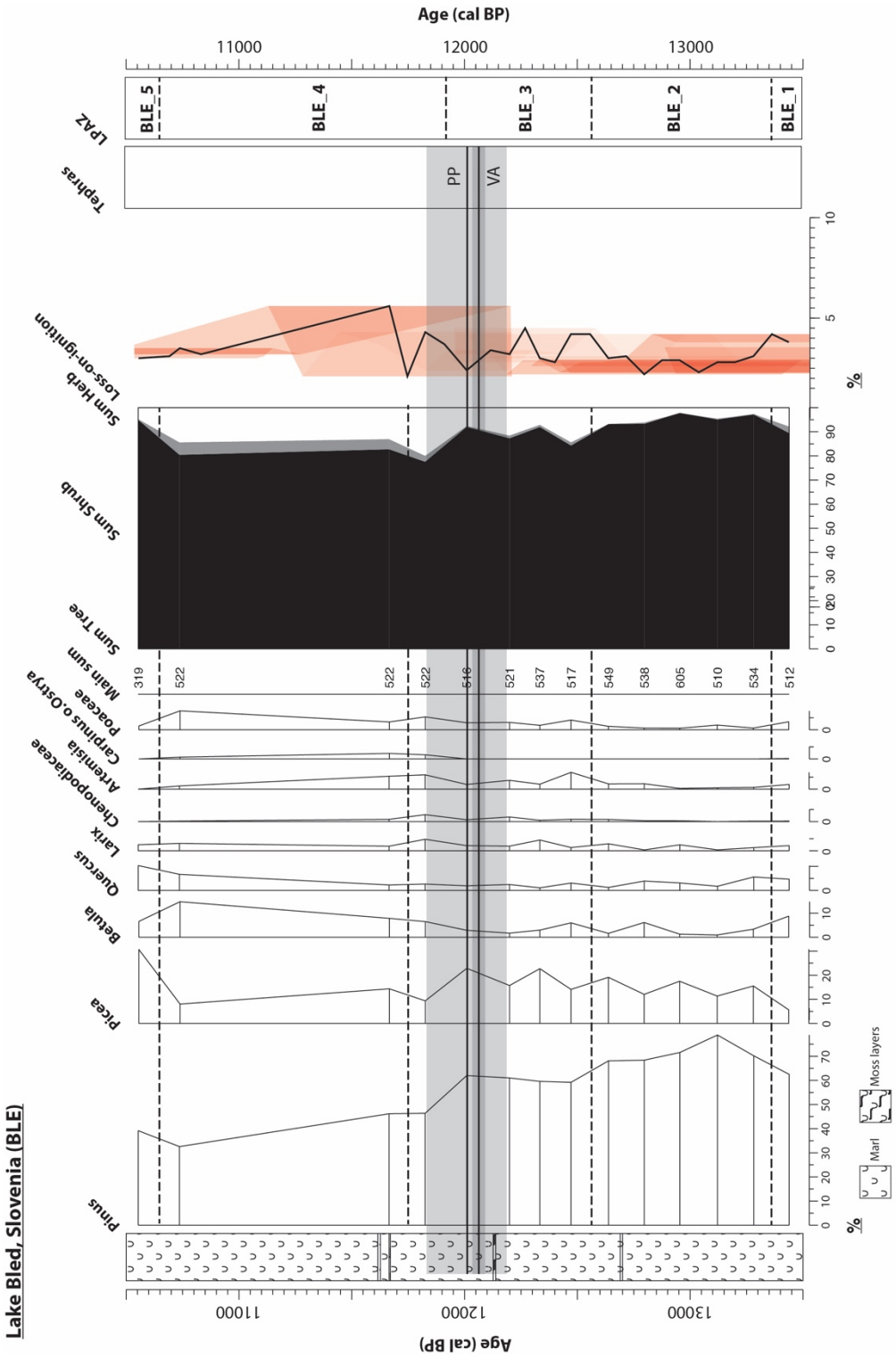


**Figure 7.44** Pollen percentage record of key taxa from Lake Bled. The record is plotted against calibrated age ($\mu \pm 1\sigma$ ). All values are presented against TLP. Lithology presented as described by Andrič et al. (2009). Percentage loss-on-ignition (LOI) is plotted. LPAZ are divided based upon changes in major taxa and CONISS. The Laacher See (LST) and Vedde Ash (VA)were identified by Lane et al. (2011b) and are plotted with this study' s new age estimate at $\mu \pm 1\sigma$ . Light shading shows $1\sigma$ age error.

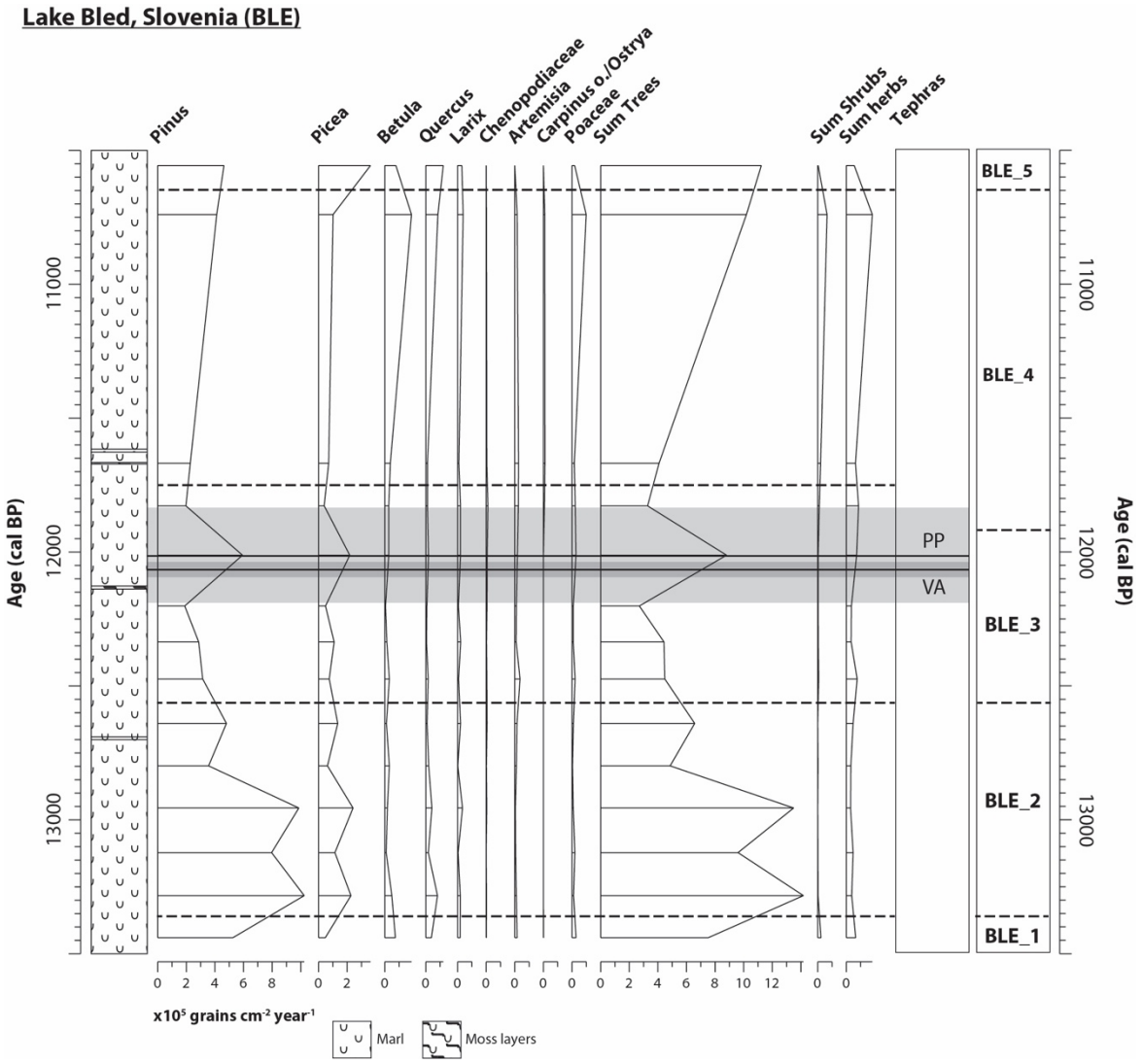


**Figure 7.45** Pollen accumulation rate (PAR) record of key taxa from Lake Bled. The record is plotted against calibrated age (μ±1σ). Lithology presented as described by Andrič et al. (2009). LPAZ are divided based upon changes in major taxa and CONISS. The Laacher See (LST) and Vedde Ash (VA)were identified by Lane et al. (2011b) and are plotted with this study's new age estimate at μ±1σ. Light shading shows 1σ age error.

### 7.2.12.1 Statistical analysis

Statistical analysis was performed on Bled's terrestrial percentage pollen dataset using taxa with an abundance of >2%. DCA results shown in Table 7.36 show short axis lengths, indicating PCA is the most appropriate statistical analysis along with PrC.

**Table 7.36** Detrended correspondence analysis results for Lake Bled. The dataset shows short axis lengths and that axis 1 explains the most variation compared to the other axis.

| | DCA1 | DCA2 | DCA3 | DCA4 |
|---|---|---|---|---|
| **Eigenvalue** | 0.1163 | 0.04475 | 0.23598 | 0.025096 |
| **Axis length** | 0.9496 | 0.66415 | 0.359334 | 0.391481 |

PCA results are shown in Figure 7.46. Axis 1 represents 46% of data variability while axis 2 represents 23.7% of the variability. Along axis 1, taxa that plot negatively include *Corylus*, *Abies* and Poaceae while only two taxa plot positively; *Pinus* and *Picea*. Taxa that have a stronger trend with axis two include *Ulmus, Quercus, Artemisia* and Chenopodiaceae.

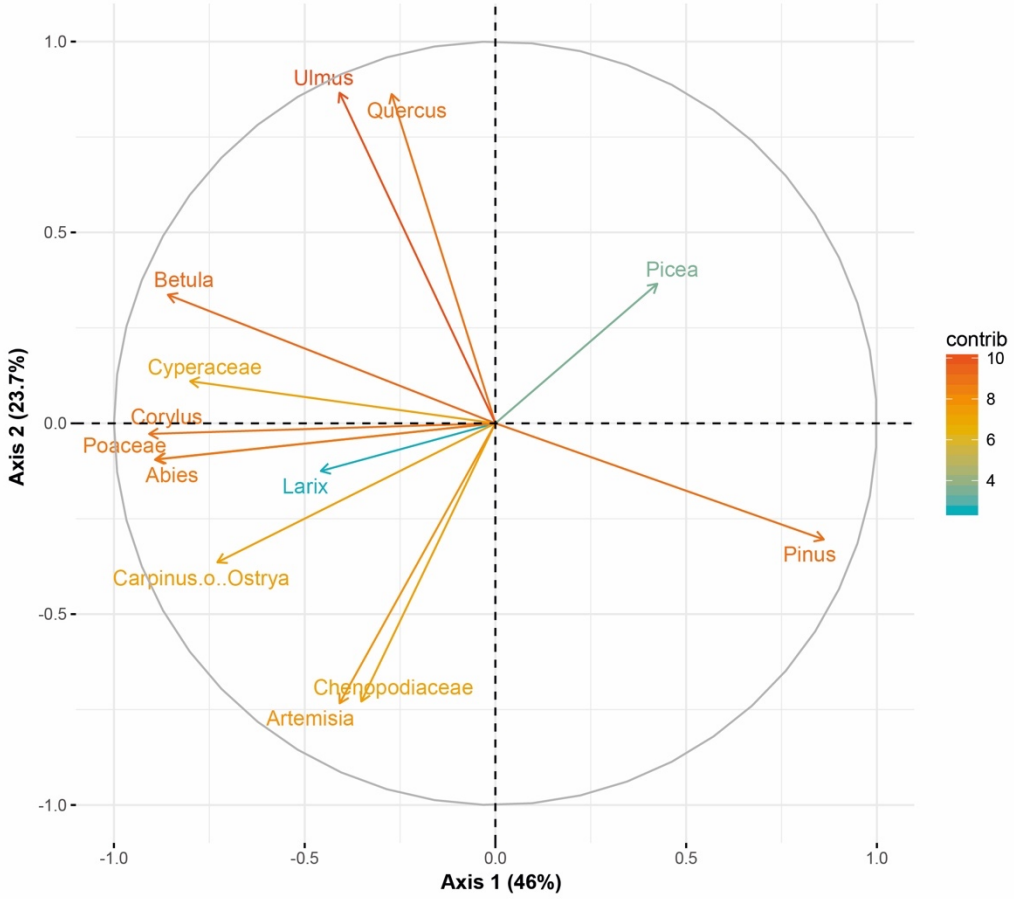


**Figure 7.46** Ordination diagram of the PCA results from Lake Bled. The two axis, axis 1 and 2, present first two principal components. The pollen taxa are placed along the axis with the length and colour of the arrow indicating the taxa dominance along the axis. Due to the poor resolution during the EH, there is a mix of taxa associated with Axis 1.

PrC modelling was undertaken using the PCA-based output approach, as indicated by DCA results. Further confirmation was seen when a CoA-based output resulted in convergence in more iterations (6 versus 5 PCA) with less data variance captured (76.2% versus 78.35% PCA).

PrC modelled output captured variance in the data with shifts to positive values. Only one major oscillation was identified with no additional oscillations in the EH period (Figure 7.47, Table 7.37).

**Table 7.37** Vegtation oscillations identified in the PrC for Lake Bled. Symbols depict:↑ increases and ↓ decreases in taxa percentage.

| Oscillation | Depth (cm) | Age (μ±1σ, cal. BP) | Key taxa influence |
|---|---|---|---|
| BLE_MO | 148-108 | 12,576±174 to 11,925±114 | ↑ *Picea;* ↓ *Pinus* |

### 7.2.12.2 Palaeoclimatic and palaeoenvironmental interpretation

The following section discussion will focus on reconstructing the climate and environmental history of Lake Bled using the pollen data previously presented. Based upon age modelling, identification of VA and the PP tephra with clear vegetational changes, LPAZ can be correlated to LGIT periods of the Allerød (BLE_1-2), YD (BLE_3) and EH (BLE_4).

**Allerød-YD transition (12,576±174 cal. BP)**

The beginning of the record shows a rise in tree taxa, namely *Pinus*, with a small percentage of NAP such as Poaceae (Figure 7.44). *Pinus* then decreased while thermophilous taxa of *Quercus* and *Piceae* increased, indicating mixed forest development. LOI showed variable organic matter <5%. This can be linked to warmer temperatures of the Allerød (Andrič et al., 2009).

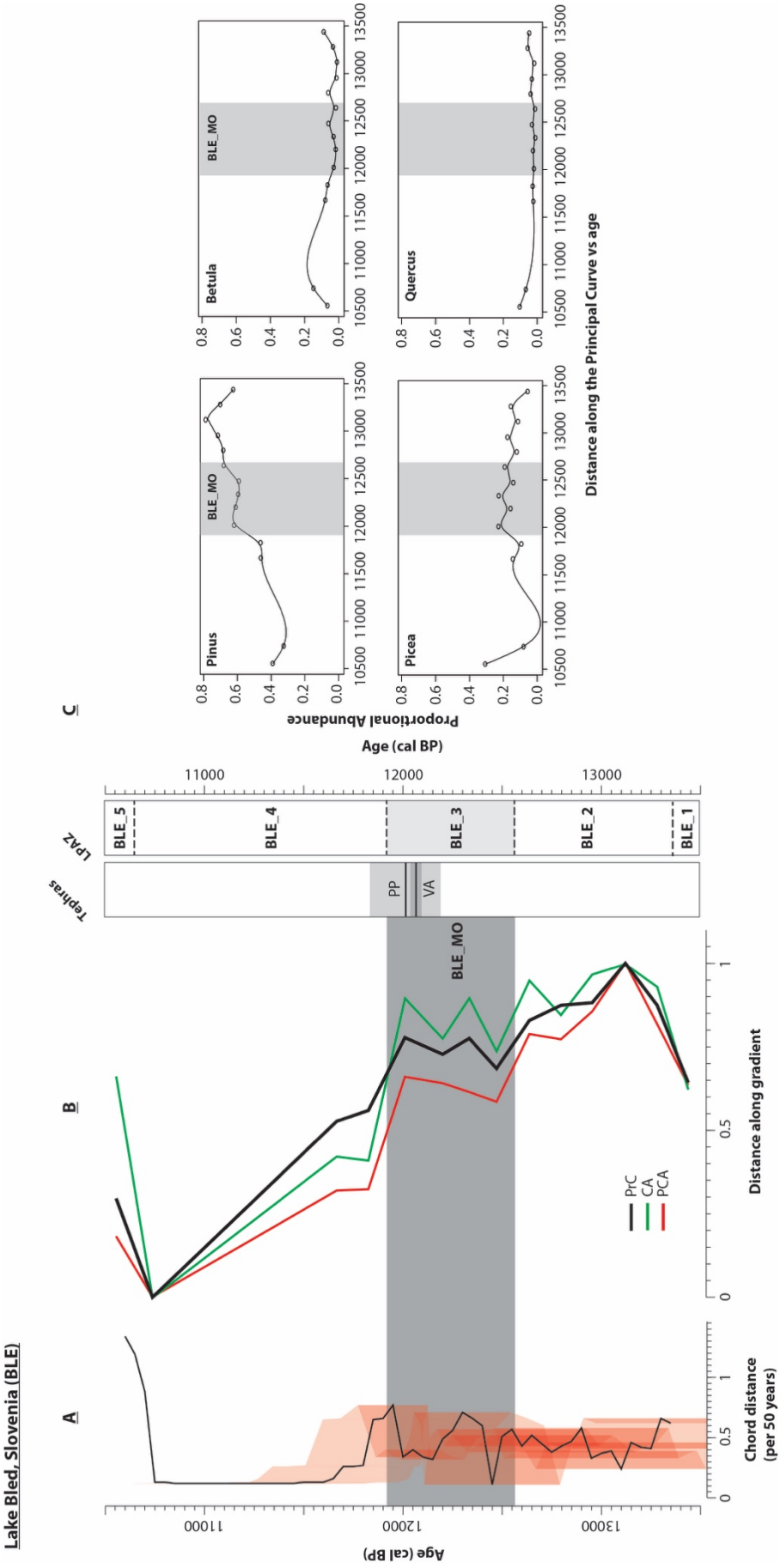


**Figure 7.47** The statistical results for the pollen percentage data from Lake Bled. A) RoC analysis for every 50 years. The values presented are exaggerated to provide clearer results into periods of significant change. The higher the bar, the more significant the composition's change was. Light shading shows 1σ age error. B) The results of the different ordination tests (PCA, CoA and PrC). The grey boxes highlight oscillations identified from the PrC curve. C) The key taxa response curves modelled through the PrC. The grey boxes show the timing of the oscillations from the main PrC. Changes in the abundance of individual taxa at certain times provide insight into which taxa are driving the change. The record is plotted against calibrated age (μ ±1σ ) with light shading showing 1σ age error.

At 12,576 ± 174 cal. BP, herbaceous taxa of *Artemisia* and Poaceae increased as taxa of *Quercus* and *Pinus* declined (Figure 7.44). *Larix* was present indicating cooler and drier climatic conditions, possibly more continental (Willis et al. 2000; Pokorny et al., 2002, 2010; Andrič et al., 2009). LOI increased linked to a decrease in vegetation on the surrounding landscape which resulted in additional runoff that has organic matter. This evidence shows the landscape became more open as climate deteriorated. This is also seen in other regional pollen records (e.g. Pokorny et al., 2002; 2010).

**YD-EH transition (11,925 ± 114 cal. BP)**

After the deposition of the VA, *Artemisia* increased while *Picea* and *Pinus* continued to decline. At 11,925 ± 114 cal. BP tree taxa of *Betula, Picea* and *Quercus* increased while *Artemisia* and Chenopodiaceae declined. LOI also sharply increased (Figure 7.44) Reforestation of the landscape began as climatic conditions became warmer showing the transition into the EH period (e.g. Pokorny et al., 2002)

**Earliest Holocene oscillations**

With a lack of samples throughout the EH, it was hard to investigate the vegetation changes at Bled (Figure 7.44). There was an overall increase in tree taxa, particularly thermophilous taxa of *Quercus* with a decline in open herbaceous taxa of *Artemisia* and Chenopodiaceae. This shows reforestation, dominated by pine-forests after the YD as temperatures warmed. No additional EH vegetation oscillations or environmental responses were identified.

### 7.2.13 Lake Brazi, Romania

Lake Brazi core TDB was collected, sampled and pollen counted by Magyari et al. (2012) and Pál et al. (2018). Fifty-eight of these samples were dated to the LGIT in this study with a continuous sample resolution of 1cm. TLP counts ranged from >300-550. Five LPAZ (TDB_*n*) were identified (Table 7.38, Figure 7.47) PAR was also calculated (Figure 7.47).

**Table 7.38** The local pollen assemblage zones for Lake Brazi. Included are the name of zones, depth, ages for the beginning and end of the zones (μ±1σ) with key taxa observations and changes within each zone. Symbols depict:↑ increases and ↓ decreases in taxa percentage; ↕ oscillating or ↔ stability of values for particular taxa; ▲ taxa peak; ● taxa present at <5%; ✕ taxa disappears in that zone.

| Zone | Composite Depth (cm) | Age (μ±1σ, cal. BP) | Taxa changes through zone | Key taxa | LOI | Lithology |
|---|---|---|---|---|---|---|
| **TDB_1** | 581-570.5 | 13,493±235 to 12,874±175 | ↑ *Pinus Dip., Betula nana;* ↓ *Pinus Hap. Artemisia,* Poaceae; ● *Alnus, Ulmus, Quercus,* Chenopodiaceae | *Pinus Diploxylon,* Poaceae | ↑ then ↓ | Silty clay to silty clay gyttja |
| **TDB_2** | 570.5-555.5 | 12,874±175 to 11,485±199 | ↑ *Artemisia,* Poaceae, Chenopodiaceae; ↓ *P. Dip.;* ● *P. Hap., B. alba, B. nana, Picea* | *Artemisia,* Poaceae, Chenopodiaceae | ● | Silty clay gyttja |
| **TDB_3** | 555.5-545.5 | 11,485±199 to 11,124±68 | ▲ ↕*P. Dip., P. Hap*; ↑ *P. Hap., Alnus viridis, Ulmus;* ↓ *Artemisia,* Poaceae, Chenopodiaceae; ● *B. alba, B. nana, Picea* | *Pinus Diploxylon* | ↑ | Silty clay to Silty clay gyttja |
| **TDB_4** | 545.5-531.5 | 11,124±68 to 10,733±216 | ▲ *A. viridis*; ↑ *Ulmus, Picea abies, Quercus;* ↓ *P. Dip.;* ● *B. alba, B. nana, Artemisia,* Poaceae | *Pinus Diploxylon, Alnus viridis, Ulmus* | ↔ | Silty clay gyttja |
| **TDB_5** | 531.5-524 | 10,733±216 to 10,448±167 | ↑ *Ulmus, Picea abies, Quercus;* ↓ *P. Dip.;* ● *B. alba, B. nana, Artemisia,* Poaceae | *Picea, Ulmus, Quercus* | ↑ | Silty clay gyttja to Herbaceous silty clay gyttja |

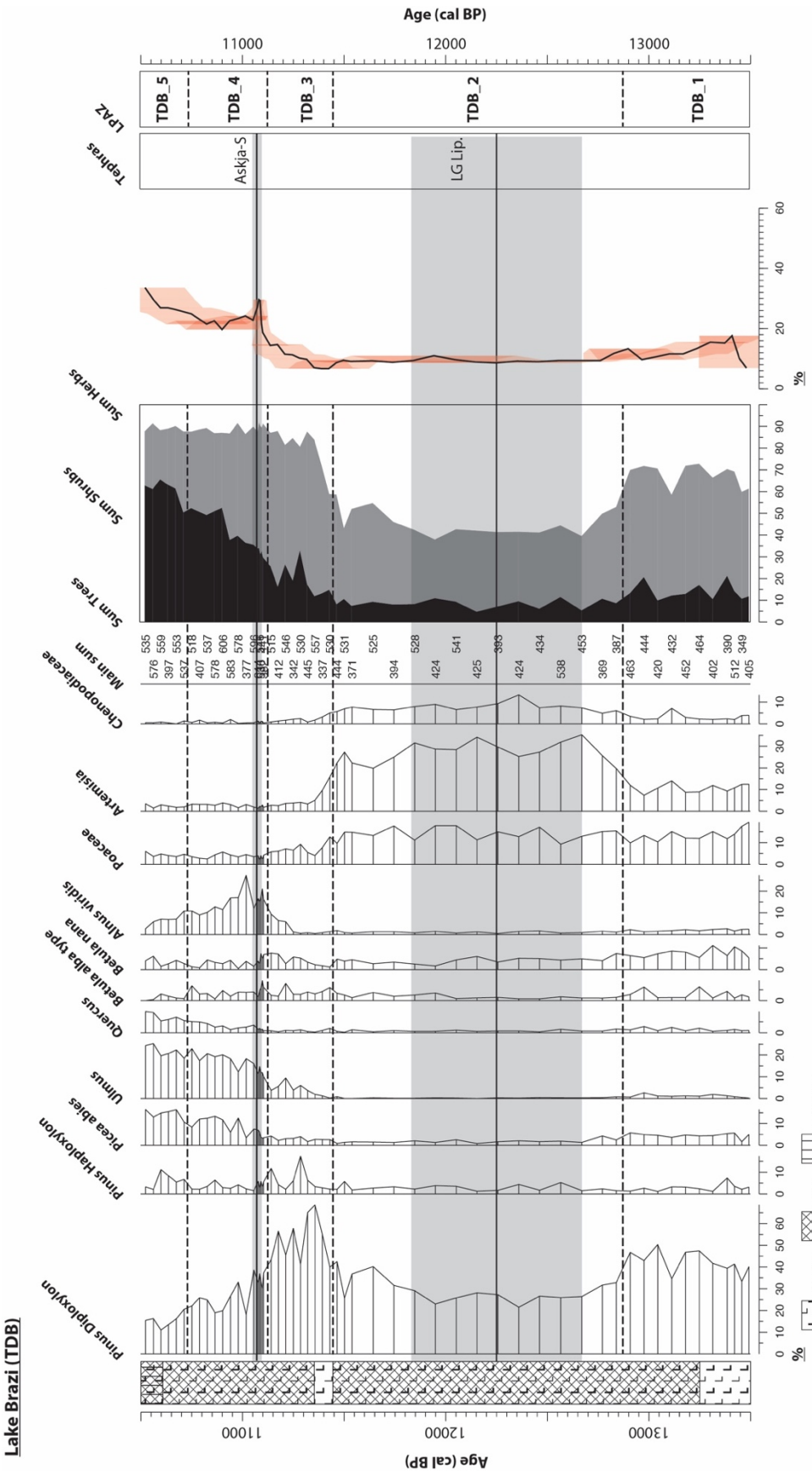


**Figure 7.48** Pollen percentage record of key taxa from Lake Brazi. The record is plotted against calibrated age (μ ±1σ ). All values are presented against TLP. Lithology presented as described by Magyari et al. (2012). Percentage LOI is plotted. LPAZ are divided based upon changes in major taxa and CONISS. *Pinus* subgenus Diploxylon is believed to represent *Pinus mugo* and the subgenus Haploxylon represents *P. cembra* (Magyari et al., 2012). The Late Glacial Lipari (LG Lipari) and Askja-S tephra identified in this study and by Kearney et al. (2018) are plotted with this study' s new age estimate at μ ±1σ . Light shading shows 1σ age error.

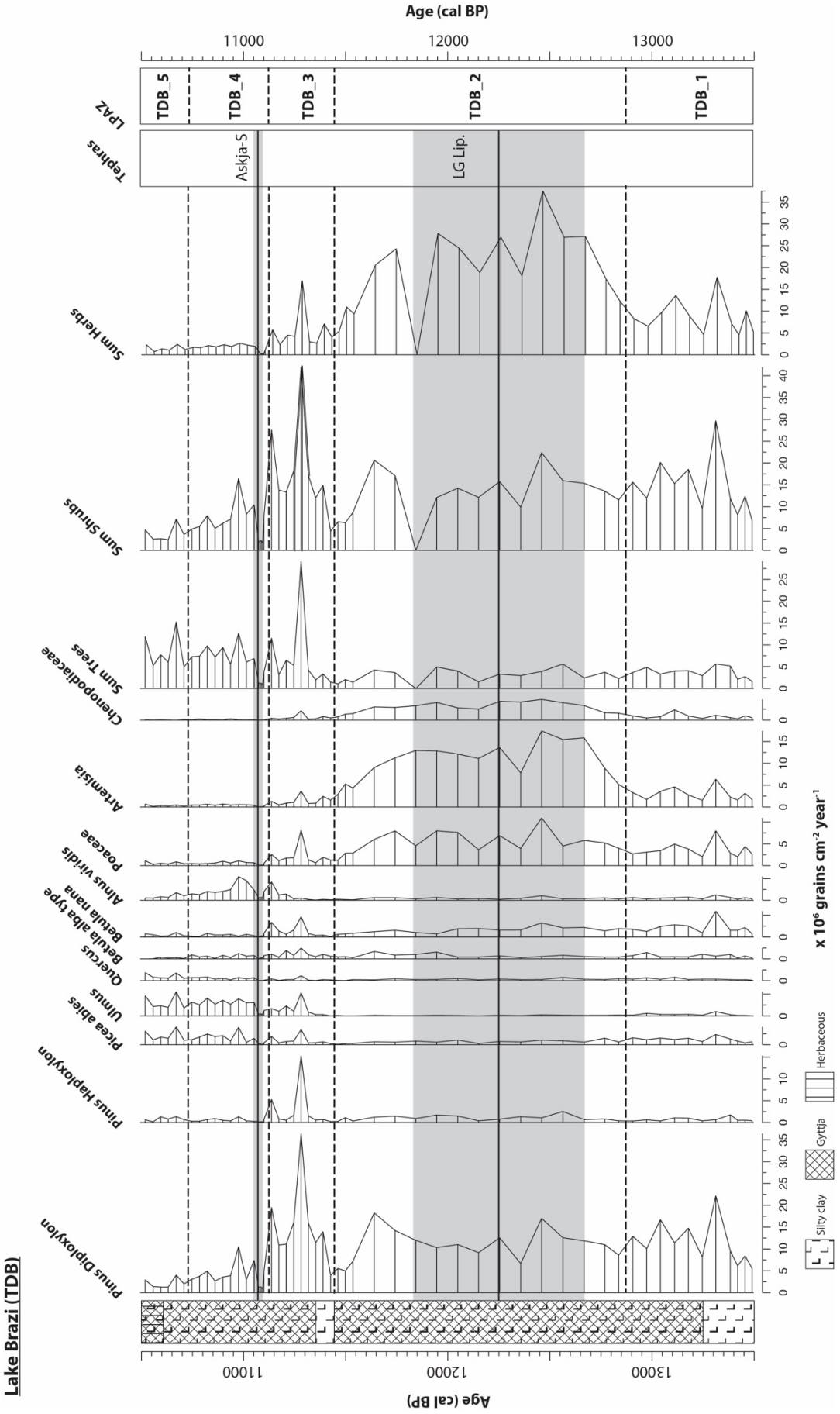
Lake Brazi (TDB)
Age (cal BP)
11000
12000
13000
LPAZ
TDB_5
TDB_4
TDB_3
TDB_2
TDB_1
Tephras
Askja-S
LG Lip.
Sum Herbs
Sum Shrubs
Sum Trees
Chenopodiaceae
Artemisia
Poaceae
Alnus viridis
Betula nana
Betula alba type
Quercus
Ulmus
Picea abies
Pinus Haploxylon
Pinus Diploxylon
0 5 10 15 20 25 30 35
0 5 10 15 20 25 30 35 40
0 5 10 15 20 25
0 5 10 15
0 5
0
0 5 10
Silty clay
Gyttja
Herbaceous
x 10⁶ grains cm⁻² year⁻¹

**Figure 7.49** Pollen accumulation rate (PAR) record of key taxa from Lake Brazi. The record is plotted against calibrated age (μ±1σ). Lithology presented as described by Magyari et al. (2012). Percentage LOI is plotted. LPAZ are divided based upon changes in major taxa and CONISS. Pinus subgenus Diploxylon is believed to represent Pinus mugo and the subgenus Haploxylon represents P. cembra (Magyari et al., 2012). The Late Glacial Lipari (LG Lipari) and Askja-S tephra identified in this study and by Kearney et al. (2018) are plotted with this study's new age estimate at μ±1σ. Light shading shows 1σ age error.

#### 7.2.13.1 Statistical analysis

Statistical analysis was conducted on terrestrial percentage pollen data from Brazi with taxa of abundances >5%. DCA results in Table 7.39 show short-axis lengths. The length were within >1.5-3SD indicating that PCA and CoA, and therefore PrC, are appropriate to explore the data.

**Table 7.39** Detrended correspondence analysis results for Lake Brazi. The dataset shows short axis lengths and that axis 1 explains the most variation compared to the other axis.

| | DCA1 | DCA2 | DCA3 | DCA4 |
|---|---|---|---|---|
| **Eigenvalue** | 0.3406 | 0.09161 | 0.02707 | 0.017882 |
| **Axis length** | 1.9564 | 1.26419 | 0.60734 | 0.559672 |

Figure 7.50 presents the PCA results. Axis 1 explains 49.5% of data variability, while axis 2 explains 18.6%. Taxa that plot negatively along axis 1 includes taxa associated with open-steppe habitats; *Artemisia* (most significant contributor), *Betula nana* and Poaceae, while taxa plotting positively are deciduous tree taxa of *Ulmus, Picea abies* and *Quercus*. Intermediate taxa, and those that plot along axis 2, include *Pinus* Diploxylon*, Pinus* Haploxylon and *Betula alba.*

To identify addition data variation, the PrC modelling used a CoA-based output. This CoA output converged in fewer iterations than PCA when similar penalty values were applied (5 versus 9 PCA). Both captured similar data variance (89.7% versus 89.8% PCA).

Variance within the modelled PrC were identified through negative changes or a pause in the distance along the gradient. As a result, one major oscillation were identified

along with three additional oscillations (Figure 7.51). Taxa associated with these changes are described in Table 7.40.

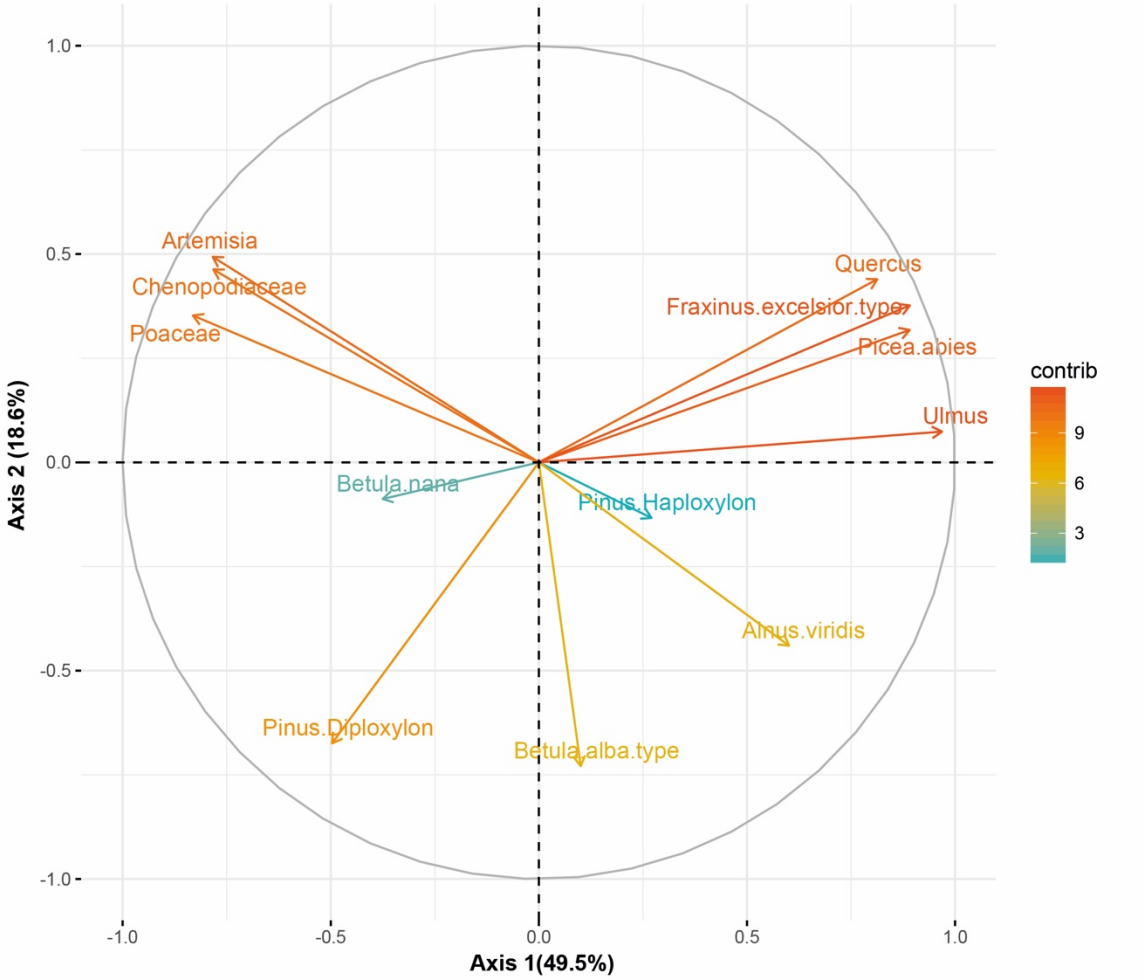


**Figure 7.50** Ordination diagram of the PCA results from Lake Brazi. The two axis, axis 1 and 2, present first two principal components. The pollen taxa are placed along the axis with the length and colour of the arrow indicating the taxa dominance along the axis. *Pinus* subgenus Diploxylon is believed to represent *Pinus mugo* and the subgenus Haploxylon represents *P. cembra* (Magyari et al., 2012). Along axis 1, tree taxa associated with warmer climates plot positively while open, colder taxa plot negatively.

**Table 7.40** Vegtation oscillations identified in the PrC for Lake Brazi. Symbols depict:↑ increases and ↓ decreases in taxa percentage

| Oscillation | Depth (cm) | Age (μ±1σ, cal. BP) | Key taxa influence |
|---|---|---|---|
| TDB_MO | 570.5-555.5 | 12,874±175 to 11,485±199 | ↓ *Pinus* Diploxylon, ↑*Artemisia* |
| TDB_E1 | 554.5-546.5 | 11,449±199 to 11,161±110 | ↓ *Pinus mugo,* ↓*Pinus cembra*, ↑*Artemisia,* ↑ |
| TDB_E2 | 543.5-537.5 | 11,096±33 to 10,962±152 | ↑*Alnus viridis,* ↓ *Pinus mugo,* ↑*Artemisia* |
| TDB_E3 | 534.5-530.5 | 10,846±197 to 10,695±218 | ↑*Alnus viridis,* ↓ *Pinus mugo* |

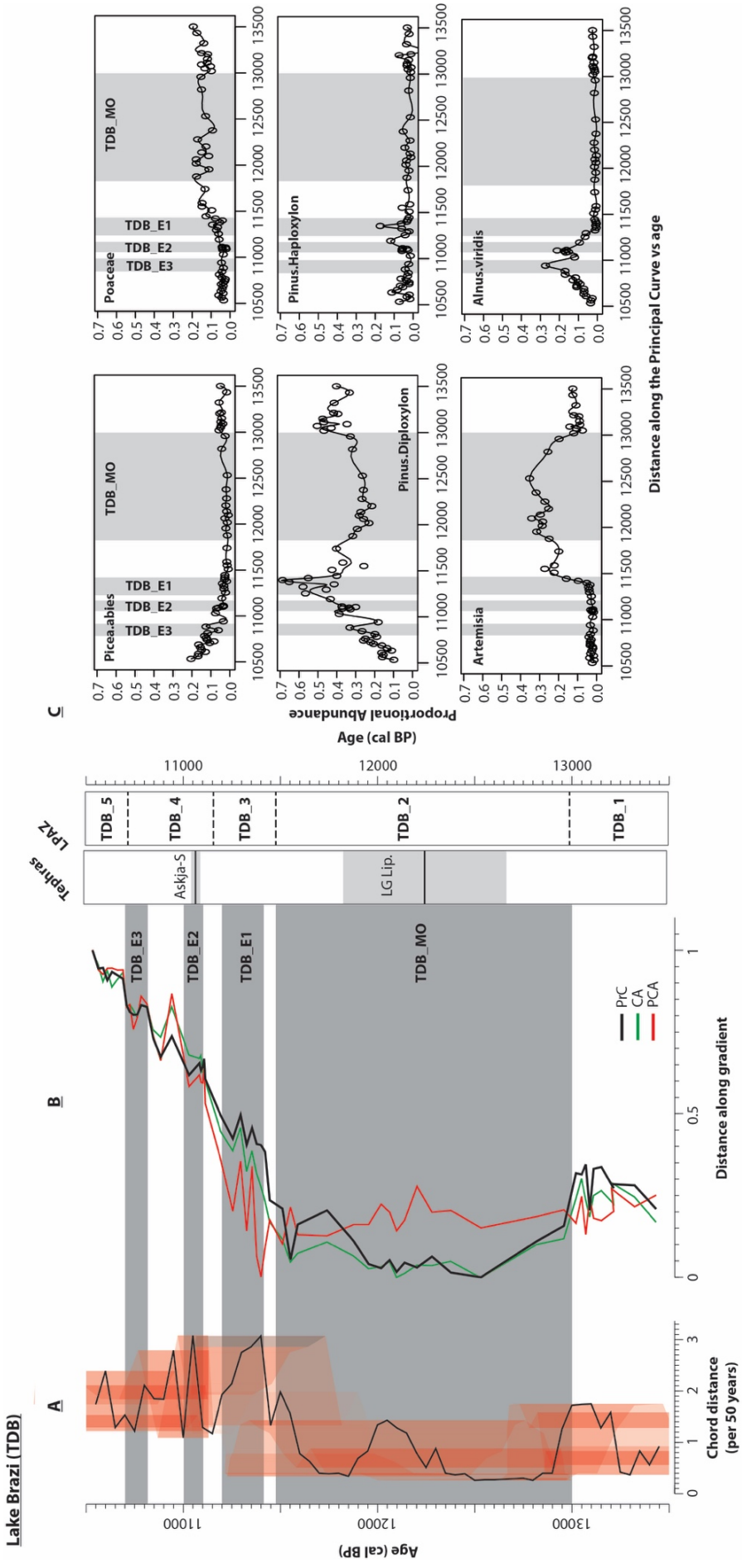


**Figure 7.51 The statistical results for the pollen percentage data from Lake Brazi**. A) RoC analysis for every 50 years. The values presented are exaggerated to provide clearer results into periods of significant change. The higher the bar, the more significant the composition' s change was. Light shading shows 1σ age error. B) The results of the different ordination tests (PCA, CoA and PrC). The grey boxes highlight oscillations identified from the PrC curve. C) The key taxa response curves modelled through the PrC. The grey boxes show the timing of the oscillations from the main PrC. Changes in the abundance of individual taxa at certain times provide insight into which taxa are driving the change. The record is plotted against calibrated age (μ ±1σ ) with light shading showing 1σ age error.

### 7.2.13.2 Palaeoclimatic and palaeoenvironmental interpretation

This section will focus on reconstructing the climate and environmental history of Lake Brazi using the pollen data previously presented. Based upon age modelling, identification of the Askja-S with the new LG Lipari tephra and evident vegetational changes, LPAZ can be correlated to periods of the LGIT of the Allerød (TDB_1), YD (TDB_2) and EH (TDB_3-5).

**Allerød-YD transition (12,874 ± 175 cal. BP)**

*Pinus* taxa was the dominant vegetational component of the local landscape during this period (Figure 7.48). Magyari et al. (2012) identified the *Pinus* taxa as *P. mugo* (part of the *Pinus* subgenus Diploxylon) and *P. cembra* (part of the subgenus Haploxylon). Both these taxa are found in mountainous areas (Huntley and Birks, 1983). Other tree taxa of *Picea abies* and *Betula nana* expanded at this higher elevation indicating woodland development while herbaceous taxa of *Artemisia* and Poaceae declined as they were outcompeted. Thermophilous deciduous taxa of *Ulmus* and *Quercus* expanded into the record (Figure 7.48). There was a slight increase in organic matter during this time. The pollen assemblage presented here was indicative of the Allerød period in Romania (e.g. Wohlfarth et al., 2001; Bjorkman et al., 2002).

At 12,874 ± 175 cal. BP, woody taxa declined (Figure 7.48). *Pinus* taxa declined, specifically *Pinus* subgenus Diploxylon, along with *Picea.* The herbaceous taxa associated with cold, steppe tundra of *Artemisia* and Chenopodiaceae increased. LOI showed a slight decline in the organic matter around this time with little lithological change (Figure 7.48). There was a marked decline in deciduous taxa (e.g. *Ulmus, Quercus, Alnus*) as temperatures cooled. Overall, this signals the onset of the YD (e.g. Wohlfarth et al., 2001; Bjorkman et al., 2002).

**YD-EH transition (11,485 ± 199 cal. BP)**

*Artemisia* and Chenopodiaceae continue to increase as cold steppe developed as the woodland was deforested (Figure 7.48; Magyari et al., 2012). The climate continued to be cold and dry with snow present (Magyari et al., 2012). Overall, tree taxa PAR does decrease over this period as the tree line descends (Figure 7.49).

At 11,485±199 cal. BP, *Pinus* subgenus Diploxylon and Haploxylon increased along with *Ulmus* (Figure 7.48). Taxa associated with cold steppe (e.g. *Artemisia* and Chenopodiaceae) declined. The deciduous tree taxa of *Ulmus*, *Alnus* and *Quercus* reappeared in the pollen record indicating the start of migration out of their local tree refugia (Björkman et al., 2003; Feurdean and Bennike, 2004; Tanţău et al., 2003, 2006, 2014; Magyari et al., 2009; Gridean et al., 2015; Vincze et al., 2017). Organic matter started to increase (Figure 7.48). Overall, the climate became warmer with the pollen assemblage indicative of the start of the EH (e.g. Bjorkman et al., 2002; Feurdean and Bennike, 2004)

**Earliest Holocene oscillations**

Climate continued to warm as thermophilous tree taxa continue to migrate into the record at Brazi. Tree taxa influx increased with deciduous taxa being the main contributors from lower elevations (Figure 7.48; Magyari et al., 2012).

Three vegetation events were identified in the EH. At 11,449 ± 199 cal. BP, a plateau followed by two positive peaks were observed in the PrC (Figure 7.51). This was accompanied by an increase in vegetation turnover indicated by a peak in RoC (Figure 7.51). The PrC is possible identifying oscillating decreases in *Pinus* subgenus Diploxylon and a decrease in Haploxylon. This was also seen in PAR at this time, indicating a decrease in pollen productivity (Figure 7.49; Magyari et al., 2012). There was a decrease in woody taxa (tree and shrubs) with an increase in herbaceous taxa, mainly *Artemisia,* Poaceae and

Chenopodiaceae indicating a forest disturbance (Figure 7.48). There was no evident change in lithology, yet there was a decline of ~1-2% in LOI at this time. A second event at 11,096 ± 33 cal. BP with a peak in PrC was seen. This was driven by a peak in *Alnus viridis* and a decline in *Pinus mugo* with a rise in open herbaceous taxa. There was a rise in LOI values. RoC showed a peak in vegetation turnover. The final event at 10,846 ± 197 cal. BP, was a trough in the PrC values. An increase in *Alnus viridis* and a decline in *Pinus mugo* drove this change. No response was seen in herbaceous taxa in Figure 7.48. There was a decline in RoC values.

## 7.3. Chapter summary

This chapter summaries both the chronological and palynological results from the sites that were selected from across Europe using the site selection criteria in Chapter 3. Firstly, the chronology results from the large age model provided refined age estimates using radiocarbon dating for the tephra layers involved, namely the LG Lipari, LST, VA, Hässeldalen and Askja-S tephra. The large age model, with the cross-correlation of these tephras, allowed many of the thirteen sites to have an improved chronology across the LGIT.

By providing a reliable age model for these sites, the timing and identification of vegetation response to climatic and environmental changes was investigated. Using raw pollen counts provided by primary investigators at each site, pollen percentage and PAR were calculated, allowing insight into vegetational changes across the LGIT. The implementation of PCA on these pollen records allowed changes in climate (mainly temperature and precipitation) to be identified as the main driver of vegetation change. This provided confirmation in vegetation response was to climate events during the LGIT. As a result, LPAZ from each site could be correlated to the chronostratigraphy of the Allerød, YD and EH period. Additional identification of centennial-scale vegetation response to climate

oscillations within the EH period was undertaken by using the statistical tool of PrC. Numerous vegetation events in response to possible climatic cooling events were identified at each site.

This results chapter provides information in the timing and characteristic of vegetation response during the LGIT across Europe. In the next chapters, this information will provide insight into the identification, timing and characteristic of vegetation transitions to abrupt climatic change on millennial-scale (the YD, in Chapter 8) and centennial-scale (in the EH period, in Chapter 9).

# Chapter 8

## The timing of millennial-scale vegetation response: the onset and termination of the Younger Dryas

This chapter discusses the timing of the onset and termination of the Younger Dryas (YD) in terrestrial vegetation across Europe. Section 8.1 focuses on the identification of the onset and termination of the stadial across Europe in the terrestrial vegetation record with additional lines of evidence from other proxies. Section 8.2 discusses the magnitude of these changes across the European regional transect. Section 8.3 presents the timing of the onset and termination of the YD at each site with comparisons to the Greenland Ice Core (GIC) record in section 8.4. The temporal structure of the YD across Europe allows for the potential climatic mechanism(s) behind the deterioration in environmental conditions to be inferred in section 8.5. Section 8.6 evaluates the results of this chapter before conclusions are drawn in section 8.7.

These sites have an independent chronology as well as either the identification of the Laacher See tephra (LST) and/or the Vedda Ash (VA). These well-dated tephra marker layers bracket the YD providing improvements in the precision and accuracy of age-models that incorporate them. The secondary sites of Hässeldala and Czechowskie are included in the larger age-model but do not include these tephras. However, they provide further understanding into the (a)synchronous nature of the climatic shift. The newly dated Late Glacial Lipari (LG Lipari) tephra to the YD at Brazi allowed the inclusion of the site. The varve sequence of Meerfelder Maar, west Germany (Brauer et al., 1999) was also used as an independently dated record to examine the synchronicity of the YD across Europe.

## 8.1 Identification of the Younger Dryas across Europe

The millennial-scale climatic oscillation of the YD stadial (outlined in section 2.2.1) was of considerable magnitude and brought about a distinct environmental response that it is seen in numerous records and proxies across Europe (e.g. Lowe and Watson, 1993).

The sites presented in this study demonstrate a terrestrial vegetation response to a large-scale climatic cooling (Chapter 7). Even with distinct regional environmental diversity from northern to southern Europe, there is evidence of extensive vegetational changes (Figure 8.1). At each site, pollen, lithology and, where available, addition proxies respond to a climatic downturn. This climatic oscillation affected the landscape surrounding each site.

### 8.1.1 Kråkenes, Norway

The transition into the YD at Kråkenes is with the change to cold-adapted vegetation communities of arctic/alpine environments (Birks et al., 2000; Birks and Birks, 2013). There was high vegetation overturn on the landscape, reflected in both the Principal Curve (PrC) and Rate of Change (RoC, Figure 8.1), replacing the previous Allerød pioneering vegetation of temperate-shrubs and herbs. Macrofossil records from the site show a similarly dramatic change in taxa (Birks and Birks, 2013). The deterioration of climatic conditions allowed a local glacier to develop and affect the local catchment rapidly, resulting in a switch to glacial silts in the lithostratigraphy (Birks et al., 2000; Lohne et al., 2013). The landscape became more open, causing an increase of inwashed sediment and a drop in LOI values. In chironomid-inferred temperatures (C-IT), there was a drop of ~5ºC at this transition (Brooks and Birks, 2001). This decline in summer temperatures affected the pollen production of taxa, indicated by Pollen Accumulation Rate (PAR). Conditions across the local region saw an increase in snow and permafrost (Birks et al., 2004; Birks and Birks, 2013).

PrC and RoC indicate the transition to the earliest Holocene (EH) with a rapid vegetation response. Temperate shrubs and herbs quickly replaced Arctic/alpine vegetation as mid-alpine grassland taxa colonised bare ground. The lithostratigraphy switched rapidly from glacial sediment to gyttja (Lohne et al., 2013). The local glacier disappeared soon after the EH onset, associated with climatic amelioration (Lohne et al., 2013). Rising summer temperatures indicated by the C-IT show an initial rise from 10 ± 1.3°C to ~11 ± 1.1°C before plateauing and then continuing to rise to 12 ± 1.1°C (Brooks and Birks, 2000; Birks and Birks, 2013).

The vegetation recorded at Kråkenes includes *Betula*. Due to the presence of *Betula nana* macrofossils, this taxon was believed to have existed locally (Birks et al., 2000). Differentiation between the species is difficult due to the pollen morphological similarities (Birks, 1968). Many investigators put both taxa under *Betula* even though there are different ecological conditions for each taxon. As a result, the continued presence of *Betula* within the pollen records may or may not relate to the persistence of *B.nana* on the landscape. The PrC and RoC values are directly affected, which may not show the full extent of the vegetation decline and composition turnover with a climatic deterioration. Previous investigators for other sites (e.g. Kråkenes, Birks et al., (2000) and Crudale, Whittington et al., (2015)), have suggested that *B.nana* is present, yet do not distinguish between the taxa in their records. As a result, the magnitude of vegetation change should be interpreted cautiously.

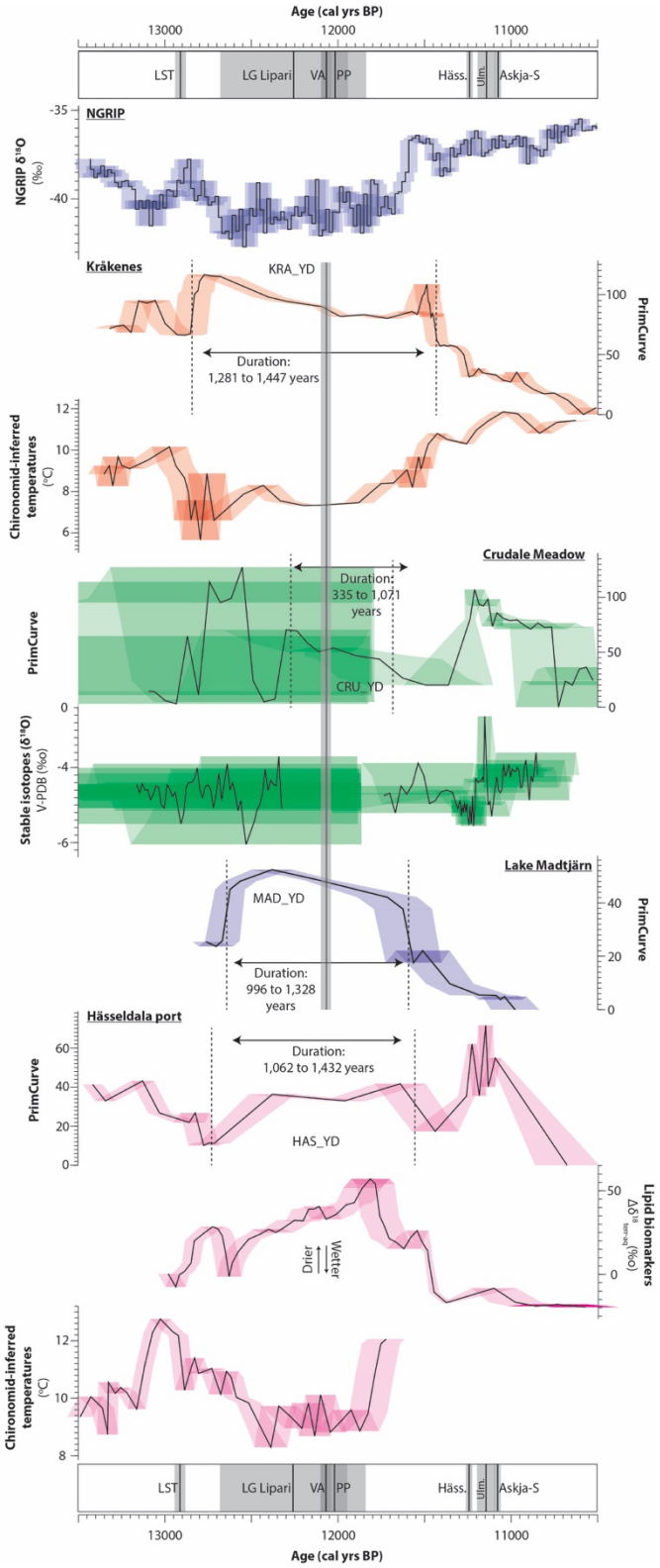


**Figure 8.1** Comparison of the Principal Curve (PrC) applied to the pollen data from the sites. The light colour band shows 1σ (68.2%) age uncertainty. Dashed line is YD period with min/max years of duration CONISS. Additional proxy data is also displayed were available. Kråkenes, Chironomid-inferred temperature (Brooks and Birks, 2001); Crudale bulk oxygen stable isotope (Whittington et al., 2015); Hässeldala port, chironomid-inferred temperature and lipid biomarkers (Wohlfarth et al., 2017). Tephras identified at each site are also shown: LST = Laacher See Tephra; LG Lip. = Late Glacial Lipari; VA = Vedde Ash; Häss. = Hässeldalen; Ulm. = Ulmener Maar; Ask. = Askja-S.

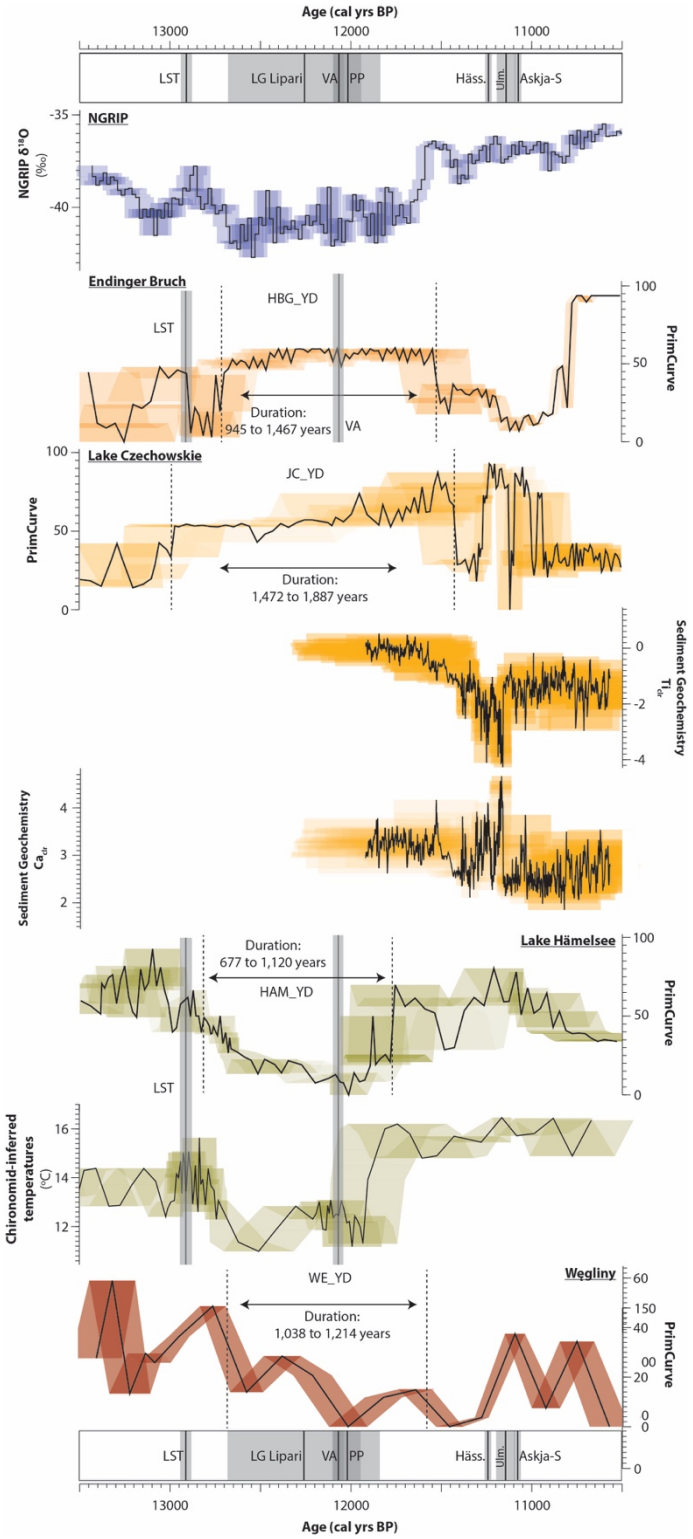


**Figure 8.1 (cont.)** Comparison of the Principal Curve (PrC) applied to the pollen data from the sites. The light colour band shows 1σ (68.2%) age uncertainty. Dashed line is YD period with min/max years of duration CONISS. Additional proxy data is also displayed were available. Kråkenes, Chironomid-inferred temperature (Brooks and Birks, 2001); Crudale bulk oxygen stable isotope (Whittington et al., 2015); Hässeldala port, chironomid-inferred temperature and lipid biomarkers (Wohlfarth et al., 2017). Tephras identified at each site are also shown: LST = Laacher See Tephra; LG Lip. = Late Glacial Lipari; VA = Vedde Ash; Häss. = Hässeldalen; Ulm. = Ulmener Maar; Ask. = Askja-S.

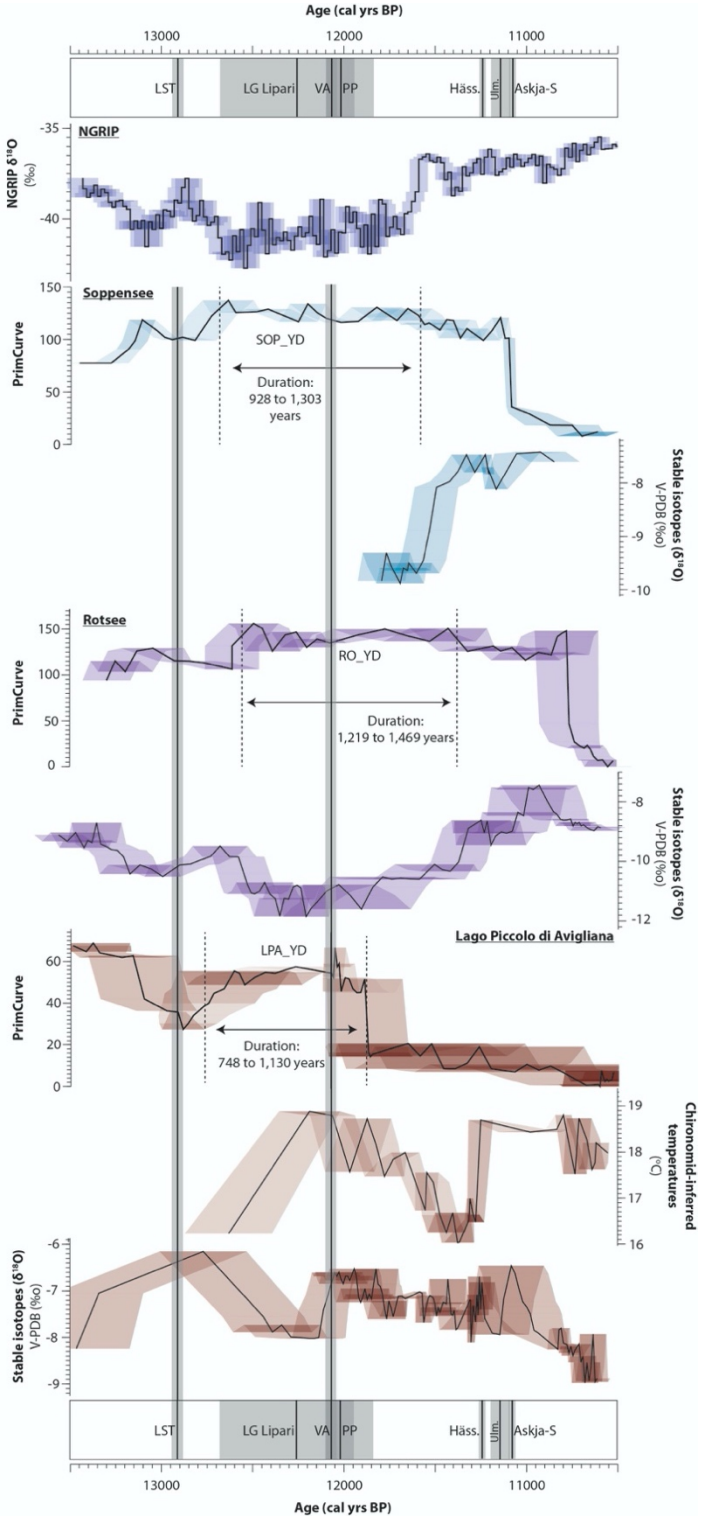


**Figure 8.1 (cont.)** Comparison of the Principal Curve (PrC) applied to the pollen data from the sites. The light colour band shows 1σ (68.2%) age uncertainty. Dashed line is YD period with min/max years of duration CONISS. Additional proxy data is also displayed were available. Kråkenes, Chironomid-inferred temperature (Brooks and Birks, 2001); Crudale bulk oxygen stable isotope (Whittington et al., 2015); Hässeldala port, chironomid-inferred temperature and lipid biomarkers (Wohlfarth et al., 2017). Tephras identified at each site are also shown: LST = Laacher See Tephra; LG Lip. = Late Glacial Lipari; VA = Vedde Ash; Häss. = Hässeldalen; Ulm. = Ulmener Maar; Ask. = Askja-S.

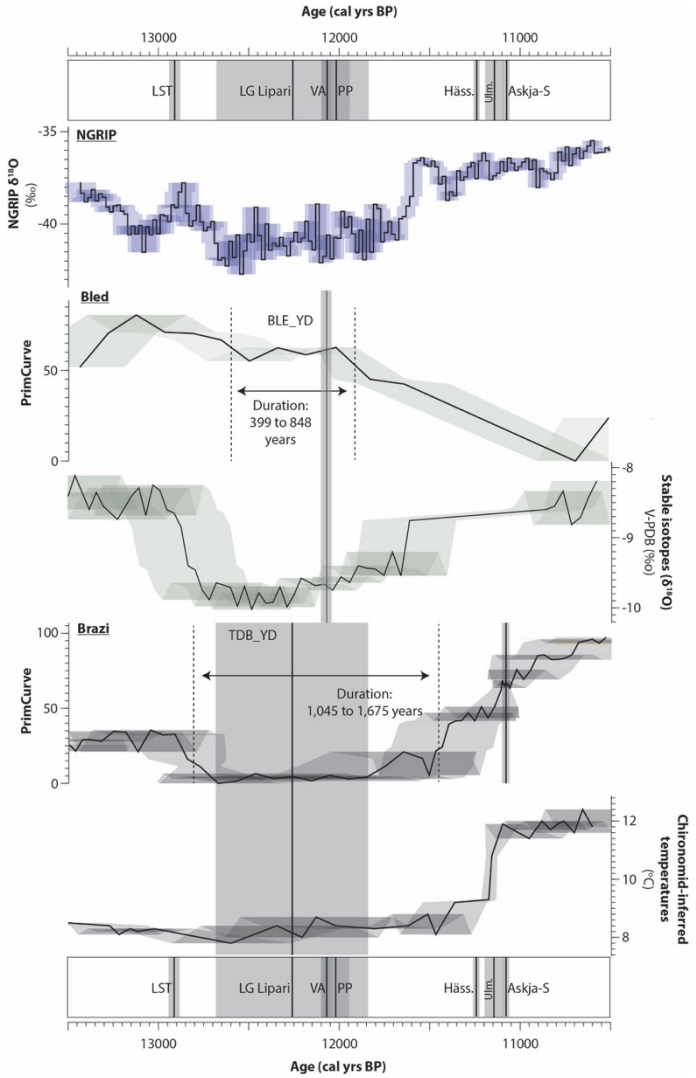


**Figure 8.1 (cont.)** Comparison of the Principal Curve (PrC) applied to the pollen data from the sites. The light colour band shows 1σ (68.2%) age uncertainty. Dashed line is YD period with min/max years of duration CONISS. Additional proxy data is also displayed were available. Kråkenes, Chironomid-inferred temperature (Brooks and Birks, 2001); Crudale bulk oxygen stable isotope (Whittington et al., 2015); Hässeldala port, chironomid-inferred temperature and lipid biomarkers (Wohlfarth et al., 2017). Tephras identified at each site are also shown: LST = Laacher See Tephra; LG Lip. = Late Glacial Lipari; VA = Vedde Ash; Häss. = Hässeldalen; Ulm. = Ulmener Maar; Ask. = Askja-S.

### 8.1.2 Crudale Meadow, Scotland

At the transition into the YD, there is rapid vegetation overturn indicated by the PrC curve (Figure 8.1). Climatic deterioration sees heathland vegetation that developed during the Allerød replaced by arctic tundra taxa (*Artemisia*, Lactuceae undiff.). The landscape became more open, with a decline in PAR, indicating a downturn in local pollen production.

Other sites across Scotland show a similar vegetation response (e.g. Whittington et al., 1996; Edwards and Whittington, 1997, 2010). There is a lithostratigraphic change from marl to siliciclastic sediment. The low LOI values and increase in magnetic susceptibility encountered by Whittington et al. (2015) indicates a rise in allogenic material as the landscape became unstable (Battarbee et al. 2001).

Further evidence provided by the sudden depletion and termination of $\delta^{18}O$ values at the site indicates a drop in temperature (Whittington et al., 2015). The $\delta^{18}O$ record is equated to temperature changes by Whittington et al. (2015), linked to isotopic fractionation in the mid-latitudes (Leng and Marshall, 2004; Whittington et al., 2015). Temperature declines of ~5$^{o}$C are recorded in C-IT for Scotland at this transition (Brooks et al., 2012).

The termination of the YD at Crudale sees a decline in arctic tundra vegetation to a landscape dominated by grasslands. A rise in LOI values shows increased landscape stability. Marl begins to be re-deposited as the temperature rose rapidly. This climatic amelioration is also recorded in $\delta^{18}O$ values by Whittington et al. (2015) (Figure 8.1). The expansion of the thermophilous shrub taxon, *Corylus*, into the pollen catchment area, provides additional evidence for improved climatic conditions. However, throughout the EH period, there is no major woody component compared to other sites (e.g. Lowe and Walker, 1986; Abrook, 2019). Either harsh climatic conditions, migratory lags or inappropriate ecotonal conditions (i.e. soil development) (Bunting, 1996) may have influenced this vegetation assemblage. As a result, this grassland development is a reflection of the EH period in the Orkney Islands (Abrook et al., 2019).

However, there should be consideration of inwashed pollen grains affecting the pollen record during the YD. The PrC chord distance during the YD is lower than the Allerød and EH variations (Figure 8.1). The magnitude of the YD is known worldwide to be larger compared to these shorter centennial-scale climatic oscillations (e.g. Lowe and Watson,

1993; Ruth et al., 2007). The increase in PAR after the deposition of the VA correlates to increased pollen inwash. The Principal Curve Analysis (PCA) for this site shows that *Empetrum* is unusually responding to a different variable than other taxa (Figure 7.10). These *Empetrum* pollen grains are likely to be reworked during the YD. The inwash of *Empetrum* pollen from Allerød deposits is common during the YD in Scotland (Birks and Birks, 2014). Whittington et al. (2015) did note that pollen grains were more eroded during this period. As a result, the PrC curve may not be reflecting an accurate representation of vegetation turnover during the YD.

### 8.1.3 Lake Madtjärn, Sweden

The onset of the YD is a transition to an open tundra landscape. The deterioration of climatic conditions deforests *Betula* and *Pinus* woodlands. The PrC shows a rapid vegetation composition turnover (Figure 8.1). Other sites in the region also show similar palynological changes with sparse terrestrial vegetation cover (e.g. Björck et al., 1994; Wohlfarth et al., 2006). Understanding the absolute changes of vegetation composition on the landscape from this record was not possible due to the lack of data to calculate PAR. As a result, it is difficult to determine how much pine was part of the local vegetation (Seppä and Hicks, 2006).

The EH transition sees an expansion of heathland of *Empetrum* and Poaceae with the reforestation of *Betula*. Birch trees are known to expand into northern Europe in response to this climatic warming (Theuerkauf et al., 2014). The sediments gradually change to a fine clay gyttja that is higher in organic content, though there is no LOI data to confirm this (Björck et al., 1996). Nonetheless, the landscape is becoming stable as seen in other pollen records for the region (e.g. Berglund et al., 1994; Heider, 2004).

### 8.1.4 Hässeldala port, Sweden

The transition to the YD stadial is an expansion of cold steppe-tundra, mainly *Artemisia*, with the contraction of birch tree woodland in the percentage pollen record. Defining the transition in PrC values is difficult and is due to insufficient proxy resolution across the LGIT (Figure 8.1). However, the onset is taken at 12,733 ± 63 cal. BP. Organic matter decreases, associated with a decline in lake productivity (Ampel et al., 2014; Wohlfarth et al., 2017). The landscape becomes largely open and treeless. C-IT show cooler conditions of <10ºC with lipid biomarkers ($\Delta\delta D_{terr\text{-}aq}$) indicating drier conditions (Muschitiello and Wohlfarth, 2015; Wohlfarth et al., 2017). Diatoms from the site show taxa associated with colder temperatures and longer lake ice-cover (Ampel et al., 2014).

The EH transition sees an expansion of heathland taxon of *Empetrum* with a sharp decline in steppe-tundra. Birch woodland does not expand until later in the EH, yet macrofossils indicate a local occurrence of the birch tree taxon (Wohlfarth et al., 2006). The PrC values and percentage pollen define the end of the YD based on only two pollen samples. As a result, it is difficult to ascertain if this is the correct timing for this transition. The lithological changes with gyttja sediment and a rise in LOI values reflect an increase in organic matter (Wohlfarth et al., 2017). A rise in C-IT to ~12ºC and a change to wetter conditions from $\Delta\delta D_{terr\text{-}aq}$, confirms climatic amelioration (Figure 8.1, Muschitiello and Wohlfarth, 2015; Wohlfarth et al., 2017). Similar vegetation responses to the YD stadial transitions are seen across Sweden (e.g. Berglund, 1966; Wohlfarth et al., 2018).

During the whole of the YD stadial, *Corylus* is recorded (Figure 7.15). *Corylus* is considered not to have migrated to the region until later, ~10,450 cal. BP, originating from the Alps ~11,600 cal. BP (Theuerkauf et al., 2014). The data provided showed a maximum of fifteen grains during the YD, with two *Corylus* grains from another core at the site (Core 6). The pollen grains of *Betula* are similar in morphology. Coupling this with a rise in

crumpled/eroded pollen grains inwashed into the lake during the stadial it may have resulted in a misidentification of *Betula* pollen. As a result, the PrC values have possibly been influenced by this, which need to be taken into consideration.

### 8.1.5 Endinger Bruch, Germany

The onset of the YD is seen with an opening of the birch/pine woodland as these taxa decline and herbaceous taxa expand. The proposed decline in summer temperatures to 11-12$^{o}$C during the stadial would have had detrimental effects on tree pollen production (Isarin and Bohncke, 1999). However, these temperatures are still within the thermal ranges of pine and birch taxa (Ibid). As a result, birch/pine stands would be common rather than a closed forest (de Klerk, 2002). The vegetation transition is observed in the PrC is in high-resolution contrast to the interpolated RoC. A decrease in LOI values and accumulation of sandy/silty sediments within the lithostratigraphy indicate increased upland erosion with the reduction in vegetation (de Klerk, 2002). The delayed change in lithostratigraphy to silt/sand gyttja is due to a lag in lake productivity according to de Klerk (2002).

Expansion of *Betula* and *Pinus* indicates a transition into the EH climatic amelioration, dated to 11,516 ± 137 cal. BP. Percentage pollen values show a closing of the forest as shrubs and herbaceous pollen are easily outcompeted. The rise in wild grasses is associated with an increase in *Phragmites* (reed species) along the lake edge as wetland vegetation expanded with ideal climatic conditions (de Klerk, 2002). The gradual rise of LOI and shift to detrital gyttja indicates organic production and landscape stability as vegetation succession began (e.g. Theuerkauf et al., 2014).

### 8.1.6 Lake Czechowskie, Poland

The transition into the YD stadial saw a decline in the birch-pine woodland that dominated the landscape while tundra-steppe taxa expanded. The shade-intolerant *Juniperus* shrub and herbaceous taxa occupied open areas (Thomas et al., 2007). PrC values with RoC pick up this transition indicating a widespread vegetation change on the local landscape (Figure 8.1). Theuerkauf et al. (2012) highlighted a latitudinal ecotone limit of 53° to the local occurrence of *Pinus* during the YD due to either harsh atmospheric conditions or permafrost (de Klerk, 2008). The sedimentological changes from calcite to faint laminations also indicate that climatic deterioration affected lake productivity (Brauer et al., 1999). No LOI values were available for this record. However, Słowiński et al. (2017) recorded an increase in allochthonous inwash at neighbouring Tzechowskie that disrupted varve preservation. Similar inwash may be happening at Czechowskie. Other records from the northern region of Poland and Germany show similar vegetational response to this climatic deterioration (e.g. de Klerk, 2008; Theurerkauf et al., 2014; Słowiński et al., 2017).

The expansion of pine-birch woodland signalled the termination of the YD at 11,423 ± 143 cal. BP. Rising temperatures and improvement in soil conditions allowed *Pinus* to re-establish dominance on the local landscape (Theuerkauf et al., 2014). The forest became quickly closed, resulting in a decline in herbaceous taxa with the disappearance of *Artemisia* as the YD ends (Kołaczek, 2013). The formation of calcareous diatomaceous varves shows climatic amelioration in the spring and summer to allow calcite precipitation (Wulf et al., 2013). Other records demonstrate similar EH vegetation responses (e.g. de Klerk, 2008; Kołaczek, 2013).

### 8.1.7 Lake Hämelsee, Germany

The onset of the YD at Hämelsee is gradual with an opening up of the birch/pine forest and a rise in herbaceous taxa. This transition is hard to identify in the PrC curve with RoC showing no large vegetational composition change, in contrast to other sites in northern Europe (Figure 8.1, e.g. Litt and Stebich, 1999; Brauer et al., 2001). Previous investigators at the site have also encountered gradual vegetation changes into the YD (Merkt and Müller, 1999). There is further evidence provided by a gradual sedimentological change (LOI) at the site. Merkt and Müller (1999) suggested that the reworking of shallower lake sediments during the transition resulted in this indistinct transition. The lithostratigraphic change to homogenous sediments indicates inwash of clastic sediments due to catchment instability and cryoturbation (Merkt and Müller, 1999; Brauer et al., 1999). The site's C-IT record shows no distinct temperature decline at this transition as seen at other sites (e.g. van Asch et al., 2012), presumably due to the effect of reworked lake sediments. Nonetheless, there is C-IT decline of ~2°C to ~11.5°C in summer temperatures to the coldest point in the early YD (Figure 8.1).

The termination of the YD is presented in the PrC curve is by the expansion of *Betula* woodland and decline of herbaceous taxa. There are similar vegetation responses in the region (e.g. Litt and Stebich, 1999; Bos, 2001). At the EH onset, there is an increase in C-IT to ~16°C (Figure 8.1). With climatic amelioration, the rapid reforestation of *Betula* from open forests to high coverage of the landscape is due to ideal local conditions recorded in Western Germany with oceanic climates and gleylic soils (Theuerkauf et al., 2014). LOI values show a rise in organic matter in the catchment as biomass and landscape stability increased with improving climatic conditions.

### 8.1.8 Węgliny, Poland

Defining the onset of the YD is difficult at Węgliny due to the lack of vegetational changes associated with deteriorating climatic conditions. The PrC values are highly variable across the whole LGIT record, with no clear distinctions for the YD onset and termination (Figure 8.1). Jurochnik and Nalepka (2013) attribute this to a lag in vegetation response to climatic changes. The distal location of the site may have mitigated the impact of North Atlantic changes in oceanic circulation during the LGIT (Isarin and Renssen, 1999). However, there are additional factors. Insufficient proxy resolution with the limited number of identified taxa might have restricted the identification of vegetation responses to climatic oscillations if a response existed. Pollen changes between successive samples may be the result of statistical bias (de Klerk, 2007). Comparison to other sites in central Poland does show clear vegetation overturn during the LGIT (e.g. Gosler et al., 1999; Pawłowski et al., 2016). Further investigation with the application of higher resolution pollen analysis may provide further insight into vegetational shifts.

Nonetheless, from the data provided, the YD onset is recorded by an opening of the pine-birch woodland to expanding herbaceous taxa. A decline in organic matter is linked to increased fluvial erosion and weathering as the climate deteriorated (Brauer et al., 1999). The distinction between *Betula* tree and *B. nana* is not made in the record by Joruchnik and Nalepka (2013), yet there is a decline in *Betula*.

The reforestation of pine-birch woodland with the decline of *Artemisia* defines the termination of the YD. Rising LOI values show increased biomass on the landscape. The appearance of *Alnus* further indicates a rise in temperatures associated with the EH period with C-IT records in the region showing a summer temperature increase to 16.5$^{o}$C (Pawłonski et al., 2015, 2016) and reduction in cold herbaceous taxa (e.g. Gosler et al., 1999; Pawłonski et al., 2016).

### 8.1.9 Soppensee and Rotsee, Switzerland

Soppensee and Rotsee will be discussed together due to the close proximity of these pollen records. The YD onset at both sites sees an opening of the pine forest with birch stands with the shade-intolerant taxa of *Juniperus* and *Artemisia* expanding (Thomas et al., 2007). The PrC curve shows a clear YD transition with vegetation turnover (Figure 8.1). Macrofossil remains reflect this vegetation composition change with a decline in both *Betula* and *Pinus* (Lotter, 1992a, 1999). Both sites are below the treeline limit during the onset of the YD resulting in composition change rather than drastic deforestation (Lotter et al., 1992a, 1999; Wick and Tinner, 1997). There is little lithostratigraphic shift in both core sediments, indicating that changes in vegetation composition did not significantly affect landscape stability or minerogenic inwash. Rotsee did record a decline in lower LOI values as lake productivity fell (Lotter et al., 1992a). The transition is reflected clearly in the bulk stable-isotope record ($\delta^{18}O$) for Rotsee (Figure 8.1). The changes in $\delta^{18}O$ values are to temperature-dependent isotopic fractionation at mid-latitudes (Figure 8.1; Lotter et al., 1992a; Leng and Marshall, 2004; Verbruggen et al., 2010). There is an apparent decrease in $\delta^{18}O$ values as temperatures declined at Rotsee. This climatic cooling resulted in deforestation of areas across the northern Alps (e.g. Lotter et al., 1992, 2000; Wick, 2000).

Both palynological records show an increase in birch and pine woodland with the onset of the EH climatic amelioration. Herbaceous taxa and *Juniperus* declined with increased as the landscape became more stable. This transition is not definitive in the PrC values due to limited vegetation composition changes on the landscape (Figure 8.1). The lower altitude of Rotsee and Soppensee resulted in a less pronounced shift to EH vegetation as they were within their vegetational ecotones (Wick, 2000). The $\delta^{18}O$ record at Soppensee begins around the EH transition as temperatures warmed (Figure 8.1, Lotter et al., 1992). The higher $\delta^{18}O$ values from both sites show climatic warming (Lotter et al., 1992;

Verbruggen et al., 2010) with C-IT for the region showing a rise of ~1.5ºC in summer (Heiri et al., 2003)

### 8.1.10 Lago Piccolo di Avigliana, Italy

The transition into the YD at LPA sees a decline in thermophilous tree taxa of *Quercus* from the preceding Allerød period. The mixed deciduous oak forests opened and were dominated by *Betula-Pinus* with herbaceous taxa. There are no PAR calculations for the site, but *Pinus* macrofossils indicate local occurrence (Finsinger et al., 2011). The PrC values reflect this change in vegetation composition (Figure 8.1). A decline in landscape biomass increased minerogenic inwash (Battarbee et al., 2000; Finsinger et al., 2011). C-IT record showed a deterioration in the climate with a 1.5ºC decrease in temperature (Finsinger et al., 2008). Evidence from the $\delta^{18}O$ record, reflecting air temperature changes, shows a subdued cooling response (Finsinger et al., 2008). The interplay of moisture sources may also affect $\delta^{18}O$ values (Leng and Marshall, 2004; Finsinger et al., 2008). The decline in temperatures resulted in a partial *Quercus* population decline affecting pollen production of the taxa (Finsinger et al., 2011).

PrC values show the termination of the YD and transition into the EH (Figure 8.1). There is a widespread vegetation turnover with an expansion of thermophilous tree taxa, mainly *Quercus*, and a contraction of heliophilous taxa. C-IT also shows a rapid increase by 2.5ºC at the transition (Larocque and Finsinger, 2008) and throughout the broader region (e.g. Heiri et al., 2007; Magny et al., 2012; Joannin et al., 2013). At the same time, bulk $\delta^{18}O$ shows a strong rise in values linked to changes in seasonality and rainfall (Finsinger et al., 2008; Zanchetta et al., 2007). However, issues with contamination of $\delta^{18}O$ by detrital carbonates and a decline of lake levels affecting chironomid assemblages make direct links to climatic change difficult (Finsinger et al., 2008). Evidence from other sites shows a rise

of 2-3ºC before the YD termination (e.g. Heiri and Millet, 2005; Ilyashuk et al., 2009). *Quercus* expands rapidly in LPA and other southern Alp sites after the termination of the YD (e.g. Gobet et al., 2000; Vescovi et al., 2007; Finsinger et al., 2011)

### 8.1.11 Lake Bled, Slovenia

The transition into the YD at Bled is with an opening of the birch woodland and expansion of herbaceous taxa associated with colder environments. The PrC values do not adequately define the YD onset due to either insufficient proxy resolution or the limitation of using percentage data in calculating PrC values (Figure 8.1). There is limited vegetation overturn displayed in the percentage data compared to PAR. Nonetheless, tree taxa are at lower densities, indicated by lower influx rates (Figure. 7.45). The open environment led to soil erosion in the catchment with oscillations in LOI values (Battarbee et al., 2001). Climatic conditions recorded by $\delta^{18}O$ values, linked to changing air temperature, imply cooler temperatures at the YD onset (Andrič et al., 2009). There are similar vegetation responses in other records in the region (e.g. Pokorný et al., 2002; 2010; Stefanova and Ammann, 2003).

The reforestation of pine and deciduous forest taxa and decline of herbaceous taxa indicate the termination of the YD. Adequately defining the transition in percentage and PrC records is difficult due to poor pollen resolution during the EH. The enrichment in $\delta^{18}O$ values indicates gradual warming due to $\delta^{18}O$ having higher sample resolution across the transition (Andrič et al., 2009; Figure 8.1). There are similar vegetation responses seen by Pokorný et al. (2002) and Stefanova and Ammann (2003).

### 8.1.12 Lake Brazi, Romania

The onset of the YD stadial is with a reduction in the pine tree forest and expansion of steppe tundra taxa. Macrofossils of *Pinus mugo* (*Pinus* subgenus Diploxylon) have been identified in the record at this time indicating local survival. However, *Pinus cembra* (stone pine, dwarf pine, *Pinus* subgenus Haploxylon) become locally established as the treeline altitude recedes (Magyari et al., 2012; Orbán et al., 2018). *P.cembra* can tolerate harsh temperatures and higher altitudes (Caudullo and de Rigo, 2016). The treeline contracts to a similar elevation as Brazi (Magyari et al., 2012; Orbán et al., 2017). Thermophilous taxa of *Ulmus* and *Quercus* decline to lower elevations with climatic deterioration (Feurdean et al., 2007; Magyari et al., 2009, 2012). The observed transition in PrC and RoC values show extensive vegetational changes and reduced biomass with a reduction in woody taxa influx (Figure 8.1). There is little lithological change at the onset of the stadial with a slight decline in organic matter due to the presence of snow and ice cover, reducing lake productivity (Magyari et al., 2012). The C-IT shows a slight decline in summer temperatures with climatic deterioration (Figure 8.1, Tóth et al., 2012). However, the influence of the local glacier and the possible resilience of the assemblage to cooler temperatures may have resulted in this slight decline, with the greatest temperature change seen in winter (Figure 8.1; Feurdean et al., 2008a, b; Tóth et al., 2012). There are similar vegetation responses across the region (e.g. Tanţău et al., 2003; Feurdean and Bennike, 2004; Feurdean et al., 2007; Lascu et al., 2015).

The termination of the YD saw the re-establishment of *Pinus* woodland with the expansion of thermophilous deciduous taxa from local refugia (Gridean et al., 2015; Vincze et al., 2017). The treeline extended past Brazi, with pine macrofossils indicating a local open boreal woodland (Magyari et al., 2012; Orbán et al., 2017). The rise in organic matter shows increased biomass on the landscape and lake productivity (Tóth et al., 2012). C-IT summer

temperatures increase by ~0.5°C with a second increase of ~0.7°C around ~10,800 cal. BP (Figure 8.1; Tóth et al., 2012). Kråkenes also experienced a second C-IT increase (Tóth et al., 2012; Brooks and Birks, 2001). However, Brazi has a muted increase in comparison due to a local glacier (Reuther et al., 2007). Overall, the climate is becoming warmer with a pollen assemblage indicative of the start of the EH. This rapid vegetation response is similar to other sites in the region (e.g. Tanţău et al., 2003; Feurdean and Bennike, 2004; Feurdean et al., 2007; Lascu et al., 2015).

## 8.2 The magnitude of Younger Dryas vegetation response across Europe

The magnitude and characteristics of vegetation response during the transition into and out of the YD varies across Europe. The magnitude of inferred vegetation response used the relative PrC value changes with the maximum value minus the minimum value across the transitions. The relative change value was divided by the highest PrC value across the whole LGIT and multiplied by 100 to obtain a percentage change.

### 8.2.1 The Younger Dryas onset

Across Europe, the YD onset is observed. In the northern Europe, arctic tundra becomes dominant (Kråkenes, Crudale and Madtjärn). The central sites (Hässeldala, Endinger Bruch, Czechowskie, Hämelsee and Węgliny) experience an opening of the woodland with an expansion in herbaceous taxa. Southern sites (LPA, Bled and Brazi) see a decline in thermophilous trees and a rise herbaceous taxa. Figure 8.2 presents the magnitude of change across this transition.

The largest percentage shifts are in the northern sites of Kråkenes (42%), Crudale (51%) and Madtjärn (50%). The transition into the YD at these sites showed an abrupt decline in woody taxa as the local landscape became more open and treeless, dominated by

herbaceous arctic taxa. Previous authors have also noted that this transition is sharp and distinct, both in vegetation and sedimentary response (Björck et al., 1996; Birks et al., 2000; Wohlfarth et al., 2006, 2017; Whittington et al., 2015). Birks and Birks (2014) noted that small changes in temperature during the early YD resulted in large scale vegetation and local catchment response. The magnitude of change may not be reflected in the vegetation shift expressed in the PrC values due to problems associated with the level of taxa identification, mainly *Betula*. At northern sites during the YD, the sub-species of *Betula nana* is present. This dwarf shrub has different, harsher ecological tolerances than its counterpart of *Betula* tree (Beck et al., 2016). However, there is no distinction between these two subgenera due to similar pollen morphologies (Birks, 1968). The continued presence of "*Betula*" influences the PrC values resulting in a subdued shift in values (Birks et al., 2000; Whittington et al., 2015).

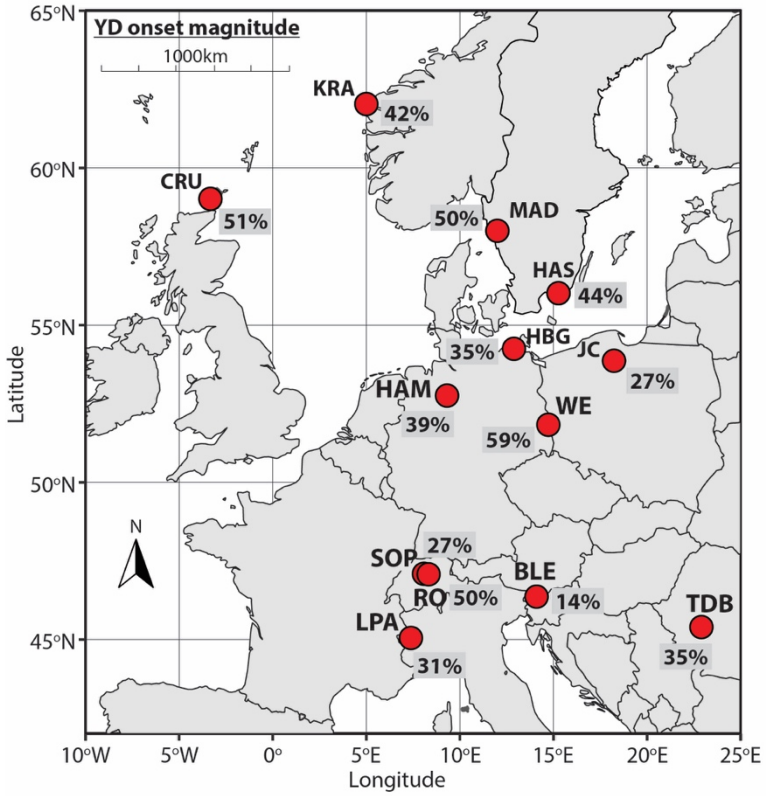


**Figure 8.2** Map of sites across Europe with percentage change in the PrC for the onset of the Younger Dryas. Site codes: KRA = Kråkenes; CRU = Crudale Meadow; MAD = Lake Madtjärn; HAS = Hässeldala port; HBG = Endinger Bruch; JC = Czechowskie; HAM = Lake Hämelsee; WE = Węgliny; MFM = Meerfelder Maar; SOP = Soppensee; RO = Rotsee; LPA = Lago Piccolo di Avigliana; BLE = Lake Bled; TDB = Lake Brazi

The central European sites of Hässeldala (44%), Endinger Bruch (35%), Hämelsee (39%) and Czechowskie (27%) show a lower magnitude response in comparison to northern sites. These vegetation records show a contraction in Allerød pine-birch woodlands with an expansion of shrub and herbaceous taxa as the landscape opened. However, at Hässeldala and Hämelsee, the PrC does not sufficiently identify the YD shift. Poor sampling resolution at Hässeldala as applied to the record is in contrast to other sites. While at Hämelsee reworking of surrounding lake sediments has resulted in a gradual vegetation transition (Merkt and Müller, 1999). As a result, it is difficult to determine the magnitude of the shift for both sites. Nonetheless, the magnitude of vegetation shifts are less than that experienced at the northern sites.

The vegetational response at the southern sites of Soppensee (27%), Rotsee (32%), LPA (31%) and the eastern site of Brazi (35%) show a similar response to central European sites (Figure 8.2). A similar change in landscape vegetation is seen, with an opening of the Allerød woodland and an increase in herbaceous taxa. The landscapes remain largely stable reflecting minor lithostratigraphic and LOI changes compared to northern sites.

At Bled vegetation shifts of 14% and Węgliny with 59%, the YD transition is hard to identify using the PrC. These values are different compared to other sites of similar latitude (Figure 8.2). The pollen records at both sites show little vegetation overturn during the LGIT. However, this could be the product of insufficient sample resolution at both sites which fails to capture variation in the vegetation during the LGIT.

The climatic deterioration into the YD resulted in a varying magnitude of vegetation response across Europe. The greatest response was observed in northern Europe as local Allerød vegetation declined and arctic taxa expanded. The propagation of the climatic retrogression across central and southern Europe resulted in a reduced magnitude of vegetation change with many sites retaining the majority of the birch-pine woodland.

The vegetational change at northern sites exceeded suggested ecological thresholds, resulting in widespread vegetation overturn (Scheffer and Carpenter, 2003; Williams et al., 2011). The changes in atmospheric circulation believed to be due to reduced AMOC from freshwater inputs resulted in the southward shift of the polar front and the Westerlies with declines in temperatures and precipitation (e.g. Clark et al., 2002). Changes in temperature and precipitation govern vegetation patterns across Europe (Prentice et al., 1991; Birks and Birks, 2014). The most considerable changes in temperature and precipitation are in northern latitudes with a ~2-5$^{o}$C decline in C-IT in comparison to ~0.5-1.5$^{o}$C shift in central and southern latitudes (Brooks and Birks, 2001; Brooks et al., 2012; van Asch et al., 2012; Birks and Birks, 2014). Additional local site factors such as increased soil disturbance (Kråkenes), wind strength (Crudale) and competition (Madtjärn) further influenced vegetation change within the record (Bunting, 1996; Birks et al., 2000; Birks and Birks, 2014).

The limited vegetation change at central and southern sites is in response to disseminated climatic changes along the latitudinal gradient due to weakening influence of the North Atlantic Ocean. Changes in temperature and precipitation are not as significant compared to Northern latitudes (Birks and Birks, 2014; Moreno et al., 2014). As a result, the vegetation populations at these sites do not pass their ecological thresholds. The continued presence of *Betula* and rise of *Juniperus* populations indicate that thermal limits (>12$^{o}$C) during the summer were not exceeded (Thomas et al., 2007; Birks and Birks, 2014) with decreased precipitation governing *Betula/Pinus* populations. Pollen production would have been affected with woody taxa restricted to smaller woodlands or tree stands.

The sites of Soppensee, Rotsee, LPA and Brazi are at high altitude southern sites. Davis and Shaw (2001) highlighted that vegetation at higher altitudes is closer to their ecological threshold. The role of altitude results in a greater magnitude of vegetational change into the stadial, compared to lower altitudes (Ammann et al., 1993). However, the

lack of similar elevated records in central and northern Europe, requires further investigation as to the role of altitude on vegetation shifts.

### 8.2.2 The Younger Dryas termination

The onset of climatic amelioration at the termination of the YD resulted in an expansion of scrub and woodland taxa as herbaceous taxa declined. Figure 8.3 shows the magnitude of change experienced across Europe. There are no clear latitudinal or altitudinal trends in the magnitude of vegetation response to increases in temperature. The changes in PrC values along these transitions highlight local conditions and vegetation succession that governed the level of vegetation response.

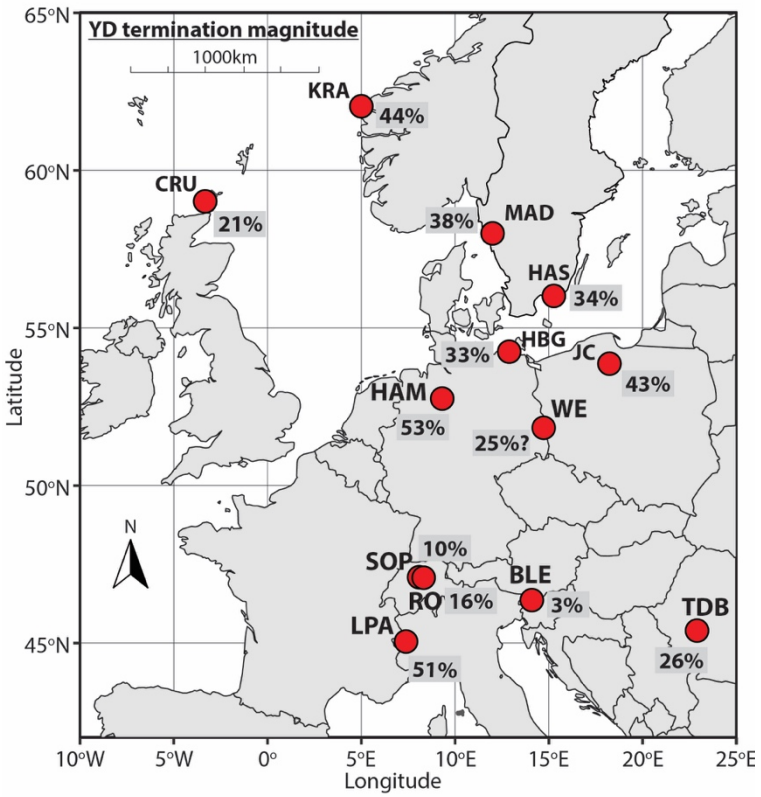


**Figure 8.3** Map of sites across Europe with percentage change in the PrC for the termination of the Younger Dryas. ? = uncertainty of YD termination. Site codes: KRA = Kråkenes; CRU = Crudale Meadow; MAD = Lake Madtjärn; HAS = Hässeldala port; HBG = Endinger Bruch; JC = Czechowskie; HAM = Lake Hämelsee; WE = Węgliny; MFM = Meerfelder Maar; SOP = Soppensee; RO = Rotsee; LPA = Lago Piccolo di Avigliana; BLE = Lake Bled; TDB = Lake Brazi

The sites which recorded considerable vegetation shifts in PrC values are Hämelsee (53%) and LPA (51%). At Hämelsee, there is a sharp rise in *Betula*, a result of ideal soil and climatic conditions (Theuerkauf et al., 2014). The sites of Czechowskie and Endinger Bruch see a similar expansion of woody taxa with the closing of the YD open-woodland landscape.

At LPA, expansion of thermophilous tree taxa (e.g. *Quercus*) was rapid. Increased solar radiation and temperatures allowed these taxa to recolonise open landscape at higher altitudes recorded at LPA (Finsinger et al., 2006; Vescovi et al., 2007). The other alpine sites of Soppensee (10%) and Rotsee (16%) show lower magnitudes of change with the closing of the birch-pine forests after the YD, resulting in little vegetational overturn (Lotter et al., 1992a; 2001).

The lowest magnitude response is at Bled (3%). However, due to insufficient proxy resolution throughout the EH, the full extent of vegetation change was not recorded. Also, at Węgliny there are similar issues (Figure 8.3). However, these sites were still included in this investigation to provide a continental scale insight into the YD stadial across Europe for regions that lack detailed pollen records. Due to the low pollen resolution, the magnitude of the YD at Bled and Węgliny cannot be accurately constrained.

In comparison to other northern latitude sites of Madtjärn and Kråkenes, Crudale shows a smaller vegetation change at the termination of the YD. Several factors may be influenced this. Firstly, the establishment of extensive grasslands at the site, due to local climatic conditions and migration factors, impede the establishment of tree and shrub taxa. There is no significant vegetational overturn (Bunting, 1996). Also, taphonomic problems associated with the inwash of Allerød *Empetrum* negatively affected the PrC values during the YD (Lowe and Watson, 1993; Ruth et al., 2007). Finally, the problem of distinguishing *Betula* and *Betula nana* also affected PrC values (Birks, 1968). As a result, the magnitude of vegetation shift at Crudale should be carefully interpreted.

## 8.3 Timing of the Younger Dryas vegetation response

### 8.3.1 Younger Dryas onset

There are new modelled age estimates for the AL-YD transition in terrestrial vegetation for sites in Table 8.1. The age probability for each site are at 68.2% and 95.4% ranges shown in Figure 8.4. These ranges are approximately equivalent to 1σ and 2σ, respectively. Included are secondary sites that were also involved in the large age model, yet lack the identification of the LST and/or the VA (Hässeldala, Czechowskie and Brazi). At 68.2% probability interval, there is evidence for a time-transgression across Europe for the transition into the YD. However, this time-transgression is not strongly evident at the age probability range of 95.4%. This could suggest rapid vegetation response to shifting climate that cannot be seen due to this larger age uncertainty. Therefore, the discussion will focus on the potential climatic mechanisms for the tentatively identified asynchrony in these records while bearing in mind the lower probability.

**Table 8.1** Summary of modelled ages for the onset of the Younger Dryas.

| Site | Median age | Mean age ± 1 sigma | 68.4% age probability | 95.4% age probability |
|---|---|---|---|---|
| Kråkenes | 12,835 | 12,842 ± 68 | 12,835 – 12,756 | 12,976 – 12,725 |
| Crudale | 12,180 | 12,270 ± 322 | 12,291 – 12,038 | 12,813 – 11,995 |
| Madtjärn | 12,654 | 12,763 ± 54 | 12,805 – 12,715 | 12,890 – 12,655 |
| Hässeldala port | 12,795 | 12,801 ± 61 | 12,854 – 12,732 | 12,936 – 12,689 |
| Endinger Bruch | 12,683 | 12,667 ± 135 | 12,913 – 12,392 | 12,913 – 12,392 |
| Czechowskie | 13,034 | 12,986 ± 193 | 13,188 – 12,908 | 13,272-12,548 |
| Hämelsee | 12,710 | 12,716 ± 55 | 12,758 – 12,654 | 12,835 – 12,611 |
| Węgliny | 12,673 | 12,672 ± 58 | 12,719 – 12,628 | 12,784 – 12,560 |
| Soppensee | 12,688 | 12,680 ± 97 | 12,789 – 12,599 | 12,866 – 12,480 |
| Rotsee | 12,682 | 12,674 ± 49 | 12,728 – 12,644 | 12,755 – 12,559 |
| Bled | 12,571 | 12,576 ± 174 | 12,710 – 12,432 | 12,937 – 12,177 |
| LPA | 12,852 | 12,798 ± 152 | 12,952 – 12,775 | 12,972 – 12,444 |
| Brazi | 12,811 | 12,874 ± 175 | 12,916 - 12696 | 13,317 – 12,678 |

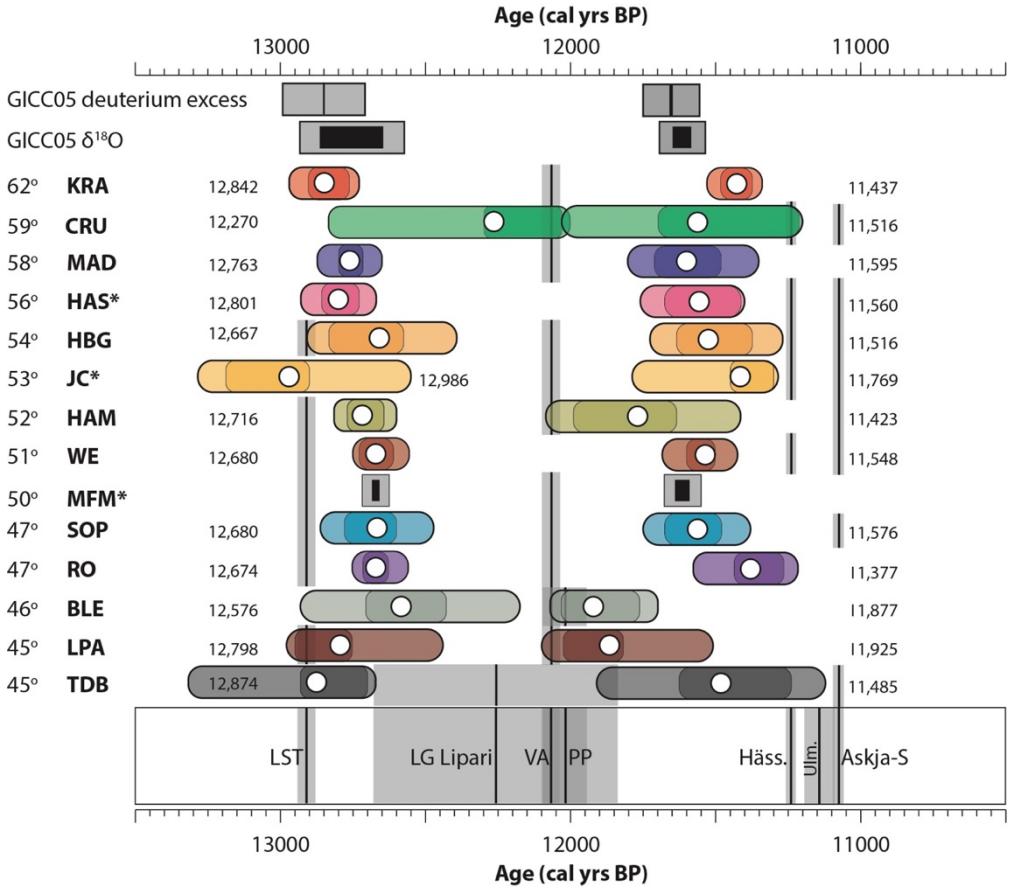


**Figure 8.4** Schematic of the ages for the onset (left side) and termination (right side) for the Younger Dryas across sites in Europe against latitude. Median age of the corresponding terrestrial pollen transitions. The onset and termination of Meerfelder Maar (MFM) is inferred from varve chronology by Brauer et al. (1999, 2000). Bars presented are age estimates for the transitions presented at 68.2% (1σ) and 95.4% (2σ) age probability as described in Table 8.1 and 8.2. The GICC05 with maximum counting errors from Rasmussen et al. (2006) and transferred to IntCal13 timescale using INTIMATE integration tool (Bronk Ramsey, 2015; Adolphi and Muscheler, 2016). Site codes: KRA = Kråkenes; CRU = Crudale Meadow; MAD = Lake Madtjärn; HAS = Hässeldala port; HBG = Endinger Bruch; JC = Czechowskie; HAM = Lake Hämelsee; WE = Węgliny; MFM = Meerfelder Maar; SOP = Soppensee; RO = Rotsee; LPA = Lago Piccolo di Avigliana; BLE = Lake Bled; TDB = Lake Brazi. Tephras identified at each site are also shown: LST = Laacher See Tephra; LG Lip. = Late Glacial Lipari; VA = Vedde Ash; Häss. = Hässeldalen; Ulm. = Ulmener Maar; Ask. = Askja-S.

The sites that show a time-transgression at 68.2% probability include the following in latitudinal order: Kråkenes, Węgliny, Rotsee, and Bled in Figure 8.4. Also, the MFM high-resolution, independently dated record shows time-transgression at the transition of the YD onset compared to the most northern sites (Figure 8.4). These ages indicate north to

south environmental shift, possibly linked to large-scale reorganisation of the atmospheric circulation as Europe transitioned into the colder YD period (Ruddiman et al., 1977; Rach et al., 2014; Muschitiello and Wohlfarth, 2015). The North Atlantic Ocean sea ice expanded from around Iceland to ~57° south (Karpuz and Jansen, 1992; Bodén, 1997; Isarin et al., 1998) which resulted in a strong thermal gradient between the cooler northern and warmer southern Europe/Africa (Isarin et al., 1998; Bakke et al., 2009; Rach et al., 2014). The polar front was possibly gradually displaced further south (Bakke et al., 2009; Rach et al., 2014), resulting in the northern sites of Kråkenes and Madtjärn reaching and passing their critical vegetation thresholds first before the more southern sites of Rotsee and Bled.

In contrast, Czechowskie shows an earlier transition into the YD than other European sites at 12,986 ± 193 cal. BP (Figure 8.4). The proposed southward migration of the polar front across Europe is inconsistent here, suggesting a possible separate atmospheric mechanism at the onset of the YD. The Scandinavian Ice Sheet (SIS) was still present across the northern part of Europe, encompassing the majority of Norway and Sweden and re-advancing during the late Allerød period (e.g. Lohne et al., 2007; Mangerud et al., 2016). The presence of this substantial ice sheet, along with the possible amplification role of Baltic lake-ice cover (Wohlfarth et al., 2007), may have resulted in an anticyclonic circulation over the SIS, weakening the influence of the Westerly winds from the North Atlantic with increasing dominance of the Easterly winds (Yu and Harrison, 1995; Harrison et al., 1996; Lauterbach et al., 2011; Collins et al., 2018). Eastern Europe may have been influenced more by the cooler air advancing southwards from the SIS and resulted in an earlier YD onset at Czechowskie before the rest of northern and central Europe. Collins et al. (2018) also recorded this early eastern European propagation of the YD in biomarker hydrogen isotopic composition at Lake Trezechowskie, situated next to Czechowskie. The terrestrial vegetation at Czechowskie may have responded to increased continentality at the YD onset.

Additional investigations have also highlighted the influence of the effect of the SIS on atmospheric circulation for other eastern European records during the LGIT (e.g. Strančikaitė et al., 2008; Lauterbach et al., 2011).

The YD onset at Brazi is recorded at a similar time to Kråkenes while being the furthest southern site. This site is situated at the highest altitude of 1740m a.s.l., close to the treeline during the LGIT (Magyari et al., 2009; Orbàn et al., 2017; Vincze et al., 2017). The vegetation may have been close to an ecological and climatic threshold, resulting in a similar timing for the YD onset to northern and central Europe (Scheffer et al., 2009). This may have resulted in a rapid vegetation response to climatic cooling.

The sites that present time-transgression at 68.2% probability may reflect an accurate vegetation response associated with atmospheric re-organisation and crossing ecological thresholds at the time of the YD onset. However, possible issues with chronology, pollen resolution and identification should be considered when drawing the time-transgression conclusion at this lower and the higher (95.4%) statistical interval.

The age models presented for Wegliny and Bled show an evident lack of radiocarbon dates over the YD (Figure 8.5). The ages presented are from the interpolation between tephras identified at each site; each has either the LST or VA, not both. If both were present at each site, these well-dated tephra marker layers that bracketed the YD onset would allow further refinement of ages, especially where there was an apparent lack of datable material (Lane et al., 2011a, 2012a). Examples of this are Endinger Bruch, and LPA that have both LST and VA identified and also a lack of radiocarbon dates across the YD (Figure 8.5). Both sites show overlap in timings at 68.2% probability with other sites, indicating that the proposed transgression at this uncertainty interval could be due to chronological imprecision and inaccuracy.

Lake Czechowskie also lacks radiocarbon dates and the presence of tephra layers through the whole of the YD period (Figure 8.5). There is one radiocarbon date present within the Allerød period. In contrast, the pollen resolution at the site is very high across the YD onset transition (i.e. 2cm, equating to ~30-50 ± ~70-200 cal. BP). This high-resolution results in the distinct definition of the transition within the pollen record, yet the lack of complementary high chronological resolution influences in these age discrepancies (Wohlfarth et al., 2006).

Additional discrepancies in chronology are within the site of Crudale with large age uncertainties and a clear difference in timing for the YD onset (Figure 8.4). At Crudale, there is a lack of radiocarbon which results in large age uncertainties of 322 years (1σ) for the timing of the transition into the YD (Figure 8.5). In addition, the pollen and the cryptotephra layers used in creating the chronology are from different cores and then cross-correlated to a master depth by LOI and lithological changes. This produces additional age-uncertainty. Crudale shows an anomaly observed across Europe for the onset of the YD which, rather than being a certain vegetation lag, is likely due to chronological problems. However, the well-dated tephras of the VA, Askja-S and Hässeldalen allow this important site to have a chronology.

Overall, the precision and accuracy of the chronologies presented for these sites across Europe modelled in this thesis must be improved to allow greater statistical confidence in the identification of asynchrony for the YD onset. As Lane et al. (2011a) and Blaauw et al. (2018) highlighted, an age model is as accurate as the dates used. Nonetheless, asynchrony in the YD onset across Europe may exist as indicated by the results presented here. To further test this hypothesis, issues surrounding chronological and proxy resolution needs to be addressed.

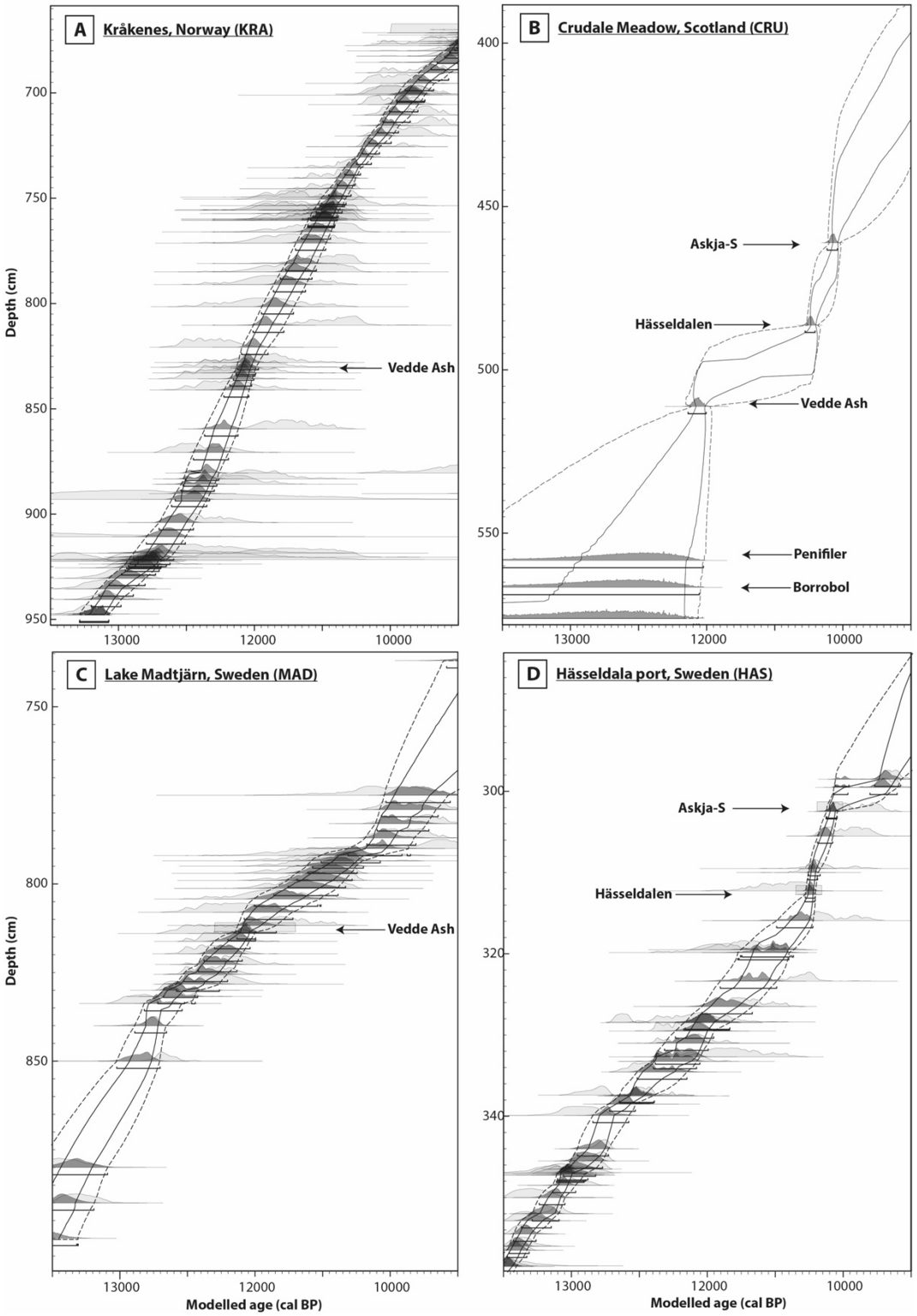


**Figure 8.5** Individual age model results for each site involved in the large age model showing the Younger Dryas stadial identified in terrestrial vegetation record. Y-axis shows depth with the position of the individual tephras identified at each site. X-axis plots modelled (95.4% probability interval) age ranges for each calibrated radiocarbon date. With outlier analysis applied to the age model, outliers detected were down-weighted and are shown in lighter grey colour. The models were generated in OxCal. version 4. 3.2 (Bronk Ramsey et al ) using the IntCal13 atmospheric calibration curve (Reimer et al., 2013).

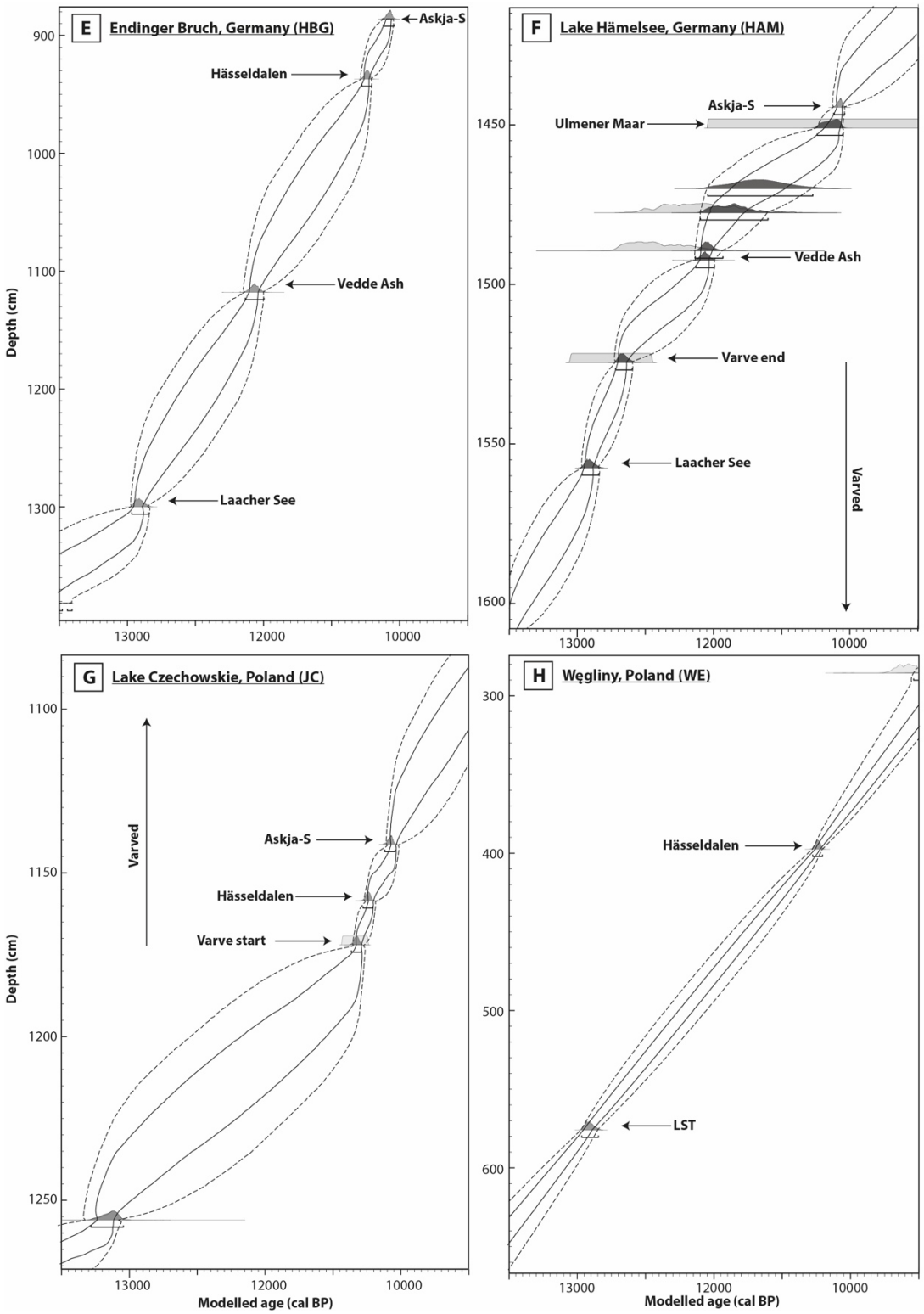


**Figure 8.5 (cont.)** Individual age model results for each site involved in the large age model showing the Younger Dryas stadial identified in terrestrial vegetation record. Y-axis shows depth with the position of the individual tephras identified at each site. X-axis plots modelled (95.4% probability interval) age ranges for each calibrated radiocarbon date. With outlier analysis applied to the age model, outliers detected were down-weighted and are shown in lighter grey colour. The models were generated in OxCal. version 4. 3.2 (Bronk Ramsey et al ) using the IntCal13 atmospheric calibration curve (Reimer et al., 2013).

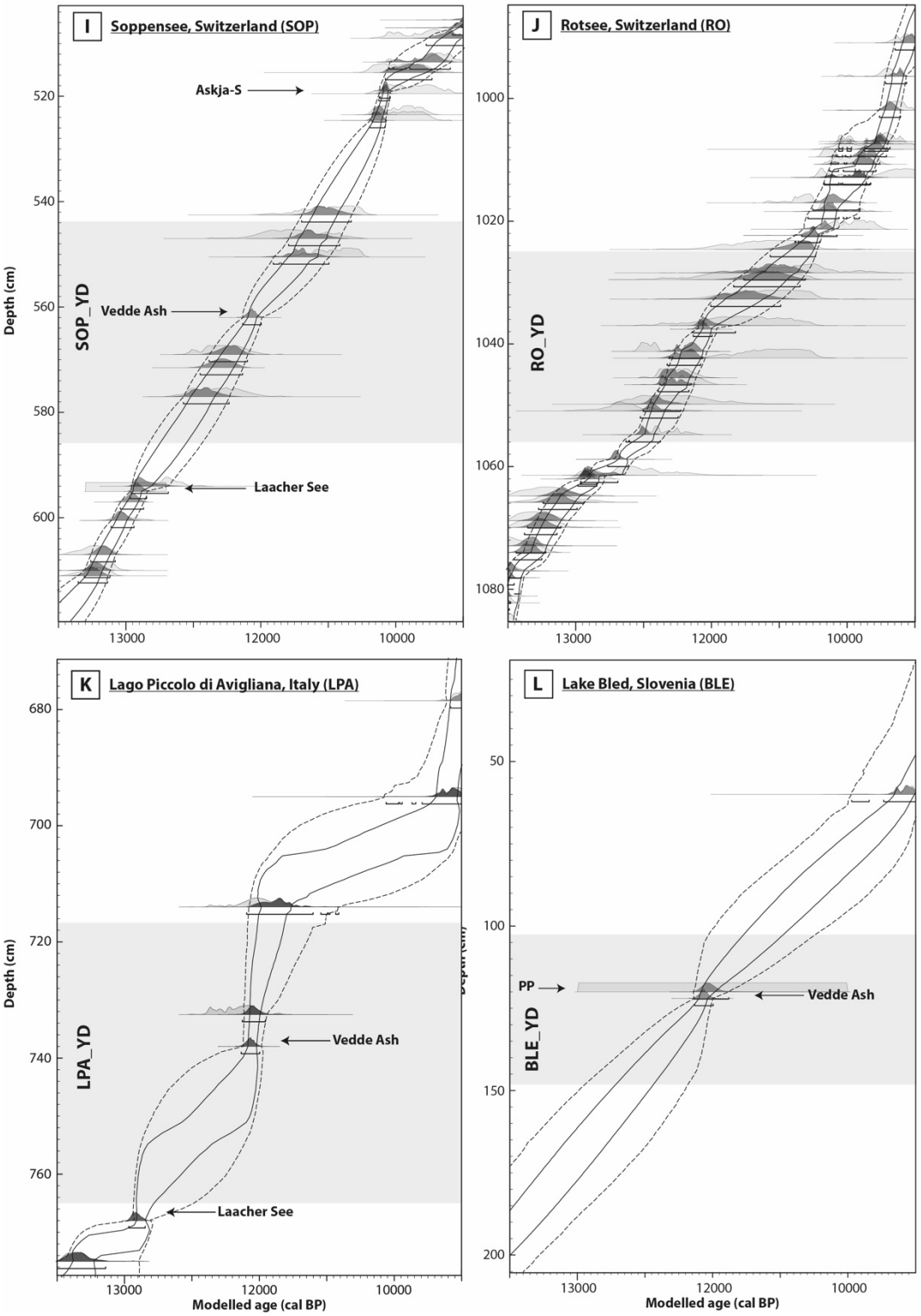


**Figure 8.5 (cont.)** Individual age model results for each site involved in the large age model showing the Younger Dryas stadial identified in terrestrial vegetation record. Y-axis shows depth with the position of the individual tephras identified at each site. X-axis plots modelled (95.4% probability interval) age ranges for each calibrated radiocarbon date. With outlier analysis applied to the age model, outliers detected were down-weighted and are shown in lighter grey colour. The models were generated in OxCal. version 4. 3.2 (Bronk Ramsey et al ) using the IntCal13 atmospheric calibration curve (Reimer et al., 2013).

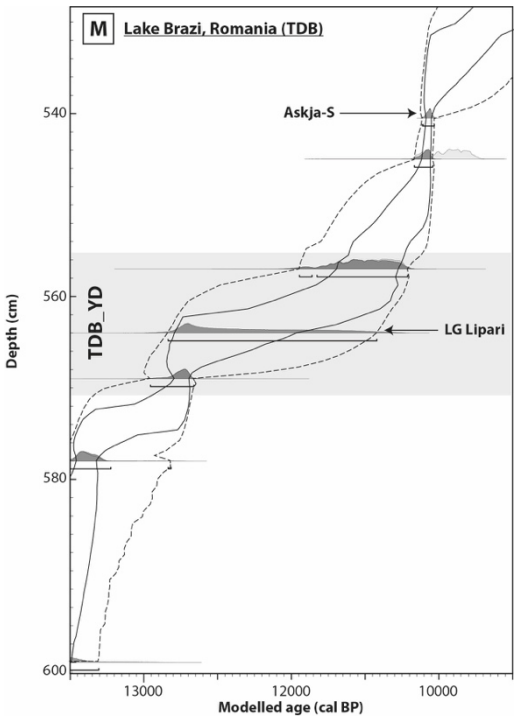


**Figure 8.5 (cont.)** Individual age model results for each site involved in the large age model showing the Younger Dryas stadial identified in terrestrial vegetation record. Y-axis shows depth with the position of the individual tephras identified at each site. X-axis plots modelled (95.4% probability interval) age ranges for each calibrated radiocarbon date. With outlier analysis applied to the age model, outliers detected were down-weighted and are shown in lighter grey colour. The models were generated in OxCal. version 4. 3.2 (Bronk Ramsey et al ) using the IntCal13 atmospheric calibration curve (Reimer et al., 2013).

### 8.3.2 Younger Dryas termination

The newly modelled age estimates (Table 8.2) for the timing of the YD termination with the transition into the EH period across Europe are shown in Figure 8.4. Displayed are the chronological uncertainties of 68.2% (~1σ) and 95.4% (~2σ) probability ranges. The secondary sites of Hässeldala and Czechowskie are also displayed. At 68.2%, there is evidence for time-transgression for the termination of the EH, yet this is not clearly seen at 95.4% probability ranges.

**Table 8.2** Summary of modelled ages for the termination of the Younger Dryas.

| Site | Median age | Mean age ± 1 sigma | 68.4% age probability | 95.4% age probability |
|---|---|---|---|---|
| Kråkenes | 11,432 | 11,437 ± 46 | 11,475 – 11,388 | 11,534 – 11,348 |
| Crudale | 11,516 | 11,561 ± 255 | 11,703 – 11,220 | 12,041 – 11,217 |
| Madtjärn | 11,597 | 11,595 ± 117 | 11,719 – 11,477 | 11,815 – 11,360 |
| Hässeldala port | 11,536 | 11,560 ± 103 | 11,670 – 11,422 | 11,778 – 11,400 |
| Endinger Bruch | 11,505 | 11,516 ± 137 | 11,627 – 11,360 | 11,788 – 11,255 |
| Czechowskie | 11,371 | 11,423 ± 143 | 11,436 – 11,301 | 11,737 – 11,284 |
| Hämelsee | 11,784 | 11,769 ± 171 | 11,977 – 11,638 | 12,076 – 11,422 |
| Węgliny | 11,547 | 11,548 ± 59 | 11,590 – 11,505 | 11,663 – 11,430 |
| Soppensee | 11,584 | 11,576 ± 94 | 11,671 – 11,486 | 11,754 – 11,378 |
| Rotsee | 11,359 | 11,377 ± 92 | 11,425 – 11,259 | 11,573 – 11,234 |
| Bled | 11,936 | 11,925 ± 114 | 12,033 – 11,862 | 12,116 – 11,707 |
| LPA | 11,896 | 11,877 ± 151 | 12,027 – 11,822 | 12,102 – 11,527 |
| Brazi | 11,465 | 11,485 ± 199 | 11,621 – 11,241 | 11,924 – 11,129 |

At 68.2% probability, there is asynchrony with the younger ages for the YD termination at southern sites of LPA at 11,877 ± 151 cal. BP and Bled at 11,925 ± 114 cal. BP with progressively older ages towards northern sites such as Soppensee at 11,576 ± 94 cal. BP, Węgliny at 11,548 ± 59 cal. BP, Madtjärn at 11,595 ± 117 cal. BP and the most northerly site of Kråkenes at 11,437 ± 46 cal. BP (Table 8.2; Figure 8.4). A shorter YD duration is seen at the southern sites LPA and Bled compared to the northern sites of Madtjärn and Kråkenes (Figure 8.4). This time-transgression can be associated with the northward withdrawal of the polar front. Towards the end of the YD, the ocean warmed, and salinity began to return to pre-YD concentrations. This result in the breakup and recession of sea-ice towards Iceland with the polar front migrating back northwards to similar latitudes to the present day (Bakke et al., 2004; Rach et al., 2014; Muschitiello and Wohlfarth, 2015). As a result, southern sites would be likely to respond first, as seen at 68.2% probability range.

Both LPA and Bled are at the boundary of two influential air masses, the North Atlantic and the Mediterranean (Bout-Roumazeilles et al., 2007; Finsinger et al., 2008; Lane et al., 2012a, 2013). The shifts in the influence of these different climatic dynamics are reliant on the strength and position of the westerlies, the North Atlantic Oscillation and the Inter-Tropical Convergence Zone. As a result, LPA and Bled are sensitive to any atmospheric changes or re-organisation (Finsinger et al., 2008; Lane et al., 2012b,c). Both sites have thermophilous taxa, mainly *Quercus*, present throughout the YD period (Finsinger et al., 2006, 2008; Andrič et al., 2009). These taxa are especially susceptible to changes in rising temperatures, especially with the migration of *Corylus* during the EH (Huntley and Birks, 1983; Finsinger et al., 2006). The tree taxa at LPA took advantage of the climatic amelioration with large magnitude expansion at the YD termination, seen with other sites across the Southern Alps (e.g. Gobet et al., 2000; Vescovi et al., 2007). All these factors may have resulted in the early termination of the YD at these sites compared to their more northern counterparts. They continued to experience prolonged stadial climatic and environmental conditions under the influence of the westerlies and polar front.

The YD termination at Czechowskie at 11,423 ± 143 cal. BP takes place later compared to the sites of Madtjärn and Hässeldala at 68.2% (Figure 8.4). Persistent cooler conditions in NE Poland can be linked to the continued influence of the easterlies as anticyclonic atmospheric conditions continued over the SIS. The SIS was still a substantial ice sheet over Scandinavia even during the EH (Yu and Harrison, 1995). Further amplification of these colder and continental conditions brought on by the Easterlies is from the continued Baltic Sea ice (Yu and Harrison, 1995; Wohlfarth et al., 2007; Lauterbach et al., 2011). As a result, the YD associated vegetation may have continued at Czechowskie even after vegetation in Europe crossed their climatic thresholds to the EH. Other eastern

European sites also experienced a delay to the YD termination (e.g. Strančikaitė et al., 2008; Lauterbach et al., 2011).

Once again, at 68.2% probability ranges, these sites seem to reflect an authentic time-transgression of vegetational response to the YD termination possibly linked to the retreat of the polar front as sea-ice retreated. However, chronological and proxy resolution at each site should be kept in mind when drawing these conclusions. The same conclusion cannot be clearly observed at 95.4% at the majority of sites (Figure 8.4).

At 95.4% probability ranges, Bled continues to show an older YD termination range of 12,116-11,707 cal. BP (95.4%). However, the proxy resolution at Bled is poor during the YD-EH transition, with only three samples dated to the whole of the EH period (section 7.2.12.; Andrič et al., 2009). The placement of boundaries or pollen zones is reliant upon the proxy resolution performed on the record, which in turn affects the proposed timing of the transition at a site (Wohlfarth et al., 2006; de Klerk et al., 2007). With one sample defining the end of the YD at Bled, followed by a proxy hiatus of ~40cm, equivalent to ~1,000 years of the EH, this record can present uncertainties in establishing the correct timing of the YD termination in southern Europe. However, with LPA showing a similar age for the YD termination, within the uncertainty, gives support to this early age at Bled (Figure 8.4).

Sites that may have issues with chronology are Crudale and Hämelsee. The large age uncertainties at Crudale have been previously discussed and continue to affect the precision for the age of the YD termination. The identification of the YD VA, Hässeldalen and Askja-S tephras later in the EH, resulted in a reduction of age uncertainty for the end of the YD (Figure 8.4). At Hämelsee, the age for the YD termination is older at 11,769 ± 171 cal. BP compared to other sites in central Europe (Endinger Bruch, Węgliny and Soppensee). The

site has several dates spanning the end of the YD, resulting in large age uncertainties (Figure 8.5).

At Rotsee, the YD termination is younger at 11,377 ± 92 cal BP compared to Soppensee at 11,576 ± 94 cal. BP. Both sites are situated at a similar latitude and altitude and have largely identical vegetational responses to the YD (section 8.2.2; Figure 8.4; Lotter et al., 1992a). This age discrepancy may be due to the dating material used to produce the age model for Rotsee. The chronology for the site was produced from radiocarbon ages by Lotter and Zbinden (1989) and an additional forty duplicated radiocarbon measurements from archived material (Richard Staff personal communication). They underwent radiocarbon preparation technique at different times. The difference in the age for the termination at Rotsee can be due to either difference in the radiocarbon method preparation, instrument performance and use of archived material (e.g. modern carbon contamination; Wohlfarth et al., 1998). In addition, problems associated with cross-correlating three different cores (dating cores RL300, RL305 and pollen core RL205) to one master core (RL05). One or all these factors may have resulted in the difference in the age of the YD termination compared to the other European sites. Ideally, proxy investigations with high-resolution chronology and cryptotephra investigations should be undertaken on one core to reduce the errors associated with cross-core correlations (Abrook, 2019). However, at 95.4% probability range, there is an overlap in ages with Soppensee.

Brazi responds at a similar time to LPA and Bled due to its relative proximity and the climatic and environmental characteristics of the site. Brazi is at the boundary at three major air circulations; the North Atlantic, Mediterranean and Siberian High (Fitzsimmon et al., 2013; Haliuc et al., 2017; Longman et al., 2017a, b; Obreht et al., 2017) in addition to being a refugia for thermophilous taxa (e.g. Picea, Ulmus, Quercus and Alnus (Björckman et al., 2002, 2003; Feurdean and Bennike, 2004; Feurdean et al., 2007; Magyari et al., 2009;

2012). However, the termination of the YD is at a similar time to central and northern European sites at 11,485 ± 199 cal. BP, with greater imprecision (Figure 8.4). Chronological problems associated with a lack of datable macrofossils during the LGIT (Magyari et al., 2012; Hubay et al., 2018) and the dating uncertainties associated with the LG Lipari during the YD, has resulted in an imprecise age that extends over the timings of all other European sites' YD transitions. Additional radiocarbon dates and identification of the VA isochron in the record would assist in demonstrating asynchronicity at greater probability.

The age uncertainty at all sites increases for the YD-EH period compared to the Allerød-YD (Table 8.1 and 8.2) even with many of the sites with radiocarbon dates over the YD transition (Kråkenes, Madtjärn, Hässeldala, Hämelsee, Soppensee, Rotsee, LPA and Brazi). There is a radiocarbon plateau during the YD-EH period (section 2.4.2-3; Guilderson et al., 2005). As a result, identifying if there is climatic asynchronicity across Europe becomes challenging to determine through radiocarbon dating alone. An increase in the number of radiocarbon dates around this period, in conjunction with widespread, well-dated tephras, can reduce these uncertainties. This is seen with Kråkenes where a total of seventy-two radiocarbon dates has produced a highly precise chronology for the site across the YD (Figure 8.5).

When comparing Kråkenes to the independent varve chronology of MFM, time-transgression is seen at 95.4% with 12,690 ± 30 varve years (Figure 8.4, Brauer et al., 1999), lending support to the retreat of the polar front and overall influence of the North Atlantic. Lane et al. (2013) also highlighted a time-transgression between these sites related to the movement of the polar front seen during the YD stadial. Both high-resolution chronologies, coupled with a similar proxy resolution, supplemented by tephrochronology, are essential to improve accuracy. However, with the best evidence presented in this thesis, it is currently

difficult to see a clear time-transgression across Europe with the chronological uncertainties presented.

## 8.4 Correlation to the Greenland Ice Cores

The environmental transitions identified across Europe are compared to the Greenland ice-cores (GIC) to provide insight into the (a)synchronicity of the onset and termination of the YD on a hemispheric scale. The GIC has routinely been used to compare the timing of events across the LGIT to terrestrial records as a result of their annual resolution, usually by wiggle-matching, resulting in assumptions of synchronicity (section 2.1; e.g. Magyari et al., 2012). To allow independent comparisons of the European terrestrial records to the GIC, the ice-core chronology GICC05 (b2k) is transferred to the IntCal13 timescale using the time transfer function calculated by Adolphi and Muscheler (2016) (section 2.5.2; cal. BP; Rasmussen et al., 2006; Lowe et al., 2008; Bronk Ramsey et al., 2015).

The GIC proposed chronostratigraphic equivalent of the YD is the Greenland Stadial 1 (GS-1). Section 2.1 highlights the possible problems with this assumption. Nonetheless, changes in deuterium excess define this period (Rasmussen et al., 2006: Lowe et al., 2008), linked to shifts in moisture sources as the atmosphere circulation underwent major reorganisation (Masson-Delmotte et al., 2005; Jouzel et al., 2007; Steffenson et al., 2008). This shift was rapid, happening within 1-3 years (Steffenson et al., 2008). However, the stable oxygen isotope values ($\delta^{18}O$), a proxy mainly for past air temperature through temperature fractionation (Dansgaard, 1993), show a gradual decline of ~200 years as temperature declined in GS-1 (Steffenson et al., 2008). In contrast, the warming into the EH at the end of GS-1 at 11,700 b2k took 60 years in $\delta^{18}O$ records, while 1-3 years in deuterium excess (Steffenson et al., 2008). Additional measurements of dust content, $Ca^{2+}$ (both from

low-latitude desert sources) and annual layer thickness show a gradual rise in the onset and termination of GS-1 (Steffenson et al., 2008). Generally, published regional comparisons use the GIC $\delta^{18}O$ record due to this gradual transition (e.g. Marshall et al., 2002; Magyari et al., 2012). However, the start of GS-1 as defined by Rasmussen et al. (2006, 2014) is at the point of the largest shift in deuterium excess (Lowe et al., 2008).

Figure 8.4 compares the ages of the YD onset transition defined in the pollen records across Europe to deuterium excess and $\delta^{18}O$ changes in the GIC. Changes in temperatures recorded by $\delta^{18}O$ are largely synchronous with vegetation responses across Europe and Greenland, within chronological uncertainty. This suggests that proposed issues with pollen lagging behind climate are very limited for large amplitude climatic events, with a possible maximum lag of <50 years (Prentice et al., 1991; Clark et al., 1998). The timing of the transition recorded in deuterium excess, related to changes in atmospheric circulation, overlap with many of the European records (Kråkenes, Hässeldala, Czechowskie, LPA and Brazi). The changes recorded at these sites could be due to responses in moisture content. However, taking into account the problems of chronology for the sites of Czechowskie, LPA and Brazi, the changes of moisture are hard to decipher. Also, changes in vegetation are linked to several factors including moisture, temperature, soil, evapotranspiration, length of the growing season (Huntley, 1991; Prentice et al., 1991). The timing of vegetational response at Kråkenes, with the changes in deuterium excess, has been described by Lohne et al. (2013) and linked to the proximity of both sites to the North Atlantic. Kråkenes is the most northern site resulting in an earlier response to changes in both temperature and moisture sources as the jet stream shifted south.

At Czechowskie, the pollen record shows an earlier response to the YD onset compared to GIC deuterium excess and $\delta^{18}O$ at 68.2% probability. A different independent climatic driver may be responsible for this, e.g. the SIS effects on the local atmospheric

circulation of eastern Europe. However, when comparing records with different chronological resolution and associated large chronological uncertainties, neither Kråkenes or Czechowskie are responding at a similar time to deuterium excess rather than $\delta^{18}O$ (Figure 8.4).

A comparison between GIC (deuterium excess and $\delta^{18}O$ record) and pollen records across Europe are made. Previous investigations focusing on the timing of the YD end across Europe identified a synchronous response to the GIC (e.g. Lane et al., 2012a; Rach et al., 2014). However, at 68.2% probability ranges, there is an earlier transition to the EH at the southern sites of Bled and LPA compared to the GIC deuterium excess and $\delta^{18}O$ (Figure 8.4). As the polar front withdrew, due to sea-ice retreat, these southern sites may have warmed before the higher latitude of the GIC, which was still possibly under the influence of the YD North Atlantic circulation (Isarin and Renssen, 1999; Clark et al., 2002 ). However, the problems of radiocarbon age precision compared to the annually resolved GIC limits the ability to detect a chronological offset (Brauer et al., 2014). The annually dated record of MFM shows a largely synchronous YD termination with GIC deuterium excess and $\delta^{18}O$ records (within MCE, Figure 8.4), indicating a time-transgression for the YD across Europe may not exist or be so rapid it cannot be seen in this study due to the age uncertainties. Other factors, such as proxy resolution and different proxy sensitivity, may also make it challenging to identify clear temporal differences. However, pollen records are responding rapidly suggesting problems with chronological resolution are possibly mainly influencing the results here.

## 8.5 Proposed climatic driver

With the evidence previously presented on the proposed timing of the transitions into and out of the YD, a discussion based upon the proposed mechanisms of the climatic change

is possible (Figure 8.6). The central hypothesis linked to the climatic shift into the YD is due to changes in the North Atlantic Thermohaline Circulation. An additional scenario can also be presented with an earlier cooling in central Europe (Czechowskie) due to SIS affecting localised atmospheric circulations.

The climatic shift into the YD has been linked to large freshwater influxes into the North Atlantic, resulting in weakening of the AMOC (Issarin and Renssen, 1999; Broecker et al., 1989). Where this freshwater originated from has long been debated, with sources from Lake Agassiz (Broecker et al., 1985), the Laurentide ice-sheet (Broecker et al., 1989; Clark et al., 2001), the Arctic (Tarasov and Peltier, 2005) and/or the Scandinavian Ice sheet (Björck et al., 1979; Muschitiello et al., 2015). Nonetheless, the input of fresh water from a terrestrial source into the North Atlantic resulted in a decrease in sea surface salinity, reducing density and the formation of the North Atlantic Deep Water (NADW) to transport oceanic heat from the tropics to higher northern latitudes (Clark et al., 2001). From around ~13,000 cal. BP, an expansion in sea-ice into the Nordic Sea, is seen (Karpuz and Jansen, 1992; Cabedo-Sanz et al., 2013; Müller and Stein, 2014). With the increased sea-ice cover, there were alterations in air temperature and heat feedback mechanisms (Li et al., 2005), resulting in cooler temperatures and a larger thermal gradient between the higher and lower latitudes. Steep pressure gradients produced may have resulted in the deflection of the jet stream and the polar front from latitudes close to Iceland to the more southern position of ~52$^{o}$N. The Westerlies were possibly deflected south to sites as far as the Iberian peninsula (Naughton et al., 2019).

This thermal gradient resulted in a stable high-pressure circulation across the northern latitudes, providing ideal conditions for the growth and re-advancement of the SIS (Lohne et al., 2007; Ma). This resulted in the reduced influence and blocking of the deflected moist Westerlies with the colder, drier Easterlies affecting eastern European sites (Yu and

Harrison, 1995; Harrison et al., 1996; Lauterbach et al., 2011; Collins et al., 2018). The region's vegetation passed its climatic threshold before other northern and central sites (Lauterbach et al., 2011; Collins et al., 2018).

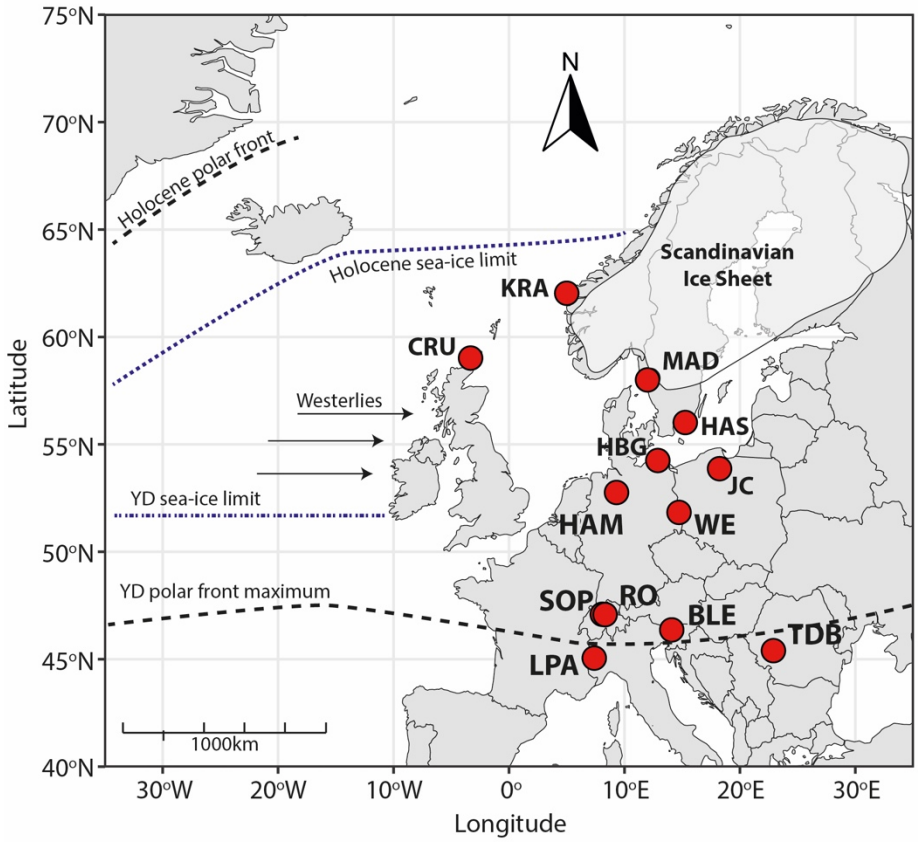


**Figure 8.6** Map showing the changing atmospheric circulation pattern during YD/GS-1. Changes in the position of the sea-ice and polar front compared to the Holocene (Broecker et al., 1988; Isarin et al., 1998; Brauer et al., 2008). Scandinavian Ice Sheet margin limits from Lundqvist and Wohlfarth (2001) and Mangerud et al. (2016). The position of the Easterlies adapted from Yu and Harrison (1995) and Lauterbach et al. (2011). The high pressure over the SIS generated the easterlies, blocking the Westerlies over eastern Europe. Site codes are GIC= Greenland Ice Cores; KRA = Kråkenes; CRU = Crudale Meadow; MAD = Lake Madtjärn; HAS = Hässeldala port; HBG = Endinger Bruch; JC = Czechowskie; HAM = Lake Hämelsee; WE = Węgliny; MFM = Meerfelder Maar; SOP = Soppensee; RO = Rotsee; LPA = Lago Piccolo di Avgliana; BLE = Lake Bled; TDB = Lake Brazi

At 68.2% probability, the blocking and weakening of the Westerlies by the re-advancing SIS, may have resulted in Czechowskie witnessing colder, drier environmental conditions before northern sites. Muschitiello and Wohlfarth (2015) dated the YD transition at Sluggan bog, Ireland around this time. The location of Sluggan resulted in the direct

influence of the North Atlantic and sea-ice expansion. A time-transgression of the YD onset is then seen with the most northern site Kråkenes passing its vegetational critical summer threshold as the polar front shifts south, followed by central European sites and then southern sites such as Bled.

The transition into the EH is explained with the northward migration of the polar front as the sea-ice margin retreated (Bakke et al., 2009; Cabedo-Sanz et al., 2013; Gil et al., 2015) and the AMOC circulation strengthened (Thornalley et al., 2011; Naughton et al., 2019). An early YD termination is seen at the most southern sites of LPA and Bled at 68.2% uncertainty, while central and northern sites experiencing extended YD conditions while the polar front and Westerlies continued to retreat further north. The eastern site of Czechowskie recorded a later EH onset as the SIS influenced and prolonged the blocking of the Westerlies.

However, the chronological precision of the "best" sites presented here, the time-transgression of the YD onset and termination is difficult to determine. Even with Bayesian modelling and the additional well-dated tephra layers of the LST and VA, the age uncertainties presented for these records could be larger than the duration of the transitions (Lane et al., 2011a, 2013). At 95.4%, a hypothesis of major atmospheric re-organisation may be happening in decadal timescales on a continental scale. This has been seen within the GIC in comparison to annually laminated records (Steffenson et al., 2008; Bakke et al., 2009; Lane et al., 2013; Rach et al., 2014). As a result, where there are no annually laminated records, palaeoenvironmental records should have higher resolution chronology supplemented with tephrochronology in order to provide further insight into this possible time-transgression scenario upon a continental scale.

## 8.6 Evaluating climatic synchronicity across Europe

The timing of the transition into the YD is underpinned by two well-dated, widely identified tephra marker layers of the LST and VA. The refined age of these tephras and the large scale age-depth modelling presented in this study, has provided insight into the timing of the YD transition across Europe through the comparison of vegetation response at different sites. The VA is identified at the majority of the sites mid-way through the YD. This provides a key chronological tie-point for both the onset and termination of the YD (Lane et al., 2011a, 2012c). However, not all sites have both the LST and VA. Northern sites particularly lack the identification of the LST as they are outside the known eruption dispersal area (Wulf et al., 2013). As a result, the chronological uncertainties are overlapping with the LST eruption age (Figure 8.4). If the LST was present, the uncertainty surrounding the YD onset would be enhanced and depicted as taken place before or after the LST. However, with the lack of tephra, resilience needs to be improved with high-resolution radiocarbon dating. This is particularly true with Brazi, where the only the YD tephra identified, the LG Lipari, has a large age error and has only been described and dated at this site (Chapter 7). The VA, identified at Brazi, is not a clear isochron. Further investigation is needed to improve the chronological precision of the YD transitions in Romania. Nonetheless, future improvements on the eruption age of the LG Lipari and identification of a clear VA isochron will allow testing of the time-transgression of the YD in south-eastern Europe.

The placement and definition of a transition can affect the “timing” of the YD transitions. The placement of these transitions is mainly dependent on proxy resolutions (Wohlfarth et al., 2006; Engels et al., 2016). Each site in this thesis has different proxy resolutions from the high-resolution conducted at Kråkenes and Hämelsee to the contrasting lower resolution of Węgliny. For the termination of the YD at Bled, the limited sample

resolution is not ideal and may negatively influence the timing of the YD. High-resolution proxy sampling will give improved accuracy.

Presenting age uncertainties for the onset and termination of the YD can aid the understanding in the overall interpretation of the timing of these transitions as well as understanding the limitations of the records (Bennett, 1994; Blaauw et al., 2010; Blaauw, 2018). As this discussion demonstrates, there is no clear answer as a result of the age uncertainties involved. Sites with very few or no radiocarbon dates (especially, Crudale), and other sites which lack tephra layers during the YD (especially, Czechowskie), have resulted in large age uncertainties. The presence of a radiocarbon plateau at the time of the YD-EH transition may have generated larger age uncertainties at all sites (Figure 8.4; Ammann and Lotter, 1989; Lotter et al., 1992; Bartlein et al., 1995). There are implications for interpreting diachroneity across Europe in vegetation response. By increasing the number of radiocarbon dates across the YD transitions, especially where there is a lack of well-dated tephra layers will minimise these uncertainties. As seen with Kråkenes compared to other sites in this thesis, the number of dates used in a model can influence the age uncertainties and thus the accuracy of the timing of the transitions (Lane et al., 2011a).

## 8.7 Chapter summary

There is recognition of a possible time-transgression of vegetation response across Europe, be it at 68.4% probability range, for the onset and termination of the YD. Independent chronologies supplemented by well-dated tephra layers have made this possible. The spatiotemporal differences of the YD through vegetation response can be investigated and compared to the climate changes seen in Greenland. The current dominant hypothesis of changes in the North Atlantic circulation by freshwater influxes resulted in migration (retreat) of the polar front could be supported. The significant re-organisation of

the atmospheric circulation, perhaps within decadal timescales, resulted in rapid climatic changes. Vegetation in northern sites passed their critical climatic threshold first at the onset of the YD. At the termination of the YD, the southern sites passed their climatic threshold before northern sites. However, the influence of the SIS on atmospheric circulations resulted in eastern Europe witnessing colder temperatures before and after northern and central Europe. Improvements in the current chronologies by increasing the number of radiocarbon dates at selected sites, with the use of potential tephrostratigraphic lattices across Europe, would help to resolve the large age uncertainties and further test the time-transgressive response and ecological coupling to the YD climatic downturn.

# Chapter 9

# The timing of centennial-scale vegetation response(s) in the earliest Holocene

This chapter discusses the identification and timing of earliest Holocene (EH) oscillations in terrestrial vegetation across Europe. Section 9.1 focuses on the identification of EH events using the adapted criteria of Watts (1970) and the numerical analysis undertaken as outlined in Chapter 3. There is additional evidence for climatic events from other proxies, where available. Section 9.2 discusses the magnitude of the EH oscillations identified across a regional transect. Section 9.3 focuses on the timing of the identified climatic oscillations at each site, with comparison to the Greenland ice-core (GIC) record in section 9.4. A review of the proposed climatic drivers of the EH events is inferred in section 9.5. Section 9.6 evaluates the results of this chapter with a discussion on the timing of these events equate to the proposed Preboreal Oscillation (PBO) of Björck et al. (1997).

The primary sites used in this chapter have the Hässeldalen and Askja-S tephras identified within their records. Wohlfarth et al. (2006) proposed these tephras bracket an EH climatic event termed the Preboreal Oscillation (Björck et al., 1997). The large age-model from this study provide refined ages for these tephras. Not all of the sites in the large-age model have the Askja-S and Hässeldalen tephras. However, as the sites of Kråkenes, Lake Madtjärn, Rotsee, LPA and Bled were also involved in this age model and have a precise and accurate chronology, they were also used to provide further understanding into the timing of EH climatic shifts as secondary sites.

## 9.1 Identification of vegetation revertences across Europe

A numerical assessment was crucial to distinguish a 'signal' from the 'noise' in the pollen data sets (Ammann et al., 2000). Without doing so, there would be the risk of bias with identifying minor vegetation oscillations to one's hypothesis. For each site, Principal Curve (PrC) and Rate of Change (RoC) were calculated. The results of PrC are shown in Figure 9.1. Inflexions and plateaus in the PrC values reflect periods of vegetational change and stability, respectively. PrC was chosen as the main method to identify vegetation EH oscillations due to capturing more minor variance within a dataset compared to CONISS and other ordination techniques (Simpson and Birks, 2012; Abrook et al., 2019). Table 9.1 describes if these vegetation changes are associated with a climatic oscillation as per the adapted criteria of Watts (1970) and Abrook (2019). A combination of these methods, along with additional supporting information from other site proxies, allow for the identification of vegetation revertences associated with climatic events (see section 3.3.4). PrC values allowed the calculation of the magnitudes of shifts for the identified vegetation events (Figure 9.2).

Due to the numerous terms previously used to define the EH climatic cooling events within pollen records (e.g. Rammelbeck phase, Youngest Dryas, Piottino Oscillation) and the problems associated with them (see Section 2.4.3), each vegetation revertence/event identified at the sites will have a neutral associated number (i.e. sitecode_En) to avoid biased assumptions prior to discussion in later sections (de Klerk, 2007).

**Table 9.1** The adapted criteria from Watts (1970) and Abrook (2019, with **) for identifying vegetation revertences associated with climatic events within pollen records. * highlights secondary sites that do not have Hässeldalen and/or Askja-S tephra within their records. The tick indicates the criterion was met while a the cross shows the criterion was not met. A question mark relates that the record may contain the right data; N/A = there is no data available for that part of the criterion.

| Site | Event | Good modern standard of pollen record | Clear evidence of climatic reversion | >1 distinct pollen taxon | Distinctive sedimentological change | Evidence for climatic deterioration | >1 pollen sample** | Evidence from other proxies** | Vegetation revertence identified? |
|---|---|---|---|---|---|---|---|---|---|
| **Kråkenes*** | KRA_E1 | ✓ | ? | ✓ | ✓? (LOI) | x? | ✓ | ✓ (C-IT) | Yes? |
| | KRA_E2 | ✓ | x | ✓ | x? (LOI?) | x | ✓ | x | No |
| | KRA_E3 | ✓ | x | ✓ | x | x | x | x | No |
| **Crudale** | CRU_E1 | ✓ | ✓ | ✓ | ✓ (LOI) | ✓ | ✓ | ✓ ($\delta^{18}O$) | **Yes** |
| **Madtjärn*** | MAD_E1 | ✓ | x? | ✓ | x | x | x | NA | No |
| | MAD_E2 | ✓ | ✓ | ✓ | ✓ (strat) | ✓ | ✓? | NA | **Yes** |
| **Hässeldala** | HAS_E1 | ✓ | ✓ | ✓ | ✓ (strat, LOI) | ✓ | ✓ | ✓ ($\Delta\delta D_{terr\text{-}aq}$) | **Yes** |
| **Endinger Bruch** | HBG_E1 | ✓ | ✓? | ✓ | x | x? | ✓ | NA | No? |
| | HBG_E2 | ✓ | x? | ✓ | ✓ (LOI) | ? | ✓ | NA | No? |
| **Hämelsee** | HAM_E1 | ✓ | ✓ | ✓ | ✓ (strat, LOI) | ✓ | ✓ | ✓ (C-IT) | **Yes** |
| | HAM_E2 | ✓ | ✓ | ✓ | ✓ (LOI) | ✓ | ✓ | ✓ (C-IT) | **Yes** |
| **Czecho -wskie** | JC_E1 | ✓ | ✓ | ✓ | ✓(XRF) | ✓ | ✓ | ✓ (Geochem) | **Yes** |
| | JC_E2 | ✓ | ✓ | ✓ | ✓(XRF) | ✓ | ✓ | ✓ (Geochem) | **Yes** |
| **Węgliny** | WE_E1 | ✓ | ? | ✓ | ✓ (LOI) | x? | x | NA | Yes? |
| **Soppensee** | SOP_E1 | ✓ | x | ✓ | x | x | ✓ | x | No |
| | SOP_E2 | ✓ | ✓ | ✓ | ? (NA LOI) | ✓ | ✓ | ✓($\delta^{18}O$) | **Yes** |
| **Rotsee*** | RO_E1 | ✓ | ✓ | ✓ | ✓ (LOI) | ✓ | ✓ | ✓ ($\delta^{18}O$) | **Yes** |
| **LPA*** | LPA_E1 | ✓ | x | ✓ | x | x | ✓ | x | No |
| | LPA_E2 | ✓ | ✓ | ✓ | ✓ (LOI) | ✓ | ✓ | ✓ ($\delta^{18}O$, C-IT) | **Yes** |
| | LPA_E3 | ✓ | x | ✓ | x | x | x | x | No |
| **Bled*** | x | x | x | x | x | x | x | x | NA |
| **Brazi** | TDB_E1 | ✓ | ✓ | ✓ | ✓ (LOI) | ✓ | ✓ | ✓ (C-IT) | **Yes** |
| | TDB_E2 | ✓ | x | ✓ | x | x? | ✓ | ✓? (C-IT) | No |
| | TDB_E3 | ✓ | x | x | x | x | ✓ | ✓? (C-IT) | No |

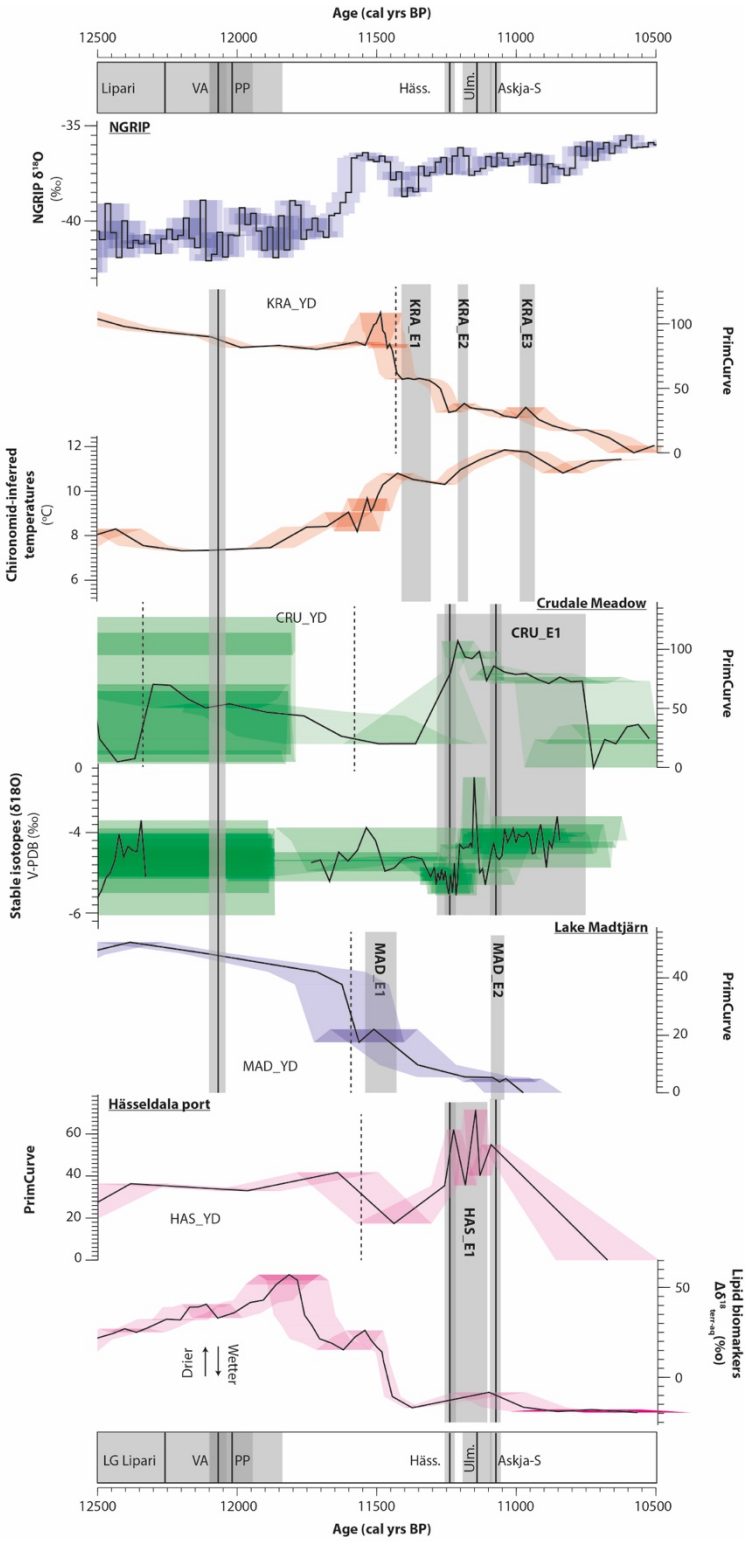


**Figure 9.1** Comparison of the Principal Curve (PrC) applied to the pollen data from the sites studied in this project with the vegetation events seen in the PrC highlighted at each site. The light colour shows 1σ age uncertainty. Additional proxy data is also displayed were available. Kråkenes, chironomid-inferred temperature (Brooks and Birks, 2001); Crudale bulk oxygen stable isotope (Whittington et al., 2015); Hässeldala port, chironomid-inferred temperature and lipid biomarkers (Wohlfarth et al., 2017). Tephras identified at each site are also shown: LST = Laacher See Tephra; LG Lip. = Late Glacial Lipari; VA = Vedde Ash; Häss. = Hässeldalen; Ulm. = Ulmener Maar; Askja-S.

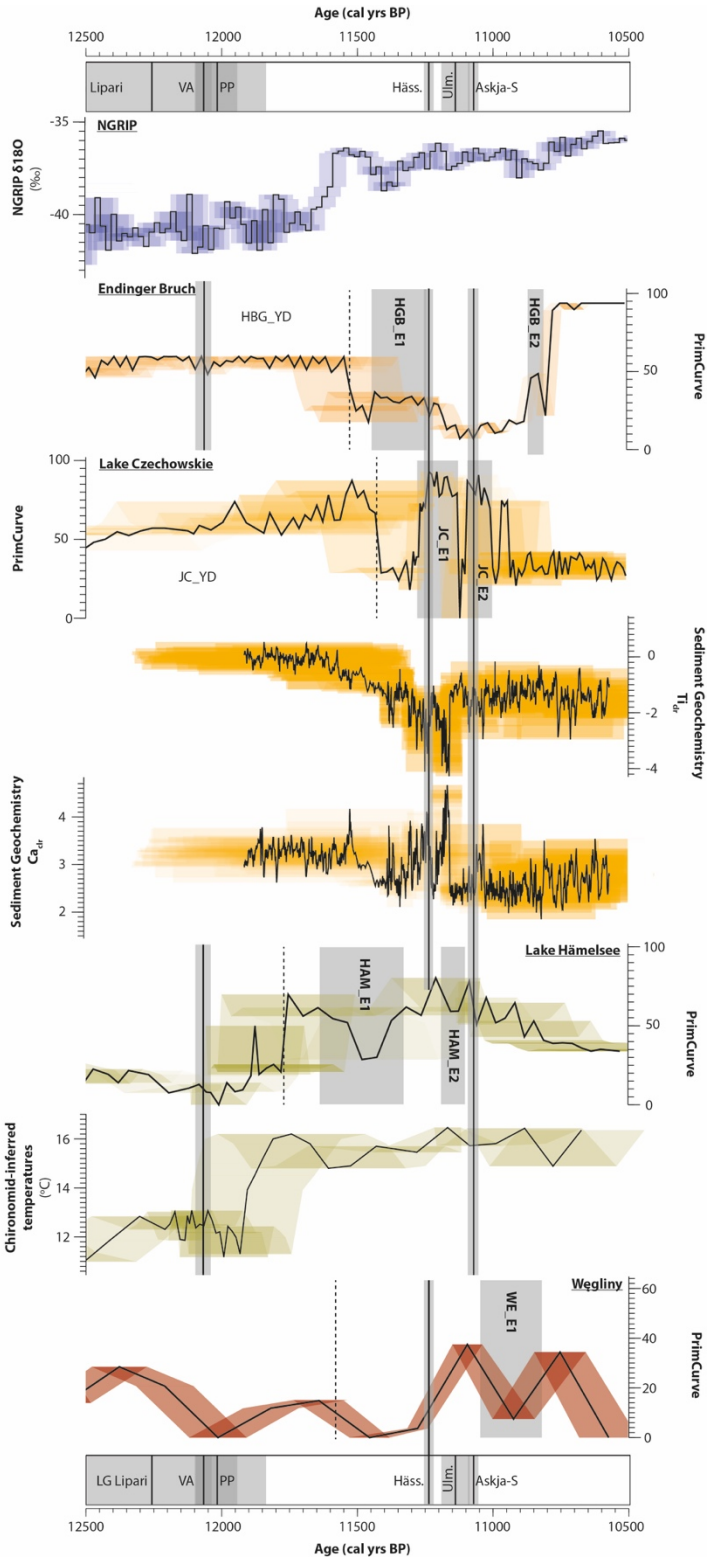


**Figure 9.1 cont.** Comparison of the Principal Curve (PrC) applied to the pollen data from the sites studied in this project with the vegetation events seen in the PrC highlighted at each site. The light colour shows 1σ age uncertainty. Additional proxy data is also displayed were available. Czechowskie, sediment XRF geochemistry (Ott et al., 2016); Hämelsee, chironomid-inferred temperature (Engels pers. Comms.). Tephras identified at each site are also shown: LST = Laacher See Tephra; LG Lip. = Late Glacial Lipari; VA = Vedde Ash; Häss. = Hässeldalen; Ulm. = Ulmener Maar; Askja-S.

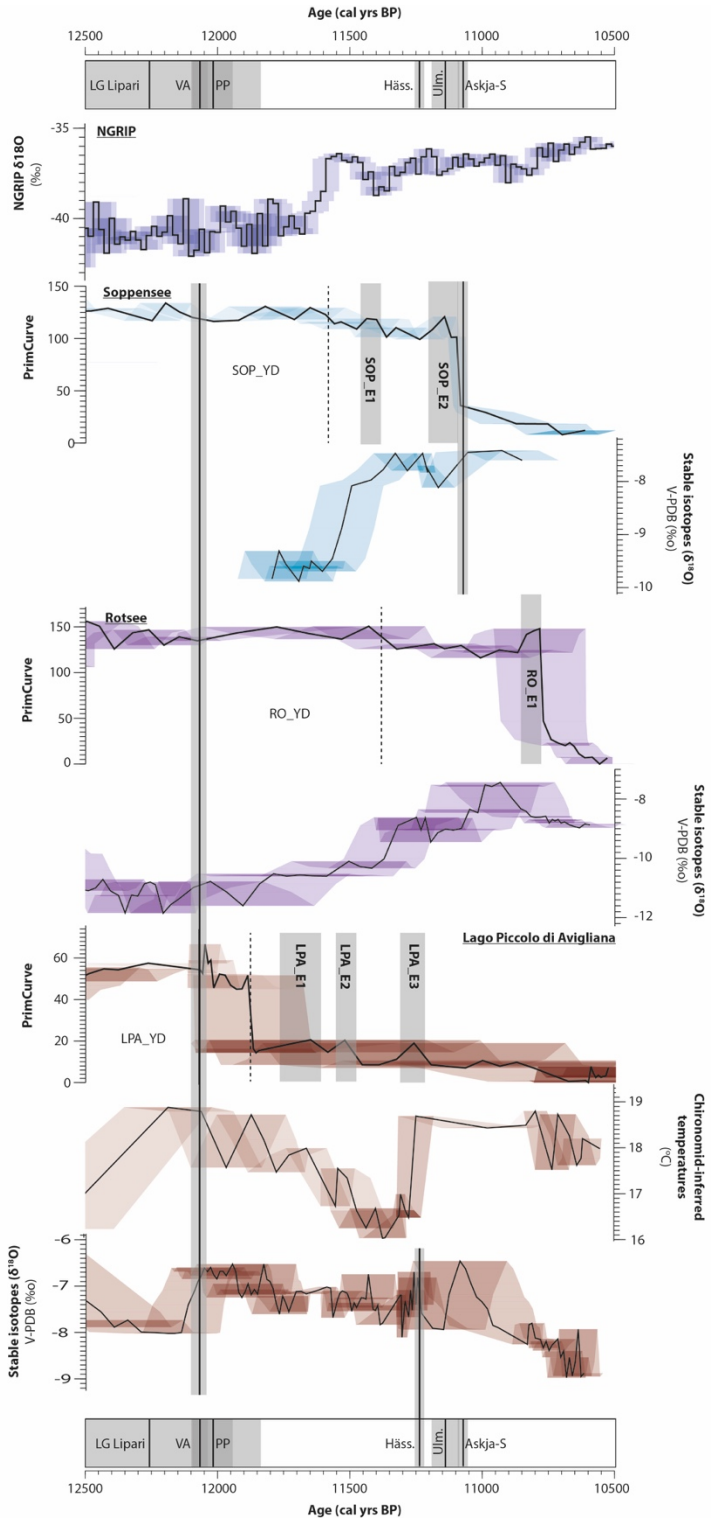


**Figure 9.1 cont.** Comparison of the Principal Curve (PrC) applied to the pollen data from the sites studied in this project with the vegetation events seen in the PrC highlighted at each site. The light colour shows 1σ age uncertainty. Additional proxy data is also displayed were available. Soppensee, bulk oxygen stable isotope record (Lotter et al., 1999); Rotsee, bulk oxygen stable isotope (Verbuggen et al., 2010); Lago Piccolo di Avigliana, bulk oxygen stable isotope and chironomid inferred temperature (Finsinger et al., 2008). Tephras identified at each site are also shown: LST = Laacher See Tephra; LG Lip. = Late Glacial Lipari; VA = Vedde Ash; Häss. = Hässeldalen; Ulm. = Ulmener Maar; Askja-S.

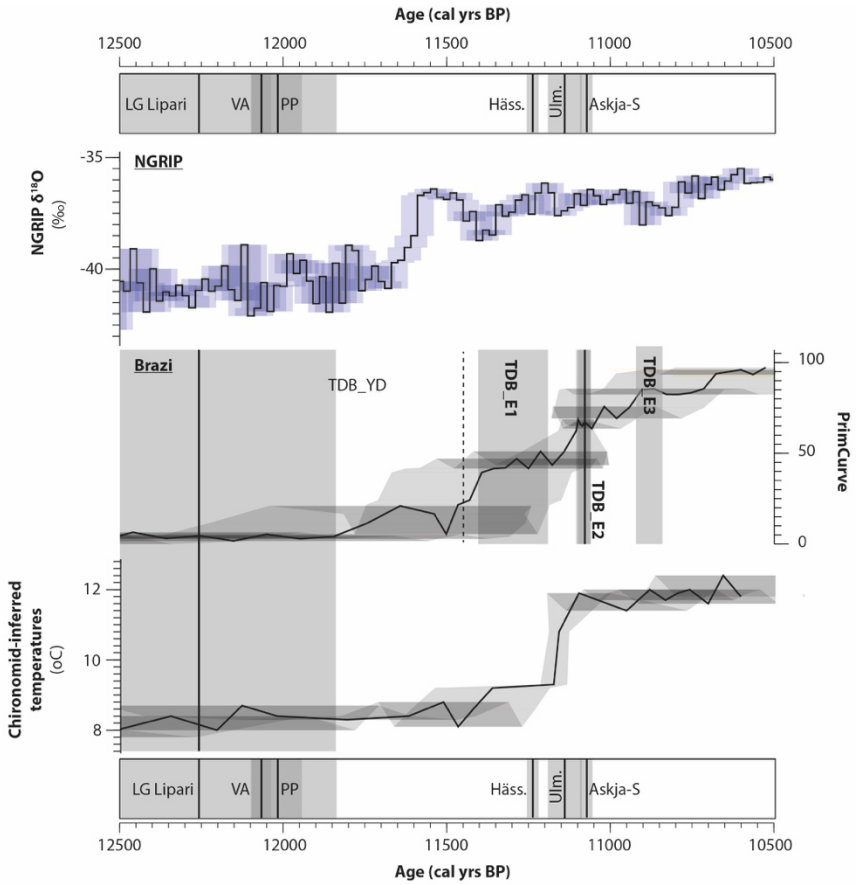


**Figure 9.1 cont**. Comparison of the Principal Curve (PrC) applied to the pollen data from the sites studied in this project with the vegetation events seen in the PrC highlighted at each site. The light colour shows 1σ age uncertainty. Additional proxy data is also displayed were available. Brazi, chironomid-inferred temperature (Tóth et al., 2012). Tephras identified at each site are also shown: LST = Laacher See Tephra; LG Lip. = Late Glacial Lipari; VA = Vedde Ash; Häss. = Hässeldalen; Ulm. = Ulmener Maar; Askja-S.

### 9.1.1 Kråkenes, Norway

PrC, RoC and percentage pollen data allowed the identification of three vegetational events (Figure 9.1, Table 9.1). The earliest event at 11,399 ± 43 to 11,321 ± 35 cal. BP is seen with a plateau in the PrC soon after the EH onset, indicating a cessation in vegetational development. The magnitude of this event is small, at 1.5% percentage change in PrC (Figure 9.2). The *Carex*-type taxon with sedge taxa *Filipendula* and *Rumex* are driving this, showing either a change in: 1) hydrology; 2) infilling of lake edges; or 3) spread of taxa due to natural vegetation succession of the EH. The expansion of wetland taxa, possibly from close to the shoreline of Kråkenes, may indicate a decline in the local lake level, linked to a drier climate,

allowing these taxa to take advantage of uncolonized ground (Usinger, 2004). However, the expansion of *Filipendula* is indicative of succession in Norway (Birks et al., 2000, 2008). *Betula* also declines during this time in percentage and PAR, reflecting a regional vegetational change with far-travelled pollen transport or more localised decline of *B.nana* (Birks, 1994; Birks et al., 2000). The chironomid inferred-temperatures (C-IT) and coleopteran mutual climatic ranges (MCR) show a cooling at this time, which has been linked to the PBO by Brooks and Birks (2001) (Figure 9.1; after Brooks and Birks, 2000; Lemdahl, 2000). There is little change in LOI values. As a result, it is unclear if KRA_E1 is represented by successional change or driven by a climatic event. The drop in temperatures indicated by C-IT may have postponed the migration of tree birch into the region (Brooks and Birks, 2001; Birks et al., 2012; Theuerkauf et al., 2014), with the type of vegetation present at the site being resilient to colder temperatures. This may have resulted in a lack of response in Kråkenes vegetation.

The second event of KRA_E2 at 11,177 ± 31 to 11,066 ± 83 cal. BP is controlled by a rise in *Empetrum* and *Betula* while *Carex*-type and Salix declined. There is a vegetational shift of 6%. At this time, *Betula* trees was migrating into the area with macrofossils found at the site (Birks, 1994; Birks et al., 2000). The rise in *Rumex* and *Poaceae* indicate a disturbance and opening of the shrub-type woodland. The C-IT shows a rise during KRA_E2 with an oscillation observed in LOI values (Figure 9.1). This proposed revertence may correspond to a climatic drying as suggested by the dominance of *Empetrum*. However, there is a regional expansion of these taxa as recorded at other sites in Norway with the Kråkenes PrC identifying a vegetation succession rather than a response to a climatic event (e.g. Birks, 1994; Vorren et al., 2009; Birks et al., 2012, 2014).

The youngest vegetation event at Kråkenes, KRA_E3 is at 10,985 ± 46 to 10,945 ± 51 cal. BP. The increase in *Rumex* and the decline in *Betula* show an opening and disturbance of the vegetation, a similar degree of species turnover seen at the onset of the YD. This inference

from a single sample does not fully satisfy the criteria for vegetation revertence, suggesting it could be an outlier (Table 9.1).

There is difficulty in interpreting these three vegetation changes as revertences to a climatic event. The small vegetation change observed is due to the background trend of vegetation development of Kråkenes' ecosystem during the EH. Birks et al. (2000) did not previously identify any clear vegetation response to EH cooling events. Other Norwegian palaeoenvironmental records also show a lack of response (Aarnes et al., 2012; Birks et al., 2014). The landscape is mostly alpine-tundra, dominated by dwarf-shrub taxa that are mainly resistant to cooler temperatures. These are the proposed conditions of the EH climatic oscillations witnessed in Europe (Björck et al., 1997; Rasmussen et al., 2006). Kråkenes' vegetation was possibly resilient to these smaller, shorter amplitude cooling events compared to the larger, more extended magnitude of the YD stadial (Williams et al., 2011; Muschitiello and Wohlfarth, 2015). Brooks and Birks (2001) identified a cooling EH oscillation with a decline of ~0.6ºC during the summer. The lack of a clear vegetation response with a decline in summer temperatures could be due to the resilient nature of the plant assemblage at Kråkenes. However, this temperature decline may have impeded the migration of tree birch into the area (Brooks and Birks, 2001). In contrast, chironomid assemblages are known to be sensitive to changes in summer-temperatures, resulting in a rapid response to any decline in temperature (Lotter et al., 2012).

Additional records from Norway have identified EH cooling oscillations in pollen records (Seppä et al., 2002; Birks et al., 2012), chironomid records (e.g. Nesje et al., 2014) and localised glacial pauses in retreats or advances (Nesje and Dahl, 1993; Bakke et al., 2005). As a result, vegetation succession may have driven the terrestrial change at Kråkenes as the vegetation was possibly resilient to lower amplitude cooling events (Birks and Birks, 2013).

### 9.1.2 Crudale Meadow, Scotland

Crudale demonstrates a single vegetation revertence, dated to 11,296 ± 127 to 10,945 ± 51 cal. BP. An increase in *Empetrum* and an overall decline in *Betula* drove a rise and then a pause in the PrC values. The rise in *Empetrum* is indicative of colder, drier conditions seen during the colder CRU_YD and in other EH Scottish pollen records (e.g. Charman, 1994; Kelly et al., 2016). This event is long in duration and may encompass two separate climatic oscillations.

Whittington et al. (2015) identified two separate $\delta^{18}O$ isotopic signals in contrast to the one short vegetation event. Whittington et al. (2015) linked variations in $\delta^{18}O$ values to changes in climatic conditions. This is assumed to be temperature driven due to the isotopic fractionation between air temperature and rainfall at mid-latitudes (Leng and Marshall, 2004; Whittington et al., 2015). The initial rise in *Empetrum* and increase in herbaceous taxa (e.g. *Artemisia*) show an opening in the developing woodland. *Betula* pollen production and growth was possibly affected by a drop in summer temperatures (Paus, 1995; Barnekow and Sandgren, 2001). The $\delta^{18}O$ values confirm this temperature decline (Figure 9.1; after Whittington et al., 2015). *Empetrum* then declined, yet was still a dominant part of the landscape as *Betula* does not recover. The pollen accumulation rate (PAR, see section 7.2.2) shows this second vegetation event. The second decline in $\delta^{18}O$ is also showing a temperature decline (Whittington et al., 2015). The lack of two clearly defined vegetation revertences in the pollen record could be due to proxy resolution.

The vegetation response of this event is larger in magnitude than the YD onset at 68% change in the PrC values (Figure 9.2). In comparison, the amplitude of centennial-scale cooling events is smaller than the YD stadial across other European sites (Figure 9.2). The re-working of *Empetrum* during the YD at Crudale may have inflated the apparent CRU_E1 vegetation response (Whittington et al., 2001; Abrook et al., 2019). The PCA highlights that separate

drivers influence *Empetrum* compared to other taxa in the record (Figure 7.2.2). The magnitude of this event may have possibly been inflated and requires careful interpretation.

### 9.1.3 Lake Madtjärn, Sweden

The PrC identifies two vegetation revertences, with supporting evidence provided by RoC. The earlier vegetation revertence (MAD_E1), dated to 11,486 ± 108 to 11,435 ± 103 cal. BP is indicated by higher PrC values and characterised by a peak in *Pinus* and rise in *Empetrum*. The event met the majority of the revertence criteria (Table 9.1). It is debatable if this is related to a climatic event. A rise in *Pinus* may indicate an increase in aridity with cooler temperatures. This taxon prefers dry soils and is cold hardy (Huntley and Birks, 1983; Sakai, 1983; Theuerkauf et al., 2014). Other disturbed ground taxa, *Rumex* and *Artemisia,* do persist during this event providing an additional line of evidence for a climatic downturn. However, the early peak in *Pinus* could be due to the dominance of this taxon in the pollen record. The high production and wind-blow pollen may have suppressed the presence of other local taxa (Huntly and Birks, 1983; Hicks, 1999; Birks et al., 1996). There is no PAR data for this site from this study, which prevents further insight into if this a representation of a true *Pinus* peak in the percentage pollen data. Björck et al. (1996) has displayed a summary concentration data for Madtjärn, with a pollen concentration decline at this depth. A vegetational response to a climatic event seems plausible, yet with the lack of PAR data, it is insufficient to depict MAD_E1 as a clear vegetation revertence.

There is a second vegetation revertence (MAD_E2) at 11,297 ± 103 to 11,051 ± 91 cal. BP. A peak in *Empterum* and a decline in *Betula* and *Pinus* show a reversion to a more open landscape. The peak of *Betula nana* is debatable due to the problems of identifying the shrub and tree species of this genus (Birks, 1968). Björck et al. (1997) used Madtjärn to identify the PBO in terrestrial pollen records. This second event is associated with a decline in organic

content. While there is a vegetation revertence with a response to decreases in temperatures, MAD_E2 is over several samples for certain taxon and could theoretically be a result of natural variability. However, as this event meets the majority of the criteria for a vegetation revertence to be identified (Table 9.1), in addition to previous authors work, MAD_E2 is seen as a vegetation revertence.

The length of the Madtjärn record limits further identification of vegetation revertences during the EH. There are numerous records in Sweden that identify several cooling oscillations during the EH. A decline in trees and a rise in herbaceous taxa are associated with colder temperatures, observed in several other pollen records (e.g. Björck et al., 1997; Björck and Wastegård, 1999). Other evidence for several EH cooling events include several glacial re-advances and retreats in Sweden (Lundqvist, 1988; Wastegård, 1998).

### 9.1.4 Hässeldala port, Sweden

At Hässeldala there is a single, chronologically well-constrained event, dated to 11,236 ± 18 to 11,112 ± 27 cal. BP (Figure 9.1). Under the revertence criteria, this is a clear vegetation revertence (Table 9.1). The oscillating peaks in PrC values indicate a period of landscape instability characterised by the collapse of *Pinus* and decline of *Betula*. RoC shows a high vegetation turnover. There is an oscillation of *Pinus* throughout this complex event. While this demonstrates revertence, the pollen record suggests an opening of the developing birch woodland as opposed to a landscape-wide clearance of woody taxa. The sharp decline in LOI values provides additional evidence for this climatic event. The rise of the shrub taxa *Juniperus* and *Salix* also shows an opening of the birch woodland (Wohlfarth et al., 2006, 2017). Suggested climatic conditions are continental, with cooling affecting pollen production of tree taxa during the summer (Theurkauf et al., 2014). The data from the nearby site of Madtjärn MAD_E2 contrast with this, showing a rise in *Pinus* with a decline in *Betula*. Hässeldala pollen

may indicate a continental climate associated with central Europe, while Madtjärn is possibly under the influence of the SIS (Björck et al., 1996).

Further evidence of EH climatic events is provided by changes in leaf-wax derived hydrogen isotopes, $\delta D_{terr\text{-}aq}$, which provides insight into evapotranspiration (Wohlfarth et al., 2017). Wohlfarth et al. (2017) identified a drying event before HAS_E1 (Figure 9.1), which they proposed to be the PBO as defined by Björck et al. (1997). The authors proposed that the associated vegetation response seen in HAS_E1 was evidence of a vegetation lag to this drying climatic oscillation.There is insufficient pollen resolution at Hässeldala to detect additional vegetation revertences during the EH. The proposed drying event in $\delta D_{terr\text{-}aq}$ could be associated with a vegetation revertence. However, with only one sample over this period compared to the higher resolution of the $\delta D_{terr\text{-}aq}$, vegetation response to drying is debatable. The decline in $\delta D_{terr\text{-}aq}$ during HAS_E1 shows a wetter climate in contrast to the pollen record indicating a drier, colder condition (Figure 9.1). Changes in $\delta D_{terr\text{-}aq}$ may also be related to changes in moisture source for the isotopes (Gat, 1996; Rach et al., 2014). A change in atmospheric circulation during this time may have resulted in drier conditions as recorded by the vegetation.

The magnitude of this vegetation revertence at 43% in PrC values is equal to the magnitude recorded during the HAS_YD. HAS_E1 PrC shows more prominent peaks than for the HAS_YD (Figure 9.1). The CoA-based solution to model PrC presents realistic values with the YD larger in magnitude than HAS_E1. However, this model was only capturing 56.9% of the data variation, indicating that the PCA-based solution used in this discussion is appropriate. The poor pollen resolution throughout the record, with only six samples recorded during HAS_YD, may have resulted in a lower magnitude of change in PrC values for the HAS_YD. The questionable identification of *Corylus* within the YD (see Chapter 9) may have resulted in

the HAS_E1 magnitude being over-estimated, meaning that the magnitude should be carefully interpreted.

### 9.1.5 Endinger Bruch, Germany

There are two events identified using PrC, RoC and percentage pollen data (Figure 9.1, Table 9.1). The first event, dated to 11,447 ± 128 to 11,242 ± 22 cal. BP, is indicated by a pause in the PrC. A peak in wild grasses and a pause in *Pinus* and *Betula* characterise this event. This pollen response can be attributed to either a climatic oscillation or vegetation succession.

The rise in wild grasses is associated with the expansion of the reed species *Phragmites* along the lakeshore (de Klerk, 2002; Bos et al., 2005). *Cyperaceae* and *Filipendula* are also present, suggesting a wetland belt around the lake (Jahns, 2007). Wild grasses are pioneering vegetation and expand rapidly on open, disturbed landscapes (Huntley and Birks, 1983). The early expansion of wild grasses soon after the EH onset could be a consequence of *Betula* not expanding quickly enough to colonise the open landscape after the YD. Additional evidence provided by LOI shows a gradual increase in organic carbon, indicating landscape stabilisation. The rise in wild grasses may also reflect a climatic oscillation. A drier, more continental climate would have lowered the lake levels allowing these taxa to colonise exposed ground (Usinger, 2004). The decline of *Betula* at this time further suggests that there is a possible climatic response. However, wild grasses, particularly *Phragmites* a reed species, are a strong pollen producer resulting in over-representation in the percentage pollen record (Jahns, 2007). This possibly led to suppression of other taxa, possibly *Betula*. Unfortunately, no complete concentration pollen for all the depths was received. There are no PAR calculations and no additional proxy data available to verify this wild grass peak. Here, as suggested by de Klerk (2002), it is concluded that this change was possibly due to vegetational succession.

The youngest event, dated to 10,871 ± 21 to 10,818 ± 22 cal. BP, is a peak in the PrC driven by a rise in *Pinus* and a decline in *Betula*. *Corylus*, having recently migrated into the region due to EH amelioration, slightly declines in the percentage pollen record (Theuerkauf et al., 2014). Similar taxa response is seen in the YD with a dominance of *Pinus* as temperatures dropped and the climate became more continental (i.e. drier). There was also a decline in LOI. A climatic event resulted in the birch woodland opening up. However, herbaceous taxa do not rise during this period which may indicate that cooler temperatures impacted upon *Betula* pollen production or flowering, with long-distance pollen transport of *Pinus* (Usinger, 2004; Hicks, 2006; Fiłoc et al., 2018). Other records across central Europe show similar environmental changes around this time associated with an increase in climate continentality, as demonstrated in pollen concentration records (e.g. Andersen et al., 2007; Fiłoc et al., 2018) and lowering of lake levels (e.g. Kalis et al., 2003; Kulesza et al., 2012). However, the calculation of PAR for this record would provide additional insight into the drivers of this vegetation change.

The PrC curve for Endinger Bruch shows additional peaks during the EH period. One such peak is between the Hässeldalen and Askja-S tephras (Figure 9.1). The PrC data failed to identify vegetation revertence due to similar-sized PrC oscillations in values during the HBG_YD. The high-resolution pollen record possibly created “noise” from the minor fluctuations in the percentage record and was modelled by the PrC, resulting in these type of oscillating peaks. The current events picked out of the pollen record are seen over several samples. As a result, these minor peaks in the EH are not identified as vegetation revertences. RoC evidence supports this interpretation.

### 9.1.6 Lake Czechowskie, Poland

There is evidence for two EH climatic events. The PrC curve reveals two peaks at 11,284 ± 34 to11,126 ± 49 cal. BP and 11,097 ± 38 to 11,004 ± 85 cal. BP with a drop in chord distance and recovery of taxa between the peaks. The magnitude of these shifts is at 81% and 68% of percentage change in PrC values (Figure 9.2). A rise in *Betula* and decline in *Pinus* (with little change in other taxa) drive these PrC events. In PAR, only these two taxa are affected. There is a sharp decline in *Pinus* pollen supply to the sediment. The climatic deterioration may have resulted in a decline in the pollen production and flowering of *Pinus*. *Betula*, in contrast, has a higher tolerance to lower temperatures (Fiłoc et al., 2018). The colder temperatures did not result in deforestation of these trees as there is no clear rise in herbaceous taxa. Other authors have suggested that the rise in *Betula* is also due to wetter conditions during the EH (e.g. Bos et al., 2001; de Klerk, 2007; Fiłoc et al., 2018). However, there is no increase in percentage or PAR data for wetland taxa (see section 7.2.6). The temperature was possibly a dominating driver for these events (Fiłoc et al., 2018).

The identification of two separate vegetation revertences, associated with two possible climatic oscillations of similar conditions, are separated by a short recovery of *Pinus*. This is typical of pine forest recovery and expansion in the EH of central Europe (Theuerkauf et al., 2014; Fiłoc et al., 2018). This reforestation occurred over many samples (equating to ~20 years), allowing division into different vegetation events for the peaks in the PrC curve. X-Ray Fluorescence (XRF) geochemistry provides further evidence (Figure 9.1; Ott et al., 2016).

The peaks in PrC correspond to a decline in titanium (Ti). Ti is a proxy for inwash into the lake with calcium (Ca) linked to calcium carbonate production, indicating drier conditions (Kylander et al., 2013; Davies et al., 2015). The lower values of Ti and higher Ca during these proposed climatic events gives support for a colder, drier EH climatic condition (Davies et al., 2015; Ott et al., 2016).

The increase in *Pinus* pollen between JC_E1 and JC_E2 with Ti and Ca also showing changes to wetter conditions, allows two vegetation revertences associated with climatic oscillations to be identified (Figure 9.1). Other records within the region have shown similar vegetation responses with several EH oscillations (e.g. de Klerk, 2007; Lauterbach et al., 2011; Fiłoc et al., 2018).

After JC_E2, there are additional peaks in the PrC and pollen data (percentage and PAR). Identifying these as vegetation revertences associated with climatic events is difficult. The noise in the high-resolution record at this point may have influenced the modelling PrC values. During the JC_YD similar peaks are observed. As a result, these PrC changes are possibly modelling natural variability.

### 9.1.7 Lake Hämelsee, Germany

Two vegetation revertences were identified through a combination of PrC and RoC in conjunction with the PAR record for Hämelsee. The first, dated to 11,619 ± 199 to 11,346 ± 176 cal. BP, sees a decline in PrC values (Figure 9.1). This event saw an opening of the birch woodland with an EH *Betula* minimum and increase in herbaceous taxa (see section 7.2.7). The decline of birch can be associated with a drop in temperature in central Europe (Theuerkauf et al., 2014). *Pinus* remains stable during this event and does not seem to take advantage of the opening of the landscape compared to Poaceae. The drop in LOI values shows a wide landscape response, that can be linked to a climatic deterioration as organic matter input into the lake declines (Battarbee et al., 2001). Further evidence provided by chironomid inferred temperatures (C-IT) records a drop of 1°C (Figure 9.1).

This event is similar to Endinger Bruch HBG_E1 in vegetation turnover, with an EH peak in Poaceae/wild grasses soon after the YD. However, before HAM_E1, there is a peak in *Betula* as it swiftly recolonises the landscape after the YD (Theuerkauf et al., 2014). This

further supports that HAM_E1 is a climatic response in contrast to HBG_E1 which is possibly a vegetation succession response. This is due to no prior *Betula* peak is recorded at HBG to compete with the expansion of wild grasses.

The youngest event, dated to 11,137 ± 51 to 11,006 ± 93 cal. BP, is identified in the PAR record driven by a decline in both *Betula* and *Pinus*. The percentage pollen data and PrC for this vegetation revertence show variability with no apparent clear changes. However, the palynological data presented by PAR shows a clear vegetation revertence for HAM_E2 to meet the Watts (1970) criteria. This vegetation decline sees a decrease in pollen production and flowering of *Betula* and *Pinus* (Browicz, 1979; Paus, 2010; Fiłoc et al., 2018). This climatic oscillation resulted in a drop in temperatures with C-IT from the site showing a decline of ~0.5ºC (Figure 9.1). The climatic deteriorations that are driving multiple vegetation shifts at Hämelsee during the EH and also recorded in several other vegetation records across the region (e.g. Bos and Urz, 2003; Jahns, 2007; Dreibrodt et al., 2010; Theuerkauf et al., 2014).

The identification of HAM_E2 using PAR over PrC highlights the limitations of basing vegetation revertence detections on changes in the PrC values alone. The modelling of PrC uses percentage data which is reliant on the interdependency of each taxon (Davis and Deevey, 1964). Where a climatic oscillation affects all taxa in a record simultaneously, i.e. through reducing pollen production, the percentage does not show vegetation revertence. As a result other lines of evidence are need to confirm a climatic event along with PrC.

### 9.1.8 Węgliny, Poland

There is only one vegetation event identified, dated to 11,004±85 to 10,836±61 cal. BP, using a single low-resolution sample by Jurochnik and Nalepka (2013). The increase in herbaceous taxa shows an opening of the landscape. However, this could be due to natural variability rather than a climatic response (Williams et al., 2011). Sampling at a higher

resolution during the EH may provide further evidence for a revertence over additional samples. The site experienced limited vegetational turnover during the YD due to possible internal site-specific factors (e.g. soil, competition). Similar factors possibly affected centennial-scale oscillations during the EH (Seddon et al., 2015). As a result, possible vegetational revertences could not be clearly identified at this time (Table 9.1).

### 9.1.9 Soppensee, Switzerland

The PrC identified two vegetation revertences with additional evidence provided by PAR and RoC. The oldest event, SOP_E1, dated from 11,504 ± 92 cal. BP to 11,381 ± 87 cal. BP, and is driven by a peak in *Pinus* and a decline in *Betula*. These taxa respond in a similar manner during the YD, lending validity to a climatic oscillation during the EH. However, there is limited opening in the pine-birch woodland as herbaceous taxa (e.g. *Artemisia*, Poaceae) show a slight increase.

Identifying this as a vegetation revertence linked to climatic change is difficult. Across the EH, the PrC curve shows several oscillations of similar magnitude to that experienced during the YD. Several samples record SOP_E1 with limited changes in the PAR record. Further evidence from the stable isotopes ($\delta^{18}O$) show enrichment at this time related to warming temperatures (Lotter et al., 1999; Figure 9.1). As a result, this variability could be possibly a response to a climatic warming and be part of natural succession.

SOP_E2 sees similar changes in *Pinus* and *Betula* at 11,212 ± 60 to 11,089 ± 22 cal. BP. However, the $\delta^{18}O$ demonstrates an apparent depletion in values, indicating a drop in temperature or moisture (Lotter et al., 1999; Figure 9.1). The peak in *Pinus* may result from increased aridity (Schwörer et al., 2014). Evidence from C-IT in the region shows a decline of temperatures of ~1ºC around this time (Heiri et al., 2004; Ilyashuk et al., 2009; Larocque-

Tobler et al., 2010; Samartin et al., 2016). As a result, SOP_E2 is a vegetation revertence possibly linked to a EH climatic oscillation.

Lotter et al. (1992a) identified a cooling event in the northern Alps during the EH period. However, within the pollen record the vegetation response was difficult to identify (Lotter et al., 1992a, 1999). The re-examination of the records using PrC allowed the identification of a vegetational revertence linked to a climatic oscillation. The magnitude of these vegetational shifts is small, lending support that vegetation response to EH events was subtle (Figure 9.2). There is no further identification of EH vegetation revertences after SOP_E2. The dominance of *Corylus* in the record shows that succession drove the vegetation changes rather than climate during the rest of EH period.

### 9.1.10 Rotsee, Switzerland

A single vegetation revertence was identified as a peak in the PrC values and dated to 10,847 ± 61 cal. BP to 10,774 ± 77 cal. BP (Figure 9.1). A peak in *Pinus* and a decline in *Betula* over several samples drove this change (see section 7.2.10). As seen in Soppensee, this vegetation change may indicate colder, drier conditions with little change in overall forest composition (Lotter et al., 1992a; Schwörer et al., 2014). PAR depicts a more apparent decline in all taxa during this event as pollen production fell. *Artemesia* and Poaceae do increase. The migration of *Corylus* into the northern Alps could have been delayed due to this drop in temperature. PAR shows a decline in *Corylus* after an initial rise in the taxa. This thermophilous species is sensitive to colder temperatures and aridity during the EH (Huntley, 1993).

Stable isotopes also record climatic deteriorations during the EH (Figure 9.1; Verbruggen et al., 2010). During RO_E1, $\delta^{18}O$ values begin to decline, indicating a change to cooler conditions (Verbruggen et al., 2010). However, at this time, *Corylus* starts to migrate into the area and becomes dominant (Lotter et al., 1992a, 1999). The C-IT records in the Alps

also record a decline in temperatures around this time (e.g. Heiri et al., 2004; Ilyashuk et al., 2009; Larocque-Tobler et al., 2010). An apparent depletion in $\delta^{18}O$ values, linked to cooler temperatures, is also observed before RO_E1.

No vegetation revertence were identified at this time by the PrC curve, due to several factors. Firstly, the pollen record may not have recorded the climatic event associated with the isotopic changes. The magnitude of the event is either too small in amplitude or short to result in a vegetational shift (Lotter et al., 1992a). Many authors have noted the weakening influence of the North Atlantic the further a site is from the North Atlantic (e.g. Björck et al., 1997; Heiri et al., 2014; Candy et al., 2016; Pál et al., 2018). However, with the large change in isotopic values of ~1.5‰ shift and subsequent temperature decline, a response in vegetation may have occurred. The identification of RO_E1 shows that the record does respond to proposed lower amplitude climatic events during the EH (Björck et al., 1997; Rasmussen et al., 2007).

Secondly, the pollen record resolution may be insufficient to detect changes in vegetation during the EH. The sample resolution equates to ~70-100 years for each point (±<100-year error). The EH climatic event durations are estimated between ~50-150 years (Björck et al., 1997; Bond et al., 2001; Rasmussen et al., 2007) providing evidence that the pollen resolution may possibly be adequate to record this isotopic shift with a duration of ~150 years.

Finally, the vegetation response can lag behind isotopic changes by around two decades (e.g. Ammann et al., 2000; Słowinski et al., 2017). The isotopic event before RO_E1 may be linked to the same climatic oscillation. A lag of around 50-100 years is calculated here. This lag is too large to be possibly attributed to delayed vegetation response. However, as discussed in section 9.3.2, there are possible inherited chronological problems associated with either the material dated or cross-core correlations. The difficulty with cross-core correlations may have resulted in an artificial lag between the pollen and the isotopes.

One or all of these problems may have resulted in these challenges. Both proxies may or may not have recorded a response to the same climatic event. This emphasises the need to undertake multi-proxy and high-resolution chronology on the same core to resolve these problems.

### 9.1.11 Lago Piccolo di Avigliana, Italy

There are three events identified through peaks in the PrC curve (Figure 9.1, Table 9.1). The earliest event, at 11,552 ± 353 to 11,487 ± 370 cal. BP, is with a PrC peak from a single data point. The decline in *Quercus robur* and a short rise in *Betula* drive this change. The herbaceous taxa do not change, which would have been associated with colder climatic conditions, as seen in the YD (i.e. *Artemisia, Rumex* and Poaceae). LOI values remain stable during this time. As a result, changes in vegetation composition are inferred, rather than an opening of the landscape. The decrease in the thermophilous tree of *Q. robur* indicates a decline in temperatures, while a rise in *Betula* may demonstrate an increase in moisture (Finsinger et al., 2006, 2008; Theuerkauf et al., 2014). Many records in Europe identified EH events as being wetter and colder (e.g. Bos et al., 2001; Fiłoc et al., 2018). In central Europe, Magny et al. (2007) recorded several increases in lake levels during the EH period. However, under the adapted criteria of Watts (1970), vegetation revertence cannot be fully implied (Table 9.1). With only one sample defining this change, and with the lack of PAR data available, the vegetation composition could conjecturally be a response to natural variability. Additional data points are needed over these depths to verify this.

The second event of LPA_E2, at 11,357 ± 395 to 11,160 ± 402 cal. BP is driven by an opening of the *Q. robur-Pinus* woodland with an increase in the open and disturbed ground herbaceous taxon of *Artemisia*. A more significant magnitude shift of 15% change is recorded in PrC (Figure 9.2). The peak in *Artemisia* is similar to levels experienced during the cold and

dry YD (Finsinger et al., 2006, 2008, 2011). An enrichment in $\delta^{18}O$ values soon after LPA_E1, linked to a decline in groundwater into the lake, is possibly due to increasing aridity (Figure 9.1; Finsinger et al., 2008). The low-resolution C-IT from LPA shows a decline of ~0.2°C associated with this event. Other records in the region show a decline of ~0.5°C (Heiri et al., 2007; Larocque and Finsinger, 2008). As a result, this vegetation change may correspond to a climatic oscillation. Other records in the region show colder and drier conditions during the EH period (e.g. Magny et al., 2006; Finsinger et al., 2010; Joannin et al., 2012, 2013; Di Rita et al., 2013).

The youngest vegetation event of LPA_E3, at 10,593 ± 144 to 10,584 ± 140 cal. BP has a peak in the PrC curve. However, under the criteria outlined in Table 9.1, a vegetation revertence could not be identified. Changes in vegetation are limited to one sample. Information from PAR would provide additional insight into this event as a vegetation revertence or natural fluctuations.

### 9.1.12 Lake Bled, Slovenia

The poor pollen resolution during the EH showed no vegetation events. Only three samples are available for the whole period. This is due to the aims and objectives of the primary investigation undertaken Andrič et al. (2009) which looked at the whole core from the Oldest Dryas to the Holocene period. As this site was involved in the large-age model, it had to be considered here to explore the EH oscillations, though it did not have the Hässledalen or Askja-S tephras. Vegetational changes, especially in response to lower magnitude climatic oscillation, may have been recorded at the site. Overall, due to the resolution of the pollen during the EH at Bled, this site was excluded from the remaining discussion.

### 9.1.13 Lake Brazi, Romania

The PrC curve for Brazi shows variability across the EH period (Figure 9.1). There are three vegetation events identified with further evidence provided by RoC, percentage pollen data and PAR to prove if these are vegetation revertences were linked to climatic oscillations (Watts, 1970).

The earliest event, TDB_E1, is dated to 11,449 ± 199 to 11,161 ± 110 cal. BP with a plateau and oscillation in the PrC curve (Figure 9.1). Vegetational development can be seen as being stopped before reaching a threshold and then shifted to a new state to be in equilibrium with the new climate (Williams et al., 2011; Scheffer and Carpenter 2003). There are declines in the pine taxa (*Pinus mugo* (*Pinus* subgenus Diploxylon)and *Pinus cembra* (*Pinus* subgenus Haploxylon)) seen in PAR, showing a decrease in pollen production. Vegetation composition shifts to more alpine meadow taxa (e.g. *Artemisia*, Chenopodiaceae) as the climate became colder. The treeline altitude declined with limited changes in LOI (Magyari et al., 2012). The C-IT showed a decline of 0.7$^{o}$C in summer temperatures during this time (Tóth et al., 2012). The decline of pine taxa indicates a decline in the growing season as these taxa are susceptible to late frost (Huntley and Birks, 1983; Ballian et al., 2016; Caudullo and de Rigo, 2016). Temperate cold tree *Alnus viridis* increases and is associated with wetter conditions possibly associated with the winter season, as shown by stable isotope values from diatoms (Magyari et al., 2013; Mauri and Caudullo, 2016; Pál et al., 2018). TDB_E1 has been identified as a vegetation revertence possibly associated with a climatic event.

The second event of TDB_E2, at 11,096 ± 33 to 10,962 ± 152 cal. BP, is driven by a peak in *A. viridis* and a decline in *P. mugo*. Taxa associated with the disturbed ground also increase. A small change of 5% change is recorded in PrC values (Figure 9.2). PAR shows a sharp decline in pollen production (see section 7.2.13). There is a high increase in sedimentation rate at this point compared to the rest of the core resulting in an artificial low in

PAR (Seppä and Hicks, 2006). As a result, PAR is not admissible as an additional line of evidence. This vegetation revertence may correspond to climatic cooling and increased moisture. However, the C-IT show a temperature plateau before increasing sharply by ~2°C (Figure 9.1; Tóth et al., 2012). LOI values show a peak at this time (Figure 7.48). As a result, the PrC may be highlighting a vegetation change that could be associated natural variation rather than being driven by a climatic oscillation.

The youngest event at 10,846 ± 197 to 10,695 ± 218 cal. BP corresponds to a trough in the PrC curve (Figure 9.1). An increase in *A. viridis* and a decline in *P. mugo* drove this change. Further evidence provided by PAR shows a rise in all taxa, indicating possibly natural variability is resulting in vegetation change on the landscape. There is a recorded decrease of ~0.5°C in the C-IT (Figure 9.1; Tóth et al., 2012) during TDB_E3. However, C-IT shows similar variability for the remainder of this EH period. As a result, the evidence possibly indicates a natural variability that was modelled by the PrC. Further troughs in the PrC curve are seen afterwards, with no response of taxa associated with colder climatic conditions as observed in the YD. This further highlights that several lines of evidence are needed to ascertain if a change in the PrC curve is possibly due to climate or other natural drivers, e.g. succession.

## 9.2 The magnitude of EH vegetation response across Europe

Björck et al. (1997) have highlighted that individual sites will respond differently to climatic events during the Holocene. This is due to site-specific settings with individual plant assemblages responding. The vegetation revertences identified at each site show subtle differences in the magnitude of terrestrial vegetation response which varies across latitudes (Figure 9.2). Changes in atmospheric circulations are known to affect terrestrial vegetation

through changes in temperature and moisture (Williams et al., 2002; Seppä and Bennet, 2003). These effects are propagated across the region.

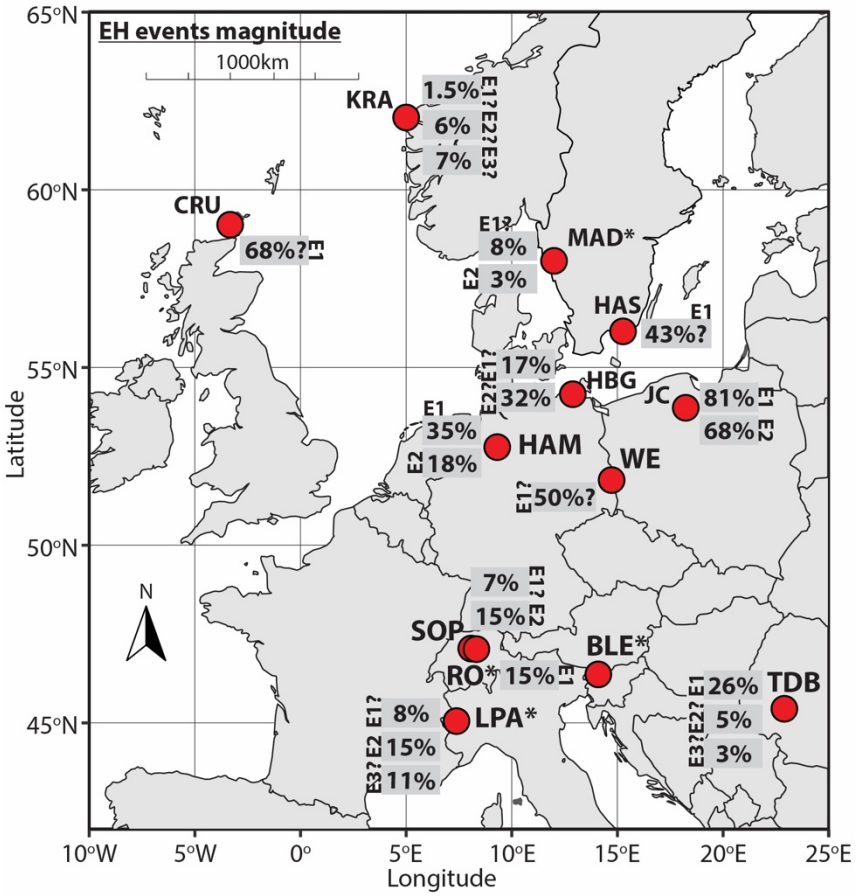


**Figure 9.2** Map of sites across Europe with percentage change (magnitude) in the PrC for the different vegetation events during the earliest Holocene period. * = secondary site; E1? = uncertainty if the vegetation events is a revertence and can be linked to climatic oscillations; 68%? = query around the magnitude of change records. Site codes: KRA = Kråkenes; CRU = Crudale Meadow; MAD = Lake Madtjärn; HAS = Hässeldala port; HBG = Endinger Bruch; JC = Czechowskie; HAM = Lake Hämelsee; WE = Węgliny; MFM = Meerfelder Maar; SOP = Soppensee; RO = Rotsee; LPA = Lago Piccolo di Avgliana; BLE = Lake Bled; TDB = Lake Brazi

The highest latitude site of Madtjärn shows a low magnitude vegetation revertence associated with a climatic event compared to central and southern sites (Figure 9.2). Kråkenes also shows lower magnitude changes due to the vegetation resilience to climatic oscillations. The magnitude at Crudale CRU_E1 is questioned due to the possible inflation from re-worked pollen during CRU_YD, as well as likely encompassing two EH events. Nonetheless, the lower magnitude or lack of response in terrestrial vegetation to centennial-scale climatic oscillations

can be due to several factors. Firstly, the vegetation at these sites was predominantly pioneer taxon of tundra-like composition, which was cold-adapted (Whittington et al., 2015; Brooks and Birks, 2001; Abrook et al., 2019). There is no tree-birch within these northern assemblages during the EH, resulting in a lack of response at Kråkenes and other sites (Brooks and Birks, 2000; Birks et al., 2014). This vegetation is resilient, resulting in a higher climatic threshold before a new vegetation state (Grimme et al., 2000; Schegger and Carpenter, 2003; Williams et al., 2011). With a smaller magnitude climatic event, the resilience of the local vegetation communities would have mitigated the vegetation response at these sites (Williams et al., 2011).

Secondly, the northern location of the sites results in the vegetation being under the constant influence close coastal sea ice and cold winds (Birks et al., 2000; Vorren et al., 2009; Muschitiello and Wohlfarth, 2015; Wohlfarth et al., 2017). Changes in the North Atlantic Ocean circulation or position of sea ice and cold winds (i.e. polar front) associated with EH oscillations might have had little effect on the vegetation (Björck et al., 1997).

Finally, the position of Kråkenes and Madtjärn are close to the SIS (Björck et al., 1997; Birks et al., 2000). The area could act as a buffer in reducing the extreme seasonal and temperature changes during the EH, as well as directly influencing the type of resilient biota recorded at these sites (Muschitiello and Wohlfarth, 2015). As a result, one or a combination of these factors could have reduced the expression of EH climatic oscillations within their pollen records.

EH climatic events seem to have a stronger impact on vegetation at sites situated between 56 and 51$^{o}$N with larger magnitudes of change seen in PrC values (Figure 9.2). All these sites had developed or were developing a woodland in the EH. Changes in temperatures and/or moisture availability may have resulted in an opening of this woodland landscape. There are also additional vegetation revertences recorded at these sites compared to northern and

southern locations. Theurekauf et al. (2014) also recorded a pronounced decline in birch-woodland at sites along these latitudinal gradients. These sites are situated close to the North Atlantic Ocean which could suggest a possible climatic driver (Bakke et al., 2009; Candy et al., 2016).

The more southern and eastern sites of Soppensee, Rotsee, LPA and Brazi show a lower magnitude response, with a change in vegetation composition rather than an opening of the landscape (Figure 9.2). There is a reduced influence of the North Atlantic and atmospheric circulations further inland (Magyari et al., 2012; Heiri et al., 2014; Brooks and Langdon, 2014; Pál et al., 2018). These sites are also at a higher altitude than central and northern sites. Altitude may have exerted an additional control over the vegetation responses, resulting in larger vegetation shifts for these sites latitudinal position (Ammann et al., 2000). High altitude vegetation assemblages may have been closer to their ecological thresholds (Lotter et al, 1992a; Ammann et al., 2000; Wick, 2000).

Brazi is the highest site and located close to the treeline with the pollen record sensitive to perturbations in temperature and treeline position (Magyari et al., 2009, 2012; Orbán et al., 2017; Vincze et al., 2017). Brazi may have had a smaller climatic threshold to cross compared to other sites investigated. Also, the site is at the boundary of major air circulations which may have resulted in a larger vegetational response. Speleothem isotope records from the region show the distal influence of the North Atlantic compared to the Mediterranean circulation during the EH period (Constantin et al., 2007). A combination of these factors resulted in Brazi having a more considerable vegetational change.

Comparisons between sites of similar elevation across a latitudinal transect of Europe would provide further insight into the interplay between altitude controls with climatic events. There is also an evident lack of sites between 51 and 47°N (Figure 9.2). More sites across the region would provide further insight into latitudinal control.

## 9.3 Timing of proposed vegetation revertences

Figure 9.3 and Table 9.2 presents the modelled age estimates for the identified vegetation revertences linked to changes in climatic oscillations from sites in Europe. Ages are presented at 68.2% (~1σ of the distribution) and 95.4% (~2σ of the distribution) probability ranges .

The sites of Madtjärn, Hässeldala, Soppensee, Rotsee, LPA and Brazi have recorded one vegetation revertence associated with climatic oscillations (Figure 9.3). While the site of Hämelsee and Czechowskie there have been several abrupt climatic events identified in quick succession within their terrestrial vegetation records (Figure 9.3). Several other central and north-western European pollen records have also several environmental responses identified in during the EH (e.g. Ralska-Jasiewiczowa et al., 2003; Fiłoc et al., 2018). The overlap in age probability ranges between the sites and these events presented in Figure 9.3 makes it difficult to ascertain if the additional events are the same or are a response to different climatic oscillations. The record at Crudale presents one long event (CRU_E1) which may encompass two separate oscillations.

**Table 9.2** Summary of modelled ages for the onset and terminations for vegetation revertences associated with climatic events in the earliest Holocene

| | | Event onset | | | | Event termination | | | |
|---|---|---|---|---|---|---|---|---|---|
| **Site** | **Event** | **Median age** | **Mean age ± 1 sigma** | **68.4% age probability** | **95.4% age probability** | **Median age** | **Mean age ± 1 sigma** | **68.4% age probability** | **95.4% age probability** |
| Crudale | CRU_E1 | 11,252 | 11,296 ± 127 | 11,280 – 11,212 | 11,614-11,188 | 10,746 | 10,746 ± 173 | 10,955 – 10,592 | 11,067 – 10,418 |
| Madtjärn | MAD_E2 | 11,288 | 11,297 ± 103 | 11,380 – 11,196 | 11,526-11,094 | 11,055 | 11,051 ± 91 | 11,138 – 10,983 | 11,226 – 10,827 |
| Hässeldala | HAS_E1 | 11,235 | 11,236 ± 18 | 11,253 – 11,216 | 11,274-11,201 | 11,111 | 11,112 ± 27 | 11,137 – 11,081 | 11,168 – 11,062 |
| Czechowskie | JC_E1 | 11,284 | 11,284 ± 34 | 11,321 – 11,248 | 11,346-11,220 | 11,115 | 11,126 ± 49 | 11,156 – 11,062 | 11,230 – 11,051 |
| | JC_E2 | 11,089 | 11,097 ± 38 | 11,114 – 11,056 | 11,189-11,040 | 11,030 | 11,004 ± 85 | 11,093 – 10,978 | 11,119 – 10,816 |
| Hämelsee | HAM_E1 | 11,621 | 11,619 ± 199 | 11,831 – 11,423 | 12,022-11232 | 11,316 | 11,346 ± 176 | 11,441 – 11,126 | 11,713 – 11,063 |
| Hämelsee | HAM_E2 | 11,131 | 11,137 ± 51 | 11,175 – 11,067 | 11,235-11,054 | 11,035 | 11,006 ± 93 | 11,095 – 10,987 | 11,123 – 10,803 |
| Soppensee | SOP_E2 | 11,207 | 11,212 ± 60 | 11,259 – 11,145 | 11,334-11,101 | 11,087 | 11,089 ± 22 | 11,107 – 11,064 | 11,136 – 11,049 |
| Rotsee | RO_E1 | 10,825 | 10,847 ± 85 | 10,889 – 10,761 | 11,097-10,721 | 10,755 | 10,774 ± 77 | 10,789 – 10,707 | 11,050 – 10,668 |
| LPA | LPA_E2 | 11,403 | 11,357 ± 395 | 11,897 – 11,052 | 11,991-10,624 | 11,130 | 11,160 ± 402 | 11,451 – 10,563 | 11,881 – 10,516 |
| Brazi | TDB_E1 | 11,426 | 11,449 ± 199 | 11,600 – 11,218 | 11,873-11,092 | 11,418 | 11,161 ±110 | 11,167 – 11,065 | 11,418 – 11,043 |

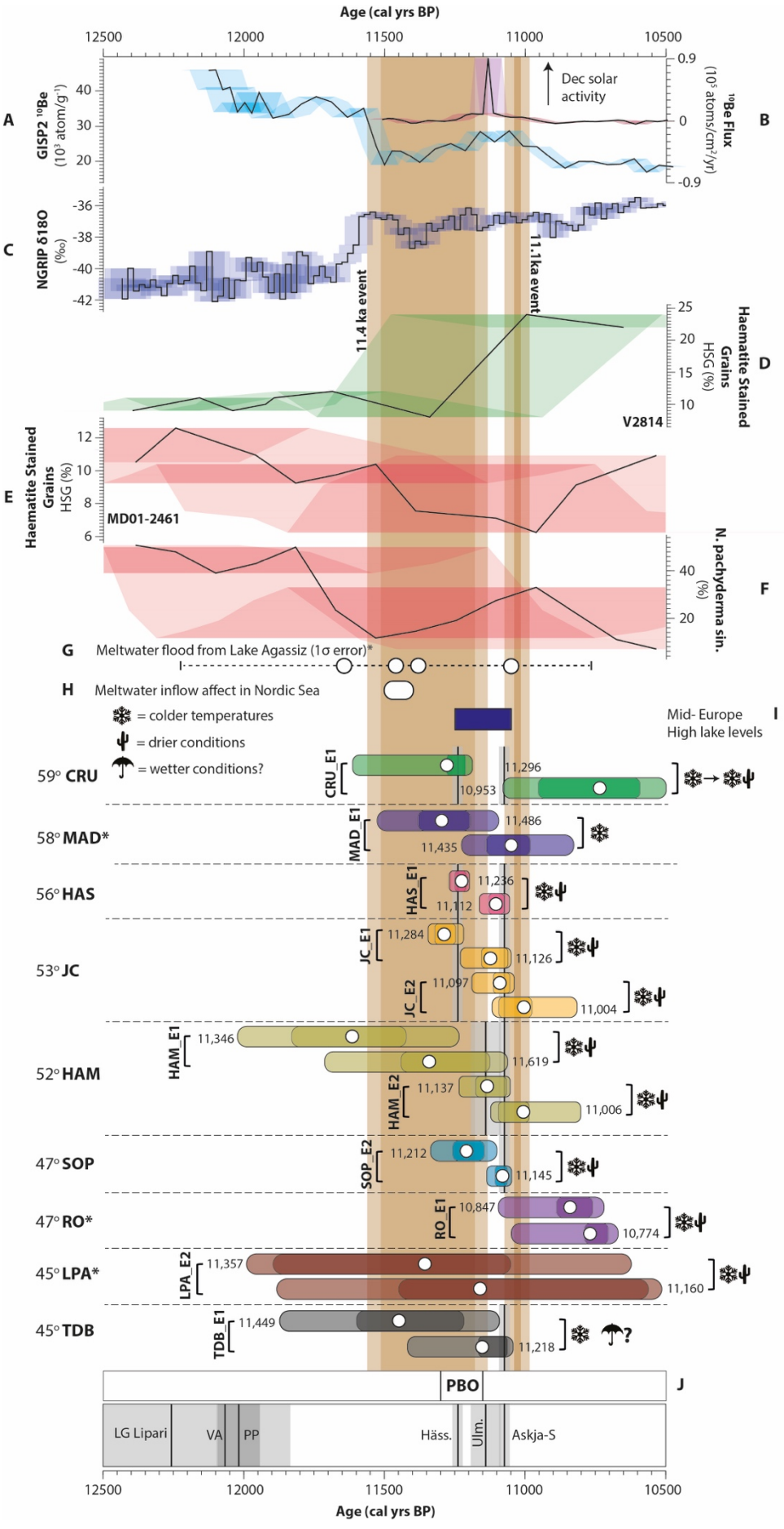
Age (cal yrs BP)
12500
12000
11500
11000
10500
A
GISP2 ¹⁰Be (10³ atom/g⁻¹)
Dec solar activity
¹⁰Be Flux (10⁵ atoms/cm²/yr)
B
C
NGRIP δ18O (‰)
11.4 ka event
11.1ka event
D
Haematite Stained Grains HSG (%)
V2814
E
MD01-2461
F
N. pachyderma sin. (%)
G
Meltwater flood from Lake Agassiz (1σ error)*
H
Meltwater inflow affect in Nordic Sea
= colder temperatures
= drier conditions
= wetter conditions?
Mid- Europe High lake levels
I
59° CRU
CRU_E1
11,296
10,953
58° MAD*
MAD_E1
11,486
11,435
56° HAS
HAS_E1
11,236
11,112
53° JC
JC_E1
11,284
11,126
JC_E2
11,097
11,004
52° HAM
HAM_E1
11,346
11,619
HAM_E2
11,137
11,006
47° SOP
SOP_E2
11,212
11,145
47° RO*
RO_E1
10,847
10,774
45° LPA*
LPA_E2
11,357
11,160
45° TDB
TDB_E1
11,449
11,218
J
PBO
LG Lipari
VA
PP
Häss.
Ulm.
Askja-S

**Figure 9.3** The timings between vegetation revertences in response to earliest Holocene climatic oscillations across the sites re-evaluated in this study in comparison to: A) Cosmogenic nuclides concentration of $^{10}$Be in the GISP2 ice core (Finkel et al., 1997) and B) GRIP and GISP2 ice cores (Bond et al., 2001); C) NGRIP $\delta^{18}$O record with the earliest Holocene 11.4ka and 11.1ka events highlighted (Rasmussen et al., 2007, 2014); D) Haematite stained grains record from the marine core of V2814 as a proxy for ice-rafted debris (IRD) from Bond et al. (1997, 2001) with re-modelled ages using the IntCal13 curve in this study; E) HSG from marine core MD01-2461 in the North Atlantic with F) *N.pachyderma* increase linked to increase ice rafting, based on re-modelled ages using the IntCal13 curve and Vedde Ash age from this study (Peck et al., 2007); G) Re-modelled ages for meltwater floods from Lake Agassiz (Finsinger et al., 2012); H) Timings of effects of meltwater influx believed to be from the Baltic sea ice upon benthic foraminifera in Nordic sea, not upon updates ages (Husum and Hald, 2002); I) Mid-European high lake level stands during the earliest Holocene based on ages by Magny (2004) and Magny et al. (2007). Coloured shading on A-F is 1σ age error (68.2%). The ages of vegetation revertences across Europe are at 68.2% (1σ) and 2σ (95.4%) probability ranges. Symbols next to each event denote the proposed climatic conditions experienced at each site from the pollen record.

The timing of EH events recorded in the terrestrial vegetation record across Europe show no evidence for climatic asynchrony due to the overlap at 68.2% and 95.4% age probability ranges (Figure 9.3). From the timing of these events, the assumption is that they could be responding rapidly to climatic forcing.

The changes in the atmospheric circulation, possibly driven by either shifts of the North Atlantic Ocean circulation into a colder state (Björck et al., 1996, 1997; Clark et al., 2001) or changes in solar input (Björck et al., 2001; van der Pilcht et al., 2004), associated with a centennial-scale climatic event resulted rapid vegetational responses to colder conditions. However, there are other considerations before assumptions of synchronicity of the climatic event. The presence of a radiocarbon plateau at ~10,000-9,000 and 9,600-9,500 $^{14}$C years coincides with the timing of these events (Björck et al., 1997, 2001; Bos et al., 2007; Reimer et al., 2013). The large age errors produced could have reduced the potential of identifying climatic asynchrony.

Also, many of the sites lack enough dates during the period that would reduce these uncertainties (Blaauw et al., 2018). LPA has age uncertainties of ~350-400years (±1σ) with the

single vegetation revertence identified. This is due to the lack of radiocarbon dates and large errors associated with the dating of material around this time (section 7.1.2.5).

Despite these chronological problems, the identification of the Hässeldalen and Askja-S tephras across many sites in Europe provides ideal isochronous markers to test the onset and termination of EH climatic events. Wohlfarth et al. (2006) highlighted that these tephras are propose to have occurred before (Hässeldalen) and after (Askja-S) an EH cooling event, the classic PBO of Björck et al. (1997). Many other investigators have also verified this claim in their records (e.g. Ott et al., 2016, Kelly et al., 2016). However, as seen in Figure 9.3 with additional vegetation revertences before and after these tephra layers, caution should be advised when using the Hässeldalen and Askja-S tephras to search for an EH event between these tephras specifically.

The question of whether EH abrupt climatic events are synchronous across Europe can be addressed with the clear vegetation revertences identified in many sites that encompass one or both tephras, with the refinement of age uncertainties around these marker layers.

### 9.3.1 Onset of earliest Holocene cooling events

The northern sites of Crudale, Hässeldala, Endinger Bruch and Czechowskie have both the Hässeldalen and Askja-S tephras (Figure 9.3). At Crudale, the vegetation revertence occurs before the Hässeldalen tephra. While at Hässeldala, the HAS_E1 occurs between the two tephras. There are two vegetation revertences at Czechowskie, JC_E1 starting before the Hässeldalen tephra and terminating 50 years before the Askja-S tephra. At Endinger Bruch, the vegetation change seen before the Hässeldalen tephra (HBG_E1) provides additional evidence that this was successional rather than a climatic event. No other northern sites with the Hässeldalen tephra has an earlier vegetation revertence. At Hämelsee, there is a similarly timed event. With large age uncertainties associated with limited radiocarbon dates during the EH

and no Hässeldalen tephra identified in the Hämelsee record, further evidence suggests that HBG_E1 is possibly a localised natural succession.

Comparing these sites allows the formation of a tentative hypothesis for climate time-transgression. There is a difference in the timing of CRU_E1 with HAS_E1 using the Hässeldalen tephra as an isochronous marker. CRU_E1 onset is before this tephra while HAS_E1 onset is after. This difference could possibly be due to the displacement of the polar front resulted in a north to south environmental shift. With the position of Hässeldala at 56ºN, at the margins of the polar and Atlantic air masses, the sensitivity of this site to changes in the atmospheric circulation would be clearly expressed (Lane et al., 2013; Muschitiello and Wohlfarth, 2015; Candy et al., 2016). The potential vegetation revertence at Węgliny (WE_E1) after the Hässeldalen could lend further validation to this theory. However, there is insufficient pollen resolution at Węgliny to confirm this time-transgression. To the best of my knowledge, no other investigation has examined or identified climatic asynchronicity with centennial-scale events within palaeoenvironmental records.

In contrast, the onset of the event of JC_E1 at Czechowskie shows an early transition before the Hässeldalen tephra. This shows possible inconsistency with a time-transgression scenario. A different atmospheric circulation, similar to that observed in the YD (Chapter 8), may have influenced the vegetation response at the site. The SIS was still present across Scandinavia, with advancement and pauses in ice retreat dated to EH climatic events (e.g. Lundqvist, 1988; Wastegård, 1998). There was ice cover still present in the Baltic Sea (Wohlfarth et al., 2007). The weakening of the Westerlies from the atmospheric blocking and cooler air from the Easterlies may have resulted in the vegetation response before the rest of Europe, or at least before Hässeldala port (Yu and Harrison, 1995; Harrison et al., 1996; Lauterbach et al., 2011; Collins et al., 2018). However, no investigations have highlighted the importance of SIS atmospheric blocking during EH cooling events. With the similar timing for

the onset for JC_E1 and CRU_E1, it suggests possible similar timing of rapid vegetation change.

Low proxy resolution at Hässeldala may have resulted in the later onset of EH cooling, with varying sample resolution throughout the EH interval. Before the Hässeldalen tephra, there is a proxy sample resolution of ~200 years. In contrast, there is a ~20-30 year resolution implemented between the two EH tephras, adequate to detect short duration EH climatic events of 50-150 years (e.g. Hoek and Bohncke, 2002; Bos et al., 2017). The proxy resolution applied pre-HAS_E1 may have missed the beginning or additional cooling events. As a result, the difference in timing of the EH cooling event could have been a product of variable proxy resolution rather than time-transgression.

Further determining the validity of genuine asynchronicity across Europe for the onset of the EH cooling events is limited as the Hässeldalen tephra has only been identified in sites of northern Europe (e.g. Davies et al., 2003; Ott et al., 2016; Timms et al., 2017, 2019). However, sites with a high-resolution chronology, i.e. Madtjärn, Czechowskie and Soppensee, overlap in age probability ranges show that there is currently not strong evidence for climatic asynchrony.

### 9.3.2 Termination of earliest Holocene cooling events

With the plethora of caveats discussed in the previous sections, it is hard to determine if the earliest EH vegetation revertences identified in the records across Europe are responding to the same climatic event. However, the Askja-S tephra can help in examining the timing of cooling event terminations. This tephra is identified widely across Europe, providing a useful isochronous marker (section 6.3.1).

At the northern site of Crudale, CRU_E1 extends ~330 years after the Askja-S tephra (Figure 9.3). In contrast, HAS_E1, JC_E1, HAM_E1, SOP_E2 and TDB_E1 terminate before

the deposition of the Askja-S (Figure 9.3). Time-transgression can be hypothesised, linked to the northward withdrawal of the polar front. Reductions in sea ice, due to either a change in AMOC or solar forcing, resulted in the migration of the polar front to modern-day latitudes (Björck et al., 1997, 2001; Clark et al., 2001; van der Pilchet et al., 2004). Crudale experienced extended cooling in contrast to the other sites with the Askja-S tephra (Figure 9.3). However, there are issues with CRU_E1 being one long cooling event. The vegetation revertence identified at Crudale possibly encompassed two individual cooling events. Due to inadequate pollen resolution or the resilience of the vegetation at the site to cooler climatic conditions, there was no clear second vegetation revertence identified in the PrC (see section 9.1.2). However, the stable isotope record presents two separate climatic events (Whittington et al., 2015). At Czechowskie and Hämelsee there is a second vegetation revertence during the EH (Figure 9.3). The earliest events of JC_E1 and HAM_E1 terminate before the Askja-S tephra, while the second event, JC_E2 and HAM_E2, start before and progress over the deposition of this tephra layer. This evidence highlights the possibility that CRU_E1 is composed of two events. As a result, there cannot be a clear comparison between the termination of CRU_E1 and the earliest EH vegetation revertences seen at other sites.

The secondary sites of Madtjärn and LPA provide insight into the timing of the termination of the earliest EH event. Within age probability ranges, there is no evidence for time-transgression in the termination of this earliest EH event across Europe. There is a rapid propagation of climatic changes upon a regional scale with atmospheric circulation re-organisation, resulting in synchronous termination of the event.

### 9.3.3 Additional younger earliest Holocene cooling events

Hämelsee and Czechowskie show an additional vegetation revertence (Figure 9.3). The events of HAM_E2 and JC_E2 start before the Askja-S tephra, ~11,110 cal. BP, and finish

within uncertainty, synchronously (HAM_E2: 70 ± 93 years, JC_E2: 72 ± 85 years) after the deposition of this tephra. The evidence provided by other proxies at these sites suggests an additional climatic oscillation (Ott et al., 2016; Stefan Engels, personal communication). Identifying similarly timed vegetation revertences across other European sites is limited due to several factors. Firstly, insufficient pollen resolution may have limited the detection of additional separate cooling events. At Hässeldala, there is only one pollen sample after the deposition of the Askja-S tephra (section 7.2.4). The proxy resolution at Crudale resulted in a lack of recognition for identifying different vegetation revertences. The pollen record at Madtjärn terminates soon after MAD_E1 (Björck et al., 1996, 1997).

At Soppensee, vegetation succession soon became the primary driver for vegetational change in the EH. There is a high abundance of *Corylus* after the deposition of the Askja-S tephra as the taxon migrated into the area (Huntley, 1993; Theuerkauf et al., 2014; Finsinger et al., 2006). *Corylus* is resilient to cooler temperatures compared to other thermophilous taxa (Huntley, 2003; Finsinger et al., 2006). Once this taxon became established and dominant in the landscape, further cooling events (possibly of smaller amplitude and not propagated as far south compared to the first) resulted in little vegetation response.

The lack of additional events at southern and eastern sites, particularly Brazi, may possible be due to the distal influence of the North Atlantic Ocean. There would have been a weaker expression of smaller amplitude climatic events in the terrestrial vegetation record (Bakke et al., 2009; Candy et al., 2016). During the EH, Brazi was possibly under the influence of an eastern Mediterranean circulation, leading to a further weaker expression of the additional EH climatic events (Constantin et al., 2007; Pál et al., 2018).

At Rotsee, there was a young vegetation revertence recorded at 10,847 ± 85 to 10,774 ± 77 cal. BP. There is no synchronicity with the earliest EH events across Europe (Figure 9.3) However, this could be due to problems with dating chronology, discussed in Chapter 8. The

timing of *Corylus* expansion in the record provides further evidence for dating problems. The *Corylus* expansion into the Alps is dated to ~11,000 cal. BP (Finsinger et al., 2006). At Soppensee *Corylus* expansion is recorded ~11,100 cal. BP. In contrast Rotsee, located close by, dates *Corylus* expansion to ~10,800 cal. BP. There is no large physical barrier, i.e. a mountain range or large lake between these two sites to delay *Corylus* migration by ~300 years. The seed dispersal is quick for this taxon (Finsinger et al., 2006). As a result, the timing of the expansion of hazel should be broadly similar at both sites. However, chronological problems experienced at Rotsee continue to affect the timing of climatic events into the EH.

Evidence provided by other proxies at these southern and eastern sites shows a lack of response to a second climatic oscillation around the same time as Hämelsee and Czechowskie. Where the Askja-S tephra is identified at other sites, there is a lack of environmental response (Figure 9.1). This confirms that the second climatic oscillation may have been smaller in amplitude than the first, resulting in a weaker or a lack of ecosystem response in records located further from the North Atlantic Ocean.

Overall, the Askja-S tephra has provided a valuable marker to identify and investigate a second climatic oscillation across northern and central Europe. Identifying this tephra marker layer in other high-resolution records across Europe would allow further investigation into the propagation and characteristics of EH cooling.

## 9.4 Correlation to the Greenland Ice Core records

The vegetation revertences identified across Europe are compared to climatic events identified in the Greenland ice core records (GIC; Figure 9.3). The timing of EH cooling events in terrestrial palaeoenvironmental and in the GICs are routinely compared (e.g. Björck et al., 1996, 1997; Blockley et al., 2018). To allow independent comparisons of the European

terrestrial records to the GICs, the Greenland ice-core chronology (GICC05) (b2k) is transferred to the IntCal13 timescale (cal. BP) using the time transfer function calculated by Adolphi and Muscheler with the use of the Integration tool from the INTIMATE database (2016) (Rasmussen et al., 2006; Lowe et al., 2008; Bronk Ramsey et al., 2015).

There are several EH climatic events identified in the GIC records through shifts in $\delta^{18}O$ values and snow accumulation rates (Rasmussen et al., 2007). Around 50 years after the termination of GS-1, there is a decline of 1-2‰ in $\delta^{18}O$ values and a 10-15% reduction in accumulation rate (Rasmussen et al., 2007). The $\delta^{15}N$ values measure a decline in temperatures at this time in GISP2 (Kobashi et al., 2008). This oscillation is named the '11.4ka event' and dated to 11,585-11,255 b2k (97-96 MCE) with the lowest values centred around 11.5 to 11.4ka b2k (Rasmussen et al., 2007). A second, less pronounced $\delta^{18}O$ anomaly termed the '11.1ka event' has only been identified in NGRIP, centred around 11.1 ka b2k (Rasmussen et al., 2007; Blockley et al., 2018). Rasmussen et al. (2007) found no accumulation anomalies with this event. There are questions over whether the 11.1ka event is representative of a climatic event or a result of changing local conditions (Rasmussen et al., 2007). However, Blockley et al. (2018) identified pronounced climatic events at Star Carr, dated to the 11.4ka and 11.1ka events through high-precision Bayesian modelling and environmental analysis.

Figure 9.3 compares the timings of the GICs 11.4ka and 11.1ka events to the vegetation revertences identified in the European pollen record. These GICs events overlap in age probability ranges of the vegetation revertences identified in the terrestrial records. This overlap makes it hard to distinguish which vegetation revertence can be assigned to which GICs event. However, focusing on the onset for each vegetation revertence, synchronicity ca be tested between the GICs and pollen records.

In the majority of European records, there is a delay to the onset of the 11.4ka event, at 1σ. The vegetation revertences are happening around the coldest part of the GICs event (Figure

9.3). Sites which have the Hässeldalen and/or the Askja-S tephras have a refined timing for the delayed onset of this GICs cooling event (Crudale, Hässeldala, Czechowskie and Soppensee). These tephras have not been identified in the ice cores (Paul Albert, personal communication), limiting the direct comparison in the timing of these cooling events between the different archives. The secondary sites of Kråkenes and Madtjärn also show a later onset at 1σ, confirming a proposed delay in vegetation response to climatic cooling. The sites of Hämelsee, LPA and Brazi show a simultaneous response to the onset of the 11.4ka, yet problems with chronology at these sites previously discussed have resulted in large age uncertainties.

The delay in response to climatic cooling presented in Figure 9.3 at the 68.2% probability range could be due to a time-transgression. The earliest response at GICs may be due to being the furthest northern sites. In contrast, there may be issues with comparing the different proxies. Changes in terrestrial vegetation have been proposed as being slower than changes recorded in $\delta^{18}O$ due to migration rates, seed dispersal, taxa recruitment (mature individuals added to the species population in an area) resulting in a lag to abrupt climatic changes (Huntley, 1991; Ammann et al., 2000; Williams et al., 2011; Słowiński et al., 2017).

At greater probability of 95.4% range, the sites of Crudale, Madtjärn, Hämelsee, LPA and Brazi show synchronous vegetation changes with the onset of the 11.4ka event, possibly indicating large-scale, near simultaneous propagation of climatic changes through alterations in atmospheric circulation. However, the onset of these vegetation revertences presents a complicated picture. There are no clear timings on EH oscillation onsets across a latitudinal gradient (Figure 9.3) This may be related to problems with chronology and the lack of additional radiocarbon dates at these sites. The record at Crudale has well-known tephra layers to create an age-depth model for the record. Additional dating could reduce the large age uncertainties associated with this site. Hämelsee and LPA have large age uncertainties at this time, possibly due to the radiocarbon plateau. This plateau may also be affecting the secondary

site of Madtjärn's ages, especially with the lack of EH tephras identified. In contrast, Hässeldala, Czechowskie and Soppensee show a delay in vegetation response to the 11.4ka event at 95.4% probability range. These sites have better dating controls (radiocarbon and tephras), resulting in higher precision throughout this period.

The termination of these vegetation revertences and GICs 11.4ka are compared (Figure 9.3). There is a delay to the termination of vegetation revertences in comparison to the ending of the 11.4ka event. However, with some sites identifying an additional EH event, along with the GICs 11.1ka event (Hämelsee, Czechowskie and possibly Crudale), deciphering the response of these pollen records to a particular GICs event is extremely difficult with the age uncertainties presented. This delay to the termination could be due to the prolonged vegetation response to a second climatic event presented by the 11.1ka event. There is an overlap in age uncertainty presented at all sites to the timing of the 11.1ka event (Figure 9.3). However, testing this hypothesis is difficult as the Askja-S tephra has not been identified in GICs. Also, there are problems for comparing radiocarbon ages to the high-resolution record of the GICs, as demonstrated here. Determining if there is a valid offset between the records, due to either climatic mechanisms or proxy resolution or sensitivity, is difficult.

Previous investigators have identified synchronicity when comparing EH vegetation events to GICs, namely the 11.4ka event (e.g. Björck et al., 1997; Bos et al., 2007; Fiłoc et al., 2018). However, disentangling the vegetation response to EH climatic cooling in GICs is extremely difficult. The overlap in age probability ranges for vegetation revertences and GICs event requires further investigation with additional high-resolution dating and proxy resolution, supplemented by tephrochronology.

## 9.5 Proposed climatic drivers

The timing of the centennial-scale climatic oscillations allows investigation into the climatic mechanisms behind climatic oscillations. There are several proposed hypothesis for the climatic drivers behind the EH cooling events, including freshwater input into the North Atlantic Ocean (e.g. Fisher et al., 2012; Nesje et al., 2004 ) and/or changes in solar activity (e.g. Bond et al., 2001; van der Pilcht et al., 2004). The timing of vegetation revertences in this study allows for these different hypothesis' to be explored.

Figure 9.3 presents the vegetation revertences in a broader climatic context with comparisons to timings of: A) solar activity using $^{10}$Be records from the GICs; B) re-modelled dates for a freshwater outburst from Lake Agassiz (Finsinger et al., 2012) and proglacial lakes of northern Europe (Nesje et al., 2004, not remodelled); and C) re-modelled ages for ice-rafted debris (IRD) layers from Bond et al. (1997) core V2814 and MD01-2461 (Peck et al., 2007).

The initial freshwater outburst from Lake Agassiz (Finsinger et al., 2012) and the Baltic ice lake (e.g. Hald and Hagen, 1998; Husum and Hald, 2002; Nesje et al., 2004) occurred before the first EH event recorded in the terrestrial vegetation (Figure 9.3). This may have resulted in the disruption and weakening of the AMOC reducing heat transported to the northern latitudes (Clark et al., 2002; Renssen et al., 2007). As a result, sea-ice expanded into the Nordic Sea as indicated by an increase in IRD and stratification of the water column within marine records (Figure 9.3; Bond et al., 2001; Husum and Hald, 2002; Renssen et al., 2007). The polar front may have been displaced south, resulting in cooler conditions recorded in the pollen records across Europe (Figure 9.3). The time-transgressive nature of the polar front migration is difficult to determine due to the chronological precision of radiocarbon dating (Olsson, 2009; Lane et al., 2011b). However, it is probably within decadal timescales, indicating quick atmospheric reorganisation and vegetation response.

Changes in solar activity may have also played a vital role in the expression of cooling events in the EH period. After the initial freshwater impulse, there was a marked increase in cosmogenic nuclides in GIC, indicating decreased solar activity (Figure 9.3; Bond et al., 2001). Vegetation revertences are identified during this period. The variations in solar activity may have affected the climate in two ways. Firstly, through changes in the atmospheric circulation with the North Atlantic Oscillation (NAO) through the 'top-down' mechanism (see Chapter 2). Secondly, through the 'bottom-up' mechanism associated with the oceanic system resulting in increased IRD events (see section 2.3.2; Bond et al., 2001; Renssen et al., 2007; Engels and van Geel, 2012). As solar activity decreased, the stratospheric polar vortex weakened, resulting in a cold ozone layer forming and a negative NAO dominating. Such a situation resulted in colder temperatures and different precipitation patterns across Europe as storm tracks were displaced south (Magny et al., 2006, 2007). Comparisons to marine records also show overlap in age uncertainty with solar minima and IRD events, particular the Bond event 8 linked to the PBO (Figure 9.3; Bond et al., 2001).

As the timing of freshwater influxes into the North Atlantic happen before this solar minima, it seems more likely that a meltwater event was the main climatic driver behind the earliest EH oscillation identified in pollen records (Figure 9.3). The sites closest to the North Atlantic Ocean show the largest magnitude of the vegetational shifts, highlighting the ocean as an important driver of changing climatic conditions (Figure 9.2). The identification of a second climatic oscillation soon after the first event within central European records overlaps with the solar minima (Figure 9.3). Only northern and central European sites record a clear second event. It can be suggested that the North Atlantic Ocean likely amplified the solar minimum. The results of the GCM simulation used by Renssen et al. (2006) suggested that reduced solar activity affects the AMOC and sea-ice extent. Sites at higher latitudes were under the confluence of the changing polar front position. After the first EH event, the polar front may

have withdrew north as the sea-ice retreated following the proposed initial changes in the AMOC. Solar activity then proceeded to drop, possibly resulting in prolonged convection shutdown around the Nordic sea as radiative forcing declined (Renssen et al., 2006). Sea-ice may then have expanded again, shifting the polar front further south. The northern and central sites experienced an additional cooling event around 30 years after the end of the first EH oscillation (Figure 9.3; Usinger et al., 2004; Stančikaitė et al., 2009; Paus et al., 2015; Fiłoc et al., 2018). The additional cooling event of the 11.1ka event was seen in the GICs. However, this was not propagated as far south as no second vegetation or any other proxy response to cooler climatic conditions was recorded at this time.

If solar forcing was the main driver for this second oscillation identified in this study, all records across Europe may have shown a second event. A decrease in solar radiation can affect stratospheric processes resulting in changes to a negative NAO (Haigh, 1996; van Geel et al., 1999; Magny et al., 2007). This would have resulted in changes in temperature and precipitation across the latitudes which would have affected the vegetation assemblages at all sites (Magny et al., 2007; Martin-Puertas et al., 2012; Magyari et al., 2012). However, there is no clear second event identified in southern sites vegetation record (Figure 9.3) or other proxies (e.g. Lotter et al., 1992; Kyrikou et al., 2019). This could be due to other factors linked to the records themselves as previously discussed (proxy sensitivity, resolution, cross-core correlations, the resilience of assemblages). However, vegetation at sites further to the south and east may not have passed their climatic threshold to a second lower amplitude climatic oscillation (Alley et al., 2003; Scheffer and Carpenter, 2003; Williams et al., 2011; Heiri et al., 2014; Candy et al., 2016). As a result, it could be suggested that the North Atlantic Ocean was the main driver for the initial climatic cooling seen across EH Europe. With a decrease in solar activity afterwards, there was a positive oceanic feedback that possibly amplified this solar

minima across the northern latitudes of Europe (Bond et al., 2001; Renssen et al., 2007; Engels and van Geel, 2012).

Disentangling the major driver of the EH cooling events is also difficult due to the problems of chronology and proxy resolution of marine records and their comparisons to the finer resolution and precision dated terrestrial records. The large age uncertainties (>200-year error) associated with IRD events reported in Figure 9.3 are larger than the proposed duration of EH climatic events (Bond et al., 2001; Björck et al., 1997). Large age uncertainties in marine records are the result of: 1) sedimentation rates which can result in poor proxy resolution for sub-millennial scale climatic events (Polyak et al., 2010); and 2) coupled with problems of marine reservoir effect on radiocarbon dates samples (e.g. Ascough et al., 2005). Comparison to centennial-scale climatic events is difficult (Polyak et al., 2010). Many investigators have used the original Bond et al. (1997, 2001) raw data to correlate EH events to IRD events (e.g. Florescu et al., 2019). The original age-depth model did not use a calibration curve. The newly modelled ages from this study (Appendix 5) show a large age uncertainty which needs to be taken into account when making assumptions of synchronicity.

### 9.6 Evaluating climatic synchronicity across Europe

The results from this research show the complexity in the identification and timing of EH climatic oscillations. The period has two widely detected tephra marker layers of the Hässeldalen and Askja-S seen in several records across Europe. The refinement of both tephra ages, particularly the Askja-S, in this project has improved age precision and constrained chronological uncertainty for many records during the EH. This is particularly useful with the demonstrated occurrence of one or more EH climatic oscillations coinciding with these eruptions.

However, not all sites have both of these isochronous maker layers with many of these sites confined to northern Europe, limiting the investigation into potential climatic time-transgression across a continental-scale latitudinal gradient. Nonetheless, even within this small northern region, the presence of these tephra layers was not able to clearly show a time-transgressive nature to these EH oscillations. The widespread deposition of the Askja-S from northern to south-eastern Europe is a helpful marker to improve age uncertainty and identification of a possible additional EH event, particularly in northern and central Europe. This further demonstrates the importance of these two tephras in constraining rapid climatic events and integrating palaeoenvironmental records across a large spatial area (Lane et al., 2013; Davies et al., 2015). Ideally, both tephra layers would be within the GICs to allow direct comparisons to this important palaeoenvironmental record. However, currently, these layers have not been found.

Using these two co-existing tephras as prior knowledge into identifying an EH climatic event between these marker layers can be useful (Wohlfarth et al., 2006; Ott et al., 2016). However, caution is advised when identifying these tephras in records without confirmation with geochemical analysis, as related climatic events have been shown here to start before and continue after the depositions of these isochronous markers.

Once again, as demonstrated in Chapter 8, utilising and presenting ages at 68.2% and 95.4% ranges for the EH climatic events allows further understanding into the timing of centennial-scale climatic oscillations across Europe. It also allows insight into the possible weaknesses of methods or records to be explored (Bennett, 1994; Blaauw, 2010; Blaauw et al., 2018). Sites with limited radiocarbon dates (LPA) lack of one or both tephras (Hämelsee and Rotsee, respectively) coupled with large age errors and variations in proxy resolution (Hässeldala), can result in difficulty in disentangling clear timings of climatic events across a gradient. Also, there is a radiocarbon plateau during the EH period, which has resulted in age

uncertainties at all sites (Björck et al., 1997; van der Pilcht et al., 2004). Increasing the number of radiocarbon dates across this period may help to reduce these age uncertainties (Ammann and Lotter, 1989; Blaauw et al., 2018), as might developments in the radiocarbon calibration curve (Reimer et al., in preparation). Even with the use of well-dated tephra horizons, age uncertainty overlap at different sites can make it difficult to clearly distinguish if time-transgression seen in the terrestrial records.

Even with the improvements in chronological uncertainty made here, with the use of tephra layers and Bayesian age modelling, it is difficult to resolve if an environmental response to climatic changes is synchronous or not at the centennial-, decadal-timescales. This could be partly due to reaching the limits of radiocarbon dating precision (~20-30 years in optimum situations, Olsson, 2009). The high resolution dating at Kråkenes with <70 samples for the LGIT period does provide very refined and precise ages. However, at many sites, this is not possible, usually because of a lack of suitable dating material or other constraints (e.g. hardwater effect). Tephra layers improve this, but their use is very dependent on ash dispersal directions and understanding of the taphonomic processes if these layers are identified (Pyne-O'Donnell, 2007; Davies et al., 2012; Timms et al., 2019). The temporal duration of the events discussed here within the EH appears to be beyond the levels of precision currently undertaken for radiocarbon dating (Lowe and Walker, 2000). This is even with the application of Bayesian modelling and tephrochronology (Blaauw et al., 2018). As demonstrated by Lane et al. (2013), the annually laminated records with tephra horizons may provide the best opportunity to make comparisons at a sub-centennial scale and further test the possible time-transgressive nature of EH climatic events.

### 9.6.1 Identifying the classic PBO of Björck et al. (1996, 1997)

The classic Preboreal Oscillation was dated in terrestrial pollen records from northern Europe by Björck et al. (1997), dated to 11,300-11,150 cal. BP. Since this publication, numerous investigators have identified this climatic event within different archives (see section 2.3. for details). The term PBO has been used inconsistently throughout the literature with numerous events of different ages being assigned this term (e.g. Fiłoc et al., 2018).

This continental-scale study of EH climatic events from the terrestrial vegetation record, using refined chronology and tephrochronology, has provided ages for these events. Is there a PBO in these records as defined by Björck et al. (1997)? Figure 9.3 shows that there is at least one cooling event registered in the majority of terrestrial pollen records across Europe. There is a large scale response to the coldest EH oscillation that is depicted in the GIC, the 11.4ka event. It could be suggested that a response seen in terrestrial records to this 'ice-PBO' is the terrestrial equivalent of the PBO.

However, it is shown here that complications arise when several, quick succession climatic events are identified in the same record and overlap in age probabilities. The EH is characterised by multiple cooling events (Figure 9.3). Identifying these climatic events within the terrestrial pollen record is dependent on the sensitivity of the site under investigation. As seen in Kråkenes and Crudale, pollen records show different responses compared to other proxy records at the same site with no or prolonged vegetation deterioration. In addition, the further south a site is located from the North Atlantic, the less chance a second climate event is recorded. Sites close to the ocean do show a clear environmental response in all records. Yet, the timing of these responses is also very dependent on the resolution of the proxy and the chronological controls at the site. Many other investigators have shown additional EH oscillations across Europe within the pollen record (e.g. Bohncke and Hoek, 2007; Fiłoc et al., 2018), stable isotopes (e.g. Whittington et al., 1996, 2015) and glacial moraines (e.g. Nesje and

Dahl, 1993; Bakke et al., 2005) with many giving all these different oscillations the term "PBO" (e.g. Fiłoc et al., 2018).

As a result, unless the investigative approach is wide-ranging, with the use of independent evidence and dating with the addition of refined isochronous tephra markers during the EH, the researcher cannot be confident which climatic event identified in their record is the earliest or oldest EH climatic response. For this reason, the term PBO is misleading and should no longer be used.

## 9.7 Chapter summary

The refined ages for the Hässeldalen and Askja-S tephras produced within this study have provided insight into the earliest Holocene centennial-scale climatic events and their temporal and spatial expression across Europe. Identifying vegetation revertences as a result of climatic oscillations was made possible through using the Principal Curve in conjunction with evidence from Pollen Accumulation Rate and other proxies. This technique resulted in the identification of EH oscillations across Europe with the additional events identified in sites in northern and central Europe. The refined age for the Askja-S tephra was key to identifying and validating a second EH oscillation at these sites. The lack of this second EH event seen in southern and eastern European records with the Askja-S tephra could be due to low amplitude characteristic of this cooling event. By combining the evidence from other proxies and the magnitude of terrestrial vegetation change, it is suggested that the main climatic driver of the first EH oscillation is possibly the North Atlantic Ocean. Freshwater influx changed the oceanic circulation and the potentially the position of the polar front. The timing of solar minimum soon after was possibly amplified by the North Atlantic Ocean through the 'bottom-up' mechanism resulting in a second cooling event only witnessed in northern and central European sites, suggesting a localised change in the polar front. The identification of the Askja-S tephra

helps recognise and verify this event in records across Europe. As a result, the Preboreal Oscillation dated by Björck et al. (1997) may be associated with the first EH event. However, caution should be used when calling an oscillation the PBO unless high-resolution proxy and dating have been undertaken with tephrochronology to verify the timing of this event.

# Chapter 10

# Synthesis and conclusions

The main aim of this thesis was to investigate and assess the synchroneity or asynchrony of different temporal scale climatic oscillations during the Last Glacial-Interglacial Transition (LGIT). The millennial-scale climatic event of the Younger Dryas (YD) and the earliest Holocene (EH) centennial-scale oscillations provided ideal periods to investigate climatic change across Europe. This thesis was the first study to use this particular approach to look at the potential propagation of climatic oscillations on a continental scale. Through the methods employed in this study, a greater understanding into the climatic drivers and variable spatiotemporal response for both the YD and EH climatic oscillations across Europe was achieved.

## 10.1 Cryptotephra investigations in Romania – summary of findings

- Tephra shards at both primary study sites, Lake Lia and Brazi, originated from Anatolian, Mediterranean and Icelandic volcanic centres, identified using major and trace element analysis. This highlights the pivotal link that Romanian and the central eastern European regional cryptotephra records can provide in correlating between sedimentary archives in the North Atlantic region, Europe and the Mediterranean.
- The adaptation of the cryptotephra laboratory procedures from using a 25µm to a 15µm sized mesh was essential in retaining and subsequently identifying the fine grain ash particles produced from distal eruptions.
- Three different clear cryptotephra horizons were successfully identified from three different volcanic centres:

1. The Askja-S tephra from Iceland in both Lia and Brazi. This discovery extends the known ash dispersal for this tephra from north-west to south-eastern Europe. The identification of this tephra layer was crucial in understanding the timing of the EH oscillations (Chapter 9).
2. The Late Glacial Lipari (LG Lipari) tephra layer was identified in both Lia and Brazi. Chronological modelling produced an age of 12,156 ± 421 cal BP (1σ) for this eruption. The use of major, minor AND trace element analysis was vital for this tephra to be distinguished from other known Lipari eruptions.
3. Identified in Lia was an isochron with tephra shards from an EH Ischia eruption. At Lia, the age is refined for this tephra to 11,084 ± 66 cal. BP (1σ).

- Throughout both records, there were rhyolitic glass shards with high-silica (>75%) determined to be from Anatolia through major, minor and trace element geochemistry. No definitive correlations to eruptions or volcanoes were made due to the lack of published glass geochemistry and poor chronological controls on known past volcanic eruption for the region.
- Other tephras were also identified in both sites' records, including: 1) Vedde-Ash like shards yet lacking a clear isochron; 2) An EH Pantellerite shard; 3) A single shard of Neapolitan Yellow Tuff geochemistry in Lia.

## 10.2 The (a)synchronicity of millennial and centennial-scale climatic oscillation across Europe

Thirteen of the 'best' dated pollen records were collected from published and unpublished literature using a selection criteria (section 3.1.2) that included independent dating from radiocarbon dates and tephra layers to provide insight into the temporal and spatial response to the YD and EH oscillations across Europe.

### 10.2.1 The Younger Dryas

- There is possibly time-transgression in the onset and termination of the YD stadial across Europe.
- The onset of the YD was time-transgressive from northern to southern Europe at 68.2% probability. Weakening of the Atlantic Meridional Overturning Circulation (AMOC) is suggested as resulting in the southward expansion of sea-ice into the Nordic Sea and displacement of the polar front southward. However, eastern Europe may have cooled before northern Europe due to blocking of atmospheric circulation by the Scandinavian Ice Sheet. The largest magnitude of vegetation change was experienced at northern sites compared to central and southern sites. This highlights the weakening effect of the North Atlantic Ocean and associated changes in atmospheric circulation (Ruddiman et al., 1981; Issarin and Renssen, 1999; Muschitiello and Wohlfarth et al., 2015; Candy et al., 2016).
- However, at 95.4% probability there is not strong enough evidence to say that there is climatic asynchronicity for the YD onset due to chronological uncertainties associated with both dating and proxy resolution. These issues identified through this investigation with the 'best' palaeoenvironmental records may have limited insight into the asynchrony of this millennial-scale oscillation.
- There is no strong evidence of asynchrony for the YD onset between terrestrial pollen records across Europe and the Greenland ice-core records. Instead, this transition saw a rapid large-scale atmospheric reorganisation and terrestrial vegetation response happening on short timescale.
- The timing of the termination for the YD across Europe saw the southern sites respond to climatic amelioration first before northern sites. The local site conditions and

vegetation assemblages governed the level of vegetation response to climatic amelioration.

### 10.2.2 The earliest Holocene oscillations

- This study has improved the age estimates for the Hässeldalen and Askja-S tephras. The Hässeldalen tephra has a refined age of 11,239 ± 18 cal. BP. The Askja-S tephra has a refined age of 11,076 ± 19 cal. BP.
- The use of statistical analysis via PrC, Rate of Change (RoC) and additional proxy information were vital to identifying the onset and termination of events in the EH period. The PrC allowed further understanding of the magnitude of vegetation change for the climatic transitions.
- Single vegetation revertences linked to abrupt climate change were identified at northern and southern sites. In contrast, two vegetation revertences were identified at central European sites only. Central Europe experienced the biggest magnitude of vegetation shifts for both events. Within the NGRIP ice-core, two climatic oscillations have also been seen. The age uncertainties between the pollen and ice-core records overlap with the coldest part of the older GIC EH 11.4ka event.
- The identification of the Hässeldalen and Askja-S tephras within the records improved age uncertainties for the EH oscillations and helped identify/not identify the second EH cooling event across Europe. No time-transgression was record for both events across the continent, indicating a rapid vegetation response to changing climate.
- Two different climatic drivers are given for the EH oscillations. The first event was driven by a disruption to the AMOC by freshwater, allowing for sea-ice to expand into the Nordic Sea, shifting the polar front south. The second event experienced in central Europe was possibly due to a decrease in solar radiation at this time the effects of which

may have been amplified by the North Atlantic Ocean (van der Pilcht et al., 2004; Renssen et al., 2006; Wanner et al., 2011; Engels and van Geel, 2012). Declining sea surface temperatures may have resulted in a resurgence of sea-ice shifting the polar front south again. However, due to the lower amplification of this climatic event, the polar front potentially remained at central latitudes. No southern sites responded to this second oscillation.

## 10.3 Synthesis and future research

This study has demonstrated the importance of producing precise and accurate chronologies for palaeoenvironmental records. Through the application of tephrochronology, Bayesian age-modelling and the INTIMATE Integration tool to integrate records, there has been advancement in the knowledge of (a)synchronicity of different temporal-scale climatic oscillations during the LGIT on a continental scale.

Even with these chronological tools, the dating resolution of some of the 'best' sites limited the ability to identify time-transgression across Europe. These results emphasise the importance of producing an appropriate number of dates for a sequence to improve chronological precisions (Blaauw et al., 2018). The more dates that are fed into a model, the more precise the chronology can become. The high-resolution dating at Kråkenes provides by far the most precise chronology. However, the practicality of undertaking this type of higher resolution dating is limited in many records due to cost, time and the lack of the appropriate material that can be dated. Nonetheless, future investigations should strive to have appropriate levels of dating and the addition of tephrochronology.

The palynological resolution undertaken at each site varies. The identification of a climatic transition depends on the proxy resolution applied across the LGIT (Wohlfarth et al., 2006; Engels et al., 2016). High-resolution proxy sampling allows an accurate transition to be

determined. Once again, palaeoenvironmental records should undergo high-resolution proxy sampling in addition to dating to provide a precise and accurate climatic and environmental record from the same core.

Lane et al. (2013) have also shown that time-transgression can be on decadal timescales. The uncertainties produced in this thesis are the most precise achievable from these datasets, yet no definitive evidence for time-transgression for abrupt climate change was identified. The IntCal13 radiocarbon plateau at the YD/EH transition and during the EH resulted in larger age uncertainties at all sites. We may be currently reaching a limit for using radiocarbon to look at the timing for abrupt transitions (Olsson, 2009; Lane et al., 2011). Future investigations may hinge on using annually resolved archives with the deposition of tephra layers close to the timing of climatic oscillations to allow comparisons on decadal scales.

The re-modelling and subsequent new ages for the Hässeldalen and Askja-S tephras in this study allowed for high precision dates during the EH. With the imminent release of the IntCal20 radiocarbon calibration curve (Reimer et al., in review), age accuracies for the LGIT will improve.

Throughout this thesis, the use of tephra layers was key to understanding the temporal and spatial characteristics of climatic transitions during the LGIT. The application of using a 15μm sieve mesh size was crucial to retaining and identifying small, ultra-distal tephra shards, particularly the shards of the Askja-S in Romania. As a result, future cryptotephra investigations should also follow this method to identify other ultra-distal and widely identified, useful tephra layers within palaeoenvironmental records

This study provided insight into time-transgression across the European continent. However, there is a spatial gap between the latitudes of 47-50$^{o}$, where there are minimal palaeoenvironmental records (Moreno et al., 2014). As a result, more studies are required at

these latitudes to further understand the temporal and spatial response for abrupt LGIT oscillations.

This thesis used one proxy (pollen) of several that were currently available to reconstruct the climatic complexity of the LGIT. Several studies have highlighted that undertaking different approaches using different proxies is powerful in providing further understanding into abrupt climatic transitions (e.g. Finsinger et al., 2006; Abrook, 2019). This is particularly useful when pollen records are assumed to lag behind climatic changes (Davis and Shaw, 2001; Williams et al., 2011). Future investigations should look at investigating time-transgression using other proxies response to abrupt climate events and allow quantitative reconstructions of past climatic conditions (Moreno et al., 2014). This includes stable isotopes, chironomids and deuterium isotopic biomarker reconstructions, which provide potentially useful tools for investigating the (a)synchronicity of abrupt climatic oscillations (e.g. Sachse et al., 2012; Candy et al., 2016; Abrook, 2019).

Overall, this thesis provides a foundation for investigating time-transgression for understanding abrupt climate change during the LGIT using the chronological methods employed. Future investigations should learn from the results of this thesis and apply the suggestions given throughout to provide high-quality terrestrial records for the palaeo-community to use. By using well-dated records, accepting chronological uncertainties and discarding the use of tuned palaeoenvironmental records, insight into climate asynchrony can be further explored.

## References


Aarnes, I., Bjune, A.E., Birks, H.H., Balascio, N.L., Bakke, J., Blaauw, M. (2012) Vegetation responses to rapid climatic changes during the last deglaciation 13,500–8,000 years ago on southwest Andøya, arctic Norway. *Vegetation history and Archaeobotany*, 21:1, 17-35.

Abrook, A. M. (2019) Environmental response to abrupt climatic change during the Last Glacial-Interglacial Transition (ca. 16-8 Cal. Ka BP): delineating climatic drivers and landscape response during millennial- and centennial-scale climatic variability. *PhD thesis*, Royal Holloway, University of London. 424 p.

Abrook, A.M., Matthews, I.P., Milner, A.M., Candy, I., Palmer, A.P., Timms, R.G. (2019) Environmental variability in response to abrupt climatic change during the Last Glacial-Interglacial Transition (16-8 cal. ka BP): evidence from Mainland, Orkney. *Scottish Journal of Geology*. In press.

Adolphi, F. and Muscheler, R. (2016) Synchronizing the Greenland ice core and radiocarbon timescales over the Holocene–Bayesian wiggle-matching of cosmogenic radionuclide records. *Climate of the Past*, 12:1, 15-30.

Adolphi, F., Muscheler, R., Svensson, A., Aldahan, A., Possnert, G., Beer, J., Sjolte, J., Björck, S., Matthes, K., Thiéblemont, R. (2014) Persistent link between solar activity and Greenland climate during the Last Glacial Maximum. *Nature Geoscience*, 7:9, 662.

Adolphi, F., Ramsey, C.B., Erhardt, T., Edwards, R.L., Cheng, H., Turney, C.S., Cooper, A., Svensson, A., Rasmussen, S.O., Fischer, H., Muscheler, R. (2018) Connecting the Greenland ice-core and U⁄ Th timescales via cosmogenic radionuclides: testing the synchroneity of Dansgaard–Oeschger events. *Climate of the Past*, *14*.

Aharon, P. (2003) Meltwater flooding events in the Gulf of Mexico revisited: implications for rapid climate changes during the last deglaciation. *Paleoceanography and palaeoclimatology*, 18:4, 1-14.

Albert, P.G., Tomlinson, E.L., Lane, C.S., Wulf, S., Smith, V.C., Coltelli, M., Keller, J., Castro, D.L., Manning, C.J., Müller, W., Menzies, M.A. (2013) Late glacial explosive activity on Mount Etna: Implications for proximal–distal tephra correlations and the synchronisation of Mediterranean archives. *Journal of Volcanology and Geothermal Research*, 265, 9-26.

Albert, P.G., Hardiman, M., Keller, J., Tomlinson, E.L., Smith, V.C., Bourne, A.J., Wulf, S., Zanchetta, G., Sulpizio, R., Müller, U.C., Pross, J., Ottolini, L., Matthews, I.P., Blockley, S.P.E., Menzies, M.A. (2015) Revisiting the Y-3 tephrostratigraphic marker: a new diagnostic glass geochemistry, age estimate, and details on its climatostratigraphical context. *Quaternary Science Reviews,* 118, 105-121.

Albert, P.G., Tomlinson, E.L., Smith, V.C., Traglia, F.D., Pistolesi, M., Morris, A., Donato, P., Rose, R.D., Sulpizio, R., Keller, J., Rosi, M., Menzies, M. (2017) Glass geochemistry of pyroclastic deposits form the Aeolian Islands in the last 50ka: a proximal database for tephrochronology. *Journal Volcanology and Geothermal Research*, 33, 81-107.

Albert, P.G., Smith, V.C., Suzuki, T., McLean, D., Tomlinson, E.L., Miyabuchi, Y., Kitaba, I., Mark, D.F., Moriwaki, H., Members, S.P., Nakagawa, T. (2019) Geochemical characterisation of the Late Quaternary widespread Japanese tephrostratigraphic markers and correlations to the Lake Suigetsu sedimentary archive (SG06 core). *Quaternary Geochronology*, 52, 103-131.

Alley, R.B., Marotzke, J., Nordhaus, W.D., Overpeck, J.T., Peteet, D.M., Pielke, R.A., Pierrehumbert, R.T., Rhines, P.B., Stocker, T.F., Talley, L.D., Wallace, J.M. (2003) Abrupt climate change. *science*, 299:5615, 2005-2010.

Ammann, B. and Lotter, A.F. (1989) Late-Glacial radiocarbon and palynostratigraphy on the Swiss Plateau. *Boreas*, 18:2, 109-126.

Ammann, B., Birks, H.J.B., Brooks, S.J., Eicher, U., von Grafenstein, U., Hofmann, W., Lemdahl, G., Schwander, J., Tobolski, K., Wick, L. (2000) Quantification of biotic responses to rapid climatic changes around the Younger Dryas—a synthesis. *Palaeogeography, Palaeoclimatology, Palaeoecology*, 159:3-4, 313-347.

Ampel, L., Kylander, M. E., Steinthorsdottir, M., Wohlfarth, B. (2014) Abrupt climate change and early lake development – the Lateglacial diatom flora at Hässeldala Port, southeastern Sweden. *Boreas*, 44, 94–102.

Andersen, B. G. (1975) Glacial geology of northern Nordland, North Norway. *Norges Geologiske Undersøkelse*, 320, 74 .

Andersson, G. (1896) Svenska växtvärldens historia. *In* Norsted, P. A. and Söner, B. Stockholm, 136 pp.

Andresen, C.S., Björck, S., Jessen, C., Rundgren, M. (2007) Early Holocene terrestrial climatic variability along a North Atlantic island transect: palaeoceanographic implications. *Quaternary Science Reviews*, 26, 1989-1998.

Andrews, J.T., Jennings, A.E., Kerwin, M., Kirby, M., Manley, W., Miller, G.H., Bond, G., MacLean, B. (1995) A Heinrich-like event, H-0 (DC-0): Source (s) for detrital carbonate in the North Atlantic during the Younger Dryas Chronozone. *Paleoceanography*, 10:5, 943-952.

Andrič, M., Massaferro, J., Eicher, U., Ammann, B., Leuenberger, M.C., Martinčič, A., Marinova, E., Brancelj, A. (2009) A multi-proxy Late-glacial palaeoenvironmental record from Lake Bled, Slovenia. *Hydrobiologia*, 631:1, 121-141.

Ascough, P., Cook, G., Dugmore, A. (2005) Methodological approaches to determining the marine radiocarbon reservoir effect. *Progress in Physical Geography*, 29:4, 532-547.

Bakke, J., Dahl, S.O., Paasche, Ø., Løvlie, R., Nesje, A. (2005) Glacier fluctuations, equilibrium-line altitudes and palaeoclimate in Lyngen, northern Norway, during the Lateglacial and Holocene. *The Holocene*, 15:4, 518-540.

Bakke, J., Lie, Ø., Heegaard, E., Dokken, T., Haug, G.H., Birks, H.H., Dulski, P., Nilsen, T., (2009) Rapid oceanic and atmospheric changes during the Younger Dryas cold period. *Nature Geoscience*, 2:3, 202-205.

Baldini, L.M., McDermott, F., Baldini, J.U., Arias, P., Cueto, M., Fairchild, I.J., Hoffmann, D.L., Mattey, D.P., Müller, W., Nita, D.C. (2015) Regional temperature, atmospheric circulation, and sea-ice variability within the Younger Dryas Event constrained using a speleothem from northern Iberia. *Earth and Planetary Science Letters*, 419, 101-110.

Ballantyne, C.K. (2010) Extent and deglacial chronology of the last British-Irish ice sheet: implications of exposure age using cosmogenic isotopes. *Journal of Quaternary Science*, 25:4, 515-534.

Ballian, D., Ravazzi, C., De Rigo, D., Caudullo, G. (2016) Pinus mugo in Europe: Distribution, habitat, usage and threats. *In*: San-Miguel-Ayanz, J., de Rigo, D., Caudullo, G., Houston Durrant, T., Mauri, A. (Eds.), *European Atlas of Forest Tree Species*. Publication Office EU, Luxembourg, 124-125.

Bányai, J. (1964) The eruptive age of Lake Szent Anna twin craters (A Szent Anna-tavi ikerkráter erupciójának kora; in Hungarian). *Földrajzi Értesítő (Hung. Geogr. Bull.) XIII,* 1, 57–66.

Barnekow, L. and Sandgren, P. (2001) Palaeoclimate and tree-line changes during the Holocene based on pollen and plant macrofossil records from six lakes at different altitudes in northern Sweden. *Review of Palaeobotany and Palynology*, 117:1-3, 109-118.

Bartlein, P.J., Edwards, M.E., Shafer, S.L., Barker Jr, E.D. (1995) Calibration of radiocarbon ages and the interpretation of paleoenvironmental records. *Quaternary Research*, 44:3, 417-424.

Bartolomé, M., Moreno, A., Sancho, C., Stoll, H.M., Cacho, I., Spötl, C., Belmonte, Á., Edwards, R.L., Cheng, H., Hellstrom, J.C. (2015) Hydrological change in Southern Europe responding to increasing North Atlantic overturning during Greenland Stadial 1. *Proceedings of the National Academy of Sciences*, 112:21, 6568-6572.

Barton, R.N.E., Lane, C.S., Albert, P.G., White, D., Collcutt, S.N., Bouzouggar, A., Ditchfield, P., Farr, L., Oh, A., Ottolini, L., Smith, V.C. (2015) The role of cryptotephra in refining the chronology of Late Pleistocene human evolution and cultural change in North Africa. *Quaternary Science Reviews*, 118, 151-169.

Battarbee, R.W., Cameron, N.G., Golding, P., Brooks, S.J., Switsur, R., Harkness, D., Appleby, P., Oldfield, F., Thompson, R., Monteith, D.T., McGovern, A. (2001) Evidence for Holocene climate variability from the sediments of a Scottish remote mountain lake. *Journal of Quaternary Science: Published for the Quaternary Research Association*, 16:4, 339-346.

Beck, P., Caudullo, G., de Rigo, D., Tinner, W. (2016) *Betula pendula, Betula pubescens* and other birches in Europe: distribution, habitat, usage and threats. In: San-Miguel-Ayanz, J., de Rigo, D., Caudullo, G., Houston Durrant, T., Mauri, A. (Eds.), *European Atlas of Forest Tree Species*. Publication Office EU, Luxembourg, 70-73.

Behre, K.E. (1978) Die Klimaschwankungen im europäischen Präboreal. Petermanns Geographische Mitteilungen, *2*, 97-102.

Belis, C.A., Finsinger, W., Ammann, B. (2008) The late glacial–Holocene transition as inferred from ostracod and pollen records in the Lago Piccolo di Avigliana (Northern Italy). *Palaeogeography, palaeoclimatology, palaeoecology*, 264:3-4, 306-317.

Bell, J.N.B. and Tallis, J.H. (1973) Empetrum nigrum L. *Journal of Ecology*, 61:1, 289-305.

Bennett, K.D. (1994) Confidence intervals for age estimates and deposition times in late-Quaternary sediment sequences. *The Holocene*, 4:4, 337-348.

Bennett, K.D. (1996) Determination of the number of zones in a biostratigraphical sequence. *New Phytologist*, 132, 155-170.

Bennett, K.D., Willis, K.J. (2001) Pollen. *In*: Smol, J.P., Birks, H.J.B., and Last, W.M. (Eds.). *Tracking Environmental Change Using Lake Sediments. Volume 3: Terrestrial, Algal and Siliceous Indicators.* Dordrecht, The Netherlands: Kluwer Academic Publishers, 5-32.

Bennett, K.D. and Humphry, R.W. (1995) Analysis of late-glacial and Holocene rates of vegetational change at two sites in the British Isles. *Review of Palaeobotany and Palynology*, 85, 263-287.

Bennett, K., (1995) psimpoll, Version 4.27. Retrieved January 2018. http://www.chrono.qub.ac.uk/psimpoll/psimpoll.html

Bennion, H., Simpson, G.L., Goldsmith, B.J. (2015). Assessing degradation and recovery pathways in lakes impacted by eutrophication using the sediment record. *Frontiers in Ecology and Evolution*, 3, 1-20.

Berglund, B. E. (1966) Late-Quaternary vegetation in eastern Blekinge, south-eastern Sweden. *Opera Botanica*. 12, 5–180.

Berglund, B.E., Björck, S., Lemdahl, G., Bergsten, H., Nordberg, K., Kolstrup, E. (1994) Late Weichselian environmental change in southern Sweden and Denmark. *Journal of Quaternary Science*, 9:2, 127-132.

Bergman, J., Wastegård, S., Hammarlund, D., Wohlfarth, B., Roberts, S.J. (2004) Holocene tephra horizons at Klocka Bog, west-central Sweden: aspects of reproducibility in subarctic peat deposits. *Journal of Quaternary Science*, 19:3, 241-249.

Birks, H.H. and Ammann, B. (2000) Two terrestrial records of rapid climatic change during the glacial–Holocene transition (14,000–9,000 calendar years BP) from Europe. *Proceedings of the National Academy of Sciences*, 97:4, 1390-1394.

Birks, H. J. B. and Birks, H. H. (2008) Biological responses to rapid climate change at the Younger Dryas – Holocene transition at Kråkenes, western Norway. *The Holocene*, 18:1, 19–30.

Birks, H.H. and Birks, H.J.B., (2000) Future uses of pollen analysis must include plant macrofossils. *Journal of biogeography*, 27:1, 31-35.

Birks, H.H. and Birks, H.J.B. (2013) Vegetation responses to late-glacial climate changes in western Norway. *Preslia*, 85:3, 215-237.

Birks, H.H. and Wright, H.E. (2000) Introduction to the reconstruction of the late-glacial and early-Holocene aquatic ecosystems at Kråkenes Lake, Norway. *Journal of Paleolimnology*, 23:1, 1-5.

Birks, H.H., Aarnes, I., Bjune, A.E., Brooks, S.J., Bakke, J., Kühl, N., Birks, H.J.B. (2014) Lateglacial and early-Holocene climate variability reconstructed from multi-proxy records on Andøya, northern Norway. *Quaternary Science Reviews*, 89, 108-122.

Birks, H.H., Battarbee, R.W., Birks, H.J.B. (2000) The development of the aquatic ecosystem at Kråkenes Lake, western Norway, during the late glacial and early Holocene-a synthesis. *Journal of Paleolimnology*, 23:1, 91-114.

Birks, H.H., Gulliksen, S., Haflidason, H., Mangerud, J., Possnert, G. (1996) New radiocarbon dates for the Vedde Ash and the Saksunarvatn Ash from western Norway. *Quaternary research*, 45:2, 119-127.

Birks, H.H., Jones, V.J., Brooks, S.J., Birks, H.J.B., Telford, R.J., Juggins, S., Peglar, S.M., (2012) From cold to cool in northernmost Norway: Lateglacial and early Holocene multi-proxy environmental and climate reconstructions from Jansvatnet, Hammerfest. *Quaternary Science Reviews*, 33, 100-120.

Birks, H.H., Larsen, E., Birks, H.J.B. (2005). Did tree-*Betula*, *Pinus* and *Picea* survive the last glaciation along the west coast of Norway. A review of the evidence, in light of Kullman (2002). *Journal of Biogeography*, 32:8, 1461-1471.

Birks, H.H., Vorren, K.D., Birks, H.J.B. (1996) Holocene tree-lines, dendrochronology and palaeoclimate. *PalaÈoklimaforschung/Palaeoclimate Research*, 20, 1-18.

Birks, H.J. (1974) Numerical zonation's of Flandrian pollen data. *New Phytologist*, 73:2, 351-358.

Birks, H.J.B. (1968) The identification of Betula nana pollen. *New Phytologist*, 67, 309-341.

Bjorck, S. and Möller, P. (1987) Late Weichselian environmental history in southeastern Sweden during the deglaciation of the Scandinavian ice sheet. *Quaternary Research*, 28, 1–37.

Björck, J. and Wastegård, S. (1999) Climate oscillations and tephrochronology in eastern middle Sweden during the last glacial–interglacial transition. *Journal of Quaternary Science*, 14:5, 399-410.

Björck, S. and Digerfeldt, G. (1991) Allerød-Younger Dryas sea level changes in southwestern Sweden and their relation to the Baltic Ice Lake development. *Boreas*, 20:2, 115-133.

Björck, S., Kromer, B., Johnsen, S., Bennike, O., Hammarlund, D., Lemdahl, G., Possnert, G., Rasmussen, T.L., Wohlfarth, B., Hammer, C.U., Spurk, M. (1996) Synchronized terrestrial atmospheric deglacial records around the North Atlantic. *Science*, 274:5290, 1155-1160.

Björck, S., Muscheler, R., Kromer, B., Andresen, C.S., Heinemeier, J., Johnsen, S.J., Conley, D., Koç, N., Spurk, M., Veski, S. (2001) High-resolution analyses of an early Holocene climate event may imply decreased solar forcing as an important climate trigger. *Geology*, 29:12, 1107-1110.

Björck, S., Rundgren, M., Ingolfsson, O., Funder, S. (1997) The Preboreal oscillation around the Nordic Seas: terrestrial and lacustrine responses. *Journal of Quaternary Science*, 12, 455-465.

Björck, S., Walker, M.J., Cwynar, L.C., Johnsen, S., Knudsen, K.L., Lowe, J.J., Wohlfarth, B. (1998) An event stratigraphy for the Last Termination in the North Atlantic region based on the Greenland ice-core record: a proposal by the INTIMATE group. *Journal of Quaternary Science: Published for the Quaternary Research Association*, 13:4, 283-292.

Björkman, L., Feurdean, A., Cinthio, K., Wohlfarth, B., Possnert, G. (2002) Lateglacial and early Holocene vegetation development in the Gutaiului Mountains, northwestern Romania. *Quaternary Science Reviews*, 21, 1039-1059.

Blaauw, M. (2010) Methods and code for 'classical' age-modelling of radiocarbon sequences. *quaternary geochronology*, 5:5, 512-518.

Blaauw, M., Christen, J.A., Bennett, K.D., Reimer, P.J. (2018) Double the dates and go for Bayes—Impacts of model choice, dating density and quality on chronologies. *Quaternary Science Reviews*, 188, 58-66.

Blockley, S. P. E., Donnell, S. D. F. P., Lowe, J. J., Matthews, I. P., Stone, A., Pollard, A. M., Turney, C. S. M., Molyneux, E. G. (2005) A new and less destructive laboratory procedure for the physical separation of distal glass tephra shards from sediments. *Quaternary Science Reviews*, 24, 1952–1960.

Blockley, S., Candy, I., Matthews, I., Langdon, P., Langdon, C., Palmer, A., Lincoln, P., Abrook, A., Taylor, B., Conneller, C., Bayliss, A., MacLeod, A., Deeprose, L., Darvill, C., Kearney, R., Beaven, N., Staff, R., Bamforth, M., Taylor, M., Milner, N. (2018) The resilience of postglacial hunter-gatherers to abrupt climate change. *Nature ecology & evolution*, 2:5, 810.

Blockley, S.P., Lane, C.S., Hardiman, M., Rasmussen, S.O., Seierstad, I.K., Steffensen, J.P., Svensson, A., Lotter, A.F., Turney, C.S., Ramsey, C.B. and Intimate Members (2012) Synchronisation of palaeoenvironmental records over the last 60,000 years, and an extended INTIMATE event stratigraphy to 48,000 b2k. *Quaternary Science Reviews*, 36, 2-10.

Blockley, S.P., Lowe, J.J., Walker, M.J., Asioli, A., Trincardi, F., Coope, G.R., Donahue, R.E. (2004) Bayesian analysis of radiocarbon chronologies: examples from the European Late-glacial. *Journal of Quaternary Science*, 19:2, 159-175.

Blockley, S.P.E., Lane, C.S., Lotter, A.F., Pollard, A.M. (2007) Evidence for the presence of the Vedde Ash in central Europe. *Quaternary Science Reviews*, 26:25-28, 3030-3036.

Blockley, S.P.E., Pyne-O'Donnell, S.D.F., Lowe, J.J., Matthews, I.P., Stone, A., Pollard, A.M., Turney, C.S.M., Molyneux, E.G. (2005) A new and less destructive laboratory procedure for

the physical separation of distal glass tephra shards from sediments. *Quaternary Science Reviews*, 24:16-17, 1952-1960.

Bohncke, S.J.P. and Hoek, W.Z. (2007) Multiple oscillations during the Preboreal as recorded in a calcareous gyttja, Kingbeekdal, The Netherlands. *Quaternary Science Reviews*, 26:15-16, 1965-1974.

Bodén, P., Fairbanks, R.G., Wright, J.D., Burckle, L.H. (1997) High-resolution stable isotope records from southwest Sweden: the drainage of the Baltic Ice Lake and Younger Dryas ice margin oscillations. *Paleoceanography*, 12:1, 39-49.

Boettger, T., Hiller, A., Junge, F.W., Mania, D., Kremenetski, K., (2009) Late Glacial/Early Holocene environmental changes in Thuringia, Germany: stable isotope record and vegetation history. *Quaternary International*, 203:1-2, 105-112.

Bogaard, P.V. and Schmincke, H.U. (1985) Laacher See Tephra: A widespread isochronous late Quaternary tephra layer in central and northern Europe. *Geological Society of America Bulletin*, 96:12, 1554-1571.

Böhm, E., Lippold, J., Gutjahr, M., Frank, M., Blaser, P., Antz, B., Fohlmeister, J., Frank, N., Andersen, M.B., Deininger, M. (2015) Strong and deep Atlantic meridional overturning circulation during the last glacial cycle. *Nature*, 517, 73-76.

Bohncke, S.J.P. and Hoek, W.Z. (2007) Multiple oscillations during the Preboreal as recorded in a calcereous gyttja, Kingbeekdal, The Netherlands. *Quaternary Science Reviews*, 26, 1965-1974.

Bond, G.C., Mandeville, C., Hoffmann, S. (2001) Were rhyolitic glasses in the Vedde Ash and in the North Atlantic's Ash Zone 1 produced by the same volcanic eruption? *Quaternary Science Reviews*, 20:11, 1189-1199.

Bos, J.A. (2001) Lateglacial and Early Holocene vegetation history of the northern Wetterau and the Amöneburger Basin (Hessen), central-west Germany. *Review of Palaeobotany and Palynology*, 115:3-4, 177-204.

Bos, J.A., Huisman, D.J., Kiden, P., Hoek, W.Z., van Geel, B. (2005) Early Holocene environmental change in the Kreekrak area (Zeeland, SW-Netherlands): a multi-proxy analysis. *Palaeogeography, Palaeoclimatology, Palaeoecology*, 227:4, 259-289.

Bos, J.A. and Urz, R. (2003) Late Glacial and early Holocene environment in the middle Lahn river valley (Hessen, central-west Germany) and the local impact of early Mesolithic people—pollen and macrofossil evidence. *Vegetation History and Archaeobotany*, 12:1, 19-36.

Bos, J.A., van Geel, B., van der Plicht, J., Bohncke, S.J. (2007) Preboreal climate oscillations in Europe: wiggle-match dating and synthesis of Dutch high-resolution multi-proxy records. *Quaternary Science Reviews*, 26:15-16, 1927-1950.

Bos, J.A.A., Dambeck, R., Kalis, A.J., Schweizer, A., Thiemeyer, H. (2008) Palaeoenvironmental changes and vegetation history of the northern Upper Rhine Graben

(southwestern Germany) since the Lateglacial. *Netherlands Journal of Geosciences/Geologie en Mijnbouw*, 87:1, 67-90.

Botta, F., Dahl-Jensen, D., Rahbek, C., Svensson, A., Nogués-Bravo, D. (2019) Abrupt Change in Climate and Biotic Systems. *Current Biology*, 29:19, R1045-R1054.

Bourne, A.J., Lowe, J.J., Trincardi, F., Asioli, A., Blockley, S.P.E., Wulf, S., Matthews, I.P., Piva, A., Vigliotti, L. (2010) Distal tephra record for the last ca 105,000 years from core PRAD 1-2 in the central Adriatic Sea: implications for marine tephrostratigraphy. *Quaternary Science Reviews*, 29(23-24), 3079-3094.

Bout-Roumazeilles, V., Combourieu Nebout, N., Peyron, O., Cortijo, E., Landais, A., Masson-Delmotte, V. (2007) Connection between South Mediterranean climate and North African atmospheric circulation during the last 50,000 yr BP North Atlantic cold events. *Quaternary Science Reviews*, 26, 3197-3215.

Brauer, A., Endres, C., Negendank, J.F. (1999) Lateglacial calendar year chronology based on annually laminated sediments from Lake Meerfelder Maar, Germany. *Quaternary International*, 61:1, 17-25.

Brauer, A., Hajdas, I., Blockley, S.P., Ramsey, C.B., Christl, M., Ivy-Ochs, S., Moseley, G.E., Nowaczyk, N.N., Rasmussen, S.O., Roberts, H.M., Spötl, C. (2014) The importance of independent chronology in integrating records of past climate change for the 60–8 ka INTIMATE time interval. *Quaternary Science Reviews*, 106, 47-66.

Brauer, A., Haug, G.H., Dulski, P., Sigman, D.M., Negendank, J.F. (2008) An abrupt wind shift in western Europe at the onset of the Younger Dryas cold period. *Nature Geoscience*, 1:8, 520-523.

Brauer, A., Litt, T., Negendank, J.F., Zolitschka, B. (2001) Lateglacial varve chronology and biostratigraphy of lakes Holzmaar and Meerfelder Maar, Germany. *Boreas*, 30:1, 83-88.

Braun, M., Hubay, K., Magyari, E., Veres, D., Papp, I., Bálint, M. (2013). Using linear discriminant analysis (LDA) of bulk lake sediment geochemical data to reconstruct lateglacial climate changes in the South Carpathian Mountains. *Quaternary International*, 293, 114-122.

Broecker, W.S. (2006) Abrupt climate change revisited. *Global and Planetary Change*, 54:3-4, 211-215.

Broecker, W.S., Andree, M., Wolfli, W., Oeschger, H., Bonani, G., Kennett, J., Peteet, D. (1988) The chronology of the last deglaciation: Implications to the cause of the Younger Dryas event. *Paleoceanography*, 3:1, 1-19.

Broecker, W.S., Denton, G.H., Edwards, R.L., Cheng, H., Alley, R.B., Putnam, A.E. (2010) Putting the Younger Dryas cold event into context. *Quaternary Science Reviews*, 29:9-10, 1078-1081.

Broecker, W.S., Kennett, J.P., Flower, B.P., Teller, J.T., Trumbore, S., Bonani, G. Wolfli, W. (1989) Routing of meltwater from the Laurentide Ice Sheet during the Younger Dryas cold episode. *Nature*, 341:6240, 318.

Broecker, W.S., Peteet, D.M., Rind, D. (1985) Does the ocean–atmosphere system have more than one stable mode of operation?. *Nature*, 315:6014, 21.

Bronk Ramsey, C. (1994) Analysis of chronological information and radiocarbon calibration: the program OxCal. *Archaeological Computing Newsletter*, 41*,* 11-16.

Bronk Ramsey, C. (1995) Radiocarbon calibration and analysis of stratigraphy: the OxCal program. *Radiocarbon*, 37:2, 425-430.

Bronk Ramsey, C. (2017) OxCal project, Version 4.3. Retrieved April 2017. https://c14. arch.ox.ac.uk/oxcal/OxCal.html.

Bronk Ramsey, C. (2008). Deposition models for chronological records. *Quaternary Science Reviews,* 27(1-2), 42-60.

Bronk Ramsey, C., (2009a) Dealing with outliers and offsets in radiocarbon dating. *Radiocarbon*, 51:3, 1023-1045.

Bronk Ramsey, C. (2009b) Bayesian analysis of radiocarbon dates. *Radiocarbon*, 51, 337-360.

Bronk Ramsey, C. and Lee, S. (2013) Recent and planned developments of the program OxCal. Radiocarbon, 55:2, 720-730.

Bronk Ramsey, B., Blaauw, M., Kearney, R., Staff, R.A. (2019) The importance of open access to chronological information: the IntChron initiative. *Radiocarbon*, 1-11.

Bronk Ramsey, C., Albert, P., Blockley, S., Hardiman, M., Lane, C., Macleod, A., Matthews, I. P., Muscheler, R., Palmer, A., Staff, R.A. (2014) Integrating timescales with time-transfer functions: A practical approach for an INTIMATE database, *Quaternary Science Reviews*, 106, 67–80.

Bronk Ramsey, C., Albert, P.G., Blockley, S.P., Hardiman, M., Housley, R.A., Lane, C.S., Lee, S., Matthews, I.P., Smith, V.C., Lowe, J.J. (2015) Improved age estimates for key Late Quaternary European tephra horizons in the RESET lattice. *Quaternary Science Reviews*, 118, 18-32.

Bronk Ramsey, C., Blaauw, M., Kearney, R., Staff, R.A. (2019) The importance of open access to chronological information: the IntChron initiative. *Radiocarbon*. In press.

Bronk Ramsey, C. (2008) Deposition models for chronological records. *Quaternary Science Reviews*, 27:1-2, 42-60.

Brooks, S.J., Birks, H.J.B. (2001) Chironomid-inferred air temperatures from Lateglacial and Holocene sites in north-west Europe: progress and problems. *Quaternary Science Reviews*, 20:16-17, 1723-1741.

Brooks, S.J., Matthews, I.P., Birks, H.H., Birks, H.J.B. (2012) High resolution Lateglacial and early-Holocene summer air temperature records from Scotland inferred from chironomid assemblages. *Quaternary Science Reviews*, 41, 67-82.

Brooks, S.J. and Langdon, P.G. (2014) Summer temperature gradients in northwest Europe during the Lateglacial to early Holocene transition (15–8 ka BP) inferred from chironomid assemblages. *Quaternary International*, 341, 80-90.

Browicz, K. (1979) Geograficzne rozmieszczenie brzoz (Geographical distribution of birches). *In*: Brzozy e Betula L. Nasze Drzewa Lesne (Birches e Betula L. Our forest trees). Monografie popularno-naukowe, Tom 7. PWN Warszawa-Poznan, p. 73.

Buczkó, K., Magyari, E., Soróczki-Pinter, E., Hubay, K., Braun, M., Bálint, M. (2009) Diatom based evidence for abrupt climate changes during the Late Glacial in the Southern Carpathian Mountains. *Central European Geology*, 52:1, 1-20.

Buczkó, K., Magyari, E.K., Braun, M., Bálint, M. (2013) Diatom-inferred lateglacial and Holocene climatic variability in the South Carpathian Mountains (Romania). *Quaternary International (Advancing Pleistocene and Holocene climate change research in the Carpathian-Balkan region),* 293, 123–135.

Buczkó, K., Szurdoki, E., Braun, M., Magyari, E. (2018) Reconciling diverse diatom-based lake responses to climate change in four mountain lakes in the South-Carpathian Mountains during the last 17 kyrs. *Quaternary International*, 477, 117-137.

Buizert, C., Adrian, B., Ahn, J., Albert, M., Alley, R.B., Baggenstos, D., Bauska, T.K., Bay, R.C., Bencivengo, B.B., Bentley, C.R., Brook, E.J. (2015) Precise interpolar phasing of abrupt climate change during the last ice age. *Nature*, 520:7549, 661.

Bunting, M.J. (1996) Holocene vegetation and environment of Orkney.' In: Hall, A.M. (Ed.). *The Quaternary of Orkney: Field Guide*, Cambridge: Quaternary Research Association, 20–29.

Cabedo-Sanz, P., Belt, S.T., Knies, J., Husum, K. (2013) Identification of contrasting seasonal sea ice conditions during the Younger Dryas. *Quaternary Science Reviews*, 79, 74-86.

Candy, I., Abrook, A., Elliot, F., Lincoln, P., Matthews, I.P., Palmer, A. (2016) Oxygen isotopic evidence for high-magnitude, abrupt climatic events during the Lateglacial Interstadial in north-west Europe: analysis of a lacustrine sequence from the site of Tirinie, Scottish Highlands. *Journal Of Quaternary Science*, 31:6, 607-621.

Caron, B., Siani, G., Sulpizio, R., Zanchetta, G., Paterne, M., Santacroce, R., Tema, E., Zanella, E. (2012) Late Pleistocene to Holocene tephrostratigraphic record from the Northern Ionian Sea. *Marine Geology*, 311,.41-51.

Cassidy, M., Watt, S.F., Palmer, M.R., Trofimovs, J., Symons, W., Maclachlan, S.E., Stinton, A.J. (2014) Construction of volcanic records from marine sediment cores, 138, 137-155.

Caudullo, G. and de Rigo, D. (2016) Pinus cembra in Europe: distribution, habitat, usage and threats. *In*: San-Miguel-Ayanz, J., de Rigo, D., Caudullo, G., Houston Durrant, T., Mauri, A. (Eds.), *European Atlas of Forest Tree Species*. Publication Office EU, Luxembourg, 120-121.

Charman, D.J. (1994) Late-glacial and Holocene vegetation history of the Flow Country, northern Scotland. *New phytologist*, 127:1, 155-168.

Chiu, T.C., Fairbanks, R.G., Cao, L., Mortlock, R.A. (2007) Analysis of the atmospheric $^{14}C$ record spanning the past 50,000 years derived from high-precision $^{230}Th/^{234}U/^{238}U$, $^{231}Pa/^{235}U$ and $^{14}C$ dates on fossil corals. *Quaternary Science Reviews*, 26, 18-36.

Civetta, L., Cornette, Y., Gillot, P.Y., Orsi, G. (1988) The eruptive history of Pantelleria (Sicily Channel) in the last 50 ka. *Bulletin of Volcanology*, 50:1, 47-57.

Civetta, L., Gallo, G., Orsi, G. (1991) Sr-and Nd-isotope and trace-element constraints on the chemical evolution of the magmatic system of Ischia (Italy) in the last 55 ka. *Journal of Volcanology and Geothermal Research*, 46:3-4, 213-230.

Clark, P.U., Marshall, S.J., Clarke, G.K., Hostetler, S.W., Licciardi, J.M., Teller, J.T. (2001) Freshwater forcing of abrupt climate change during the last glaciation. *Science*, 293:5528, 283-287.

Clark, P.U., Pisias, N.G., Stocker, T.F.,Weaver, A.J. (2002) The role of the thermohaline circulation in abrupt climate change: *Nature*, 415, 863–869.

Clark, J.S., Fastie, C., Hurtt, G., Jackson, S.T., Johnson, C., King, G.A., Lewis, M., Lynch, J., Pacala, S., Prentice, C., Schupp, E.W., Webb, T., III, Wyckoff, P. (1998) Reid's paradox of rapid plant migration. Dispersal theory and interpretation of palaeoecological record. *BioScience*, 48, 13–24.

Colella, A. and Hiscott, R.N. (1997) Pyroclastic surges of the Pleistocene Monte Guardia sequence (Lipari island, Italy): depositional processes. *Sedimentology*, 44:1, 47-66.

Colinvaux, P.A. (1978) On the use of the word "absolute" in pollen statistics. *Quaternary Research,* 9, 132-193.

Collins, J., Aichner B., Schnek, F., Engels, S., Lane, C., Maas, D., Neugebauer, I., Ott, F., Słowinski, M., Wulf, S., Brauer, A., Sachse, D. (2018) Influence of the Scandinavian Ice Sheet on spatiotemporal patterns of European hydroclimate during the Younger Dryas from decadally resolved lacustrine biomarker records. *Geophysical Research Abstracts*, 20.

Constantin, S., Bojar, A.V., Lauritzen, S.E., Lundberg, J. (2007) Holocene and Late Pleistocene climate in the sub-Mediterranean continental environment: a speleothem record from Poleva Cave (Southern Carpathians, Romania). *Palaeogeography, Palaeoclimatolgy, Palaeoecology,* 243, 322-338.

Cook, E., Davies, S.M., Guðmundsdóttir, E.R., Abbott, P.M., Pearce, N.J. (2018) First identification and characterization of Borrobol-type tephra in the Greenland ice cores: new deposits and improved age estimates. *Journal of quaternary science*, 33:2, 212-224.

Coope, G.R. and Lemdahl, G. (1995) Regional differences in the Lateglacial climate of northern Europe based on coleopteran analysis. *Journal of Quaternary Science*, 10:4, 391-395.

Coope, G.R., Lemdahl, G., Lowe, J.J., Walkling, A. (1998) Temperature gradients in northern Europe during the last glacial–Holocene transition (14-9 14C kyr BP) interpreted from coleopteran assemblages. *Journal of Quaternary Science: Published for the Quaternary Research Association*, 13:5, 419-433.

Cortese, M., Frazzetta, G., La Volpe, L. (1986) Volcanic history of Lipari (Aeolian Islands, Italy) during the last 10,000 years. *Journal of Volcanology and Geothermal Research*, 27:1-2, 117-133.

Crisci, G.M., De Rosa, R., Lanzafame, G., Mazzuoli, R., Sheridan, M.F., Zuffa, G.G. (1981) Monte Guardia Sequence: a Late-Pleistocene Eruptive Cycle on Lipari (Italy). *Bulletin of Volcanology*, 44, 241–255.

Cullen, V.L (2015) Tephrochronology as a tool for assessing the synchronicity of Middle Plaeolithic and Upper Palaeolithic techno-complexes in the Caucasus. *DPhil thesis*, University of Oxford.

Cullen, V. L., Smith, V. C. and Arz, H. W. (2014) The detailed tephrostratigraphy of a core from the south-east Black Sea spanning the last 60 ka, *Journal of Quaternary Science*, 29, 675–690.

Cwynar, L.C. and Watts, W.A. (1989) Accelerator-mass spectrometer ages for late-glacial events at Ballybetagh, Ireland. *Quaternary Research*, 31:3, 377-380.

Dansgaard, W., Johnsen, S.J., Clausen, H.B., Dahl-Jensen, D., Gundestrup, N.S., Hammer, C.U., Hvidberg, C.S., Steffensen, J.P., Sveinbjörnsdóttir, A.E., Jouzel, J., Bond, G. (1993). Evidence for general instability of past climate from a 250-kyr ice- core record. *Nature*, 364:6434, 218-220.

Dansgaard, W., Johnsen, S.J., Clausen, H.B., Dahl-Jensen, D., Gundestrup, N., Hammer, C.U., Oeschger, H. (1984) North Atlantic climatic oscillations revealed by deep Greenland ice cores. *Climate processes and climate sensitivity*, 29, 288-298.

Davies, S. M. (2015) Cryptotephras: the revolution in correlation and precision dating. *Journal of Quaternary Science*, 30:2, 114–130.

Davies, S. M., Elmquist, M., Bergman, J., Wohlfarth, B. and Hammarlund, D. (2007) Cryptotephra sedimentation processes within two lacustrine sequences from west central Sweden, *The Holocene*, 17:3, 319–330.

Davies, S.J., Lamb, H.F., Roberts, S.J (2015) Micro-XRF Core Scanning in Palaeolimnology: Recent developments. *In*: Croudace, I.W., Rothwell, R.G. (Eds) Mirco-XRF Studies of Sediment Cores: Applications of a non-destructive tool for the environmental sciences, Springer, pg189.

Davies, S.M., Abbott, P.M., Pearce, N.J., Wastegård, S., Blockley, S.P. (2012) Integrating the INTIMATE records using tephrochronology: rising to the challenge. *Quaternary Science Reviews*, 36, 11–27.

Davies, S.M., Elmquist, M., Bergman, J., Wohlfarth, B., Hammarlund, D. (2007) Cryptotephra sedimentation processes within two lacustrine sequences from west central Sweden. *The Holocene*, 17:3, 319-330.

Davies, S.M., Hoek, W.Z., Bohncke, S.J., Lowe, J.J., O'Donnell, S.P., Turney, C.S. (2005) Detection of Lateglacial distal tephra layers in the Netherlands. *Boreas*, 34:2, 123-135.

Davies, S.M., Wastegård, S., Wohlfarth, B. (2003) Extending the limits of the Borrobol Tephra to Scandinavia and detection of new early Holocene tephras. *Quaternary Research*, 59, 345-352.

Davis, M.B. and Deevey, E.S. (1964) Pollen accumulation rates: estimates from late-glacial sediment of Roger Lake. *Science*, 145, 1293-1295.

Davis, M.B. and Shaw, R.G. (2001) Range shifts and adaptive responses to Quaternary climate change. *Science*, 292:5517, 673-679.

de Klerk, P. (2002) Changing vegetation patterns in the Endinger Bruch area (Vorpommern, NE Germany) during the Weichselian Lateglacial and early Holocene. *Review of Palaeobotany and Palynology*, 119:3-4, 275-309.

de Klerk, P. (2008) Patterns in vegetation and sedimentation during the Weichselian Late-glacial in north-eastern Germany. *Journal of Biogeography*, 35:7, 1308-1322.

de Klerk, P., Couwenberg, J., Joosten, H. (2007) Short-lived vegetational and environmental change during the Preboreal in the Biebrza Upper Basin (NE Poland). *Quaternary Science Reviews*, 26:15-16, 1975-1988.

de Rita, D., Dolfi, D., Cimarelli, C. (2008) Occurrence of Somma-Vesuvius fine ashes in the tephrostratigraphy record of Panarea, Aeolian Islands. *Journal of Volcanology and Geothermal Research*, 177:1, 197–207.

de Vita, S., Sansivero, F., Orsi, G., Marotta, E.,(2006) Cyclical slope instability and volcanism related to volcano-tectonism in resurgent calderas: the Ischia island (Italy) case study. *Engineering Geology*, 86, 148–165.

De'ath, G. (1999) Principal curves: a new technique for indirect and direct gradient analysis. *Ecology*, 80:7, 2237-2253.

Deino, A.L., Orsi, G., de Vita, S., Piochi, M. (2004) The age of the Neapolitan Yellow Tuff caldera-forming eruption (Campi Flegrei caldera Italy) assessed by $^{40}Ar/^{39}Ar$ dating method. *Journal of Volcanology and Geothermal Research*, 133:1-4, 157-170.

Donato, P., Albert, P.G., Crocitti, M., De Rosa, R., Menzies, M.A. (2016) Tephra layers along the southern Tyrrhenian coast of Italy: links to the X-5 & X-6 using volcanic glass geochemistry. *Journal of Volcanology and Geothermal Research*, 317, 30-41.

Di Genova, D., Romano, C., Hess, K.U., Vona, A., Poe, B.T., Giordano, D., Dingwell, D.B., Behrens, H. (2013) The rheology of peralkaline rhyolites from Pantelleria Island. *Journal of Volcanology and Geothermal Research*, 249, 201-216.

Di Roberto, A., Smedile, A., Del Carlo, P., De Martini, P.M., Iorio, M., Petrelli, M., Pantosti, D., Pinzi, S., Todrani, A. (2018) Tephra and cryptotephra in a~ 60,000-year-old lacustrine sequence from the Fucino Basin: new insights into the major explosive events in Italy. *Bulletin of Volcanology*, 80:3, 20.

Di Vito, M.A., Sulpizio, R., Zanchetta, G., D'Orazio, M. (2008) The late Pleistocene pyroclastic deposits of the Campanian Plain: new insights into the explosive activity of Neapolitan volcanoes. J *Journal of Volcanology and Geothermal Research*, 177:1, 19-48.

Dreibrodt, S., Lomax, J., Nelle, O., Lubos, C., Fischer, P., Mitusov, A., Reiss, S., Radtke, U., Nadeau, M., Grootes, P.M., Bork, H.R. (2010) Are mid-latitude slopes sensitive to climatic oscillations? Implications from an Early Holocene sequence of slope deposits and buried soils from eastern Germany. *Geomorphology*, 122:3-4, 351-369.

Drescher-Schneider, R., De Beaulieu, J.L., Magny, M., Walter-Simonnet, A.V., Bossuet, G., Millet, L., Brugiapaglia, E., Drescher, A. (2007) Vegetation history, climate and human impact over the last 15,000 years at Lago dell'Accesa (Tuscany, Central Italy). *Vegetation History and Archaeobotany*, 16:4, 279-299.

Dugmore, A.J. and Newton, A.J. (1997) Holocene tephra layers in the Faroe Islands. *Frodskaparrit* 45, 141-154.

Dugmore, A.J., Newton, A.J. (2012) Isochrons and beyond: maximising the use of tephrochronology in geomorphology. *Jökull*, 62, 39-52.

Eastwood, W.J., Pearce, N.J.G., Westgate, J.A., Perkins, W.T., Lamb, H.F., Roberts, N. (1999) Geochemistry of Santorini tephra in lake sediments from southwest Turkey. *Global Planetary Change*, 21:1-3, 17-29.

Eawag, A.L., Eicher, U., Siegenthaler, U., Birks, H.J.B. (1992) Late-glacial climatic oscillations as recorded in Swiss lake sediments. *Journal of Quaternary Science*, 7:3, 187-204.

Edwards, K.J. and Whittington, G. (1997) A 12 000-year record of environmental change in the Lomond Hills, Fife, Scotland: vegetational and climatic variability. *Vegetation History and Archaeobotany*, 6:3, 133-152.

Edwards, K.J. and Whittington, G. (2010) Lateglacial palaeoenvironmental investigations at Wester Cartmore Farm, Fife and their significance for patterns of vegetation and climate change in east-central Scotland. *Review of Palaeobotany and Palynology*, 159:1-2, 14-34.

Eicher, U. (1980) Pollen-und Sauerstoffisotopenanalysen an spätglazialen Profilen vom Gerzensee, Faulenseemoos und vom Regenmoos ob Boltigen. *Mitteilung der Naturforschenden Gesellschaft Bern*, 37, 65-80.

Eicher, U. and Siegenthaler, U. (1976) Palynological and oxygen isotope investigations on Late-glacial cores from Swiss lakes. *Boreas*, 5, 109–117.

Endres, C. (1997) Warvenchronologie und radiokarbondatierungen an holozaenen und spaetglazialen sedimenten des meerfelder maares (unpublished PhD thesis). Universitaet Potsdam, Germany, p. 98.

Engels, S. and van Geel, B. (2012) The effects of changing solar activity on climate: contributions from palaeoclimatological studies. *Journal of Space Weather and Space Climate*, *2*, A09.

Engels, S., Brauer, A., Buddelmeijer, N., Martín-Puertas, C., Rach, O., Sachse, D., Van Geel, B. (2016) Subdecadal-scale vegetation responses to a previously unknown late-Allerød climate fluctuation and Younger Dryas cooling at Lake Meerfelder Maar (Germany). *Journal of Quaternary Science*, 31:7, 741-752.

Farcas, S., de Beaulieu, J.L., Reille, M., Coldea, G., Diaconeasa, B., Goeury, C., Goslar, T., Jull, T. (1999) First 14C dating of Late Glacial and Holocene pollen sequences from Romanian Carpathes, *Académie des sciences*, 322, 799-807.

Feurdean, A. and Bennike, O. L. E. (2004) Late Quaternary palaeoecological and palaeoclimatological reconstruction in the Gutaiului Mountains, northwest Romania. *Journal of Quaternary Science*, 19:8, 809–827.

Feurdean, A., Klotz, S., Brewer, S., Mosbrugger, V., Tămaş, T., Wohlfarth, B. (2008a) Lateglacial climate development in NW Romania – Comparative quantitative pollen-based methods. *Palaeogeogrpahy, Palaeoclimatology, Palaeoecology*. 265, 121-133.

Feurdean, A., Klotz, S., Mosbrugger, V., Wohlfarth, B. (2008b) Pollen-based quantitative reconstructions of Holocene climate variability NW Romania. *Palaeogeogrpahy, Palaeoclimatology, Palaeoecology*. 260, 494-504.

Feurdean, A., Perşoiu, A., Tanţău, I., Stevens, T., Magyari, E.K., Onac, B.P., Marković, S., Andrič, M., Connor, S., Fărcaş, S., Gałka, M. (2014) Climate variability and associated vegetation response throughout Central and Eastern Europe (CEE) between 60 and 8 ka. *Quaternary Science Reviews*, 106, 206-224.

Feurdean, A., Wohlfarth, B., Björkman, L., Tantau, I., Bennike, O., Willis, K.J., Farcas, S., Robertsson, A.M. (2007) The influence of refugia population on Lateglacial and early Holocene vegetational change in Romania. *Review of Palaeobotany and Palynology*, 145, 305-320.

Fiłoc, M., Kupryjanowicz, M., Rzodkiewicz, M., Suchora, M. (2018) Response of terrestrial and lake environments in NE Poland to Preboreal cold oscillations (PBO). *Quaternary International*, 475, 101-117.

Finsinger, W., Belis, C., Blockley, S.P., Eicher, U., Leuenberger, M., Lotter, A.F., Ammann, B. (2008) Temporal patterns in lacustrine stable isotopes as evidence for climate change during the late glacial in the Southern European Alps. *Journal of Paleolimnology*, 40:3, 885-895.

Finsinger, W., Colombaroli, D., De Beaulieu, J.L., Valsecchi, V., Vannière, B., Vescovi, E., Chapron, E., Lotter, A.F., Magny, M., Tinner, W. (2010) Early to mid-Holocene climate

change at Lago dell'Accesa (central Italy): climate signal or anthropogenic bias? *Journal of Quaternary Science*, 25:8, 1239-1247.

Finsinger, W., Fevre, J., Orbán, I., Pál, I., Vincze, I., Hubay, K., Birks, H.H., Braun, M., Tóth, M., Magyari, E.K. (2018) Holocene fire-regime changes near the treeline in the Retezat Mts.(Southern Carpathians, Romania). *Quaternary International*, 477, 94-105.

Finsinger, W., Lane, C.S., van Den Brand, G.J., Wagner-Cremer, F., Blockley, S.P.E., Lotter, A.F. (2011) The lateglacial Quercus expansion in the southern European Alps: rapid vegetation response to a late Allerød climate warming?. *Journal of Quaternary Science*, 26:7, 694-702.

Finsinger, W. and Tinner, W. (2006) Holocene vegetation and land-use changes in response to climatic changes in the forelands of the southwestern Alps, Italy. *Journal of Quaternary Science*, 21:3, 243-258.

Firestone, R.B., West, A., Kennett, J.P., Becker, L., Bunch, T.E., Revay, Z.S., Schultz, P.H., Belgya, T., Kennett, D.J., Erlandson, J.M., Dickenson, O.J., Goodyear, A.C., Harris, R.S., Howard, G.A., Kloosterman, J.B., Lechler, P., Mayewski, P.A., Montgomery, J., Poreda, R., Darrah, T., Que Hee, S.S., Smitha, A.R., Stich, A., Topping, W., Wittke, J.H., Wolbach, W.S. (2007) Evidence for an extraterrestrial impact 12,900 years ago that contributed to the megafaunal extinctions and the Younger Dryas cooling. *PNAS*, 104, 16016-16021.

Fisher, R.V. (1964) Maximum size, median diameter, and sorting of tephra. *Journal of Geophysical Research*, 69:2, 341-355.

Fisher, T.G., Smith, D.G., Andrews, J.T. (2002) Preboreal oscillation caused by a glacial Lake Agassiz flood. *Quaternary Science Reviews*, 21, 873-878.

Fitzsimmons, K.E., Hambach, U., Veres, D., Iovita, R. (2013) The Campanian Ignimbrite eruption: new data on volcanic ash dispersal and its potential impact on human evolution. *PLoS One*, 8:6, 65839.

Florescu, G., Brown, K.J., Carter, V.A., Kuneš, P., Veski, S., Feurdean, A. (2019) Holocene rapid climate changes and ice-rafting debris events reflected in high-resolution European charcoal records. *Quaternary Science Reviews*, 222, 105877.

Forni, F., Lucchi, F., Peccerillo, A., Tranne, C.A., Rossi, P.L., Frezzotti, M.L. (2013) Stratigraphy and geological evolution of the Lipari volcanic complex (central Aeolian archipelago). *Geological Society, London, Memoirs*, 37:1, 213-279.

Friedrich, M., Kromer, B., Spurk, M., Hofmann, J., Kaiser, K.F. (1999) Paleoenvironment and radiocarbon calibration as derived from Lateglacial/Early Holocene tree-ring chronologies. *Quaternary International*, 61:1, 27-39.

Gauch, H.G., Whittaker, R.H., Wentworth, T.R. (1977) A comparative study of reciprocal averaging and other ordination techniques. *Journal of Ecology*, 65, 157-174.

Gervais, P. (1867–69) Zoologie et Paléontologie Générales: Nouvelles Recherches sur les Animaux Vértetebrés Vivants et Fossiles (two volumes). Bertrand, Paris, 263 pp.

Geyh, M., Schotterer, U., Grosjean, M. (1998) Temporal changes of the $^{14}C$ reservoir effect in lakes. *Radiocarbon*, 40, 921-931.

Ghenea, C. (1967) Prezenta unui tuf vulcanic in Villafranchianul din Depresiunea Valaha (in Romanian). *Studii Tehnice si Economice,* H3, 39-47.

Giescke, T. and Fontana, S.L. (2008) Revisiting pollen accumulation rates from Swedish lake sediments. *The Holocene*, 18, 293-305.

Gil, I.M., Keigwin, L.D., Abrantes, F. (2015) The deglaciation over Laurentian Fan: History of diatoms, IRD, ice and fresh water. *Quaternary Science Reviews*, 129, 57-67.

Gobet, E., Tinner, W., Bigler, C., Hochuli, P.A., Ammann, B. (2005) Early-Holocene afforestation processes in the lower subalpine belt of the Central Swiss Alps as inferred from macrofossil and pollen record. *The Holocene*, 15, 672–686.

Gobet, E., Tinner, W., Hubschmid, P., Jansen, I., Wehrli, M., Ammann, B.,Wick, L. (2000) Influence of human impact and bedrock differences on the vegetational history of the Insubrian Southern Alps. *Vegetation History and Archaeobotany*, 9:3, 175-187.

Godwin, H. (1962) Half-life of radiocarbon. *Nature*, 195, 984.

Gordon, A.D., Birks, H.J.B. (1972) Numerical methods in Quaternary palaeoecology I. Zonation of pollen diagrams. *New Phytologist*, 71:5, 961-979.

Goslar, T., Arnold, M., Bard, E., Kuc, T., Pazdur, M.F., Ralska-Jasiewiczowa, M., Tisnerat, N., Rozanski, K., Walanus, A., Wickik, B., Wieckowski, K. (1995) High concentrations of atmospheric $^{14}C$ during the Younger Dryas cold episode. *Nature*, 377, 414-417.

Goslar, T., Bałaga, K., Arnold, M., Tisnerat, N., Starnawska, E., Kuźniarski, M., Chróst, L., Walanus, A., Więckowski, K. (1999) Climate-related variations in the composition of the Late Glacial and early Holocene sediments of Lake Perespilno (eastern Poland). *Quaternary Science Reviews*, 18:7, 899-911.

Gray, L.J., Beer, J., Geller, M., Haigh, J.D., Lockwood, M., Matthes, K., Cubasch, U., Fleitmann, D., Harrison, G., Hood, L., Luterbacher, J. (2010) Solar influences on climate. *Reviews of Geophysics*, 48:4, 1-53.

Giaccio, B., Niespolo, E.M., Pereira, A., Nomade, S., Renne, P.R., Albert, P.G., Arienzo, I., Regattieri, E., Wagner, B., Zanchetta, G., Gaeta, M. (2017) First integrated tephrochronological record for the last~ 190 kyr from the Fucino Quaternary lacustrine succession, central Italy. *Quaternary Science Reviews*, 158, 211-234.

Gridean, R., Feurdean, A., Hurdu, B., Fărcas, S., Tanţău, I. (2015) Lateglacial/Holocene transition to mid-Holocene: Vegetation responses to climate changes in the Apuseni Mountains (NW Romania). *Quaternary International*, 388, 76-86.

Grime, J.P., Brown, V.K., Thompson, K., Masters, G.J., Hillier, S.H., Clarke, I.P., Askew, A.P., Corker, D., Kielty, J.P. (2000) The response of two contrasting limestone grasslands to simulated climate change. *Science*, 289:5480, 762-765.

Grimm, E.C. (1987) 'CONISS' a FORTRAN 77 program for stratigraphically constrained cluster analysis by the method of incremental sum of squares.' *Computers & Geosciences*, 13:1, 13-35.

Grimm, E.C. and Jacobson, G.L. (1992) Fossil-pollen evidence for abrupt climate changes during the past 18,000 years in eastern North America. *Climate Dynamics*, 6, 179-184.

Gudmundsdöttir, E.R., Eiríksson, J., Larsen, G. (2011) Identification and definition of primary and reworked tephra in Late Glacial and Holocene marine shelf sediments off North Iceland. *Journal of Quaternary Science*, 26:6, 589-602.

Gudmundsson, M.T., Thordarson, T., Höskuldsson, Larsen, G., Björnsson, H., Prata, F.J., Oddsson, B., Magnússin, E., Högnadottir, Petersen, G.N., Hayward, C.L., Stevenson, J.A., Jonsdottir, I. (2012) Ash generation and distribution from the April-May 2010 eruption of Eyjafjallajökull, Iceland. *Scientific Reports*, 2:572, 1-12.

Guilderson, T.P., Reimer, P.J., Brown, T.A. (2005) The boon and bane of radiocarbon dating. *Science,* 307:5708, 362-364.

Guiter, F., Andrieu-Ponel, V., Digerfeldt, G., Reille, M., de Beaulieu, J.L., Ponel, P. (2005) Vegetation history and lake-level changes from the Younger Dryas to the present in Eastern Pyrenees (France): pollen, plant macrofossils and lithostratigraphy from Lake Racou (2000 m asl). *Vegetation history and Archaeobotany*, 14:2, 99-118.

Haflidason, H., Regnéll, C., Pyne-O'Donnell, S., Svendsen, J.I. (2019) Extending the known distribution of the Vedde Ash into Siberia: occurrence in lake sediments from the Timan Ridge and the Ural Mountains, northern Russia. *Boreas*, 48:2, 444-451.

Haigh, J. D. (1996) The impact of solar variability on climate. *Science*, 272, 981–984.

Hajdas, I., Ivy, S.D., Beer, J., Bonani, G., Imboden, D., Lotted, A.F., Sturm, M., Suter, M. (1993) AMS radiocarbon dating and varve chronology of Lake Soppensee: 6000 to 12000 14 C years BP. *Climate dynamics*, 9:3, 107-116.

Hajdas, I., Zolitschka, B., Ivy-Ochs, S.D., Beer, J., Bonani, G., Leroy, S.A.G., Negendank, J.W., Ramrath, M., Suter, M. (1995) AMS radiocarbon dating of annually laminated sediments from lake Holzmaar, Germany. *Quaternary Science Reviews*, 14:2, 137-143.

Hald, M. and Hagen, S. (1998) Early preboreal cooling in the Nordic seas region triggered by meltwater. *Geology*, 26, 615–618.

Haliuc, A., Veres, D., Brauer, A., Hubay, K., Hutchinson, S.M., Begy, R., Braun, M. (2017) Palaeohydrological changes during the mid and late Holocene in the Carpathian area, central-eastern Europe. *Global and Planetary Change*, 152, 99-114.

Hall, A. (1996) *Igneous Petrology. 2nd ed*. London. Longman Group.

Hamann, Y., Wulf, S., Ersoy, O., Ehrmann, W., Aydar, E., Schmiedl, G. (2010) First evidence of a distal early Holocene ash layer in Eastern Mediterranean deep-sea sediments derived from the Anatolian volcanic province. *Quaternary Research*, 73, 497- 506.

Harangi, S., Molnár, M., Vinkler, A.P., Kiss, B., Jull, A.J.T., Leonard, A.G. (2010) Radiocarbon Dating the Last Volcanic Eruptions of Ciomadul Volcano, Southeast Carpathians, Eastern-Central Europe. *Radiocarbon*, 52, 1498-1507.

Harangi, S., Molnár, K., Schmitt, A.K., Dunkl, I., Seghedi, I., Novothny, Á., Molnár, M., Kiss, B., Ntaflos, T., Mason, P.R., Lukács, R. (2020) Fingerprinting the Late Pleistocene tephras of Ciomadul volcano, eastern–central Europe. *Journal of Quaternary Science*, in press.

Harning, D.J., Thordarson, T., Geirsdóttir, Á., Zalzal, K., Miller, G.H. (2018) Provenance, stratigraphy and chronology of Holocene tephra from Vestfirðir, Iceland. *Quaternary Geochronology*, 46, 59-76.

Harrison, S.P., Yu, G., Tarasov, P.E. (1996) Late Quaternary lake-level record from northern Eurasia. *Quaternary Research*, 45:2, 138-159.

Hastie, T., Stuetzle, W. (1989). Principal curves. *Journal of the American Statistical Association*, 84, 502–516

Heider, V. (2004) Late Pleistocene and Holocene paleolimnology and climate history in Southern Sweden reconstructed from chironomid, diatom and pollen records, *PhD thesis,* Tehnische Universität Carolo-Wilhemina zu Braunschweig, 147 p.

Heiri, O., Brooks, S.J., Renssen, H., Bedford, A., Hazekamp, M., Ilyashuk, B., Jeffers, E.S., Lang, B., Kirilova, E., Kuiper, S., Millet, L. (2014) Validation of climate model-inferred regional temperature change for late-glacial Europe. *Nature communications*, 5, 4914.

Heiri O, Millet L. (2005) Reconstruction of Late Glacial summer temperatures from chironomid assemblages in Lac Lautrey (Jura, France). *Journal of Quaternary Science*, 20: 33–44.

Heiri, O., Cremer, H., Engels, S., Hoek, W.Z., Peeters, W., Lotter, A.F. (2007a) Lateglacial summer temperatures in the Northwest European lowlands: a chironomid record from Hijkermeer, the Netherlands. *Quaternary Science Reviews*, 26:19-21, 2420-2437.

Heiri, O., Filippi, M.L., Lotter, A.F. (2007b) Lateglacial summer temperature in the Trentino area (Northern Italy) as reconstructed by fossil chironomid assemblages in Lago di Lavarone (1100 m asl). *Acta Geologica*, *82*, 299-308.

Heiri, O. and Lotter, A.F. (2005) Holocene and Lateglacial summer temperature reconstruction in the Swiss Alps based on fossil assemblages of aquatic organisms: a review. *Boreas*, 34:4, 506-516.

Heiri, O., Lotter, A.F., Hausmann, S., Kienast, F. (2003) A chironomid-based Holocene summer air temperature reconstruction from the Swiss Alps. *The Holocene*, 13:4, 477-484.

Hicks, S. (2006) When no pollen does not mean no trees. *Vegetation History and Archaeobotany*, 15, 253–261.

Hicks, S. and Hyvaèrinen, H. (1999) Pollen influx values measured in different sedimentary environments and their paleoecological implications. *Grana*, 38, 228-242.

Hoek W. (2001) Vegetation response to the 14.7 and 11.5 ka cal. BP climate transitions: is vegetation lagging climate? *Global and Planetary Change*, 30, 103–115.

Hoek, W.Z. and Bohncke, S.J.P. (2001) Oxygen-isotope wiggle matching as a tool for synchronising ice-core and terrestrial records over Termination 1. *Quaternary Science Reviews*, 20:11, 251-1264.

Horváth, E. (2001) Marker horizons in the loesses of the Carpathian Basin. *Quaternary International*, 76, 157-163.

Housley, R., MacLeod, A., Nalepka, D., Jurochnik, A., Masojc, M., Davies, L., Lincoln, P., Bronk Ramsey, C., Gamble, C.S., Lowe, J.J. (2013) Teprostratigraphy of a Lateglacial lake sediment sequence at Węgliny, southwest Poland. *Quaternary Science Reviews*, 77, 4-18.

Hubay, K., Molnár, M., Orbán, I., Braun, M., Bíró, T., Magyari, E. (2018) Age–depth relationship and accumulation rates in four sediment sequences from the Retezat Mts, South Carpathians (Romania). *Quaternary International*, 477, 7-18.

Hunt, J.B. (1994) The mobility and re-deposition of the Hekla 1991 Tephra, and the effects of wind and snow. *Münchener Geographische Abhandlungen. Band B*, 12, 157-175.

Hunt, J.B. and Hill, P.G. (1993) Tephra geochemistry: a discussion of some persistent analytical problems. *The Holocene*, 3:3, 271-278.

Huntley, B. (1991) How plants respond to climate change: migration rates, individualism and the consequences for plant communities. *Annals of Botany*, 67, 15-22.

Huntley, B. (1993) Rapid early Holocene migration and high abundance of hazel (Corylus avellana L.): alternative hypotheses. In: Chambers, F.M. (Ed.), Climate change and human impact on the landscape. Chapman & Hall, London.

Huntley, B. and Birks, H.J.B. (1983). *An atlas of past and present pollen maps for Europe: 0-13,000 years ago*, Cambridge: Cambridge University Press, 688 pp.

Husum, K. and Hald, M. (2002) Early Holocene cooling events in Malangenfjord and the adjoining shelf, north-east Norwegian Sea. *Polar Research*, 21, 267-274.

Ilyashuk, B., Gobet, E., Heiri, O., Lotter, A.F., van Leeuwen, J.F., van der Knaap, W.O., Ilyashuk, E., Oberli, F., Ammann, B. (2009) Lateglacial environmental and climatic changes at the Maloja Pass, Central Swiss Alps, as recorded by chironomids and pollen. *Quaternary Science Reviews*, 28:13-14, 1340-1353.

Isarin, R.F. and Bohncke, S.J. (1999) Mean July temperatures during the Younger Dryas in northwestern and central Europe as inferred from climate indicator plant species. *Quaternary Research*, 51:2, 158-173.

Isarin, R.F., Renssen, H., Vandenberghe, J. (1998) The impact of the North Atlantic Ocean on the Younger Dryas climate in northwestern and central Europe. *Journal of Quaternary Science: Published for the Quaternary Research Association*, 13:5, 447-453.

Ivy-Ochs, S., Kerschner, H., Reuther, A., Preusser, F., Heine, K., Maisch, M., Kubik, P.W., Schlüchter, C. (2008) Chronology of the last glacial cycle in the European Alps. *Journal of Quaternary Science*, 23:6-7, 559-573.

Jacobson, G.L. and Grimm, E.C. (1986) A numerical analysis of Holocene Forest and Prairie Vegetation in Central Minnesota. *Ecology*, 67:4, 958-966.

Jahns, S. (2007) Palynological investigations into the Late Pleistocene and Holocene history of vegetation and settlement at the Löddigsee, Mecklenburg, Germany. *Vegetation History and Archaeobotany*, 16:2-3, 157-169.

Jackson, S.T. (2012) Representation of flora and vegetation in Quaternary fossil assemblages: known and unknown knowns and unknowns. *Quaternary Science Reviews*, 49, 1-15.

Jancsik, P. (2001) A Retyezát-hegység (The Retezat Mountains). *Pallas–Akadémia Könyvkiadó*, Csíkszereda, 140.

Jensen, B.J.L., Pyne-O'Donnell, S., Plunkett, G., Froese, D.G., Hughes, P.D.M., Sigi, M., McConnell, J.R., Amesbury, M.J., Blackwell, P.G., van den Bogaard, C., Buck, C.E., Charman, D.J., Clague, J.J., Hall, v.A., Koch, J., Mackay, H., Mallon, G., McColl, L., Pilcher, J.R. (2014). Transatlantic distribution of the Alaskan White River Ash. *Geology*, 42:10, 875-878.

Joannin, S., Vannière, B., Galop, D., Peyron, O., Haas, J.N., Gilli, A., Chapron, E., Wirth, S.B., Anselmetti, F.S., Desmet, M., Magny, M. (2013) Climate and vegetation changes during the Lateglacial and early-middle Holocene at Lake Ledro (southern Alps, Italy). *Climate of the Past*, 9, 913-933.

Jóhannsdöttir, G. (2007) Mid Holocene to Late Glacial Tephrochronology in West Iceland as Revealed in Three Lacustrine Environments. *MSc Thesis in Geology*. University of Iceland.

Jones, G., Davies, S.M., Farr, G.J., Bevan, J. (2017) Identification of the Askja-S Tephra in a rare turlough record from Pant-y-Llyn, south Wales. *Proceedings of the Geologists' Association*, 128:4, 523-530.

Jones, G., Lane, C.S., Brauer, A., Davies, S.M., De Bruijn, R., Engels, S., Haliuc, A., Hoek, W.Z., Merkt, J., Sachse, D., Turner, F., (2018) The Lateglacial to early Holocene tephrochronological record from Lake Hämelsee, Germany: a key site within the European tephra framework. *Boreas*, 47:1, 28-40.

Jouzel, J., Stievenard, M., Johnsen, S.J., Landais, A., Masson-Delmotte, V., Sveinbjornsdottir, A., Vimeux, F., Von Grafenstein, U., White, J.W. (2007) The GRIP deuterium-excess record. *Quaternary Science Reviews*, 26:1-2, 1-17.

Jochum, K.P., Stoll, B., Herwig, K., Willbold, M., Hofmann, A.W., Amini, M., Aarburg, S., Abouchami, W., Hellebrand, E., Mocek, B., Raczek, I. (2006) MPI-DING reference glasses for in situ microanalysis: New reference values for element concentrations and isotope ratios. *Geochemistry, Geophysics, Geosystems*, 7:2, 1-44.

Juggins, S. (2017). Rioja: Analysis of Quaternary Science Data, R package Version 0.9-15.1. [Software] (http://cran.r-project.org/package=rioja).

Jurochnik, A. and Nalepka, D. (2013) Late Glacial and Holocene plant cover in Węgliny, Lubsza Plain, south-west Poland, based on pollen analysis. *Acta Palaeobotanica*, 53:2, 191-233.

Kahmen, A., Hoffmann, B., Schefuß, E., Arndt, S.K., Cernusak, L.A., West, J.B., Sachse, D. (2013). Leaf water deuterium enrichment shapes leaf wax n-alkane δD values of angiosperm plants II: Observational evidence and global implications. *Geochimica et Cosmochimica Acta*, 111, 50-63.

Kaiser, K., Lorenz, S., Germer, S., Juschus, O., Küster, M., Libra, J., Bens, O., Hüttl, R.F., (2012) Late Quaternary evolution of rivers, lakes and peatlands in northeast Germany reflecting past climatic and human impact–an overview. *E&G Quaternary Science Journal*, 61:2, 103-132.

Kalis, A.J., Merkt, J., Wunderlich, J. (2003) Environmental changes during the Holocene climatic optimum in central Europe d human impact and natural causes. *Quaternary Science Reviews*, 22, 33-79.

Karátson, D., Wulf, S., Veres, D., Magyari, E.K., Gertiser, R., timar-Gabor, A., Novothny, Á., Telbisz, T., Szalai, Z., Anechitei-Deacu, V., Appelt, O., Bormann, M., Jánosi, Cs., Hubay, K., Schäbitz. (2016) The latest explosive eruptions of Ciomadul (Csomád) volcano, East Carpathians – A tephrostratigraphic approach for the 51-29 ka BP time interval. *Journal of Volcanology and Geothermal Research*, 319, 29-51.

Karkanas, P., White, D., Lane, C.S., Stringer, C., Davies, W., Cullen, V.L., Smith, V.C., Ntinou, M., Tsartsidou, G., Kyparissi-Apostolika, N. (2015) Tephra correlations and climatic events between the MIS6/5 transition and the beginning of MIS3 in Theopetra Cave, central Greece. *Quaternary Science Reviews*, 118, 170-181.

Karpuz, N.K. and Jansen, E. (1992) A high-resolution diatom record of the last deglaciation from the SE Norwegian Sea: Documentation of rapid climatic changes. *Paleoceanography*, 7:4, 499-520.

Kearney, R., Albert, P.G., Staff, R.A., Pál, I., Veres, D., Magyari, E., Ramsey, C.B. (2018) Ultra-distal fine ash occurrences of the Icelandic Askja-S Plinian eruption deposits in Southern Carpathian lakes: new age constraints on a continental scale tephrostratigraphic marker. *Quaternary Science Reviews*, 188, 174–182.

Kelly, T.J., Hardiman, M., Lovelady, M., Lowe, J.J., Matthews, I.P., Blockley, S.P.E. (2016) Scottish early Holocene vegetation dynamics based on pollen and tephra re- cords from Inverlair and Loch Etteridge, Inverness-shire. *Proceedings of the Geologists' Association*, 128, 125-135.

Kletetschka, G., Vondrák, D., Hruba, J., van der Knaap, W.O., van Leeuwen, J.F.N., Heurich, M. (2019) Laacher See tephra discovered in the Bohemian Forest, Germany, east of the eruption. *Quaternary geochronology*, 51, 130-139.

Kobashi, T., Severinghaus, J.P., Barnola, J.M. (2008) 4±1.5 ºC abrupt warming 11,270 yr ago identified from trapped air in Greenland ice. *Earth and Planetary Science Letters*, 268:3-4, 397-407.

Kołaczek, P. (2010). The development of Late Glacial and Holocene vegetation and human impact near Grodzisko Nowe in the Lower San Valley (Sandomierz Basin, Poland SE). *Acta Palaeobotanica*, 50:2, 101-117.

Kołaczek, P., Kupryjanowicz, M., Karpińska-Kołaczek, M., Szal, M., Winter, H., Danel, W., Pochocka-Szwarc, K. and Stachowicz-Rybka, R. (2013) The Late Glacial and Holocene development of vegetation in the area of a fossil lake in the Skaliska Basin (north-eastern Poland) inferred from pollen analysis and radiocarbon dating. *Acta Palaeobotanica*, 53:1, 23-52.

Koponai, J., Magyari, E.K., Buczkó, Iepure, S., Namiotko, T., Czakó, D., Kövér, C., Braun, M. (2011) Cladocera response to Late Glacial to Early Holocene climate change in a South Carpathian mountain lake. *Hydrobiologia*, 676, 223-235.

Koren, J.H., Svendsen, J.I., Mangerud, J., Furnes, H. (2008) The Dimna Ash e a 12.8 $^{14}$C ka-old volcanic ash in Western Norway. *Quaternary Science Reviews*, 27:1, 85-94.

Kulesza, P., Suchora, M., Pidek, I.A., Alexandrowicz, W.P. (2011) Chronology and directions of Late Glacial paleoenvironmental changes: A multi-proxy study on sediments of Lake Słone (SE Poland). *Quaternary International*, 238:1-2, 89-106.

Kulesza, P., Suchora, M., Pidek, I.A., Dobrowolski, R., Alexandrowicz, W.P. (2012) The Holocene palaeoenvironmental changes reflected in the multi-proxy studies of Lake Słone sediments (SE Poland). *Palaeogeography, Palaeoclimatology, Palaeoecology*, 363, 79-98.

Kwiecien, O., Arz, H.W., Lamy, F., Wulf, S., Bahr, A., Rohl, U., Haug, G.H. (2008) Estimated reservoir age of the black sea since the last glacial. *Radiocarbon*, 50, 99-118.

Kyrikou, S., Kouli, K., Triantaphyllou, M.V., Dimiza, M.D., Gogou, A., Panagiotopoulos, I.P., Anagnostou, C., Karageorgis, A.P. (2019) Late Glacial and Holocene vegetation patterns of Attica: A high-resolution record from Elefsis Bay, southern Greece. *Quaternary International*, In press.

Lane, C. S., Blockley, S. P. E., Ramsey, C. B., Lotter, A. F. (2011a) Tephrochronology and absolute centennial scale synchronisation of European and Greenland records for the last glacial to interglacial transition: A case study of Soppensee and NGRIP. *Quaternary International*, 246:1–2, 145–156.

Lane, C.S., Andric, M., Cullen, V.L., Blockley, S.P.E. (2011b) The occurrence of distal Icelandic and Italian tephra in the Lateglacial of Lake Bled, Slovenia. *Quaternary Science Reviews*, 30, 1013-1018.

Lane, C.S., Blockely, S.P.E., Mangerud, J., Smith, V.C., Lohne, Ø.S., Tomlindon, E.L., Matthews, I.P., Lotter, A.F. (2012b) Was the 12.1ka Iceland vedde ash one of a kind? *Quaternary Science Reviews*, 33, 87-99.

Lane, C.S., Blockley, S.P.E., Lotter, A.F., Finsinger, W., Filippi, M.L. and Matthews, I.P. (2012c) A regional tephrostratigraphic framework for central and southern European climate

archives during the Last Glacial to Interglacial transition: comparisons north and south of the Alps. *Quaternary Science Reviews*, *36*, pp.50-58.

Lane, C.S., Brauer, A., Blockley, S.P.E., Dulski, P. (2013) Volcanic ash reveals time-transgressive abrupt climate change during the Younger Dryas. Geology 41, 1251-1254.

Lane, C.S., Brauer, A., Martín-Puertas, C., Blockley, S.P., Smith, V.C., Tomlinson, E.L. (2015) The Late Quaternary tephrostratigraphy of annually laminated sediments from Meerfelder Maar, Germany. *Quaternary Science Reviews*, 122, 192-206.

Lane, C.S., Cullen, V.L., White, D., Bramham-Law, C.W.F., Smith, V.C. (2014) Cryptotephra as a dating and correlation tool in archaeology. *Journal of Archaeological Sciences*, 42, 42-50.

Lane, C.S., De Klerk, P., Cullen, V.L. (2012a) A tephrochronology for the Lateglacial palynological record of the Endinger Bruch (Vorpommern, north-east Germany). *Journal of Quaternary Science*, 27, 141-149.

Lane, C.S., Engels, S., Staff, R.A., McGuire, A., Kearney, R. Does the Gerzensee Oscilaltion correlate to Greenland Interstadial 1b? A cautionary note on tuning chronologies for short lived climate oscillations. *In preparation*

Lane, C.S., Lowe, D.J., Blockley, S.P.E., Suzuki, T., Smith, V.C. (2017) Advancing tephrochronology as a global dating tool: Applications in volcanology, archaeology, and palaeoclimatic research. *Quaternary Geochronology*, 40, 1-7.

Lang, B., Bedford, A., Brooks, S.J., Jones, R.T., Richardson, N., Birks, H.J.B., Marshall, J.D., (2010) Early-Holocene temperature variability inferred from chironomid assemblages at Hawes Water, northwest England. *The Holocene*, 20:6, 943-954.
Larocque-Tobler, I., Heiri, O., Wehrli, M. (2010) Late Glacial and Holocene temperature changes at Egelsee, Switzerland, reconstructed using subfossil chironomids. *Journal of Paleolimnology*, 43:4, 649-666.

Larocque, I., Finsinger, W. (2008) Late-glacial chironomid-based temperature reconstructions for Lago Piccolo di Avigliana in the southwestern Alps (Italy). *Palaeogeography, Palaeoclimatology, Palaeoecology*, 257:1-2, 207-223.

Larocque, I., Hall, R.I., Grahn, E. (2001) Chironomids as indicators of climate change: a 100-lake training set from a subarctic region of northern Sweden (Lapland). *Journal of Paleolimnology*, 26:3, 307-322.

Larsen, J.J. and Noe-Nygaard, N. (2014) Lateglacial and early Holocene tephrostratigraphy and sedimentology of the Store Slotseng basin, SW Denmark: a multi-proxy study. *Boreas*, 43, 349–361.

Lascu, I., Wohlfarth, B., Onac, B. P., Björck, S., Kromer, B. (2015) A Late Glacial paleolake record from an up-dammed river valley in Transylvania, Romania. *Quaternary International*, 388, 87–96.

Latałowa, M. and Borówka, R.K. (2006) The Allerød/Younger Dryas transition in Wolin Island, northwest Poland, as reflected by pollen, macrofossils, and chemical content of an

organic layer separating two aeolian series. *Vegetation History and Archaeobotany*, 15:4, 321-331.

Lauterbach, S., Brauer, A., Andersen, N., Danielopol, D.L., Dulski, P., Huels, M., Milecka, K., Namiotko, T., Plessen, B., Grafenstein, U.V., Declakes Participants (2011) Multi-proxy evidence for early to mid-Holocene environmental and climatic changes in northeastern Poland. *Boreas*, 40:1, 57-72.

Lawson, I., Frogley, M., Bryant, C., Preece, R., Tzedakis, P. (2004) The Lateglacial and Holocene environmental history of the Ioannina basin, north-west Greece. *Quaternary Science Reviews*, 23:14-15, 1599-1625.

Le Bas, M.J., Le Maitre, R.W., Streckeisen, A., Zanettin, B. (1986) A chemical classification of volcanic rocks based on the total alkali-silica diagram. *Journal of Petrology*, 27, 745–750.

Lee, S., Ramsey, C.B., Hardiman, M. (2013) Modelling the age of the Cape Riva (Y-2) tephra. *Radiocarbon*, 55(2–3), 741-747.

Legendre, P. and Birks, H.J.B. (2012) From Classical to Canonical Ordination *In*: Birks, H.J.B., Lotter, A.F., Juggins, S., and Smol, J.P (Eds.). *Tracking Environmental Change Using Lake Sediments. Volume 5: Data Handling and Numerical Techniques.* Dordrecht, The Netherlands: Kluwer Academic Publishers, pp. 201-248.

Lemdahl, G. (2000) Late-glacial and early-Holocene Coleoptera assemblages as indicators of local environment and climate at Kråkenes Lake, western Norway. *Journal of Paleolimnology*, 23:1, 57-66.

Leng, M.J. and Marshall, M.D. (2004) Palaeoclimate interpretation of stable isotope data from lake sediment archives. *Quaternary Science Reviews*, 23:7-8, 811-831.

Leunda, M., González-Sampériz, P., Gil-Romera, G., Aranbarri, J., Moreno, A., Oliva-Urcia, B., Sevilla-Callejo, M., Valero-Garcés, B. (2017) The Late-Glacial and Holocene Marboré Lake sequence (2612 m asl, Central Pyrenees, Spain): testing high altitude sites sensitivity to millennial scale vegetation and climate variability. *Global and planetary change*, 157, 214-231.

Li, C., Battisti, D.S., Schrag, D.P., Tziperman, E. (2005) Abrupt climate shifts in Greenland due to displacements of the sea ice edge. *Geophysical Research Letters*, 32:19, 1-4.

Libby, W.F., Anderson, E.C., Arnold, J.R. (1949) Age determination by radiocarbon content: world-wide assay of natural radiocarbon. *Science,* 109, 227-228.

Lilja, C., Lind, E.M., Moren, B., Wastegård, S. (2013) A Lateglacialeearly Holocene tephrochronology for SW Sweden. *Boreas*, 42, 544-554.

Lind, E.M., Lilja, C., Wastegård, S., Pearce, N.J. (2016) Revisiting the Borrobol tephra. *Boreas*, 45, 629–643.

Lind, E.M. and Wastegård, S. (2011) Tephra horizons contemporary with short early Holocene climate fluctuations: new results from the Faroe Islands. *Quaternary International*, 246:1-2, 157-167.

Lind, E.M., Wastegård, S., Larsen, J.J. (2013) A late Younger Dryas-Early Holocene tephrostratigraphy for Fosen, Central Norway. *Journal of Quaternary Science*, 28:8, 803-811.

Litt, T. and Stebich, M. (1999) Bio-and chronostratigraphy of the lateglacial in the Eifel region, Germany. *Quaternary International*, 61:1, 5-16.

Lohne, O. y. S., Mangerud, J., Birks, H.H. (2013) Precise $^{14}C$ ages of the Vedde and Saksunarvatn ashes and the Younger Dryas boundaries from western Norway and their comparison with the Greenland Ice Core (GICC05) chronology. *Journal of Quaternary Science*, 28:5, 490-500.

Lohne, Ø.S., Bondevik, S., Mangerud, J., Svendsen, J.I. (2007) Sea-level fluctuations imply that the Younger Dryas ice-sheet expansion in western Norway commenced during the Allerød. *Quaternary Science Reviews*, 26:17-18, 2128-2151.

Longman, J., Ersek, V., Veres, D., Salzmann, U. (2017a) Detrital events and hydroclimate variability in the Romanian Carpathians during the mid-to-late Holocene. *Quaternary Science Reviews*, 167, 78-95.

Longman, J., Veres, D., Ersek, V., Salzmann, U., Hubay, K., Bormann, M., Wennrich, V., Schäbitz, F. (2017b) Periodic input of dust over the Eastern Carpathians during the Holocene linked with Saharan desertification and human impact. *Climate of the Past*, 13, 897-917.

Lotter, A. (1988) Paläoökologische und paläolimnologische Studie des Rotsees bei Luzern. Pollen-, grossrest-, diatomeen- und sedimentanalytische Untersuchungen. *Dissertationes Botanicae*, *124*, 187.

Lotter, A.F. (1999) Late-glacial and Holocene vegetation history and dynamics as shown by pollen and plant macrofossil analyses in annually laminated sediments from Soppensee, central Switzerland. *Vegetation History and Archaeobotany*, 8:3, 165-184.

Lotter, A.F. (1989) Evidence of annual layering in Holocene sediments of Soppensee, Switzerland. *Aquatic Sciences*, 51, 19-30.

Lotter, A.F. (2001) The palaeolimnology of Soppensee (Central Switzerlabnd), as evidenced by diatom, pollen, and fossil-pigment analyses. *Journal of Paleolimnology*, 25:1, 65-79.

Lotter, A.F., Eicher, U., Siegenthaler, U., Birks, H.J.B. (1992a) Late-Glacial climatic oscillations as recorded in Swiss lake sediments. *Journal of Quaternary Science*, 7:3, 187-204.

Lotter, A.F., Ammann, B., Sturm, M. (1992b) Rates of change and chronological problems during the late-glacial period. *Climate Dynamics*, 6, 233-239.

Lotter, A.F., Birks, H.J.B., Eicher, U., Hofmann, W., Schwander, J., Wick, L. (2000) Younger Dryas and Allerød summer temperatures at Gerzensee (Switzerland) inferred from fossil pollen

and cladoceran assemblages. *Palaeogeography, Palaeoclimatology, Palaeoecology*, 159:3-4, 349-361.

Lotter, A.F., Heiri, O., Brooks, S.J., van Leeuwen, J.F., Eicher, U., Ammann, B. (2012) Rapid summer temperature changes during Termination 1a: high-resolution multi-proxy climate reconstructions from Gerzensee (Switzerland). *Quaternary Science Reviews*, 36, 103-113.

Lowe, D.J. (2011) Tephrochronology and its application: A review. *Quaternary Geochronology*, 6, 107-153.

Lowe, J. and Turney, C. S. M. (1997) Vedde Ash discovered in a small lake basin on the Scottish mainland Vedde Ash layer discovered in a small lake basin on the Scottish mainland. *Journal of the Geological Society*, 154, 605-612.

Lowe, J. J., Ramsey, C. B., Housley, R. A., Lane, C. S. and Tomlinson, E. L. (2015) The RESET project: constructing a European tephra lattice for refined synchronisation of environmental and archaeological events during the last c. 100 ka. *Quaternary Science Reviews*, 118, 1–17.

Lowe, J. J., Rasmussen, S. O., Bjork, S., Hoek, W. Z., Steffensen, J. P., Walker, M. J. C., Yu, Z. C., INTIMATE Members (2008) Synchronisation of palaeoenvironmental events in the North Atlantic region during the Last Termination: a revised protocol recommended by the INTIMATE group. *Quaternary Science Reviews*, 27, 6–17.

Lowe, J. J., Walker, M. J. C., Scott, E. M., Harkness, D. D., Bryant, C. L., Davies, S. M. (2004) A coherent high-precision radiocarbon chronology for the Late-glacial sequence at Sluggan Bog, Co. Antrim, Northern Ireland. *Journal of Paleolimnology*, 19:2, 147–158.

Lowe, J., Matthews, I., Mayfield, R., Lincoln, P., Palmer, A., Staff, R., Timms, R. (2019) On the timing of retreat of the Loch Lomond ('Younger Dryas') Readvance icefield in the SW Scottish Highlands and its wider significance. *Quaternary Science Reviews*, 219, 171-186.

Lowe, J.J. (2001). Abrupt climatic changes in Europe during the last glacial–interglacial transition: the potential for testing hypotheses on the synchroneity of climatic events using tephrochronology. *Global and Planetary Change*, 30:1, 73-84.

Lowe, J.J. and Walker, M.J.C. (1986) Lateglacial and early Flandrian environmental history of the Isle of Mull, Inner Hebrides, Scotland. *Earth and Environmental Science Transactions of The Royal Society of Edinburgh*, 77:1, 1-20.

Lowe, J.J. andWalker, M.J.C. (2014). *Reconstructing Quaternary Environments, Third Edition.* Abingdon: Routledge, 538 pp.

Lowe, J.J., Blockley, S.P.E., Trincardi, F., Asioli, A., Cattaneo, A., Matthews, I.P., Pollard, A.M., Wulf, S. (2007) Age modelling of late Quaternary marine sequences in the Adriatic: towards improved precision and accuracy using volcanic event stratigraphy. *Continental Shelf Research,* 27, 560-582.

Lowe, J.J., Palmer, A.P., Carter-Champion, A., MacLeod, A.M., Ramirez-Rojas, I., Timms, R.G.O. (2017) Stratigraphy of a Lateglacial lake basin sediment sequence at Turret Bank,

Upper Glen Roy, Lochaber: implications for the age of the Turret Fan. *Proceedings of Geologist' Association*, 128, 110–124.

Lowe, J.J., Rasmussen, S.O., Björck, S., Hoek, W.Z., Steffensen, J.P., Walker, M.J., Yu, Z.C., Intimate Group (2008) Synchronisation of palaeoenvironmental events in the North Atlantic region during the Last Termination: a revised protocol recommended by the INTIMATE group. *Quaternary Science Reviews*, 27:1-2, 6-17.

Lowe, J.J. and Walker, M.J. (2000) Radiocarbon Dating the Last Glacial-Interglacial Transition (ca. 14–9 $^{14}$C Ka BP) in Terrestrial and Marine Records: The Need for New Quality Assurance Protocols. *Radiocarbon*, 42, 53-68.

Lowe, D.J., Pearce, N.J., Jorgensen, M.A., Kuehn, S.C., Tryon, C.A., Hayward, C.L. (2017) Correlating tephras and cryptotephras using glass compositional analyses and numerical and statistical methods: Review and evaluation. *Quaternary Science Reviews*, 175, 1-44.

Lucchi, F., Tranne, C.A., De Astis, G., Keller, J., Losito, R., Morche, W. (2008) Stratigraphy and significance of Brown Tuffs on the Aeolian Islands (southern Italy). *Journal of Volcanology and Geothermal Research*, 177, 49–70.

Lucchi, F., Tranne, C.A., Forni, F., Rossi, P.L. (2013) Geological map of the island of Lipari, scale 1:10 000 (Aeolian archipelago). *In*: Lucchi, F., Peccerillo, A., Keller, J., Tranne, C.A., Rossi, P.L. (Eds.), The Aeolian Islands Volcanoes. Geological Society, London, Memoirs 37.

Lundqvist, J. (1986) Late Weichselian glaciation and deglaciation in Scandinavia. *Quaternary Science Reviews*, 5, 269-292.

MacArthur, R.H. (1957) On the relative abundance of bird species. *Proceedings of the National Academy of Science,* 43, 293-295.

Macdonald, R. (1974) Nomenclature and petrochemistry of the peralkaline over-saturated extrusive rocks. *Bulletin of Volcanology*, 38, 498-516.

Macleod, A. and Davies, S. M. (2016) Caution in cryptotephra correlation: resolving Lateglacial chemical controversies at Sluggan Bog. *Journal of Quaternary Science*, 31, 406–415.

MacLeod, A., Matthews, I.P., Lowe, J.J., Palmer, A.P., Albert, P.G. (2015) A second tephra isochron for the Younger Dryas period in northern Europe: the Abernethy Tephra. *Quaternary Geochronology*, 28, 1-11.

Magny, M., de Beaulieu, J.-L., Drescher-Schneider, R., Vanniere, B., Walter- Simonnet, A.V., Millet, L., Bossuet, G., Peyron, O. (2006) Climatic oscillations in central Italy during the Last Glacial-Holocene transition: the record from Lake Accesa. *Journal of Quaternary Science*, 21:4, 311-320.

Magny, M., Leroux, A., Bichet, V., Gauthier, E., Richard, H., Walter-Simonnet, A.V. (2013) Climate, vegetation and land use as drivers of Holocene sedimentation: a case study from Lake Saint-Point (Jura Mountains, eastern France). *The Holocene*, 23:1, 137-147.

Magny, M., Vannière, B., Calo, C., Millet, L., Leroux, A., Peyron, O., Zanchetta, G., La Mantia, T., Tinner, W. (2011) Holocene hydrological changes in south-western Mediterranean as recorded by lake-level fluctuations at Lago Preola, a coastal lake in southern Sicily, Italy. *Quaternary Science Reviews*, 30:19-20, 2459-2475.

Magny, M., Vannière, B., De Beaulieu, J.L., Bégeot, C., Heiri, O., Millet, L., Peyron, O., Walter-Simonnet, A.V. (2007) Early-Holocene climatic oscillations recorded by lake-level fluctuations in west-central Europe and in central Italy. *Quaternary Science Reviews*, 26:15-16, 1951-1964.

Magyari, E.K., Braun, M., Buczko, K., Kern, Z., Laszlo, P., Hubay, K. (2009a) Radiocarbon chronology of glacial lake sediments in the Retezat Mts (South Carpathians, Romania): a window to Late Glacial and Holocene climatic and palaeoenvironmental changes. *Central European Geology*, 52, 225-248.

Magyari, E.K., Buczko , K., Jakab, G., Braun, M., Pa l, Z., Karatson, D., Papp, P. (2009b) Palaeolimnology of the last crater lake in the Eastern Carpathian Mountains: a multiproxy study of Holocene hydrological changes. *Hydrobiologia*, 631, 29-63.

Magyari, E.K., Demény, A., Buczkó, K., Kern, Z., Vennemann, T., Fórizs, I., Vincze, I., Braun, M., Kováccs, J.I., Udvardi, B., Veres, D. (2013) A 13,600-year diatom oxygen isotope record from the South Carpathians (Romania): Reflection of winter conditions and possible links with North Atlantic circulation changes. *Quaternary International*, 293, 136-149.

Magyari, E.K., Jakab, G., Ba lint, M., Kern, Z., Buczko , K., Braun, M. (2012) Rapid vegetation response to Lateglacial and early Holocene climatic fluctuation in the South Carpathian Mountains (Romania). *Quaternary Science Reviews*, 35, 116-130.

Mahood, G.A. and Hildreth, W. (1986) Geology of the peralkaline volcano at Pantelleria, Strait of Sicily. *Bulletin of Volcanology*, 48:2-3, 143-172.

Mangerud, J., Aarseth, I., Hughes, A.L., Lohne, Ø.S., Skår, K., Sønstegaard, E., Svendsen, J.I. (2016) A major re-growth of the Scandinavian Ice Sheet in western Norway during Allerød-Younger Dryas. *Quaternary Science Reviews*, 132, 175-205.

Mangerud, J., Andersen, S. T., Berglund, B. E., Donner, J. J. (1974) Quaternary stratigraphy of Norden, a proposal for terminology and classification. *Boreas*, 3:3, 109-126.

Mangerud, J., Goehring, B.M., Lohne, Ø.S., Svendsen, J.I., Gyllencreutz, R., (2013) Collapse of marine-based outlet glaciers from the Scandinavian ice sheet. *Quaternary Science Reviews*, 67, 8-16.

Marchini, G., Zanchetta, G., Santacroce, R., Vigliotti, L., Capotondi, L., Sulpizio, R., (2014) Tephrostratigraphy of marine core AD91-17 (Adriatic sea) revised. *Alpine and Mediterranean Quaternary*, 27:2, 77-84.

Margari, V., Pyle, D.M., Bryant, C., Gibbard, P.L. (2007) Mediterranean tephra stratigraphy revisited: results from a long terrestrial sequence on Lesvos Island, Greece. *Journal of Volcanology and Geothermal Research*, 163:1-4, 34-54.

Marshall, J.D., Jones, R.T., Crowley, S.F., Oldfield, F., Nash, S., Bedford, A. (2002) A high resolution late-glacial isotopic record from Hawes Water, northwest England: Climatic oscillations: Calibration and comparison of palaeotemperature proxies. *Palaeogeography, Palaeoclimatology, Palaeoecology*, 185:1-2, 25-40.

Martin-Puertas, C., Matthes, K., Brauer, A., Muscheler, R., Hansen, F., Petrick, C., Aldahan, A., Possnert, G., Van Geel, B. (2012) Regional atmospheric circulation shifts induced by a grand solar minimum. *Nature Geoscience*, 5:6, 397.

Martin-Puertas, C., Tjallingii, R., Bloemsma, M., Brauer, A. (2017) Varved sediment responses to early Holocene climate and environmental changes in Lake Meerfelder Maar (Germany) obtained from multivariate analyses of micro X-ray fluorescence core scanning data. *Journal of Quaternary Science*, 32:3, 427-436.

Martinson, D.G., Pisias, N.G., Hays, J.D., Imbrie, J., Moore, T.C., Shackleton, N.J. (1987) Age dating and the orbital theory of the ice ages: Development of a high-resolution 0 to 300,000-year chronostratigraphy 1. *Quaternary research*, 27:1, 1-29.

Mârza, I. (1991) The Volcanic Tuffs from the Transylvanian Basin, Romania. *University of Cluj-Napoca*, Special Issue 3, 550.

Masson-Delmotte, V., Jouzel, J., Landais, A., Stievenard, M., Johnsen, S.J., White, J.W.C., Werner, M., Sveinbjornsdottir, A., Fuhrer, K. (2005) GRIP deuterium excess reveals rapid and orbital-scale changes in Greenland moisture origin. *Science*, 309:5731, 118-121.

Mastrolorenzo, G., Pappalardo, L., Troise, C., Panizza, A., De Natale, G. (2008) Probabilistic tephra hazard maps for the Neapolitan area: quantitative volcanological study of Campi Flegrei eruptions. *Journal of Geophysical Research: Solid Earth*, 113(B7).

Matthews, I.P., Birks, H.H., Bourne, A.J., Brooks, S.J., Lowe, J.J., Macleod, A., Pyne-O'Donnell, S.D.F. (2011) New age estimates and climatostratigraphic correlations for the Borrobol and Penifiler Tephras: evidence from Abernethy Forest Scot- land. *Journal of Quaternary Science*, 26:3, 247-252.

Mauri, A. and Caudullo, G. (2016) Alnus viridis in Europe: Distribution, habitat, usage and threats. *In*: San-Miguel-Ayanz, J., de Rigo, D., Caudullo, G., Houston Durrant, T., Mauri, A. (Eds.), *European Atlas of Forest Tree Species*. Publication Office EU, Luxembourg, 68.

McLean, D., Albert, P.G., Nakagawa, T., Staff, R.A., Suzuki, T., Smith, V.C. (2016) Identification of the Changbaishan 'Millennium'(B-Tm) eruption deposit in the Lake Suigetsu (SG06) sedimentary archive, Japan: synchronisation of hemispheric-wide palaeoclimate archives. *Quaternary Science Reviews*, 150, 301-307.

McLean, D., Albert, P.G., Nakagawa, T., Suzuki, T., Staff, R.A., Yamada, K., Kitaba, I., Haraguchi, T., Kitagawa, J., Members, S.P., Smith, V.C. (2018) Integrating the Holocene tephrostratigraphy for East Asia using a high-resolution cryptotephra study from Lake Suigetsu (SG14 core), central Japan. *Quaternary Science Reviews*, 183, 36-58.

McManus, J.F., Francois, R., Gherardi, J.M., Keigwin, L.D., Brown-Leger, S. (2004) Collapse and rapid resumption of Atlantic meridional circulation linked to deglacial climate changes. *Nature*, 428, 834–837.

Meehl, G. A., W. M. Washington, T. M. L. Wigley, J. M. Arblaster, A. Dai (2003) Solar and greenhouse gas forcing and climate response in the 20th century. *Journal of Climatology*, 16, 426–444.

Merkt, J. and Müller, H. (1999) Varve chronology and palynology of the Lateglacial in Northwest Germany from lacustrine sediments of Hämelsee in Lower Saxony. *Quaternary International*, 61:1, 41-59.

Mîndrescu, M. and Veres, D. (2016) Recent contributions and prospects for climate variability studies in Central and Eastern Europe. *Quaternary International*, 415, 1-5.

Moles, J.D., McGarvie, D., Stevenson, J.A., Sherlock, S.C., Abbott, P.M., Jenner, F.E., Halton, A.M. (2019) Widespread tephra dispersal and ignimbrite emplacement from a subglacial volcano (Torfajökull, Iceland). *Geology*, 47:6, 577-580.

Moore, P.D., Webb, J.A., Collinson, M.E. (1991). *Pollen Analysis.* Oxford: Blackwell Scientific Publications, 216 pp.

Moreno, A., Svensson, A., Brooks, S.J., Connor, S., Engels, S., Fletcher, W., Genty, D., Heiri, O., Labuhn, I., Perşoiu, A., Peyron, O. (2014) A compilation of Western European terrestrial records 60–8 ka BP: towards an understanding of latitudinal climatic gradients. *Quaternary Science Reviews*, 106, 167-185.

Moriwaki, H., Nakamura, N., Nagasako, T., Lowe, D.J., Sangawa, T. (2016) The role of tephras in developing a high-precision chronostratigraphy for palaeoenviron- mental reconstruction and archaeology in southern Kyushu, Japan, since 30,000 cal. BP: an integration. *Quaternary International*, 397, 79-92.

Mortensen, M.F., Birks, H.H., Christensen, C., Holm, J., Noe-Nygaard, N., Odgaard, B.V., Olsen, J., Rasmussen, K.L. (2011) Lateglacial vegetation development in Denmark–new evidence based on macrofossils and pollen from Slotseng, a small-scale site in southern Jutland. *Quaternary Science Reviews*, 30:19-20, 2534-2550.

Mortensen, M.F., Henriksen, P.S., Christensen, C., Petersen, P.V.,Olsen, J. (2014) Vegetation development in south-east Denmark during the Weichselian Late Glacial: palaeoenvironmental studies close to the Palaeolithic site of Hasselø. *Danish Journal of Archaeology*, 3:1, 33-51.

Müller, J. and Stein, R. (2014) High-resolution record of late glacial and deglacial sea ice changes in Fram Strait corroborates ice–ocean interactions during abrupt climate shifts. *Earth and Planetary Science Letters*, 403, 446-455.

Murton, J.B., Bateman, M.D., Dallimore, S.R., Teller, J.T., Yang, Z. (2010) Identification of Younger Dryas outburst flood path from Lake Agassiz to the Arctic ocean. *Nature*, 464, 740-743.

Muscheler, R., Adolphi, F., Knudsen, M.F. (2014) Assessing the differences between the IntCal and Greenland ice-core time scales for the last 14,000 years via the common cosmogenic radionuclide variations. *Quaternary Science Reviews*, 106, 81-87.

Muscheler, R., Beer, J., Wagner, G., Finkel, R.C. (2000) Changes in deep-water formation during the Younger Dryas event inferred from $^{10}$Be and $^{14}$C records. *Nature*, 408, 567-570.

Muschitiello, F., Pausata, F.S., Watson, J.E., Smittenberg, R.H., Salih, A.A., Brooks, S.J., Whitehouse, N.J., Karlatou-Charalampopoulou, A., Wohlfarth, B., (2015) Fennoscandian freshwater control on Greenland hydroclimate shifts at the onset of the Younger Dryas. *Nature communications*, *6*, 8939.

Muschitiello, F. and Wohlfarth, B. (2015) Time-transgressive environmental shifts across Northern Europe at the onset of the Younger Dryas. *Quaternary Science Reviews*, 109, 49-56.

Narcisi, B. (2002) Tephrostratigraphy of the Late Quaternary lacustrine sediments of Lago di Pergusa (central Sicily). *Bollettino della Società Geologica Italiana*, 12:2, 211–219.

Naughton, F., Costas, S., Gomes, S.D., Desprat, S., Rodrigues, T., Goñi, M.S., Renssen, H., Trigo, R., Bronk-Ramsey, C., Oliveira, D., Salgueiro, E. (2019) Coupled ocean and atmospheric changes during Greenland stadial 1 in southwestern Europe. *Quaternary Science Reviews*, 212, 108-120.

Negri, A., Capotondi, L., Keller, J. (1999) Calcareous nannofossils, planktonic foraminifera and oxygen isotopes in the Late Quaternary Sapropels of the Ionian Sea. *Marine Geology*, 157, 89–103.

Nesje A and Dahl SO. (1993) Lateglacial and Holocene glacier fluctuations and climate variations in western Norway — a review. *Quaternary Science Reviews*, 12, 255–261.

Nesje, A., Dahl, S.O., Bakke, J. (2004) Were abrupt Lateglacial and early-Holocene climatic changes in northwest Europe linked to freshwater outbursts to the North Atlantic and Arctic Oceans? *The Holocene*, 14:2, 299-310.

Neugebauer, I., Wulf, S., Schwab, M.J., Serb, J., Plessen, B., Appelt, O., Brauer, A. (2017) Implications of S1 tephra findings in Dead Sea and Tayma palaeolake sediments for marine reservoir age estimation and palaeoclimate synchronisation. *Quaternary Science Reviews*, 170, 269-275.

Newhall, C.G. and Self, S. (1982) The volcanic explosivity index (VEI) an estimate of explosive magnitude for historical volcanism. *Journal of Geophysical Research*, 87, 1231-1238.

Nolan, S.R., Bloemendal, J., Boyle, J.F., Jones, R.T., Oldfield, F., Whitney, M. (1999) Mineral magnetic and geochemical records of late Glacial climatic change from two northwest European carbonate lakes. *Journal of Paleolimnology*, 22:1, 97-107.

Norðdahl, H. and Hjort, C. (1993) Lateglacial raised beaches and glacier recession in the PistilfjörÐur-Bakkafloi area, Northeast Iceland. *Jokull*, 43, 33-44.

Ntinou, M., Kyparissi-Apostolika, N. (2016) Local vegetation dynamics and human habitation from the last interglacial to the early Holocene at Theopetra cave, central Greece: the evidence from wood charcoal analysis. *Vegetation history and archaeobotany*, 25:2, 191-(206.

Obreht, I., Hambach, U., Veres, D., Zeeden, C., Bösken, J., Stevens, T., Markovic, S.B., Klasen, N., Brill, D., Burow, C., Lehmkuhl F. (2017) Shift of large-scale atmospheric systems over Europe during late MIS 3 and implications for Modern Human dispersal. *Scientific Reports*, 7:5848, 1-10.

Obreht, I., Zeeden, C., Hambach, U., Veres, D., Markovi c, S. b., Bösken, J., Svircev, Z., Bacevic, N., Gavrilov, M.B., Lehmkuhl, F. (2016) Tracing the influence of Medi- terranean climate on Southeastern Europe during the past 350,000 years. *Science Reports*, 6, 36334.

Odgaard, B. V. (1995) Fossil pollen as a record of past biodiversity. *Journal of Biogeography*, 26:1, 7–17.

Oksanen, J., Blanchet, F.G., Kindt, R., Legendre, P., Minchin, P.R., O'hara, R.B., Simpson, G.L., Solymos, P., Stevens, M.H.H., Wagner, H., Oksanen, M.J. (2018). Package 'vegan' Community ecology package, R package version 2.5-2 [Software] https://cran.ism.ac.jp/web/packages/vegan/vegan.pdf

Olsson, I.U. (2009) Radiocarbon dating history: early days, questions, and problems met. *Radiocarbon*, 51, 1-43.

Orbán, I., Birks, H.H., Vincze, I., Finsinger, W., Pál, I., Marinova, E., Jakab, G., Braun, M., Hubay, K., Bíró, T., Magyari, E.K. (2018) Treeline and timberline dynamics on the northern and southern slopes of the Retezat Mountains (Romania) during the late glacial and the Holocene. *Quaternary International*, 477, 59-78.

Ott, F., Wulf, S., Serb, J., Słowinski, M., Obremska, M., Tjallingii, R., Błaszkiewicz, M., Brauer, A. (2016) Constraining the time span between the Early Holocene Hasseldalen and Askja-S Tephras through varve counting in the Lake Czechowskie sediment record, Poland. *Journal of Quaternary Science*, 31, 103– 113.

Pál, I., Buczkó, K., Vincze, I., Finsinger, W., Braun, M., Biró, T., Magyari, E.K. (2018) Terrestrial and aquatic ecosystem responses to early Holocene rapid climate change (RCC) events in the South Carpathian Mountains, Romania. *Quaternary International*, 477, 79-93.

Paterne, M., Guichard, F., Labeyrie, J. (1988) Explosive activity of the South Italian volcanoes during the past 80,000 years as determined by marine tephrochronology. *Journal of Volcanology and Geothermal Research*, 34:3-4, 153-172.

Paus, A. (1995) The Late Weichselian and early Holocene history of tree birch in south Norway and the Bølling Betula time-lag in northwest Europe. *Review of Palaeobotany and Palynology*, 85:3-4, 243-262.

Paus, A. (2010) Vegetation and environment of the Rødalen alpine area, Central Norway, with emphasis on the early Holocene. *Vegetation History and Archaeobotany*, 19, 29-51.

Paus, A., Boessenkool, S., Brochmann, C., Epp, L.S., Fabel, D., Haflidason, H., Linge, H.,

(2015) Lake Store finnsjøen – a key for understanding Lateglacial/early Holocene vegetation and ice sheet dynamics in the central Scandes Mountains. *Quaternary Science Reviews*, 121, 36-51.

Pawłowski, D., Borówka, R.K., Kowalewski, G.A., Luoto, T.P., Milecka, K., Nevalainen, L., Okupny, D., Tomkowiak, J., Zieliński, T. (2016) Late Weichselian and Holocene record of the paleoenvironmental changes in a small river valley in Central Poland. *Quaternary Science Reviews*, 135, 24-40.

Pawłowski, D., Płóciennik, M., Brooks, S.J., Luoto, T.P., Milecka, K., Nevalainen, L., Peyron, O., Self, A., Zieliński, T. (2015) A multiproxy study of Younger Dryas and Early Holocene climatic conditions from the Grabia River paleo-oxbow lake (central Poland). *Palaeogeography, Palaeoclimatology, Palaeoecology*, 438, 34-50.

Pearce, N. J. G., Perkins, W. T., Westgate, J. A., Wade, S. C. (2011) Trace-element microanalysis by LA-ICP-MS: the quest for comprehensive chemical characterisation of single, sub-10 mm volcanic glass shards. *Quaternary International*, 246, 57–81.

Pearce, J.A., Bender, J.F., De Long, S.E., Kidd, W.S.F., Low, P.J., Güner, Y., Saroglu, F., Yilmaz, Y., Moorbath, S., Mitchell, J.G. (1990) Genesis of collision volcanism in Eastern Anatolia, Turkey. *Journal of Volcanology and Geothermal Research*, 44:1-2, 189-229.

Peccerillo, A. and Taylor, S.R. (1976) Geochemistry of Eocene calc-alkaline volcanic rocks from the Kastamonu area, northern Turkey. *Contributions to mineralogy and petrology*, 58, 63-81.

Pedro, J.B., Van Ommen, T.D., Rasmussen, S.O., Morgan, V.I., Chappellaz, J., Moy, A.D., Masson-Delmotte, V., Delmotte, M. (2011) The last deglaciation: timing the bipolar seesaw.

Peteet, D. (1995) Global Younger Dryas? *Quaternary International*, 28, 93-104.

Pilcher, J., Bradley, R.S., Francus, P., Anderson, L. (2005) A Holocene tephra record from the Lofoten Islands, arctic Norway. *Boreas*, 34, 136-156.

Plunkett, G. and Pilcher, J.R. (2018) Defining the potential source region of volcanic ash in northwest Europe during the Mid-to Late Holocene. *Earth Science Reviews*, 179, 20–37.

Pokorný, P. (2002) A high-resolution record of Late-Glacial and Early-Holocene climatic and environmental change in the Czech Republic. *Quaternary International*, 91:1, 101-122.

Pokorný, P., Šída, P., Chvojka, O., Žáčková, P., Kuneš, P., Světlík, I., Veselý, J. (2010) Palaeoenvironmental research of the Schwarzenberg Lake, southern Bohemia, and exploratory excavations of this key Mesolithic archaeological area. *Památky archeologické*, 101.

Pollard, A.M., Blockley, S.P.E., Lane, C.S. (2006). 'Some numerical considerations in the geochemical analysis of distal microtephra. *Applied Geochemistry*, 21:10, 1692-1714.

Praetorius, S.K., McManus, J.F., Oppo, D.W.,Curry, W.B. (2008) Episodic reductions in bottom-water currents since the last ice age. *Nature Geoscience*, 1, 449–452.

Preece, R.C. and Bridgland, D.R. (1999) Holywell Coombe, Folkestone: a 13,000 year history of an English chalkland valley. *Quaternary Science Reviews*, 18:8-9, 1075-1125.

Prentice, I.C. (1980) Multidimensional scaling as a research tool in Quaternary palynology: a review of theory and methods. *Review of Palaeobotany and Palynology*, 31, 71-104.

Prentice, I.C. (1988) Records of vegetation in time and space: The principles of pollen analysis. *In*: Huntley, B., Webb, T. (Eds.) Vegetation History, Dordrecht: Kluwer Academic Publishers, 17–42.

Prentice, I.C., Bartlein, P.J., Webb III, T. (1991) Vegetation and climate change in eastern North America since the last glacial maximum. *Ecology*, 72:6, 2038-2056.

Pyne-O'Donnell, S.D.F. (2007) Three new distal tephras in sediments spanning the Last Glacial-Interglacial transition in Scotland. *Journal of Quaternary Science*, 22, 559–570.

Pyne-O'Donnell, S. (2011) The taphonomy of Last Glacial – Interglacial Transition (LGIT) distal volcanic ash in small Scottish lakes. *Boreas*, 40:1, 131-145.

Pyne-O'Donnell, S.D.F., Blockley, S.P.E., Turney, C.S.M., Lowe, J.J. (2008) Distal volcanic ash layers in the Lateglacial Interstadial (GI-1): problems of stratigraphic discrimination. *Quaternary Science Reviews*, 27, 72–84.

Rach, O., Brauer, A., Wilkes, H., Sachse, D. (2014) Delayed hydrological response to Greenland cooling at the onset of the Younger Dryas in western Europe. *Nature Geoscience*, 7:2, 109-112.

Rahmstorf, S., 2002. Ocean circulation and climate during the past 120,000 years. *Nature*, 419:6903, 207.

Ralska-Jasiewiczowa, M., Goslar, T., Różański, K., Wacnik, A., Czernik, J., Chróst, L. (2003) Very fast environmental changes at the Pleistocene/Holocene boundary, recorded in laminated sediments of Lake Gościąż, Poland. *Palaeogeography, Palaeoclimatology, Palaeoecology*, 193:2, 225-247.

Ram, M., Donarummo Jr, J., Sheridan, M. (1996) Volcanic ash from Icelandic ~57,300 yr BP eruption found in GISP2 (Greenland) ice core. *Geophysical Research Letters*, 23:22, 3167-3169.

Ranner, P.H., Allen, J.R., Huntley, B. (2005) A new early Holocene cryptotephra from northwest Scotland. *Journal of Quaternary Science: Published for the Quaternary Research Association*, 20:3, 201-208.

Rasmussen, S.O., Andersen, K.K., Svensson, A.M., Steffensen, J.P., Vinther, B.M., Clausen, H.B., Siggaard-Andersen, M.L., Johnsen, S.J., Larsen, L.B., Dahl-Jensen, D., Bigler, M. (2006) A new Greenland ice core chronology for the last glacial termination. *Journal of Geophysical Research: Atmospheres*, 111:D6.

Rasmussen, S.O., Bigler, M., Blockley, S.P., Blunier, T., Buchardt, S.L., Clausen, H.B., Cvijanovic, I., Dahl-Jensen, D., Johnsen, S.J., Fischer, H., Gkinis, V. (2014) A stratigraphic

framework for abrupt climatic changes during the Last Glacial period based on three synchronized Greenland ice-core records: refining and extending the INTIMATE event stratigraphy. *Quaternary Science Reviews*, 106, 14-28.

Rasmussen, S.O., Vinther, B.M., Clausen, H.B., Andersen, K.K. (2007) Early Holocene climate oscillations recorded in three Greenland ice cores. *Quaternary Science Reviews*, 26:15-16, 1907-1914.

Reille, M. and Lowe, J.J. (1993) A re-evaluation of the vegetation history of the eastern Pyrenees (France) from the end of the last glacial to the present. *Quaternary Science Reviews*, 12:1, 47-77.

Reimer, P.J., Baillie, M.G., Bard, E., Bayliss, A., Beck, J.W., Blackwell, P.G., Ramsey, C.B., Buck, C.E., Burr, G.S., Edwards, R.L., Friedrich, M. (2009) IntCal09 and Marine09 radiocarbon age calibration curves, 0–50,000 years cal BP. *Radiocarbon*, 51:4, 1111-1150.

Reimer, P.J., Bard, E., Bayliss, A., Beck, J.W., Blackwell, P.G., Ramsey, C.B., Buck, C.E., Cheng, H., Edwards, R.L., Friedrich, M., Grootes, P.M. (2013) IntCal13 and Marine13 radiocarbon age calibration curves 0–50,000 years cal BP. *Radiocarbon*, 55:4, 1869-1887.

Reimer, P.J., Austin, W.E.N., Bard, E., Bayliss, A., Blackwell, P.G., Bronk Ramsey, C., Butzine, M., Cheng, H., Edwards, L., Friedrich, M., Grootes, P.M., Guilderson, T.P., Hajdas, I., Heaton, T.J., Hogg, A.G., Hughen, K.A., Kromer, B., Manning, S.W., Muscheler, R., Palmer, J.G., Pearson, C., van der Pilcht, J., Reimer, R.W., Richards, D., Scott, E.M., Southon, J.R., Turney, C.S.MM., Wacker, L., Adophi, F., Büntgen, U., Capano, M., Fahrni, S., Fogtmann-Schulzm A., Friedrich, R., Kudsk, S., Miyake, F., Olsen, J., Reining, F., Sakamoto, M., Sookdeo, A., Talamo, S. (2020) The IntCal20 Northern Hemisphere radiocarbon calibration curve (0-55kcal BP) Radiocarbon, in review.

Renssen, H. and Isarin, R.F.B. (1997) Surface temperature in NW Europe during the Younger Dryas: AGCM simulation compared with temperature reconstructions. *Climate Dynamics*, 14:1, 33-44.

Renssen, H., Goosse, H., Muscheler, R. (2006) Coupled climate model simulation of Holocene cooling events: solar forcing triggers oceanic feedback. *Climate of the Past Discussions*, 2:3, 209-232.

Renssen, H. and Isarin, R.F. (2001) The two major warming phases of the last deglaciation at ~14.7 and ~11.5 ka cal BP in Europe: climate reconstructions and AGCM experiments. *Global and Planetary Change*, 30:1-2, 117-153.

Renssen, H., Mairesse, A., Goosse, H., Mathiot, P., Heiri, O., Roche, D.M., Nisancioglu, K.H., Valdes, P.J. (2015) Multiple causes of the Younger Dryas cold period. *Nature Geoscience*, 8:12, 946-949.

Reuther, A.U., Urdea, P., Geiger, C., Ivy-Ochs, S., Niller, H.P., Kubik, P.W., Heine, K (2007) Late Pleistocene glacial chronology of the Pietrele Valley, Retezat Mountains, Southern Carpathians constrained by $^{10}$Be exposure ages and pedology investigation. *Quaternary International*, 164:65, 151-169.

Reyer, C.P., Rammig, A., Brouwers, N., Langerwisch, F., Gibson, D. (2015) Forest resilience, tipping points and global change processes. *Journal of Ecology*, 103:1, 1-4.

Ribera, I. and Vogler, A.P. (2004) Speciation of Iberian diving beetles in Pleistocene refugia (Coleoptera, Dytiscidae). *Molecular Ecology*, 13:1, 179-193.

Ruddiman W.F. and McIntyre, A. (1981) The mode and mechanism of the last deglaciation: oceanic evidence. *Quaternary Research*, 16, 125–34

Ruddiman, W.F. and Glover, L.K. (1972) Vertical mixing of ice rafted volcanic ash in north Atlantic sediments. *Geological Society of America Bulletin,* 83, 2817-2836.

Ruszkiczay-Rüdiger, Z., Kern, Z., Urdea, P., Braucher, R., Madarász, B., Schimmelpfennig, I., ASTER team (2016) Revised deglaciation history of the Pietrele-Stânişoara glacial complex, Retezat Mts, Southern Carpathians, Romania. *Quaternary International*, 415, 216-229.

Ruth, U., Bigler, M., Röthlisberger, R., Siggaard-Andersen, M.L., Kipfstuhl, S., Goto-Azuma, K., Hansson, M.E., Johnsen, S.J., Lu, H., Steffensen, J.P. (2007) Ice core evidence for a very tight link between North Atlantic and east Asian glacial climate. *Geophysical Research Letters*, 34:3.

Sachse, D., Billault, I., Bowen, G.J., Chikaraishi, Y., Dawson, T.E., Feakins, S.J., Freeman, K.H., Magill, C.R., McInerney, F.A., Van der Meer, M.T., Polissar, P. (2012) Molecular paleohydrology: interpreting the hydrogen-isotopic composition of lipid biomarkers from photosynthesizing organisms. *Annual Review of Earth and Planetary Sciences*, 40, 221-249.

Sæmundsson, K. (1991) The geology of the krafla system (jarðfraeði kröflukerfisins). *In*: Garðarsson, A., Einarsson, A. (Eds.), Nattúra My vatns. Hið íslenska nattúrufraeðifelag, Reykjavík, 25-95.

Sakai, A. (1983). Comparative study of freezing resistance of conifers with special reference to cold adaptation and its evolutive aspects. *Canadian Journal of Botany*, 61, 2323-2332.

Samartin, S., Heiri, O., Vescovi, E., Brooks, S.J., Tinner, W. (2012) Lateglacial and early Holocene summer temperatures in the southern Swiss Alps reconstructed using fossil chironomids. *Journal of Quaternary Science*, 27:3, 279-289.

Satow, C., Tomlinson, E.L., Grant, K.M., Albert, P.G., Smith, V.C., Manning, C.J., Ottolini, L., Wulf, S., Rohling, E.J., Lowe, J.J., Blockley, S.P.E. (2015) A new contribution to the Late Quaternary tephrostratigraphy of the Mediterranean: Aegean Sea core LC21. *Quaternary Science Reviews*, 117, 96-112.

Scaillet, S., Vita-Scaillet, G., Rotolo, S.G. (2013) Millennial-scale phase relationships between ice-core and Mediterranean marine records: insights from high- precision $^{40}Ar/^{39}Ar$ dating of the Green Tuff of Pantelleria, Sicily Strait. *Quaternary Science Reviews*, 78, 141154.

Scheffer, M., Bascompte, J., Brock, W.A., Brovkin, V., Carpenter, S.R., Dakos, V., Held, H., Van Nes, E.H., Rietkerk, M., Sugihara, G. (2009) Early-warning signals for critical transitions. *Nature*, 461:7260, 53.

Scheffer, M. and Carpenter, S.R. (2003) Catastrophic regime shifts in ecosystems: linking theory to observation. *Trends in ecology & evolution*, 18:12, 648-656.

Schenk, F., Väliranta, M., Muschitiello, F., Tarasov, L., Heikkilä, M., Björck, S., Brandefelt, J., Johansson, A.V., Näslund, J.O., Wohlfarth, B., (2018) Warm summers during the Younger Dryas cold reversal. *Nature communications*, 9:1, 1634.

Schmidt, R., van den Bogaard, C., Merkt, J., Müller, J. (2002) A new Lateglacial chronostratigraphic tephra marker for the south-eastern Alps: the Neapolitan Yellow Tuff (NYT) in Langsee (Austria) in the context of a regional biostratigraphy and palaeoclimate. *Quaternary International*, 88, 45-56.

Schmitt, A.K., Danisik, M., Evans, N.J., Siebel, W., Kiemele, E., Aydin, F., Harvey, J. (2011) Acigöl rhyolite field, Central Anatolia (part 1): high-resolution dating of eruption episodes and zircon growth rates. *Contribution to Mineral Petrolology,* 162, 1215-1231.

Schoene, B., Condon, D.J., Morgan, L., McLean, N. (2013) Precision and accuracy in geochronology. *Elements*, 9:1, 19-24.

Schwander, J., Eicher, U., Ammann, B., (2000) Oxygen isotopes of lake marl at Gerzensee and Leysin (Switzerland), covering the Younger Dryas and two minor oscillations, and their correlation to the GRIP ice core. *Palaeogeography, Palaeoclimatology, Palaeoecology*, 159:3-4, 203-214.

Schwörer, C., Henne, P.D., Tinner, W. (2014) A model-data comparison of Holocene timberline changes in the Swiss Alps reveals past and future drivers of mountain forest dynamics. *Global change biology*, 20:5, 1512-1526.

Seddon, A.W., Macias-Fauria, M., Willis, K.J. (2015) Climate and abrupt vegetation change in Northern Europe since the last deglaciation. *The Holocene*, 25:1, 25-36.

Seppä, H. and Hicks, S. (2006) Integration of modern and past pollen accumulation rate (PAR) records across the arctic tree-line: a method for more precise vegetation reconstructions. *Quaternary Science Reviews*, 25:13-14, 1501-1516.

Seppä, H. and Bennett, K.D. (2003) Quaternary pollen analysis: recent progress in palaeoecology and palaeoclimatology. *Progress in Physical Geography*, 27:4, 548-579.

Seppä, H. (2007) Pollen analysis, principles. In: Elias, S.A. (Editor) *Encyclopaedia of Quaternary Science*, Elsevier Science, vol. 3, 2486-2497.

Seppälä, A., Matthes, K., Randall, C.E., Mironova, I.A. (2014) What is the solar influence on climate? Overview of activities during CAWSES-II. *Progress in Earth and Planetary Science*, 1:1, 1-12.

Shane, P. (2000) Tephrochronology: A New Zealand case study. *Earth-Science Reviews*, 49:1-4, 223-259.

Shumilovskikh, L.S., Novenko, E., Giesecke, T. (2017). Long-term dynamics of the East European forest-steppe ecotone. *Journal of Vegetation Science*, 29:3, 416-426.

Siani, G., Sulpizio, R., Paterne, M., Sbrana, A. (2004) Tephrostratigraphy study for the last 18,000 14C years in a deep-sea sediment sequence for the South Adriatic. *Quaternary Science Reviews*, 23:23-24, 2485-2500.

Sigurdsson, H., McIntosh, W.C., Dunbar, N., Lacasse, C., Carey, S.N. (1998) Thorsmork Ignimbrite in Iceland; possible source of North Atlantic ash zone 2. *In*: *AGU 1998 Spring Meeting. Eos (Transactions, American Geophysical Union)*, 79, 377.

Sigvaldason, G.E. (2002) Volcanic and tectonic processes coinciding with glaciation and crustal rebound: an early Holocene rhyolitic eruption in the Dyngjufjöll volcanic centre and the formation of the Askja caldera, north Iceland. *Bulletin of Volcanology*, 64, 192-205.

Simpson, G.L. and Birks, H.J.B. (2012). Statistical learning in Palaeolimnology. *In*: Birks, H.J.B., Lotter, A.F., Juggins, S., and Smol, J.P (Eds.). *Tracking Environmental Change Using Lake Sediments. Volume 5: Data Handling and Numerical Techniques.* Dordrecht, The Netherlands: Kluwer Academic Publishers, pp. 249-327.

Słowiński, M., Zawiska, I., Ott, F., Noryśkiewicz, A.M., Plessen, B., Apolinarska, K., Rzodkiewicz, M., Michczyńska, D.J., Wulf, S., Skubała, P., Kordowski, J. (2017) Differential proxy responses to late Allerød and early Younger Dryas climatic change recorded in varved sediments of the Trzechowskie palaeolake in Northern Poland. *Quaternary Science Reviews*, 158, 94-106.

Smith, V. C., Isaia, R., Pearce, N. J. G. (2011) Tephrostratigraphy and glass compositions of post- 15 kyr Campi Flegrei eruptions: implications for eruption history and chronostratigraphic markers. *Quaternary Science Reviews*, 30:25–26, 3638–3660.

Speranza, F., Landi, P., Caracciolo, F.D.A., Pignatelli, A., (2010) Paleomagnetic dating of the most recent silicic eruptive activity at Pantelleria (Strait of Sicily). *Bulletin of Volcanology*, 72:7, 847-858.

Stančikaitė, M., Gedminienė, L., Edvardsson, J., Stoffel, M., Corona, C., Gryguc, G., Uogintas, D., Zinkutė, R., Skuratovič, Ž., Taraškevičius, R. (2017) Holocene vegetation and hydroclimatic dynamics in SE Lithuania–Implications from a multi-proxy study of the Čepkeliai bog. *Quaternary International*, 501, 219-239.

Stančikaitė, M., Kisielienė, D., Moe, D., Vaikutienė, G. (2009) Lateglacial and early Holocene environmental changes in northeastern Lithuania. *Quaternary International*, 207:1-2, 80-92.

Starkel, L. (1991) Environmental changes at the Younger Dryas-Preboreal transition and during the early Holocene: some distinctive aspects in central Europe. *The Holocene*, 1:3, 234-242.

Stefanova, I. and Ammann, B. (2003) Lateglacial and Holocene vegetation belts in the Pirin Mountains (southwestern Bulgaria). *The Holocene*, 13:1, 97-107.

Steffensen, J. P., Andersen, K. K., Bigler, M., Clausen, H. B., Dahl-jensen, D., Fischer, H., Goto-azuma, K., Hansson, M., Johnsen, S. J., Jouzel, J., Masson-delmotte, V., Popp, T., Rasmussen, S. O., Röthlisberger, R., Ruth, U., Stauffer, B., Sveinbjörnsdóttir, Á. E., Svensson, A., White, J. W. C. (2008) High-Resolution Greenland Ice Core Data Show Abrupt Climate Change Happens in Few Years. *Science*, 321:5889, 680-684.

Steinhilber, F., Beer, J., Fröhlich, C. (2009) Total solar irradiance during the Holocene. *Geophysical Research Letters*, 36:19, 1-5.

Stevenson, J.A., Loughlin, S.C., Font, A., Fuller, G.W., MacLeod, A., Oliver, I.W., Jackson, B., Horwell, C.J., Thordarson, T., Dawson, I. (2013) UK monitoring and deposition of tephra from the May (2011 eruption of Grímsvötn, Iceland. *Journal of Applied Volcanology*, 2:1, 3.

Striberger, J., Björck, S., Holmgren, S., Hamerlík, L. (2012) The sediments of Lake Lögurinnda unique proxy record of Holocene glacial meltwater variability in eastern Iceland. *Quaternary Science Reviews*, 38, 76-88.

Sugita, S. (1994) Pollen representation of vegetation in Quaternary sediments: theory and method in patchy vegetation. *Journal of ecology*, 881-897.

Sulpizio, R., Zanchetta, G., Orazio, M. D., Vogel, H., Wagner, B., Geomineralogico, D. (2010) Tephrostratigraphy and tephrochronology of lakes Ohrid and Prespa, Balkans. *Biogeosceiences*, 7, 3273–3288.

Sumita, M. and Schmincke, H-U. (2013) Impact of volcanism on the evolution of Lake Van I: evolution of explosive volcanism of Nemrut Volcano (eastern Anatolia) during the past >400,000 years. *Bulletin of Volcanology*, 75, 1-32.

Sun, S. and McDonough, W.F. (1989) Chemical and isotopic systematics of 630 oceanic basalts: implications for mantle composition and processes. *In*: Saunders, A.D., Norry, M.J. (Eds.), *Magmatism in Ocean Basins*. 631.

Talbot, M.R. (1990) A review of the palaeohydrological interpretation of carbon and oxygen isotopic ratios in primary lacustrine carbonates. *Chemical Geology: Isotope Geoscience Section*, 80:4, 261-279.

Tamburrino, S., Insinga, D.D., Sprovieri, M., Petrosino, P., Tiepolo, M. (2012) Major and trace element characterization of tephra layers offshore Pantelleria Island: insights into the last (200 ka of volcanic activity and contribution to the Mediterranean tephrochronology. *Journal of Quaternary Science*, 27:2, 129-140.

Tanţău, I., Reille, M., Beaulieu, J. D. E., Farcas, S. (2006) Late Glacial and Holocene vegetation history in the southern part of Transylvania (Romania): pollen analysis of two sequences from Avrig. *Journal of Quaternary Science*, 21:1, 49–61.

Tanţău, I., Reille, M., Farcas, S., Goslar, T., Paterne, M. (2003) Vegetation history in the Eastern Romanian Carpathians : pollen analysis of two sequences from the Mohos¸ crater. *Vegetation History and Archaeobotany*, 12:2, 113–125.

Tarasov, L. and Peltier, W.R. (2005) Arctic freshwater forcing of the Younger Dryas cold reversal. *Nature*, 435:7042, 662.

Tauber, H. (1965) Differential pollen dispersal and the interpretation of pollen diagrams. *Danmarks Geologiske Undersøgelse*II, 89, 1-69.

Telford, R.J., Heegaard, E., Birks., H.J.B. (2004) All age-depth models are wrong: but how badly? *Quaternary Science Reviews*, 23, 1-5.

Teller, J.T., Leverington, D.W., Mann, J.D. (2002) Freshwater outbursts to the oceans from glacial Lake Agassiz and their role in climate change during the last deglaciation. *Quaternary Science Reviews*, 21, 879-887.

ter Braak, C.J. and Prentice, I.C. (1988). A theory of gradient analysis. *Advances in Ecological Research*, 18, 271-317.

Textor, C., Sachs, P.M., Graf, H.F., Hansteen, T.H. (2003) The 12 900 years BP Laacher See eruption: estimation of volatile yields and simulation of their fate in the plume. *Geological Society, London, Special Publications*, 213, 307-328.

Theuerkauf, M. and Joosten, H. (2012) Younger Dryas cold stage vegetation patterns of central E urope–climate, soil and relief controls. *Boreas*, 41:3, 391-407.

Theuerkauf, M., Bos, J.A., Jahns, S., Janke, W., Kuparinen, A., Stebich, M., Joosten, H. (2014) Corylus expansion and persistent openness in the early Holocene vegetation of northern central Europe. *Quaternary Science Reviews*, 90, 183-198.

Thomas, P.A., El-Barghathi, M., Polwart, A. (2007) Biological flora of the British Isles: Juniperus communis L. *Journal of Ecology*, 95:6, 1404-1440.

Thompson, R. (1980) Use of the word "influx' in palaeolimnological studies. *Quaternary Research*, 14, 269-270.

Thórarinsson, S. (1944) Tefrokronologiska studier på Island. *Geografiska Annaler* 26, 1–217.

Thornalley, D.J., McCave, I.N., Elderfield, H. (2011) Tephra in deglacial ocean sediments south of Iceland: stratigraphy, geochemistry and oceanic reservoir ages. *Journal of Quaternary Science*, 26:2, 190-198.

Timms, R.G., Matthews, I.P., Lowe, J.J., Palmer, A.P., Weston, D.J., MacLeod, A., Blockley, S.P. (2019) Establishing tephrostratigraphic frameworks to aid the study of abrupt climatic and glacial transitions: a case study of the Last Glacial-Interglacial Transition in the British Isles (c. 16-8 ka BP). *Earth-science reviews*, 192, 34-64.

Timms, R.G.O., Matthews, I.P., Palmer, A.P., Candy, I. (2018) Toward a tephrostratigraphic framework for the British Isles: a Last Glacial to Interglacial Transition (LGIT c. 16-8 ka) case study from Crudale Meadow, Orkney. *Quaternary Geochronology*, 46, 28–44.

Timms, R.G.O., Matthews, I.P., Palmer, A.P., Candy, I., Abel, L. (2017) A high-resolution tephrostratigraphy from Quoyloo Meadow, Orkney, Scotland: implications for the

tephrostratigraphy of NW Europe during the Last Glacial-Interglacial Transition. *Quaternary Geochronology*, 40, 67-81.

Tinner, W., Conedera, M., Ammann, B., Lotter, A.F. (2005) Fire ecology north and south of the Alps since the last ice age. *The Holocene*, 15:8, 1214-1226.

Tipping, R.M. (1989). Devensian Lateglacial Vegetation History at Loch Barnluasgan, Argyllshire, Western Scotland. *Journal of Biogeography*, 16:5, 435–447.

Tipping, R. (1991) The climatostratigraphic subdivision of the Devensian Lateglacial: evidence from a pollen site near Oban, western Scotland. *Journal of biogeography*, 89-101.

Tomlinson, E.L., Albert, P.G., Wulf, S., Brown, R.J., Smith, V.C., Keller, J., Orsi, G., Bourne, A.J., Menzies, M.A. (2014) Age and geochemistry of tephra layers from Ischia, Italy: constraints from proximal-distal correlations with Lago Grande di Monticchio. *Journal of volcanology and Geothermal Research*, 287, 22-39.

Tomlinson, E.L., Arienzo, I., Civetta, L., Wulf, S., Smith, V.C., Hardiman, M., Lane, C.S., Carandenta, A., Orsi, G., Rosi, M., Muller, W., Menzies, M.A. (2012a) Geochemistry of the Phlegraean Fields (Italy) proximal sources for major Mediterranean tephras: implications for the dispersal of Plinian and co-ignimbritic components of explosive eruptions. *Geochimica et Cosmochimica Acta*, 93, 102-128.

Tomlinson, E.L., Arienzo, I., Wulf, S., Smith, V.C., Carandente, A., Civetta, L., Hardiman, M., Lane, C.S., Orsi, G., Rosi, M., Thirlwall, M. (2012b) Geochemistry of the Plegraean Fields (Italy) proximal Campi Flegrei sources for major Mediterranean tephras (C-1, C-2, Y-3 & Y-5). *Geochim. Cosmochim. Acta*, 93:10, 102-128

Tomlinson, E.L., Thordarson, T., Müller, W., Thirlwall, M., Menzies, M.A. (2010) Microanalysis of tephra by LA-ICP-MS—strategies, advantages and limitations assessed using the Thorsmörk Ignimbrite (Southern Iceland). *Chemical Geology*, 279:3-4, 73-89.

Tomlinson, E.L., Smith, V.C., Albert, P.G., Aydar, E., Civetta, L., Cioni, R., Çubukçu, E., Gertisser, R., Isaia, R., Menzies, M.A., Orsi, G., Rosi, M., Zanchetta, G. (2015) The major and trace element glass composition of the productive Mediterranean volcanic sources: tools for correlating distal tephra layers in and around Europe. *Quaternary Science Reviews*, 118, 48-66.

Tóth, M., Magyari, E.K., Brooks, S.J., Braun, M., Buczko , K., Ba lint, M., Heiri, O. (2012) A chironomid-based reconstruction of late glacial summer temperatures in the southern Carpathians (Romania). *Quaternary Research*, 77, 122-131.

Tóth, M., Magyari, K., Brooks, S. J., Braun, M., Buczkó, K., Bálint, M., Heiri, O. (2015) A chironomid-based reconstruction of late glacial summer temperatures in the southern Carpathians (Romania). *Quaternary Research*, 77, 122–131.

Tryon, C. A., Logan, M. A. V, Mouralis, D., Kuhn, S., Slimak, L., Balkan-atl, N. (2009) Building a tephrostratigraphic framework for the Paleolithic of Central Anatolia, Turkey. *Journal of Archaeological Science*, 36:3, 637–652.

Turney, C.S., Harkness, D.D., Lowe, J.J. (1997) Rapid Communication: the use of microtephra horizons to correlate Late-glacial lake sediment successions in Scotland. *Journal of Quaternary Science,* 12:6, 525–531.

Turney, C.S.M. (1998) Extraction of rhyolitic component of Vedde microtephra from minerogenic lake sediments. *Journal of Paleolimnology*, 19, 199-206.

Turney, C.S., Lowe, J.J., Wastegård, S., Cooper, R., Roberts, S.J. (2001) The development of a tephrochronological framework for the last glacial-Holocene transition in NW Europe. *Tephras: Chronology and Archaeology. Les dossiers de l'Archeo-Logis, Goudet*, 101, 109.

Turney, C.S.M., Den Burg, K.V., Wastegård, S., Davies, S.M., Whitehouse, N.J., Pilcher, J.R., Callaghan, C. (2006) North European last glacial–interglacial transition (LGIT; 15–9 ka) tephrochronology: extended limits and new events. *Journal of Quaternary Science: Published for the Quaternary Research Association*, 21:4, 335-345.

Urdea, P. (2004) The Pleistocene glaciation of the Romanian Carpathians. *In*: Ehlers, J., P.L. Gibbard (Eds) *Quaternary Glaciations-Extent and Chronology*, Part I, 301–308.

van der Bilt, W.G.M., Lane, C.S., Bakke, J. (2017) Ultra-distal Kamchatkan ash on Artic Svalbard: Towards hemispheric cryptotephra correlation. *Quaternary Science Reviews*, 164, 230-235.

Usinger, H. (2004) Vegetation and climate of the lowlands of northern Central Europe and adjacent areas around the Younger Dryas–Preboreal transition–with special emphasis on the Preboreal oscillation. *In*: Hunters in a Changing World, Terberger, T., Eriksen, B.V. (Eds) *Environment and Archaeology of the Pleistocene-Holocene Transition (ca. 11 000–9000 B.C.) in Northern Europe*, Marie Leidorf Publisher: Rahden, 1–26.

van Asch, N., Kloos, M.E., Heiri, O., de Klerk, P., Hoek, W.Z. (2012) The Younger Dryas cooling in northeast Germany: summer temperature and environmental changes in the Friedländer Groβe Wiese region. *Journal of Quaternary Science*, 27:5, 531-543.

van der Plicht, J., Van Geel, B., Bohncke, S.J.P., Bos, J.A.A., Blaauw, M., Speranza, A.O.M., Muscheler, R., Björck, S. (2004) The Preboreal climate reversal and a subsequent solar-forced climate shift. *Journal of Quaternary Science*, 19:3, 263-269.

van Dinter, M., Birks, H. H. (1996) Distinguishing fossil *Betula nana* and *B. pubescens* using their wingless fruits: implications for the late-glacial vegetational history of western Norway. *Vegetation History and Archaeobotonay*, 5, 229–240.

van Geel, B., Raspopov, O.M., Renssen, H., Van der Plicht, J., Dergachev, V.A., Meijer, H.A.J. (1999) The role of solar forcing upon climate change. *Quaternary Science Reviews*, 18:3, 331-338.

van Raden, U.J., Colombaroli, D., Gilli, A., Schwander, J., Bernasconi, S.M., van Leeuwen, J., Leuenberger, M., Eicher, U. (2013). High-resolution Late-Glacial chronology for the Gerzensee lake record (Switzerland): $\delta^{18}O$ correlation between a Gerzensee-stack and NGRIP.*Palaeogeography, Palaeoclimatology, Palaeoecology*, 391, 13-24.

Verbruggen, F., Heiri, O., Reichart, G.J., Lotter, A.F. (2010) Chironomid $\delta^{18}O$ as a proxy for past lake water $\delta^{18}O$: a Lateglacial record from Rotsee (Switzerland). *Quaternary Science Reviews*, 29:17-18, 2271-2279.

Veres, D. and Mîndrescu, M. (2013) Advancing Pleistocene and Holocene climate change research in the Carpathian-Balkan region. *Quaternary International*, 293, 1-4.

Vescovi, E., Ravazzi, C., Arpenti, E., Finsinger, W., Pini, R., Valsecchi, V., Wick, L., Ammann, B., Tinner, W. (2007) Interactions between climate and vegetation during the Lateglacial period as recorded by lake and mire sediment archives in Northern Italy and Southern Switzerland. *Quaternary Science Reviews*, 26:11-12, 1650-1669.

Vincze, I., Orbán, I., Birks, H.H., Pál, I., Finsinger, W., Hubay, K., Marinova, E., Jakab, G., Braun, M., Biró, T., Tóth, M. (2017) Holocene treeline and timberline changes in the South Carpathians (Romania): Climatic and anthropogenic drivers on the southern slopes of the Retezat Mountains. *The Holocene*, 27:11, 1613-1630.

Vogel, H., Zanchetta, G., Sulpizio, R., Wagner, B., Nowaczyk, N. (2010) A tephrostratigraphic record for the last glacial–interglacial cycle from Lake Ohrid, Albania and Macedonia. *Journal of Quaternary Science: Published for the Quaternary Research Association*, 25:3, 320-338.

von Fichtel, J.E. (1780) Beytrag Zur Mineralgeschichte Von Siebenbürgen. Zweyter Theil Welcher Die Geschichte Des Steinsalzes enthält. Raspische Buchhandlung, Nürnberg, pp 134.

Von Post, L. (1946) The prospect for pollen analysis in the studys of earths climatic history. *New Phytol*, 45, 193-217.

Vorren, K.D., Elverland, E., Blaauw, M., Ravna, E.K., Jensen, C.A. (2009) Vegetation and climate c. 12 300–9000 cal. yr BP at Andøya, NW Norway. *Boreas*, 38:3, 401-420.

Wacnik, A. (2009) From foraging to farming in the Great Mazurian Lake District: palynological studies on Lake Miłkowskie sediments, northeast Poland. *Vegetation History and Archaeobotany*, 18:3, 187-203.

Waelbroeck, C., Duplessy, J., Michel, E. (2001) The timing of the last deglaciation in North Atlantic climate records. *Nature*, 412, 548-548.

Walker, M.J.C., Björck, S., Lowe, J.J. (2001) Integration of ice core, marine and terrestrial records (INTIMATE) from around the North Atlantic region: an introduction. *Quaternary Science Reviews*, 20:11, 1169-1174.

Walker, M.J.C., Coope, G.R., Sheldrick, C., Turney, C.S.M., Lowe, J.J., Blockley, S.P.E., Harkness, D.D. (2003). Devensian Lateglacial environmental changes in Britain: a multi-proxy environmental record from Llanilid, South Wales, UK. *Quaternary Science Reviews*, 22:5-7, 475-520.

Walker, M., Johnsen, S., Rasmussen, S.O., Popp, T., Steffensen, J.P., Gibbard, P., Hoek, W., Lowe, J., Andrews, J., Björck, S., Cwynar, L.C. (2009) Formal definition and dating of the GSSP (Global Stratotype Section and Point) for the base of the Holocene using the Greenland

NGRIP ice core, and selected auxiliary records. *Journal of Quaternary Science: Published for the Quaternary Research Association*, 24:1, 3-17.

Wanner, H., Solomina, O., Grosjean, M., Ritz, S.P., Jetel, M. (2011) Structure and origin of Holocene cold events. *Quaternary Science Reviews*, 30, 3109-3123.

Wastegård, S. (1998) Deglaciation chronology and marine environments in southwestern Sweden. *Boreas*, 27, 178-194.

Wastegård, S., Björck, S., Possnert, G., Wohlfarth, B. (1998) Evidence for the occurrence of Vedde Ash in Sweden: radiocarbon and calendar age estimates. *Journal of Quaternary Science: Published for the Quaternary Research Association*, 13:3, 271-274.

Wastegård, S., Gudmundsdóttir, E.R., Lind, E.M., Timms, R.G.O., Björck, S., Hannon, G.E., Olsen, J., Rundgren, M. (2018) Towards a Holocene tephrochronology for the Faroe Islands, North Atlantic. *Quaternary Science Reviews*, 195, 195–214.

Wastegård, S., Turney, C.S.M., Lowe, J.J., Roberts, S.J. (2000b) New discoveries of the Vedde Ash in southern Sweden and Scotland. *Boreas*, 29, 72–78.

Wastegård, S., Wohlfarth, B., Subetto, D. A., Sapelko, T. V (2000a) Extending the known distribution of the Younger Dryas Vedde Ash into northwestern Russia. *Journal of Quaternary Science*, 15, 581–586.

Watts, W.A., Allen, J.R.M., Huntley, B. (1996) Vegetation history and palaeoclimate of the last glacial period at Lago Grande di Monticchio, southern Italy. Quaternary Science Reviews, 15:2, 133-153.

Watt, S.F., Gilbert, J.S., Folch, A., Phillips, J.C., Cai, X.M. (2015) An example of enhanced tephra deposition driven by topographically induced atmospheric turbulence. *Bulletin of Volcanology*, 77:5, 35.

Watts, W.A. (1970) Criteria for identification of Late-glacial climatic oscillations, with special reference to the Bølling Oscillation. *American Quaternary Association, 1st Meeting Abstracts (1970),* 144-145.

Westgate, J.A., Gorton, M.P. (1981) Correlation techniques in tephra studies. In: Self, S., Sparks, R.S.J. (Eds.), Tephra Studies. Reidel, Dordrecht, pp. 73-94.

Whitmore, J., Gajewski, K., Sawada, M., Williams, J. W., Shuman, B., Bartlein, P. J. (2005) Modern pollen data from North America and Greenland for multi-scale paleoenvironmental applications. *Quaternary Science Reviews*, 24, 1828–1848.

Whittington, G., Edwards, K.J., Zanchetta, G., Keen, D.H., Bunting, M.J., Fallick, A.E., Bryant, C.L. (2015) Lateglacial and early Holocene climates of the Atlantic margins of Europe: Stable isotope, mollusc and pollen records from Orkney, Scotland. *Quaternary Science Reviews*, 122, 112-130.

Whittington, G., Fallick, A.E., Edwards, K.J. (1996) Stable oxygen isotope and pollen records from eastern Scotland and a consideration of Late-glacial and early Holocene climate change

for Europe. Journal of Quaternary Science: *Published for the Quaternary Research Association*, 11:4, 327-340.

Wick, L., Tinner, W. (1997) Vegetation changes and umbertine fluctuations in the Central Alps as indicators of Holocene climatic oscillations. *Arctic and Alpine Research*, 29:4, 445-458.

Wick, L. (2000) Vegetational response to climatic changes recorded in Swiss Late Glacial lake sediments. *Palaeogeography, Palaeoclimatology, Palaeoecology*, 159:3-4, 231-250.

Wiersma, A.P., Roche, D.M., Renssen, H. (2011) Fingerprinting the 8.2 ka event climate response in a coupled climate model. *Journal of Quaternary Science*, 26:1, 118-127.

Wijk, S. (1986). Performance of *Salix herbacea* in an alpine snow-bed gradient.' *Journal of Ecology*, 675-684.

Williams, J.W., Blois, J.L., Shuman, B.N. (2011) Extrinsic and intrinsic forcing of abrupt ecological change: case studies from the late Quaternary. *Journal of Ecology*, 99:3, 664-677.

Williams, J.W., Post, D.M., Cwynar, L.C., Lotter, A.F., Levesque, A.J. (2002) Rapid and widespread vegetation responses to past climate change in the North Atlantic region. *Geology*, 30:11, 971-974.

Willkomm, H., Erlenkeuser, H. (1973) $C^{14}$ measurements on water, plants and sediments of lakes. In: *Proceedings of the Eighth International Radiocarbon Dating Conference*. Lower Hutt, New Zealand, 18–25 October 1972, 312–323.

Wohlfarth, B., Blaauw, M., Davies, S.M., Andersson, M., Wastegård, S., Hormes, A., Possnert, G. (2006) Constraining the age of Lateglacial and early Holocene pollen zones and tephra horizons in southern Sweden with Bayesian probability methods. *Journal of Quaternary Science*, 21, 321–334.

Wohlfarth, B., Hannon, G., Feurdean, A., Ghergari, L., Onac, B.P. (2001) Reconstruction of climatic and environmental changes in NW Romania during the early part of the last deglaciation (~15,000-13,600 cal yr BP). *Quaternary Science Reviews*, 20, 1897-1914.

Wohlfarth, B., Skog, G., Possnert, G., Holmquist, B. (1998) Pitfalls in the AMS radiocarbon-dating of terrestrial macrofossils. *Journal of Quaternary Science,* 13, 137-145.

Wohlfarth, B., Lacourse, T., Bennike, O., Subetto, D., Tarasov, P., Demidov, I., Filimonova, L. and Sapelko, T. (2007) Climatic and environmental changes in north-western Russia between 15,000 and 8000 cal yr BP: a review. *Quaternary Science Reviews*, 26:13-14, 1871-1883.

Wohlfarth, B., Luoto, T.P., Muschitiello, F., Väliranta, M., Björck, S., Davies, S.M., Kylander, M., Ljung, K., Reimer, P.J., Smittenberg, R.H. (2018) Climate and environment in southwest Sweden 15.5–11.3 cal. ka BP. *Boreas*, 47:3, 687-710.

Wohlfarth, B., Muschitiello, F., L Greenwood, S., Andersson, A., Kylander, M., Smittenberg, R.H., Steinthorsdottir, M., Watson, J., Whitehouse, N.J. (2017) Hässeldala–a key site for Last Termination climate events in northern Europe. *Boreas*, 46:2, 143-161.

Wohlfarth, B., Skog, G., Possnert, G., Holmquist, B. (1998) Pitfalls in the AMS radiocarbon-dating of terrestrial macrofossils. *Journal of Quaternary Science,* 13, 137-145.

Wulf, S., Kraml, M., Kuhn, T., Schwarz, M., Inthorn, M., Keller, J., Kuscu, I., Halbach, P., (2002) Marine tephra from the Cape Riva eruption (22 ka) of Santorini in the Sea of Marmara. *Marine Geology*, 183(1-4), 131-141.

Wulf, S., Dräger, N., Ott, F., Serb, J., Appelt, O., GuÐmundsdóttir, E., van den Bogaard, C., Słowinski, M., Błaszkiewicz, M., Brauer, A. (2016a) Holocene tephrostratigraphy of varved sediment records from Lakes Tiefer See (NE Germany) and Czechowskie (N Poland). *Quaternary Science Reviews,* 132, 1–14.

Wulf, S., Fedorowicz, S., Veres, D., Łanczont, M., Karátson, D., Gertisser, R., Bormann, M., Magyari, E., Appelt, O., Hambach, U., Gozhyk, P.F., (2016b) The 'Roxolany Tephra'(Ukraine): new evidence for an origin from Ciomadul volcano, East Carpathians. *Journal of Quaternary Science*, 31:6, 565-576.

Wulf, S., Kraml, M., Keller, J. (2008) Towards a detailed distal tephrostratigraphy in the Central Mediterranean: the last 20,000 yrs record of Lago Grande di Monticchio. *Journal of Volcanology and Geothermal Research*, 177, 118-132.

Wulf, S., Kraml, M., Keller, J., Negendank, J.F.W. (2004) Tephrochronology of the 100 ka lacustrine sediment record of Lago Grande di Monticchio (southern Italy). *Quaternary International*, 122, 7–30.

Wulf, S., Ott, F., Słowiński, M., Noryśkiewicz, A.M., Dräger, N., Martin-Puertas, C., Czymzik, M., Neugebauer, I., Dulski, P., Bourne, A.J., Błaszkiewicz, M. (2013) Tracing the Laacher See Tephra in the varved sediment record of the Trzechowskie palaeolake in central Northern Poland. *Quaternary Science Reviews*, 76, 129-139.

Yu, G.E. and Harrison, S.P. (1995) Holocene changes in atmospheric circulation patterns as shown by lake status changes in northern Europe. *Boreas*, 24:3, 260-268.

Yılmaz, Y., Güner, Y., Şaroğlu, F. (1998) Geology of the Quaternary volcanic centres of the East Anatolia. *Journal of volcanology and geothermal research*, 85:1-4, 173-210.

Zanchetta, G., Drysdale, R.N., Hellstrom, J.C., Fallick, A.E., Isola, I., Gagan, M.K., Pareschi, M.T. (2007) Enhanced rainfall in the Western Mediterranean during deposition of sapropel S1: stalagmite evidence from Corchia cave (Central Italy). *Quaternary Science Reviews*, 26:3-4, 279-286.

Zanchetta, G., Sulpizio, R., Roberts, N., Cioni, R., Eastwood, W.J., Siani, G., Caron, B., Paterne, M., Soantacroce, R. (2011) Tephrostratigraphy, chronology and climatic events of the Mediterranean basin during the Holocene: an overview. *The Holocene,* 21,33-52.

Zbinden, H., Andree, M., Oeschger, H., Ammann, B., Lotter, A., Bonani, G., Wölfli, W. (1989) Atmospheric radiocarbon at the end of the last glacial: an estimate based on AMS radiocarbon dates on terrestrial macrofossils from lake sediments. *Radiocarbon*, 31:3, 795-804.

Zolitschka, B., Negendank, J.F.W., Lottermoser, B.G. (1995) Sedimentological proof and dating of the Early Holocene volcanic eruption of Ulmener Maar (Vulkaneifel, Germany). *Geologische Rundschau*, 84, 213-219.

Zoller, H. (1960) Pollenanlytische Untersuchungen zur Vegetationsgeschlichte der insubrishen Schweiz, *Denkerschr. Schweiz. Naturforschience Ges.,* 83, 45-156.

# Appendix 1. Abbreviations

CA – calc-alkaline
CoA – Correspondence Analysis
DCA – Detrended Correspondence Analysis
EH – Early Holocene period
GI – Greenland interstadial
GIC – Greenland ice cores
GS – Greenland stadial
HKCA – High-K calc-alkaline
INTIMATE – INTegrating Ice, MArine and TErresterial records
LG – Last Glacial
LG Lipari – Late Glacial Lipari
LGIT – Last Glacial-Interglacial transition
LGM – Last Glacial Maximum
LGdM - Lago Grande di Monticchio
LOI – Loss on ignition
LST – Laacher See tephra
MEGT - Mount Epomeo Green Tuff
NAP – Non Arboreal pollen
NYT – Neapolitan Yellow Tuff
PAR – Pollen Accumulation Rate
PBO – Preboreal Oscillation
PCA – Principal Component Analysis
PP – Pomici Principali tephra
PrC- Principal Curve Analysis
PROLONG – Providing long environmental records of Late Quaternary climate oscillations in the Retezat Mountains
RoC – Rate of Change Analysis
Saks – Saksunarvatn ash
VA – Vedde Ash
VdG – Vallone del Gabellotto
YD – Younger Dryas

*Hässeldala port is correctly spelt following the Swedish spelling for the site

# Appendix 2 – Tephra geochemistry data

**Table A2.1** Lake Lia tephra geochemistry – non-normalised major and minor geochemistry data

| Depth (cm) | label | OxT Number | Probe date | Beam diam. | $Na_2O$ | MgO | $Al_2O_3$ | $SiO_2$ | $P_2O_5$ | Cl | $K_2O$ | CaO | $TiO_2$ | MnO | $FeO_t$ | Total |
|---|---|---|---|---|---|---|---|---|---|---|---|---|---|---|---|---|
| 576 | LIA_576 | 12039 | 070918 | 5 | 4.25 | 0.03 | 12.38 | 70.58 | 0.02 | 0.36 | 4.81 | 0.66 | 0.05 | 0.04 | 1.32 | 94.49 |
| | LIA_576 | 11833 | 240118 | 5 | 3.80 | 0.05 | 12.40 | 72.17 | 0.04 | 0.35 | 4.93 | 0.69 | 0.11 | 0.03 | 1.46 | 96.03 |
| | LIA_576 | 11833 | 240118 | 5 | 3.88 | 0.02 | 12.30 | 73.31 | 0.03 | 0.33 | 4.86 | 0.65 | 0.11 | 0.07 | 1.63 | 97.19 |
| | LIA_576 | 12039 | 070918 | 5 | 4.02 | 0.04 | 12.32 | 71.50 | 0.00 | 0.38 | 4.88 | 0.71 | 0.05 | 0.03 | 1.38 | 95.31 |
| | LIA_576 | 11833 | 240118 | 5 | 5.18 | 0.24 | 13.20 | 70.38 | 0.05 | 0.15 | 3.57 | 1.36 | 0.31 | 0.17 | 3.78 | 98.41 |
| | LIA_576 | 11833 | 240118 | 5 | 4.16 | 0.25 | 12.06 | 73.84 | 0.03 | 0.10 | 2.50 | 1.62 | 0.35 | 0.16 | 2.35 | 97.43 |
| | LIA_576 | 12039 | 070918 | 5 | 4.72 | 0.24 | 11.77 | 72.01 | 0.05 | 0.05 | 2.55 | 1.54 | 0.33 | 0.09 | 2.48 | 95.84 |
| | LIA_576 | 12039 | 070918 | 5 | 3.73 | 0.01 | 11.70 | 71.45 | 0.00 | 0.10 | 3.82 | 0.88 | 0.07 | 0.07 | 1.26 | 93.10 |
| | LIA_576 | 12039 | 070918 | 5 | 3.29 | 0.13 | 11.55 | 72.92 | 0.08 | 0.06 | 3.30 | 1.25 | 0.19 | 0.06 | 1.30 | 94.13 |
| | LIA_576 | 11833 | 240118 | 5 | 3.70 | 0.07 | 11.71 | 71.31 | 0.01 | 0.12 | 2.51 | 1.02 | 0.14 | 0.10 | 1.63 | 92.34 |
| | LIA_576 | 12039 | 070918 | 5 | 4.08 | 0.04 | 11.75 | 72.44 | 0.00 | 0.13 | 3.69 | 0.53 | 0.07 | 0.03 | 0.60 | 93.35 |
| 589 | LIA_589 | 11364 | 010517 | 10 | 3.74 | 0.01 | 12.05 | 73.68 | 0.00 | 0.11 | 3.96 | 0.57 | 0.02 | 0.07 | 0.78 | 94.99 |
| | LIA_589 | 10864 | 291116 | 5 | 3.27 | 0.02 | 11.96 | 70.16 | 0.00 | 0.38 | 4.56 | 0.55 | 0.07 | 0.09 | 1.16 | 92.20 |
| | LIA_589 | 11592 | 191017 | 5 | 3.65 | 0.08 | 11.87 | 71.80 | 0.00 | 0.10 | 3.21 | 0.52 | 0.02 | 0.06 | 0.74 | 92.05 |
| | LIA_589 | 11592 | 191017 | 5 | 4.07 | 0.01 | 11.74 | 71.79 | 0.01 | 0.09 | 3.22 | 0.48 | 0.00 | 0.07 | 0.90 | 92.40 |
| 591 | LIA_591 | 11591 | 230118 | 5 | 3.63 | 0.03 | 12.33 | 75.73 | 0.00 | 0.11 | 4.54 | 0.51 | 0.16 | 0.03 | 0.50 | 97.58 |
| | LIA_591 | 11591 | 230118 | 5 | 3.73 | 0.00 | 11.88 | 73.49 | 0.01 | 0.12 | 2.95 | 0.60 | 0.02 | 0.00 | 0.82 | 93.61 |
| | LIA_591 | 11591 | 230118 | 5 | 3.77 | 0.04 | 12.19 | 74.42 | 0.03 | 0.09 | 3.34 | 0.59 | 0.09 | 0.03 | 0.71 | 95.30 |
| | LIA_591 | 11591 | 230118 | 5 | 3.63 | 0.09 | 11.95 | 75.00 | 0.02 | 0.11 | 2.77 | 0.68 | 0.13 | 0.09 | 1.18 | 95.64 |
| 600 | LIA_600 | 11927 | 070918 | 5 | 4.17 | 0.30 | 12.09 | 74.25 | 0.08 | 0.05 | 2.53 | 1.64 | 0.34 | 0.10 | 2.41 | 97.96 |

| Depth (cm) | label | OxT Number | Probe date | Beam diam. | $Na_2O$ | MgO | $Al_2O_3$ | $SiO_2$ | $P_2O_5$ | Cl | $K_2O$ | CaO | $TiO_2$ | MnO | $FeO_t$ | Total |
|---|---|---|---|---|---|---|---|---|---|---|---|---|---|---|---|---|
| | LIA_600 | 11927 | 070918 | 5 | 4.35 | 0.29 | 12.32 | 74.49 | 0.06 | 0.04 | 2.52 | 1.62 | 0.30 | 0.04 | 2.51 | 98.56 |
| 600 | LIA_600 | 11927 | 070918 | 5 | 4.50 | 0.24 | 11.95 | 73.21 | 0.01 | 0.08 | 2.46 | 1.64 | 0.32 | 0.08 | 2.27 | 96.78 |
| | LIA_600 | 11927 | 070918 | 5 | 4.37 | 0.24 | 11.79 | 72.65 | 0.09 | 0.05 | 2.48 | 1.58 | 0.38 | 0.12 | 2.50 | 96.25 |
| | LIA_600 | 11927 | 070918 | 5 | 4.30 | 0.23 | 11.75 | 73.70 | 0.05 | 0.08 | 2.47 | 1.64 | 0.30 | 0.09 | 2.41 | 97.02 |
| | LIA_600 | 11927 | 070918 | 5 | 4.46 | 0.24 | 11.64 | 69.95 | 0.09 | 0.07 | 2.44 | 1.57 | 0.32 | 0.06 | 2.57 | 93.42 |
| | LIA_600 | 11927 | 070918 | 5 | 3.69 | 0.18 | 12.19 | 75.03 | 0.05 | 0.07 | 2.49 | 1.65 | 0.29 | 0.04 | 2.56 | 98.24 |
| | LIA_600 | 11927 | 070918 | 5 | 4.09 | 0.07 | 11.91 | 70.29 | 0.00 | 0.36 | 4.72 | 0.76 | 0.08 | 0.00 | 1.40 | 93.69 |
| | LIA_600 | 11927 | 070918 | 5 | 4.84 | 0.00 | 10.68 | 72.46 | 0.00 | 0.32 | 4.06 | 0.14 | 0.06 | 0.11 | 2.25 | 94.93 |
| 603 | LIA_603 | 10863 | 091216 | 5 | 4.09 | 0.24 | 12.27 | 75.86 | 0.01 | 0.08 | 2.53 | 1.66 | 0.29 | 0.13 | 2.79 | 99.94 |
| | LIA_603 | 10863 | 091216 | 5 | 4.43 | 0.21 | 12.05 | 74.64 | 0.02 | 0.08 | 2.58 | 1.58 | 0.29 | 0.06 | 2.79 | 98.73 |
| | LIA_603 | 10863 | 091216 | 5 | 4.46 | 0.24 | 12.34 | 75.54 | 0.06 | 0.07 | 2.60 | 1.57 | 0.33 | 0.16 | 2.49 | 99.87 |
| | LIA_603 | 10863 | 091216 | 5 | 4.36 | 0.26 | 11.86 | 75.02 | 0.08 | 0.10 | 2.52 | 1.62 | 0.27 | 0.07 | 2.59 | 98.74 |
| | LIA_603 | 10863 | 121016 | 10 | 4.20 | 0.25 | 12.32 | 74.49 | 0.07 | 0.11 | 2.59 | 1.50 | 0.33 | 0.16 | 2.57 | 98.58 |
| | LIA_603 | 10863 | 121016 | 10 | 4.56 | 0.26 | 12.23 | 74.18 | 0.04 | 0.08 | 2.55 | 1.60 | 0.28 | 0.13 | 2.57 | 98.48 |
| | LIA_603 | 10863 | 121016 | 10 | 4.15 | 0.25 | 12.21 | 73.60 | 0.05 | 0.08 | 2.47 | 1.57 | 0.27 | 0.09 | 2.55 | 97.27 |
| | LIA_603 | 10863 | 121016 | 10 | 4.37 | 0.29 | 12.32 | 75.00 | 0.07 | 0.09 | 2.57 | 1.71 | 0.27 | 0.05 | 2.57 | 99.30 |
| | LIA_603 | 10863 | 121016 | 10 | 4.43 | 0.26 | 12.27 | 74.30 | 0.02 | 0.06 | 2.70 | 1.54 | 0.26 | 0.10 | 2.37 | 98.30 |
| | LIA_603 | 10863 | 091216 | 5 | 3.90 | 0.04 | 12.35 | 72.15 | 0.01 | 0.37 | 4.78 | 0.66 | 0.03 | 0.02 | 1.24 | 95.55 |
| 607 | LIA_607 | 11593 | 171017 | 5 | 3.96 | 0.03 | 12.24 | 69.62 | 0.00 | 0.38 | 4.83 | 0.70 | 0.06 | 0.01 | 1.12 | 92.96 |
| | LIA_607 | 11593 | 171017 | 5 | 3.84 | 0.00 | 11.95 | 70.58 | 0.00 | 0.38 | 5.26 | 0.56 | 0.09 | 0.00 | 1.01 | 93.66 |
| | LIA_607 | 11593 | 171017 | 5 | 3.89 | 0.02 | 11.99 | 69.90 | 0.00 | 0.38 | 4.97 | 0.67 | 0.09 | 0.03 | 1.43 | 93.37 |
| | LIA_607 | 11593 | 171017 | 5 | 3.82 | 0.05 | 12.37 | 70.82 | 0.00 | 0.34 | 4.75 | 0.71 | 0.10 | 0.00 | 1.61 | 94.58 |
| | LIA_607 | 11593 | 171017 | 5 | 3.95 | 0.03 | 12.17 | 70.01 | 0.00 | 0.35 | 4.77 | 0.63 | 0.17 | 0.00 | 1.24 | 93.33 |

| Depth (cm) | label | OxT Number | Probe date | Beam diam. | $Na_2O$ | MgO | $Al_2O_3$ | $SiO_2$ | $P_2O_5$ | Cl | $K_2O$ | CaO | $TiO_2$ | MnO | $FeO_t$ | Total |
|---|---|---|---|---|---|---|---|---|---|---|---|---|---|---|---|---|
| | LIA_607 | 11593 | 171017 | 5 | 3.74 | 0.03 | 12.08 | 71.32 | 0.00 | 0.31 | 4.69 | 0.64 | 0.01 | 0.08 | 1.07 | 93.97 |
| 607 | LIA_607 | 11593 | 171017 | 5 | 4.14 | 0.01 | 12.26 | 71.16 | 0.04 | 0.36 | 4.69 | 0.59 | 0.03 | 0.12 | 1.31 | 94.72 |
| | LIA_607 | 11593 | 171017 | 5 | 3.71 | 0.01 | 12.17 | 69.36 | 0.00 | 0.33 | 4.95 | 0.73 | 0.11 | 0.14 | 3.43 | 94.94 |
| 610 | LIA_610 | 12040 | 070918 | 5 | 3.85 | 0.07 | 12.52 | 71.92 | 0.00 | 0.39 | 4.72 | 0.83 | 0.07 | 0.11 | 1.58 | 96.07 |
| | LIA_610 | 12040 | 070918 | 5 | 4.15 | 0.02 | 12.14 | 71.86 | 0.03 | 0.35 | 4.81 | 0.71 | 0.09 | 0.00 | 1.28 | 95.43 |
| | LIA_610 | 12040 | 070918 | 5 | 3.98 | 0.01 | 12.44 | 71.66 | 0.01 | 0.36 | 4.71 | 0.70 | 0.09 | 0.08 | 1.22 | 95.25 |
| | LIA_610 | 12040 | 070918 | 5 | 3.84 | 0.04 | 12.22 | 71.64 | 0.08 | 0.39 | 4.61 | 0.73 | 0.06 | 0.06 | 1.27 | 94.94 |
| | LIA_610 | 12040 | 070918 | 5 | 4.06 | 0.08 | 12.09 | 71.60 | 0.00 | 0.40 | 4.65 | 0.63 | 0.07 | 0.13 | 1.28 | 95.00 |
| | LIA_610 | 11840 | 240118 | 5 | 3.63 | 0.03 | 12.29 | 71.86 | 0.00 | 0.33 | 5.05 | 0.66 | 0.10 | 0.12 | 1.19 | 95.25 |
| | LIA_610 | 11840 | 240118 | 5 | 5.40 | 0.19 | 13.02 | 68.98 | 0.02 | 0.16 | 3.48 | 1.36 | 0.29 | 0.13 | 3.81 | 96.85 |
| | LIA_610 | 12040 | 070918 | 5 | 5.08 | 0.19 | 12.75 | 66.48 | 0.04 | 0.26 | 3.33 | 1.32 | 0.29 | 0.09 | 3.68 | 93.52 |
| 612 | LIA_612 | 12041 | 050918 | 10 | 3.91 | 0.02 | 11.75 | 72.38 | 0.02 | 0.11 | 3.33 | 0.58 | 0.01 | 0.03 | 0.80 | 92.92 |
| | LIA_612 | 12041 | 060918 | 5 | 4.86 | 0.03 | 13.16 | 72.89 | 0.03 | 0.04 | 1.94 | 0.36 | 0.06 | 0.06 | 0.75 | 94.19 |
| | LIA_612 | 12041 | 060918 | 5 | 4.02 | 0.03 | 12.25 | 74.71 | 0.01 | 0.10 | 3.44 | 0.58 | 0.06 | 0.00 | 0.78 | 95.98 |
| | LIA_612 | 11834 | 240118 | 5 | 4.38 | 0.17 | 11.89 | 74.83 | 0.04 | 0.03 | 2.28 | 1.08 | 0.27 | 0.04 | 0.84 | 95.85 |
| | LIA_612 | 11834 | 240118 | 5 | 3.72 | 0.04 | 12.49 | 72.08 | 0.03 | 0.39 | 4.74 | 0.71 | 0.13 | 0.06 | 1.40 | 95.81 |
| | LIA_612 | 11834 | 240118 | 5 | 3.65 | 0.04 | 12.35 | 71.62 | 0.04 | 0.35 | 4.82 | 0.75 | 0.05 | 0.02 | 1.54 | 95.22 |
| | LIA_612 | 11834 | 240118 | 5 | 4.15 | 0.06 | 11.97 | 71.30 | 0.02 | 0.43 | 4.69 | 0.64 | 0.09 | 0.10 | 1.34 | 94.79 |
| | LIA_612 | 12041 | 060918 | 5 | 3.73 | 0.04 | 12.49 | 72.47 | 0.00 | 0.32 | 4.97 | 0.62 | 0.03 | 0.05 | 1.36 | 96.07 |
| | LIA_612 | 11834 | 240118 | 5 | 4.18 | 0.02 | 12.44 | 71.81 | 0.05 | 0.40 | 4.77 | 0.71 | 0.12 | 0.07 | 1.49 | 96.06 |
| | LIA_612 | 12041 | 060918 | 5 | 7.06 | 0.23 | 17.65 | 60.99 | 0.00 | 0.67 | 6.24 | 1.13 | 0.45 | 0.17 | 2.33 | 96.92 |
| | LIA_612 | 12041 | 060918 | 5 | 7.20 | 0.30 | 18.21 | 61.60 | 0.05 | 0.71 | 6.52 | 1.16 | 0.50 | 0.17 | 2.52 | 98.95 |
| | LIA_612 | 11834 | 240118 | 5 | 7.33 | 0.25 | 17.84 | 61.08 | 0.03 | 0.70 | 6.24 | 1.17 | 0.50 | 0.25 | 2.29 | 97.68 |

| Depth (cm) | label | OxT Number | Probe date | Beam diam. | $Na_2O$ | MgO | $Al_2O_3$ | $SiO_2$ | $P_2O_5$ | Cl | $K_2O$ | CaO | $TiO_2$ | MnO | $FeO_t$ | Total |
|---|---|---|---|---|---|---|---|---|---|---|---|---|---|---|---|---|
| 613 | LIA_613 | 11928 | 050918 | 10 | 3.69 | 0.01 | 12.26 | 70.40 | 0.00 | 0.38 | 4.76 | 0.75 | 0.08 | 0.05 | 1.30 | 93.67 |
| 613 | LIA_613 | 11928 | 050918 | 10 | 4.08 | 0.02 | 12.02 | 71.16 | 0.01 | 0.33 | 4.91 | 0.68 | 0.04 | 0.11 | 1.31 | 94.66 |
| | LIA_613 | 11928 | 050918 | 10 | 3.76 | 0.02 | 11.99 | 70.39 | 0.00 | 0.35 | 4.61 | 0.60 | 0.06 | 0.00 | 1.40 | 93.18 |
| | LIA_613 | 11928 | 050918 | 10 | 5.26 | 0.20 | 13.34 | 70.18 | 0.05 | 0.19 | 3.61 | 1.38 | 0.30 | 0.23 | 3.67 | 98.42 |
| | LIA_613 | 11928 | 060918 | 5 | 5.45 | 0.23 | 13.59 | 70.32 | 0.07 | 0.19 | 3.42 | 1.30 | 0.27 | 0.08 | 3.89 | 98.81 |
| | LIA_613 | 11928 | 060919 | 5 | 7.40 | 0.33 | 18.65 | 61.91 | 0.05 | 0.77 | 6.42 | 1.05 | 0.52 | 0.26 | 2.56 | 99.92 |
| | LIA_613 | 11928 | 060920 | 5 | 7.79 | 0.31 | 18.12 | 62.07 | 0.03 | 0.70 | 6.16 | 1.13 | 0.58 | 0.27 | 2.36 | 99.54 |
| | LIA_613 | 11928 | 050918 | 10 | 7.59 | 0.28 | 17.06 | 58.45 | 0.06 | 0.69 | 5.87 | 1.12 | 0.52 | 0.21 | 2.43 | 94.28 |
| | LIA_613 | 11920 | 050918 | 10 | 6.32 | 0.03 | 7.05 | 65.92 | 0.00 | 0.98 | 3.89 | 0.42 | 0.32 | 0.28 | 7.81 | 93.0221 |
| 631 | LIA_631 | 12042 | 060918 | 5 | 3.91 | 0.03 | 12.25 | 72.11 | 0.00 | 0.39 | 4.67 | 0.69 | 0.04 | 0.05 | 1.42 | 95.57 |
| | LIA_631 | 12042 | 060918 | 5 | 3.91 | 0.00 | 12.72 | 71.23 | 0.04 | 0.34 | 4.56 | 0.71 | 0.07 | 0.02 | 1.16 | 94.75 |
| | LIA_631 | 11835 | 240118 | 5 | 3.97 | 0.01 | 12.37 | 73.14 | 0.02 | 0.38 | 4.80 | 0.70 | 0.05 | 0.06 | 1.48 | 97.00 |
| | LIA_631 | 11835 | 240118 | 5 | 3.93 | 0.02 | 12.55 | 72.71 | 0.00 | 0.37 | 4.66 | 0.61 | 0.13 | 0.05 | 1.48 | 96.50 |
| | LIA_631 | 11835 | 240118 | 5 | 3.44 | 0.02 | 12.10 | 69.71 | 0.01 | 0.38 | 4.96 | 0.61 | 0.15 | 0.15 | 1.46 | 92.99 |
| | LIA_631 | 11835 | 240118 | 5 | 3.96 | 0.00 | 12.62 | 73.16 | 0.09 | 0.35 | 4.76 | 0.70 | 0.06 | 0.09 | 1.49 | 97.28 |
| | LIA_631 | 11835 | 240118 | 5 | 3.88 | 0.03 | 12.25 | 71.75 | 0.04 | 0.38 | 4.82 | 0.71 | 0.05 | 0.03 | 1.38 | 95.32 |
| | LIA_631 | 11835 | 240118 | 5 | 3.58 | 0.05 | 12.66 | 73.50 | 0.04 | 0.36 | 4.81 | 0.84 | 0.04 | 0.02 | 1.31 | 97.22 |
| | LIA_631 | 11835 | 240118 | 5 | 5.09 | 0.22 | 13.29 | 70.25 | 0.01 | 0.15 | 3.59 | 1.41 | 0.17 | 0.28 | 3.98 | 98.45 |
| | LIA_631 | 11835 | 240118 | 5 | 3.75 | 0.01 | 11.94 | 74.47 | 0.05 | 0.10 | 3.50 | 0.63 | 0.04 | 0.01 | 0.73 | 95.23 |
| | LIA_631 | 11835 | 240118 | 5 | 3.80 | 0.01 | 12.27 | 75.02 | 0.02 | 0.13 | 3.62 | 0.54 | 0.06 | 0.05 | 0.90 | 96.41 |
| | LIA_631 | 12042 | 050918 | 10 | 3.58 | 0.07 | 11.16 | 71.47 | 0.01 | 0.12 | 3.75 | 1.09 | 0.12 | 0.02 | 0.86 | 92.24 |
| | LIA_631 | 12042 | 050918 | 10 | 3.93 | 0.03 | 11.53 | 72.50 | 0.00 | 0.13 | 2.88 | 0.79 | 0.11 | 0.10 | 1.11 | 93.11 |
| | LIA_631 | 12042 | 050918 | 10 | 3.61 | 0.07 | 11.22 | 71.79 | 0.02 | 0.12 | 3.41 | 0.91 | 0.07 | 0.01 | 0.95 | 92.19 |

| Depth (cm) | label | OxT Number | Probe date | Beam diam. | $Na_2O$ | MgO | $Al_2O_3$ | $SiO_2$ | $P_2O_5$ | Cl | $K_2O$ | CaO | $TiO_2$ | MnO | $FeO_t$ | Total |
|---|---|---|---|---|---|---|---|---|---|---|---|---|---|---|---|---|
| 631 | LIA_631 | 12042 | 060918 | 5 | 3.75 | 0.02 | 11.93 | 73.34 | 0.01 | 0.10 | 3.42 | 0.58 | 0.05 | 0.04 | 0.89 | 94.12 |
| 633 | LIA_633 | 11836 | 240118 | 5 | 3.68 | 0.00 | 11.94 | 71.24 | 0.01 | 0.37 | 4.91 | 0.54 | 0.09 | 0.24 | 1.16 | 94.19 |
| | LIA_633 | 11836 | 240118 | 5 | 3.84 | 0.04 | 12.17 | 71.90 | 0.01 | 0.36 | 4.88 | 0.67 | 0.11 | 0.07 | 1.42 | 95.46 |
| | LIA_633 | 11836 | 240118 | 5 | 3.69 | 0.04 | 12.47 | 72.07 | 0.02 | 0.37 | 4.69 | 0.67 | 0.10 | 0.11 | 1.31 | 95.54 |
| | LIA_633 | 11836 | 240118 | 5 | 3.54 | 0.01 | 12.29 | 72.19 | 0.02 | 0.36 | 4.80 | 0.68 | 0.01 | 0.13 | 1.45 | 95.50 |
| | LIA_633 | 11836 | 240118 | 5 | 3.43 | 0.01 | 12.49 | 73.27 | 0.00 | 0.38 | 4.79 | 0.68 | 0.06 | 0.13 | 1.54 | 96.76 |
| | LIA_633 | 11836 | 240118 | 5 | 3.69 | 0.04 | 11.99 | 71.19 | 0.02 | 0.31 | 4.81 | 0.64 | 0.08 | 0.00 | 1.48 | 94.26 |
| | LIA_633 | 11836 | 240118 | 5 | 3.82 | 0.04 | 12.43 | 72.31 | 0.00 | 0.37 | 4.87 | 0.69 | 0.11 | 0.09 | 1.26 | 95.99 |
| | LIA_633 | 11836 | 240118 | 5 | 3.92 | 0.06 | 12.09 | 71.59 | 0.00 | 0.40 | 4.90 | 0.75 | 0.06 | 0.09 | 1.27 | 95.12 |
| | LIA_633 | 12043 | 150419 | 5 | 4.09 | 0.05 | 12.71 | 72.25 | 0.02 | 0.38 | 4.94 | 0.58 | 0.08 | 0.03 | 1.29 | 96.42 |
| | LIA_633 | 11836 | 240118 | 5 | 2.97 | 0.06 | 12.25 | 72.41 | 0.02 | 0.18 | 5.08 | 0.72 | 0.07 | 0.06 | 0.45 | 94.27 |
| | LIA_633 | 12043 | 150419 | 5 | 3.98 | 0.02 | 12.83 | 72.34 | 0.03 | 0.38 | 4.79 | 0.74 | 0.13 | 0.09 | 1.54 | 96.86 |
| | LIA_633 | 12043 | 150419 | 5 | 5.60 | 0.89 | 13.28 | 61.37 | 0.23 | 0.19 | 2.49 | 2.79 | 0.95 | 0.27 | 6.10 | 94.17 |
| | LIA_633 | 11836 | 240118 | 5 | 3.42 | 0.01 | 11.93 | 72.56 | 0.00 | 0.14 | 3.21 | 0.56 | 0.04 | 0.12 | 0.86 | 92.86 |
| | LIA_633 | 12043 | 150419 | 5 | 4.03 | 0.01 | 12.18 | 72.88 | 0.00 | 0.15 | 3.18 | 0.53 | 0.00 | 0.02 | 0.89 | 93.87 |
| | LIA_633 | 12043 | 150419 | 5 | 3.94 | 0.00 | 12.00 | 72.65 | 0.00 | 0.08 | 3.38 | 0.53 | 0.01 | 0.02 | 0.77 | 93.40 |
| | LIA_633 | 12043 | 150419 | 5 | 3.96 | 0.02 | 12.25 | 74.14 | 0.02 | 0.12 | 3.16 | 0.55 | 0.01 | 0.04 | 0.89 | 95.15 |
| | LIA_633 | 12043 | 150419 | 5 | 3.94 | 0.00 | 11.77 | 73.26 | 0.04 | 0.08 | 3.48 | 0.47 | 0.05 | 0.02 | 0.60 | 93.72 |
| | LIA_633 | 12043 | 150419 | 5 | 2.42 | 0.10 | 12.28 | 73.48 | 0.00 | 0.18 | 5.38 | 1.09 | 0.04 | 0.06 | 0.96 | 95.99 |
| 637 | LIA_637 | 11837 | 230118 | 5 | 4.75 | 0.00 | 11.00 | 73.10 | 0.02 | 0.35 | 4.37 | 0.14 | 0.06 | 0.13 | 2.37 | 96.28 |
| | LIA_637 | 11837 | 230118 | 5 | 3.62 | 0.05 | 12.03 | 71.71 | 0.03 | 0.37 | 4.79 | 0.66 | 0.00 | 0.08 | 1.18 | 94.53 |
| | LIA_637 | 11837 | 230118 | 5 | 3.79 | 0.03 | 12.07 | 70.97 | 0.03 | 0.34 | 4.85 | 0.68 | 0.09 | 0.09 | 1.22 | 94.17 |
| | LIA_637 | 11837 | 230118 | 5 | 4.10 | 0.03 | 12.00 | 71.06 | 0.00 | 0.37 | 4.78 | 0.74 | 0.13 | 0.03 | 1.47 | 94.71 |

| Depth (cm) | label | OxT Number | Probe date | Beam diam. | $Na_2O$ | MgO | $Al_2O_3$ | $SiO_2$ | $P_2O_5$ | Cl | $K_2O$ | CaO | $TiO_2$ | MnO | $FeO_t$ | Total |
|---|---|---|---|---|---|---|---|---|---|---|---|---|---|---|---|---|
| 637 | LIA_637 | 11837 | 230118 | 5 | 3.88 | 0.02 | 12.11 | 70.83 | 0.01 | 0.36 | 4.78 | 0.66 | 0.11 | 0.13 | 1.23 | 94.13 |
| | LIA_637 | 11837 | 230118 | 5 | 3.62 | 0.00 | 12.18 | 72.13 | 0.00 | 0.35 | 4.83 | 0.56 | 0.10 | 0.00 | 1.21 | 94.97 |
| | LIA_637 | 11837 | 230118 | 5 | 3.99 | 0.07 | 11.85 | 72.64 | 0.03 | 0.11 | 2.77 | 0.97 | 0.09 | 0.00 | 0.96 | 93.47 |
| | LIA_637 | 11837 | 230118 | 5 | 3.40 | 0.04 | 11.80 | 72.01 | 0.03 | 0.14 | 3.32 | 0.65 | 0.04 | 0.00 | 0.76 | 92.19 |
| | LIA_637 | 11837 | 230118 | 5 | 3.71 | 0.05 | 12.05 | 72.68 | 0.00 | 0.11 | 3.12 | 0.54 | 0.06 | 0.01 | 0.87 | 93.19 |
| 686 | LIA_686 | 12044 | 070918 | 5 | 3.26 | 0.03 | 11.78 | 74.07 | 0.02 | 0.16 | 3.92 | 0.65 | 0.07 | 0.00 | 1.02 | 94.98 |
| | LIA_686 | 12044 | 070918 | 5 | 3.12 | 0.00 | 11.49 | 72.56 | 0.05 | 0.13 | 3.90 | 0.60 | 0.09 | 0.01 | 0.97 | 92.90 |
| | LIA_686 | 12044 | 070918 | 5 | 3.85 | 0.09 | 11.61 | 72.95 | 0.06 | 0.14 | 2.88 | 0.91 | 0.04 | 0.09 | 0.89 | 93.51 |
| | LIA_686 | 12044 | 070918 | 5 | 4.23 | 0.02 | 11.88 | 73.23 | 0.03 | 0.13 | 2.96 | 0.55 | 0.06 | 0.03 | 0.71 | 93.83 |
| | LIA_686 | 12044 | 070918 | 5 | 3.30 | 0.06 | 11.64 | 72.60 | 0.00 | 0.10 | 2.63 | 0.73 | 0.08 | 0.00 | 0.96 | 92.09 |
| | LIA_686 | 11121 | 291116 | 5 | 3.18 | 0.12 | 11.70 | 72.39 | 0.03 | 0.12 | 3.04 | 0.92 | 0.12 | 0.07 | 1.02 | 92.72 |
| | LIA_686 | 11121 | 291116 | 5 | 3.72 | 0.11 | 11.80 | 73.34 | 0.00 | 0.13 | 2.28 | 0.88 | 0.11 | 0.00 | 0.86 | 93.24 |
| | LIA_686 | 11121 | 291116 | 5 | 3.76 | 0.06 | 11.83 | 72.64 | 0.01 | 0.12 | 3.29 | 0.99 | 0.03 | 0.04 | 1.15 | 93.92 |
| | LIA_686 | 11121 | 291116 | 5 | 3.46 | 0.01 | 11.93 | 75.31 | 0.03 | 0.30 | 5.00 | 0.42 | 0.09 | 0.00 | 1.06 | 97.61 |
| | LIA_686 | 11121 | 291116 | 5 | 3.86 | 0.00 | 12.50 | 72.40 | 0.00 | 0.36 | 4.59 | 0.63 | 0.10 | 0.04 | 1.29 | 95.78 |
| | LIA_686 | 11363 | 191017 | 5 | 3.65 | 0.03 | 12.36 | 72.45 | 0.00 | 0.38 | 4.78 | 0.68 | 0.03 | 0.05 | 1.35 | 95.76 |
| | LIA_686 | 11363 | 191017 | 5 | 4.73 | 0.00 | 11.27 | 71.54 | 0.00 | 0.43 | 4.43 | 0.34 | 0.20 | 0.22 | 2.70 | 95.87 |
| 713 | LIA_713 | 11122 | 291116 | 5 | 3.39 | 0.06 | 11.61 | 73.20 | 0.02 | 0.12 | 3.38 | 0.56 | 0.04 | 0.00 | 0.80 | 93.20 |
| 769 | LIA_769 | 11366 | 191017 | 5 | 4.39 | 0.03 | 11.90 | 73.38 | 0.01 | 0.10 | 3.20 | 0.56 | 0.01 | 0.09 | 0.80 | 94.47 |
| | LIA_769 | 11366 | 191017 | 5 | 3.43 | 0.02 | 11.87 | 73.81 | 0.00 | 0.11 | 4.32 | 0.66 | 0.07 | 0.12 | 0.91 | 95.32 |
| | LIA_769 | 10881 | 291116 | 5 | 3.41 | 0.11 | 11.51 | 72.52 | 0.04 | 0.13 | 2.90 | 0.95 | 0.04 | 0.01 | 1.04 | 92.65 |
| | LIA_769 | 10881 | 291116 | 5 | 4.19 | 0.05 | 11.98 | 73.94 | 0.00 | 0.09 | 3.63 | 0.49 | 0.03 | 0.05 | 0.80 | 95.25 |

| Depth (cm) | label | OxT Number | Probe date | Beam diam. | $Na_2O$ | MgO | $Al_2O_3$ | $SiO_2$ | $P_2O_5$ | Cl | $K_2O$ | CaO | $TiO_2$ | MnO | $FeO_t$ | Total |
|---|---|---|---|---|---|---|---|---|---|---|---|---|---|---|---|---|
| 796 | LIA_796 | 11365 | 171017 | 5 | 3.68 | 0.06 | 11.70 | 73.19 | 0.03 | 0.11 | 2.60 | 0.96 | 0.14 | 0.01 | 1.02 | 93.48 |
| | LIA_796 | 11365 | 171017 | 5 | 4.42 | 0.05 | 11.94 | 75.02 | 0.00 | 0.15 | 2.45 | 0.63 | 0.06 | 0.06 | 1.00 | 95.79 |
| | LIA_796 | 11365 | 171017 | 5 | 3.83 | 0.03 | 11.69 | 73.35 | 0.00 | 0.09 | 2.77 | 0.54 | 0.04 | 0.07 | 0.99 | 93.41 |
| | LIA_796 | 11926 | 050918 | 10 | 4.32 | 0.06 | 11.39 | 73.00 | 0.01 | 0.15 | 3.03 | 0.73 | 0.03 | 0.07 | 1.15 | 93.94 |
| | LIA_796 | 11926 | 050918 | 10 | 4.04 | 0.07 | 11.59 | 72.15 | 0.00 | 0.11 | 2.49 | 0.83 | 0.07 | 0.02 | 0.89 | 92.26 |
| | LIA_796 | 11926 | 050918 | 10 | 3.96 | 0.06 | 11.75 | 72.93 | 0.01 | 0.14 | 2.73 | 0.82 | 0.08 | 0.10 | 1.28 | 93.84 |
| | LIA_796 | 11926 | 060918 | 5 | 4.24 | 0.00 | 11.86 | 72.85 | 0.04 | 0.12 | 2.83 | 0.62 | 0.03 | 0.04 | 0.74 | 93.37 |
| | LIA_796 | 11926 | 060918 | 5 | 4.12 | 0.06 | 11.94 | 73.28 | 0.00 | 0.09 | 2.94 | 0.59 | 0.09 | 0.00 | 0.80 | 93.90 |
| | LIA_796 | 10865 | 191017 | 5 | 3.99 | 0.02 | 11.74 | 72.26 | 0.02 | 0.09 | 3.15 | 0.61 | 0.00 | 0.06 | 0.66 | 92.58 |
| | LIA_796 | 10865 | 091216 | 5 | 3.95 | 0.04 | 11.99 | 73.09 | 0.00 | 0.11 | 3.31 | 0.55 | 0.06 | 0.05 | 0.74 | 93.88 |
| | LIA_796 | 10865 | 091216 | 5 | 3.86 | 0.03 | 11.91 | 73.67 | 0.01 | 0.11 | 3.41 | 0.52 | 0.00 | 0.05 | 0.81 | 94.39 |
| | LIA_796 | 11926 | 050918 | 10 | 4.03 | 0.03 | 12.01 | 73.14 | 0.00 | 0.09 | 3.43 | 0.55 | 0.05 | 0.06 | 0.87 | 94.25 |
| | LIA_796 | 11926 | 060918 | 5 | 3.75 | 0.06 | 12.27 | 73.99 | 0.00 | 0.10 | 3.49 | 0.53 | 0.06 | 0.12 | 0.89 | 95.25 |
| | LIA_796 | 10865 | 191017 | 5 | 4.05 | 0.03 | 11.92 | 73.31 | 0.01 | 0.11 | 3.48 | 0.50 | 0.02 | 0.08 | 0.96 | 94.49 |
| | LIA_796 | 11365 | 171017 | 5 | 3.72 | 0.03 | 12.08 | 73.59 | 0.04 | 0.11 | 3.49 | 0.59 | 0.10 | 0.07 | 0.77 | 94.58 |
| | LIA_796 | 10865 | 091216 | 5 | 4.05 | 0.04 | 12.21 | 73.42 | 0.02 | 0.12 | 3.54 | 0.54 | 0.02 | 0.08 | 0.88 | 94.91 |
| | LIA_796 | 11926 | 050918 | 10 | 3.25 | 0.08 | 11.34 | 72.71 | 0.00 | 0.17 | 3.49 | 1.12 | 0.15 | 0.00 | 1.11 | 93.42 |
| | LIA_796 | 11365 | 171017 | 5 | 3.49 | 0.02 | 12.06 | 74.01 | 0.00 | 0.10 | 3.58 | 0.71 | 0.04 | 0.10 | 0.97 | 95.09 |
| | LIA_796 | 11926 | 060918 | 5 | 3.58 | 0.05 | 11.32 | 72.55 | 0.04 | 0.14 | 3.68 | 0.78 | 0.03 | 0.03 | 1.08 | 93.26 |
| | LIA_796 | 11365 | 171017 | 5 | 3.50 | 0.05 | 11.73 | 73.61 | 0.00 | 0.11 | 3.90 | 0.82 | 0.08 | 0.00 | 0.44 | 94.25 |
| | LIA_796 | 11365 | 171017 | 5 | 2.50 | 0.05 | 11.89 | 74.63 | 0.03 | 0.09 | 4.98 | 0.74 | 0.02 | 0.00 | 0.91 | 95.84 |
| | LIA_796 | 11365 | 171017 | 5 | 2.40 | 0.03 | 12.28 | 76.20 | 0.03 | 0.17 | 5.27 | 1.00 | 0.06 | 0.01 | 0.70 | 98.16 |
| | LIA_796 | 11365 | 171017 | 5 | 2.58 | 0.06 | 11.51 | 71.46 | 0.01 | 0.22 | 5.00 | 0.91 | 0.06 | 0.11 | 0.96 | 92.88 |

| Depth (cm) | label | OxT Number | Probe date | Beam diam. | $Na_2O$ | MgO | $Al_2O_3$ | $SiO_2$ | $P_2O_5$ | Cl | $K_2O$ | CaO | $TiO_2$ | MnO | $FeO_t$ | Total |
|---|---|---|---|---|---|---|---|---|---|---|---|---|---|---|---|---|
| 796 | LIA_796 | 10865 | 191017 | 5 | 1.93 | 0.05 | 12.22 | 74.13 | 0.00 | 0.10 | 5.20 | 0.97 | 0.11 | 0.01 | 0.95 | 95.64 |
| | LIA_796 | 11926 | 050918 | 10 | 2.77 | 0.06 | 11.55 | 73.45 | 0.01 | 0.13 | 5.20 | 0.60 | 0.07 | 0.00 | 0.92 | 94.77 |
| | LIA_796 | 11365 | 171017 | 5 | 4.43 | 0.45 | 18.12 | 60.31 | 0.04 | 0.67 | 8.31 | 2.11 | 0.45 | 0.01 | 2.85 | 97.76 |
| 805 | LIA_805 | 11838 | 230118 | 5 | 4.04 | 0.06 | 11.63 | 73.52 | 0.05 | 0.12 | 2.79 | 0.76 | 0.10 | 0.04 | 1.09 | 94.19 |
| | LIA_805 | 11838 | 230118 | 5 | 3.56 | 0.04 | 11.80 | 71.83 | 0.01 | 0.14 | 3.11 | 0.91 | 0.11 | 0.09 | 1.14 | 92.73 |
| | LIA_805 | 11838 | 230118 | 5 | 3.36 | 0.03 | 11.60 | 73.05 | 0.02 | 0.11 | 3.19 | 0.66 | 0.06 | 0.03 | 1.10 | 93.21 |
| | LIA_805 | 11838 | 230118 | 5 | 3.55 | 0.02 | 11.92 | 73.87 | 0.00 | 0.14 | 3.48 | 0.51 | 0.03 | 0.00 | 0.73 | 94.26 |
| | LIA_805 | 11838 | 230118 | 5 | 2.97 | 0.04 | 11.33 | 72.00 | 0.07 | 0.09 | 4.06 | 0.57 | 0.00 | 0.00 | 0.97 | 92.11 |
| | LIA_805 | 11838 | 230118 | 5 | 3.19 | 0.03 | 11.52 | 72.07 | 0.00 | 0.11 | 3.76 | 0.59 | 0.12 | 0.13 | 0.67 | 92.20 |
| | LIA_805 | 11838 | 230118 | 5 | 3.92 | 0.02 | 11.82 | 73.38 | 0.03 | 0.12 | 3.41 | 0.58 | 0.00 | 0.00 | 0.81 | 94.07 |
| | LIA_805 | 11838 | 230118 | 5 | 3.25 | 0.02 | 11.64 | 73.62 | 0.02 | 0.12 | 4.10 | 0.61 | 0.09 | 0.08 | 0.94 | 94.49 |
| | LIA_805 | 11838 | 230118 | 5 | 3.16 | 0.01 | 11.90 | 72.36 | 0.00 | 0.13 | 3.29 | 0.61 | 0.00 | 0.00 | 0.77 | 92.23 |
| | LIA_805 | 11838 | 230118 | 5 | 3.24 | 0.01 | 11.78 | 73.01 | 0.01 | 0.10 | 3.96 | 0.62 | 0.09 | 0.06 | 0.85 | 93.73 |
| | LIA_805 | 11838 | 230118 | 5 | 3.80 | 0.11 | 11.26 | 71.54 | 0.01 | 0.11 | 3.28 | 1.00 | 0.12 | 0.09 | 0.96 | 92.29 |
| | LIA_805 | 11838 | 230118 | 5 | 3.04 | 0.07 | 11.41 | 72.47 | 0.02 | 0.13 | 3.49 | 0.88 | 0.08 | 0.06 | 1.14 | 92.78 |
| 815 | LIA_815 | 11841 | 240118 | 5 | 3.63 | 0.11 | 11.79 | 72.12 | 0.05 | 0.14 | 2.80 | 0.95 | 0.17 | 0.18 | 0.94 | 92.88 |
| | LIA_815 | 11841 | 240118 | 5 | 3.55 | 0.07 | 11.49 | 72.26 | 0.01 | 0.12 | 2.94 | 0.95 | 0.13 | 0.10 | 0.88 | 92.50 |
| | LIA_815 | 11841 | 240118 | 5 | 3.88 | 0.06 | 11.58 | 72.89 | 0.00 | 0.14 | 2.74 | 0.72 | 0.06 | 0.14 | 1.17 | 93.39 |
| | LIA_815 | 11841 | 240118 | 5 | 3.86 | 0.06 | 11.53 | 73.53 | 0.00 | 0.12 | 2.61 | 0.72 | 0.11 | 0.07 | 1.45 | 94.04 |
| | LIA_815 | 11841 | 240118 | 5 | 4.41 | 0.03 | 11.83 | 73.65 | 0.00 | 0.11 | 2.63 | 0.53 | 0.01 | 0.03 | 0.79 | 94.02 |
| | LIA_815 | 11841 | 240118 | 5 | 3.96 | 0.03 | 11.53 | 72.77 | 0.00 | 0.14 | 2.78 | 0.76 | 0.07 | 0.00 | 1.10 | 93.14 |
| | LIA_815 | 11841 | 240118 | 5 | 3.74 | 0.07 | 11.63 | 73.44 | 0.00 | 0.15 | 2.72 | 0.73 | 0.06 | 0.03 | 0.99 | 93.55 |
| | LIA_815 | 11841 | 240118 | 5 | 3.20 | 0.02 | 11.72 | 72.41 | 0.02 | 0.15 | 4.07 | 0.52 | 0.08 | 0.00 | 0.96 | 93.15 |

| Depth (cm) | label | OxT Number | Probe date | Beam diam. | $Na_2O$ | MgO | $Al_2O_3$ | $SiO_2$ | $P_2O_5$ | Cl | $K_2O$ | CaO | $TiO_2$ | MnO | $FeO_t$ | Total |
|---|---|---|---|---|---|---|---|---|---|---|---|---|---|---|---|---|
| | LIA_815 | 11841 | 240118 | 5 | 3.45 | 0.02 | 11.77 | 72.07 | 0.00 | 0.13 | 3.28 | 0.63 | 0.05 | 0.05 | 0.80 | 92.25 |
| 829 | LIA_829 | 11839 | 230118 | 5 | 4.14 | 0.04 | 12.07 | 73.86 | 0.02 | 0.09 | 2.87 | 0.67 | 0.10 | 0.02 | 0.72 | 94.59 |
| | LIA_829 | 11839 | 230118 | 5 | 3.39 | 0.01 | 11.33 | 73.22 | 0.00 | 0.07 | 4.06 | 0.60 | 0.11 | 0.00 | 0.97 | 93.77 |
| | LIA_829 | 11839 | 230118 | 5 | 3.52 | 0.02 | 11.71 | 72.94 | 0.01 | 0.10 | 3.31 | 0.55 | 0.03 | 0.00 | 0.91 | 93.09 |
| | LIA_829 | 11839 | 230118 | 5 | 4.21 | 0.01 | 11.95 | 73.05 | 0.02 | 0.11 | 2.75 | 0.51 | 0.01 | 0.00 | 0.53 | 93.16 |

**Table A2.2** Lake Brazi tephra major and minor geochemistry – non-normalised

| Depth (cm) | label | OxT Number | Probe date | Beam diam. | $Na_2O$ | MgO | $Al_2O_3$ | $SiO_2$ | $P_2O_5$ | Cl | $K_2O$ | CaO | $TiO_2$ | MnO | $FeO_t$ | Total |
|---|---|---|---|---|---|---|---|---|---|---|---|---|---|---|---|---|
| 540 | TDB_540 | 11434 | 010517 | 10 | 4.23 | 0.25 | 11.87 | 72.25 | 0.05 | 0.07 | 2.51 | 1.66 | 0.33 | 0.15 | 2.52 | 95.89 |
| | TDB_540 | 11434 | 010517 | 10 | 4.09 | 0.23 | 12.30 | 74.36 | 0.03 | 0.05 | 2.59 | 1.65 | 0.29 | 0.06 | 2.42 | 98.08 |
| | TDB_540 | 11587 | 260118 | 5 | 3.98 | 0.05 | 12.90 | 72.95 | 0.01 | 0.42 | 4.80 | 0.72 | 0.06 | 0.10 | 1.32 | 97.30 |
| | TDB_540 | 11587 | 260118 | 5 | 3.89 | 0.01 | 12.40 | 74.02 | 0.01 | 0.09 | 3.29 | 0.55 | 0.05 | 0.09 | 0.93 | 95.33 |
| | TDB_540 | 11587 | 260118 | 5 | 3.56 | 0.05 | 12.00 | 75.63 | 0.01 | 0.12 | 3.59 | 0.56 | 0.01 | 0.00 | 0.73 | 96.25 |
| | TDB_540 | 11587 | 260118 | 5 | 3.78 | 0.03 | 12.42 | 74.15 | 0.01 | 0.08 | 3.73 | 0.57 | 0.01 | 0.05 | 0.68 | 95.50 |
| | TDB_540 | 11587 | 260118 | 5 | 4.21 | 0.04 | 12.53 | 74.20 | 0.00 | 0.10 | 3.18 | 0.80 | 0.10 | 0.00 | 0.88 | 96.02 |
| 541 | TDB_541 | 11588 | 260118 | 5 | 5.21 | 0.00 | 11.46 | 73.04 | 0.04 | 0.38 | 3.71 | 0.22 | 0.04 | 0.07 | 2.25 | 96.43 |
| | TDB_541 | 11588 | 260118 | 5 | 3.44 | 0.09 | 12.62 | 72.50 | 0.05 | 0.14 | 4.77 | 0.74 | 0.10 | 0.00 | 1.08 | 95.53 |
| | TDB_541 | 11512 | 260617 | 5 | 3.83 | 0.06 | 12.46 | 71.30 | 0.03 | 0.36 | 4.88 | 0.73 | 0.07 | 0.07 | 1.44 | 95.23 |
| | TDB_541 | 11512 | 260617 | 5 | 3.25 | 0.01 | 11.71 | 72.73 | 0.04 | 0.10 | 4.38 | 0.66 | 0.06 | 0.02 | 0.96 | 93.92 |
| | TDB_541 | 11512 | 260617 | 5 | 4.35 | 0.22 | 11.87 | 73.68 | 0.01 | 0.07 | 2.46 | 1.48 | 0.33 | 0.12 | 2.44 | 97.04 |
| | TDB_541 | 11588 | 260118 | 5 | 4.31 | 0.17 | 12.39 | 75.65 | 0.04 | 0.05 | 2.62 | 1.50 | 0.33 | 0.21 | 2.41 | 99.69 |
| | TDB_541 | 11588 | 260118 | 5 | 4.23 | 0.25 | 11.56 | 70.19 | 0.07 | 0.13 | 2.40 | 1.54 | 0.25 | 0.20 | 2.50 | 93.33 |
| 546 | TDB_546 | 11583 | 250117 | 5 | 3.19 | 0.03 | 11.78 | 73.42 | 0.00 | 0.12 | 3.87 | 0.60 | 0.07 | 0.05 | 0.91 | 94.04 |
| | TDB_546 | 11583 | 250117 | 5 | 4.05 | 0.06 | 12.11 | 74.64 | 0.01 | 0.09 | 3.08 | 0.80 | 0.04 | 0.00 | 0.97 | 95.85 |
| | TDB_546 | 11583 | 250117 | 5 | 3.66 | 0.00 | 12.11 | 74.03 | 0.00 | 0.07 | 3.64 | 0.57 | 0.01 | 0.04 | 0.72 | 94.84 |
| | TDB_546 | 11583 | 250117 | 5 | 3.65 | 0.02 | 11.99 | 74.34 | 0.02 | 0.11 | 3.77 | 0.55 | 0.02 | 0.04 | 0.69 | 95.21 |
| | TDB_546 | 11583 | 250117 | 5 | 3.66 | 0.05 | 12.51 | 73.07 | 0.03 | 0.40 | 4.80 | 0.73 | 0.08 | 0.09 | 1.30 | 96.73 |
| | TDB_546 | 11583 | 250117 | 5 | 4.99 | 0.20 | 13.05 | 69.03 | 0.02 | 0.21 | 3.34 | 1.29 | 0.22 | 0.15 | 3.70 | 96.20 |

| Depth (cm) | label | OxT Number | Probe date | Beam diam. | $Na_2O$ | MgO | $Al_2O_3$ | $SiO_2$ | $P_2O_5$ | Cl | $K_2O$ | CaO | $TiO_2$ | MnO | $FeO_t$ | Total |
|---|---|---|---|---|---|---|---|---|---|---|---|---|---|---|---|---|
| 549 | TDB_549 | 11513 | 260617 | 5 | 3.60 | 0.04 | 12.57 | 72.64 | 0.00 | 0.35 | 4.86 | 0.64 | 0.08 | 0.10 | 1.37 | 96.25 |
| 554 | TDB_554 | 11584 | 070918 | 5 | 4.01 | 0.05 | 11.71 | 72.88 | 0.00 | 0.12 | 3.40 | 0.61 | 0.05 | 0.05 | 0.74 | 93.62 |
| | TDB_554 | 11584 | 070918 | 5 | 3.89 | 0.00 | 11.76 | 72.59 | 0.01 | 0.13 | 3.68 | 0.57 | 0.01 | 0.07 | 0.74 | 93.46 |
| | TDB_554 | 11584 | 070918 | 5 | 3.30 | 0.04 | 11.86 | 72.98 | 0.01 | 0.11 | 4.12 | 0.52 | 0.00 | 0.15 | 0.78 | 93.87 |
| 556 | TDB_556 | 11590 | 171017 | 5 | 4.01 | 0.02 | 12.11 | 71.56 | 0.01 | 0.10 | 3.30 | 0.87 | 0.03 | 0.10 | 1.20 | 93.31 |
| | TDB_556 | 11590 | 171017 | 5 | 4.10 | 0.01 | 11.71 | 72.71 | 0.01 | 0.12 | 3.00 | 0.79 | 0.10 | 0.07 | 1.16 | 93.78 |
| | TDB_556 | 11590 | 171017 | 5 | 4.12 | 0.00 | 11.76 | 72.25 | 0.03 | 0.09 | 3.14 | 0.50 | 0.10 | 0.13 | 0.89 | 93.01 |
| | TDB_556 | 11590 | 171017 | 5 | 3.85 | 0.06 | 11.70 | 71.93 | 0.01 | 0.10 | 3.35 | 0.55 | 0.05 | 0.04 | 0.71 | 92.36 |
| | TDB_556 | 11590 | 171017 | 5 | 4.31 | 0.00 | 11.68 | 72.67 | 0.00 | 0.09 | 3.46 | 0.59 | 0.00 | 0.00 | 0.60 | 93.38 |
| | TDB_556 | 11590 | 171017 | 5 | 4.04 | 0.03 | 11.73 | 72.88 | 0.00 | 0.14 | 3.34 | 0.56 | 0.04 | 0.13 | 0.86 | 93.75 |
| | TDB_556 | 11590 | 171017 | 5 | 4.15 | 0.02 | 11.79 | 71.57 | 0.03 | 0.09 | 3.73 | 0.53 | 0.01 | 0.12 | 0.79 | 92.84 |
| | TDB_556 | 11590 | 171017 | 5 | 3.99 | 0.01 | 11.64 | 71.82 | 0.00 | 0.11 | 3.59 | 0.56 | 0.01 | 0.02 | 0.88 | 92.62 |
| | TDB_556 | 11590 | 171017 | 5 | 3.95 | 0.01 | 11.71 | 71.80 | 0.00 | 0.12 | 3.69 | 0.54 | 0.04 | 0.00 | 0.86 | 92.73 |
| | TDB_556 | 11590 | 171017 | 5 | 3.70 | 0.01 | 11.75 | 71.72 | 0.00 | 0.14 | 3.70 | 0.55 | 0.06 | 0.06 | 0.87 | 92.56 |
| | TDB_556 | 11590 | 171017 | 5 | 4.38 | 0.03 | 11.65 | 72.60 | 0.04 | 0.13 | 2.84 | 0.48 | 0.06 | 0.00 | 0.71 | 92.93 |
| | TDB_556 | 11590 | 171017 | 5 | 3.03 | 0.05 | 11.56 | 71.87 | 0.00 | 0.12 | 3.95 | 0.59 | 0.06 | 0.01 | 0.94 | 92.17 |
| | TDB_556 | 11362 | 010517 | 10 | 3.90 | 0.04 | 11.93 | 72.83 | 0.01 | 0.10 | 2.62 | 0.53 | 0.02 | 0.00 | 0.76 | 92.74 |
| | TDB_556 | 11362 | 010517 | 10 | 3.04 | 0.04 | 11.90 | 72.30 | 0.05 | 0.12 | 3.65 | 0.74 | 0.03 | 0.07 | 0.89 | 92.81 |
| | TDB_556 | 11362 | 010517 | 10 | 3.73 | 0.04 | 11.98 | 72.46 | 0.04 | 0.12 | 3.16 | 0.56 | 0.02 | 0.09 | 0.63 | 92.82 |
| | TDB_556 | 11362 | 010517 | 10 | 3.30 | 0.09 | 11.92 | 72.63 | 0.01 | 0.14 | 2.78 | 1.03 | 0.12 | 0.03 | 0.89 | 92.95 |
| | TDB_556 | 11362 | 010517 | 10 | 3.64 | 0.03 | 12.27 | 72.75 | 0.02 | 0.10 | 3.62 | 0.61 | 0.04 | 0.03 | 0.80 | 93.91 |
| | TDB_556 | 11362 | 010517 | 10 | 3.69 | 0.01 | 12.10 | 73.41 | 0.02 | 0.10 | 4.01 | 0.57 | 0.00 | 0.06 | 0.71 | 94.70 |

| Depth (cm) | label | OxT Number | Probe date | Beam diam. | $Na_2O$ | MgO | $Al_2O_3$ | $SiO_2$ | $P_2O_5$ | Cl | $K_2O$ | CaO | $TiO_2$ | MnO | $FeO_t$ | Total |
|---|---|---|---|---|---|---|---|---|---|---|---|---|---|---|---|---|
| 556 | TDB_556 | 11362 | 010517 | 10 | 3.87 | 0.05 | 11.71 | 72.70 | 0.00 | 0.13 | 1.99 | 0.71 | 0.03 | 0.05 | 1.15 | 92.40 |
| 556 | TDB_556 | 11590 | 070918 | 5 | 3.66 | 0.09 | 11.68 | 72.44 | 0.00 | 0.13 | 2.80 | 1.01 | 0.11 | 0.03 | 1.08 | 93.04 |
| | TDB_556 | 11590 | 070918 | 5 | 3.75 | 0.03 | 11.87 | 72.42 | 0.00 | 0.10 | 3.84 | 0.60 | 0.04 | 0.01 | 0.71 | 93.39 |
| | TDB_556 | 11590 | 070918 | 5 | 4.05 | 0.02 | 11.62 | 73.01 | 0.00 | 0.09 | 3.58 | 0.55 | 0.07 | 0.02 | 0.79 | 93.79 |
| | TDB_556 | 11590 | 070918 | 5 | 4.48 | 0.02 | 11.67 | 72.69 | 0.00 | 0.10 | 3.37 | 0.50 | 0.06 | 0.09 | 0.77 | 93.77 |
| | TDB_556 | 11590 | 070918 | 5 | 3.93 | 0.01 | 11.97 | 73.50 | 0.03 | 0.09 | 3.65 | 0.52 | 0.03 | 0.14 | 0.77 | 94.64 |
| | TDB_556 | 11590 | 171017 | 5 | 3.96 | 0.00 | 12.30 | 69.76 | 0.00 | 0.39 | 4.64 | 0.65 | 0.06 | 0.00 | 1.37 | 93.13 |
| | TDB_556 | 11590 | 171017 | 5 | 3.88 | 0.02 | 12.29 | 70.78 | 0.00 | 0.41 | 4.72 | 0.65 | 0.10 | 0.05 | 1.11 | 94.01 |
| | TDB_556 | 11590 | 171017 | 5 | 4.07 | 0.04 | 12.36 | 70.89 | 0.00 | 0.32 | 4.75 | 0.67 | 0.12 | 0.03 | 1.37 | 94.62 |
| | TDB_556 | 11590 | 171017 | 5 | 3.93 | 0.02 | 12.04 | 70.35 | 0.00 | 0.35 | 5.05 | 0.66 | 0.04 | 0.09 | 1.31 | 93.84 |
| | TDB_556 | 11590 | 171017 | 5 | 3.93 | 0.03 | 11.84 | 69.49 | 0.01 | 0.37 | 4.74 | 0.78 | 0.06 | 0.03 | 1.16 | 92.44 |
| | TDB_556 | 11590 | 171017 | 5 | 3.80 | 0.03 | 11.73 | 69.16 | 0.04 | 0.41 | 4.71 | 0.68 | 0.11 | 0.11 | 1.42 | 92.20 |
| | TDB_556 | 11590 | 171017 | 5 | 3.77 | 0.01 | 11.82 | 70.08 | 0.03 | 0.42 | 4.82 | 0.56 | 0.04 | 0.07 | 1.17 | 92.79 |
| | TDB_556 | 11362 | 010517 | 10 | 3.79 | 0.01 | 12.43 | 71.18 | 0.00 | 0.34 | 4.92 | 0.67 | 0.05 | 0.03 | 1.35 | 94.79 |
| | TDB_556 | 11362 | 010517 | 10 | 3.65 | 0.02 | 12.31 | 71.84 | 0.03 | 0.35 | 5.04 | 0.58 | 0.06 | 0.04 | 1.39 | 95.31 |
| | TDB_556 | 11590 | 070918 | 5 | 4.02 | 0.05 | 12.51 | 71.74 | 0.02 | 0.09 | 3.87 | 0.91 | 0.08 | 0.07 | 1.28 | 94.64 |
| | TDB_556 | 11590 | 070918 | 5 | 3.78 | 0.02 | 11.91 | 70.67 | 0.00 | 0.35 | 4.94 | 0.67 | 0.01 | 0.09 | 1.31 | 93.75 |
| | TDB_556 | 11590 | 070918 | 5 | 4.17 | 0.05 | 12.46 | 71.98 | 0.00 | 0.36 | 4.66 | 0.68 | 0.08 | 0.02 | 1.27 | 95.72 |
| | TDB_556 | 11590 | 070918 | 5 | 4.35 | 0.03 | 12.17 | 71.22 | 0.01 | 0.34 | 4.69 | 0.61 | 0.01 | 0.07 | 1.15 | 94.67 |
| | TDB_556 | 11362 | 010517 | 10 | 3.60 | 0.05 | 12.44 | 71.84 | 0.02 | 0.40 | 4.88 | 0.68 | 0.03 | 0.05 | 1.34 | 95.33 |
| 559 | TDB_559 | 11514 | 191017 | 5 | 3.71 | 0.04 | 11.72 | 73.81 | 0.00 | 0.09 | 3.68 | 0.60 | 0.07 | 0.16 | 0.81 | 94.69 |
| | TDB_559 | 11514 | 191017 | 5 | 3.59 | 0.03 | 11.60 | 72.32 | 0.00 | 0.11 | 3.33 | 0.54 | 0.07 | 0.09 | 0.73 | 92.40 |
| | TDB_559 | 11514 | 191017 | 5 | 3.74 | 0.02 | 12.00 | 73.57 | 0.04 | 0.10 | 3.59 | 0.56 | 0.04 | 0.03 | 0.79 | 94.49 |

| Depth (cm) | label | OxT Number | Probe date | Beam diam. | $Na_2O$ | MgO | $Al_2O_3$ | $SiO_2$ | $P_2O_5$ | Cl | $K_2O$ | CaO | $TiO_2$ | MnO | $FeO_t$ | Total |
|---|---|---|---|---|---|---|---|---|---|---|---|---|---|---|---|---|
| 559 | TDB_559 | 11514 | 260617 | 5 | 2.60 | 0.13 | 12.51 | 74.15 | 0.04 | 0.21 | 5.21 | 0.55 | 0.17 | 0.11 | 0.59 | 96.26 |
| 559 | TDB_559 | 11514 | 260617 | 5 | 3.26 | 0.03 | 11.68 | 72.90 | 0.00 | 0.12 | 3.57 | 0.61 | 0.05 | 0.04 | 0.85 | 93.13 |
| | TDB_559 | 11514 | 260617 | 5 | 3.45 | 0.07 | 12.08 | 70.59 | 0.00 | 0.42 | 4.78 | 0.59 | 0.06 | 0.09 | 1.28 | 93.41 |
| | TDB_559 | 11514 | 260617 | 5 | 3.84 | 0.03 | 12.57 | 72.69 | 0.03 | 0.38 | 4.97 | 0.69 | 0.05 | 0.10 | 1.30 | 96.66 |
| | TDB_559 | 11514 | 260617 | 5 | 3.73 | 0.04 | 12.28 | 71.71 | 0.00 | 0.36 | 4.79 | 0.68 | 0.02 | 0.00 | 1.27 | 94.89 |
| 561 | TDB_561 | 11832 | 150419 | 5 | 3.56 | 0.00 | 12.34 | 71.72 | 0.01 | 0.40 | 4.95 | 0.72 | 0.06 | 0.05 | 1.37 | 95.17 |
| | TDB_561 | 11832 | 150419 | 5 | 5.16 | 0.21 | 12.76 | 68.62 | 0.05 | 0.17 | 3.41 | 1.36 | 0.24 | 0.14 | 3.62 | 95.74 |
| 564 | TDB_564 | 11517 | 171017 | 5 | 3.73 | 0.02 | 12.27 | 71.03 | 0.04 | 0.42 | 4.65 | 0.69 | 0.02 | 0.14 | 1.48 | 94.49 |
| | TDB_564 | 11517 | 171017 | 5 | 4.17 | 0.00 | 12.22 | 71.32 | 0.08 | 0.30 | 4.85 | 0.58 | 0.07 | 0.10 | 1.08 | 94.78 |
| | TDB_564 | 11517 | 171017 | 5 | 3.88 | 0.03 | 12.49 | 71.82 | 0.03 | 0.42 | 4.83 | 0.68 | 0.10 | 0.09 | 1.42 | 95.79 |
| | TDB_564 | 11517 | 171017 | 5 | 3.66 | 0.00 | 12.01 | 71.11 | 0.04 | 0.35 | 4.86 | 0.63 | 0.06 | 0.12 | 1.42 | 94.27 |
| | TDB_564 | 11517 | 171017 | 5 | 3.97 | 0.00 | 12.32 | 71.22 | 0.07 | 0.38 | 4.70 | 0.65 | 0.04 | 0.07 | 1.34 | 94.76 |
| | TDB_564 | 11517 | 171017 | 5 | 3.84 | 0.03 | 12.23 | 71.20 | 0.00 | 0.33 | 4.80 | 0.73 | 0.14 | 0.16 | 1.38 | 94.82 |
| | TDB_564 | 11517 | 171017 | 5 | 4.05 | 0.03 | 12.25 | 71.09 | 0.04 | 0.41 | 4.85 | 0.59 | 0.08 | 0.07 | 1.26 | 94.73 |
| | TDB_564 | 11517 | 171017 | 5 | 3.62 | 0.01 | 12.07 | 70.37 | 0.01 | 0.42 | 4.73 | 0.65 | 0.00 | 0.06 | 1.32 | 93.27 |
| | TDB_564 | 11517 | 171017 | 5 | 3.66 | 0.04 | 12.25 | 71.20 | 0.00 | 0.36 | 4.77 | 0.70 | 0.09 | 0.09 | 1.50 | 94.67 |
| | TDB_564 | 11517 | 171017 | 5 | 3.43 | 0.03 | 12.17 | 71.03 | 0.03 | 0.38 | 4.64 | 0.68 | 0.09 | 0.06 | 1.44 | 94.00 |
| | TDB_564 | 11517 | 171017 | 5 | 4.45 | 0.04 | 12.25 | 71.12 | 0.04 | 0.35 | 4.67 | 0.66 | 0.04 | 0.04 | 1.35 | 95.01 |
| | TDB_564 | 11292 | 030317 | 10 | 3.83 | 0.02 | 12.59 | 72.45 | 0.01 | 0.39 | 4.76 | 0.73 | 0.10 | 0.10 | 1.45 | 96.44 |
| | TDB_564 | 11292 | 030317 | 10 | 3.76 | 0.00 | 12.60 | 72.48 | 0.03 | 0.38 | 4.84 | 0.67 | 0.12 | 0.11 | 1.44 | 96.44 |
| | TDB_564 | 11292 | 030317 | 10 | 3.11 | 0.04 | 11.72 | 73.14 | 0.01 | 0.13 | 4.01 | 0.61 | 0.08 | 0.10 | 1.06 | 94.00 |
| | TDB_564 | 11292 | 030317 | 10 | 3.76 | 0.00 | 12.40 | 71.84 | 0.00 | 0.38 | 4.82 | 0.65 | 0.07 | 0.03 | 1.29 | 95.24 |

| Depth (cm) | label | OxT Number | Probe date | Beam diam. | $Na_2O$ | MgO | $Al_2O_3$ | $SiO_2$ | $P_2O_5$ | Cl | $K_2O$ | CaO | $TiO_2$ | MnO | $FeO_t$ | Total |
|---|---|---|---|---|---|---|---|---|---|---|---|---|---|---|---|---|
| 564 | TDB_564 | 11292 | 030317 | 10 | 3.69 | 0.03 | 12.38 | 73.11 | 0.00 | 0.41 | 4.94 | 0.68 | 0.08 | 0.10 | 1.36 | 96.77 |
| 564 | TDB_564 | 11292 | 030317 | 10 | 3.79 | 0.02 | 12.57 | 72.72 | 0.04 | 0.30 | 4.87 | 0.69 | 0.07 | 0.06 | 1.29 | 96.45 |
| | TDB_564 | 11292 | 030317 | 10 | 3.80 | 0.04 | 12.18 | 70.67 | 0.00 | 0.38 | 4.75 | 0.77 | 0.03 | 0.13 | 1.39 | 94.13 |
| | TDB_564 | 11292 | 030317 | 10 | 3.49 | 0.00 | 12.31 | 72.55 | 0.00 | 0.35 | 5.15 | 0.61 | 0.10 | 0.06 | 1.28 | 95.90 |
| | TDB_564 | 11292 | 030317 | 10 | 3.59 | 0.02 | 12.63 | 73.18 | 0.04 | 0.36 | 5.02 | 0.61 | 0.11 | 0.12 | 1.33 | 97.00 |
| | TDB_564 | 11292 | 030317 | 10 | 3.47 | 0.00 | 12.53 | 73.45 | 0.02 | 0.37 | 4.64 | 0.69 | 0.09 | 0.07 | 1.51 | 96.84 |
| 570 | TDB_570 | 11585 | 171017 | 5 | 3.51 | 0.18 | 11.92 | 70.42 | 0.05 | 0.30 | 5.70 | 0.49 | 0.19 | 0.10 | 2.04 | 94.90 |
| | TDB_570 | 11585 | 171017 | 5 | 2.12 | 0.05 | 12.00 | 73.68 | 0.03 | 0.09 | 5.66 | 0.75 | 0.00 | 0.08 | 0.44 | 94.89 |
| | TDB_570 | 11585 | 171017 | 5 | 3.79 | 0.01 | 11.54 | 71.73 | 0.02 | 0.12 | 3.20 | 0.60 | 0.07 | 0.00 | 0.97 | 92.05 |
| | TDB_570 | 11585 | 171017 | 5 | 3.09 | 0.06 | 11.46 | 71.35 | 0.03 | 0.12 | 3.81 | 0.83 | 0.07 | 0.15 | 1.15 | 92.12 |
| | TDB_570 | 11585 | 171017 | 5 | 3.47 | 0.06 | 12.14 | 73.28 | 0.04 | 0.11 | 4.35 | 0.70 | 0.07 | 0.00 | 1.10 | 95.32 |
| 575 | TDB_575 | 11586 | 171017 | 5 | 2.52 | 0.06 | 11.90 | 73.65 | 0.02 | 0.07 | 5.56 | 0.92 | 0.05 | 0.00 | 0.34 | 95.09 |
| | TDB_575 | 11586 | 171017 | 5 | 3.98 | 0.00 | 11.78 | 71.62 | 0.01 | 0.11 | 3.59 | 0.56 | 0.01 | 0.00 | 0.81 | 92.47 |
| | TDB_575 | 11586 | 171017 | 5 | 3.45 | 0.00 | 11.61 | 71.84 | 0.00 | 0.09 | 4.15 | 0.61 | 0.11 | 0.00 | 0.97 | 92.84 |
| | TDB_575 | 11586 | 171017 | 5 | 2.33 | 0.07 | 11.48 | 72.72 | 0.00 | 0.16 | 5.70 | 0.89 | 0.04 | 0.08 | 0.77 | 94.24 |
| | TDB_575 | 11586 | 171017 | 5 | 2.04 | 0.06 | 11.71 | 72.20 | 0.03 | 0.10 | 5.84 | 0.85 | 0.05 | 0.06 | 0.82 | 93.76 |
| | TDB_575 | 11586 | 171017 | 5 | 2.27 | 0.03 | 11.80 | 73.07 | 0.00 | 0.20 | 5.41 | 1.04 | 0.05 | 0.07 | 0.96 | 94.89 |
| | TDB_575 | 11586 | 171017 | 5 | 2.30 | 0.08 | 11.75 | 72.34 | 0.00 | 0.24 | 5.66 | 1.08 | 0.00 | 0.04 | 1.02 | 94.51 |
| | TDB_575 | 11586 | 171017 | 5 | 3.30 | 0.03 | 12.08 | 72.99 | 0.00 | 0.22 | 4.59 | 0.78 | 0.07 | 0.01 | 0.39 | 94.47 |
| 582 | TDB_582 | 11515 | 260617 | 5 | 3.75 | 0.03 | 12.40 | 73.40 | 0.01 | 0.08 | 3.26 | 0.60 | 0.07 | 0.02 | 1.06 | 94.67 |
| 588 | TDB_588 | 11435 | 070918 | 5 | 4.18 | 0.03 | 11.98 | 74.13 | 0.00 | 0.12 | 3.04 | 0.45 | 0.04 | 0.00 | 0.82 | 94.79 |
| | TDB_588 | 11435 | 070918 | 5 | 3.99 | 0.03 | 11.67 | 73.69 | 0.02 | 0.12 | 2.56 | 0.77 | 0.08 | 0.05 | 1.15 | 94.12 |
| | TDB_588 | 11435 | 070918 | 5 | 2.70 | 0.08 | 11.76 | 73.23 | 0.00 | 0.04 | 5.27 | 1.19 | 0.08 | 0.02 | 0.44 | 94.81 |

| Depth (cm) | label | OxT Number | Probe date | Beam diam. | $Na_2O$ | MgO | $Al_2O_3$ | $SiO_2$ | $P_2O_5$ | Cl | $K_2O$ | CaO | $TiO_2$ | MnO | $FeO_t$ | Total |
|---|---|---|---|---|---|---|---|---|---|---|---|---|---|---|---|---|
| 588 | TDB_588 | 11435 | 070918 | 5 | 2.08 | 0.06 | 11.42 | 71.94 | 0.02 | 0.17 | 5.73 | 0.92 | 0.06 | 0.03 | 0.62 | 93.04 |
| | TDB_588 | 11435 | 171017 | 5 | 3.42 | 0.10 | 11.39 | 71.74 | 0.06 | 0.12 | 3.11 | 1.07 | 0.14 | 0.00 | 0.88 | 92.03 |
| | TDB_588 | 11435 | 171017 | 5 | 4.15 | 0.03 | 11.81 | 72.28 | 0.05 | 0.12 | 3.68 | 0.58 | 0.02 | 0.05 | 0.79 | 93.56 |
| | TDB_588 | 11435 | 171017 | 5 | 1.84 | 0.00 | 11.79 | 71.29 | 0.00 | 0.11 | 6.65 | 0.53 | 0.03 | 0.00 | 0.67 | 92.91 |
| | TDB_588 | 11435 | 171017 | 5 | 3.91 | 0.06 | 11.40 | 72.49 | 0.00 | 0.12 | 2.83 | 0.78 | 0.10 | 0.00 | 1.16 | 92.85 |
| | TDB_588 | 11435 | 171017 | 5 | 3.74 | 0.11 | 11.58 | 71.59 | 0.02 | 0.13 | 2.78 | 1.00 | 0.12 | 0.03 | 1.10 | 92.21 |
| | TDB_588 | 11435 | 171017 | 5 | 4.01 | 0.04 | 11.79 | 72.56 | 0.00 | 0.11 | 3.22 | 0.56 | 0.06 | 0.08 | 0.74 | 93.16 |
| | TDB_588 | 11435 | 171017 | 5 | 3.61 | 0.04 | 11.84 | 72.57 | 0.00 | 0.10 | 3.80 | 0.51 | 0.00 | 0.00 | 0.91 | 93.39 |
| | TDB_588 | 11435 | 171017 | 5 | 2.65 | 0.10 | 11.83 | 72.07 | 0.00 | 0.21 | 5.23 | 1.11 | 0.09 | 0.02 | 0.98 | 94.28 |
| | TDB_588 | 11435 | 171017 | 5 | 3.56 | 0.09 | 11.64 | 72.31 | 0.00 | 0.11 | 3.37 | 0.95 | 0.13 | 0.08 | 1.13 | 93.38 |
| | TDB_588 | 11435 | 171017 | 5 | 3.65 | 0.00 | 11.77 | 72.19 | 0.04 | 0.10 | 3.26 | 0.54 | 0.01 | 0.04 | 0.80 | 92.40 |
| | TDB_588 | 11435 | 171017 | 5 | 4.10 | 0.02 | 11.57 | 72.16 | 0.04 | 0.10 | 3.12 | 0.61 | 0.08 | 0.00 | 1.00 | 92.81 |
| | TDB_588 | 11435 | 171017 | 5 | 3.68 | 0.01 | 12.18 | 72.69 | 0.03 | 0.25 | 4.85 | 0.76 | 0.09 | 0.13 | 1.48 | 96.17 |
| 599 | TDB_599 | 11831 | 240118 | 5 | 3.32 | 0.05 | 11.63 | 73.19 | 0.05 | 0.12 | 3.43 | 0.96 | 0.05 | 0.04 | 0.83 | 93.67 |
| | TDB_599 | 11831 | 240118 | 5 | 3.61 | 0.10 | 11.86 | 73.04 | 0.01 | 0.12 | 3.22 | 0.88 | 0.14 | 0.00 | 1.02 | 94.00 |
| | TDB_599 | 11831 | 240118 | 5 | 3.92 | 0.00 | 11.75 | 73.04 | 0.00 | 0.08 | 3.27 | 0.50 | 0.01 | 0.20 | 0.68 | 93.46 |
| | TDB_599 | 11831 | 240118 | 5 | 4.00 | 0.01 | 11.54 | 72.41 | 0.04 | 0.10 | 3.28 | 0.62 | 0.04 | 0.02 | 0.72 | 92.79 |
| | TDB_599 | 11831 | 240118 | 5 | 3.72 | 0.04 | 11.93 | 73.57 | 0.03 | 0.09 | 3.75 | 0.92 | 0.10 | 0.00 | 0.84 | 94.98 |
| | TDB_599 | 11831 | 240118 | 5 | 3.97 | 0.07 | 11.79 | 72.98 | 0.03 | 0.08 | 3.70 | 0.61 | 0.05 | 0.02 | 0.74 | 94.04 |
| | TDB_599 | 11831 | 240118 | 5 | 3.22 | 0.11 | 11.50 | 72.70 | 0.00 | 0.13 | 2.87 | 0.95 | 0.11 | 0.04 | 0.92 | 92.55 |
| | TDB_599 | 11831 | 240118 | 5 | 3.46 | 0.13 | 11.31 | 73.02 | 0.00 | 0.13 | 3.45 | 1.05 | 0.14 | 0.00 | 1.04 | 93.74 |
| | TDB_599 | 11831 | 240118 | 5 | 3.19 | 0.05 | 11.67 | 74.68 | 0.05 | 0.10 | 4.26 | 0.60 | 0.04 | 0.13 | 0.80 | 95.56 |
| | TDB_599 | 11831 | 240118 | 5 | 2.84 | 0.03 | 11.54 | 72.93 | 0.00 | 0.12 | 4.25 | 0.53 | 0.06 | 0.07 | 0.77 | 93.13 |

| Depth (cm) | label | OxT Number | Probe date | Beam diam. | $Na_2O$ | MgO | $Al_2O_3$ | $SiO_2$ | $P_2O_5$ | Cl | $K_2O$ | CaO | $TiO_2$ | MnO | $FeO_t$ | Total |
|---|---|---|---|---|---|---|---|---|---|---|---|---|---|---|---|---|
| 599 | TDB_599 | 11831 | 240118 | 5 | 2.15 | 0.10 | 11.46 | 72.09 | 0.00 | 0.12 | 5.72 | 1.03 | 0.09 | 0.09 | 0.97 | 93.81 |
| | TDB_599 | 11831 | 240118 | 5 | 3.43 | 0.03 | 11.65 | 73.51 | 0.02 | 0.12 | 3.80 | 0.59 | 0.09 | 0.02 | 0.93 | 94.20 |
| | TDB_599 | 11831 | 240118 | 5 | 2.56 | 0.05 | 12.01 | 73.97 | 0.06 | 0.20 | 4.87 | 1.05 | 0.10 | 0.01 | 0.96 | 95.84 |
| | TDB_599 | 11831 | 240118 | 5 | 2.70 | 0.03 | 11.43 | 72.56 | 0.02 | 0.12 | 3.73 | 0.62 | 0.01 | 0.02 | 0.99 | 92.25 |
| | TDB_599 | 11831 | 240118 | 5 | 3.07 | 0.03 | 11.78 | 72.83 | 0.05 | 0.10 | 4.37 | 0.56 | 0.04 | 0.04 | 1.00 | 93.87 |
| | TDB_599 | 11831 | 240118 | 5 | 3.34 | 0.05 | 11.44 | 72.16 | 0.02 | 0.10 | 3.59 | 0.61 | 0.05 | 0.04 | 0.89 | 92.29 |
| | TDB_599 | 11831 | 240118 | 5 | 2.96 | 0.05 | 11.64 | 72.09 | 0.00 | 0.09 | 3.82 | 0.97 | 0.10 | 0.01 | 1.30 | 93.03 |

**Table A2.3** Secondary standard of StHS6/80-G for major geochemistry analysis with the date of analysis

| Probe date | Beam diam. | $Na_2O$ | MgO | $Al_2O_3$ | $SiO_2$ | $P_2O_5$ | Cl | $K_2O$ | CaO | $TiO_2$ | MnO | $FeO_t$ | Analytical Total |
|---|---|---|---|---|---|---|---|---|---|---|---|---|---|
| 121016 | 10 | 4.40 | 1.99 | 17.68 | 63.30 | 0.14 | 0.03 | 1.34 | 5.30 | 0.72 | 0.16 | 4.25 | 99.32 |
| 121016 | 10 | 4.55 | 1.94 | 17.79 | 63.49 | 0.15 | 0.00 | 1.26 | 5.23 | 0.73 | 0.08 | 4.50 | 99.73 |
| 121016 | 10 | 4.67 | 1.99 | 17.67 | 63.26 | 0.13 | 0.02 | 1.37 | 5.30 | 0.72 | 0.09 | 4.42 | 99.63 |
| 121016 | 10 | 4.63 | 2.01 | 17.44 | 63.08 | 0.14 | 0.04 | 1.32 | 5.25 | 0.70 | 0.10 | 4.49 | 99.20 |
| 121016 | 10 | 4.40 | 1.92 | 17.59 | 63.10 | 0.13 | 0.02 | 1.23 | 5.28 | 0.74 | 0.08 | 4.44 | 98.92 |
| 121016 | 10 | 4.49 | 2.01 | 17.52 | 63.43 | 0.16 | 0.01 | 1.33 | 5.18 | 0.76 | 0.10 | 4.38 | 99.37 |
| 121016 | 10 | 4.12 | 1.94 | 17.39 | 63.28 | 0.16 | 0.00 | 1.27 | 5.23 | 0.71 | 0.05 | 4.58 | 98.73 |
| 291116 | 5 | 4.41 | 1.97 | 18.08 | 63.69 | 0.16 | 0.01 | 1.27 | 5.28 | 0.73 | 0.08 | 4.51 | 100.21 |
| 291116 | 5 | 4.66 | 1.97 | 18.05 | 63.60 | 0.16 | 0.01 | 1.29 | 5.22 | 0.71 | 0.08 | 4.49 | 100.24 |
| 291116 | 5 | 4.96 | 1.93 | 17.99 | 64.20 | 0.11 | 0.02 | 1.30 | 5.34 | 0.75 | 0.11 | 4.53 | 101.24 |
| 291116 | 5 | 4.53 | 2.00 | 17.90 | 63.81 | 0.15 | 0.01 | 1.30 | 5.20 | 0.71 | 0.12 | 4.44 | 100.17 |
| 291116 | 5 | 4.46 | 2.00 | 17.52 | 64.17 | 0.10 | 0.00 | 1.26 | 5.46 | 0.79 | 0.13 | 4.41 | 100.31 |
| 291116 | 5 | 4.46 | 1.94 | 17.44 | 64.13 | 0.06 | 0.00 | 1.25 | 5.32 | 0.75 | 0.11 | 4.43 | 99.89 |
| 091216 | 5 | 4.42 | 2.02 | 17.68 | 63.85 | 0.18 | 0.03 | 1.29 | 5.18 | 0.67 | 0.04 | 4.40 | 99.75 |
| 091216 | 5 | 4.67 | 2.02 | 17.70 | 63.54 | 0.18 | 0.00 | 1.34 | 5.36 | 0.74 | 0.06 | 4.45 | 100.06 |
| 091216 | 5 | 4.48 | 1.97 | 17.34 | 63.98 | 0.16 | 0.01 | 1.35 | 5.26 | 0.73 | 0.06 | 4.51 | 99.86 |
| 091216 | 5 | 4.51 | 2.06 | 17.67 | 63.67 | 0.19 | 0.04 | 1.30 | 5.24 | 0.75 | 0.00 | 4.65 | 100.08 |
| 091216 | 5 | 4.57 | 1.98 | 17.26 | 63.55 | 0.17 | 0.02 | 1.29 | 5.43 | 0.70 | 0.00 | 4.03 | 98.98 |
| 091216 | 5 | 4.71 | 2.04 | 17.71 | 64.05 | 0.23 | 0.03 | 1.24 | 5.39 | 0.69 | 0.06 | 4.49 | 100.66 |
| 010517 | 10 | 4.63 | 1.91 | 17.57 | 62.79 | 0.04 | 0.00 | 1.36 | 5.25 | 0.70 | 0.08 | 4.43 | 98.76 |
| 010517 | 10 | 4.45 | 1.96 | 17.64 | 62.73 | 0.10 | 0.01 | 1.33 | 5.40 | 0.75 | 0.06 | 4.19 | 98.63 |
| 010517 | 10 | 4.44 | 1.94 | 17.46 | 63.47 | 0.09 | 0.00 | 1.34 | 5.20 | 0.69 | 0.07 | 4.33 | 99.04 |
| 010517 | 10 | 4.77 | 1.99 | 17.46 | 63.53 | 0.12 | 0.00 | 1.25 | 5.32 | 0.67 | 0.09 | 4.26 | 99.47 |

| Probe date | Beam diam. | $Na_2O$ | MgO | $Al_2O_3$ | $SiO_2$ | $P_2O_5$ | Cl | $K_2O$ | CaO | $TiO_2$ | MnO | $FeO_t$ | Analytical Total |
|---|---|---|---|---|---|---|---|---|---|---|---|---|---|
| 010517 | 10 | 4.51 | 2.01 | 17.70 | 64.04 | 0.16 | 0.01 | 1.26 | 5.36 | 0.74 | 0.05 | 4.33 | 100.16 |
| 010517 | 10 | 4.66 | 2.01 | 17.73 | 63.54 | 0.17 | 0.02 | 1.27 | 5.29 | 0.74 | 0.09 | 4.37 | 99.88 |
| 260617 | 5 | 4.49 | 1.91 | 17.67 | 64.05 | 0.16 | 0.00 | 1.35 | 5.19 | 0.69 | 0.09 | 4.51 | 100.11 |
| 260617 | 5 | 4.18 | 1.93 | 17.68 | 64.19 | 0.17 | 0.01 | 1.36 | 5.34 | 0.74 | 0.09 | 4.18 | 99.87 |
| 260617 | 5 | 4.38 | 1.92 | 17.66 | 63.89 | 0.17 | 0.02 | 1.20 | 5.18 | 0.68 | 0.10 | 4.30 | 99.49 |
| 260617 | 5 | 4.61 | 1.96 | 17.58 | 63.80 | 0.14 | 0.01 | 1.30 | 5.10 | 0.69 | 0.02 | 4.56 | 99.78 |
| 260617 | 5 | 4.55 | 1.98 | 17.84 | 63.44 | 0.15 | 0.02 | 1.25 | 5.31 | 0.75 | 0.02 | 4.61 | 99.91 |
| 260617 | 5 | 4.42 | 2.00 | 17.47 | 63.61 | 0.15 | 0.01 | 1.37 | 5.30 | 0.70 | 0.10 | 4.22 | 99.34 |
| 260617 | 5 | 4.40 | 1.93 | 17.60 | 64.13 | 0.17 | 0.03 | 1.38 | 5.23 | 0.75 | 0.01 | 4.74 | 100.38 |
| 260617 | 5 | 4.81 | 1.98 | 17.65 | 64.02 | 0.14 | 0.02 | 1.32 | 5.25 | 0.71 | 0.10 | 4.16 | 100.16 |
| 260617 | 5 | 4.38 | 1.96 | 17.66 | 63.89 | 0.14 | 0.01 | 1.28 | 5.23 | 0.68 | 0.06 | 4.25 | 99.55 |
| 260617 | 5 | 4.49 | 1.91 | 17.67 | 64.05 | 0.16 | 0.00 | 1.35 | 5.19 | 0.69 | 0.09 | 4.51 | 100.11 |
| 260617 | 5 | 4.18 | 1.93 | 17.68 | 64.19 | 0.17 | 0.01 | 1.36 | 5.34 | 0.74 | 0.09 | 4.18 | 99.87 |
| 260617 | 5 | 4.38 | 1.92 | 17.66 | 63.89 | 0.17 | 0.02 | 1.20 | 5.18 | 0.68 | 0.10 | 4.30 | 99.49 |
| 260617 | 5 | 4.61 | 1.96 | 17.58 | 63.80 | 0.14 | 0.01 | 1.30 | 5.10 | 0.69 | 0.02 | 4.56 | 99.78 |
| 260617 | 5 | 4.55 | 1.98 | 17.84 | 63.44 | 0.15 | 0.02 | 1.25 | 5.31 | 0.75 | 0.02 | 4.61 | 99.91 |
| 260617 | 5 | 4.42 | 2.00 | 17.47 | 63.61 | 0.15 | 0.01 | 1.37 | 5.30 | 0.70 | 0.10 | 4.22 | 99.34 |
| 260617 | 5 | 4.40 | 1.93 | 17.60 | 64.13 | 0.17 | 0.03 | 1.38 | 5.23 | 0.75 | 0.01 | 4.74 | 100.38 |
| 260617 | 5 | 4.81 | 1.98 | 17.65 | 64.02 | 0.14 | 0.02 | 1.32 | 5.25 | 0.71 | 0.10 | 4.16 | 100.16 |
| 260617 | 5 | 4.38 | 1.96 | 17.66 | 63.89 | 0.14 | 0.01 | 1.28 | 5.23 | 0.68 | 0.06 | 4.25 | 99.55 |
| 171017 | 5 | 4.65 | 1.89 | 17.74 | 63.92 | 0.19 | 0.00 | 1.40 | 5.22 | 0.70 | 0.07 | 4.16 | 99.94 |
| 171017 | 5 | 4.60 | 1.90 | 17.64 | 64.19 | 0.13 | 0.02 | 1.33 | 5.30 | 0.70 | 0.14 | 4.68 | 100.62 |
| 171017 | 5 | 4.91 | 2.04 | 17.50 | 63.35 | 0.17 | 0.01 | 1.27 | 5.21 | 0.61 | 0.10 | 4.56 | 99.73 |
| 171017 | 5 | 4.57 | 1.93 | 17.71 | 63.59 | 0.18 | 0.00 | 1.24 | 5.17 | 0.76 | 0.08 | 4.27 | 99.49 |
| 171017 | 5 | 4.80 | 1.88 | 17.69 | 63.05 | 0.18 | 0.00 | 1.33 | 5.23 | 0.73 | 0.06 | 4.37 | 99.32 |
| 171017 | 5 | 4.59 | 1.86 | 17.42 | 62.85 | 0.18 | 0.02 | 1.29 | 5.07 | 0.74 | 0.18 | 4.41 | 98.60 |

| Probe date | Beam diam. | $Na_2O$ | MgO | $Al_2O_3$ | $SiO_2$ | $P_2O_5$ | Cl | $K_2O$ | CaO | $TiO_2$ | MnO | $FeO_t$ | Analytical Total |
|---|---|---|---|---|---|---|---|---|---|---|---|---|---|
| 171017 | 5 | 4.42 | 1.89 | 17.67 | 63.36 | 0.18 | 0.02 | 1.28 | 5.07 | 0.67 | 0.09 | 4.40 | 99.04 |
| 171017 | 5 | 4.94 | 1.88 | 17.83 | 63.53 | 0.19 | 0.00 | 1.37 | 5.11 | 0.70 | 0.07 | 4.68 | 100.29 |
| 171017 | 5 | 5.07 | 1.93 | 17.56 | 62.33 | 0.17 | 0.01 | 1.30 | 5.37 | 0.75 | 0.00 | 4.19 | 98.68 |
| 171017 | 5 | 4.79 | 1.92 | 17.79 | 63.29 | 0.16 | 0.00 | 1.24 | 5.27 | 0.69 | 0.04 | 4.33 | 99.53 |
| 191017 | 5 | 4.51 | 1.97 | 17.32 | 63.06 | 0.19 | 0.00 | 1.31 | 5.22 | 0.73 | 0.20 | 4.06 | 98.56 |
| 191017 | 5 | 4.38 | 1.97 | 17.25 | 63.52 | 0.24 | 0.01 | 1.27 | 5.27 | 0.71 | 0.20 | 4.40 | 99.25 |
| 191017 | 5 | 4.80 | 1.92 | 17.55 | 63.32 | 0.18 | 0.00 | 1.35 | 5.25 | 0.76 | 0.09 | 4.28 | 99.50 |
| 191017 | 5 | 4.59 | 2.03 | 17.45 | 63.64 | 0.13 | 0.01 | 1.37 | 5.15 | 0.61 | 0.08 | 4.33 | 99.40 |
| 191017 | 5 | 4.68 | 1.89 | 17.54 | 63.84 | 0.14 | 0.03 | 1.29 | 5.16 | 0.71 | 0.00 | 4.27 | 99.56 |
| 191017 | 5 | 4.62 | 1.96 | 17.83 | 63.25 | 0.16 | 0.02 | 1.27 | 5.20 | 0.71 | 0.00 | 4.32 | 99.35 |
| 191017 | 5 | 4.49 | 1.94 | 17.45 | 63.07 | 0.13 | 0.01 | 1.35 | 5.29 | 0.76 | 0.16 | 4.38 | 99.02 |
| 191017 | 5 | 4.39 | 1.93 | 17.59 | 63.52 | 0.17 | 0.03 | 1.25 | 5.42 | 0.70 | 0.12 | 4.44 | 99.56 |
| 191017 | 5 | 4.65 | 1.89 | 17.73 | 63.49 | 0.16 | 0.01 | 1.32 | 5.24 | 0.81 | 0.00 | 4.39 | 99.70 |
| 191017 | 5 | 4.51 | 1.87 | 17.56 | 63.98 | 0.14 | 0.02 | 1.22 | 5.39 | 0.76 | 0.03 | 4.48 | 99.95 |
| 251017 | 5 | 4.54 | 1.90 | 17.94 | 63.56 | 0.13 | 0.00 | 1.27 | 5.13 | 0.76 | 0.06 | 4.41 | 99.70 |
| 251017 | 5 | 4.50 | 1.88 | 17.84 | 63.54 | 0.13 | 0.00 | 1.36 | 5.11 | 0.66 | 0.08 | 4.20 | 99.30 |
| 251017 | 5 | 4.45 | 1.88 | 17.62 | 63.56 | 0.11 | 0.00 | 1.27 | 5.22 | 0.70 | 0.11 | 4.05 | 98.96 |
| 251017 | 5 | 4.74 | 1.91 | 17.72 | 63.36 | 0.15 | 0.01 | 1.32 | 5.40 | 0.71 | 0.01 | 4.41 | 99.76 |
| 251017 | 5 | 4.40 | 1.92 | 17.79 | 63.94 | 0.11 | 0.01 | 1.32 | 5.21 | 0.73 | 0.07 | 4.53 | 100.04 |
| 251017 | 5 | 4.63 | 1.92 | 17.86 | 63.61 | 0.07 | 0.00 | 1.34 | 5.27 | 0.69 | 0.04 | 4.56 | 100.00 |
| 251017 | 5 | 4.48 | 1.90 | 17.39 | 63.74 | 0.09 | 0.01 | 1.27 | 5.30 | 0.65 | 0.12 | 4.37 | 99.31 |
| 230118 | 5 | 4.62 | 1.99 | 17.86 | 63.72 | 0.22 | 0.03 | 1.33 | 5.39 | 0.72 | 0.00 | 4.08 | 99.96 |
| 230118 | 5 | 4.78 | 1.96 | 18.14 | 64.51 | 0.15 | 0.00 | 1.24 | 5.27 | 0.74 | 0.06 | 4.46 | 101.31 |
| 230118 | 5 | 4.42 | 2.04 | 17.61 | 63.72 | 0.13 | 0.01 | 1.29 | 5.17 | 0.69 | 0.08 | 4.09 | 99.25 |
| 230118 | 5 | 4.95 | 2.01 | 17.38 | 63.48 | 0.20 | 0.00 | 1.27 | 5.12 | 0.66 | 0.10 | 4.58 | 99.75 |
| 230118 | 5 | 4.42 | 2.01 | 17.63 | 63.38 | 0.21 | 0.00 | 1.28 | 5.17 | 0.61 | 0.08 | 4.48 | 99.27 |

| Probe date | Beam diam. | $Na_2O$ | MgO | $Al_2O_3$ | $SiO_2$ | $P_2O_5$ | Cl | $K_2O$ | CaO | $TiO_2$ | MnO | $FeO_t$ | Analytical Total |
|---|---|---|---|---|---|---|---|---|---|---|---|---|---|
| 230118 | 5 | 4.37 | 1.86 | 17.76 | 64.52 | 0.13 | 0.02 | 1.32 | 5.19 | 0.73 | 0.12 | 4.48 | 100.50 |
| 230118 | 5 | 4.35 | 1.89 | 17.31 | 63.61 | 0.11 | 0.00 | 1.30 | 5.18 | 0.74 | 0.03 | 4.75 | 99.27 |
| 240118 | 5 | 4.62 | 1.95 | 17.75 | 64.15 | 0.21 | 0.02 | 1.39 | 5.28 | 0.72 | 0.05 | 4.46 | 100.59 |
| 240118 | 5 | 4.51 | 1.97 | 17.77 | 64.33 | 0.14 | 0.01 | 1.24 | 5.24 | 0.63 | 0.14 | 4.31 | 100.30 |
| 240118 | 5 | 4.52 | 2.10 | 17.56 | 63.67 | 0.19 | 0.01 | 1.37 | 5.25 | 0.75 | 0.15 | 4.58 | 100.14 |
| 240118 | 5 | 4.44 | 2.05 | 17.48 | 63.02 | 0.16 | 0.00 | 1.32 | 5.25 | 0.75 | 0.06 | 4.41 | 98.94 |
| 240118 | 5 | 4.35 | 2.01 | 17.38 | 63.27 | 0.24 | 0.02 | 1.37 | 5.28 | 0.62 | 0.05 | 4.35 | 98.94 |
| 240118 | 5 | 4.38 | 1.96 | 17.54 | 63.64 | 0.21 | 0.03 | 1.31 | 5.18 | 0.69 | 0.08 | 4.13 | 99.13 |
| 240118 | 5 | 4.51 | 1.97 | 17.42 | 62.62 | 0.18 | 0.03 | 1.27 | 5.14 | 0.67 | 0.02 | 4.53 | 98.36 |
| 260118 | 5 | 4.78 | 1.92 | 17.83 | 63.67 | 0.18 | 0.01 | 1.32 | 5.31 | 0.81 | 0.11 | 4.54 | 100.48 |
| 260118 | 5 | 4.66 | 1.98 | 17.77 | 64.38 | 0.20 | 0.00 | 1.36 | 5.22 | 0.79 | 0.08 | 4.37 | 100.82 |
| 260118 | 5 | 4.87 | 1.86 | 17.98 | 63.92 | 0.17 | 0.00 | 1.40 | 5.40 | 0.79 | 0.08 | 4.51 | 100.98 |
| 260118 | 5 | 4.45 | 2.00 | 17.83 | 63.94 | 0.23 | 0.00 | 1.39 | 5.35 | 0.69 | 0.15 | 4.58 | 100.62 |
| 260118 | 5 | 4.57 | 1.92 | 17.84 | 63.71 | 0.15 | 0.01 | 1.33 | 5.16 | 0.72 | 0.09 | 4.46 | 99.96 |
| 050918 | 10 | 4.58 | 1.87 | 17.78 | 64.40 | 0.13 | 0.01 | 1.27 | 5.27 | 0.73 | 0.03 | 4.35 | 100.42 |
| 050918 | 10 | 4.71 | 1.99 | 17.50 | 63.96 | 0.09 | 0.01 | 1.30 | 5.08 | 0.71 | 0.07 | 4.20 | 99.60 |
| 050918 | 10 | 4.29 | 1.87 | 17.67 | 63.95 | 0.08 | 0.01 | 1.31 | 5.22 | 0.66 | 0.05 | 4.26 | 99.36 |
| 050918 | 10 | 4.74 | 1.89 | 17.67 | 63.97 | 0.18 | 0.02 | 1.28 | 5.30 | 0.66 | 0.08 | 4.60 | 100.40 |
| 050918 | 10 | 4.48 | 1.94 | 17.75 | 64.18 | 0.10 | 0.03 | 1.25 | 5.24 | 0.73 | 0.05 | 4.33 | 100.10 |
| 050918 | 10 | 4.54 | 1.94 | 17.46 | 63.74 | 0.16 | 0.02 | 1.27 | 5.24 | 0.71 | 0.06 | 4.20 | 99.34 |
| 050918 | 10 | 4.70 | 1.98 | 18.00 | 63.91 | 0.18 | 0.01 | 1.30 | 5.30 | 0.71 | 0.06 | 4.51 | 100.66 |
| 050918 | 10 | 4.89 | 1.98 | 18.12 | 63.77 | 0.17 | 0.01 | 1.27 | 5.29 | 0.68 | 0.09 | 4.49 | 100.76 |
| 060918 | 5 | 4.66 | 1.82 | 17.80 | 63.66 | 0.13 | 0.02 | 1.33 | 5.13 | 0.73 | 0.08 | 4.26 | 99.63 |
| 060918 | 5 | 4.75 | 2.00 | 18.13 | 63.80 | 0.15 | 0.03 | 1.33 | 5.34 | 0.75 | 0.06 | 4.36 | 100.70 |
| 060918 | 5 | 4.74 | 1.93 | 17.38 | 63.51 | 0.18 | 0.03 | 1.33 | 5.28 | 0.77 | 0.06 | 4.49 | 99.69 |

| Probe date | Beam diam. | $Na_2O$ | MgO | $Al_2O_3$ | $SiO_2$ | $P_2O_5$ | Cl | $K_2O$ | CaO | $TiO_2$ | MnO | $FeO_t$ | Analytical Total |
|---|---|---|---|---|---|---|---|---|---|---|---|---|---|
| 060918 | 5 | 5.00 | 1.96 | 17.81 | 63.89 | 0.11 | 0.00 | 1.31 | 5.33 | 0.63 | 0.09 | 4.37 | 100.50 |
| 070918 | 5 | 4.59 | 1.98 | 17.47 | 63.48 | 0.10 | 0.03 | 1.26 | 5.41 | 0.67 | 0.05 | 4.45 | 99.49 |
| 070918 | 5 | 4.64 | 1.98 | 17.60 | 63.32 | 0.15 | 0.02 | 1.33 | 5.25 | 0.75 | 0.05 | 4.40 | 99.47 |
| 070918 | 5 | 4.90 | 2.04 | 17.53 | 63.18 | 0.14 | 0.00 | 1.30 | 5.29 | 0.69 | 0.04 | 4.49 | 99.59 |
| 070918 | 5 | 4.75 | 1.93 | 17.48 | 62.86 | 0.15 | 0.01 | 1.27 | 5.37 | 0.77 | 0.03 | 4.36 | 98.99 |
| 070918 | 5 | 4.79 | 1.93 | 17.35 | 63.60 | 0.19 | 0.00 | 1.24 | 5.14 | 0.68 | 0.11 | 4.15 | 99.17 |
| 070918 | 5 | 4.85 | 2.04 | 17.61 | 63.74 | 0.12 | 0.02 | 1.26 | 5.23 | 0.75 | 0.07 | 4.28 | 99.95 |
| 070918 | 5 | 4.37 | 1.92 | 17.78 | 63.27 | 0.19 | 0.01 | 1.25 | 5.32 | 0.75 | 0.07 | 4.60 | 99.54 |
| 070918 | 5 | 4.35 | 1.88 | 17.51 | 62.97 | 0.15 | 0.01 | 1.29 | 5.43 | 0.73 | 0.01 | 4.24 | 98.56 |
| 070918 | 5 | 4.86 | 1.90 | 17.31 | 62.80 | 0.15 | 0.00 | 1.30 | 5.30 | 0.75 | 0.12 | 4.42 | 98.91 |
| 150419 | 5 | 4.81 | 1.99 | 18.03 | 63.98 | 0.15 | 0.01 | 1.27 | 5.16 | 0.75 | 0.09 | 4.47 | 100.69 |
| 150419 | 5 | 4.64 | 2.00 | 17.57 | 63.60 | 0.15 | 0.00 | 1.32 | 5.22 | 0.72 | 0.00 | 4.34 | 99.56 |
| 150419 | 5 | 4.68 | 2.07 | 17.90 | 63.53 | 0.19 | 0.01 | 1.28 | 5.22 | 0.73 | 0.11 | 4.62 | 100.34 |
| 150419 | 5 | 5.09 | 2.05 | 17.50 | 63.90 | 0.17 | 0.01 | 1.37 | 5.21 | 0.76 | 0.06 | 4.24 | 100.36 |
| 150419 | 5 | 4.65 | 2.00 | 17.42 | 63.60 | 0.20 | 0.01 | 1.33 | 5.26 | 0.70 | 0.10 | 4.28 | 99.55 |
| 150419 | 5 | 4.98 | 2.01 | 17.64 | 63.79 | 0.20 | 0.02 | 1.24 | 5.28 | 0.72 | 0.09 | 4.67 | 100.65 |
| 150419 | 5 | 4.56 | 1.97 | 17.87 | 63.69 | 0.19 | 0.00 | 1.28 | 5.36 | 0.73 | 0.07 | 4.36 | 100.08 |

**Table A2.4** Secondary standard of ATHOG for major geochemistry analysis with the date of analysis

| Probe date | Beam diam. | $Na_2O$ | MgO | $Al_2O_3$ | $SiO_2$ | $P_2O_5$ | Cl | $K_2O$ | CaO | $TiO_2$ | MnO | $FeO_t$ | Analytical Total |
|---|---|---|---|---|---|---|---|---|---|---|---|---|---|
| 121016 | 10 | 4.15 | 0.07 | 12.39 | 75.42 | 0.03 | 0.00 | 2.80 | 1.64 | 0.25 | 0.11 | 3.14 | 100.00 |
| 121016 | 10 | 4.11 | 0.12 | 12.13 | 74.99 | 0.05 | 0.02 | 2.97 | 1.66 | 0.26 | 0.10 | 3.17 | 99.58 |
| 121016 | 10 | 3.99 | 0.11 | 11.97 | 74.63 | 0.01 | 0.04 | 2.67 | 1.75 | 0.31 | 0.00 | 3.61 | 99.09 |
| 121016 | 10 | 4.08 | 0.10 | 12.31 | 75.30 | 0.00 | 0.04 | 2.78 | 1.66 | 0.25 | 0.07 | 3.40 | 99.99 |
| 121016 | 10 | 4.14 | 0.08 | 12.09 | 75.16 | 0.02 | 0.03 | 2.63 | 1.67 | 0.24 | 0.14 | 3.08 | 99.28 |
| 121016 | 10 | 4.30 | 0.09 | 12.05 | 74.61 | 0.02 | 0.03 | 2.82 | 1.70 | 0.22 | 0.04 | 3.41 | 99.29 |
| 121016 | 10 | 4.11 | 0.09 | 12.24 | 74.68 | 0.04 | 0.03 | 2.66 | 1.65 | 0.25 | 0.01 | 3.43 | 99.19 |
| 291116 | 5 | 4.43 | 0.11 | 12.56 | 74.87 | 0.04 | 0.03 | 2.71 | 1.70 | 0.26 | 0.02 | 3.32 | 100.04 |
| 291116 | 5 | 4.07 | 0.09 | 12.49 | 75.15 | 0.02 | 0.03 | 2.64 | 1.60 | 0.25 | 0.20 | 3.19 | 99.71 |
| 291116 | 5 | 4.12 | 0.11 | 12.36 | 75.92 | 0.06 | 0.05 | 2.62 | 1.76 | 0.27 | 0.19 | 3.11 | 100.57 |
| 291116 | 5 | 4.00 | 0.10 | 12.06 | 75.84 | 0.03 | 0.02 | 2.67 | 1.69 | 0.27 | 0.11 | 3.23 | 100.03 |
| 291116 | 5 | 4.10 | 0.06 | 12.07 | 75.82 | 0.08 | 0.03 | 2.55 | 1.71 | 0.25 | 0.13 | 3.09 | 99.90 |
| 291116 | 5 | 4.20 | 0.10 | 12.17 | 76.07 | 0.06 | 0.03 | 2.59 | 1.76 | 0.27 | 0.08 | 3.32 | 100.64 |
| 091216 | 5 | 4.11 | 0.10 | 12.41 | 75.81 | 0.03 | 0.05 | 2.68 | 1.71 | 0.29 | 0.11 | 3.10 | 100.39 |
| 091216 | 5 | 4.34 | 0.12 | 12.04 | 75.44 | 0.00 | 0.04 | 2.69 | 1.72 | 0.26 | 0.12 | 3.15 | 99.93 |
| 091216 | 5 | 4.55 | 0.12 | 12.11 | 75.75 | 0.03 | 0.01 | 2.74 | 1.78 | 0.25 | 0.17 | 3.07 | 100.58 |
| 091216 | 5 | 4.18 | 0.12 | 12.27 | 75.69 | 0.00 | 0.04 | 2.70 | 1.71 | 0.30 | 0.13 | 3.29 | 100.42 |
| 091216 | 5 | 4.11 | 0.08 | 12.28 | 75.42 | 0.00 | 0.04 | 2.75 | 1.70 | 0.31 | 0.07 | 3.30 | 100.06 |
| 091216 | 5 | 4.27 | 0.08 | 12.27 | 75.59 | 0.00 | 0.05 | 2.80 | 1.66 | 0.26 | 0.14 | 3.21 | 100.32 |
| 010517 | 10 | 4.03 | 0.10 | 12.23 | 74.23 | 0.00 | 0.04 | 2.78 | 1.70 | 0.23 | 0.12 | 3.18 | 98.64 |
| 010517 | 10 | 4.39 | 0.10 | 12.26 | 74.58 | 0.03 | 0.03 | 2.71 | 1.70 | 0.28 | 0.09 | 3.07 | 99.22 |
| 010517 | 10 | 4.25 | 0.11 | 12.33 | 74.94 | 0.01 | 0.05 | 2.80 | 1.62 | 0.30 | 0.12 | 3.22 | 99.75 |
| 010517 | 10 | 3.97 | 0.06 | 12.34 | 74.60 | 0.05 | 0.03 | 2.70 | 1.65 | 0.28 | 0.11 | 3.34 | 99.13 |
|  | 10 | 4.31 | 0.08 | 12.30 | 75.10 | 0.00 | 0.02 | 2.84 | 1.73 | 0.24 | 0.13 | 3.24 | 100.00 |

| Probe date | Beam diam. | $Na_2O$ | MgO | $Al_2O_3$ | $SiO_2$ | $P_2O_5$ | Cl | $K_2O$ | CaO | $TiO_2$ | MnO | $FeO_t$ | Analytical Total |
|---|---|---|---|---|---|---|---|---|---|---|---|---|---|
| 010517 | 10 | 4.24 | 0.12 | 12.40 | 75.60 | 0.05 | 0.02 | 2.70 | 1.68 | 0.28 | 0.13 | 3.37 | 100.58 |
| 260617 | 5 | 4.26 | 0.08 | 12.28 | 75.85 | 0.01 | 0.03 | 2.75 | 1.71 | 0.20 | 0.09 | 3.28 | 100.55 |
| 260617 | 5 | 4.06 | 0.15 | 12.27 | 75.77 | 0.01 | 0.05 | 2.74 | 1.65 | 0.24 | 0.13 | 3.06 | 100.12 |
| 260617 | 5 | 4.39 | 0.11 | 12.41 | 75.62 | 0.04 | 0.03 | 2.75 | 1.72 | 0.21 | 0.11 | 3.20 | 100.59 |
| 260617 | 5 | 4.25 | 0.11 | 12.29 | 75.72 | 0.02 | 0.04 | 2.71 | 1.71 | 0.23 | 0.12 | 3.09 | 100.28 |
| 260617 | 5 | 4.05 | 0.12 | 12.23 | 75.51 | 0.00 | 0.02 | 2.66 | 1.64 | 0.29 | 0.16 | 3.51 | 100.18 |
| 260617 | 5 | 4.12 | 0.10 | 12.36 | 75.27 | 0.02 | 0.02 | 2.78 | 1.68 | 0.25 | 0.01 | 3.13 | 99.74 |
| 260617 | 5 | 4.19 | 0.12 | 12.16 | 75.36 | 0.00 | 0.03 | 2.65 | 1.63 | 0.20 | 0.10 | 3.09 | 99.52 |
| 260617 | 5 | 4.15 | 0.09 | 12.22 | 75.77 | 0.05 | 0.03 | 2.72 | 1.74 | 0.27 | 0.06 | 3.36 | 100.45 |
| 260617 | 5 | 4.09 | 0.05 | 12.18 | 75.68 | 0.02 | 0.04 | 2.70 | 1.55 | 0.23 | 0.04 | 3.32 | 99.90 |
| 171017 | 5 | 4.04 | 0.10 | 12.18 | 75.64 | 0.05 | 0.06 | 2.71 | 1.76 | 0.27 | 0.02 | 3.35 | 100.20 |
| 171017 | 5 | 4.12 | 0.07 | 12.17 | 75.41 | 0.02 | 0.02 | 2.79 | 1.78 | 0.32 | 0.05 | 3.62 | 100.38 |
| 171017 | 5 | 4.31 | 0.12 | 12.26 | 74.77 | 0.02 | 0.07 | 2.73 | 1.77 | 0.26 | 0.16 | 3.24 | 99.71 |
| 171017 | 5 | 4.26 | 0.15 | 11.92 | 74.41 | 0.04 | 0.08 | 2.69 | 1.77 | 0.27 | 0.16 | 3.36 | 99.12 |
| 171017 | 5 | 4.09 | 0.06 | 12.10 | 74.68 | 0.04 | 0.00 | 2.70 | 1.72 | 0.22 | 0.19 | 3.15 | 98.94 |
| 191017 | 5 | 4.23 | 0.07 | 12.15 | 75.51 | 0.00 | 0.06 | 2.70 | 1.76 | 0.28 | 0.11 | 3.16 | 100.04 |
| 191017 | 5 | 4.41 | 0.08 | 12.17 | 75.11 | 0.03 | 0.05 | 2.63 | 1.78 | 0.27 | 0.14 | 2.85 | 99.53 |
| 191017 | 5 | 3.92 | 0.09 | 11.94 | 74.90 | 0.07 | 0.05 | 2.77 | 1.76 | 0.29 | 0.03 | 2.91 | 98.73 |
| 191017 | 5 | 3.98 | 0.08 | 11.99 | 74.99 | 0.00 | 0.03 | 2.69 | 1.75 | 0.25 | 0.06 | 2.97 | 98.78 |
| 191017 | 5 | 4.28 | 0.09 | 12.22 | 74.63 | 0.05 | 0.04 | 2.65 | 1.66 | 0.25 | 0.06 | 2.97 | 98.91 |
| 251017 | 5 | 4.44 | 0.11 | 12.54 | 75.16 | 0.00 | 0.03 | 2.68 | 1.72 | 0.24 | 0.08 | 3.24 | 100.24 |
| 251017 | 5 | 3.92 | 0.11 | 12.50 | 74.91 | 0.06 | 0.04 | 2.76 | 1.66 | 0.23 | 0.00 | 3.17 | 99.36 |
| 251017 | 5 | 4.08 | 0.09 | 12.22 | 75.14 | 0.06 | 0.04 | 2.79 | 1.71 | 0.25 | 0.02 | 3.41 | 99.80 |
| 251017 | 5 | 4.19 | 0.07 | 12.31 | 75.16 | 0.05 | 0.02 | 2.69 | 1.64 | 0.26 | 0.05 | 3.36 | 99.81 |
| 251017 | 5 | 3.88 | 0.09 | 12.21 | 75.51 | 0.00 | 0.03 | 2.77 | 1.66 | 0.32 | 0.07 | 3.26 | 99.81 |
| 251017 | 5 | 4.18 | 0.12 | 12.39 | 75.24 | 0.07 | 0.02 | 2.63 | 1.69 | 0.27 | 0.14 | 3.42 | 100.18 |

| Probe date | Beam diam. | $Na_2O$ | MgO | $Al_2O_3$ | $SiO_2$ | $P_2O_5$ | Cl | $K_2O$ | CaO | $TiO_2$ | MnO | $FeO_t$ | Analytical Total |
|---|---|---|---|---|---|---|---|---|---|---|---|---|---|
| 251017 | 5 | 4.20 | 0.12 | 12.45 | 75.02 | 0.02 | 0.02 | 2.71 | 1.77 | 0.24 | 0.16 | 3.39 | 100.09 |
| 230118 | 5 | 4.24 | 0.10 | 12.51 | 76.23 | 0.02 | 0.03 | 2.73 | 1.54 | 0.30 | 0.20 | 3.16 | 101.06 |
| 230118 | 5 | 4.03 | 0.09 | 12.62 | 76.02 | 0.04 | 0.03 | 2.71 | 1.74 | 0.24 | 0.08 | 3.05 | 100.65 |
| 230118 | 5 | 3.75 | 0.10 | 12.63 | 76.83 | 0.04 | 0.03 | 2.66 | 1.64 | 0.27 | 0.16 | 3.29 | 101.39 |
| 230118 | 5 | 4.02 | 0.11 | 12.38 | 76.53 | 0.03 | 0.04 | 2.79 | 1.71 | 0.23 | 0.17 | 2.95 | 100.97 |
| 230118 | 5 | 4.17 | 0.12 | 11.93 | 74.41 | 0.03 | 0.02 | 2.70 | 1.74 | 0.21 | 0.19 | 3.15 | 98.65 |
| 230118 | 5 | 4.18 | 0.10 | 12.29 | 75.30 | 0.00 | 0.04 | 2.70 | 1.59 | 0.32 | 0.11 | 3.05 | 99.68 |
| 240118 | 5 | 4.17 | 0.11 | 12.45 | 76.03 | 0.01 | 0.03 | 2.70 | 1.65 | 0.30 | 0.20 | 3.33 | 100.98 |
| 240118 | 5 | 4.01 | 0.08 | 12.52 | 75.99 | 0.00 | 0.02 | 2.79 | 1.57 | 0.22 | 0.08 | 3.18 | 100.45 |
| 240118 | 5 | 4.12 | 0.14 | 12.61 | 76.01 | 0.00 | 0.02 | 2.70 | 1.71 | 0.22 | 0.14 | 3.39 | 101.06 |
| 240118 | 5 | 4.10 | 0.10 | 12.51 | 75.93 | 0.06 | 0.03 | 2.70 | 1.72 | 0.32 | 0.06 | 3.04 | 100.57 |
| 240118 | 5 | 4.05 | 0.06 | 12.22 | 75.82 | 0.05 | 0.02 | 2.76 | 1.57 | 0.26 | 0.05 | 3.21 | 100.07 |
| 240118 | 5 | 4.12 | 0.11 | 12.34 | 75.75 | 0.02 | 0.05 | 2.70 | 1.68 | 0.26 | 0.14 | 3.20 | 100.37 |
| 240118 | 5 | 4.06 | 0.11 | 12.29 | 75.75 | 0.00 | 0.03 | 2.71 | 1.64 | 0.29 | 0.12 | 3.50 | 100.51 |
| 260118 | 5 | 4.06 | 0.06 | 12.80 | 75.27 | 0.00 | 0.02 | 2.69 | 1.77 | 0.30 | 0.18 | 3.19 | 100.34 |
| 260118 | 5 | 4.10 | 0.12 | 12.72 | 75.55 | 0.03 | 0.00 | 2.78 | 1.67 | 0.30 | 0.02 | 3.13 | 100.41 |
| 260118 | 5 | 4.12 | 0.07 | 12.49 | 75.47 | 0.06 | 0.03 | 2.78 | 1.62 | 0.24 | 0.09 | 3.14 | 100.11 |
| 260118 | 5 | 4.51 | 0.11 | 12.31 | 75.70 | 0.06 | 0.05 | 2.75 | 1.71 | 0.24 | 0.04 | 3.10 | 100.58 |
| 260118 | 5 | 4.26 | 0.08 | 12.49 | 75.73 | 0.03 | 0.03 | 2.59 | 1.75 | 0.23 | 0.02 | 3.02 | 100.23 |
| 260118 | 5 | 4.19 | 0.14 | 12.25 | 75.70 | 0.02 | 0.04 | 2.67 | 1.71 | 0.24 | 0.06 | 2.98 | 100.02 |
| 050918 | 10 | 3.93 | 0.08 | 12.55 | 75.71 | 0.00 | 0.03 | 2.69 | 1.68 | 0.28 | 0.11 | 3.24 | 100.30 |
| 050918 | 10 | 4.54 | 0.08 | 12.52 | 75.36 | 0.00 | 0.03 | 2.61 | 1.62 | 0.19 | 0.08 | 3.22 | 100.26 |
| 050918 | 10 | 4.39 | 0.08 | 12.52 | 75.66 | 0.02 | 0.04 | 2.70 | 1.65 | 0.24 | 0.12 | 3.01 | 100.43 |
| 050918 | 10 | 4.18 | 0.11 | 12.25 | 75.24 | 0.02 | 0.03 | 2.78 | 1.67 | 0.27 | 0.12 | 3.12 | 99.79 |
| 050918 | 10 | 4.21 | 0.09 | 12.28 | 75.59 | 0.03 | 0.05 | 2.69 | 1.65 | 0.27 | 0.09 | 3.07 | 100.01 |
| 251017 | 5 | 4.20 | 0.12 | 12.45 | 75.02 | 0.02 | 0.02 | 2.71 | 1.77 | 0.24 | 0.16 | 3.39 | 100.09 |

| Probe date | Beam diam. | $Na_2O$ | MgO | $Al_2O_3$ | $SiO_2$ | $P_2O_5$ | Cl | $K_2O$ | CaO | $TiO_2$ | MnO | $FeO_t$ | Analytical Total |
|---|---|---|---|---|---|---|---|---|---|---|---|---|---|
| 050918 | 10 | 4.36 | 0.12 | 12.20 | 75.38 | 0.03 | 0.03 | 2.67 | 1.58 | 0.25 | 0.08 | 3.09 | 99.80 |
| 050918 | 10 | 4.35 | 0.11 | 12.39 | 75.91 | 0.03 | 0.02 | 2.58 | 1.70 | 0.21 | 0.12 | 3.08 | 100.49 |
| 050918 | 10 | 4.46 | 0.08 | 12.55 | 75.71 | 0.05 | 0.02 | 2.64 | 1.71 | 0.22 | 0.10 | 3.31 | 100.84 |
| 60918 | 5 | 4.01 | 0.08 | 12.44 | 75.84 | 0.02 | 0.05 | 2.74 | 1.72 | 0.31 | 0.04 | 3.31 | 100.57 |
| 60918 | 5 | 4.23 | 0.11 | 12.46 | 75.75 | 0.00 | 0.04 | 2.74 | 1.69 | 0.29 | 0.03 | 3.17 | 100.51 |
| 60918 | 5 | 4.02 | 0.09 | 12.20 | 75.69 | 0.00 | 0.05 | 2.77 | 1.69 | 0.17 | 0.00 | 3.15 | 99.83 |
| 60918 | 5 | 4.26 | 0.09 | 12.50 | 75.86 | 0.05 | 0.04 | 2.71 | 1.69 | 0.21 | 0.11 | 3.20 | 100.71 |
| 60918 | 5 | 3.89 | 0.11 | 12.52 | 75.35 | 0.05 | 0.04 | 2.78 | 1.73 | 0.20 | 0.10 | 3.14 | 99.89 |
| 60918 | 5 | 4.40 | 0.16 | 12.18 | 75.62 | 0.00 | 0.02 | 2.75 | 1.69 | 0.29 | 0.10 | 2.92 | 100.13 |
| 070918 | 5 | 3.98 | 0.09 | 12.44 | 75.37 | 0.05 | 0.03 | 2.71 | 1.70 | 0.28 | 0.07 | 3.32 | 100.04 |
| 070918 | 5 | 4.13 | 0.10 | 12.55 | 75.54 | 0.06 | 0.07 | 2.73 | 1.66 | 0.27 | 0.05 | 3.39 | 100.54 |
| 070918 | 5 | 4.53 | 0.10 | 12.35 | 75.46 | 0.03 | 0.02 | 2.79 | 1.68 | 0.30 | 0.08 | 3.18 | 100.54 |
| 070918 | 5 | 4.09 | 0.10 | 12.22 | 75.02 | 0.02 | 0.03 | 2.67 | 1.69 | 0.26 | 0.13 | 3.01 | 99.24 |
| 070918 | 5 | 4.12 | 0.09 | 12.13 | 75.22 | 0.01 | 0.05 | 2.74 | 1.79 | 0.24 | 0.13 | 3.26 | 99.78 |
| 070918 | 5 | 4.30 | 0.10 | 12.36 | 75.79 | 0.01 | 0.03 | 2.62 | 1.67 | 0.27 | 0.02 | 3.20 | 100.36 |
| 070918 | 5 | 4.18 | 0.11 | 12.49 | 76.10 | 0.01 | 0.03 | 2.80 | 1.66 | 0.22 | 0.13 | 3.28 | 100.99 |
| 070918 | 5 | 4.14 | 0.06 | 12.30 | 75.70 | 0.02 | 0.04 | 2.77 | 1.67 | 0.19 | 0.11 | 3.18 | 100.19 |
| 070918 | 5 | 4.24 | 0.10 | 12.47 | 75.24 | 0.00 | 0.04 | 2.75 | 1.59 | 0.20 | 0.11 | 2.99 | 99.72 |
| 150419 | 5 | 4.08 | 0.11 | 12.50 | 74.89 | 0.00 | 0.01 | 2.73 | 1.58 | 0.26 | 0.12 | 3.33 | 99.61 |
| 150419 | 5 | 4.25 | 0.10 | 12.36 | 75.04 | 0.00 | 0.03 | 2.68 | 1.75 | 0.27 | 0.09 | 3.29 | 99.84 |
| 150419 | 5 | 4.01 | 0.10 | 12.51 | 74.95 | 0.03 | 0.04 | 2.85 | 1.71 | 0.26 | 0.12 | 3.36 | 99.94 |
| 150419 | 5 | 4.11 | 0.09 | 12.30 | 75.42 | 0.06 | 0.03 | 2.68 | 1.69 | 0.27 | 0.10 | 3.05 | 99.80 |
| 150419 | 5 | 4.02 | 0.10 | 12.14 | 75.65 | 0.03 | 0.02 | 2.64 | 1.67 | 0.24 | 0.17 | 3.09 | 99.78 |
| 150419 | 5 | 4.14 | 0.11 | 12.16 | 75.43 | 0.04 | 0.04 | 2.73 | 1.72 | 0.26 | 0.13 | 3.43 | 100.19 |
| 150419 | 5 | 4.43 | 0.12 | 12.18 | 75.47 | 0.05 | 0.04 | 2.76 | 1.67 | 0.16 | 0.12 | 3.24 | 100.24 |
| 150419 | 5 | 4.34 | 0.08 | 12.16 | 75.68 | 0.04 | 0.04 | 2.79 | 1.74 | 0.21 | 0.17 | 3.05 | 100.30 |

**Table A2.5** Secondary standard of GOR132 for major geochemistry analysis with the date of analysis

| Probe date | Beam diam. | $Na_2O$ | MgO | $Al_2O_3$ | $SiO_2$ | $P_2O_5$ | Cl | $K_2O$ | CaO | $TiO_2$ | MnO | $FeO_t$ | Analytical Total |
|---|---|---|---|---|---|---|---|---|---|---|---|---|---|
| 121016 | 10 | 0.80 | 22.27 | 11.17 | 45.41 | 0.01 | 0.00 | 0.04 | 8.50 | 0.34 | 0.17 | 10.15 | 98.86 |
| 121016 | 10 | 0.72 | 22.17 | 11.07 | 45.48 | 0.02 | 0.01 | 0.03 | 8.41 | 0.29 | 0.23 | 10.25 | 98.68 |
| 121016 | 10 | 0.70 | 22.16 | 10.85 | 45.60 | 0.04 | 0.00 | 0.07 | 8.44 | 0.24 | 0.11 | 10.23 | 98.44 |
| 121016 | 10 | 0.83 | 22.32 | 10.87 | 45.16 | 0.04 | 0.01 | 0.03 | 8.46 | 0.35 | 0.16 | 10.34 | 98.57 |
| 121016 | 10 | 0.71 | 22.01 | 10.57 | 45.45 | 0.02 | 0.00 | 0.03 | 8.42 | 0.29 | 0.10 | 10.19 | 97.79 |
| 121016 | 10 | 0.71 | 22.10 | 10.93 | 45.04 | 0.04 | 0.00 | 0.02 | 8.31 | 0.24 | 0.12 | 10.07 | 97.59 |
| 291116 | 5 | 0.70 | 22.30 | 11.10 | 45.71 | 0.02 | 0.01 | 0.05 | 8.27 | 0.31 | 0.13 | 10.47 | 99.08 |
| 291116 | 5 | 0.79 | 22.31 | 11.24 | 45.81 | 0.05 | 0.01 | 0.03 | 8.34 | 0.29 | 0.13 | 9.93 | 98.92 |
| 291116 | 5 | 0.80 | 22.48 | 11.10 | 46.03 | 0.03 | 0.00 | 0.04 | 8.61 | 0.29 | 0.04 | 10.43 | 99.85 |
| 291116 | 5 | 0.79 | 22.03 | 10.83 | 45.98 | 0.01 | 0.02 | 0.03 | 8.60 | 0.35 | 0.14 | 10.11 | 98.91 |
| 291116 | 5 | 0.88 | 22.23 | 10.78 | 45.67 | 0.08 | 0.01 | 0.05 | 8.52 | 0.30 | 0.07 | 10.21 | 98.82 |
| 291116 | 5 | 0.85 | 22.23 | 10.78 | 46.01 | 0.06 | 0.01 | 0.05 | 8.80 | 0.26 | 0.15 | 10.16 | 99.35 |
| 091216 | 5 | 0.80 | 22.56 | 11.01 | 45.91 | 0.07 | 0.01 | 0.05 | 8.70 | 0.31 | 0.13 | 10.12 | 99.65 |
| 091216 | 5 | 0.75 | 22.81 | 11.07 | 45.65 | 0.09 | 0.01 | 0.05 | 8.43 | 0.31 | 0.17 | 9.93 | 99.28 |
| 091216 | 5 | 0.83 | 22.95 | 10.93 | 45.98 | 0.02 | 0.00 | 0.03 | 8.49 | 0.31 | 0.16 | 10.22 | 99.91 |
| 091216 | 5 | 0.81 | 22.60 | 10.94 | 45.89 | 0.07 | 0.01 | 0.05 | 8.44 | 0.32 | 0.20 | 10.04 | 99.36 |
| 091216 | 5 | 0.91 | 22.73 | 10.93 | 45.95 | 0.05 | 0.00 | 0.02 | 8.43 | 0.34 | 0.24 | 10.33 | 99.92 |
| 091216 | 5 | 0.76 | 22.83 | 10.75 | 45.88 | 0.03 | 0.01 | 0.05 | 8.57 | 0.31 | 0.10 | 10.59 | 99.87 |
| 010517 | 10 | 0.75 | 22.07 | 10.90 | 45.06 | 0.05 | 0.01 | 0.05 | 8.58 | 0.24 | 0.11 | 10.35 | 98.17 |
| 010517 | 10 | 0.87 | 22.42 | 11.11 | 45.27 | 0.05 | 0.00 | 0.03 | 8.55 | 0.30 | 0.13 | 9.95 | 98.68 |
| 010517 | 10 | 0.89 | 22.21 | 10.84 | 45.52 | 0.04 | 0.02 | 0.03 | 8.75 | 0.27 | 0.13 | 9.73 | 98.43 |
| 010517 | 10 | 0.82 | 22.43 | 10.90 | 45.64 | 0.03 | 0.00 | 0.03 | 8.47 | 0.33 | 0.19 | 9.74 | 98.58 |
| 010517 | 10 | 0.92 | 22.18 | 10.97 | 45.56 | 0.06 | 0.00 | 0.03 | 8.57 | 0.28 | 0.12 | 9.93 | 98.62 |
| 010517 | 10 | 0.67 | 22.17 | 11.07 | 45.34 | 0.02 | 0.01 | 0.04 | 8.48 | 0.33 | 0.17 | 10.28 | 98.58 |

| Probe date | Beam diam. | $Na_2O$ | MgO | $Al_2O_3$ | $SiO_2$ | $P_2O_5$ | Cl | $K_2O$ | CaO | $TiO_2$ | MnO | $FeO_t$ | Analytical Total |
|---|---|---|---|---|---|---|---|---|---|---|---|---|---|
| 260617 | 5 | 0.77 | 21.86 | 10.99 | 45.68 | 0.05 | 0.02 | 0.00 | 8.27 | 0.31 | 0.13 | 9.38 | 97.46 |
| 260617 | 5 | 0.83 | 22.12 | 11.16 | 45.99 | 0.00 | 0.01 | 0.03 | 8.33 | 0.37 | 0.14 | 9.86 | 98.85 |
| 260617 | 5 | 0.71 | 22.11 | 11.08 | 45.91 | 0.02 | 0.00 | 0.02 | 8.36 | 0.36 | 0.11 | 9.81 | 98.49 |
| 260617 | 5 | 0.78 | 22.06 | 10.90 | 45.83 | 0.01 | 0.00 | 0.02 | 8.48 | 0.30 | 0.15 | 10.24 | 98.78 |
| 260617 | 5 | 0.84 | 22.47 | 10.96 | 45.93 | 0.01 | 0.00 | 0.05 | 8.42 | 0.31 | 0.23 | 10.14 | 99.34 |
| 260617 | 5 | 0.80 | 22.27 | 10.88 | 45.60 | 0.05 | 0.00 | 0.03 | 8.28 | 0.28 | 0.07 | 9.99 | 98.24 |
| 260617 | 5 | 0.83 | 22.38 | 10.93 | 46.07 | 0.08 | 0.01 | 0.03 | 8.24 | 0.30 | 0.24 | 10.43 | 99.53 |
| 260617 | 5 | 0.73 | 22.31 | 11.03 | 45.89 | 0.05 | 0.00 | 0.03 | 8.37 | 0.33 | 0.09 | 10.70 | 99.53 |
| 260617 | 5 | 0.76 | 22.16 | 10.91 | 45.64 | 0.01 | 0.00 | 0.06 | 8.42 | 0.34 | 0.23 | 9.84 | 98.36 |
| 171017 | 5 | 0.60 | 24.88 | 9.93 | 46.79 | 0.02 | 0.02 | 0.02 | 6.24 | 0.32 | 0.10 | 9.72 | 98.63 |
| 171017 | 5 | 0.56 | 25.39 | 9.69 | 45.73 | 0.06 | 0.00 | 0.04 | 6.12 | 0.23 | 0.22 | 9.63 | 97.68 |
| 171017 | 5 | 0.53 | 25.59 | 9.84 | 45.95 | 0.02 | 0.00 | 0.06 | 5.91 | 0.29 | 0.21 | 9.71 | 98.12 |
| 171017 | 5 | 0.41 | 25.51 | 9.84 | 45.62 | 0.00 | 0.01 | 0.03 | 6.14 | 0.28 | 0.19 | 10.08 | 98.10 |
| 171017 | 5 | 0.56 | 25.58 | 10.04 | 45.32 | 0.04 | 0.00 | 0.05 | 6.19 | 0.29 | 0.21 | 10.19 | 98.45 |
| 171017 | 5 | 0.65 | 25.19 | 9.90 | 45.27 | 0.10 | 0.01 | 0.07 | 6.32 | 0.32 | 0.15 | 9.53 | 97.50 |
| 171017 | 5 | 0.54 | 25.57 | 9.77 | 45.66 | 0.00 | 0.00 | 0.05 | 6.11 | 0.27 | 0.16 | 9.84 | 97.96 |
| 171017 | 5 | 0.79 | 25.43 | 9.62 | 46.30 | 0.03 | 0.02 | 0.04 | 6.18 | 0.29 | 0.14 | 9.64 | 98.48 |
| 171017 | 5 | 0.73 | 25.29 | 9.65 | 45.63 | 0.05 | 0.00 | 0.05 | 6.14 | 0.28 | 0.21 | 10.20 | 98.22 |
| 171017 | 5 | 0.65 | 25.41 | 9.89 | 45.93 | 0.06 | 0.01 | 0.07 | 6.22 | 0.28 | 0.16 | 10.08 | 98.75 |
| 191017 | 5 | 0.55 | 25.26 | 9.93 | 46.21 | 0.04 | 0.00 | 0.07 | 6.10 | 0.34 | 0.05 | 9.58 | 98.14 |
| 191017 | 5 | 0.49 | 25.50 | 9.64 | 46.06 | 0.01 | 0.00 | 0.00 | 6.10 | 0.28 | 0.21 | 9.72 | 98.02 |
| 191017 | 5 | 0.56 | 25.41 | 9.75 | 46.41 | 0.06 | 0.02 | 0.05 | 6.22 | 0.28 | 0.10 | 9.82 | 98.66 |
| 191017 | 5 | 0.66 | 25.36 | 9.80 | 45.96 | 0.05 | 0.00 | 0.04 | 6.09 | 0.34 | 0.13 | 9.71 | 98.14 |
| 191017 | 5 | 0.58 | 25.33 | 9.71 | 45.94 | 0.06 | 0.00 | 0.06 | 6.05 | 0.28 | 0.21 | 9.97 | 98.18 |
| 191017 | 5 | 0.61 | 25.31 | 10.03 | 45.65 | 0.08 | 0.02 | 0.04 | 6.21 | 0.24 | 0.15 | 10.05 | 98.39 |
| 191017 | 5 | 0.49 | 25.55 | 9.88 | 45.51 | 0.02 | 0.01 | 0.05 | 6.29 | 0.28 | 0.16 | 9.69 | 97.94 |

| Probe date | Beam diam. | $Na_2O$ | MgO | $Al_2O_3$ | $SiO_2$ | $P_2O_5$ | Cl | $K_2O$ | CaO | $TiO_2$ | MnO | $FeO_t$ | Analytical Total |
|---|---|---|---|---|---|---|---|---|---|---|---|---|---|
| 191017 | 5 | 0.48 | 25.45 | 9.63 | 45.32 | 0.02 | 0.01 | 0.04 | 6.16 | 0.31 | 0.27 | 9.36 | 97.04 |
| 251017 | 5 | 0.79 | 22.16 | 11.08 | 45.31 | 0.01 | 0.00 | 0.03 | 8.63 | 0.26 | 0.15 | 10.06 | 98.46 |
| 251017 | 5 | 0.92 | 21.76 | 11.05 | 45.59 | 0.01 | 0.01 | 0.04 | 8.38 | 0.30 | 0.11 | 10.07 | 98.23 |
| 251017 | 5 | 0.85 | 21.75 | 11.29 | 45.43 | 0.05 | 0.02 | 0.04 | 8.50 | 0.32 | 0.17 | 10.52 | 98.94 |
| 251017 | 5 | 0.77 | 22.03 | 10.96 | 45.86 | 0.08 | 0.01 | 0.03 | 8.41 | 0.29 | 0.11 | 9.96 | 98.51 |
| 251017 | 5 | 0.65 | 22.05 | 10.95 | 45.34 | 0.09 | 0.01 | 0.05 | 8.26 | 0.32 | 0.19 | 10.24 | 98.14 |
| 251017 | 5 | 0.78 | 21.97 | 10.86 | 45.61 | 0.05 | 0.00 | 0.01 | 8.29 | 0.28 | 0.23 | 10.40 | 98.49 |
| 251017 | 5 | 0.74 | 22.00 | 11.00 | 45.48 | 0.02 | 0.00 | 0.03 | 8.37 | 0.30 | 0.09 | 10.24 | 98.28 |
| 230118 | 5 | 0.71 | 22.08 | 11.25 | 46.12 | 0.07 | 0.00 | 0.01 | 8.42 | 0.18 | 0.08 | 10.60 | 99.52 |
| 230118 | 5 | 0.88 | 22.24 | 11.02 | 46.14 | 0.01 | 0.00 | 0.04 | 8.37 | 0.33 | 0.19 | 10.59 | 99.81 |
| 230118 | 5 | 0.83 | 22.48 | 10.94 | 45.77 | 0.12 | 0.00 | 0.02 | 8.30 | 0.27 | 0.13 | 10.07 | 98.93 |
| 230118 | 5 | 0.90 | 22.49 | 10.79 | 45.51 | 0.11 | 0.00 | 0.02 | 8.64 | 0.27 | 0.08 | 10.16 | 98.98 |
| 230118 | 5 | 0.67 | 22.60 | 10.77 | 45.22 | 0.08 | 0.00 | 0.05 | 8.40 | 0.31 | 0.16 | 10.19 | 98.44 |
| 230118 | 5 | 0.80 | 22.50 | 10.84 | 45.71 | 0.10 | 0.01 | 0.04 | 8.44 | 0.24 | 0.17 | 9.96 | 98.80 |
| 230118 | 5 | 0.90 | 22.15 | 10.63 | 45.57 | 0.13 | 0.01 | 0.04 | 8.36 | 0.26 | 0.10 | 10.41 | 98.55 |
| 240118 | 5 | 0.75 | 21.92 | 11.08 | 46.22 | 0.03 | 0.00 | 0.04 | 8.34 | 0.32 | 0.10 | 10.29 | 99.08 |
| 240118 | 5 | 0.91 | 22.34 | 10.79 | 45.55 | 0.02 | 0.00 | 0.05 | 8.50 | 0.25 | 0.21 | 10.32 | 98.95 |
| 240118 | 5 | 0.87 | 22.19 | 10.81 | 45.22 | 0.01 | 0.00 | 0.01 | 8.38 | 0.31 | 0.25 | 9.93 | 97.98 |
| 240118 | 5 | 0.94 | 22.48 | 10.67 | 45.21 | 0.03 | 0.00 | 0.03 | 8.27 | 0.32 | 0.04 | 9.92 | 97.90 |
| 240118 | 5 | 0.78 | 22.45 | 10.61 | 45.02 | 0.07 | 0.00 | 0.07 | 8.48 | 0.22 | 0.17 | 10.37 | 98.25 |
| 240118 | 5 | 0.74 | 22.52 | 10.75 | 45.33 | 0.05 | 0.00 | 0.00 | 8.43 | 0.33 | 0.22 | 10.26 | 98.63 |
| 240118 | 5 | 0.70 | 22.28 | 10.54 | 44.83 | 0.05 | 0.00 | 0.05 | 8.36 | 0.28 | 0.25 | 10.39 | 97.74 |
| 260118 | 5 | 0.82 | 21.69 | 11.07 | 45.66 | 0.09 | 0.00 | 0.03 | 8.36 | 0.30 | 0.11 | 10.11 | 98.25 |
| 260118 | 5 | 0.75 | 21.77 | 11.03 | 45.91 | 0.06 | 0.00 | 0.03 | 8.30 | 0.27 | 0.13 | 10.53 | 98.78 |
| 260118 | 5 | 0.89 | 22.29 | 11.07 | 46.02 | 0.06 | 0.00 | 0.04 | 8.14 | 0.34 | 0.12 | 9.87 | 98.83 |
| 260118 | 5 | 0.68 | 22.39 | 10.85 | 45.59 | 0.11 | 0.01 | 0.04 | 8.34 | 0.25 | 0.14 | 10.41 | 98.81 |

| Probe date | Beam diam. | $Na_2O$ | MgO | $Al_2O_3$ | $SiO_2$ | $P_2O_5$ | Cl | $K_2O$ | CaO | $TiO_2$ | MnO | $FeO_t$ | Analytical Total |
|---|---|---|---|---|---|---|---|---|---|---|---|---|---|
| 260118 | 5 | 0.78 | 22.20 | 11.08 | 45.88 | 0.05 | 0.02 | 0.05 | 8.62 | 0.30 | 0.29 | 10.38 | 99.65 |
| 260118 | 5 | 0.92 | 22.12 | 11.14 | 45.66 | 0.03 | 0.00 | 0.03 | 8.52 | 0.28 | 0.19 | 10.26 | 99.14 |
| 050918 | 10 | 0.86 | 22.04 | 10.88 | 45.65 | 0.03 | 0.00 | 0.04 | 8.60 | 0.29 | 0.11 | 10.04 | 98.55 |
| 050918 | 10 | 0.79 | 22.25 | 10.70 | 45.40 | 0.02 | 0.01 | 0.01 | 8.57 | 0.28 | 0.20 | 9.94 | 98.18 |
| 050918 | 10 | 0.96 | 22.07 | 11.01 | 45.65 | 0.03 | 0.00 | 0.03 | 8.62 | 0.27 | 0.13 | 10.51 | 99.29 |
| 050918 | 10 | 0.78 | 22.04 | 11.05 | 45.72 | 0.05 | 0.03 | 0.03 | 8.55 | 0.27 | 0.13 | 10.49 | 99.13 |
| 050918 | 10 | 0.83 | 22.20 | 10.81 | 45.68 | 0.03 | 0.01 | 0.02 | 8.37 | 0.32 | 0.21 | 10.62 | 99.11 |
| 050918 | 10 | 0.84 | 22.26 | 10.76 | 45.24 | 0.05 | 0.01 | 0.02 | 8.62 | 0.36 | 0.16 | 10.12 | 98.44 |
| 050918 | 10 | 0.85 | 22.08 | 10.86 | 45.66 | 0.02 | 0.01 | 0.01 | 8.41 | 0.34 | 0.18 | 10.52 | 98.94 |
| 050918 | 10 | 0.84 | 22.05 | 11.07 | 45.57 | 0.00 | 0.00 | 0.02 | 8.41 | 0.27 | 0.23 | 10.01 | 98.48 |
| 60918 | 5 | 0.91 | 22.04 | 11.16 | 45.70 | 0.02 | 0.02 | 0.02 | 8.35 | 0.28 | 0.17 | 10.31 | 98.98 |
| 60918 | 5 | 0.90 | 21.94 | 11.03 | 45.48 | 0.01 | 0.01 | 0.01 | 8.39 | 0.27 | 0.15 | 10.15 | 98.32 |
| 60918 | 5 | 0.80 | 22.21 | 10.90 | 45.47 | 0.03 | 0.02 | 0.03 | 8.67 | 0.33 | 0.19 | 10.09 | 98.72 |
| 60918 | 5 | 0.83 | 22.14 | 11.00 | 45.23 | 0.00 | 0.01 | 0.04 | 8.50 | 0.27 | 0.17 | 10.54 | 98.73 |
| 60918 | 5 | 0.91 | 22.29 | 10.97 | 45.89 | 0.03 | 0.01 | 0.06 | 8.57 | 0.29 | 0.11 | 10.02 | 99.15 |
| 60918 | 5 | 0.74 | 21.89 | 11.03 | 45.89 | 0.03 | 0.00 | 0.05 | 8.38 | 0.34 | 0.16 | 10.20 | 98.71 |
| 070918 | 5 | 0.88 | 22.16 | 10.82 | 45.83 | 0.08 | 0.00 | 0.04 | 8.41 | 0.30 | 0.20 | 10.36 | 99.08 |
| 070918 | 5 | 0.73 | 22.03 | 11.21 | 45.83 | 0.01 | 0.00 | 0.03 | 8.44 | 0.30 | 0.19 | 10.42 | 99.19 |
| 070918 | 5 | 0.86 | 22.22 | 11.01 | 45.86 | 0.05 | 0.02 | 0.04 | 8.42 | 0.28 | 0.16 | 10.23 | 99.16 |
| 070918 | 5 | 0.84 | 22.06 | 11.09 | 45.56 | 0.04 | 0.00 | 0.00 | 8.44 | 0.29 | 0.17 | 10.48 | 98.97 |
| 070918 | 5 | 0.92 | 22.24 | 10.96 | 45.86 | 0.02 | 0.00 | 0.04 | 8.35 | 0.31 | 0.15 | 10.31 | 99.14 |
| 070918 | 5 | 0.96 | 21.89 | 11.18 | 45.95 | 0.02 | 0.01 | 0.00 | 8.66 | 0.27 | 0.15 | 10.12 | 99.20 |
| 070918 | 5 | 0.88 | 21.81 | 11.20 | 45.81 | 0.04 | 0.01 | 0.09 | 8.53 | 0.26 | 0.10 | 10.16 | 98.88 |
| 070918 | 5 | 0.90 | 21.72 | 11.03 | 46.10 | 0.03 | 0.00 | 0.03 | 8.67 | 0.32 | 0.24 | 9.85 | 98.86 |
| 070918 | 5 | 0.92 | 22.12 | 11.21 | 45.83 | 0.00 | 0.00 | 0.06 | 8.55 | 0.42 | 0.20 | 10.29 | 99.62 |
| 150419 | 5 | 0.83 | 22.23 | 10.83 | 45.84 | 0.01 | 0.01 | 0.03 | 8.18 | 0.33 | 0.20 | 10.38 | 98.87 |

| Probe date | Beam diam. | $Na_2O$ | MgO | $Al_2O_3$ | $SiO_2$ | $P_2O_5$ | Cl | $K_2O$ | CaO | $TiO_2$ | MnO | $FeO_t$ | Analytical Total |
|---|---|---|---|---|---|---|---|---|---|---|---|---|---|
| 150419 | 5 | 0.86 | 21.99 | 10.96 | 45.46 | 0.05 | 0.00 | 0.07 | 8.27 | 0.30 | 0.15 | 10.33 | 98.45 |
| 150419 | 5 | 0.80 | 21.77 | 11.09 | 45.30 | 0.02 | 0.00 | 0.02 | 8.52 | 0.24 | 0.20 | 10.00 | 97.97 |
| 150419 | 5 | 0.89 | 22.00 | 11.08 | 45.18 | 0.03 | 0.00 | 0.03 | 8.46 | 0.30 | 0.18 | 10.30 | 98.45 |
| 150419 | 5 | 0.82 | 22.44 | 10.87 | 46.10 | 0.08 | 0.00 | 0.03 | 8.71 | 0.35 | 0.22 | 9.91 | 99.55 |
| 150419 | 5 | 0.73 | 22.02 | 11.11 | 45.71 | 0.12 | 0.00 | 0.04 | 8.43 | 0.25 | 0.20 | 10.20 | 98.80 |
| 150419 | 5 | 0.84 | 22.07 | 10.84 | 45.81 | 0.10 | 0.01 | 0.02 | 8.45 | 0.30 | 0.21 | 9.97 | 98.61 |
| 150419 | 5 | 0.83 | 21.86 | 10.94 | 46.18 | 0.08 | 0.01 | 0.03 | 8.47 | 0.33 | 0.14 | 10.23 | 99.10 |

**Table A2.6** Lake Lia trace geochemistry raw data

| **Depth (cm)** | 631 | | | | 633 | |
|---|---|---|---|---|---|---|
| **Label** | LIA_631 | LIA_631 | LIA_631 | LIA_631 | LIA_633 | LIA_633 |
| **Ca43** | 5675.6 | 5980.6 | 10828.7 | 12291.8 | 5144.0 | 4883.7 |
| **Ti47** | NA | NA | NA | NA | NA | NA |
| **Ni60** | NA | NA | NA | NA | NA | NA |
| **Rb85** | 327.3 | 314.3 | 619.1 | 97.6 | 330.0 | 324.6 |
| **Sr88** | 13.8 | 13.3 | 3.9 | 108.0 | 11.5 | 11.8 |
| **Y89** | 32.3 | 33.7 | 72.3 | 62.0 | 33.8 | 37.5 |
| **Zr90** | 132.2 | 138.9 | 969.2 | 708.2 | 138.0 | 151.5 |
| **Nb93** | 35.1 | 34.5 | 156.1 | 131.6 | 36.1 | 36.8 |
| **Ba138** | 12.0 | 18.2 | 7.9 | 655.4 | 9.8 | 9.8 |
| **La139** | 40.5 | 42.2 | 150.5 | 71.9 | 43.2 | 46.6 |
| **Ce140** | 86.6 | 88.2 | 280.6 | 165.1 | 90.9 | 95.3 |
| **Pr141** | 8.7 | 9.2 | 27.6 | 18.2 | 9.2 | 10.0 |
| **Nd146** | 32.7 | 32.7 | 88.4 | 71.2 | 34.9 | 36.2 |
| **Sm147** | 5.6 | 7.5 | 15.4 | 15.3 | 6.9 | 6.7 |
| **Eu153** | 0.2 | 0.3 | 0.9 | 3.5 | 0.3 | 0.2 |
| **Gd157** | 5.7 | 5.6 | 11.6 | 13.5 | 5.7 | 6.0 |
| **Dy163** | 5.4 | 5.7 | 10.9 | 13.1 | 5.5 | 6.3 |
| **Er166** | 3.8 | 3.4 | 7.1 | 6.8 | 3.6 | 3.7 |
| **Yb172** | 3.8 | 4.4 | 8.8 | 7.3 | 3.9 | 4.3 |
| **Lu175** | 0.5 | 0.5 | 1.3 | 0.9 | 0.5 | 0.6 |
| **Hf178** | 4.7 | 4.9 | 20.1 | 16.0 | 4.5 | 5.7 |
| **Ta181** | 2.1 | 2.2 | 6.8 | 5.9 | 2.2 | 2.3 |
| **Pb208** | 36.7 | 34.8 | 97.2 | 8.3 | 27.6 | 30.0 |
| **Th232** | 35.8 | 39.3 | 75.4 | 8.2 | 39.4 | 43.4 |
| **U238** | 12.8 | 14.2 | 24.9 | 3.3 | 13.6 | 14.3 |

Appendix 2. Tephra geochemistry data

| **Depth (cm)** | 633 | | | | | 637 |
|---|---|---|---|---|---|---|
| **Label** | LIA_633 | LIA_633 | LIA_633 | LIA_633 | LIA_633 | LIA_637 |
| **Ca43** | 5298.3 | 7164.4 | 5129.9 | 4909.4 | 6618.0 | 5270.0 |
| **Ti47** | NA | NA | NA | NA | NA | NA |
| **Ni60** | NA | NA | NA | NA | NA | NA |
| **Rb85** | 310.0 | 326.4 | 327.6 | 323.1 | 327.9 | 302.3 |
| **Sr88** | 17.0 | 10.6 | 10.8 | 11.1 | 13.1 | 13.3 |
| **Y89** | 37.1 | 43.1 | 36.9 | 35.3 | 32.2 | 37.9 |
| **Zr90** | 162.4 | 159.0 | 151.2 | 148.0 | 130.4 | 151.4 |
| **Nb93** | 35.6 | 36.7 | 36.9 | 34.7 | 34.5 | 35.4 |
| **Ba138** | 17.9 | 11.6 | 12.3 | 10.2 | 12.7 | 11.6 |
| **La139** | 49.7 | 51.6 | 46.1 | 44.5 | 41.5 | 45.7 |
| **Ce140** | 98.9 | 110.0 | 92.9 | 90.2 | 84.8 | 95.3 |
| **Pr141** | 10.3 | 12.3 | 9.7 | 9.8 | 8.8 | 10.1 |
| **Nd146** | 37.3 | 43.4 | 35.4 | 32.9 | 32.2 | 34.3 |
| **Sm147** | 7.6 | 8.5 | 6.7 | 7.5 | 7.0 | 7.6 |
| **Eu153** | 0.2 | 0.2 | 0.2 | 0.3 | 0.4 | <LOD |
| **Gd157** | 6.5 | 7.4 | 6.6 | 5.5 | 6.1 | 6.1 |
| **Dy163** | 5.8 | 7.7 | 6.8 | 5.4 | 5.8 | 6.4 |
| **Er166** | 3.8 | 4.6 | 4.1 | 3.4 | 3.1 | 4.1 |
| **Yb172** | 3.5 | 5.9 | 4.6 | 4.0 | 4.0 | 4.5 |
| **Lu175** | 0.6 | 0.7 | 0.6 | 0.6 | 0.6 | <LOD |
| **Hf178** | 6.0 | 6.1 | 5.4 | 5.5 | 4.6 | 5.6 |
| **Ta181** | 2.3 | 2.6 | 2.3 | 2.2 | 2.0 | 2.4 |
| **Pb208** | 29.7 | 30.1 | 29.1 | 27.6 | 29.4 | 28.2 |
| **Th232** | 44.1 | 48.0 | 40.7 | 39.1 | 33.7 | 43.9 |
| **U238** | 14.4 | 14.9 | 14.0 | 14.7 | 13.3 | 14.0 |

Appendix 2. Tephra geochemistry data

| **Depth (cm)** | 637 | | | 796 | | |
|---|---|---|---|---|---|---|
| **Label** | LIA_637 | LIA_637 | LIA_637 | LIA_796 | LIA_796 | LIA_796 |
| **Ca43** | 5122.0 | 4404.9 | 4571.4 | 4214.4 | 5303.0 | 5307.3 |
| **Ti47** | NA | NA | NA | NA | NA | NA |
| **Ni60** | NA | NA | NA | NA | NA | NA |
| **Rb85** | 323.9 | 309.8 | 182.9 | 172.2 | 157.5 | 177.7 |
| **Sr88** | 11.3 | 14.4 | 31.9 | 26.2 | 42.9 | 36.3 |
| **Y89** | 35.3 | 35.8 | 25.0 | 32.7 | 36.7 | 37.9 |
| **Zr90** | 141.5 | 145.8 | 57.5 | 58.9 | 94.1 | 65.9 |
| **Nb93** | 33.2 | 34.2 | 11.1 | 13.7 | 16.4 | 11.9 |
| **Ba138** | 8.3 | 23.6 | 754.9 | 603.0 | 960.8 | 752.5 |
| **La139** | 43.3 | 42.9 | 20.6 | 17.4 | 28.5 | 27.9 |
| **Ce140** | 80.7 | 85.7 | 41.2 | 37.4 | 62.6 | 58.0 |
| **Pr141** | 9.7 | 9.7 | 4.5 | 4.3 | 6.7 | 6.8 |
| **Nd146** | 30.9 | 33.1 | 17.1 | 17.2 | 25.7 | 26.4 |
| **Sm147** | 7.5 | 8.0 | 4.1 | 4.5 | 6.6 | 6.7 |
| **Eu153** | <LOD | <LOD | <LOD | 0.3 | 0.6 | 0.4 |
| **Gd157** | 5.8 | 6.7 | 3.6 | 4.9 | 5.3 | 6.7 |
| **Dy163** | 6.1 | 6.4 | 4.2 | 5.9 | 6.4 | 7.1 |
| **Er166** | 4.0 | 3.6 | 2.7 | 3.9 | 3.6 | 3.7 |
| **Yb172** | 4.8 | 4.6 | 3.4 | 3.7 | 4.2 | 4.1 |
| **Lu175** | <LOD | <LOD | <LOD | 0.5 | 0.6 | 0.6 |
| **Hf178** | 5.6 | 5.3 | 2.9 | 2.9 | 4.3 | 3.0 |
| **Ta181** | 2.2 | 2.3 | 1.4 | 1.3 | 1.2 | 1.1 |
| **Pb208** | 25.6 | 30.1 | 25.3 | 22.8 | 23.3 | 26.5 |
| **Th232** | 38.4 | 42.2 | 14.2 | 13.0 | 12.9 | 15.2 |
| **U238** | 12.5 | 13.7 | 5.8 | 5.0 | 4.5 | 4.9 |

Appendix 2. Tephra geochemistry data

| **Depth (cm)** | 796 | | 805 |
|---|---|---|---|
| **Label** | LIA_796 | LIA_796 | LIA_805 |
| **Ca43** | 8126.4 | 16421.3 | 5541.1 |
| **Ti47** | NA | NA | NA |
| **Ni60** | NA | NA | NA |
| **Rb85** | 146.3 | 372.7 | 140.4 |
| **Sr88** | 69.1 | 236.8 | 43.9 |
| **Y89** | 24.1 | 34.6 | 34.9 |
| **Zr90** | 102.8 | 422.9 | 130.6 |
| **Nb93** | 11.7 | 65.5 | 16.7 |
| **Ba138** | 897.7 | 96.1 | 784.5 |
| **La139** | 33.8 | 85.9 | 35.0 |
| **Ce140** | 64.5 | 165.7 | 73.3 |
| **Pr141** | 6.5 | 15.9 | 8.0 |
| **Nd146** | 23.1 | 60.2 | 30.7 |
| **Sm147** | 5.4 | 11.7 | 5.6 |
| **Eu153** | 0.5 | 2.0 | 0.5 |
| **Gd157** | 3.7 | 7.6 | 6.1 |
| **Dy163** | 4.1 | 6.4 | 5.5 |
| **Er166** | 2.6 | 3.5 | 4.1 |
| **Yb172** | 2.9 | 3.3 | 4.0 |
| **Lu175** | 0.3 | 0.5 | 0.5 |
| **Hf178** | 2.9 | 9.1 | 4.5 |
| **Ta181** | 1.1 | 3.3 | 1.2 |
| **Pb208** | 20.3 | 51.0 | 20.7 |
| **Th232** | 13.6 | 37.7 | 12.9 |
| **U238** | 4.1 | 13.3 | 4.2 |

**Table A2.7** Lake Brazi trace geochemistry raw data

| **Depth (cm)** | 556 | | | | | |
|---|---|---|---|---|---|---|
| **Label** | TDB_556 | TDB_556 | TDB_556 | TDB_556 | TDB_556 | TDB_556 |
| **Ca43** | 6113 | 4519 | 11919 | 6166 | 5684 | 6352 |
| **Ti47** | 298.2 | 217.9 | 2122.7 | 532.7 | 524.0 | 494.3 |
| **Ni60** | 20.8 | NA | NA | 10.5 | NA | NA |
| **Rb85** | 177.1 | 171.0 | 92.6 | 325.6 | 335.2 | 322.8 |
| **Sr88** | 37.1 | 27.2 | 130.3 | 13.9 | 18.0 | 14.4 |
| **Y89** | 34.5 | 35.9 | 85.4 | 41.6 | 40.4 | 37.9 |
| **Zr90** | 63.4 | 66.9 | 918.5 | 166.0 | 166.8 | 151.0 |
| **Nb93** | 13.6 | 13.6 | 136.8 | 36.7 | 37.2 | 35.8 |
| **Ba138** | 616.0 | 657.4 | 742.0 | 12.5 | 16.2 | 11.8 |
| **La139** | 19.5 | 18.5 | 93.1 | 50.8 | 49.8 | 45.5 |
| **Ce140** | 43.3 | 41.2 | 198.8 | 101.4 | 98.3 | 93.8 |
| **Pr141** | 4.6 | 5.0 | 23.1 | 10.8 | 10.8 | 10.0 |
| **Nd146** | 19.9 | 18.5 | 94.4 | 38.9 | 40.5 | 34.8 |
| **Sm147** | 4.9 | 5.0 | 18.4 | 8.1 | 8.3 | 6.9 |
| **Eu153** | 0.4 | 0.3 | 3.8 | 0.2 | 0.2 | 0.3 |
| **Gd157** | 4.3 | 4.3 | 15.5 | 7.4 | 6.9 | 6.3 |
| **Dy163** | 6.4 | 6.4 | 17.6 | 6.4 | 6.2 | 6.4 |
| **Er166** | 3.5 | 3.5 | 8.9 | 4.5 | 4.0 | 3.7 |
| **Yb172** | 3.9 | 4.6 | 8.4 | 4.5 | 4.9 | 4.5 |
| **Lu175** | 0.6 | 0.6 | 1.2 | 0.7 | 0.7 | 0.5 |
| **Hf178** | 2.9 | 3.0 | 21.5 | 5.7 | 6.2 | 5.4 |
| **Ta181** | 1.3 | 1.4 | 7.5 | 2.6 | 2.4 | 2.2 |
| **Pb208** | 25.6 | 49.5 | 8.3 | 31.1 | 30.7 | 27.4 |
| **Th232** | 13.1 | 14.9 | 11.6 | 49.9 | 48.2 | 40.7 |
| **U238** | 5.0 | 5.1 | 3.8 | 15.5 | 14.5 | 13.7 |

Appendix 2. Tephra geochemistry data

| **Depth (cm)** | 564 | | | | 575 | |
|---|---|---|---|---|---|---|
| **Label** | TDB_564 | TDB_564 | TDB_564 | TDB_564 | TDB_575 | TDB_575 |
| **Ca43** | 5798.9 | 5879.1 | 4906.3 | 6016.7 | 7673.7 | 7377.0 |
| **Ti47** | NA | NA | NA | NA | NA | NA |
| **Ni60** | NA | NA | NA | NA | NA | NA |
| **Rb85** | 306.6 | 338.1 | 319.5 | 313.4 | 236.2 | 246.7 |
| **Sr88** | 18.4 | 13.9 | 12.8 | 12.7 | 96.9 | 94.9 |
| **Y89** | 40.1 | 38.8 | 38.9 | 35.5 | 23.4 | 9.8 |
| **Zr90** | 166.4 | 155.5 | 162.0 | 137.9 | 71.0 | 77.1 |
| **Nb93** | 35.4 | 35.5 | 37.0 | 34.3 | 11.2 | 8.9 |
| **Ba138** | 12.4 | 16.3 | 11.5 | 12.0 | 962.4 | 815.6 |
| **La139** | 47.3 | 46.6 | 49.7 | 42.4 | 25.5 | 30.2 |
| **Ce140** | 98.8 | 96.0 | 98.7 | 88.7 | 48.5 | 49.9 |
| **Pr141** | 10.7 | 9.8 | 10.4 | 9.5 | 5.3 | 4.2 |
| **Nd146** | 35.0 | 36.7 | 37.6 | 33.1 | 17.9 | 12.2 |
| **Sm147** | 7.4 | 7.5 | 7.5 | 7.2 | 4.0 | 1.9 |
| **Eu153** | 0.2 | 0.3 | 0.2 | 0.3 | 0.7 | 0.3 |
| **Gd157** | 6.3 | 5.7 | 5.5 | 5.0 | 2.8 | 1.4 |
| **Dy163** | 7.0 | 5.7 | 6.3 | 5.9 | 3.8 | 1.7 |
| **Er166** | 4.3 | 3.8 | 3.9 | 3.3 | 2.8 | 1.1 |
| **Yb172** | 4.8 | 4.7 | 5.0 | 4.2 | 2.9 | 1.6 |
| **Lu175** | 0.7 | 0.6 | 0.7 | 0.6 | 0.5 | 0.2 |
| **Hf178** | 6.9 | 5.5 | 5.5 | 5.0 | 3.0 | 2.9 |
| **Ta181** | 2.5 | 2.3 | 2.4 | 2.0 | 1.5 | 1.0 |
| **Pb208** | NA | NA | NA | NA | 37.3 | 39.1 |
| **Th232** | 48.0 | 42.0 | 47.9 | 37.3 | 23.5 | 24.9 |
| **U238** | 14.2 | 13.5 | 14.2 | 13.1 | 10.2 | 8.0 |

Appendix 2. Tephra geochemistry data

| **Depth (cm)** | 575 | | | 588 | |
|---|---|---|---|---|---|
| **Label** | TDB_575 | TDB_575 | TDB_575 | TDB_588 | TDB_588 |
| **Ca43** | 4427.1 | 6151.3 | 4716.6 | 4849.0 | 5017.4 |
| **Ti47** | NA | NA | NA | NA | NA |
| **Ni60** | NA | NA | NA | NA | NA |
| **Rb85** | 170.3 | 282.0 | 169.2 | 163.1 | 162.1 |
| **Sr88** | 25.6 | 156.6 | 30.9 | 28.3 | 40.3 |
| **Y89** | 30.5 | 5.2 | 40.9 | 36.8 | 34.4 |
| **Zr90** | 67.3 | 89.9 | 92.1 | 81.6 | 60.0 |
| **Nb93** | 25.1 | 15.1 | 17.3 | 15.5 | 13.3 |
| **Ba138** | 691.9 | 632.3 | 959.5 | 885.4 | 624.3 |
| **La139** | 24.7 | 30.7 | 26.4 | 23.5 | 17.4 |
| **Ce140** | 50.6 | 51.0 | 57.7 | 49.9 | 37.4 |
| **Pr141** | 5.4 | 4.6 | 6.9 | 5.8 | 4.2 |
| **Nd146** | 19.4 | 13.2 | 27.4 | 24.3 | 17.1 |
| **Sm147** | 4.3 | 1.7 | 7.4 | 5.9 | 5.2 |
| **Eu153** | 0.3 | 0.3 | 0.5 | 0.4 | 0.5 |
| **Gd157** | 4.6 | 1.1 | 6.0 | 5.2 | 3.9 |
| **Dy163** | 4.9 | 0.8 | 6.7 | 6.5 | 6.1 |
| **Er166** | 3.3 | 0.6 | 4.4 | 3.8 | 3.9 |
| **Yb172** | 3.6 | 0.7 | 4.2 | 3.4 | 3.8 |
| **Lu175** | 0.5 | 0.1 | 0.7 | 0.6 | 0.6 |
| **Hf178** | 3.1 | 2.6 | 3.8 | 3.0 | 3.0 |
| **Ta181** | 2.5 | 1.3 | 1.3 | 1.1 | 1.2 |
| **Pb208** | 22.4 | 39.8 | 24.2 | 22.4 | 22.0 |
| **Th232** | 16.0 | 22.5 | 14.9 | 12.4 | 13.3 |
| **U238** | 6.2 | 7.9 | 5.0 | 4.5 | 4.8 |

**Table A2.8** Secondary standard for trace element geochemistry for StHS6/80-G

| Date | 220218 | 220218 | 220218 | 220218 | 280219 | 280219 | 280219 | 280219 | 280219 |
|---|---|---|---|---|---|---|---|---|---|
| **Run** | R2 | R2 | R3 | R3 | R1 | R1 | R2 | R2 | R3 |
| **Rb** | 31.1 | 31.2 | 31.1 | 31.1 | 30.21 | 30.67 | 31.67 | 32.15 | 30.92 |
| **Sr** | 474.0 | 478.0 | 477.9 | 476.1 | 476.95 | 445.44 | 490.73 | 482.02 | 480.00 |
| **Y** | 10.7 | 10.7 | 10.9 | 10.8 | 10.96 | 10.05 | 11.22 | 10.96 | 11.08 |
| **Zr** | 113.1 | 115.0 | 112.4 | 111.6 | 113.12 | 108.15 | 118.58 | 113.66 | 116.49 |
| **Nb** | 6.7 | 6.5 | 6.6 | 6.6 | 6.43 | 6.27 | 6.94 | 6.62 | 6.80 |
| **Ba** | 301.7 | 303.3 | 303.8 | 306.7 | 293.53 | 291.70 | 320.65 | 315.32 | 311.57 |
| **La** | 11.6 | 11.5 | 11.5 | 11.6 | 11.61 | 10.85 | 11.95 | 11.99 | 11.76 |
| **Ce** | 25.3 | 25.4 | 25.4 | 25.2 | 24.98 | 23.76 | 26.84 | 25.72 | 25.47 |
| **Pr** | 3.0 | 3.1 | 3.0 | 2.9 | 3.01 | 2.85 | 3.10 | 3.09 | 3.04 |
| **Nd** | 12.0 | 12.5 | 12.4 | 13.0 | 12.30 | 11.41 | 13.01 | 12.91 | 13.12 |
| **Sm** | 3.0 | 2.7 | 2.6 | 2.8 | 3.94 | 3.69 | 3.21 | 2.97 | 2.87 |
| **Eu** | 0.9 | 0.8 | 0.8 | 0.9 | 1.69 | 1.98 | 0.88 | 0.91 | 0.94 |
| **Gd** | 2.6 | 2.4 | 2.7 | 2.3 | 2.98 | 3.43 | 2.53 | 2.59 | 2.29 |
| **Dy** | 2.0 | 2.1 | 2.2 | 2.4 | 2.91 | 3.20 | 2.34 | 2.22 | 2.23 |
| **Er** | 1.1 | 1.1 | 1.2 | 1.2 | 2.03 | 1.58 | 1.18 | 1.22 | 1.19 |
| **Yb** | 1.2 | 1.2 | 1.2 | 1.2 | 2.62 | 3.28 | 1.31 | 1.25 | 1.09 |
| **Lu** | 0.2 | 0.2 | 0.2 | 0.2 | <LOD | <LOD | 0.16 | 0.16 | 0.18 |
| **Hf** | 2.9 | 3.2 | 2.8 | 2.9 | 3.65 | 3.40 | 3.01 | 2.90 | 3.13 |
| **Ta** | 0.4 | 0.4 | 0.4 | 0.4 | <LOD | <LOD | 0.40 | 0.40 | 0.41 |
| **Pb** | 9.4 | 9.3 | 9.1 | 9.4 | 27.03 | 9.04 | 9.59 | 9.69 | 9.33 |
| **Th** | 2.3 | 2.2 | 2.2 | 2.1 | 2.19 | 2.32 | 2.21 | 2.23 | 2.05 |
| **U** | 1.0 | 1.0 | 1.0 | 1.1 | 1.29 | 1.30 | 1.02 | 1.01 | 1.02 |
| **U** | | | | | | | | | |
| | | | | | | | | | |

Appendix 2. Tephra geochemistry data

| Date | 280219 | 280219 | 280219 | 280219 | 280219 | 280219 | 280219 |
|---|---|---|---|---|---|---|---|
| **Run** | R3 | R4 | R4 | R5 | R5 | R6 | R6 |
| **Rb** | 30.93 | 30.52 | 30.10 | 31.37 | 31.65 | 30.69 | 30.08 |
| **Sr** | 489.17 | 484.63 | 453.87 | 475.25 | 469.14 | 463.96 | 461.14 |
| **Y** | 11.22 | 11.15 | 10.42 | 10.77 | 10.59 | 10.54 | 10.47 |
| **Zr** | 115.89 | 114.74 | 107.79 | 112.22 | 112.55 | 110.24 | 109.15 |
| **Nb** | 6.73 | 6.81 | 6.50 | 6.81 | 6.63 | 6.47 | 6.47 |
| **Ba** | 311.66 | 302.84 | 290.51 | 299.30 | 295.73 | 300.11 | 292.18 |
| **La** | 11.69 | 11.52 | 11.04 | 11.58 | 11.15 | 11.43 | 10.99 |
| **Ce** | 25.73 | 26.17 | 24.44 | 25.58 | 25.13 | 25.18 | 24.62 |
| **Pr** | 2.94 | 3.05 | 2.81 | 2.90 | 2.87 | 2.92 | 2.83 |
| **Nd** | 13.09 | 12.23 | 12.03 | 12.40 | 12.44 | 12.60 | 11.90 |
| **Sm** | 2.99 | 2.72 | 2.76 | 2.92 | 2.99 | 2.83 | 2.91 |
| **Eu** | 0.92 | 0.90 | 0.86 | 0.90 | 0.95 | 0.92 | 0.87 |
| **Gd** | 2.58 | 2.68 | 2.32 | 2.32 | 2.54 | 2.44 | 2.17 |
| **Dy** | 2.22 | 2.14 | 2.09 | 2.36 | 2.25 | 2.06 | 2.23 |
| **Er** | 1.16 | 1.30 | 1.07 | 1.26 | 1.04 | 1.23 | 1.13 |
| **Yb** | 1.19 | 1.19 | 1.23 | 1.03 | 1.06 | 1.26 | 1.05 |
| **Lu** | 0.16 | 0.16 | 0.16 | 0.16 | 0.15 | 0.16 | 0.17 |
| **Hf** | 3.00 | 3.05 | 2.85 | 3.01 | 2.98 | 2.74 | 2.86 |
| **Ta** | 0.39 | 0.39 | 0.39 | 0.40 | 0.38 | 0.38 | 0.38 |
| **Pb** | 9.07 | 9.26 | 9.20 | 8.72 | 9.09 | 9.04 | 8.85 |
| **Th** | 2.29 | 2.29 | 2.03 | 2.23 | 2.19 | 2.21 | 2.03 |
| **U** | 0.99 | 1.08 | 1.00 | 1.03 | 0.97 | 1.07 | 0.97 |

# Appendix 3. Chronological problems of Lake Lia

**Figure A3.1** Pollen record for Lake Lia during the LGIT (Eniko Magyari and Ilona Pál, personal communication). The record is display on the original age model by Hubay et al. (2018) (black) and the age model (red) based on the Hubay et al. (2018) ages and tephra layers of Late Glacial Lipari and the Askja-S identified in this thesis. This figure visually displays the difference between the original age model and this study's age model. The Younger Dryas transition to the earliest Holocene (EH) is also shown. There is a clear age difference (~400 years) between these different age models for the mean age for this transition. The transition to the EH is very distinct in the pollen record. It is hard to identify the disparity between the different age models and could be linked to reworking of the tephras within the record as highlighted in Chapter 6. Due to personal communication between Eniko Magyari, it was deemed in the best interest not to use this site in this thesis so there could be no mis-representation of the pollen record.

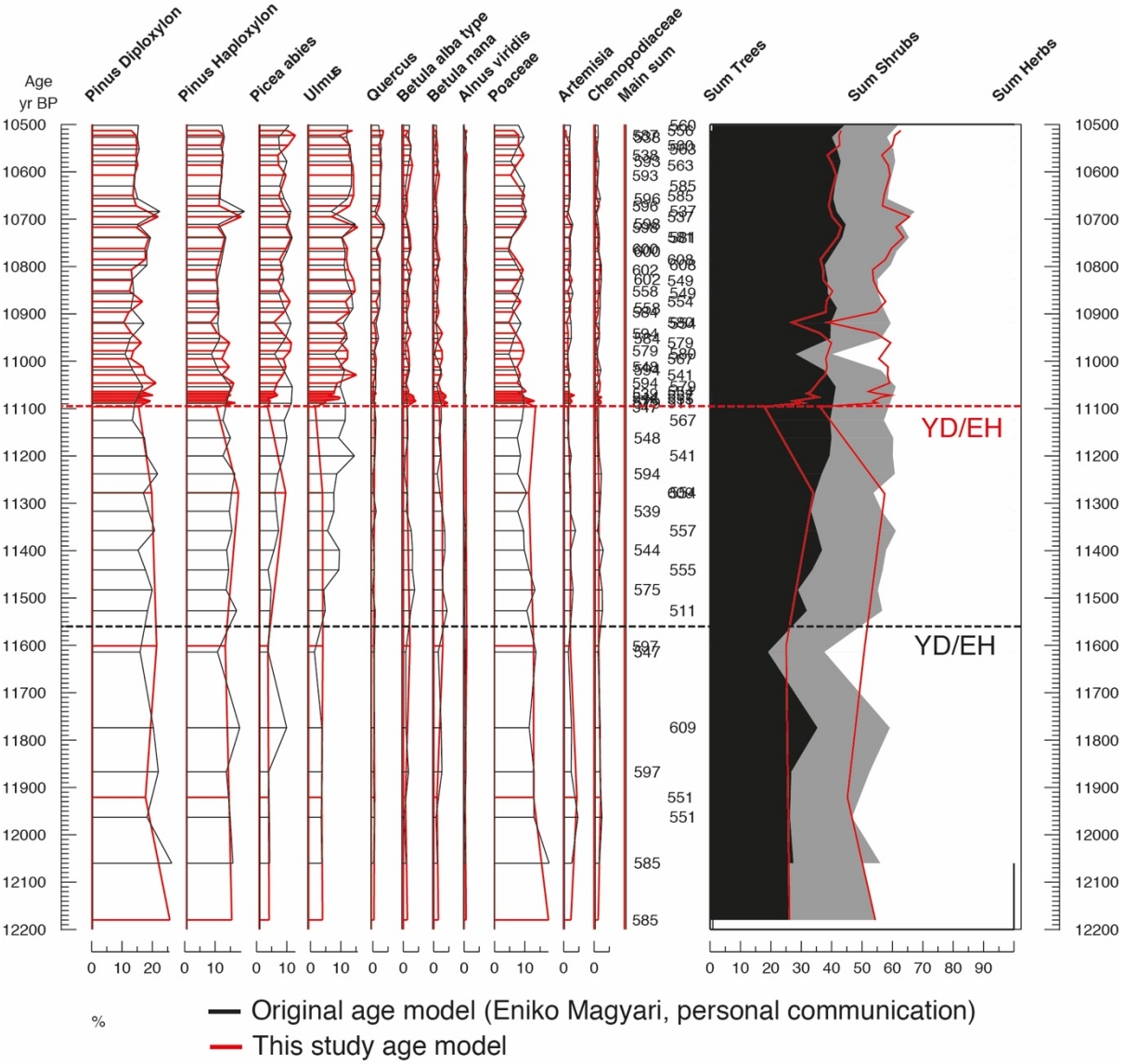

# Appendix 4 – Radiocarbon dates for sites used in the large age model

**Table A4.1** AMS $^{14}C$ dates for Kråkenes (Lohne et al., 2013, 2014) used in the large age model for this thesis. MF = macrofossil

| Lab no. | Sample depth (cm) | Material dated | $^{14}C$ age | $^{14}C$ error (1 sigma) | Used in age model |
|---|---|---|---|---|---|
| Ua-3418 | 948-947 | Terrestrial plant MF | 11380 | 85 | Yes |
| Ua-3407 | 941-940 | Terrestrial plant MF | 11220 | 90 | Yes |
| TUa-600 | 936-935 | Terrestrial plant MF | 11275 | 125 | Yes |
| TUa-597 | 931-930 | Terrestrial plant MF | 11135 | 135 | Yes |
| Tua-591 | 926-925 | Terrestrial plant MF | 10995 | 110 | Yes |
| Tua-587 | 924.5-923 | Terrestrial plant MF | 10800 | 110 | Yes |
| Tua-852A | 923-922 | Terrestrial plant MF | 11520 | 165 | Yes |
| Tua-851 | 923-921 | Terrestrial plant MF | 10980 | 120 | Yes |
| Tua-586 | 922-921 | Terrestrial plant MF | 10570 | 305 | Yes |
| Ua-3408 | 921-920 | Terrestrial plant MF | 10130 | 195 | Yes |
| Tua-589 | 919-918 | Terrestrial plant MF | 10560 | 215 | Yes |
| TUa-610 | 911.5-910 | Terrestrial plant MF | 13485 | 1555 | Yes |
| Tua-596 | 904.5-903.5 | Terrestrial plant MF | 10520 | 115 | Yes |
| Ua-3417 | 893.5-892.5 | Terrestrial plant MF | 11050 | 715 | Yes |
| Ua-3413 | 891-889.5 | Terrestrial plant MF | 8875 | 155 | No (by outlier analysis) |
| Tua-868A | 886.5-885 | Terrestrial plant MF | 10200 | 115 | Yes |
| Tua-868 | 886.5-885 | Terrestrial plant MF | 10515 | 135 | Yes |
| Tua-867A | 884-882.5 | Terrestrial plant MF | 10185 | 120 | Yes |
| Tua-867 | 884-882.5 | Terrestrial plant MF | 10420 | 175 | Yes |
| Ua-3416 | 881-880 | Terrestrial plant MF | 9205 | 200 | No (by outlier analysis) |
| Tua-599 | 871.5-870 | Terrestrial plant MF | 10510 | 115 | Yes |
| Ua-3412 | 860.5-858.5 | Terrestrial plant MF | 10130 | 75 | Yes |
| Ua-3405 | 842-840 | Terrestrial plant MF | 10345 | 105 | Yes |
| Ua-3404 | 837-834.5 | Terrestrial plant MF | 10415 | 95 | Yes |
| Ua-3403 | 834.5-831.5 | Terrestrial plant MF | 10305 | 95 | Yes |
| Ua-3402 | 831-829.5 | Terrestrial plant MF | 10300 | 110 | Yes |

| Lab no. | Sample depth (cm) | Material dated | $^{14}$C age | $^{14}$C error (1 sigma) | Used in age model |
|---|---|---|---|---|---|
| Ua-3401 | 829.5-826.5 | Terrestrial plant MF | 10230 | 90 | Yes |
| Ua-3400 | 821.5-820 | Terrestrial plant MF | 10445 | 85 | Yes |
| Ua-3411 | 811.5-809 | Terrestrial plant MF | 9900 | 110 | Yes |
| Tua-783 | 802-801 | Terrestrial plant MF | 10220 | 120 | Yes |
| Tua-598 | 792-790 | Terrestrial plant MF | 10180 | 110 | Yes |
| Ua-3415 | 786-784 | Terrestrial plant MF | 10060 | 135 | Yes |
| Tua-782 | 780-782 | Terrestrial plant MF | 9965 | 90 | Yes |
| Ua-3410 | 772.5-770 | Terrestrial plant MF | 10100 | 115 | Yes |
| Ua-3414 | 767-765 | Terrestrial plant MF | 9980 | 125 | Yes |
| Tua-590 | 761-760 | Terrestrial plant MF | 9985 | 95 | Yes |
| Tua-1180A | 760.5-760 | Gyttja | 10100 | 75 | Yes |
| Tua-585 | 760-759.5 | Terrestrial plant MF | 9960 | 100 | Yes |
| Tua-594 | 758-756.5 | Terrestrial plant MF | 9945 | 85 | Yes |
| Tua-584 | 756.5-755 | Terrestrial plant MF | 10105 | 90 | Yes |
| Tua-1179A | 756-755 | Gyttja | 10165 | 75 | Yes |
| Tua-595 | 754-753 | Terrestrial plant MF | 9815 | 110 | Yes |
| Tua-1178A | 751-750 | Gyttja | 10120 | 65 | Yes |
| Tua-588 | 750-749 | Terrestrial plant MF | 10005 | 95 | Yes |
| Tua-605 | 746-745 | Gyttja | 10200 | 110 | Yes |
| Tua-1177A | 746-745 | Terrestrial plant MF | 9950 | 55 | Yes |
| Ua-3406 | 741-740 | Terrestrial plant MF | 9880 | 85 | Yes |
| TUa-1176A | 741-740 | Gyttja | 9990 | 55 | Yes |
| Tua-780 | 736-735 | Gyttja | 9935 | 95 | Yes |
| Tua-1175A | 736-735 | Terrestrial plant MF | 9910 | 65 | Yes |
| Tua-593 | 731-730 | Terrestrial plant MF | 9600 | 100 | Yes |
| Tua-1174A | 731-730 | Gyttja | 9800 | 65 | Yes |
| Tua-1173A | 731-730 | Gyttja | 9705 | 60 | Yes |
| Tua-1172A | 721-720 | Gyttja | 9560 | 80 | Yes |

| Lab no. | Sample depth (cm) | Material dated | $^{14}$C age | $^{14}$C error (1 sigma) | Used in age model |
|---|---|---|---|---|---|
| Tua-1171A | 716-715 | Gyttja | 9465 | 70 | Yes |
| Tua-1170A | 711-710 | Gyttja | 9505 | 75 | Yes |
| Tua-1169A | 706-705 | Gyttja | 9630 | 70 | Yes |
| T-10830A | 702-700 | Gyttja | 9580 | 130 | Yes |
| Tua-1168A | 701-700 | Gyttja | 9570 | 75 | Yes |
| Tua-1167A | 696-695 | Gyttja | 9615 | 80 | Yes |
| TUA-1166A | 691-690 | Gyttja | 9465 | 75 | Yes |
| Tua-1165A | 686-685 | Gyttja | 9300 | 100 | Yes |
| Ua-3450 | 683-682 | Gyttja | 9290 | 100 | Yes |
| Tua-1008A | 681-679 | Gyttja | 9210 | 130 | Yes |
| Ua-3449 | 678-677 | Gyttja | 9450 | 90 | Yes |
| Ua-3428 | 677-676 | Terrestrial plant MF | 9190 | 85 | Yes |
| Ua-3427 | 676-675 | Gyttja | 9180 | 80 | Yes |
| Ua-3426 | 674-673 | Terrestrial plant MF | 8840 | 130 | Yes |
| Ua-3425 | 674-673 | Terrestrial plant MF | 9065 | 105 | Yes |
| Ua-3448 | 673-672 | Gyttja | 9115 | 90 | Yes |
| Ua-3424 | 673-672 | Terrestrial plant MF | 8335 | 95 | Yes |
| Ua-3423 | 672-671 | Terrestrial plant MF | 8930 | 145 | Yes |

**Table A4.2** AMS $^{14}C$ dates for Lake Madtjärn (Björck et al., 1996, 1997) used in the large age model for this thesis. The type of material dated includes twigs, leaf fragments, seeds, buds and twigs.

| Lab no. | Sample depth (cm) | Material dated | $^{14}C$ age | $^{14}C$ error (1 sigma) | Used in age model |
|---|---|---|---|---|---|
| Ua-10352 | 895-885 | *Salix* sp. MF | 11470 | 135 | Yes |
| Ua-10281 | 885-875 | *Salix* sp. MF | 11630 | 190 | Yes |
| Ua-10274 | 855-845 | *Salix* sp. MF , *Empetrum nigrum* MF | 10750 | 100 | Yes |
| Ua-10271 | 845-835 | *Dryas octopetala* MF, *Polygonum viviparum* MF, *Empetrum nigrum* MF | 11065 | 150 | Yes |
| Ua-10272 | 845-835 | *Salix* sp. MF | 10820 | 85 | Yes |
| Ua-10214 | 835-832.5 | *Salix* sp. MF, *Dryas octopetala* MF, *Saxifraga oppositifloria* MF, *Empetrum nigrum* MF | 10995 | 75 | Yes |
| Ua-10215 | 832.5-831 | *Salix* sp. MF, *Dryas octopetala* MF, *Saxifraga oppositifloria* MF, *Polygonum viviparum* MF, *Empetrum nigrum* MF | 10625 | 70 | Yes |
| Ua-10216 | 831-829.5 | *Salix* sp. MF, *Dryas octopetala* MF, *Saxifraga oppositifloria* MF | 10625 | 75 | Yes |
| Ua-10217 | 829.5-827 | *Salix* sp. MF | 10400 | 80 | Yes |
| Ua-12018 | 827-824 | *Salix* sp. MF, *Dryas octopetala* MF | 10440 | 65 | Yes |
| Ua-10219 | 824-821.5 | *Salix* sp. MF | 10340 | 70 | Yes |
| Ua-10220 | 821.5-818 | *Salix* sp. MF, *Dryas octopetala, Polygonum viviparum* MF | 10425 | 80 | Yes |
| Ua-10221 | 818-814.5 | *Salix* sp. MF, *Dryas octopetala, Polygonum viviparum* MF | 10375 | 70 | Yes |
| Ua-10270 | 814.5-813.5 | *Salix* sp. MF | 10455 | 115 | Yes |
| Ua-10222 | 813.5-810 | *Salix* sp. MF, *Dryas octopetala* MF | 10155 | 85 | Yes |
| UA-10269 | 810-806 | *Salix* sp. MF, *Dryas octopetala* MF | 10330 | 125 | Yes |
| Ua-10268 | 806-802.5 | *Salix* sp. MF, *Dryas octopetala* MF | 10185 | 115 | Yes |
| Ua-10267 | 802.5-800 | *Betula* MF, *Salix* sp. MF, *Dryas octopetala* | 10060 | 100 | Yes |

| Lab no. | Sample depth (cm) | Material dated | $^{14}$C age | $^{14}$C error (1 sigma) | Used in age model |
|---|---|---|---|---|---|
| Ua-10266 | 800-798 | *Salix* sp. MF, *Dryas octopetala* MF | 9990 | 105 | Yes |
| Ua-10265 | 798-796 | *Betula* MF, *Salix* sp. MF, *Dryas octopetala* | 10010 | 110 | Yes |
| Ua-10264 | 796-794 | *Betula* MF, *Salix* sp. MF, *Dryas octopetala* | 9995 | 100 | Yes |
| Ua-10263 | 794-793 | *Betula* MF | 9930 | 135 | Yes |
| Ua-10262 | 793-791 | *Betula* MF, *Salix* sp. MF, *Dryas octopetala* | 9935 | 165 | Yes |
| Ua-10261 | 791-789 | *Betula* MF, *Dryas octopetala* | 9395 | 115 | Yes |
| Ua-10223 | 789-785 | *Betula* MF, *Salix* sp. MF, *Dryas octopetala* MF, *Empetrum nigrum* MF | 9550 | 85 | Yes |
| Ua-10260 | 785-781 | *Betula* MF, *Salix* sp. MF, *Dryas octopetala* | 9490 | 90 | Yes |
| Ua-10259 | 781-777 | Betula MF, Salix sp. MF | 9490 | 100 | Yes |
| Ua-10258 | 777-773 | Betula MF, Salix sp. MF | 9670 | 195 | Yes |

**Table A4.3** AMS $^{14}$C dates for Hässeldala (Wohlfarth et al., 2006, 2016) on Core 5 depth used in the large age model for this thesis. MF = macrofossils

| Lab no. | Sample depth (cm) | Material dated | $^{14}$C age | $^{14}$C error (1 sigma) | Used in age model |
|---|---|---|---|---|---|
| UBA-20296 | 369.5 | *Dryas octop., Betula nana* | 12211 | 57 | Yes |
| UBA-20297 | 367.5 | *Dryas octop., Salix* sp. | 11972 | 62 | Yes |
| Ua-20516 | 366.6 | *Dryas octop, Betula nana,* Terrestrial MF | 12355 | 190 | Yes |
| UBA-20298 | 365.25 | *Dryas, Salix, Betula* | 11673 | 56 | Yes |
| UBA-20299 | 363 | *Dryas octop., Betula nana* | 11819 | 57 | Yes |
| Ua-20517 | 362.65 | *Dryas octop., Betula nana* | 11920 | 90 | Yes |
| UBA-20300 | 360.5 | *Dryas octop., Betula nana* | 11735 | 60 | Yes |
| Ua-20518 | 360.15 | *Dryas octop., Betula nana* | 11990 | 110 | Yes |
| UBA-20301 | 358.5 | *Dryas octop., Betula nana* | 11614 | 55 | Yes |
| Ua-20519 | 358.4 | *Betula nana* | 11805 | 240 | Yes |

| Lab no. | Sample depth (cm) | Material dated | $^{14}$C age | $^{14}$C error (1 sigma) | Used in age model |
|---|---|---|---|---|---|
| UBA-20302 | 356.5 | *Dryas octop., Betula nana* | 11565 | 56 | Yes |
| Ua-20520 | 356 | *Betula nana* | 11525 | 85 | Yes |
| UBA-20303 | 354.5 | *Betula nana* | 11515 | 65 | Yes |
| Ua-20521 | 352.85 | Terrestrial MF | 11490 | 85 | Yes |
| UBA-20304 | 352 | *Betula nana* | 11225 | 60 | Yes |
| Ua-20522 | 350 | *Betula nana* | 11455 | 125 | Yes |
| UBA-20305 | 348.5 | *Betula nana* | 11118 | 60 | Yes |
| Ua-20523 | 347.25 | *Betula nana,* Terrestrial MF | 11245 | 95 | Yes |
| Ua-20524 | 347.1 | *Betula nana,* Terrestrial MF | 11275 | 95 | Yes |
| Ua-20525 | 346.95 | *Betula nana* | 11200 | 165 | Yes |
| UBA-20306 | 346.5 | *Betula nana* | 10998 | 63 | Yes |
| Ua-20526 | 345.5 | *Betula nana,* Terrestrial MF | 10935 | 80 | Yes |
| UBA-20307 | 344 | *Betula nana* | 10894 | 63 | Yes |
| Ua-20527 | 339.9 | *Betula nana,* Terrestrial MF | 11070 | 135 | Yes |
| UBA-20308 | 338.5 | *Betula nana* | 10644 | 58 | Yes |
| UBA-20309 | 337.5 | *Betula nana* | 10484 | 50 | Yes |
| Ua-20528 | 337.4 | *Betula nana,* Terrestrial MF | 10935 | 80 | Yes |
| Ua-20529 | 334.55 | *Betula nana,* Terrestrial MF | 10515 | 75 | Yes |
| UBA-20310 | 333.25 | *Betula nana* | 10331 | 51 | Yes |
| Ua-16740 | 332.7 | *Betula nana* | 10165 | 95 | Yes |
| UBA-20311 | 331 | *Betula nana* | 10301 | 57 | Yes |
| UBA-23306 | 329.5 | *Betula nana* | 10331 | 53 | Yes |
| UBA-20312 | 328.5 | *Betula nana* | 10639 | 51 | No (by outlier analysis) |
| Ua-16745 | 328.4 | *Dryas octop., Betula nana* | 10285 | 95 | Yes |
| UBA-20313 | 326.5 | *Betula nana* | 10130 | 69 | Yes |
| Ua-16747 | 323.35 | *Betula nana* | 9860 | 85 | Yes |
| Ua-16750 | 319.85 | *Betula nana*, charcoal | 10205 | 85 | Yes |
| UBA-21574 | 319.5 | *Betula nana* | 10102 | 67 | Yes |

| Lab no. | Sample depth (cm) | Material dated | $^{14}$C age | $^{14}$C error (1 sigma) | Used in age model |
|---|---|---|---|---|---|
| Ua-16752 | 315.25 | *Betula nana*, *B. pubescens, Pinus sylvestris* needles | 9720 | 90 | Yes |
| Ua-16761 | 312.25 | *Betula nana*, Terrestrial MF | 9955 | 90 | Yes |
| UBA-22308 | 310 | *Betula nana* | 9864 | 47 | Yes |
| Ua-16766 | 309.5 | *Pinus sylvestris* needles | 9765 | 85 | Yes |
| Ua-16768 | 305.05 | *Pinus sylvestris* needles | 9625 | 70 | Yes |
| UBA-21575 | 302.5 | *Betula nana* | 9532 | 59 | Yes |
| UBA-21577 | 299.5 | *Betula nana* | 9442 | 52 | Yes |
| UBA-21578 | 298.5 | *Betula nana* | 9416 | 47 | Yes |
| UBA-21576 | 290.5 | *Betula,* Terrestrial MF, charcoal | 7496 | 55 | Yes |
| UBA-23309 | 280 | *Betula nana* | 9129 | 50 | Yes |
| UBA-21579 | 272.5 | Terrestrial MF | 8605 | 46 | Yes |
| UBA-21574 | 369.5 | *Dryas octop., Betula nana* | 12211 | 57 | Yes |

**Table A4.4** AMS $^{14}$C dates for Endinger Bruch (de Klerk, 2007; Lane et al., 2012) used in the large age model for this thesis. MF = macrofossils

| Lab no. | Sample depth (cm) | Material dated | $^{14}$C age | $^{14}$C error (1 sigma) | Used in age model |
|---|---|---|---|---|---|
| KL7 | 1382 | Terrestrial MF | 11950 | 70 | Yes |

**Table A4.5** AMS $^{14}C$ dates for Lake Czechowskie (Florain Ott, personal communication) used in the large age model for this thesis. MF = macrofossils

| Lab no. | Sample depth (cm) | Material dated | $^{14}C$ age | $^{14}C$ error (1 sigma) | Used in age model |
|---|---|---|---|---|---|
| Poz-52867 | 1274 | Terrestrial MF | 11900 | 50 | Yes |
| Poz-52866 | 1256 | Terrestrial MF | 11270 | 60 | Yes |
| Poz-52862 | 1054 | Terrestrial MF | 8790 | 50 | Yes |
| Poz-52810 | 1035 | Terrestrial MF | 7970 | 90 | Yes |

**Table A4.6** AMS $^{14}C$ dates for Lake Hämelsee, HÄM13 (Stefan Engels and Christine Lane, personal communication) used in the large age model for this thesis. MF = macrofossils

| Lab no. | Sample depth (cm) | Material dated | $^{14}C$ age | $^{14}C$ error (1 sigma) | Used in age model |
|---|---|---|---|---|---|
| OxA-32273 | 1694-1695 | Terrestrial MF | 12450 | 65 | Yes |
| OxA-32272 | 1683-1682 | Terrestrial MF | 12475 | 60 | Yes |
| OxA-2551-47 | 1680-1679 | *Betula* seeds | 11975 | 50 | Yes |
| OxA-2555-13 | 1490-1489 | *Betula* Seeds | 10550 | 160 | Yes |
| OxA-2555-14 | 1478-1477 | *Salix* bud scales | 10310 | 130 | Yes |

**Table A4.7** AMS $^{14}C$ dates for Wegliny (Housley et al., 2013) used in the large age model for this thesis.

| Lab no. | Sample depth (cm) | Material dated | $^{14}C$ age | $^{14}C$ error (1 sigma) | Used in age model |
|---|---|---|---|---|---|
| Poz43989 | 725-724 | Peat | 13340 | 70 | Yes |
| Poz-43987 | 666-665 | Peat | 14240 | 80 | Yes |
| Poz-44103 | 492-491 | Peat | 12880 | 70 | No |
| Poz-42399 | 456-455 | Peat | 12190 | 60 | No |
| Poz-43985 | 346-345 | Gyttja | 10440 | 50 | No |
| Poz-42398 | 286-285 | Gyttja | 9360 | 60 | Yes |
| Poz-42397 | 219-218 | Gyttja | 8660 | 50 | yes |

**Table A4.8** AMS $^{14}C$ dates for Soppensee (Hajdas et al., 1993) on SO89-17 used in the large age model for this thesis. MF = macrofossils.

| Lab no. | Sample depth (cm) | Material dated | $^{14}C$ age | $^{14}C$ error (1 sigma) | Used in age model |
|---|---|---|---|---|---|
| ETH-6809 | 633.5 | Terrestrial MF | 12150 | 90 | Yes |
| ETH-6808 | 631.5 | Terrestrial MF | 11930 | 90 | Yes |
| ETH-6807 | 624.5 | Terrestrial MF | 12040 | 90 | Yes |
| ETH-6806 | 611 | Terrestrial MF | 11385 | 90 | Yes |
| ETH-6805 | 610 | Terrestrial MF | 11300 | 85 | Yes |
| ETH-5305 | 607 | Terrestrial MF | 11380 | 105 | Yes |
| ETH-6932 | 600.5 | Terrestrial MF | 11160 | 60 | Yes |
| ETH-5290 | 594 | Terrestrial MF | 10760 | 105 | Yes |
| ETH-5303 | 590.5 | Terrestrial MF | 10070 | 155 | Yes |
| ETH-7704 | 587.5 | Terrestrial MF | 10020 | 110 | Yes |
| ETH-7703 | 577 | Terrestrial MF | 10440 | 100 | Yes |
| ETH-6929 | 569 | Terrestrial MF | 10400 | 70 | Yes |
| ETH-6803 | 550.5 | Terrestrial MF | 9965 | 75 | Yes |
| ETH-7710 | 547 | Terrestrial MF | 10135 | 100 | Yes |
| ETH-7701 | 542.45 | Terrestrial MF | 9970 | 100 | Yes |

| Lab no. | Sample depth (cm) | Material dated | $^{14}$C age | $^{14}$C error (1 sigma) | Used in age model |
|---|---|---|---|---|---|
| ETH-6623 | 524.5 | Terrestrial MF | 9595 | 70 | Yes |
| ETH-6622 | 523.5 | Terrestrial MF | 9625 | 65 | Yes |
| ETH-7700 | 519.5 | Terrestrial MF | 9530 | 95 | Yes |
| ETH-7699 | 515.5 | Terrestrial MF | 9620 | 100 | Yes |
| ETH-6620 | 513.5 | Terrestrial MF | 9940 | 70 | Yes |
| ETH-6619 | 509 | Terrestrial MF | 9475 | 5 | Yes |
| ETH-6617 | 507 | Terrestrial MF | 9255 | 60 | Yes |
| ETH-6936 | 505.5 | Terrestrial MF | 9115 | 95 | Yes |
| ETH-6616 | 501 | Terrestrial MF | 9020 | 65 | Yes |
| ETH-6615 | 497 | Terrestrial MF | 8990 | 70 | Yes |
| ETH-6614 | 495.5 | Terrestrial MF | 9020 | 75 | Yes |

**Table A4.9** AMS $^{14}C$ dates for Rotsee (Lotter and Zbiden, 1989; Zbiden et al., 1989, Richard Staff, personal communication) used in the large age model for this thesis. Depth is at RL05 core. *shows the duplicates undertaken by Richard Staff. MF = macrofossils. Terrestrial MF includes fruits and catskin scale of birch (Lotter and Zbinden, 1989).

| Lab no. | Sample depth (cm) | Material dated | $^{14}C$ age | $^{14}C$ error (1 sigma) | Used in age model |
|---|---|---|---|---|---|
| OxA-26017 (RL300)* | 996.3 | Bark | 9470 | 45 | Yes |
| C725 (RL300) | 996.3 | Terrestrial MF | 9380 | 130 | Yes |
| OxA-26018 (RL300)* | 1001.8 | Bark | 9405 | 50 | Yes |
| C846 (RL305) | 1006.9 | Terrestrial MF | 9510 | 140 | Yes |
| OxA-26022 (RL305)* | 1006.9 | Leaf fragments | 9465 | 50 | Yes |
| C727 (RL300) | 1007.3 | Terrestrial MF | 9780 | 140 | Yes |
| OxA-25922 (RL300)* | 1007.3 | Bark fragment | 9508 | 39 | Yes |
| C847 (RL305) | 1008.2 | Terrestrial MF | 9450 | 140 | Yes |
| C848 (RL305) | 1009.4 | Terrestrial MF | 9760 | 160 | Yes |
| OxA-26023 (RL305)* | 1009.4 | Bark fragment | 9665 | 45 | Yes |
| C852 (RL305) | 1010.6 | Terrestrial MF | 9630 | 150 | Yes |
| OxA-26024 (RL305)* | 1010.6 | Stem fragments | 9590 | 45 | Yes |
| C853 (RL305) | 1012.7 | Terrestrial MF | 10010 | 160 | Yes |
| OxA-26025 (RL305)* | 1012.7 | Leaf fragments | 9705 | 50 | Yes |
| OxA-25923 (RL300)* | 1012.8 | Bark | 9159 | 38 | Yes |
| C728 (RL300) | 1012.8 | Terrestrial MF | 9360 | 130 | Yes |
| OxA-26026 (RL305)* | 1016.9 | Bark fragment | 9920 | 45 | Yes |

| Lab no. | Sample depth (cm) | Material dated | $^{14}$C age | $^{14}$C error (1 sigma) | Used in age model |
|---|---|---|---|---|---|
| C854 (RL305) | 1016.9 | Terrestrial MF | 10010 | 150 | Yes |
| OxA-26019 (RL300)* | 1018.3 | Stem fragments | 9705 | 50 | Yes |
| OxA-26027 (RL305)* | 1021.2 | Leaf fragments | 9610 | 50 | Yes |
| OxA-25924 (RL300)* | 1022.2 | Twig fragments | 9880 | 40 | Yes |
| C746 (RL300) | 1022.2 | Terrestrial MF | 9840 | 140 | Yes |
| C864 (RL305) | 1024.5 | Terrestrial MF | 10010 | 150 | Yes |
| C869 (RL305) | 1028.3 | Terrestrial MF | 9870 | 150 | Yes |
| C731 (RL300) | 1029.4 | Terrestrial MF | 10120 | 140 | Yes |
| C874 (RL305) | 1032.6 | Terrestrial MF | 10010 | 150 | Yes |
| OxA-25931 (RL305)* | 1041.1 | Bark fragments | 10480 | 40 | Yes |
| C909 (RL305) | 1041.1 | Terrestrial MF | 10460 | 40 | Yes |
| C730 (RL300) | 1042.2 | Terrestrial MF | 10000 | 130 | Yes |
| OxA-25932 (RL305)* | 1045.4 | Bark | 10395 | 40 | Yes |
| C904 (RL305) | 1045.4 | Terrestrial MF | 10310 | 160 | Yes |
| OxA-25925 (RL300)* | 1046.5 | Twig fragments | 10345 | 40 | Yes |
| C905 (RL305) | 1049.7 | Terrestrial MF | 10440 | 160 | Yes |
| C968 (RL300) | 1050.8 | Terrestrial MF | 10730 | 150 | Yes |
| C901 (RL305) | 1054.7 | Terrestrial MF | 10450 | 160 | Yes |
| OxA-25933 (RL305)* | 1054.7 | Bark fragments | 10450 | 40 | Yes |
| C910 (RL305) | 1058.7 | Terrestrial MF | 11070 | 170 | Yes |
| OxA-26028 (RL305)* | 1058.7 | Bark fragments | 10755 | 50 | Yes |

| Lab no. | Sample depth (cm) | Material dated | $^{14}$C age | $^{14}$C error (1 sigma) | Used in age model |
|---|---|---|---|---|---|
| LST2 | 1061.3 | Terrestrial MF | 10640 | 160 | Yes |
| OxA-25926 (RL300)* | 1061.9 | Bark | 11005 | 45 | Yes |
| LST1 | | Terrestrial MF | 11260 | 140 | Yes |
| C915 (RL305) | 1064.7 | Terrestrial MF | 11370 | 180 | Yes |
| C780 (RL300) | 1065.7 | Terrestrial MF | 11270 | 140 | Yes |
| C919 (RL305) | 1068.7 | Terrestrial MF | 11670 | 170 | Yes |
| C978 (RL300) | 1068.7 | Terrestrial MF | 11230 | 180 | Yes |
| OxA-26020 (RL300)* | 1069.8 | Stem fragments | 9855 | 45 | Yes |
| C784 (RL300) | 1069.8 | Terrestrial MF | 11440 | 140 | Yes |
| OxA-25927 (RL300)* | 1072.8 | Stem fragments | 11435 | 34 | Yes |
| C920 (RL305) | 1072.8 | Terrestrial MF | 11740 | 180 | Yes |
| OxA-25927 | 1073.9 | Terrestrial MF | 11435 | 45 | Yes |
| C785 (RL300) | 1073.9 | Terrestrial MF | 11460 | 140 | Yes |
| OxA-26029 (RL305)* | 1076.9 | Leaf fragments | 11700 | 110 | Yes |
| C934 (RL305) | 1076.9 | Terrestrial MF | 11810 | 200 | Yes |
| OxA-25928 (RL300)* | 1078 | Twig | 11745 | 45 | Yes |
| C781 (RL300) | 1078 | Terrestrial MF | 11970 | 150 | Yes |
| OxA-26030 (RL305)* | 1081 | “sheath” fragments | 11840 | 60 | Yes |
| C939 (RL305) | 1081 | Terrestrial MF | 12060 | 220 | Yes |
| OxA-26021 (RL300)* | 1082.1 | Stem fragments | 11745 | 55 | Yes |
| C782 (RL300) | 1082.1 | Terrestrial MF | 11870 | 150 | Yes |
| | | | | | |

| Lab no. | Sample depth (cm) | Material dated | $^{14}$C age | $^{14}$C error (1 sigma) | Used in age model |
|---|---|---|---|---|---|
| OxA-25934 (RL305)* | 1085.1 | unidentified | 11695 | 45 | Yes |
| C783 (RL300) | 1086.2 | Terrestrial MF | 11800 | 140 | Yes |
| OxA-25929 (RL300)* | 1094.4 | Twigs | 12390 | 50 | Yes |
| OxA-25930 (RL300)* | 1094.4 | Twigs | 12475 | 45 | Yes |
| C791 (RL300) | 1094.4 | Terrestrial MF | 12580 | 170 | Yes |
| OxA-26031 (RL305)* | 1099.4 | Leaf fragments | 12020 | 80 | Yes |
| OxA-25935 (RL305)* | 1106.2 | Stem fragments | 12290 | 50 | Yes |
| C794 (RL305) | 1106.2 | Terrestrial MF | 12600 | 170 | Yes |
| OxA-26032 (RL305)* | 1111.7 | Stem fragments | 12460 | 65 | Yes |
| C795 (RL305) | 1111.7 | Terrestrial MF | 12750 | 180 | Yes |
| OxA-25937 (RL305)* | 1117.3 | Twig fragments | 12705 | 50 | Yes |
| OxA-25936 (RL305)* | 1117.3 | Twig fragments | 12725 | 50 | Yes |
| C796 (RL305) | 1117.3 | Terrestrial MF | 12800 | 190 | Yes |
| OxA-26033 (RL305)* | 1122.8 | Leaf fragments | 12755 | 60 | Yes |
| OxA-26034 (RL305)* | 1128.3 | Stem fragments | 12730 | 75 | Yes |
| C809 (RL305) | 1128.3 | Terrestrial MF | 12800 | 190 | Yes |
| OxA-26035 (RL305)* | 1133.9 | Twig fragments | 12905 | 65 | Yes |
| C810 (RL305) | 1139.4 | Terrestrial MF | 13540 | 210 | Yes |

| Lab no. | Sample depth (cm) | Material dated | $^{14}$C age | $^{14}$C error (1 sigma) | Used in age model |
|---|---|---|---|---|---|
| OxA-26036 (RL305)* | 1144.7 | Leaf fragments | 13060 | 70 | Yes |
| C814 (RL305) | 1144.7 | Terrestrial MF | 13290 | 200 | Yes |
| C815 (RL305) | 1148 | Terrestrial MF | 12970 | 200 | Yes |
| C818 (RL305) | 1149.6 | Terrestrial MF | 13600 | 220 | Yes |
| C830 (RL305) | 1151.2 | Terrestrial MF | 13820 | 210 | Yes |
| OxA-25938 (RL305)* | 1152.8 | Leaf fragments | 13760 | 55 | Yes |
| C831 (RL305) | 1152.8 | Terrestrial MF | 14000 | 210 | Yes |
| C823 (RL305) | 1154.4 | Terrestrial MF | 14570 | 240 | Yes |
| OxA-26037 (RL305)* | 1156 | Stem fragments | 13825 | 80 | Yes |
| C837 (RL305) | 1156 | Terrestrial MF | 14240 | 220 | Yes |

**Table A4.10** AMS $^{14}C$ dates for Lago Piccolo di Avigliana (Finsinger et al., 2006, 2008) used in the large age model for this thesis. MF = macrofossils

| Lab no. | Sample depth | Material dated | $^{14}C$ age | $^{14}C$ error (1 sigma) | Used in age model |
|---|---|---|---|---|---|
| Poz-6497 | 909 | | 14930 | 80 | Yes |
| Erl-4797 | 888 | 1 *Betula* fruit, 1 *Alnus* seed, Wood indet. | 14614 | 111 | Yes |
| Erl-4798 | 806 | 35 *Betula* fruits, 5 Betula *catkin scales* | 12,395 | 102 | Yes |
| Erl-4799 | 775 | 104 *Betula* fruits, 9 *Betula* catkin scales, 2 *Quercus* bud-scales | 11525 | 80 | Yes |
| Poz-3931 | 732.5 | 54 *Betula* fruits, 2 budscales indet. 1 *Betula* budscale, 6 *Betula* catkin scale, 2 terresterial leaf fragments, 4 *Larix* needles, 1 coniferous buedscale | 10320 | 50 | Yes |
| Erl-4800 | 714 | 1 wood indet. | 10248 | 64 | Yes |
| Poz-3918 | 695 | 3 Quercus budscale, 2 *Betula* fruits, 2 terresterial leaf fragements | 9320 | 60 | Yes |
| Poz-3930 | 678 | 2 *Quercus* budscale, 2 *Betula* fruits, 2 budscales indet., 1 Coniferous budscale | 9290 | 50 | Yes |
| Erl-4801 | 634 | 1 *Betula* fruit, 1 *Betula* catkin scale, leaf fragemens of terresterial plant | 8723 | 63 | Yes |

**Table A4.11** AMS $^{14}$C dates for Lake Bled (Andrič et al., 2009) used in the large age model for this thesis. MF = macrofossils

| Lab no. | Sample depth (cm) | Material dated | $^{14}$C age | $^{14}$C error (1 sigma) | Used in age model |
|---|---|---|---|---|---|
| Beta-217805 | 210 | *Larix* twif and needles | 11930 | 40 | Yes |
| Beta-222472 | 60 | *Larix* leaves, part of cone scale and wings of coniferous seeds | 9340 | 40 | Yes |

**Table A4.12** AMS $^{14}$C dates for Lake Brazi (Hubary et al., 2018) used in the large age model for this thesis. MF = macrofossils

| Lab no. | Sample depth | Material dated | $^{14}$C age | $^{14}$C error (1 sigma) | Used in age model |
|---|---|---|---|---|---|
| Poz-26113 | 591 | *Picea abies* conescale | 9690 | 50 | No |
| Poz-27305 | 578 | *Pinus mug*o sp.needles | 11590 | 60 | Yes |
| Poz-31716 | 569 | Macrocharcoal | 10870 | 70 | Yes |
| Poz-31715 | 557 | *Pinus mugo* needles | 9980 | 100 | Yes |
| Poz-26112 | 545 | *Pice abies* needles and seed | 9610 | 50 | Yes |
| Poz-31714 | 521 | *Pinus mugo* needles | 9150 | 50 | Yes |
| Poz-26110 | 505 | *Picea abies* needles and seed | 8810 | 50 | Yes |
| Poz-26110 | 450 | *Picea abies* needles and seed | 8240 | 50 | Yes |

**Table A4.13** AMS $^{14}$C dates for Lake Lia (Hubay et al., 2018) used in an age model for this thesis. MF = macrofossils

| Lab no. | Sample depth | Material dated | $^{14}$C age | $^{14}$C error (1 sigma) | Used in age model |
|---|---|---|---|---|---|
| DeA-3247 | 703 | Bulk sediment | 9884 | 82 | No |
| DeA-1640 | 683 | Sediment fraction <250µm | 11324 | 65 | Yes |
| DeA-1639 | 683 | Sediment fraction <250µm | 11462 | 63 | Yes |
| DeA-3270 | 624 | *Rumex alpinus*-type fruit | 9560 | 42 | Yes |
| DeA-3139 | 590 | *Pinus mugo* needle | 9521 | 43 | Yes |
| DeA-1642 | 560 | Sediment fraction <250µm | 9379 | 37 | Yes |
| DeA-1641 | 560 | Sediment fraction <250µm | 9386 | 54 | Yes |
| DeA-1643 | 494 | Sediment fraction <250µm | 8846 | 53 | Yes |
| DeA-3138 | 433 | *Pinus mugo* needle | 7987 | 45 | Yes |
| DeA-1644 | 383 | Sediment fraction <250µm | 7419 | 48 | Yes |
| DeA-3137 | 337 | *Picea abies* needle | 6147 | 43 | Yes |
| DeA-1645 | 278 | Sediment fraction <250µm | 5576 | 43 | Yes |
| DeA-3136 | 218 | *Picea abies* needle | 4057 | 40 | Yes |
| DeA-1646 | 162 | Sediment fraction <250µm | 3715 | 40 | Yes |
| DeA-3135 | 133 | Plant macrofossils | 2782 | 37 | Yes |
| DeA-3134 | 96 | *Pinus mugo* needle | 950 | 36 | Yes |
| DeA-1647 | 80 | Sediment fraction <250µm | 1018 | 35 | Yes |

**Appendix 5 – OxCal coding for all age models in this study**

**Lake Lia individual age model OxCal coding**

```
Plot()
 {
 Outlier_Model("General",T(5),U(0,4),"t");
  Sequence("Lia Core")
  {
   Date("Top", N(AD(2008),1));
  };
  P_Sequence("Lake Lia",1,0.2,U(-2,2))
  {
   Boundary("Base")
   {
    z=829;
   };
   R_Date("DeA-3247",9884,82)
   {
    Outlier();
    z=703;
   };
   R_Combine("DeA-1640/DeA-1639")
   {
    R_Date("DeA-1640",11324,65);
    R_Date("DeA-1639",11462,63);
    Outlier(0.05);
    z=683;
   };
   Date("Lipari", N(calBP(12258),421))
   {
    z=637;
   };
   R_Date("DeA-3270",9560,42)
   {
    Outlier(0.05);
    z=624;
   };
   Date("Ischia")
   {
    z=612.5;
   };
   Date("Askja-S", N(calBP(11076),19))
   {
    z=603;
   };
   R_Date("DeA-3139",9521,43)
   {
    Outlier(0.05);
    z=590;
   };
   R_Combine("DeA-1642/DeA-1641")
   {
    R_Date("DeA-1642",9379,37);
    R_Date("DeA-1641",9386,54);
    Outlier(0.05);
    z=560;
   };
   R_Date("DeA-1643",8846,53)
   {
    Outlier(0.05);
    z=494;
   };
   R_Date("DeA-3138",7987,45)
   {
    Outlier(0.05);
    z=433;
   };
   R_Date("DeA-1644",7419,48)
   {
    Outlier(0.05);
    z=383;
   };
   R_Date("DeA-3137",6147,43)
   {
    Outlier(0.05);
    z=337;
   };
   R_Date("DeA-1645",5576,43)
   {
    Outlier(0.05);
    z=278;
   };
   R_Date("DeA-3136",4057,40)
   {
    Outlier(0.05);
    z=218;
   };
   R_Date("DeA-1646",3715,40)
   {
    Outlier(0.05);
    z=162;
   };
   R_Date("DeA-3135",2782,37)
   {
    Outlier(0.05);
    z=133;
   };
   R_Date("DeA-3134",950,36)
   {
    Outlier(0.05);
    z=96;
   };
   R_Date("DeA-1647",1018,35)
   {
    Outlier(0.05);
    z=80;
   };
```

```
  Boundary("=Top")
  {
   z=0.001;
  };
 };
};
```

**Large age model OxCal coding**

```
Plot()
 {
  Outlier_Model("General",T(5),U(0,4),"t");
  Outlier_Model("SSimple", N(0,2), 0, "s");
  Sequence("Tephras")
  {
   Date("=NYT");
   Date("=LST");
   Date("=Vedde Ash");
   Date("=Hasseldalen");
   Date("=Ulmener Maar");
   Date("=Askja_S");
   Date("=Saksunarvatn Ash");
  };
  Date("=PP");
  Date("=LG Lipari");
  P_Sequence("Lake Madtjarn",1,1,U(-2,2))
  {
   Boundary("MADBase")
   {
    z=900;
   };
   R_Date("Ua-10352",11470,135)
   {
    Outlier("General", 0.05);
    z=890;
   };
   R_Date("Ua-10281",11630,190)
   {
    Outlier("General", 0.05);
    z=880;
   };
   R_Date("Ua-10274",10750,100)
   {
    Outlier("General", 0.05);
    z=850;
   };
   R_Combine("Ua-10271/Ua-10272")
   {
    R_Date("Ua-10271",11065,150)
    {
     Outlier("SSimple", 0.05);
    };
    R_Date("Ua-10272",10820,85)
    {
     Outlier("SSimple", 0.05);
    };
    Outlier("General", 0.05);
    z=840;
   };
   R_Date("Ua-10214",10995,75)
   {
    Outlier("General", 0.05);
    z=833.75;
   };
   R_Date("Ua-12015",10625,70)
   {
    Outlier("General", 0.05);
    z=831.75;
   };
   R_Date("Ua-10216",10625,75)
   {
    Outlier("General", 0.05);
    z=830;
   };
   R_Date("Ua-10217",10400,80)
   {
    Outlier("General", 0.05);
    z=828.25;
   };
   R_Date("Ua-10218",10440,65)
   {
    Outlier("General", 0.05);
    z=825.5;
   };
   R_Date("Ua-10219",10340,70)
   {
    Outlier("General", 0.05);
    z=822.75;
   };
   R_Date("Ua-10222",10425,80)
   {
    Outlier("General", 0.05);
    z=819.75;
   };
   R_Date("Ua-10221",10375,70)
   {
    Outlier("General", 0.05);
    z=816.25;
   };
   R_Date("Ua-10270",10455,115)
   {
    Outlier("General", 0.05);
    z=814;
   };
   Date("Vedde Ash",
 Top_Hat(calBP(12000),300))
   {
    z=813.5;
   };
```

Appendix 5. OxCal coding for age models

```
R_Date("Ua-10222b",10155,85)
{
 Outlier("General", 0.05);
 z=811.75;
};
R_Date("Ua-10269",10330,125)
{
 Outlier("General", 0.05);
 z=808;
};
R_Date("Ua-10268",10185,115)
{
 Outlier("General", 0.05);
 z=804.25;
};
R_Date("Ua-10267",10060,100)
{
 Outlier("General", 0.05);
 z=801.25;
};
R_Date("Ua-10266",9990,105)
{
 Outlier("General", 0.05);
 z=799;
};
R_Date("Ua-10265",10010,110)
{
 Outlier("General", 0.05);
 z=797;
};
R_Date("Ua-10264",9995,100)
{
 Outlier("General", 0.05);
 z=795;
};
R_Date("Ua-10263",9930,135)
{
 Outlier("General", 0.05);
 z=793.5;
};
R_Date("Ua-10262",9935,165)
{
 Outlier("General", 0.05);
 z=792;
};
R_Date("Ua-10261",9395,115)
{
 Outlier("General", 0.05);
 z=790;
};
R_Date("Ua-10223",9550,85)
{
 Outlier("General", 0.05);
 z=787;
};
R_Date("Ua-10260",9490,90)
{
 Outlier("General", 0.05);
 z=783;
};
R_Date("Ua-10259",9490,100)
{
 Outlier("General", 0.05);
 z=779;
};
R_Date("Ua-10258",9670,195)
{
 Outlier("General", 0.05);
 z=775;
};
Boundary("MADTop")
{
 z=737;
};
};
P_Sequence("Soppensee",1,1,U(-2,2))
{
 Boundary("VI/VII")
 {
  z=633.51;
 };
 R_Date("ETH-6809",12150,90)
 {
  Outlier("General", 0.05);
  z=633.5;
 };
 R_Date("ETH-6808",11930,90)
 {
  Outlier("General", 0.05);
  z=631.5;
 };
 R_Date("ETH-6807",12040,90)
 {
  Outlier("General", 0.05);
  z=629.5;
 };
 R_Date("ETH-6806",11385,90)
 {
  Outlier("General", 0.05);
  z=611;
 };
 R_Date("ETH-6805",11300,85)
 {
  Outlier("General", 0.05);
  z=610;
 };
 R_Date("ETH-5305", 11380, 105)
 {
  Outlier("General", 0.05);
  z=607;
```

```
};
R_Date("ETH-6932",11160,60)
{
 Outlier("General", 0.05);
 z=600.5;
};
Date("V/VI")
{
 z=597;
};
Date("LST", Top_Hat(calBP(13000),300))
{
 z=595;
};
R_Date("ETH-5290",10760,105)
{
 Outlier("General", 0.05);
 z=594;
};
R_Date("ETH-7703",10440,100)
{
 Outlier("General", 0.05);
 z=577;
};
R_Date("ETH-6929",10400,70)
{
 Outlier("General", 0.05);
 z=569;
};
Date("=Vedde Ash")
{
 z=562.0;
};
R_Date("ETH-6803",9965,75)
{
 Outlier("General", 0.05);
 z=550.5;
};
R_Date("ETH-7710",10135,100)
{
 Outlier("General", 0.05);
 z=547;
};
R_Date("ETH-7701",9970,100)
{
 Outlier("General", 0.05);
 z=542.5;
};
R_Date("II/III/ETH-6623",9595,70)
{
 Outlier("General", 0.05);
 z=524.6;
};
R_Date("ETH-6622",9625,65)
{
 Outlier("General", 0.05);
 z=523.5;
};
R_Date("ETH-7700",9530,95)
{
 Outlier("General", 0.05);
 z=519.5;
};
Date("=Askja_S")
{
 z=519.0;
};
R_Date("ETH-7699",9620,100)
{
 Outlier("General", 0.05);
 z=515.5;
};
R_Date("ETH-6620",9440,70)
{
 Outlier("General", 0.05);
 z=513.5;
};
R_Date("ETH-6619",9475,85)
{
 Outlier("General", 0.05);
 z=509;
};
R_Date("ETH-6617",9255,60)
{
 Outlier("General", 0.05);
 z=507;
};
R_Date("ETH-6936",9115,95)
{
 Outlier("General", 0.05);
 z=505.5;
};
R_Date("ETH-6616",9020,65)
{
 Outlier("General", 0.05);
 z=501;
};
R_Date("ETH-6615",8990,70)
{
 Outlier("General", 0.05);
 z=497;
};
R_Date("ETH-6614",9020,75)
{
 Outlier("General", 0.05);
 z=495.5;
};
Boundary("I/II")
{
 z=488;
```

```
 };
};
P_Sequence("Rotsee 05", 1, 1, U(-2,2))
{
 Boundary("Rotsee 1160cm")
 {
  z=1160.0;
  color="Gray";
 };
 R_Combine("RL305: 1060-1064cm")
 {
  R_Date("C837", 14240, 220)
  {
   Outlier("SSimple", 0.05);
  };
  R_Date("OxA-26037", 13825, 80)
  {
   Outlier("SSimple", 0.05);
  };
  Outlier("General", 0.05);
  z=1156.0;
 };
 R_Date("C823", 14570, 240)
 {
  Outlier("General", 0.05);
  z=1154.4;
 };
 R_Combine("RL305: 1052-1056cm")
 {
  R_Date("C831", 14000, 210)
  {
   Outlier("SSimple", 0.05);
  };
  R_Date("OxA-25938", 13760, 55)
  {
   Outlier("SSimple", 0.05);
  };
  Outlier("General", 0.05);
  z=1152.8;
 };
 R_Date("C830", 13820, 210)
 {
  Outlier("General", 0.05);
  z=1151.2;
 };
 R_Date("C818", 13600, 220)
 {
  Outlier("General", 0.05);
  z=1149.6;
 };
 R_Date("C815", 12970, 200)
 {
  Outlier("General", 0.05);
  z=1148.0;
 };
 R_Combine("RL305: 1036-1040cm")
 {
  R_Date("C814", 13290, 200)
  {
   Outlier("SSimple", 0.05);
  };
  R_Date("OxA-26036", 13060, 70)
  {
   Outlier("SSimple", 0.05);
  };
  Outlier("General", 0.05);
  z=1144.7;
 };
 R_Date("C810", 13540, 210)
 {
  Outlier("General", 0.05);
  z=1139.4;
 };
 R_Date("OxA-26035", 12905, 65)
 {
  Outlier("General", 0.05);
  z=1133.9;
 };
 R_Combine("RL305: 1024-1028cm")
 {
  R_Date("C809", 12800, 190)
  {
   Outlier("SSimple", 0.05);
  };
  R_Date("OxA-26034", 12730, 75)
  {
   Outlier("SSimple", 0.05);
  };
  Outlier("General", 0.05);
  z=1128.3;
 };
 R_Date("OxA-26033", 12755, 60)
 {
  Outlier("General", 0.05);
  z=1122.8;
 };
 R_Combine("RL305: 1016-1020cm")
 {
  R_Date("C796", 12800, 190)
  {
   Outlier("SSimple", 0.05);
  };
  R_Date("OxA-25937", 12705, 50)
  {
   Outlier("SSimple", 0.05);
  };
  R_Date("OxA-25936", 12725, 50)
  {
   Outlier("SSimple", 0.05);
  };
```

```
 Outlier("General", 0.05);
 z=1117.3;
};
R_Combine("RL305: 1012-1016cm")
{
 R_Date("C795", 12570, 180)
 {
  Outlier("SSimple", 0.05);
 };
 R_Date("OxA-26032", 12460, 65)
 {
  Outlier("SSimple", 0.05);
 };
 Outlier("General", 0.05);
 z=1111.7;
};
R_Combine("RL305: 1008-1012cm")
{
 R_Date("C794", 12600, 170)
 {
  Outlier("SSimple", 0.05);
 };
 R_Date("OxA-25935", 12290, 50)
 {
  Outlier("SSimple", 0.05);
 };
 Outlier("General", 0.05);
 z=1106.2;
};
R_Date("OxA-26031", 12020, 80)
{
 Outlier("General", 0.05);
 z=1099.4;
};
R_Combine("RL300: 862.5-867.5cm")
{
 R_Date("C791", 12580, 170)
 {
  Outlier("SSimple", 0.05);
 };
 R_Date("OxA-25929", 12390, 50)
 {
  Outlier("SSimple", 0.05);
 };
 R_Date("OxA-25930", 12475, 45)
 {
  Outlier("SSimple", 0.05);
 };
 Outlier("General", 0.05);
 z=1094.4;
};
R_Date("C979", 11880, 150)
{
 Outlier("General", 0.05);
 z=1090.3;
};
R_Date("C783", 11800, 140)
{
 Outlier("General", 0.05);
 z=1086.2;
};
R_Date("OxA-25934", 11695, 45)
{
 Outlier("General", 0.05);
 z=1085.1;
};
R_Combine("RL300: 832.5-837.5cm")
{
 R_Date("C782", 11870, 150)
 {
  Outlier("SSimple", 0.05);
 };
 R_Date("OxA-26021", 11745, 55)
 {
  Outlier("SSimple", 0.05);
 };
 Outlier("General", 0.05);
 z=1082.1;
};
R_Combine("RL305: 988-992cm")
{
 R_Date("C939", 12060, 220)
 {
  Outlier("SSimple", 0.05);
 };
 R_Date("OxA-26030", 11840, 60)
 {
  Outlier("SSimple", 0.05);
 };
 Outlier("General", 0.05);
 z=1081.0;
};
R_Combine("RL300: 822.5-827.5cm")
{
 R_Date("C781", 11970, 150)
 {
  Outlier("SSimple", 0.05);
 };
 R_Date("OxA-25928", 11745, 45)
 {
  Outlier("SSimple", 0.05);
 };
 Outlier("General", 0.05);
 z=1078.0;
};
R_Combine("RL305: 984-988cm")
{
 R_Date("C934", 11810, 200)
 {
  Outlier("SSimple", 0.05);
```

```
 };
 R_Date("OxA-26029", 11700, 110)
 {
  Outlier("SSimple", 0.05);
 };
 Outlier("General", 0.05);
 z=1076.9;
};
R_Combine("RL300: 812.5-817.5cm")
{
 R_Date("C785", 11460, 140)
 {
  Outlier("SSimple", 0.05);
 };
 R_Date("OxA-25927", 11435, 45)
 {
  Outlier("SSimple", 0.05);
 };
 Outlier("General", 0.05);
 z=1073.9;
};
R_Date("C920", 11740, 180)
{
 Outlier("General", 0.05);
 z=1072.8;
};
R_Date("C784", 11440, 140)
{
 Outlier("General", 0.05);
 z=1069.8;
};
R_Combine("RL305: 978cm")
{
 R_Date("C978", 11230, 180)
 {
  Outlier("SSimple", 0.05);
 };
 R_Date("C919", 11670, 170)
 {
  Outlier("SSimple", 0.05);
 };
 Outlier("General", 0.05);
 z=1068.7;
};
R_Date("C780", 11270, 140)
{
 Outlier("General", 0.05);
 z=1065.7;
};
R_Date("C915", 11370, 180)
{
 Outlier("General", 0.05);
 z=1064.7;
};
R_Combine("RL300: 782.5-787.5cm")
{
 R_Date("LST1", 11260, 140)
 {
  Outlier("SSimple", 0.05);
 };
 R_Date("OxA-25926", 11005, 45)
 {
  Outlier("SSimple", 0.05);
 };
 Outlier("General", 0.05);
 z=1061.9;
};
Date("=LST")
{
 z=1061.6;
};
R_Date("LST2", 10640, 160)
{
 Outlier("General", 0.05);
 z=1061.3;
};
R_Combine("RL305: 964-968cm")
{
 R_Date("C910", 11070, 170)
 {
  Outlier("SSimple", 0.05);
 };
 R_Date("OxA-26028", 10755, 50)
 {
  Outlier("SSimple", 0.05);
 };
 Outlier("General", 0.05);
 z=1058.7;
};
R_Combine("RL305: 960-964cm")
{
 R_Date("C901", 10450, 160)
 {
  Outlier("SSimple", 0.05);
 };
 R_Date("OxA-25933", 10450, 40)
 {
  Outlier("SSimple", 0.05);
 };
 Outlier("General", 0.05);
 z=1054.7;
};
R_Date("C968", 10730, 150)
{
 Outlier("General", 0.05);
 z=1050.8;
};
R_Date("C905", 10440, 160)
{
 Outlier("General", 0.05);
```

```
 z=1049.7;
};
R_Date("OxA-25925", 10345, 40)
{
 Outlier("General", 0.05);
 z=1046.5;
};
R_Combine("RL305: 952-956cm")
{
 R_Date("C904", 10310, 160)
 {
  Outlier("SSimple", 0.05);
 };
 R_Date("OxA-25932",10395,40)
 {
  Outlier("SSimple", 0.05);
 };
 Outlier("General", 0.05);
 z=1045.4;
};
R_Date("C730", 10000, 130)
{
 Outlier("General", 0.05);
 z=1042.2;
};
R_Combine("RL305: 948-952cm")
{
 R_Date("C909", 10460, 160)
 {
  Outlier("SSimple", 0.05);
 };
 R_Date("OxA-25931", 10480, 40)
 {
  Outlier("SSimple", 0.05);
 };
 Outlier("General", 0.05);
 z=1041.1;
};
Date("=Vedde Ash")
{
 z=1037.5;
};
R_Date("C889", 10130, 150)
{
 Outlier("General", 0.05);
 z=1036.9;
};
R_Date("C874", 10010, 150)
{
 Outlier("General", 0.05);
 z=1032.6;
};
R_Date("C731", 10120, 140)
{
 Outlier("General", 0.05);
 z=1029.4;
};
R_Date("C869", 9870, 150)
{
 Outlier("General", 0.05);
 z=1028.3;
};
R_Date("C864", 10010, 150)
{
 Outlier("General", 0.05);
 z=1024.5;
};
R_Combine("RL300: 682.5-687.5cm")
{
 R_Date("C746", 9840, 140)
 {
  Outlier("SSimple", 0.05);
 };
 R_Date("OxA-25924", 9880, 40)
 {
  Outlier("SSimple", 0.05);
 };
 Outlier("General", 0.05);
 z=1022.2;
};
R_Date("OxA-26027", 9610, 50)
{
 Outlier("General", 0.05);
 z=1021.2;
};
R_Date("OxA-26019", 9705, 50)
{
 Outlier("General", 0.05);
 z=1018.3;
};
R_Combine("RL305: 924-928cm")
{
 R_Date("C854", 10010, 150)
 {
  Outlier("SSimple", 0.05);
 };
 R_Date("OxA-26026", 9920, 45)
 {
  Outlier("SSimple", 0.05);
 };
 Outlier("General", 0.05);
 z=1016.9;
};
R_Date("C728", 9360, 130)
{
 Outlier("General", 0.05);
 z=1012.8;
};
R_Combine("RL305: 920-924cm")
{
```

Appendix 5. OxCal coding for age models

```
 R_Date("C853", 10010, 160)
 {
  Outlier("SSimple", 0.05);
 };
 R_Date("OxA-26025", 9705, 50)
 {
  Outlier("SSimple", 0.05);
 };
 Outlier("General", 0.05);
 z=1012.7;
};
R_Combine("RL305: 916-920cm")
{
 R_Date("C852", 9630, 150)
 {
  Outlier("SSimple", 0.05);
 };
 R_Date("OxA-26024", 9590, 45)
 {
  Outlier("SSimple", 0.05);
 };
 Outlier("General", 0.05);
 z=1010.6;
};
R_Combine("RL305: 912-916cm")
{
 R_Date("C848", 9760, 160)
 {
  Outlier("SSimple", 0.05);
 };
 R_Date("OxA-26023", 9665, 45)
 {
  Outlier("SSimple", 0.05);
 };
 Outlier("General", 0.05);
 z=1009.4;
};
R_Date("C847", 9450, 140)
{
 Outlier("General", 0.05);
 z=1008.2;
};
R_Combine("RL300: 652.5-657.5cm")
{
 R_Date("C727", 9780, 140)
 {
  Outlier("SSimple", 0.05);
 };
 R_Date("OxA-25922", 9508, 39)
 {
  Outlier("SSimple", 0.05);
 };
 Outlier("General", 0.05);
 z=1007.3;
};
R_Combine("RL305: 904-908cm")
{
 R_Date("C846", 9510, 140)
 {
  Outlier("SSimple", 0.05);
 };
 R_Date("OxA-26022", 9465, 50)
 {
  Outlier("SSimple", 0.05);
 };
 Outlier("General", 0.05);
 z=1006.9;
};
R_Date("OxA-26018", 9405, 50)
{
 Outlier("General", 0.05);
 z=1001.8;
};
R_Combine("RL300: 632.5-637.5cm")
{
 R_Date("C725", 9380, 130)
 {
  Outlier("SSimple", 0.05);
 };
 R_Date("OxA-26017", 9470, 45)
 {
  Outlier("SSimple", 0.05);
 };
 Outlier("General", 0.05);
 z=996.3;
};
R_Combine("RL300: 622.5-627.5cm")
{
 R_Date("C724", 9450, 140)
 {
  Outlier("SSimple", 0.05);
 };
 R_Date("OxA-26016", 9335, 50)
 {
  Outlier("SSimple", 0.05);
 };
 Outlier("General", 0.05);
 z=990.8;
};
Boundary("Rotsee 980cm")
{
 z=980.0;
};
};
P_Sequence("Lake Brazi",1,1,U(-2,2))
{
 Boundary("BraziBase")
 {
  z=600;
 };
```

Appendix 5. OxCal coding for age models

```
R_Date("Poz-27305",11590,60)
{
 Outlier("General", 0.05);
 z=578;
};
R_Date("Poz-31716",10870,70)
{
 Outlier("General", 0.05);
 z=569;
};
Date("LG Lipari")
{
 z=564;
};
R_Date("Poz-31715",9980,100)
{
 Outlier("General", 0.05);
 z=557;
};
R_Date("Poz-26112",9610,50)
{
 Outlier("General", 0.05);
 z=545;
};
Date("=Askja_S")
{
 z=540.5;
};
R_Date("Poz-31714",9150,50)
{
 Outlier("General", 0.05);
 z=521;
};
R_Date("Poz-26111",8810,50)
{
 Outlier("General", 0.05);
 z=505;
};
R_Date("Poz-26110",8240,50)
{
 Outlier("General", 0.05);
 z=450;
};
Boundary("BraziNotTop")
{
 z=449;
};
};
P_Sequence("WE 10/2",1,1,U(-2,2))
{
 Boundary("WE10/2 Base")
 {
  z=790;
 };
 R_Date("Poz43989",13340,70)
 {
  Outlier();
  z=724.5;
 };
 R_Date("Poz-43987",14240,80)
 {
  Outlier();
  z=666.5;
 };
 Date("=LST")
 {
  z=576;
 };
 Date("=Hasseldalen")
 {
  z=397.5;
 };
 R_Date("Poz-42398",9360,60)
 {
  Outlier("General", 0.05);
  z=285.5;
 };
 R_Date("Poz-42397",8660,50)
 {
  Outlier(0.05);
  z=218.5;
 };
 Boundary("WE10/2Nottop")
 {
  z=219;
 };
};
P_Sequence("Lago Piccolo di
Avigliana",1,1,U(-2,2))
{
 Boundary("LPA Base")
 {
  z=954;
 };
 R_Date("Poz-6497",14930,80)
 {
  Outlier("General", 0.05);
  z=909;
 };
 R_Date("Erl-4797",14614,111)
 {
  Outlier("General", 0.05);
  z=888;
 };
 R_Date("Erl-4798",12395,102)
 {
  Outlier("General", 0.05);
  z=806;
 };
 R_Date("Erl-4799",11525,80)
```

```
 {
  Outlier("General", 0.05);
  z=775;
 };
 Date("=LST")
 {
  z=768;
 };
 Date("=Vedde Ash")
 {
  z=738;
 };
 R_Date("Poz-3931",10320,50)
 {
  Outlier("General", 0.05);
  z=732.5;
 };
 R_Date("Erl-4800",10248,64)
 {
  Outlier("General", 0.05);
  z=714;
 };
 R_Date("Poz-3918",9320,60)
 {
  Outlier("General", 0.05);
  z=695;
 };
 R_Date("Poz-3930",9290,50)
 {
  Outlier("General", 0.05);
  z=678.5;
 };
 R_Date("Erl-4801",8723,63)
 {
  Outlier("General", 0.05);
  z=634;
 };
 Boundary("LPANotTop")
 {
  z=633;
 };
};
P_Sequence("Lake Bled",1,1,U(-2,2))
{
 Boundary("NYT",
Top_Hat(calBP(14000),1000))
 {
  z=240;
 };
 R_Date("Beta-217805",11930,40)
 {
  Outlier("General", 0.05);
  z=210;
 };
 Date("=Vedde Ash")
 {
  z=122;
 };
 Date("PP", Top_Hat(calBP(12000),1000))
 {
  z=120;
 };
 R_Date("Beta-222472",9340,40)
 {
  Outlier("General", 0.05);
  z=60;
 };
 Boundary("Bled Top")
 {
  z=8;
 };
};
P_Sequence("Hasseldala port",1,1,U(-2,2))
{
 Boundary("HASS end")
 {
  z=370;
 };
 R_Date("UBA-20296",12211,57)
 {
  Outlier("General", 0.05);
  z=369.5;
 };
 R_Date("UBA-20297",11972,62)
 {
  Outlier("General", 0.05);
  z=367.5;
 };
 R_Date("Ua-20516",12355,190)
 {
  Outlier("General", 0.05);
  z=366.6;
 };
 R_Date("UBA-20298",11673,56)
 {
  Outlier("General", 0.05);
  z=365.25;
 };
 R_Date("UBA-20299",11819,57)
 {
  Outlier("General", 0.05);
  z=363;
 };
 R_Date("Ua-20517",11920,90)
 {
  Outlier("General", 0.05);
  z=362.65;
 };
 R_Date("UBA-20300",11735,60)
 {
```

```
 Outlier("General", 0.05);
 z=360.5;
};
R_Date("Ua-20518",11990,110)
{
 Outlier("General", 0.05);
 z=360.15;
};
R_Date("UBA-20301",11614,55)
{
 Outlier("General", 0.05);
 z=358.5;
};
R_Date("Ua-20519",11805,240)
{
 Outlier("General", 0.05);
 z=358.4;
};
R_Date("UBA-20302",11565,56)
{
 Outlier("General", 0.05);
 z=356.5;
};
R_Date("Ua-20520",11525,85)
{
 Outlier("General", 0.05);
 z=356;
};
R_Date("UBA-20303",11515,65)
{
 Outlier("General", 0.05);
 z=354.5;
};
R_Date("Ua-20521",11490,85)
{
 Outlier("General", 0.05);
 z=352.85;
};
R_Date("UBA-20304",11225,60)
{
 Outlier("General", 0.05);
 z=352;
};
R_Date("Ua-20522",11455,125)
{
 Outlier("General", 0.05);
 z=350;
};
R_Date("UBA-20305",11118,60)
{
 Outlier("General", 0.05);
 z=348.5;
};
R_Date("Ua-20523",11245,95)
{
 Outlier("General", 0.05);
 z=347.25;
};
R_Date("Ua-20524",11275,95)
{
 Outlier("General", 0.05);
 z=347.1;
};
R_Date("Ua-20525",11200,165)
{
 Outlier("General", 0.05);
 z=346.95;
};
R_Date("UBA-20306",10998,63)
{
 Outlier("General", 0.05);
 z=346.5;
};
R_Date("Ua-20526",10935,80)
{
 Outlier("General", 0.05);
 z=345.5;
};
R_Date("UBA-20307",10894,63)
{
 Outlier("General", 0.05);
 z=344;
};
R_Date("Ua-20527",11070,135)
{
 Outlier("General", 0.05);
 z=339.9;
};
R_Date("UBA-20308",10644,58)
{
 Outlier("General", 0.05);
 z=338.5;
};
R_Date("UBA-20309",10484,50)
{
 Outlier("General", 0.05);
 z=337.5;
};
R_Date("Ua-20528",10935,80)
{
 Outlier("General", 0.05);
 z=337.4;
};
R_Date("Ua-20529",10515,75)
{
 Outlier("General", 0.05);
 z=334.55;
};
R_Date("UBA-20310",10331,51)
{
```

```
 Outlier("General", 0.05);
 z=333.25;
};
R_Date("Ua-16740",10165,95)
{
 Outlier("General", 0.05);
 z=332.7;
};
R_Date("UBA-20311",10301,57)
{
 Outlier("General", 0.05);
 z=331;
};
R_Date("UBA-23306",10331,53)
{
 Outlier("General", 0.05);
 z=329.5;
};
R_Date("UBA-20312",10639,51)
{
 Outlier("General", 0.05);
 z=328.5;
};
R_Date("Ua-16745",10285,95)
{
 Outlier("General", 0.05);
 z=328.4;
};
R_Date("UBA-20313",10130,69)
{
 Outlier("General", 0.05);
 z=326.5;
};
R_Date("Ua-16747",9860,85)
{
 Outlier("General", 0.05);
 z=323.35;
};
R_Date("Ua-16750",10205,85)
{
 Outlier("General", 0.05);
 z=319.85;
};
R_Date("UBA-21574",10102,67)
{
 Outlier("General", 0.05);
 z=319.5;
};
R_Date("Ua-16752",9720,90)
{
 Outlier("General", 0.05);
 z=315.9;
};

Date("Hasseldalen",U(calBP(11345),calBP(1
1155)))
  {
   z=312.7;
  };
  R_Date("Ua-16761",9955,90)
  {
   Outlier("General", 0.05);
   z=312.25;
  };
  R_Date("UBA-22308",9864,47)
  {
   Outlier("General", 0.05);
   z=310;
  };
  R_Date("Ua-16766",9765,85)
  {
   Outlier("General", 0.05);
   z=309.5;
  };
  R_Date("Ua-16768",9625,70)
  {
   Outlier("General", 0.05);
   z=305.5;
  };
  R_Date("UBA-21575",9532,59)
  {
   Outlier("General", 0.05);
   z=302.5;
  };

Date("Askja_S",U(calBP(11189),calBP(1100
0)))
  {
   z=302.4;
  };
  R_Date("UBA-21577",9442,52)
  {
   Outlier("General", 0.05);
   z=299.5;
  };
  R_Date("UBA-21578",9416,47)
  {
   Outlier("General", 0.05);
   z=298.5;
  };
  R_Date("UBA-23309",9129,50)
  {
   Outlier("General", 0.05);
   z=280;
  };
  R_Date("UBA-21579",8605,46)
  {
   Outlier("General", 0.05);
```

Appendix 5. OxCal coding for age models

```
 z=272.5;
 };
 Boundary("HASS Top")
 {
 z=270.5;
 };
};
P_Sequence("CRU",1,1,U(-2,2))
{
 Boundary("CRU Base")
 {
 z=576;
 };
 Date("Borrobol")
 {
 z=566.59;
 };
 Date("Penifiler")
 {
 z=558.35;
 };
 Date("=Vedde Ash")
 {
 z=511.20;
 {
 z=500;
 };
 Date("=Hasseldalen")
 {
 z=486.32;
 };
 Date("=Askja_S")
 {
 z=461.12;
 };
 R_Date("AA-36191",13245,95)
 {
 Outlier();
 z=428;
 };
 Date("=Saksunarvatn Ash")
 {
 z=385;
 };
 Boundary("CRU Top")
 {
 z=194;
 };
};
P_Sequence("HBG",1,1,U(-2,2))
{
 Boundary();
 R_Date("KL7",11950,70)
 {
 Outlier("General", 0.05);
 z=1382;
 };
 Date("=LST")
 {
 z=1300;
 };
 Date("=Vedde Ash")
 {
 z=1118;
 };
 Date("=Hasseldalen")
 {
 z=937;
 };
 Boundary("=Askja_S")
 {
 z=886;
 };
};
 P_Sequence("KrakenesLohne46",1,1,U(-
2,2))
 {
 Boundary("KRABase")
 {
 z=948;
 };
 R_Date("Ua-3418",11380,85)
 {
 Outlier("General", 0.05);
 z=947.5;
 };
 R_Date("Ua-3407",11220,90)
 {
 Outlier("General", 0.05);
 z=940.5;
 };
 R_Date("TUa-600",11275,125)
 {
 Outlier("General", 0.05);
 z=935.5;
 };
 R_Date("TUa-597",11135,135)
 {
 Outlier("General", 0.05);
 z=930.5;
 };
 R_Date("TUa-591",10995,110)
 {
 Outlier("General", 0.05);
 z=925.5;
 };
 R_Date("TUa-587",10800,110)
 {
 Outlier("General", 0.05);
 z=923.75;
```

```
};
R_Date("TUa-852A",11520,165)
{
 Outlier("General", 0.05);
 z=922.5;
};
R_Date("TUa-851",10980,120)
{
 Outlier("General", 0.05);
 z=922;
};
R_Date("TUa-586",10570,305)
{
 Outlier("General", 0.05);
 z=921.5;
};
R_Date("Ua-3408",10130,195)
{
 Outlier("General", 0.05);
 z=920.5;
};
R_Date("TUa-589",10560,215)
{
 Outlier("General", 0.05);
 z=918.5;
};
R_Date("TUa-610",13485,1555)
{
 Outlier("General", 0.05);
 z=910.75;
};
R_Date("TUa-596",10520,115)
{
 Outlier("General", 0.05);
 z=904;
};
R_Date("Ua-3417",11050,715)
{
 Outlier("General", 0.05);
 z=893;
};
R_Date("Ua-3413",8875,155)
{
 Outlier("General", 0.05);
 z=890.25;
};
R_Combine("TUa-868A/TUa-868")
{
 R_Date("TUa-868A",10200,115)
 {
  Outlier("SSimple", 0.05);
 };
 R_Date("TUa-868",10515,135)
 {
  Outlier("SSimple", 0.05);
 };
 Outlier("General", 0.05);
 z=885.75;
};
R_Combine("TUa-867A/TUa-867")
{
 R_Date("TUa-867A",10185,120)
 {
  Outlier("SSimple", 0.05);
 };
 R_Date("TUa-867",10420,175)
 {
  Outlier("SSimple", 0.05);
 };
 Outlier("General", 0.05);
 z=883.25;
};
R_Date("Ua-3416",9205,200)
{
 Outlier("General", 0.05);
 z=880.5;
};
R_Date("TUa-599",10510,115)
{
 Outlier("General", 0.05);
 z=870.75;
};
R_Date("Ua-3412",10130,75)
{
 Outlier("General", 0.05);
 z=859.5;
};
R_Date("Ua-3405",10345,105)
{
 Outlier("General", 0.05);
 z=841;
};
R_Date("Ua-3404",10415,95)
{
 Outlier("General", 0.05);
 z=835.75;
};
R_Date("Ua-3403",10305,95)
{
 Outlier("General", 0.05);
 z=833;
};
Date("=Vedde Ash")
{
 z=831;
};
R_Date("Ua-3402",10300,110)
{
 Outlier("General", 0.05);
 z=830.25;
```

```
};
R_Date("Ua-3401",10230,90)
{
 Outlier("General", 0.05);
 z=828;
};
R_Date("Ua-3400",10445,85)
{
 Outlier("General", 0.05);
 z=820.75;
};
R_Date("Ua-3411",9900,110)
{
 Outlier("General", 0.05);
 z=810.25;
};
R_Date("TUa-783",10220,120)
{
 Outlier("General", 0.05);
 z=801.5;
};
R_Date("TUa-598",10180,110)
{
 Outlier("General", 0.05);
 z=791;
};
R_Date("Ua-3415",10060,135)
{
 Outlier("General", 0.05);
 z=785;
};
R_Date("TUa-782",9965,90)
{
 Outlier("General", 0.05);
 z=781;
};
R_Date("Ua-3410",10100,115)
{
 Outlier("General", 0.05);
 z=771.25;
};
R_Date("Ua-3414",9980,125)
{
 Outlier("General", 0.05);
 z=766;
};
R_Date("TUa-590",9985,95)
{
 Outlier("General", 0.05);
 z=760.5;
};
R_Date("TUa-1180A",10100,75)
{
 Outlier("General", 0.05);
 z=760.25;
};
R_Date("TUa-585",9960,100)
{
 Outlier("General", 0.05);
 z=759.75;
};
R_Date("TUa-594",9945,85)
{
 Outlier("General", 0.05);
 z=757.25;
};
R_Date("TUa-584",10105,90)
{
 Outlier("General", 0.05);
 z=755.75;
};
R_Date("TUa-1179A",10165,75)
{
 Outlier("General", 0.05);
 z=755.5;
};
R_Date("TUa-595",9815,110)
{
 Outlier("General", 0.05);
 z=753.5;
};
R_Date("TUa-1178A",10120,65)
{
 Outlier("General", 0.05);
 z=750.5;
};
R_Date("TUa-588",10005,95)
{
 Outlier("General", 0.05);
 z=749.5;
};
R_Date("TUa-1177A",9950,55)
{
 Outlier("General", 0.05);
 z=745.5;
};
R_Combine("Ua-3406/TUa-1176A")
{
 R_Date("Ua-3406",9880,85)
 {
  Outlier("SSimple", 0.05);
 };
 R_Date("TUa-1176A",9990,55)
 {
  Outlier("SSimple", 0.05);
 };
 Outlier("General", 0.05);
 z=740.5;
};
R_Combine("TUa-780/TUa-1175A")
```

Appendix 5. OxCal coding for age models

```
{
 R_Date("TUa-780",9935,95)
 {
  Outlier("SSimple", 0.05);
 };
 R_Date("TUa-1175A",9910,65)
 {
  Outlier("SSimple", 0.05);
 };
 Outlier("General", 0.05);
 z=735.5;
};
R_Combine("TUa-593/TUa-1174A")
{
 R_Date("TUa-593",9600,100)
 {
  Outlier("SSimple", 0.05);
 };
 R_Date("TUa-1174A",9800,65)
 {
  Outlier("SSimple", 0.05);
 };
 Outlier("General", 0.05);
 z=730.5;
};
R_Date("TUa-1173A",9705,60)
{
 Outlier("General", 0.05);
 z=725.5;
};
R_Date("TUa-1172A",9560,80)
{
 Outlier("General", 0.05);
 z=720.5;
};
R_Date("TUa-1171A",9465,70)
{
 Outlier("General", 0.05);
 z=715.5;
};
R_Date("TUa-1170A",9505,75)
{
 Outlier("General", 0.05);
 z=710.5;
};
R_Date("TUa-1169A",9630,70)
{
 Outlier("General", 0.05);
 z=705.5;
};
R_Date("T-10830A",9580,130)
{
 Outlier("General", 0.05);
 z=701;
};
R_Date("TUa-1168A",9570,75)
{
 Outlier("General", 0.05);
 z=700.5;
};
R_Date("TUa-1167A",9615,80)
{
 Outlier("General", 0.05);
 z=695.5;
};
R_Date("TUa-1166A",9465,75)
{
 Outlier("General", 0.05);
 z=690.5;
};
R_Date("TUa-1165A",9300,100)
{
 Outlier("General", 0.05);
 z=685.5;
};
R_Date("Ua-3450",9290,100)
{
 Outlier("General", 0.05);
 z=682.5;
};
R_Date("TUa-1008A",9210,130)
{
 Outlier("General", 0.05);
 z=680;
};
R_Date("Ua-3449",9450,90)
{
 Outlier("General", 0.05);
 z=677.5;
};
R_Date("Ua-3428",9190,85)
{
 Outlier("General", 0.05);
 z=676.5;
};
R_Date("Ua-3427",9180,80)
{
 Outlier("General", 0.05);
 z=675.5;
};
R_Combine("Ua-3426/Ua-3425")
{
 R_Date("Ua-3426",8840,130)
 {
  Outlier("SSimple", 0.05);
 };
 R_Date("Ua-3425",9065,105)
 {
  Outlier("SSimple", 0.05);
 };
```

Appendix 5. OxCal coding for age models

```
 Outlier("General", 0.05);
 z=673.5;
 };
 R_Date("Ua-3448",9115,90)
 {
 Outlier("General", 0.05);
 z=672.5;
 };
 Date("Saksunarvatn Ash",
Top_Hat(calBP(10000),1000))
 {
 z=671.5;
 };
 R_Date("Ua-3423",8930,145)
 {
 Outlier("General",0.05);
 z=671.4;
 };
 Boundary("KRANotTop")
 {
 z=670;
 };
};
P_Sequence("HAM",1,1,U(-2,2))
{
 Boundary("HAMCore base")
 {
 z=1730;
 };
 R_Date("OxA-32273",12450,65)
 {
 Outlier("General", 0.05);
 z=1694.5;
 };
 R_Date("OxA-32272",12475,60)
 {
 Outlier("General", 0.05);
 z=1682.5;
 };
 R_Date("OxA-2551-47",11975,50)
 {
 Outlier("General", 0.05);
 z=1679.5;
 };
 Date("HAMVarve count limit",LST-
N(579,5))
 {
 z=1610;
 };
 Date("=LST")
 {
 z=1557.5;
 };
 Date("HAMVarve end",LST+N(246,5))
 {
 z=1524.5;
 };
 Date("=Vedde Ash")
 {
 z=1492.5;
 };
 R_Date("OxA-2555-13",10550,160)
 {
 Outlier("General", 0.05);
 z=1489.5;
 };
 R_Date("OxA-2555-14",10310,130)
 {
 Outlier("General", 0.05);
 z=1477.5;
 };
 Date("HAM_1470")
 {
 z=1470;
 };
 Date("Ulmener Maar",
Top_Hat(calBP(11050),1000))
 {
 z=1451;
 };
 Date("=Askja_S")
 {
 z=1444.5;
 };
 Date("=Saksunarvatn Ash")
 {
 z=1401.5;
 };
 Boundary("HAMCore top")
 {
 z=1370;
 };
};
P_Sequence("JC", 1, 1,U(-2,2))
{
 Boundary("JC base")
 {
 z=1345;
 };
 R_Date("Poz-52867",11900,50)
 {
 Outlier("General", 0.05);
 z=1274;
 };
 R_Date("Poz-52866", 11270, 60)
 {
 Outlier("General", 0.05);
 z=1256;
 };
```

```
  Date("Varve count limit",Hasseldalen-
N(86,3))
  {
   z=1172;
  };
  Date("=Hasseldalen")
  {
   z=1158.5;
  };
  Interval(N(152,10));
  Date("=Askja_S")
  {
   z=1141.25;
  };
  Date("Varve end",Askja_S+N(730,3))
  {
   z=1073;
  };
  R_Date("Poz-52862",8790,50)
  {
   Outlier("General", 0.05);
   z=1054;
  };
  R_Date("Poz-52810",7970,90)
  {
   Outlier("General", 0.05);
   z=1035;
  };
  Boundary("JCnotTop")
  {
   z=1027;
  };
 };
 Combine("=LST")
 {
  // Friedrich et al 1999 data
  // Kruft 1
  R_Date("Hd-19607",11062,27);
  Gap(15);
  R_Date("Hd-18648",11037,27);
  Gap(5);
  // Kruft 9
  R_Date("Hd-19098",11063,30);
  Gap(40);
  R_Date("Hd-19092",11066,28);
  Gap(25);
  R_Date("Hd-18622",11073,33);
  Gap(15);
  R_Date("Hd-19037",11075,28);
  Gap(5);
  // Kruft 8
  R_Date("Hd-18438",11065,22);
  Gap(0);
 };
};
```

**Sequence and Phase model for Hässeldalen and Askja-S tephra *U* age OxCal model**

```
Plot()
 {
  Outlier_Model("General",T(5),U(0,4),"t");
  Sequence()
  {
   Tau_Boundary();
   Phase()
   {
    R_Date("Ua-16752",9720,90)
    {
     Outlier(0.05);
    };
    R_Date("UBA-21574",10102,67)
    {
     Outlier(0.05);
    };
   };
   Boundary("Hasseldalen");
   Sequence("Inbetween Hass and Askja
Hassp")
   {
    R_Date("Ua-16761",9955,90)
    {
     Outlier(0.05);
    };
    R_Date("UBA-22308",9864,47)
    {
     Outlier(0.05);
    };
    R_Date("Ua-16766",9765,85)
    {
     Outlier(0.05);
    };
    R_Date("Ua-16768",9625,70)
    {
     Outlier(0.05);
    };
    R_Date("UBA-21575",9532,59)
    {
     Outlier(0.05);
    };
   };
   Boundary("Askja-S");
   Phase("post Askja")
   {
    R_Date("ETH-7699",9620,100)
    {
     Outlier(0.05);
    };
```

```
   R_Date("UBA-21577",9442,52)
   {
    Outlier(0.05);
   };
   R_Date("UBA-21578",9416,47)
   {
    Outlier(0.05);
   };
  };
  Tau_Boundary();
 };
 Difference("","Askja-S","Hasseldalen",
N(152,10));
};
```

**Bond et al. (2001) re-modelled VM2814 age model**

```
Options()
 {
 Curve="Marine13.14c";
};
Plot()
 {
 Outlier_Model("General",T(5),U(0,4),"t");
 P_Sequence("",1,1,U(-2,2))
 {
  Boundary();
  R_Date("108",11040,130)
  {
   Outlier(0.05);
   z=108;
  };
  R_Date("103",10880,130)
  {
   Outlier(0.05);
   z=103;
  };
  R_Date("95",10290,130)
  {
   Outlier(0.05);
   z=95;
  };
  R_Date("90",8810,140)
  {
   Outlier(0.05);
   z=90;
  };
  R_Date("82",8010,80)
  {
   Outlier(0.05);
   z=82;
  };
  R_Date("76.7",7100,75)
  {
   Outlier(0.05);
   z=76.7;
  };
  R_Date("74",6680,80)
  {
   Outlier(0.05);
   z=74;
  };
  R_Date("69",5960,65)
  {
   Outlier(0.05);
   z=69;
  };
  R_Date("60",5515,51)
  {
   Outlier(0.05);
   z=60;
  };
  R_Date("52",4895,70)
  {
   Outlier(0.05);
   z=52;
  };
  R_Date("44",4318,59)
  {
   Outlier(0.05);
   z=44;
  };
  R_Date("32",3540,53)
  {
   Outlier(0.05);
   z=32;
  };
  R_Date("19.5",2895,60)
  {
   Outlier(0.05);
   z=19.5;
  };
  R_Date("8",1643,60)
  {
   Outlier(0.05);
   z=8;
  };
  Boundary();
 };
};
```

**Re-modelled Finsinger et al. (2002) Early Holocene Lake Agasiz flood events**

```
Plot()
 {
  R_Date("FD1", 10015, 320);
```

```
 R_Date("FD2", 9860, 230);
 R_Date("D1", 9910, 190);
 R_Date("D2", 9710, 130);
};
```

**Re-modelled age model for Peck et al. (2007) of MD01-2461**

```
Options()
 {
 Curve="Marine13.14c";
};
Plot()
 {
 Outlier_Model("General",T(5),U(0,4),"t");
 P_Sequence("",1,1,U(-2,2))
  {
  Boundary();
  R_Date("SUERC-3306",11950,43)
  {
   Outlier(0.05);
   z=228.5;
  };
  R_Date("SUERC-3303",12551,46)
  {
   Outlier(0.05);
   z=208.5;
  };
  R_Date("SUERC-3302",11032,39)
  {
   Outlier(0.05);
   z=196.5;
  };
  R_Date("SUERC-3299",7623,29)
  {
   Outlier(0.05);
   z=134;
  };
  Boundary();
 };
};
```

Quaternary Science Reviews 188 (2018) 174–182

Contents lists available at ScienceDirect

Quaternary Science Reviews

journal homepage: www.elsevier.com/locate/quascirev

Short Communication

# Ultra-distal fine ash occurrences of the Icelandic Askja-S Plinian eruption deposits in Southern Carpathian lakes: New age constraints on a continental scale tephrostratigraphic marker

R. Kearney [a, *], P.G. Albert [a], R.A. Staff [b], I. Pál [c], D. Veres [e], E. Magyari [d], C. Bronk Ramsey [a]

[a] Research Laboratory for Archaeology and the History of Art, School of Archaeology, University of Oxford, 1 South Parks Road, Oxford, OX1 3TG, UK
[b] Scottish Universities Environmental Research Centre, University of Glasgow, Rankine Avenue, East Kilbride, South Lanarkshire, G75 0QF, UK
[c] Isotope Climatology and Environmental Research Center (ICER), Institute for Nuclear Research, Hungarian Academy of Sciences, H-4026, Debrecen, Bem tér 18/c, Hungary
[d] Eötvös Lóránd University, MTA-MTM-ELTE Research Group for Paleontology, Department of Environmental and Landscape Geography, Pázmány P. stny. 1/C, H-1117, Budapest, Hungary
[e] Romanian Academy, Institute of Speleology, Clinicilor 5, 400006, Cluj-Napoca, Romania

ARTICLE INFO

*Article history:*
Received 15 September 2017
Received in revised form
21 March 2018
Accepted 27 March 2018
Available online 10 April 2018

*Keywords:*
Askja-S tephra
Ultra-distal cryptotephra
Carpathian mountains
Tephrostratigraphy

ABSTRACT

Here we present the results of the first cryptotephra investigation of two Late glacial-Holocene lake records from the Southern Carpathian Mountains in Romania, Lake Brazi and Lake Lia. The discovery of an important Icelandic tephrostratigraphic marker, the Askja-S, in the sedimentary records of both sites significantly extends the known ash dispersal from this Plinian eruption. Bayesian age-depth modelling of available radiocarbon ($^{14}$C) data from both sedimentary records allows us to further refine the depositional age of this ultra-distal tephra. In combination with age constraints on the tephra from other well-dated European sites, we produce an updated age for this key tephrostratigraphic marker of 10,824 ± 97 cal yrs BP (95.4% range). The Askja-S tephra is stratigraphically positioned after the palaeoenvironmental proxy response to the Preboreal Oscillation at both sites. The widespread distribution of this tephra across Europe offers the potential to assess spatio-temporal variability of this climatic signal. The discovery of the Askja-S in lake records from the Southern Carpathians highlights the likelihood of finding other ultra-distal (Icelandic) cryptotephra marker layers within the region. Additionally, given the location of the Carpathian region, it offers the opportunity to further enhance and integrate tephrostratigraphic frameworks of north-western Europe with those of the Mediterranean and Anatolia regions, which will enable a more precise comparison of palaeoenvironmental archives across Europe.

© 2018 Elsevier Ltd. All rights reserved.

## 1. Introduction

The Late Glacial to Early Holocene transition (~16–8 kya) represents a period of abrupt climatic changes recorded in numerous multi-proxy palaeoenvironmental archives globally (Blockley et al., 2014; Moreno et al., 2014). These climatic changes occurred on centennial and even decadal timescales (Alley et al., 2003; Steffensen et al., 2008). Understanding the underlying driving and associated propagation mechanisms remains challenging, due to the large chronological uncertainties associated with dating methods, preventing robust inter-site comparisons of abrupt climatic transitions (Brauer et al., 2014; Bronk Ramsey et al., 2014).

The identification of widely dispersed volcanic ash (tephra) horizons can help to address these limitations (Lowe, 2011). During explosive volcanic eruptions, the fine ash component of tephra can be widely dispersed and preserved, providing time synchronous marker layers in a range of palaeoclimate records. These tephrostratigraphic markers facilitate the precise temporal comparison of disparate palaeoclimate archives (e.g. Lane et al., 2011a; Blockley et al., 2012). The identification of cryptotephra (non-visible) horizons beyond the extent of visible tephra fall layers, has enabled the application of tephrochronology over much greater areas (e.g. Jensen et al., 2014; Albert et al., 2015; van der Bilt et al., 2017). Because of this, cryptotephra horizons are becoming a powerful tool for integrating geographically disparate records, facilitating better understanding of the dynamics of abrupt climate change

* Corresponding author.
*E-mail address:* rebecca.kearney@st-annes.ox.ac.uk (R. Kearney).

https://doi.org/10.1016/j.quascirev.2018.03.035
0277-3791/© 2018 Elsevier Ltd. All rights reserved.

(e.g. Lane et al., 2013). Over the last decade, numerous European records have been subjected to detailed cryptotephra investigations, providing insights into past regional abrupt climate change, especially in northern and western Europe (e.g. MacLeod et al., 2014; Lowe et al., 2015). Yet regions such as Central Eastern Europe have been largely overlooked for cryptotephra application despite the demonstrated importance of visible distal and local tephras in providing marker horizons (Veres et al., 2013; Karátson et al., 2016). However, it is expected that the region holds significant potential for successful cryptotephra investigations due to its proximity to multiple volcanic fields, which have been active during the Late Quaternary, as well as its location at the convergence of several major air circulation patterns (Fig. 1A; Haliuc et al., 2017; Longman et al., 2017a, b; Obreht et al., 2017).

Here, we present the important discovery of an Icelandic-derived cryptotephra, the Askja-S, within two lacustrine palaeoenvironmental records from the Southern Carpathian Mountains. This provides, for the first time, a direct tephra linkage between multi-proxy palaeoclimatic archives in south-eastern Europe with those in north-western Europe.

## 2. Background

### 2.1. Askja-S tephra

The Askja-S tephra is the product of a Plinian eruption that formed the Askja caldera at the Dyngjuföll volcanic centre, Iceland (Sigvaldason, 2002). The estimated volume of this rhyolitic eruption is $1.5 \pm 0.5\ km^3$ dense-rock equivalent (DRE), relative to a Volcanic Explosivity Index (VEI) of 5 (Newhall and Self, 1982; Sigvaldason, 2002). The eruption coincided with glacial retreat in Iceland after Greenland Stadial (GS)-1. Proximal Askja-S Plinian fall deposits are distributed along the north-eastern coast of Iceland (Fig. 1A, Sæmundsson, 1991; Norðdahl and Hjort, 1993; Sigvaldason, 2002; Gudmundsdóttir et al., 2011), confirming a dominant NNE plume dispersal off Iceland.

The Askja-S was first reported distally by Davies et al. (2003) as a cryptotephra horizon in a sediment core from Hässeldala Port, Sweden. Askja-S cryptotephra has since been observed as far north as Borge, Norway (Pilcher et al., 2005), as far east as Lake Czechowskie, Poland (Wulf et al., 2016) and as far south as Soppensee, Switzerland (Lane et al., 2011b), limiting the Askja-S dispersal to mainly north-western European sites (Fig. 1A). Most recently, the

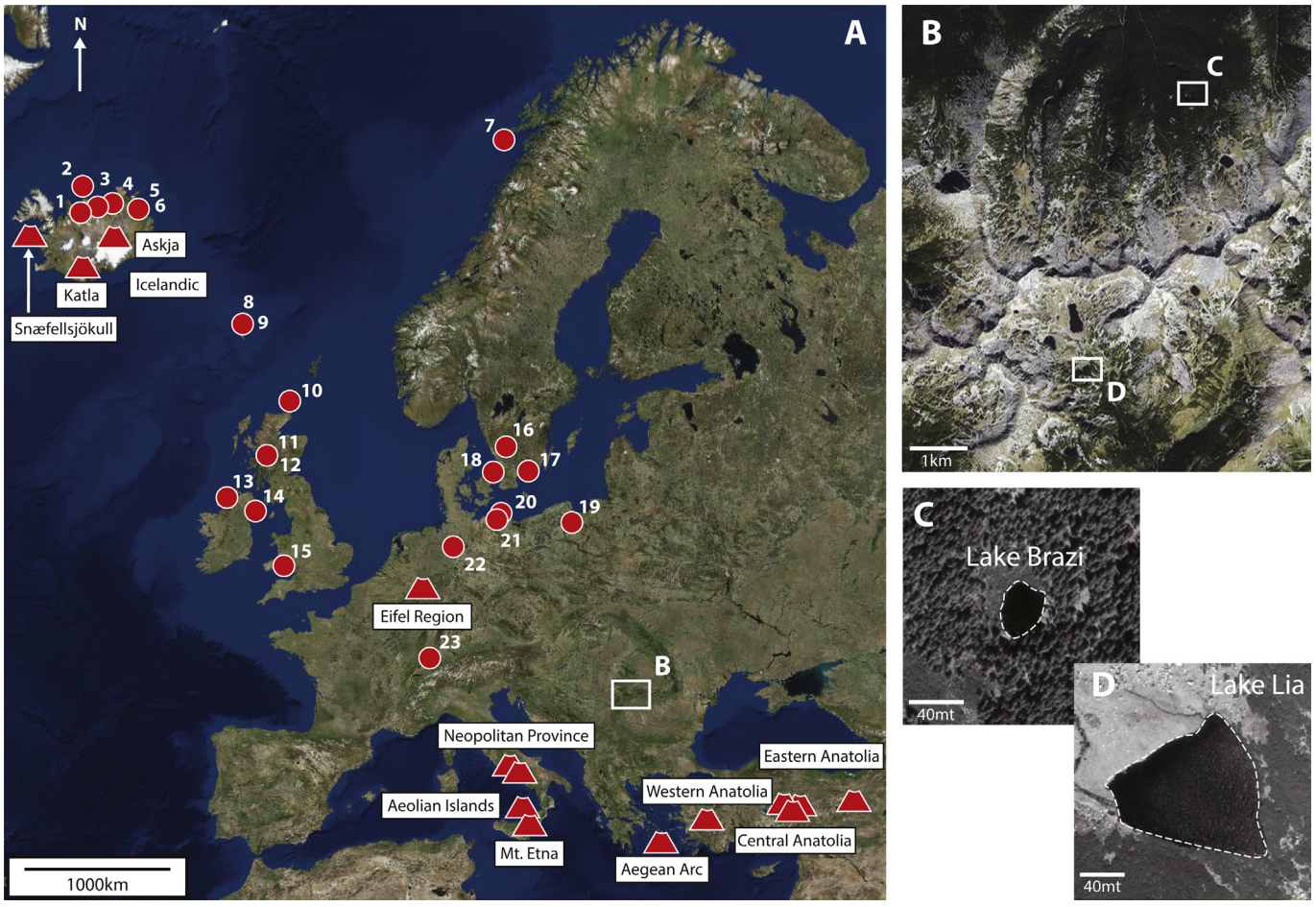


**Fig. 1.** (**A**) Landsat image (EU-DEM, 2016) of Europe showing the proximity of known active volcanic centres during the Late Glacial period and sites where the Askja-S tephra has been reported: 1) Skagafjördur (Sigvaldason, 2002); 2) MD99-2271 (Gudmundsdóttir et al., 2011); 3) Laufas (Sigvaldason, 2002); 4) Gjastykki (Sæmundsson, 1991); 5)Bakkaflói (Norðdahl and Hjort, 1993); 6) Vopnafjördur (Sigvaldason, 2002); 7) Borge Bog (Pilcher et al., 2005); 8) Høvdarhagi Bog (Lind and Wastegård., 2011); 9) Havnardalmyren (Kylander et al., 2012); 10) Quoyloo Meadow (Timms et al., 2016); 11) Inverlair (Kelly et al., 2016); 12) Turret Bank (Lowe et al., 2017); 13) Lough Nadourcan (Turney et al., 2006); 14) Long Lough (Turney et al., 2006); 15) Pant-y-Llyn (Jones et al., 2017a); 16) Mulakullegöl (Lilja et al., 2013); 17) Hässedala port (Davies et al., 2003; Wohlfarth et al., 2006); 18) Tøvelde (Larsen, 2013); 19) Lake Czechowskie (Wulf et al., 2016); 20) Endinger Bruch (Lane et al., 2012a); 21) Lake Tiefer See (Wulf et al., 2016); 22) Lake Hämelsee (Jones et al., 2017b); 23) Soppensee (Lane et al., 2011b). (**B**) Landsat image of the Retezat Mountains showing Lake Brazi (**C**) and Lake Lia (**D**).

tephra has been discovered in Pant-y-Llyn, South Wales (Jones et al., 2017a).

Several ages have been suggested for the eruption of the Askja-S (Fig. 2). At Hässeldala Port, an age of 10,810 ± 240 cal yrs BP was reported by Wohlfarth et al. (2006) which has since been supported by an age of 10,846 ± 276 cal yrs BP at Soppensee (Lane et al., 2011c, Fig. 2; all dates reported in this paper are at 95.4% probability). A younger age of 10,425 ± 75 cal yrs BP has been suggested by Lind and Wastegård (2011) from Høvdarhagi Bog, Faroe Islands, whilst a significantly older age of 11,228 ± 226 cal yrs BP has been provided by Ott et al. (2016) based on a floating varve chronology from Lake Czechowskie. Arguably, the most robust age estimate for the Askja-S tephra has been produced by Bronk Ramsey et al. (2015), through integrating radiocarbon age models from multiple palaeoenvironmental records from across Europe using the RESET (RESponse of humans to abrupt Environmental Transitions) tephra lattice, producing a refined modelled age of 10,841 ± 115 cal yrs BP.

### 2.2. Study sites

The Retezat Mountains form the western massif of the Southern Carpathian Mountains. This area was previously glaciated during the Last Glacial Maximum, with around 58 permanent glacial lakes still preserved (Magyari et al., 2009). Of these, two lakes, Brazi and Lia (Fig. 1B) were selected for cryptotephra investigation due to the extensive palaeoenvironmental investigations previously undertaken at both sites for the Late Glacial and Early Holocene periods (e.g. Magyari et al., 2012; Tóth et al., 2015; Buczkó et al., 2013; Orbán et al., 2017; Vincze et al., 2017). The chronologies of both sites are based upon radiocarbon ($^{14}$C) dating (Magyari et al., 2009, 2012; Hubay et al., 2016; Pál et al., 2016).

Lake Brazi (45°23′47″ N, 22°54′06″ E, 1740 m a.s.l., Fig. 1C) is located on the northern slope of the Retezat Mountains in a former kettle-hole setting (Magyari et al., 2009). Lake Lia (45°21′7.3″ N, 22°52′27.0″ E, 1910m a.s.l, Fig. 1D) is a small, shallow lake located 5 km from Lake Brazi on the south facing slopes of the Retezat Mountains (Orbán et al., 2017; Vincze et al., 2017).

## 3. Methods

### 3.1. Tephra sample preparation

Contiguous 5 cm resolution samples were taken across the sedimentologically identified Late Glacial to Early Holocene sequence of both Lake Brazi (TDB) and Lia (LIA) sediment cores (Magyari et al., 2009; Vincze et al., 2017). The glass shards were extracted following the density separation procedures described by Turney (1998) and Blockley et al. (2005) with a single modification where samples were sieved at 80 μm and 15 μm, rather than 80 μm and 25 μm. The tephra extraction residue (2.55 g cm$^{-3}$) of each sample was mounted on to microscope slides in Canada Balsam. Volcanic glass shards were identified and counted under a high-powdered, polarizing optical microscope. Where peaks in glass shard concentration were identified at 5 cm resolution, these depths were re-sampled at a higher resolution (1 cm) and prepared as above.

Individual glass shards from identified peaks were concentrated and mounted on to epoxy resin stubs with the use of a micromanipulator (see Lane et al., 2014). Finally, the shards were sealed in resin, sectioned and polished for geochemical analyses.

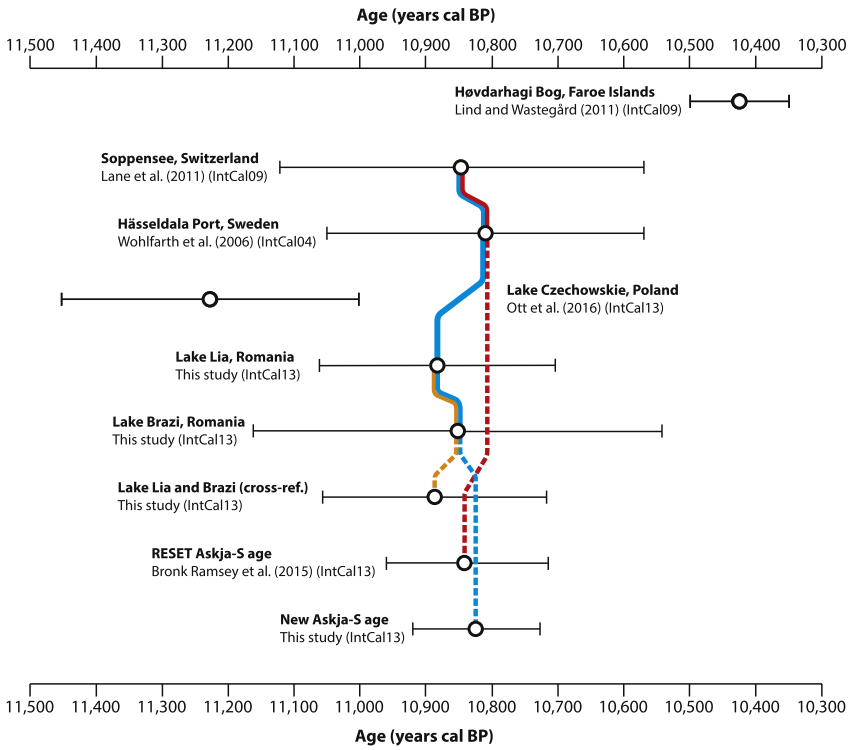


**Fig. 2.** Schematic representation of age estimates for the Askja-S tephra from published records, and newly remodelled data from this study. The red line indicates the sites cross-referenced for the Bayesian chronological modelling of Bronk Ramsey et al. (2015) to produce a refined the Askja-S age estimate as part of the RESET tephra lattice; the orange line shows the age estimate from modelling performed in the present study, cross-referencing of Lakes Brazi and Lia only; and the blue line indicates the records that were cross-referenced to produce our preferred the new Askja-S age building upon the RESET model by Bronk Ramsey et al. (2015) with the incorporation of the data from Lakes Brazi and Lia (this study). (For interpretation of the references to colour in this figure legend, the reader is referred to the Web version of this article.)

### 3.2. Geochemical analysis

Major and minor element compositions of individual glass shards were measured using a JEOL-8600 wavelength-dispersive electron microprobe (WDS-EPMA) at the Research Laboratory for Archaeology and History of Art, University of Oxford. All analyses used an accelerating voltage of 15 kV, beam current of 6 nA and 10 μm-diameter beam. Peak counting times were 30 s for all elements apart from Na (12s), Mn (40s), Cl (50s) and P (60s). The electron microprobe was calibrated using a suite of mineral standards, and the PAP absorption correction method was used for quantification. The accuracy and precision of our analyses were assessed using analyses of the MPI-DING reference glasses (Jochum et al., 2006), which were run alongside the unknown tephra samples. Data were filtered to remove accidental analyses of minerals and biogenic silica. Volcanic glass with analytical totals <95% were also removed.

### 3.3. Age-depth modelling

The original radiocarbon dates from both Lake Brazi and Lake Lia (Magyari et al., 2009, 2012; Hubay et al., 2016; Pál et al., 2016) have been re-modelled using the Bayesian statistical program OxCal (version 4.3, Bronk Ramsey, 2017) applying the IntCal13 calibration curve (Reimer et al., 2013). A 'P_Sequence' deposition model (Bronk Ramsey, 2009a) was applied for both sites utilising a variable *k* parameter to allow OxCal to independently determine the optimal variability in sedimentation rate (Bronk Ramsey and Lee, 2013). A 'general' *Outlier_Model* was applied with a 5% prior probability of any individual date being a statistical outlier (Bronk Ramsey, 2009b).

## 4. Results and discussion

### 4.1. Position and identification of cryptotephra layers

Distinct peaks in tephra shard concentration were identified in both the Lake Brazi and Lia sediment cores (Fig. 3). Robust geochemical analysis identified separate eruptions by major and minor element comparisons. For the purposes of this contribution we only present grain-specific glass geochemistry from selected peaks in glass shard concentrations in the Late glacial – early Holocene sequences of the two lakes, at 540/541 cm from the Lake Brazi sedimentary sequence (TDB_540, 288 shards $g^{-1}$; and TDB_541, 275 shards $g^{-1}$) and 603 cm in the Lake Lia record (LIA_603, 908 shards $g^{-1}$) (Fig. 3). Due to the nearly identical shard concentrations across TDB_540 and TDB_541, the positioning of the peak or isochron is taken as the mid-point of these depths (540.5 cm). Other peaks in tephra shard concentrations, with different geochemical characteristics from the distinctive Askja-S, will be discussed in future publications.

TDB_540/541 and LIA_603 are positioned within the locally described pollen zones associated with the transition from the Younger Dryas to Early Holocene (Magyari et al., 2009, 2012; Vincze et al., 2017). The modelled age of Askja-S from Lake Brazi is 10,852 ± 309 cal yrs BP and Lake Lia 10,885 ± 183 cal yrs BP (Fig. 3), within good statistical agreement of each other.

The shard morphologies of both layers exhibit a similar fluted appearance, the shards are colourless, with a maximum shard size of 20–25 μm (Fig. 3). The individual geochemical analyses of the glass shards in TDB_540/541 and LIA_603 are presented in Table 1, with selected major and minor element bi-plots shown in Fig. 4. TDB_540/541 and LIA_603 demonstrate a homogenous, rhyolitic glass composition characterised by low $K_2O$ (TDB_540/541: 2.60 ± 0.05 wt %, LIA_603: 2.60 ± 0.06 wt %; 1 s.d.) and high CaO (TDB_540/541: 1.65 ± 0.11 wt %; LIA_603: 1.61 ± 0.06 wt %; 1 s.d.). Due to this distinctive glass chemistry and the chronostratigraphic position of the TDB_540/541 and LIA_603 samples, we can confidently correlate them to the Askja-S erupted from the Dyngjuföll volcanic centre, Iceland (Sigvaldason, 2002) as well as to identified distal occurrences of ash from this eruption at multiple sites across north–western Europe (Davies et al., 2003; Pilcher et al., 2005; Lane et al., 2011b; Wulf et al., 2016; Jones et al., 2017b) (Figs. 1A and 4). The ultra-distal discovery of the Askja-S tephra, over 3000 km from volcanic source in the Southern Carpathian Mountains dramatically extends the known dispersal of fine ash (typically < 25 μm glass shards) from this Plinian eruption and, furthermore, represents the first identification of an Icelandic tephra in south-eastern Europe.

### 4.2. Chronological modelling

Owing to the occurrence of the Askja-S in both lake records, its eruption age can be subsequently refined using cross-referencing in OxCal (Bronk Ramsey, 2009a), producing an updated age of 10,889 ± 174 cal yrs BP for the deposition of this tephra within both lake records. This is within statistical agreement with the Askja-S age proposed by Bronk Ramsey et al. (2015), but contradicts the older and younger ages reported by Ott et al. (2016) and Lind and Wastegård (2011), respectively. Whilst other, younger tephras from Askja volcano have been reported (e.g. the Askja-L and Askja-H; Jóhannsdóttir, 2007, Striberger et al., 2012, Gudmundsdóttir et al., 2016), there is no evidence to date of these tephras having been identified beyond Iceland. Therefore, we presume that the divergent ages presented by Ott et al. (2016) and Lind and Wastegård (2011) are the result of problematic site chronologies, rather than the misattribution of these tephra layers.

Combining the chronological modelling of the Askja-S tephra in Lakes Brazi and Lia with the data from the other two sites, Soppensee and Hässeldala Port whose ages for the tephra are within statistical agreement with our own, improves upon the age estimate of the RESET tephra lattice by Bronk Ramsey et al. (2015, Fig. 2). The new results from the model provide a refined age of 10,824 ± 97 cal yrs BP (Fig. 2).

## 5. Future research

### 5.1. Palaeoenvironments

The discovery of an Icelandic tephra layer (Askja-S) in two palaeoenvironmental records from the Southern Carpathians provides a key tephrostratigraphic linkage between western and northern Europe with south-eastern Europe (Fig. 1). Here it is particularly important as the Askja-S tephra is chronostratigraphically positioned in the Early Holocene close to where several abrupt climatic transitions have been reported, for instance the Preboreal Oscillation (PBO, 11.5–11.4 b2k) and the '10.7 kya event' which are identified in numerous European palaeoclimate records (Björck et al., 1997; Wohlfarth et al., 2006; Lowe et al., 2015; Ott et al., 2016). However, these events remain somewhat poorly understood in terms of their environmental impacts and geographical expression (e.g. Björck et al., 1996, 1997; Wohlfarth et al., 2006). Both lakes, have undergone high-resolution, multi-proxy palaeoenvironmental investigations across this time period (e.g. Magyari et al., 2012; Buczkó et al., 2013; Tóth et al., 2015, in press; Pál et al., 2016, in press, Finsinger et al., 2014, 2016; Vincze et al., 2017). The additional identification of the Askja-S within both records, provides an ideal opportunity to investigate comparative environmental dynamics and duration of the PBO through improving chronological modelling from north-western Europe to the Southern Carpathians.

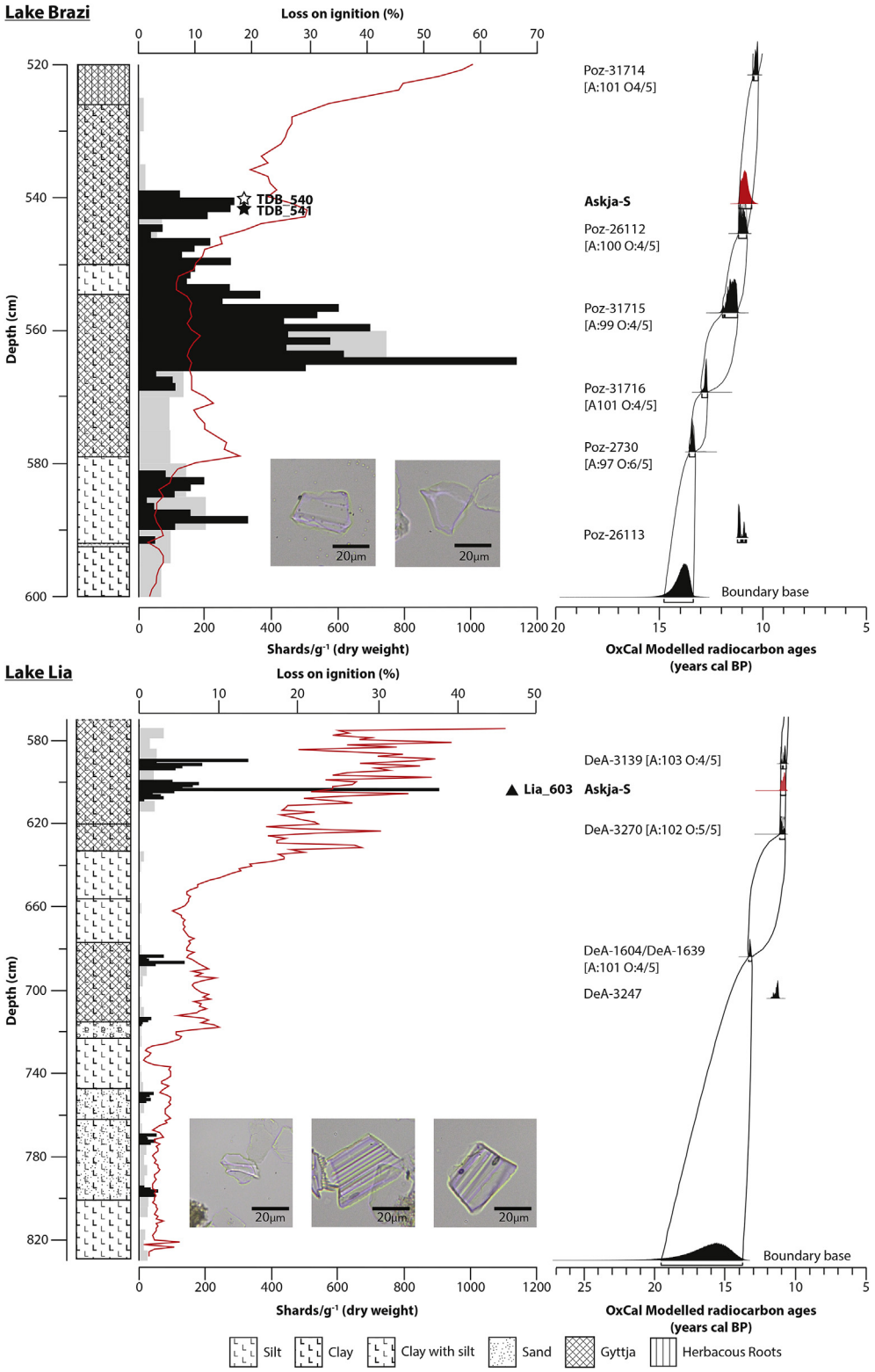


**Fig. 3.** Lithostratigraphy, loss-on-ignition, total shard concentration (from low-resolution, 5 cm contiguous scans, light grey; and from higher, 1 cm resolution scans, black) and re-modelled age-depth models for both Lake Brazi and Lake Lia focusing on the Late Glacial and Early Holocene core sections. The peaks containing the Askja-S tephra that are only discussed in this paper are highlighted. Other tephra concentration peaks will be the subject of future publications. Images of individual tephra shards from these Askja-S peaks are shown.

**Table 1**
Major element glass compositions (normalised to 100%), along with raw (non-normalised) analytical totals of individual tephra shards from Lake Brazi (TDB_540, TDB_541) and Lake Lia (LIA_603). Unnormalised data can be seen in Supplementary Material A.

| Sample | $SiO_2$ | $TiO_2$ | $Al_2O_3$ | FeOt | MnO | MgO | CaO | $Na_2O$ | $K_2O$ | $P_2O5$ | Cl | Analytical Total |
|---|---|---|---|---|---|---|---|---|---|---|---|---|
| TDB_540 | 75.35 | 0.34 | 12.37 | 2.63 | 0.16 | 0.26 | 1.73 | 4.42 | 2.61 | 0.05 | 0.08 | 95.89 |
| | 75.82 | 0.3 | 12.54 | 2.47 | 0.06 | 0.24 | 1.68 | 4.17 | 2.64 | 0.03 | 0.05 | 98.08 |
| TDB_541 | 75.93 | 0.34 | 12.23 | 2.52 | 0.12 | 0.23 | 1.53 | 4.48 | 2.54 | 0.01 | 0.07 | 97.04 |
| Mean | 75.7 | 0.33 | 12.38 | 2.54 | 0.11 | 0.24 | 1.65 | 4.36 | 2.6 | 0.03 | 0.07 | |
| SD (1σ) | 0.31 | 0.02 | 0.15 | 0.08 | 0.05 | 0.02 | 0.11 | 0.16 | 0.05 | 0.02 | 0.01 | |
| LIA_603 | 75.56 | 0.34 | 12.49 | 2.6 | 0.16 | 0.25 | 1.52 | 4.26 | 2.63 | 0.07 | 0.11 | 98.58 |
| | 75.32 | 0.29 | 12.42 | 2.61 | 0.14 | 0.27 | 1.63 | 4.63 | 2.59 | 0.04 | 0.08 | 98.48 |
| | 75.66 | 0.28 | 12.56 | 2.62 | 0.09 | 0.25 | 1.61 | 4.26 | 2.54 | 0.05 | 0.08 | 97.27 |
| | 75.53 | 0.27 | 12.41 | 2.58 | 0.05 | 0.29 | 1.72 | 4.4 | 2.59 | 0.07 | 0.09 | 99.30 |
| | 75.59 | 0.26 | 12.48 | 2.41 | 0.1 | 0.26 | 1.57 | 4.5 | 2.74 | 0.02 | 0.06 | 98.30 |
| | 75.9 | 0.29 | 12.28 | 2.79 | 0.13 | 0.24 | 1.66 | 4.09 | 2.53 | 0.01 | 0.08 | 99.94 |
| | 75.6 | 0.3 | 12.21 | 2.82 | 0.06 | 0.21 | 1.6 | 4.49 | 2.62 | 0.02 | 0.08 | 98.73 |
| | 75.63 | 0.33 | 12.36 | 2.49 | 0.16 | 0.24 | 1.58 | 4.47 | 2.61 | 0.06 | 0.07 | 99.87 |
| | 75.98 | 0.27 | 12.01 | 2.62 | 0.07 | 0.27 | 1.65 | 4.41 | 2.55 | 0.08 | 0.1 | 98.74 |
| Mean | 75.64 | 0.29 | 12.36 | 2.62 | 0.11 | 0.25 | 1.61 | 4.39 | 2.6 | 0.05 | 0.08 | |
| SD (1σ) | 0.2 | 0.03 | 0.17 | 0.13 | 0.04 | 0.02 | 0.06 | 0.16 | 0.06 | 0.03 | 0.02 | |

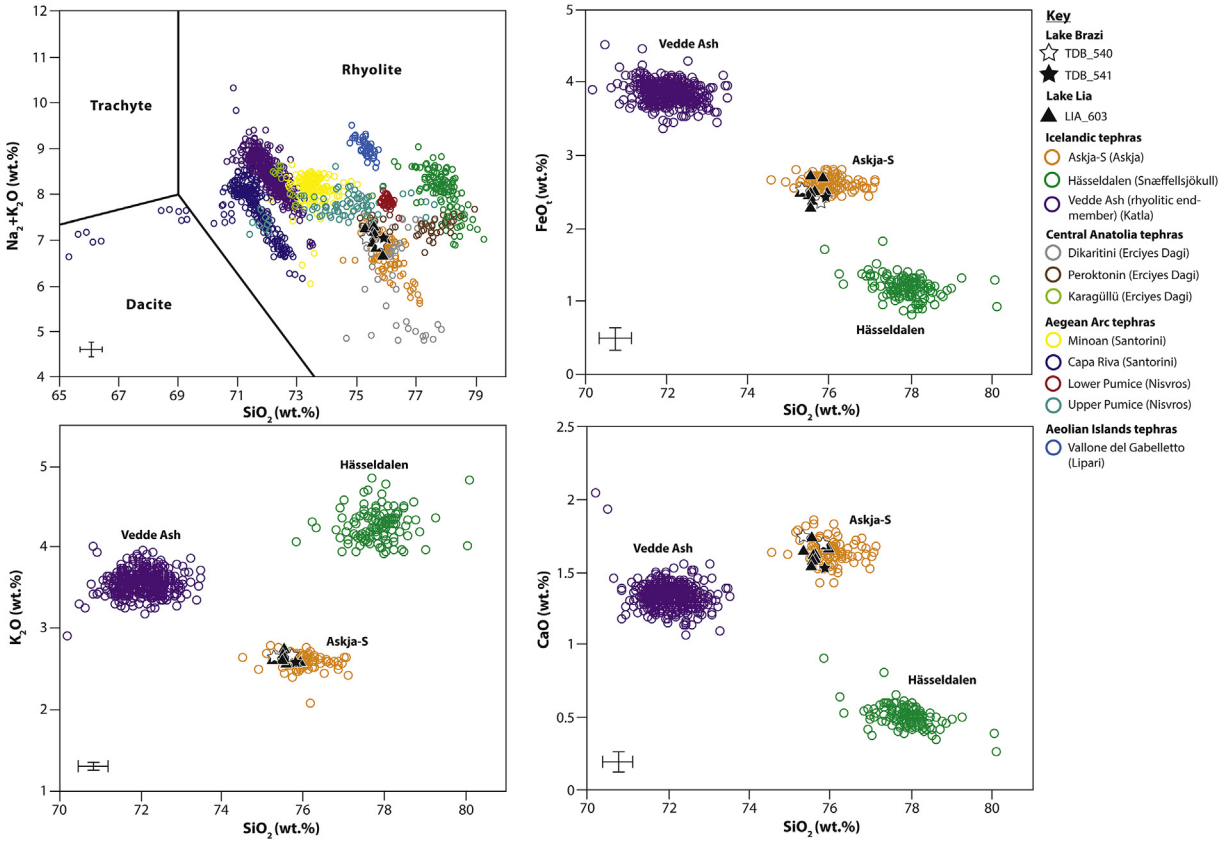


**Fig. 4.** Geochemical bi-plots of the major elemental data from Lake Brazi and Lake Lia with known rhyolitic eruptions during the Late Glacial to Early Holocene from volcanic sources close to the sites. Reference data for tephras are from Central Anatolia (Hamann et al., 2010; Cullen et al., 2014; Tomlinson et al., 2015), Aegean Arc (Eastwood et al., 1999; Kwiecien et al., 2008; Tomlinson et al., 2012, 2015; Cullen et al., 2014), Aeolian Islands (Albert et al., 2017) and Icelandic tephra (Vedde Ash: Birks et al., 1996, Wastegård et al., 1998, 2000, Turney et al., 1997, 2006, Raner et al., 2005, Pilcher et al., 2005, Davies et al., 2005, Blockley et al., 2007, Lane et al., 2011b, c, 2012a, b; Hässeldalen: Lane et al., 2012b, Housley et al., 2013, Davies et al., 2003, Lind and Wastegård, 2011, Lilja et al., 2013, Larsen and Noe-Nygaard., 2014, Wulf et al., 2016; and Askja-S: Sigvaldason, 2002, Davies et al., 2003, Turney et al., 2006, Lane et al., 2011b, Lind and Wastegård, 2011, Wulf et al., 2016, Kelly et al., 2016, Jones et al., 2017b, Lowe et al., 2017). Error bars presented are 2 standard deviations of repeat analysis of the StHs6/80-G MPI-DING standard glass.

### 5.2. Expansion of tephrostratigraphic frameworks

This finding demonstrates that the Askja-S tephra provides a powerful tephrostratigraphic marker extending from north-west Europe to south-eastern Europe. The identification of this cryptotephra horizon is not uniform across north-west European sites that have undergone detailed cryptotephra investigations, revealing a patchy distribution of this ash fall event (Jones et al., 2017a).

A number of factors could be responsible for the distal occurrences of this widespread ash dispersal from Iceland. Following an initial NNE plume dispersal off Iceland, evident in proximal

deposits (Sæmundsson, 1991; Norðdahl and Hjort, 1993; Sigvaldason, 2002), the resulting complex distribution of ash fall evidenced across Europe may have been governed by the variable/evolving concomitant weather patterns, or different atmospheric circulation at changing heights in the plume. Modern Icelandic eruptions have exhibited complicated dispersals following their initial dispersals away from Iceland, seemingly affected by these factors (e.g. Davies et al., 2010; Gudmundsson et al., 2012).

The 15 μm sieve mesh size used here was crucial to the retention and identification of the finest grain ash particles produced during this eruption (<25 μm). Routinely in cryptotephra studies, a 25 μm mesh was employed and this may also be responsible for fine grained Askja-S material not being recovered at some sites. Therefore, our findings provide encouragement for re-investigations of the temporally relevant sediments at these sites. Speculatively, the concentration of Askja-S tephra in the Lake Brazi and Lia records could have been influenced by orographic precipitation induced by the Carpathian mountain range. Additional factors such as regional bias of cryptotephra investigations (Watson et al., 2017), site-specific sedimentary taphonomic processes (Pyne-O'Donnell, 2011) and lack of continuous high-resolution cryptotephra searches (Timms et al., 2016) may all have acted to limit the currently known spatial distribution of this tephrostratigraphic marker in Europe.

Crucially, the identification of Icelandic tephra in Lake Brazi and Lake Lia, which are geographically closer to other productive volcanic regions (e.g. Italian, Aegean and Anatolian volcanoes), highlights the enormous potential of these sites for the future integration of regional tephrostratigraphic frameworks from multiple volcanic sources.

## Acknowledgements

RK is funded by the UK National Environmental Research Council (NERC; grants: NE/L002612/1) as part of the Environmental Research Doctoral Training Program at the University of Oxford. PGA and RAS are supported by Early Career Fellowships from the Leverhulme Trust (grants: ECF-2014-438 and ECF-2015-396). Drilling and palaeoenvironmental study of Lake Brazi and Lake Lia was supported by the Hungarian OTKA grant NF 101362 and GINOP-2.3.2-15-2016-00009. EU-DEM map produced using Copernicus data and information funded by the European Union – EU-DEM layers. The authors would like to thank Simon Blockley and anonymous reviewers for their comments and feedback.

## Appendix A. Supplementary data

Supplementary data related to this article can be found at https://doi.org/10.1016/j.quascirev.2018.03.035.

## References

Albert, P.G., Hardiman, M., Keller, J., Tomlinson, E.L., Smith, V.C., Bourne, A.J., Wulf, S., Zanchetta, G., Sulpizio, R., Müller, U.C., Pross, J., Ottolini, L., Matthews, I.P., Blockley, S.P.E., Menzies, M.A., 2015. Revisiting the Y-3 tephrostratigraphic marker: a new diagnostic glass geochemistry, age estimate, and details on its climatostratigraphical context. Quat. Sci. Rev. 118, 105–121.

Albert, P.G., Tomlinson, E.L., Smith, V.C., Traglia, F.D., Pistolesi, M., Morris, A., Donato, P., Rose, R.D., Sulpizio, R., Keller, J., Rosi, M., Menzies, M., 2017. Glass geochemistry of puroclatic deposits form the Aeolian Islnads in the last 50ka: a proximal database for tephrochronology. J. Volcanol. Geoth. Res. 33, 81–107.

Alley, R.B., Marotzke, J., Nordhaus, W.D., 2003. Abrupt climate change. Science 299, 2005–2010.

Birks, H.H., Guliksen, S., Haflidason, H., Mangerud, J., Possnert, G., 1996. New radiocarbon dates for the Vedde Ash and the Saksunarvatn ash from western Norway. Quat. Res.Quat. Res. 45 (2), 119–127.

Björck, S., Kromer, B., Johnsen, S., Bennike, O., Hammarlund, D., Lemdahl, G., Possnert, G., Rasmussen, T.L., Wohlfarth, B., Hammer, C.U., Spurk, M., 1996. Synchronized terrestrial Atmospheric deglacial records around the north Atlantic. Science 274, 1155–1160.

Björck, S., Rundgren, M., Ingolfsson, O., Funder, S., 1997. The Preboreal oscillation around the Nordic Seas: terrestrial and lacustrine responses. J. Quat. Sci. 12, 455–465.

Blockley, S.P.E., Donnell, S.D.F.P., Lowe, J.J., Matthews, I.P., Stone, A., Pollard, A.M., Turney, C.S.M., Molyneux, E.G., 2005. A new and less destructive laboratory procedure for the physical separation of distal glass tephra shards from sediments. Quat. Sci. Rev. 24, 1952–1960.

Blockley, S.P.E., Lane, C.S., Lotter, A.F., Pollard, A.M., 2007. Evidence for the presence fo the vedde ash in central Europe. Quat. Sci. Rev. 26 (25–28), 3030–3036.

Blockley, S.P.E., Lane, C.S., Hardiman, M., Rasumssen, S.O., Seierstad, I.K., Steffensen, J.P., Svensson, A., Lotter, A.F., Turney, C.S.M., Bronk Ramsey, C., 2012. Synchronisation of palaeoenvironmental records over the last 60,000 years, and an extended INTIMATE event stratigraphy to 48,000 b2k. Quat. Sci. Rev. 36, 2–10.

Blockley, S.P.E., Bourne, A., Brauer, A., Davies, S., Hardiman, M., Harding, P., Lane, C., MacLeod, A., Matthews, I., Pyne-O'Donnell, S., Wulf, S., Zanchetta, G., 2014. Tephrochronology and the extended INTIMATE (integration of ice-core, marine and terrestrial records) event stratigraphy 8-128ka b2k. Quat. Sci. Rev. 106, 88–100.

Brauer, A., Hajdas, I., Blockley, S.P.E., Bronk Ramsey, C., Christl, M., Ivy-Ochs, S., Moseley, G.E., Nowaczyk, N.N., Rasmussen, S.O., Roberts, H.M., Spötl, C., Staff, R.A., Svensson, A., 2014. The importance of independent chronology in integrating records of past climate change for the 60–8 ka INTIMATE time interval. Quat. Sci. Rev. 106, 47–66.

Bronk Ramsey, C., 2009a. Bayesian analysis of radiocarbon dates. Radiocarbon 51, 337–360.

Bronk Ramsey, C., 2009b. Dealing with outliers and offsets in radiocarbon dating. Radiocarbon 51 (3), 1023–1045.

Bronk Ramsey, C., Albert, P., Blockley, P., hardiman, M., Lane, C., Maclead, a., Matthews, I.P., Muscheler, R., Palmer, A., Staff, R.A., 2014. Integrating timescales with time-transfer functions: a practical approach for an INTIMATE database. Quat. Sci. Rev. 106, 67–80.

Bronk Ramsey, C., 2017. OxCal project, Version 4.3. Retrieved April 2017. https://c14.arch.ox.ac.uk/oxcal/OxCal.html.

Bronk Ramsey, C., Lee, S., 2013. Recent and planned developments of the program OxCal. Radiocarbon 55, 3–4.

Bronk Ramsey, C., Albert, P.G., Blockley, S.P.E., Hardiman, M., Housley, R.A., Lane, C.S., Lee, S., Matthews, I.P., Smith, V.C., Lowe, J.J., 2015. Improved age estimates for key Late Quaternary European tephra horizons in the RESET lattice. Quat. Sci. Rev. 118, 18–32.

Buczkó, K., Magyari, E.K., Braun, M., Bálint, M., 2013. Diatom-inferred lateglacial and Holocene climatic variability in the south carpathian mountains (Romania). Quat. Int. 293, 123–135.

Cullen, V.L., Smith, V.C., Arz, H.W., 2014. The detailed tephrostratigraphy of a core from the south-east Black Sea spanning the last ~60ka. J. Quat. Sci. 29 (7), 675–690.

Davies, S.M., Wastegård, S., Wohlfarth, B., 2003. Extending the limits of the Borrobol Tephra to Scandinavia and detection of new early Holocene tephras. Quat. Res. 59, 345–352.

Davies, S.M., Hoek, W.Z., Bohncke, S.J.P., Lowe, J.J., O'Donnell, S.P., Turney, C.S.M., 2005. Detection of Lateglacial distal tephra layers in The Netherlands. Boreas 34 (2), 123–135.

Davies, S.M., Larsen, G., Wastegård, S., Turney, C.S., Hall, V.A., Coyle, L., Thordarson, T., 2010. Widespread dispersal of Icelandic tephra: how does the Eyjafjöll eruption of 2010 compare to past Icelandic events? J. Quat. Sci. 25 (5), 605–611.

Eastwood, W.J., Pearce, N.J.G., Westgate, J.A., Perkins, W.T., Lamb, H.F., Roberts, N., 1999. Geochemistry of Santorini tephra in lake sediments from southwest Turkey. Global Planet. Change 21, 1–3, 17-29.

Finsinger, W., Kelly, R., Fevre, J., Magyari, E.K., 2014. A guide to screening charcoal peaks in macrocharcoal-area records for fire-episode reconstructions. Holocene 24, 1002–1008.

Finsinger, W., Fevre, J., Orbán, I., Pál, I., Vincze, I., Hubay, K., Birks, H.H., Braun, M., Tóth, M., Magyari, E.K., 2016. Holocene fire-regime changes near the treeline in the Retezat mts. (southern Carpathians, Romania). Quat. Int. https://doi.org/10.1016/j.quaint.2016.04.029.

Gudmundsdóttir, E.R., Eiríksson, J., Larsen, G., 2011. Identification and definition of primary and reworked tephra in Late Glacial and Holocene marine shelf sediments off North Iceland. J. Quat. Sci. 26 (6), 589–602.

Gudmundsdóttir, E.R., Larsen, G., Björck, S., Ingólfsson, Ó., Striberger, J., 2016. A new high-resolution Holocene tephra stratigraphy in eastern Iceland: improving the Icelandic and North Atlantic tephrochronology. Quat. Sci. Rev. 150, 234–249.

Gudmundsson, M.T., Thordarson, T., Höskuldsson, Larsen, G., Björnsson, H., Prata, F.J., Oddsson, B., Magnússin, E., Högnadóttir, Petersen, G.N., Hayward, C.L., Stevenson, J.A., Jónsdóttir, I., 2012. Ash generation and distribution from the April-May 2010 eruption of Eyjafjallajökull, Iceland. Sci. Rep. 2 (572), 1–12.

Haliuc, A., Veres, D., Brauer, A., Hubay, K., Hutchinson, S.M., Begy, R., Braun, M., 2017. Palaeohydrological changes during the mid and late Holocene in the Carpathian area, central-eastern Europe. Global Planet. Change 152, 99–114.

Hamann, Y., Wulf, S., Ersoy, O., Ehrmann, W., Aydar, E., Schmiedl, G., 2010. First evidence of a distal Early Holocene ash layer in eastern Mediterranean deep-sea sediments derived from the Anatolian volcanic province. Quat. Res. 73, 497–506.

Housley, R., MacLeod, A., Nalepka, D., Jurochnik, A., Masojc, M., Davies, L., Lincoln, P.,

Bronk Ramsey, C., Gamble, C.S., Lowe, J.J., 2013. Teprostratigraphy of a Late-glacial lake sediment sequence at Węgliny, southwest Poland. Quat. Sci. Rev. 77, 4–18.

Hubay, K., Molnár, M., Orbán, I., Braun, M., Biro, T., Magyari, E., 2016. Age-depth relationship and accumulation rates in four sediment sequences from the Retezat Mts, South Carpathians (Romania). Quat. Int. 1–12 in press. https://doi.org/10.1016/j.quaint.2016.09.019.

Jensen, B.J.L., Pyne-O'Donnell, S., Plunkett, G., Froese, D.G., Hughes, P.D.M., Sigi, M., McConnell, J.R., Amesbury, M.J., Blackwell, P.G., van den Bogaard, C., Buck, C.E., Charman, D.J., Clague, J.J., Hall, V.A., Koch, J., Mackay, H., Mallon, G., McColl, L., Pilcher, J.R., 2014. Transatlantic distribution of the alaskan white river ash. Geology 42 (10), 875–878.

Jochum, K.P., Stoll, B., Herwig, K., Willbold, M., Hofmann, A.W., Amini, M., et al., 2006. MPI-DING reference glasses for in situ microanalysis: new reference values for element concentrations and isotope ratios. G-cubed 7, 2.

Jóhannsdóttir, G., 2007. Mid Holocene to Late Glacial Tephrochronology in West Iceland as Revealed in Three Lacustrine Environments. MS Thesis in Geology. University of Iceland.

Jones, G., Davies, S.M., Farr, G., Bevan, J., 2017a. Identification of the Askja-S tephra in a rare turlough record from Pant-y-Llyn, South Wales. Proc. Geol. Assoc. 605, 1–9.

Jones, G., Lane, C.S., Brauer, A., Davies, S.M., de Brujin, R., Engels, S., Haliuc, A., Hoek, W.Z., Merkt, J., Sachse, D., Turner, F., Wagner-Cremer, F., 2017b. The Lateglacial to early Holocene tephrochronological record from Lake Hämerlsee, Germany: a key site within the European tephra framework. Boreas. https://doi.org/10.1111/bor.12250 in press.

Karátson, D., Wulf, S., Veres, D., Magyari, E.K., Gertisser, R., Timar-Gabor, A., Novothny, A., Telbisz, T., Szalai, Z., Anechitei-Deacu, V., Appelt, O., Bormann, M., Janosi, C., Hubay, K., Schaebitz, F., 2016. The latest explosive eruptions of Ciomadul (Csomad) volcano, East Carpathians - a tephrostratigraphic approach for the 51-29 ka BP time interval. J. Volcanol. Geoth. Res. 319, 29–51.

Kelly, T.J., Hardiman, M., Lovelady, M., Lowe, J.J., Matthews, I.P., Blockley, S.P.E., 2016. Scottish early Holocene vegetation dynamics based on pollen and tephra records from Inverlair and Loch Etteridge, Inverness-shire. Proc. Geol. Assoc. 128, 125–135.

Kwiecien, O., Arz, H.W., Lamy, F., Wulf, S., Bahr, A., Rohl, U., Haug, G.H., 2008. Estimated reservoir age of the black sea since the last glacial. Radiocarbon 50, 99–118.

Kylander, M.E., Lind, E.M., Wastegård, S., Löwemark, L., 2012. Recommendations for using XRF core scanning as a tool in tephrochronology. Holocene 22, 371–375.

Lane, C.S., Brauer, A., Blockley, S.P.E., Dulski, P., 2013. Volcanic ash reveals time-transgressive abrupt climate change during the younger dryas. Geology 41 (12), 1251–1254.

Lane, C.S., Andrič, M., Cullen, V.L., Blockley, S.P.E., 2011a. The occurrence of distal Icelandic and Italian tephra in the Lateglacial of Lake Bled, Slovenia. Quat. Sci. Rev. 30, 1013–1018.

Lane, C.S., Blockley, S.P.E., Bronk Ramsey, C., Lotter, A.F., 2011b. Tephrochronology and absolute centennial scale synchronisation of European and Greenland records for the last glacial to interglacial transition: a case study of Soppensee and NGRIP. Quat. Int. 246, 145–156.

Lane, C.S., Blockley, S.P.E., Lotter, A.F., Finsinger, W., Filippi, M.L., Matthews, I.P., 2011c. A regional tephrostratigraphic framework for central and southern European climate archives during the Last Glacial to Interglacial transition: comparisons north and south of the Alps. Quat. Sci. Rev. 36, 50–58.

Lane, C.S., De Klerk, P., Cullen, V.L., 2012a. A tephrochronology for the Lateglacial palynological record of the Endinger Bruch (Vorpommern, north-east Germany). J. Quat. Sci. 27, 141–149.

Lane, C.S., Blockely, S.P.E., Mangerud, J., Smith, V.C., Lohne, Ø.S., Tomlindon, E.L., Matthews, I.P., Lotter, A.F., 2012b. Was the 12.1ka Iceland vedde ash one of a kind? Quat. Sci. Rev. 33, 87–99.

Lane, C.S., Cullen, V.L., White, D., Bramham-Law, C.W.F., Smith, V.C., 2014. Cryptotephra as a dating and correlation tool in archaeology. J. Archaeol. Sci. 42, 42–50.

Larsen, J.J., 2013. Lateglacial and Holocene tephrostratigraphy in Denmark Volcanic Ash in a Palaeoenvironmental Context. Unpublished PhD Thesis. University of Copenhagen.

Larsen, J.J., Noe-Nygaard, N., 2014. Lateglacial and early Holocene tephrostratigraphy and sedimentology of the Store Slotsenf basin, SW Denmark: a multi-proxy study. Boreas 43, 349–361.

Lilja, C., Lind, E.M., Morén, B., Wastegård, S., 2013. A Lateglacial–early Holocene tephrochronology for SW Sweden. Boreas 42, 544–554.

Lind, E.M., Wastegård, S., 2011. Tephra horizons contemporary with short early Holocene climate fluctuations: new results from the Faroe Islands. Quat. Int. 246, 157–167.

Longman, J., Ersek, V., Veres, D., Salzmann, U., 2017a. Detrital events and hydroclimate variability in the Romanian Carpathians during the mid-to-late Holocene. Quat. Sci. Rev. 167, 78–95.

Longman, J., Veres, D., Ersek, V., Salzmann, U., Hubay, K., Bormann, M., Wennrich, V., Schäbitz, F., 2017b. Periodic input of dust over the Eastern Carpathians during the Holocene linked with Saharan desertification and human impact. Clim. Past 13, 897–917.

Lowe, D.J., 2011. Tephrochronology and its application: a review. Quat. Geochronol. 6, 107–153.

Lowe, J.J., Ramsey, C.B., Housley, R.A., Lane, C.S., Tomlinson, E.L., 2015. The RESET project: constructing a European tephra lattice for refined synchronisation of environmental and archaeological events during the last c. 100 ka. Quat. Sci. Rev. 118, 1–17.

Lowe, J.J., Palmer, A.P., Carter-Champion, A., MacLeod, A., Ramirez-Rojas, I., Timms, R.G.O., 2017. Stratigraphy of a lateglacial lake basin sediment sequence at Turret Bank, upper glen roy, Lochaber: implications for the age of the Turret fan. Proc. Geol. Assoc. 128, 110–124.

MacLeod, A., Brunnberg, L., Wastegård, S., Hand, T., Matthews, I.P., 2014. Lateglacial cryptotephra detected within clay varves in Östergötland, south-east Sweden. J. Quat. Sci. 29, 605–609.

Magyari, E.K., Braun, M., Buczkó, K., Kern, Z., László, P., Hubay, K., 2009. Radiocarbon chronology of glacial lake sediments in the Retezat Mts (South Carpathians, Romania): a window to Late Glacial and Holocene climatic and palaeoenvironmental changes. Central European Geology 52, 225–248.

Magyari, E.K., Jakab, G., Bálint, M., Kern, Z., Buczkó, K., Braun, M., 2012. Rapid vegetation response to lateglacial and early Holocene climatic fluctuation in the south carpathian mountains (Romania). Quat. Sci. Rev. 35, 116–130.

Moreno, A., Svensson, A., Brooks, S.J., Connor, S., Engels, S., Fletcher, W., Genty, D., Heiri, O., Labuhn, I., Persoiu, A., Peyron, O., Sadori, L., Valero-Garcés, B., Wulf, S., Zanchetta, G., 2014. A compilation of Western European terrestrial records 60–8 ka BP: towards an understanding of latitudinal climatic gradients. Quat. Sci. Rev. 106, 167–185.

Newhall, C.G., Self, S., 1982. The volcanic explosivity index (VEI) an estimate of explosive magnitude for historical volcanism. J. Geophys. Res. 87, 1231–1238.

Norðdahl, H., Hjort, C., 1993. Lateglacial raised beaches and glacier recession in the PistilfjörÐur-Bakkaflói area, Northeast Iceland. Jokull 43, 33–44.

Obreht, I., Hambach, U., Veres, D., Zeeden, C., Bösken, J., Stevens, T., Marković, S.B., Klasen, N., Brill, D., Burow, C., Lehmkuhl, F., 2017. Shift of large-scale atmospheric systems over Europe during late MIS 3 and implications for Modern Human dispersal. Sci. Rep. 7 (5848), 1–10.

Orbán, I., Birks, H.H., Vincze, I., Finsinger, W., Pál, I., Marinova, E., Jakab, G., Braun, M., Hubay, K., Bíró, T., Magyari, E.K., 2017. Treeline and timber- line dynamics on the northern and southern slopes of the Retezat Mountains (Romania) during the Late-Glacial and the Holocene. Quat. Int. https://doi.org/10.1016/j.quaint.2017.03.012. In press.

Ott, F., Wulf, S., Serb, J., Słowin ski, M., Obremska, M., Tjallingii, R., Błaszkiewicz, M., Brauer, A., 2016. Constraining the time span between the Early Holocene Hasseldalen and Askja-S Tephras through varve counting in the Lake Czechowskie sediment record, Poland. J. Quat. Sci. 31, 103–113.

Pál, I., Magyari, E.K., Braun, M., Vincze, I., Pálfy, J., Molnár, M., Finsinger, W., Buczko, K., 2016. Small-scale moisture availability increase during the 8.2-ka climatic event inferred from biotic proxy records in the South Carpathians (SE Romania). Holocene 26 (9), 1382–1396.

Pál, I., Buczkó, K., Vincze, I., Finsinger, W., Braun, M., Biró, T., Magyari, E., 2018. Terrestrial and aquatic ecosystem responses to early Holocene rapid climate change (RCC) events in the South Carpathian Mountains, Romania. Quat. Int. in press https://doi.org/10.1016/j.quaint.2016.11.015.

Pilcher, J., Bradley, R.S., Francus, P., Anderson, L., 2005. A Holocene tephra record from the Lofoten Islands, arctic Norway. Boreas 34, 136–156.

Pyne-O'Donnell, S., 2011. The taphonomy of Last Glacial-Interglacial Transition (LGIT) distal volcanic ash in small Scottish lakes. Boreas 40, 131–145.

Raner, P.H., Allen, J.R., Huntley, B., 2005. A new early Holocene cryptotephra from northwest Scotland. Journal of Quaternary Science 20 (3), 201–208.

Reimer, P.J., Bard, E., Bayliss, A., Beck, J.W., Blackwell, P.G., Bronk Ramsey, C., Buck, C.E., Cheng, H., Edwards, L.R., Friedrich, M., Grootes, P.M., Guilderson, T.P., Haflidason, H., Hajdas, I., Hatte, C., Heaton, T.J., Hoffmann, D.L., Hogg, A.G., Hughen, K.A., Kaiser, K.F., Kromer, B., Manning, S.W., Niu, M., Reimer, R.W., Richards, D.A., Scott, E.M., Southon, J.R., Staff, R.A., Turney, C.S.M., van der Plicht, J., 2013. IntCal13 and Marine13 radiocarbon age calibration curves 0-50,000 years cal BP. Radiocarbon 55, 1869–1887.

Sigvaldason, G.E., 2002. Volcanic and tectonic processes coinciding with glaciation and crustal rebound: an early Holocene rhyolitic eruption in the Dyngjufjöll volcanic centre and the formation of the Askja caldera, north Iceland. Bull. Volcanol. 64, 192–205.

Steffensen, J.P., Andersen, K.K., Bigler, M., Clausen, H.B., Dahl-Jensen, D., Fischer, H., Gotoazuma, K., Hansson, M., Johnsen, S.J., Jouzel, J., Masson-delmotte, V., Popp, T., Rasmussen, S.O., Röthlisberger, R., Ruth, U., Stauffer, B., Sveinbjörnsdóttir, Á.E., Svensson, A., White, J.W.C., 2008. High-resolution Greenland ice core data show abrupt climate change happens in years. Science 321 (5889), 680–684.

Striberger, J., Björck, S., Holmgren, S., Hamerlík, L., 2012. The sediments of Lake Lögurinn—a unique proxy record of Holocene glacial meltwater variability in eastern Iceland. Quat. Sci. Rev. 38, 76–88.

Sæmundsson, K., 1991. The geology of the krafla system (jarðfraeði kröflukerfisins). In: Garðarsson, A., Einarsson, A. (Eds.), Náttúra My vatns. Hið íslenska náttúrufraeðifélag, Reykjavík, pp. 25–95.

Timms, R.G.O., Matthews, I.P., Palmer, A.P., Candy, I., Abel, L., 2016. A high-resolution tephrostratigraphy from Quoyloo Meadow, Orkney, scotland: implications for the tephrostratigraphy of nw Europe during the last glacial-interglacial transition. Quat. Geochronol.

Tomlinson, E.L., Arienzo, I., Civetta, L., Wulf, S., Smith, V.C., Hardiman, M., Lane, C.S., Carandenta, A., Orsi, G., Rosi, M., Muller, W., Menzies, M.A., 2012. Geochemistry of the Phlegraean Fields (Italy) proximal sources for major Mediterranean tephras: implications for the dispersal of Plinian and co-ignimbritic components of explosive eruptions. Geochem. Cosmochim. Acta 93, 102–128.

Tomlinson, E.L., Smith, V.C., Albert, P.G., Aydar, E., Civetta, L., Cioni, R., Çubukçu, E.,

Gertisser, R., Isaia, R., Menzies, M.A., Orsi, G., Rosi, M., Zanchetta, G., 2015. The major and trace element glass composition of the productive Mediterranean volcanic sources: tools for correlating distal tephra layers in and around Europe. Quat. Sci. Rev. 118, 48–66.

Tóth, M., Magyari, K., Brooks, S.J., Braun, M., Buczkó, K., Bálint, M., Heiri, O., 2015. A chironomid-based reconstruction of late glacial summer temperatures in the southern Carpathians (Romania). Quaternary Res. 77, 122–131.

Tóth, M., Buczkó, K., Specziár, A., Heiri, O., Braun, M., Hubay, K., Czakó, D., Magyari, E., 2018. Limnological changes in south carpathian glacier-formed lakes (Retezat mEstimated reserviour age of the black sea since the last glacialountains, Romania) during the late glacial and the Holocene: a synthesis. iInt. in press https://doi.org/10.1016/j.quaint.2017.05.023.

Turney, C.S.M., Harkness, D.D., Lowe, J.J., 1997. The use of microtephra horizons to correlate late-glacial lake sediment successions in Scotland. Journal of Quaternary Science 12 (6), 525–531.

Turney, C.S.M., 1998. Extraction of rhyolitic component of Vedde microtephra from minerogenic lake sediments. J. Paleolimnol. 19, 199–206.

Turney, C.S.M., Van Den Burg, K., Wastegård, S., Davies, S.M., Whitehouse, N.J., Pilcher, J.R., Callaghan, C., 2006. North European last glacial-interglacial transition (LGIT; 15-9 ka) tephrochronology: extended limits and new events. J. Quat. Sci. 21, 335–345.

van der Bilt, W.G.M., Lane, C.S., Bakke, J., 2017. Ultra-distal Kamchatkan ash on Artic Svalbard: towards hemispheric cryptotephra correlation. Quat. Sci. Rev. 164, 230–235.

Veres, D., Lane, C.S., Timar-Gabor, A., Hambach, U., Constantin, D., Szakács, A., Fülling, A., Onac, B.P., 2013. The Campanian Ignimbrite/Y5 tephra layer – a regional stratigraphic marker for Isotope Stage 3 deposits in the Lower Danube region, Romania. Quat. Int. 293, 22–33.

Vincze, I., Orbán, I., Birks, H.H., Pál, I., Finsinger, W., Hubay, K., Marinova, E., Jakab, G., Braun, M., Biró, T., Tóth, M., Danau, C., Ferencz, I.V., Magyari, E.K., 2017. Holocene treeline and timberline changes in the South Carpathians (Romania): climatic and anthropogenic drivers on the southern slopes of the Retezat Mountains. Holocene in press. https://doi.org/10.1177/0959683617702227.

Wastegård, S., Björch, S., Possner, G., Wohlfarth, B., 1998. Evidence for the occurrence of Vedde Ash in Sweden: radiocarbon and calendar age estimates. J. Quat. Sci. 13 (3), 271–274.

Wastegård, S., Wohlfarth, B., Subetto, D.A., Sapelko, T.V., 2000. Extending the known distribution of the younger Dryas vedde ash into northwestern Russia. J. Quat. Sci. 15 (6), 581–586.

Watson, E.J., Swindles, G.T., Lawson, I.T., Savov, I.P., Wastegård, S., 2017. The presence of Holocene cryptotephra in Wales and southern England. J. Quat. Sci. 32, 493–500.

Wohlfarth, B., Blaauw, M., Davies, S.M., Andersson, M., Wastegård, S., Hormes, A., Possnert, G., 2006. Constraining the age of Lateglacial and early Holocene pollen zones and tephra horizons in southern Sweden with Bayesian probability methods. J. Quat. Sci. 21, 321–334.

Wulf, S., Dräger, N., Ott, F., Serb, J., Appelt, O., GuÐmundsdóttir, E., van den Bogaard, C., Słowin ski, M., Błaszkiewicz, M., Brauer, A., 2016. Holocene tephrostratigraphy of varved sediment records from Lakes Tiefer See (NE Germany) and Czechowskie (N Poland). Quat. Sci. Rev. 132, 1–14.